2024

Novel Strategies for early detection of Neurodegenerative Diseases

Andreia Forte

Dissertation presented to obtain the **Ph.D degree in**

Sustainable Chemistry

Oeiras, April, 2024

INSTITUTO DE TECNOLOGIA QUÍMICA E BIOLÓGICA ANTÓNIO XAVIER | UNIVERSIDADE NOVA DE LISBOA

Novel Strategies for early detection of Neurodegenerative Diseases

Andreia Sofia de Almeida Baptista Forte

Dissertation presented to obtain the Ph.D degree in Sustainable Chemistry

Instituto de Tecnologia Química e Biológica António Xavier | Universidade Nova de Lisboa

Oeiras, April, 2024

Title

Novel Strategies for early detection of Neurodegenerative Diseases

Dissertation presented to obtain the Ph.D degree in Sustainable Chemistry

Author

Andreia Sofia de Almeida Baptista Forte

Separation and Extraction Technologies Laboratory
Instituto de Tecnologia Química e Biológica António Xavier
Universidade Nova de Lisboa
Av. da República Estação Agronómica Nacional
2780-157 Oeiras
Portugal

April, 2024

I declare that the work presented in this thesis, except where otherwise stated, is based on my own research. The work was mainly performed in Cultural Heritage and Responsive Materials (CHARM) from LAQV-REQUIMTE of Nova School of Science and Technology (FCT-NOVA) and Separation and Extraction Technologies Laboratory of the Instituto de Tecnologia Química e Biológica António Xavier (ITQB-NOVA) between March 2015 and July 2021 and supervised by Professor Doctor Isabel Marrucho (ITQB-NOVA and IST-UL) and Professor Doctor Luís C. Branco (LAQV-REQUIMTE; FCT-NOVA). Financial support was provided by Fundação para a Ciência e a Tecnologia through the doctoral fellowship PD/BD/109625/2015.

Ao meu Pai, ao meu "chato"…

A dor de perdermos alguém que amamos vem, inevitavelmente, acompanhada de uma sensação de vazio e de uma saudade imensa. Esse sentimento irá acompanhar-me para sempre e terei, ao longo da vida, de aprender a viver com ele…Porque não se trata de não sentir a tua falta, trata-se de aprender a viver com a tua ausência física. As nossas memórias, essas…ficarão para sempre comigo!

Tenho a certeza de que, estejas onde estiveres, estarás sempre ao meu lado!

Obrigada por tudo!

"What we once enjoyed and deeply loved we can never lose, For all that we love deeply becomes a part of us"

Helen Keller

Acknowledgements

Primeiro que tudo, gostaria de agradecer aos meus orientadores, a Professora Doutora Isabel Marrucho e o Professor Doutor Luís Branco, pelos conhecimentos, pela disponibilidade, pelo apoio, pela compreensão e pela paciência que muitas vezes sei que foi necessária durante o longo caminho que percorremos juntos.

Gostaria de agradecer ao Professor César Laia pela disponibilidade, pelo apoio e pelos conhecimentos transmitidos durante esta etapa.

Quero também agradecer á Doutora Marta Corvo pela ajuda e conhecimentos transmitidos ao longo do trabalho. Obrigada pela enorme paciência, disponibilidade e simpatia que sempre demonstrou para comigo.

Á Doutora Clara Gomes pela sua ajuda, simpatia e disponibilidade que teve sempre para comigo.

Á Doutora Sandra Gago…ficaria bem dizer assim, mas tu és mais do que isso, és mais do que uma pessoa que me ensinou muito no trabalho. Por isso, á minha Sandra, …o que dizer?! Obrigada por tudo! Não só me ensinaste no laboratório, como me transmitiste valores que para mim são essenciais na vida. Fomos devagarinho construindo uma bonita história de amizade e de aprendizagem. Acho que temos crescido muito juntas e espero que assim continue pela vida fora. Obrigada por todas as vezes em que, pacientemente, me ouviste e ajudaste!

Aos meus pais, pelo apoio que sempre me deram, pelas oportunidades que me proporcionaram, pela força que sempre demonstraram e me transmitiram e pela vossa fé em mim! Quero principalmente agradecer-vos pelo amor que sempre me deram, pelos valores que me transmitiram e por nunca me falharem num abraço sentido e numa palavra de carinho necessária. Vocês foram e são o meu pilar e o meu grande exemplo!

Ao meu eterno menino grande, ao meu Pedro, agradeço pelo teu amor, pela tua paciência e compreensão e por nunca desistires de mim, de nós! 21 anos depois, continuamos juntos a enfrentar e aproveitar o que a vida tem para nos dar. Só nós sabemos o que temos passado e ultrapassado juntos. Quantas vezes nos perdemos na correria da vida, mas também temos sabido reencontrar-nos. Que assim continue até deixarmos de existir. Que

continuemos a errar e a acertar juntos. Obrigada por não me deixares desistir nunca, nesta e em outras fases da nossa vida, e por toda a caminhada que temos feito lado a lado. Obrigada por me teres dado a minha maior bênção!

Ao meu maior amor, obrigada por me teres escolhido para tua mãe! Não imaginas o orgulho que tenho em ti. Todos os dias vences probabilidades, superas expectativas e mostras a todos (incluindo a mim) do que é feito um guerreiro! És a minha maior obra de arte, és perfeitinho exatamente como és, mas principalmente, és um pequeno grande ser humano! Os teus abraços são os melhores do mundo, o teu sorriso ilumina os meus dias e tudo o que pudesse dizer ou escrever seria sempre pouco para explicar o infinito amor que sinto por ti! Ensinas-me todos os dias a ser mãe e melhor pessoa!

"Se houver um amanhã em que não estejamos juntos, há algo de que te deves lembrar sempre: Tu és mais corajoso do que acreditas, mais forte do que pareces e mais inteligente do que os outros pensam. Mas o mais importante é que mesmo que um dia estejamos separados … Eu vou estar sempre contigo. "

Winnie the Pooh

(sim, porque nos desenhos e com as crianças também se aprende muito sobre a vida!)

Á minha Ana (tri-mamã), minha amiga, minha ouvinte,Obrigada pelas horas que pacientemente me ouviste, pelo ombro sempre disponível, por todas as vezes em que me chamaste a atenção e me ensinaste. Obrigada pelos nossos almoços e gargalhadas dos quais tenho imensas saudades. Tornaste todos os meus dias melhores, tornaste-me a mim melhor também…obrigada por tudo isso!

Aos meus colegas do grupo CHARM (os presentes e o que por lá foram passando), pela disponibilidade, pelos bons momentos que me proporcionaram e, principalmente, pelo carinho que sempre demonstraram para comigo. Todos, de diferentes formas, me acrescentaram algo que ficará certamente para a vida. Em especial queria agradecer á Karolina e ao Miguel pelo vosso apoio, amizade e pelos abracinhos cheios de força. Ao Artur e ao André pela vossa ajuda, disponibilidade e paciência para me aturar

sempre que vos ia chatear fosse por que motivo fosse. Á Ana Lúcia e ao Mani por me acompanharem neste caminho, quer no laboratório quer fora dele. Obrigada aos dois pela amizade que construímos e pela vossa enorme paciência. Á Noemi e ao Hugo pela preocupação, pelas longas conversas e pelo apoio que sempre tiveram para comigo. Obrigada a todos pelo vosso carinho, disponibilidade, paciência e compreensão!

Gostaria também de agradecer á minha Ana Marta, á Letícia e ao Luís Cabrita, pessoas que embora não estejam presentes todos os dias, sempre me apoiaram. Nunca me esqueço das coisas que me foram ensinando ao longo dos anos. Às vezes pode parecer que não ouvi, posso ter de cair primeiro, mas nunca me esqueço do que me ensinaram e disseram nos momentos em que precisei de vos ouvir. Minha Ana Marta, tu sabes o quanto te adoro e o que significas para mim!

Á minha Claudiiiiiinha (com aquela entoação que tu sabes!), pelas longas conversas, boa energia, pelos valores que sempre me transmitiste e pelas gargalhadas (anexadas a algum disparate que dizíamos…ou eu). Não teria sido o mesmo sem ti!

Aos meus amigos em geral (os já mencionados, mas também os que, não fazendo parte deste mundo da investigação, sempre estiveram comigo ao longo da vida) pela vossa força, capacidade de compreensão pela falta de tempo e ausências da minha parte e pela vossa capacidade de tornarem os nossos encontros em momentos de descontração e descompressão. Obrigada por me acompanharem nesta e em todas as fases da minha vida.

Por fim, queria agradecer á D. Idalina, á D. Conceição e á Isabel Rodrigues pela compreensão e por tanto me aturarem com os meus imensos pedidos.

Não termino sem pedir desculpa se, eventualmente, me esqueci de alguém. Não foi certamente por não ser importante, mas porque esta parte é, honestamente, muito difícil para mim. É difícil exprimir o quanto agradeço a todos os que passaram na minha vida e o que me deixaram. Obrigada a todos!

"Aqueles que passam por nós, não vão sós, não nos deixam sós. Deixam um pouco de si, levam um pouco de nós"

(Antoine de Saint-Exupéry)

Members of the Jury

President

Doutora Inês Antunes Cardoso Pereira, Professora Catedrática do Instituto de Tecnologia Química e Biológica António Xavier da Universidade NOVA de Lisboa, Portugal, por delegação.

Thesis Supervisors

Prof. Dr. Isabel Maria Delgado Jana Marrucho Ferreira, Associate Professor with Habilitation at Instituto Superior Técnico, Universidade de Lisboa, Portugal; Researcher at Instituto de Tecnologia Química e Biológica António Xavier, Universidade Nova de Lisboa, Portugal (supervisor).

Prof. Dr. Luís Alexandre Almeida Fernandes Cobra Branco, Principal Researcher at Departamento de Química, Faculdade de Ciências e Tecnologia, Universidade Nova de Lisboa, Portugal (co-supervisor).

Thesis Examiners

Doutor Carlos Alberto Mateus Afonso, Professor Catedrático na Faculdade de Farmácia da Universidade de Lisboa, Portugal.

Doutora Ana Maria Antunes Dias, Investigadora Auxiliar na Faculdade de Engenharia Química da Universidade de Coimbra, Portugal.

Doutor José Manuel Silva Simões Esperança, Investigador Principal na Faculdade de Ciências e Tecnologia da Universidade NOVA de Lisboa, Portugal.

Doutora Marta Cristina Parracho Cançado Corvo, Investigadora Auxiliar na Faculdade de Ciências e Tecnologia da Universidade NOVA de Lisboa, Portugal.

CONTENTS

Novel Strategies for early detection of Neurodegenerative Diseases

ABSTRACT

Neurodegenerative diseases are incurable and highly incapacitating diseases characterized by the progressive degeneration and death of neural tissues. According to World Health Organization, it is estimated that almost 50 million people have dementia worldwide and it is expected that this number triple by 2050. One of the main problems associated with this type of pathologies, is the late stage of detection implying a less effective treatment options. In this context, Magnetic resonance imaging (MRI) has gained greater attention in the most recent years. Several studies have been carried out to find new molecules with the ability to increase the contrast between tissues allowing a more accurate and early diagnosis of these diseases. Also, new molecules have been designed over the years to find new compounds that could elucidate β-amyloid aggregation through luminescent methodologies. The main goals of this thesis are focused on the development of new magnetic organic salts with potential application as MRI contrast agents. Biocompatible magnetic and luminescent Ionic Liquids (ILs) or organic salts based on the combination between choline derivative cations and Mn(II), Gd(III) or Tb(III) anion complexes were prepared. Some selected analogues of these compounds were functionalized in Mesoporous Silica Nanoparticles (MSNs) to evaluate the impact of this immobilization in their toxicity profile. Magnetic salts and MSN materials were characterized by spectroscopy (NMR, FTIR, UV-Vis, Emission); elemental analysis; ICP-MS; magnetic susceptibility; thermal properties; and about their toxicity. Finally, relaxation studies were performed to evaluate their applicability as contrast agents for MRI technique. In parallel, new ionic fluorescent probes based on Thioflavin T and Congo Red were prepared. These new materials were characterized by spectroscopy (NMR, FTIR); elemental analysis; and about

their thermal properties. Specifically, for ThT salts, UV-Vis and Emission studies were carried out and birefringence studies for Congo Red salts.

It is expected to explore in the future some of the prepared magnetic and luminescent salts for application as efficient and non-toxic MRI contrast agents.

RESUMO

As doenças neurodegenerativas são doenças incuráveis e altamente incapacitantes que são normalmente caracterizadas pela progressiva degeneração e consequente morte dos tecidos neurais. Segundo a Organização Mundial de Saúde, estima-se que quase 50 milhões de pessoas sofram atualmente de algum tipo de demência em todo o mundo e que este número triplique até 2050. Uma das principais limitações associadas a este tipo de patologias é a sua deteção tardia cuja consequência é um menor número de opções de tratamentos possíveis bem como uma menor eficácia dos mesmos. Devido às suas enormes vantagens relativamente a outros métodos atualmente usados, a Ressonância Magnética á Imagem (MRI) tem atraído um maior interesse nos últimos anos. Têm sido realizados diversos estudos de forma a encontrar novas moléculas com a capacidade de aumentar o contraste entre os tecidos permitindo um diagnóstico mais preciso e precoce das doenças neurodegenerativas. Adicionalmente, têm também sido feitos muitos estudos no sentido de encontrar novas moléculas que permitam, através de metodologias espectroscópicas (nomeadamente de Luminescência), á comunidade científica obter um maior conhecimento sobre o mecanismo de agregação da β-amiloide. Os objetivos principais desta tese baseiam-se no desenvolvimento de novos sais orgânicos magnéticos com potencial aplicação como agentes de contraste para ressonância magnética á imagem. Foram preparados líquidos iónicos ou sais orgânicos magnéticos e luminescentes biocompatíveis com base na combinação entre catiões derivados da colina e complexos metálicos de Mn (II), Gd (III) e Tb (III). Foram posteriormente selecionadas algumas estruturas cujos análogos foram funcionalizados em Nanopartículas de Sílica Mesoporosa (MSNs)

com o objetivo de avaliar o impacto dessa imobilização na toxicidade dos sais. Tanto os sais magnéticos como os nanomateriais foram caracterizados por espectroscopia (RMN, FTIR, UV-Vis, Emissão); análise elementar; ICP-MS; suscetibilidade magnética; quanto às suas propriedades térmicas; e toxicidade. Por fim, foram realizados estudos de relaxação de forma a avaliar a aplicabilidade destes novos compostos e materiais como agentes de contraste para ressonância magnética á imagem. Numa segunda parte do trabalho foram também preparados novos compostos iónicos baseados nas estruturas da Tioflavina T e Vermelho do Congo que possam ser usados como sondas fluorescentes. Esses novos materiais foram caracterizados por espectroscopia (NMR, FTIR); análise elementar; e quanto às suas propriedades térmicas. Especificamente, os sais baseados na Tioflavina T foram ainda avaliados quanto às suas propriedades de luminescência e foram efetuados estudos de birrefringência para os sais preparados a partir do Vermelho do Congo.

No futuro espera-se que alguns dos sais magnéticos e luminescentes preparados possam ser aplicados como agentes de contraste de MRI mais eficientes e não tóxicos.

KEYWORDS

• NEURODEGERATIVE DISEASES •

• MAGNETIC ORGANIC SALTS •

• MESOPOROUS SILICA NANOPARTICLES •

• MAGNETIC RESONANCE IMAGING •

• CONTRAST AGENTS •

• FLUORESCENT PROBES •

PALAVRAS-CHAVE

• DOENÇAS NEURODEGENERATIVAS •

• SAIS ORGÂNICOS MAGNÉTICOS •

• NANOPARTÍCULAS DE SÍLICA MESOPOROSA •

• RESSONÂNCIA MAGNÉTICA Á IMAGEM •

• AGENTES DE CONTRASTE •

• SONDAS FLUORESCENTES •

List of Abbreviations

ND	Neurodegenerative diseases
CNS	Central nervous system
WHO	World Health Organization
AD	Alzheimer's Disease
APO e4	Apolipoprotein allele
Aβ	β-amyloid protein
APP	Amyloid precursor protein
GABA	γ-aminobutyric acid
ILs	Ionic liquids
FDA	Food and Drugs Administration
IAChE	Acetylcholinesterase inhibitors
NMDAR	N-methyl-D-aspartate receptor
CSF	Cerebrospinal fluid
PET	Positron emission tomography
MRI	Magnetic resonance imaging
FDG-PET	Fluorodeoxyglucose-PET
SPECT	Single-photon emission computed tomography
RF	Radiofrequency
PD	Proton density
NMV	Net magnetization vector
CA	Contrast agent
r	Relaxivity
T_1	Longitudinal relaxation time
T_2	Transverse relaxation time
SBM	Solomon-Bloembergen-Morgan
HF	Hwang and Freed
BPP	Bloembergen, Purcell, and Pound
ThT	Thioflavin T
CR	Congo red

BTA	Benzothiazole aniline
SQ	Styryl-quinoxaline
K114	((trans,trans)-1-bromo-2,5-bis(4-hydroxy)styrylbenzene
BSB	((trans,trans)-1bromo-2,5-bis(3-hydroxycarbonyl-4-hydroxy)styrylbenzene
ANS	8-anilinonaphthalene-1-sulfonate
S	Singlet
T	Triplet
Φ	Quantum yield
Φ_F	Fluorescence quantum yield
τ	Lifetime decay
n_o	Ordinary ray
n_e	Extraordinary ray
RTILs	Room Temperature Ionic Liquids
API	Active pharmaceutical ingredient
ACh	Acetylcholine
acetyl-CoA	Acetyl-coenzyme A
ChAT	Choline acetyltransferase
TMA	Trimethylamine
TMAO	Trimethylamine-N-oxide
MILs	Magnetic Ionic Liquids
μ_{eff}	Effective magnetic moment
GdCAs	Gd (III)-based contrast agents formulation
χ_g	Magnetic susceptibility
MB	Bohr Magneton
SEM	Standard error of the mean
Tm	Melting temperature
Td	Decomposition temperature
PL	Photoluminescence
λ	Wavelength
k_r	Radiative constant

k_{nr}	Non-radiative constant
Δ	Ligand-field splitting parameter
ºC	Degree Celsius
K	Kelvin
DMAE	2-dimethylaminoethanol
DMAP	1-dimethylamino-2-propanol
MSN	Mesoporous silica nanoparticles
^{1}H-NMR	Proton nuclear magnetic resonance
^{13}C-NMR	Carbon-13 nuclear magnetic resonance
^{19}F-NMR	Fluorine-19 nuclear magnetic resonance
FT-IR	Fourier transform infrared
EA	Elemental analysis
ICP-MS	Inductively coupled plasma mass spectrometry
XRF	X-Ray Fluorescence
TEM	Transmission electron microscopy
TGA	Thermogravimetric analysis
XRD	X-ray diffraction
DLS	Dynamic light scattering
NLDFT	Non-local density functional theory
A_{BET}	Specific surface
D_p	Pore diameter
V_p	Pore volume
δ	Chemical-shift deviation
ū	Wavenumber
ppm	parts per million

Chapter 1

Introductory concepts

Chapter 1

Introductory concepts

1. Neurodegenerative Diseases

Neurodegenerative diseases (ND) are incurable and highly incapacitating disorders that affect the human central nervous system (CNS). These pathologies are characterized by the progressive degeneration and death of nerve cells, more commonly called neurons.[1,2] These are specialized cells that act, along with glia cells, as one of the basic building block of the CNS and communicates with other cells through connections called synapses.[3–5] Once damaged or destroyed, neurons do not have the capacity to regenerate nor can be replaced. Therefore, the neuronal loss event lead to severe damages to CNS structure and function in specific areas and, consequently, to the appearance of symptoms that depends on the affected area and whose severity increases with time.[2,5,6] Alzheimer's, Parkinson's or Huntington's diseases, amyotrophic lateral sclerosis and so many other pathologies are examples of neurodegenerative disorders. According to World Health Organization (WHO), it is estimated that almost 50 million people have dementia worldwide. Also, Alzheimer's Disease (AD) arises as the most common form of dementia representing 60 to 70% of the people that suffer with this kind of illness.[7] Usually, the first symptom related with AD is the short-term memory loss, *i.e.*, the increased difficulty in retaining recent memories. Also, poor judgment, repeating questions and increased anxiety can be included in the first symptoms that patients may suffer. With time, these and many other symptoms appear, and the severity increases greatly. In more advanced stages of the disease, the patient can feel disorientation and confusion, depression, lack of ability to perform the normal daily tasks as well as the loss of the ability to recognize family and friends. In late stages, the patients lose many important and vital body functions which leads, eventually, to death.[8]

Most of AD cases are age-related with the first clinical symptoms appearing at mid-60s, however, a small percentage of patients (2 to 10%) with this illness show an early onset form of the disease.[9] In addition to age, being female, possessing a poor education level, have a family history with AD cases, severe head trauma, race and an inheritance of a specific apolipoprotein allele (APO e4) are examples of risk factors that increases the chance of develop AD.[8,10] Also, rare autosomal dominant forms of AD with an approximate incidence smaller than 1% can be found between the patients.[9]

Despite all neurodegenerative disorders showed similar common pathological features (*e.g.* cell loss, gliosis, atrophy, and pathological protein inclusions) they can be distinguished by some details such as (i) *which neuronal populations are lost* (*e.g.* brain, spinal cord) and (ii) *which proteins are found in inclusions and their subcellular localization*. Specifically, AD is neuropathologically characterized by the formation and deposition of two different protein aggregates associated to tau and β-amyloid proteins and more commonly known as neurofibrillary tangles and amyloid plaques, respectively.[11,12] Amyloid aggregates can be found mostly within the parenchyma and in the vicinity of small vessels walls and comprises the deposition of fibrillar forms of β-amyloid (Aβ) protein.[12,13] These Aβ peptides are formed through the proteolytic cleavage from a larger protein, amyloid precursor protein or APP through two possible pathways as can be seen in Figure 1. 1.

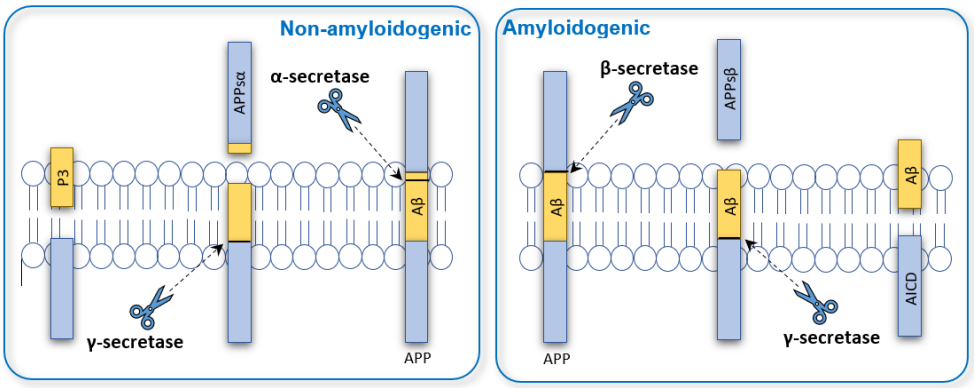

Figure 1. 1 | Scheme of APP proteolysis process. adapted from 14

Non-amyloidogenic route leads to the formation of a soluble and innocuous fragment called p3 while amyloidogenic path conducts to the formation of a fragment of β-Amyloid. This fragment presents several isoforms according to the APP cleavage site. [15–18] Although harmless to health, the most frequently Aβ form is composed by 40 (Aβ40) amino acids. With an incidence of less than 10% of the produced isoforms, Aβ42 arises as the main responsible for the formation of neurotoxic protein aggregates. This form of β-Amyloid peptide presents hydrophobic properties which leads to higher predisposition to aggregate. [19–23] According to amyloid cascade hypothesis, aggregation and, consequent deposition of β-amyloid peptide in the brain, is one of the most important causes for Alzheimer's disease. Aβ formation and its precursor structures distort synaptic neurotransmitter levels and prevent the communication between neurons which leads to a dysfunction of the synaptic process.[24–27] Neurotransmitters normally associated to AD are acetylcholine, glutamate, serotonin, dopamine, γ-aminobutyric acid (GABA) and noradrenaline. Because of this modification, a progressive loss of cognitive functions is observed.

1.1. β-Amyloid fibrils formation

Amyloid fibrillogenesis, i.e., the process or Aβ aggregates formation is carried out through a multiple step's evolution where, at each stage, an increasingly complex structure is formed (Figure 1. 2). The rearrangement of a native protein structure with a formation of a misfolded intermediate is the first step. This protein reorganization leads to an unstable β-sheet rich fibrillar intermediate with a high probability to aggregate with other β-strands into higher-order oligomers to find stability. Oligomers scaffolds act as monomers and its formation is followed by more aggregation steps where more complex intermediate structures are attained until the insoluble species named fibrils are observed. [28–32]

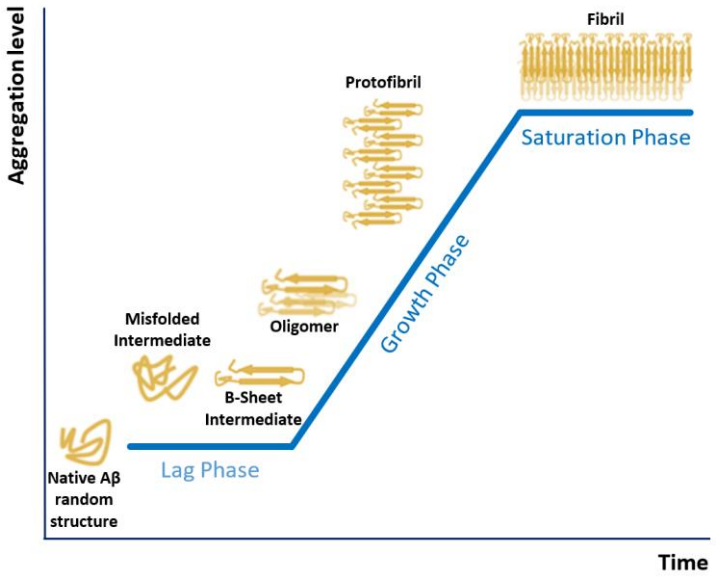

Figure 1. 2 | Process of amyloid fibrils formation. Adapted from 28,33

Recent studies suggested that synaptic process is affected before amyloid fibrils formation. Although this report is still very recent, some authors has

been attributing the synaptic process dysfunction to earlier stages of AD, i.e., to the formation and action of oligomers.[34–36] According to the literature, amyloid fibrils formation can be inhibited through oligomers stabilization via hydrogen bond between carboxylic group and the protein backbone. By using some ionic compounds, more specifically ionic liquids (ILs), it is possible to observe some differences in the fibril's formation process. In the presence of task-specific ionic liquids, it was possible to consider important observations: *i) different amount and morphology of fibril aggregates; ii) smaller protein β-sheet content; iii) higher stability of folded protein conformation; iv) some oligomers species were not converted into structures that are more complex.* [37]

1.2. Neurotransmitters and pharmacological drugs

Until 2021, none of the prescribed therapeutic drugs used for this kind of illness could stop the disease progress. It is important to note that the approved pharmacological therapies are based on the reduction of the symptoms evolution as well as to preserve the patient's mental and cognitive abilities as long as possible giving to them some life quality. From 2003, Food and Drugs Administration (FDA) approved only two drugs for therapy. Table 1. 1 presents the approved drugs used to treat AD patients. Being associated to altered neurotransmitter levels in the brain, AD symptomatic treatment was, until this year, focused on two different classes of drugs, acetylcholinesterase inhibitors (IAChE) and one antagonist of the N-methyl-D-aspartate receptor (NMDAR). IAChE and NMDAR mainly act on the cholinergic and glutamatergic systems.[38–41] In contrast, the new drugs called Aduhelm® and Leqembi®, contained as main target one of the AD pathological hallmark, β-amyloid. Patients that received these new drugs

showed a significant reduction of Aβ plaques. On the other hand, patients treated with placebo, did not present any difference in Aβ plaques content.[42]

Table 1. 1 | Drugs used for the symptomatic treatment of Alzheimer's disease.[41]

Drug	Class	Indication	Date of Introduction
Tacrine [(a)]	IAChE	Mild to moderate dementia of the Alzheimer's type	1993
Donepezil		Dementia of the Alzheimer's type	1997
Rivastigmine		Mild to moderate dementia of the Alzheimer's type	2000 (Oral) 2008 (patch)
Galantamine		Mild to moderate Alzheimer's disease	2001
Memantine	NMDA antagonist	Moderate to severe dementia of the Alzheimer's type in adult patients	2003
Aduhelm	Aβ- directed antibody	-	2021
Leqembi	monoclonal antibody	-	2023

[(a)] Tacrine was the first IAChE approved for clinical use and showed an improvement in the cognitive function of the patients, however, today it is no longer used due to their high incidence secondary effects (hepatotoxicity).

1.2.1. The cholinergic system

AD patients present smaller amounts of choline acetyltransferase. This enzyme is responsible for the synthesis of ACh neurotransmitter and, because of its reduced concentration, a decrease in ACh production can be observed. ACh neurotransmitter is involved in the learning and memory and generally, the patients experienced a cognitive decline according to their cholinergic function loss. IAChE compounds act for inhibition of acetylcholinesterase (AchE) enzyme and, thus, avoid the acetylcholine degradation in the synaptic cleft.[38,39] A significant improvement of the characteristic symptoms of AD disease using IAChE have been observed.[40]

1.2.2. The Glutamatergic System

Glutamate excitatory neurotransmitter, presented in high levels in AD patients, binds to NMDA receptor when the synaptic process is ongoing. In a mechanism of excitotoxicity, the presence of high levels of Glutamate leads to the introduction of high amounts of calcium in the nerve cells and, as a consequence, also results in the cell death by excessive stimulation. Memantine, the only non-competitive antagonist of NMDAR prescribed for AD disorder, acts making the connection Glutamate-NMDA receptor more difficult and, thus, reduces the calcium introduced in the cells. This mechanism allows to avoid the cell damage and consequent death.[11,38,40] Due to the small affinity to NMDAR, Memantine has no effect in healthy people. This drug is only activated in specific cases such as when an increase of NMDAR is observed or when the neurons are being too overly stimulated. With an increase in the disease severity (later stages), memantine shows greater efficiency since the phenomenon of excitotoxicity is also higher. Thus, this drug seems to be more effective in severe AD cases. [39,40]

1.3. Diagnosis Techniques

Currently, it is not available an efficient method to perform AD diagnosis. Pathological analysis performed during the patient's autopsy is, still today, the only method that can give a definitive diagnosis of this disorder.[43] Therefore, AD diagnosis can be made by differential analysis considering different hypotheses, which are gradually eliminated until, ideally, only one option is obtained. This differential analysis is carried out through physical examinations and cognitive assessment in order to eliminate other hypothetical diseases. Currently, three exams that can be more focused to this pathology (although it cannot serve as a definitive diagnostic method)

are being used in the clinical practice: analysis of biomarkers in the cerebrospinal fluid (CSF), positron emission tomography (PET) and magnetic resonance imaging (MRI). These techniques are important to evaluate the presence and deposition of amyloid protein, the presence of pathological tau protein as well as the brain cortical atrophy. Additionally other differential diagnosis methods such as by using glucose metabolism measurement through fluorodeoxyglucose-PET (FDG-PET) technique and brain perfusion by single-photon emission computed tomography (SPECT) can be used.[44] In Table 1. 2 these techniques are summarized according to objectives.

Table 1. 2 | Techniques used in differential diagnosis of Alzheimer's disease.

Technique	Biomarker	How it works
MRI	Brain cortical atrophy	Give images from brain atrophy, i.e., brain tissue loss. This information is correlated with characteristic cognitive deficits of AD patients. [45,46]
PET	Aβ42 plaques	^{18}F tracers [(a)] is used to detect brain amyloidosis due to high affinity of tracers to amyloid plaques. [44,47]
CSF Biomarkers	T-tau Aβ42 level	Measurement of total T-tau level and β-amyloid 1-42 for quantification of the protein concentration present in the brain. [48]
FDG-PET	Glucose metabolism [(b)]	Detects glucose metabolism changes in the brain that is correlated with synapse disfunction (direct method). [49]
SPECT	Brain perfusion [(b)]	Synaptic activity is dependent with glucose metabolism, which it can be correlated with cerebral blood flow to the brain (cerebral perfusion, indirect method). [43]

[(a)] PET tracers used in clinical practice: Florbetapir F-18 (Amyvid), Florbetaben (Neuraceq, Piramal Imaging) and [18F]-flutemetamol (Vizamyl ®)

[(b)] Radiopharmaceutical compounds used: technetium-99m-hexamethyl propylene amine oxime (99mTc-HMPAO) or technetium-99m-ethyl cysteinate diethylester (99mTc-ECD)

All these diagnosis techniques give us different valuable clues facilitating the differential diagnosis along with patient's cognitive analysis. Specifically for this work, we are interested in the study of MRI technique. In the last years, this diagnosis method has been gained greater attention as an alternative to PET technique. MRI is based on nuclear magnetic resonance spectroscopy and allows collecting images from internal structures of human body. It presents several important advantages such as its higher spatial resolution, the ability to differentiate soft tissues, it is a cheaper diagnosis method comparing to PET and no ionizing radiation is needed. In addition, it is a non-invasive method and considered harmless to the patients despite the use of high magnetic fields. However, MRI sometimes possesses a low sensitivity problem, which may lead to a poor image contrast and resolution, as well as the need to apply higher times scan. To overcome this problem, MRI can be used in combination with contrast agents. These pharmaceutical compounds are applied in order to increase the contrast enhancement.[50,51]

2. Magnetic Resonance Imaging

NMR spectroscopy, and so, Magnetic Resonance Imaging (MRI), are based on the interaction phenomenon between an external magnetic field and a particle with associated spin and charge.[52–54] Due to their inherent angular momentum and being positively charged, MRI-active nuclei has a net electrical charge. According to Faraday's law, rotating nucleus with a positive charge, i.e., a moving electric field, generates a local magnetic field usually called magnetic moment.[55,56] The proton nucleus, ^{1}H, is the most used hydrogen isotope in magnetic resonance technique. Its single proton gives to this nucleus a relatively large magnetic moment which, together with the high percentage of hydrogen in human body, allow it to be the better choice

for MRI applications.[57,58] Thus, this diagnosis method takes advantage of the high-water percentage and also the presence of fat in human tissues to obtain images of anatomic structures and physiological processes of human body.[53,57,59] The MRI technique is accomplished with the relaxation detection of water protons spins when these are under the influence of a strong magnetic field and excited by radiofrequency (RF) energy, applied in short pulses. The RF pulses, as a low-energy radiation (non-ionizing), is the reason why MRI is considered a safe imaging technique and one of the main advantages comparing to other diagnostic methods (Figure 1. 3). This process is complemented with magnetic field gradients, *i.e.*, with linear variations in the magnetic field intensity. These gradients allow to: *(1) selectively excite (focus) the anatomical area of interest and (2) encode the position of the resonating spins, which enables the construction of a three-dimension image*. Regarding to the process of spins relaxation, this concerns to the return of protons spins to equilibrium state (low-energy state).[58,60–62] These mechanisms are going to be detailed in the next section.

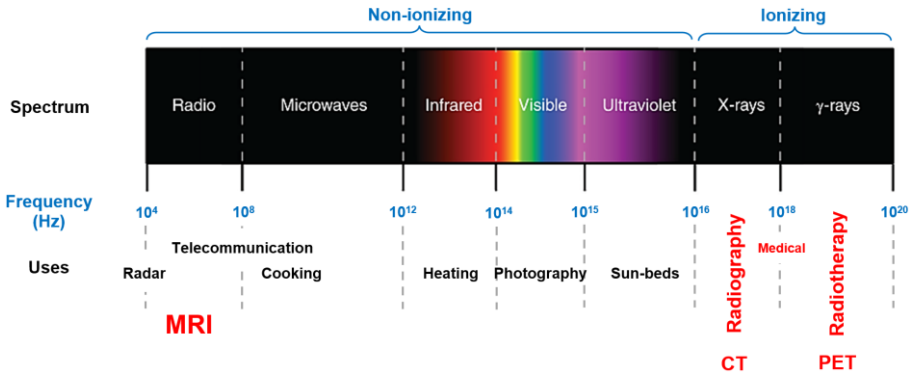

Figure 1. 3 | The electromagnetic spectrum. (adapted from 63)

2.1. MRI image contrast parameters

Image contrast in MRI experiments is affected by several factors. Some of these can be changed by the technique operator (extrinsic parameters), however, others are inherent to the body tissues and cannot be changed (intrinsic parameters).[52,58] T_1 recovery, T_2 decay and proton density (PD) are the three main intrinsic parameters responsible for the image contrast. PD is related with the number of protons available in a tissue per unit volume. Therefore, higher values of PD lead to a larger signal.[53,64] T_1 recovery and T_2 decay (longitudinal and transverse relaxation, respectively) concern to spin relaxation mechanisms. These relaxation processes emerge from protons spins excitation. In the absence of an external magnetic field, none of the protons spins orientation is preferential and they have the same energy (Figure 1. 4 (A)). However, in the presence of a strong magnetic field (B_0), an interaction between the nucleus and the applied field is established and the magnetic moments line up with B_0 in parallel and antiparallel alignments (Figure 1. 4 (B)). These two alignments have different energy levels according to the spin vector direction. When the magnetic moment and B_0 are aligned (in the same direction), a low-energy state is obtained. On the other hand, when they have opposite directions, the energy of this state increases.[53,65]

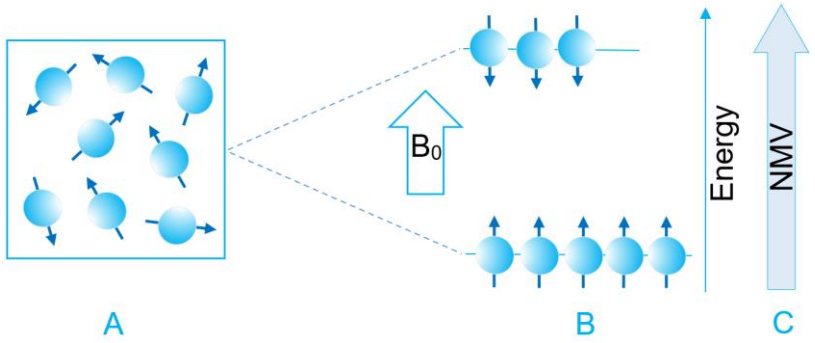

Figure 1. 4 | Hydrogen protons alignment in (A) the absence and (B) presence of an external magnetic field; (C) The net magnetization vector. (adapted from 52)

When this condition is achieved, even in small amount, there is a larger population in the low-energy state comparing to antiparallel state. This small excess of low-energy spins generates a net magnetic moment illustrated in Figure 1. 4 (C) by a vector aligned in the same direction with the external magnetic field called net magnetization vector (NMV).[58,62,64] Protons spins can be excited under the influence of the static magnetic field B_0 by the application of an additional radiofrequency (RF) magnetic field applied in short duration pulses. When the RF field is removed, specific relaxation processes are initiated and the protons spins return to their low-energy state at the same time that the NMV vector realign with B_0.[61] These relaxation mechanisms are characterized by relaxation times T_1 and T_2 whose variation on tissues (hydrogen atom environment) are the basis of MRI image contrast.[53,65]

2.1.1. T_1 recovery

T_1 recovery mechanism is characterized by the loss of energy from hydrogen nuclei to the neighbouring environment. This energy loss causes the return of protons magnetic moments to longitudinal plane, *i.e.*, allows to recover

their longitudinal magnetization (Figure 1. 5 (A)). This mechanism can be expressed by an exponential curve (Figure 1. 5 (B)) and it is characterized by a longitudinal relaxation time constant (T_1) that corresponds to the required time to longitudinal magnetization recovers 63% in a tissue. Time evolution of this process is described in Equation 1. 1.[53,65,66]

(A) **(B)**

$$\mathbf{M}_{z_\tau} = \mathbf{M_0}.(\mathbf{1} - \mathbf{e}^{-\tau/T_1}) \qquad \textbf{(Equation 1. 1)}$$

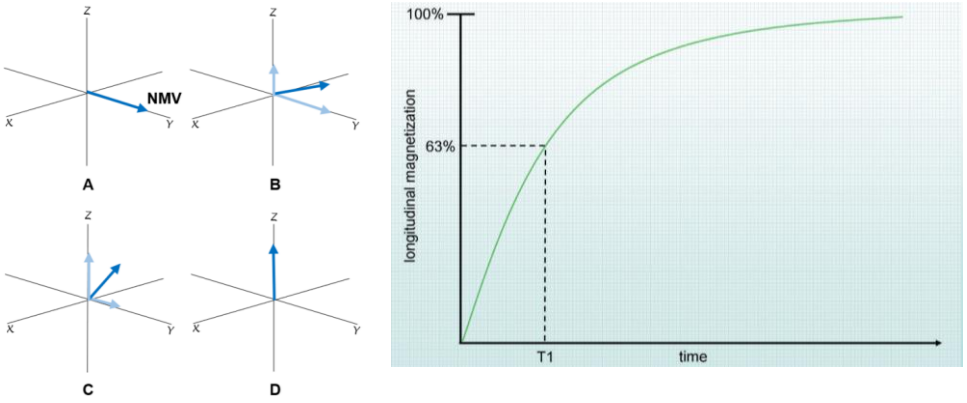

Figure 1. 5 | (A) Longitudinal relaxation process; (B) T1 recovery curve. $\boldsymbol{M_{z_\tau}}$ *is the longitudinal magnetization at time τ after removing the excitation pulse;* $\boldsymbol{M_0}$ *is the longitudinal equilibrium magnetization; and* T_1 *corresponds to* T_1 *recovery time and is the time required to increase longitudinal magnetization by a factor of e.*(adapted from 58,65)

2.1.2. T_2 decay

T_2 decay, or spin-spin relaxation, is characterized by the interaction of nearby proton magnetic fields with each other and the consequent loss of coherent transverse magnetization (Figure 1. 6 (A)). As longitudinal relaxation, also T_2 decay rate is an exponential process (Figure 1. 6 (B)), and it is characterized by a transversal relaxation constant (T_2). This constant corresponds to the

required time to obtain 63% of coherence loss in the transverse plane. Time evolution of this process is described in Equation 1. 2.[53,65,66]

(A) **(B)**

$$\mathbf{M_{xy} = M_0 . e^{-\frac{\tau}{T_2}}} \quad \textbf{(Equation 1. 2)}$$

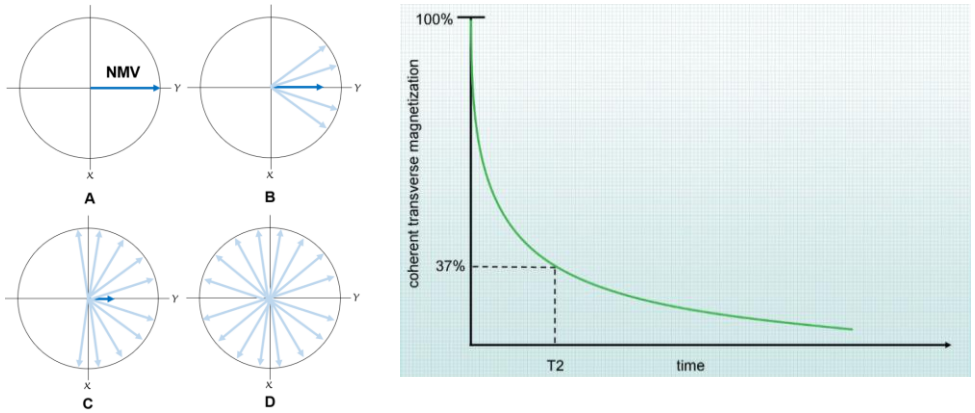

Figure 1. 6 | (A) Transverse relaxation process; (B) T2 decay curve. $\boldsymbol{M_{xy_\tau}}$ *is the transverse magnetization at time τ after removing the excitation pulse;* $\boldsymbol{M_0}$ *is the transverse equilibrium magnetization; and* T_2 *corresponds to* T_2 *decay and is the time required to reduce transverse magnetization by a factor of e.*(adapted from 58,65)

2.2. Contrast agents

As described in section 1.3, MRI possesses several important advantages over other diagnostic techniques. However, one of its major disadvantages is the reduced image contrast observed in some situations. Thus, the use of contrast agents can be relevant in order to support this technique. The function of contrast agents is focused in their ability to increase the image contrast between the target tissue, organ or structure and the surrounding tissues. There is some divergences about the classification of contrast

agents, but in general, they can be classified according to Scheme 1. 1.[51,67–70]

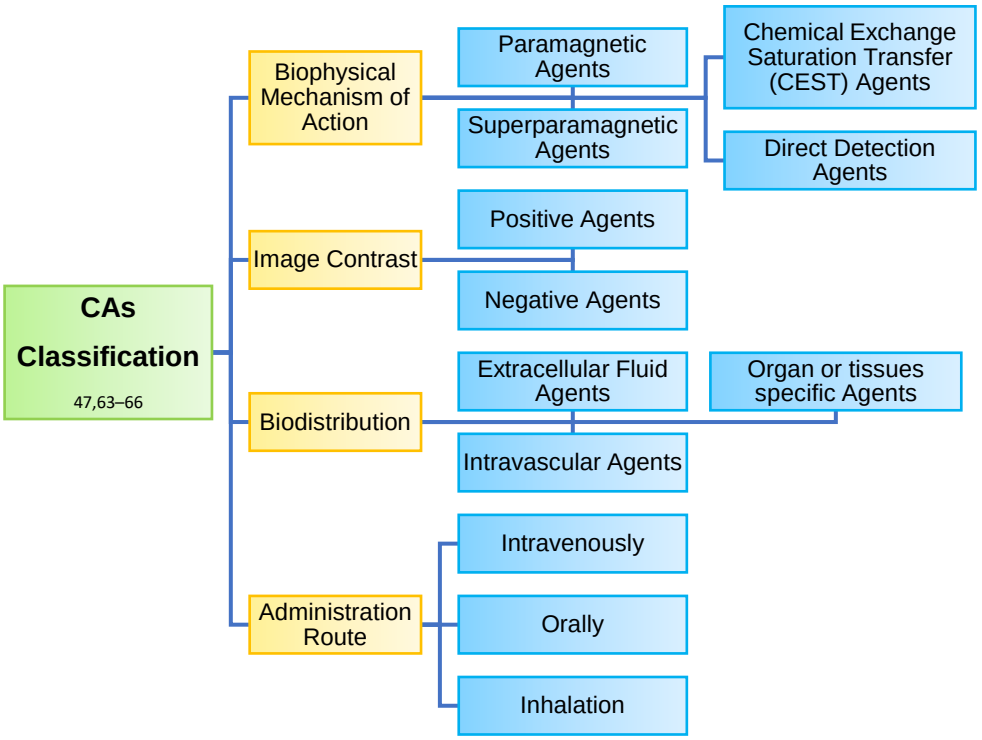

Scheme 1. 1 | General classification of the Contrast Agents

In this context, it is important to analyse in more detail the Paramagnetic CAs, in particular, their effect on image contrast as well as their role and function. Paramagnetic agents are typically correlated to metal chelates whose formulation comprise the presence of a ligand coordinated with a metal ion with a permanent magnetic moment (as a result of the presence of at least one unpaired electron). The most widely used paramagnetic commercial CAs are usually based on gadolinium (III) complexes. Although there are already reported two examples of CAs based on the manganese (II) transition metal (Mn-DPDP and a liposome encapsulation system named on

LumenHance), gadolinium (III) remains as the primordial choice with a higher success rate within commercial CAs.[69] Gadolinium (Gd) is a lanthanide element from f-block with important properties, such as its 7 unpaired electrons in the 4f orbital, the high magnetic moment and coordination efficiency with water molecules; and, also, the fact that their complexes induce a reduction of longitudinal and transversal relaxation times of water protons closer to the metal.[69,71] Nevertheless, Gd (III) has a high toxic level for the human body in its free state. This metal toxicity has been associated to several mechanisms of action including calcium channel inhibition. In the free state, Gd (III) presents a similar atomic radius as divalent calcium (Ca^{2+}). Although the mechanism by which gadolinium inhibits calcium channels is still unknown, it is recognized that Gd acts as an analogue of Ca^{2+} and inhibits its normal functioning.[72–75] With an important role as an activator in the release of the neurotransmitters during the synaptic process, blocking this mechanism as a result of its inhibition by gadolinium can induce severe biological consequences.[73,76–78] In order to avoid this gadolinium-associated toxicity, a ligand or chelate is selected to trap the free metal.[74,77] This carrier molecule and the coordination with the metal has to respect some parameters to be adequate as MRI contrast agents. One of the most important features is the ligand ability to form a thermodynamically stable metal complex to prevent the dissociation of metal-ligand bond and, consequently, the release of free metal. The thermodynamic balance between Gd^{3+} and ionic ligand species as well as the metal complex determines the final stability. Moreover, the required time for this equilibrium attainment, *i.e.*, the kinetic stability, is an important parameter. Thus, the ligand chemical properties and its ability to stablish a well-coordinated chelate allows to predict the dissociation probability and the rate of the process. Several studies to develop new ligands with a design that allows to

reduce gadolinium (III) complexes toxicity have been made. [74,79] Some commercial contrast agents organized by the nature of their ligands (macrocyclic or linear) and complexes (ionic or non-ionic) are presented in Figure 1. 7.

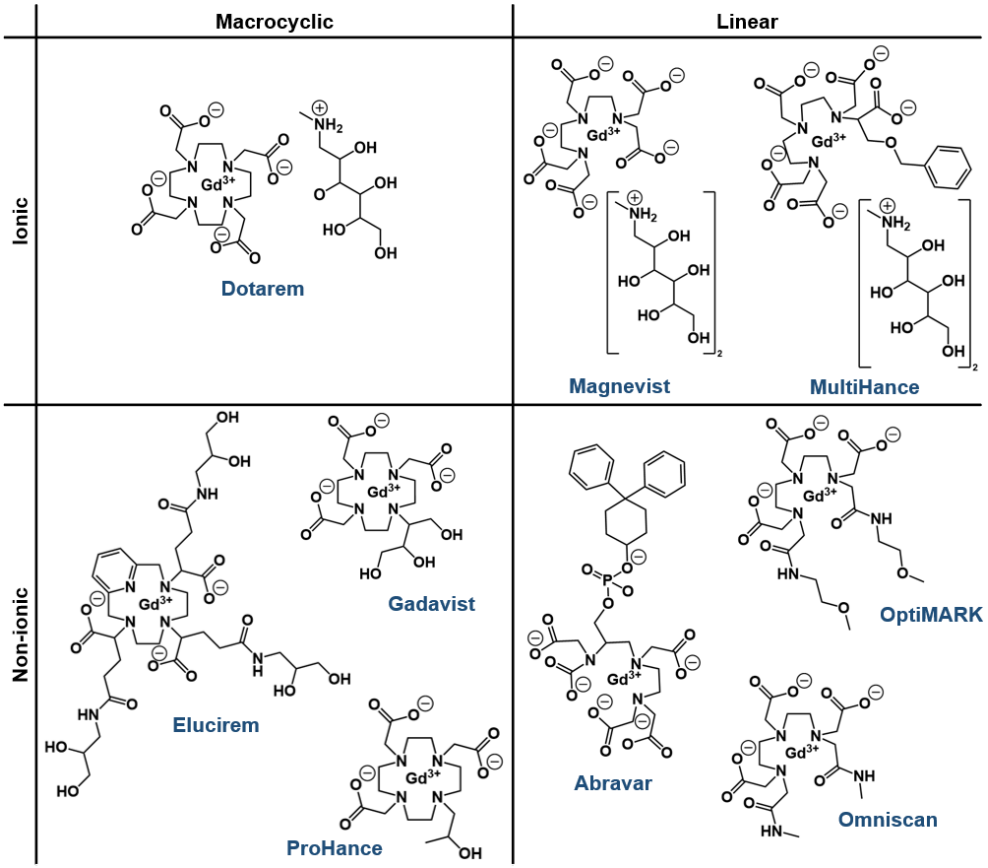

Figure 1. 7 | Commercial contrast agents structures[80]

In addition to stability, other properties such as relaxivity, biodistribution, toxicity, clearance, osmolality and viscosity must be also considered.[81] The efficiency of the contrast agent is initially evaluated or quantified by the determination of its relaxivity (r).This CAs property is associated to the ability

of a paramagnetic compound to enhance the relaxation rate, and consequently reduce relaxation times of water molecules in its vicinity in order to increase the tissue contrast.[82–84] The relaxation rate observed ($1/T_{i,obs}$) for this phenomena can be described by the Equation 1. 3 as a sum of the relaxation rates associated to the system in the absence ($1/T_{i,d}$) and in the presence ($1/T_{i,p}$) of the paramagnetic ion (contrast agent). Due to the linear dependency on contrast agent concentration ([CA]), the parameter associated to the paramagnetic ion can be rewritten and the Equation 1. 4 is obtained.

$$\frac{\mathbf{1}}{\boldsymbol{T_{i,obs}}} = \frac{\mathbf{1}}{\boldsymbol{T_{i,d}}} + \frac{\mathbf{1}}{\boldsymbol{T_{i,p}}} \qquad \textbf{(Equation 1. 3)}$$

$$\frac{\mathbf{1}}{\boldsymbol{T_{i,obs}}} = \frac{\mathbf{1}}{\boldsymbol{T_{i,d}}} + \boldsymbol{r_i}[\boldsymbol{CA}] \qquad \textbf{(Equation 1. 4)}$$

where r_i $(i = 1,2)$ *is the relaxivity, the specific concentration independent factor that characterizes the paramagnetic agent.*

Therefore, the relaxivity associated to a system with the presence of a CA corresponds to the slope of the plot described by Equation 1. 4 ($1/T_{i,obs}$ vs [CA]).[85,86]

CAs can be classified according to their effect on the contrast image, *i.e.*, to its greatest tendency to affect T_1 or T_2 relaxation times. Compounds with the ability to decrease T_1 recovery (longitudinal relaxation) are usually called T_1 agents. On the other hand, if their presence affects the T_2 decay process (transverse relaxation), they are called T_2 agents. Most compounds used as CAs for MRI are T_1 agents with a typical formulation based on Gd (III) complexes. In fact, it is important to highlight that these Gd (III)-based CAs can increase both longitudinal and transverse relaxation rates, however, its

major effect in the tissues relies in the reduction of T_1 relaxation time. T_2 contrast agents are usually based on superparamagnetic iron oxide nanoparticles.[87,88] Specifically, for T_1 agents, as illustrated in Figure 1. 8, the efficient relaxation effect associated to CAs is chemically related to the water molecules directly coordinated with the metal chelate (inner sphere) or in its surrounding (second and outer sphere).[85] Inner-sphere mechanism encompasses the direct coordination between the water molecules and the contrast agent (*i.e.*, with the paramagnetic center). A greater number of coordinated water molecules, as well as their rapidly exchange with the bulk water protons, can be useful to increase the influence of the CA on the relaxation enhancement.[84,88] However, although the major influence being related with the water molecules directly connected to the metal, the influence of the contrast agents over the relaxation rate comprises also all the different water molecules contributions. Thus, the outer-sphere mechanism concerns to the water molecules that, despite not having an effective connection with the contrast agent, can also be affected by the relaxation enhancement as a result from the CA presence. This effect results from the dipolar interaction that occurs through the diffusion of the solvent molecules (water protons) that are in the vicinity of the paramagnetic center. Additionally, a second coordination shell located between the inner and the outer-sphere space can also affect the relaxivity associated to the outer-sphere process. The so-called second-sphere mechanism comprises the water molecules that do not have a direct dative covalent bond with the paramagnetic center but are confined to a second sphere of coordination through hydrogen bonds with the polar groups of the ligand.[85,89–91]

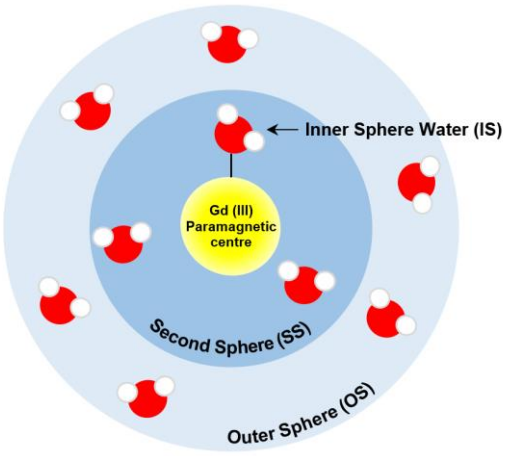

Figure 1. 8 | Scheme of different water molecules contributions to relaxation rate change (adapted from 85)

The inspiration of this NMR relaxation model that postulates a dependency relationship between the relaxation phenomenon and the water molecules in the paramagnetic ion vicinity can be essentially based on Solomon-Bloembergen-Morgan (SBM) and Hwang and Freed (HF) theories.[92] SBM hypothesizes that the relaxation has a dependency relation with the Brownian motion of water molecules around the paramagnetic species. SBM concept assumes a rigid dipolar interaction between the electron magnetic moment of the paramagnetic species (*e.g.*, Gd^{3+}) and the nuclear magnetic moment of the water protons (^{1}H) resulting in a mono-exponential decay according to Debye theory. Inspired by Bloembergen, Purcell, and Pound (BPP) model where only proton-proton interactions were considered, SBM model allowed to extend the theory to include proton-electron interactions.[92,93] This reformulation allowed to consider the greater impact that interactions between the water molecules and the paramagnetic ions have in protons relaxation. This effect is related with the higher dipole magnetic moment of the electron spin associated to the paramagnetic ion

when compared with the proton spin. Since the electron spin presents a higher dipole magnetic moment and smaller mass compared to proton spin, the interactions proton-electron (*e.g.*, ^{1}H-Gd^{3+}) are much stronger and present a greater impact in protons relaxation than proton-proton interactions.[90,93] Therefore, SBM model agrees that protons relaxation phenomena depend on the random motion of water molecules around the paramagnetic species creating an inner-sphere space already mentioned before. According to this concept and considering as the main goal the increase of CAs efficiency, it is predictable that contrast agents composed by ligands that allow to coordinate a greater number of water molecules, present higher relaxivity values. Also, other parameters such as the residence time of the coordinated water, and the molecule tumbling rate can be relevant and influence the CAs relaxivity.[84] The relaxation of water molecules presented in the outer-sphere can be explained by HF intermolecular relaxation model. This model concerns to the translational diffusion and rotational motion of non-coordinated water molecules when they are in close proximity with the contrast agent. The HF model arises as an improvement to Torrey theory through the introduction of a boundary condition correction previously neglected by this and other authors. This modification allowed to take into account a boundary problem related to the diffusion of water molecules and paramagnetic ion species and a distance of minimum approach, *i.e.* takes into account a minimum distance value between particles in order to prevent them from getting too close. Thus, the improvement prevents the diffusion of spins within a sphere whose radius is centered on the paramagnetic ion. According to HF theory, a multi-exponential decay can be obtained as a result of the assumption that the paramagnetic center (Gd^{3+}) and water molecules are two force-free hard-spheres experiencing a translational diffusion movement. [90,92–96]

3. Amyloid Probes and their Optical Properties

As mentioned in section 1.1. β-amyloid protein starts to aggregate when Aβ monomers are formed. These monomers have a β-sheet conformation and seem to provide a good scaffold for protein self-assembly. The monomers start to interact with each other and a more insoluble, β-sheet repetitive and complex structure - Aβ senile plaques or fibrils - is formed.[97] Due to β-sheet-repetitive conformation, small molecules have been shown a particular high affinity to interact with amyloid plaques. Thus, several studies in order to develop specific molecules for selective staining and imaging of Aβ aggregates have been made.[98,99] The discovery of new probes as efficient tools to detect these aggregates formation can be specially relevant to elucidate the molecular mechanisms associated to protein aggregation as well as to obtain an earlier and accurate clinical diagnosis and therapeutics of neurodegenerative disorders. Over the last years, some conventional dyes for protein aggregation detection have been tested. The probes most studied are based on two organic scaffolds such as Thioflavin T (ThT) and Congo Red (CR) whose chemical structures are presented in Figure 1. 9.[100]

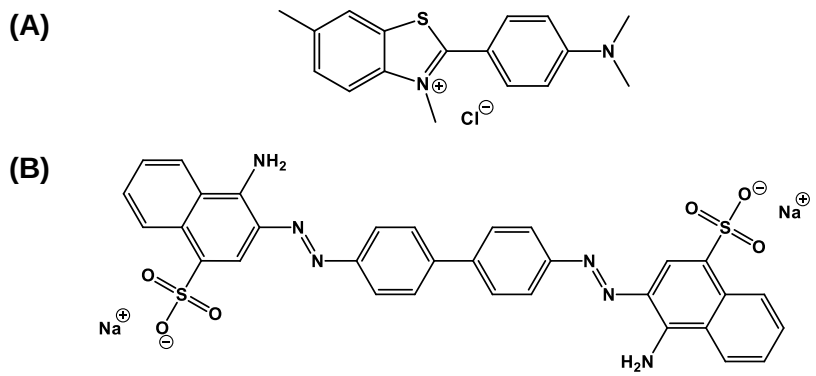

Figure 1. 9 | Scheme of some commercial probes used to detect amyloid aggregates formation: (A) Thioflavin T; (B) Congo Red.

Discovered in 1959 by Vassar and Culling, ThT is a positively charged benzothiazole-based dye. This heterobicyclic organic compound belongs to an important class of pharmaceutical drugs that presents an attractive set of biological activities, such as antitumor, antimicrobial, antifungal among others.[100,101] The detection method of this probe is focused on its intrinsic fluorescence when bounded to Aβ fibrils. In the free state, the bond between benzothiazole and aniline rings shows an ultrafast rotation (Figure 1. 10) which cause the self-quenching of the excited state and, consequently, the low emission of this compound. However, when this dye is bounded to the Aβ fibrils, this rotation movement is blocked, the excited state is preserved and ThT fluorescence increases.[100,102]

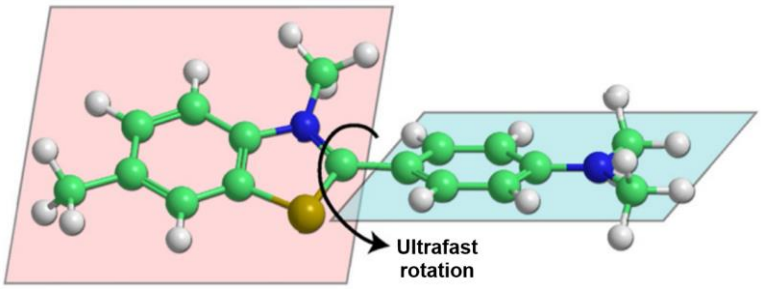

Figure 1. 10 | Thioflavin T structure and its two planer segments whose mutual rotation defines its chirality adapted from 102

The key structural feature of Congo Red is related with its two carboxylic acids groups and the space between them. Like in the case of ThT, CR is also a positive indicator of the presence of amyloid aggregates, however, the method is not based on dye fluorescence. When bounded to Aβ fibrils, CR displays a specific colour under polarized light due to its characteristic birefringence.[100,103] Thus, in the presence of amyloid aggregates, CR places between the parallel fibrils and non-polar hydrogen bonds are formed. In this

context, under the polarized light, an apple green colour associated to CR birefringence is visible allowing to positively identify amyloid aggregates.[104] The major problem of these classic probes is related with their poor selectivity. Thus, the development or discovery of compounds to overcome this drawback can be important to understand amyloid mechanism and its function in neurodegenerative disorders. Therefore, several authors propose other alternative probes to most conventional ones. Figure 1. 11 illustrated examples of ThT-based derivatives probes such as Benzothiazole aniline (BTA), thienoquinoxaline and styryl-quinoxaline (SQ) possessing higher affinity to amyloid than ThT original structure.[105] On the other hand, K114 ((trans,trans)-1-bromo-2,5-bis(4-hydroxy)styrylbenzene, arises as one of the first CR derivatives dyes. This probe as well as others such as BSB ((trans,trans)-1bromo-2,5-bis(3-hydroxycarbonyl-4-hydroxy)styrylbenzene and Chrysamine G (Figure 1. 11) are examples of CR derivatives with a high affinity to amyloid and, thus, with the ability to identify this protein aggregates. Also, these probes present a higher fluorescence behaviour comparing to CR original structure.[105]

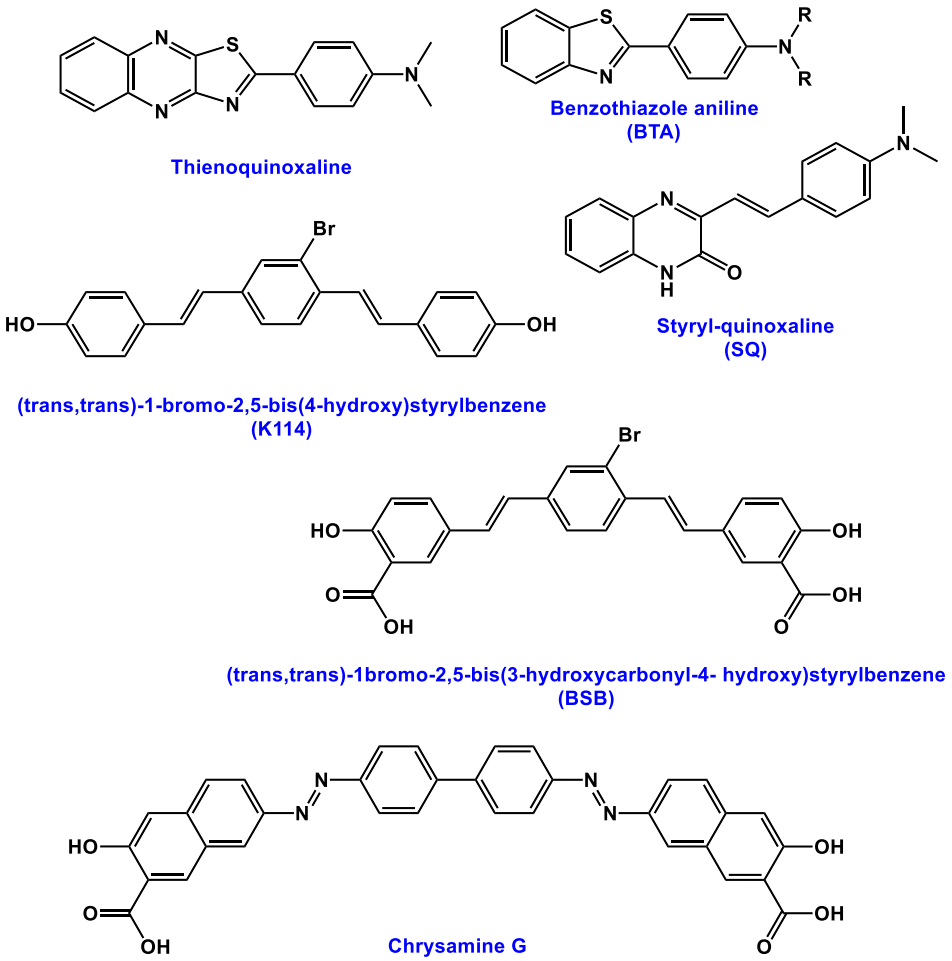

Figure 1. 11 | Structures of ThT and CR-based derivatives probes

In addition to the probes based on ThT and CR scaffolds, alternative structures such as stilbene, curcumin, perylene and thiophenes derivatives have been developed (Figure 1. 12). These probes are self-quenched in their free state but highly fluorescent when bound to Aβ.[99,106,107]

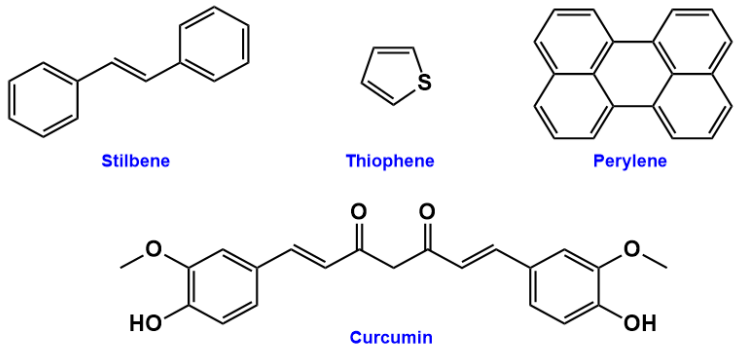

Figure 1. 12 | Strutures of probes tested for amyloid assay in vitro

Recently, can be highlighted some strategies such as

(i) the use of drugs in order to reduce the formation of Aβ fibrils (*e.g.apomorphime, a morphine derivative used in Parkinson treatment*);

(ii) the use of natural products to prevent the protein misfolding and, consequently, the Aβ formation (*e.g. Gallic acid, a grape seed extract that have been shown good results in the case of amyloid fibrils formation; and arginine, a hydrophilic aminoacid that increases the solubility of Aβ in aqueous medium*) and;

(iii) task-specific ionic liquids in order to inhibit the Aβ fibrils have been reported.[108–110]

It is important to note that this inhibitory effect is associated with the stabilization of earlier stages of the amyloid aggregation by the ionic liquids and its charge.[37] Examples of intrinsically fluorescent ionic liquids based on ruthenium, europium, rhodium and other metal complexes as well as 8-anilinonaphthalene-1-sulfonate (ANS) as fluorescent anions have been reported. In addition, quantum dots and metal nanoparticles have been also explored as alternative strategies.[105,111,112]

3.1. Luminescence

According to quantum mechanics, a molecule is organized through energy levels. The most important, and also the best known, are the electronic levels. They are related to the spatial electron's distribution and subdivided in two levels: ***the vibrational levels,*** associated to molecule vibration modes; and ***the rotational levels*** that comprise the rotational motions of the molecule. The lower energy level where the electronic, vibrational, and rotational energies are smaller is called ground state (S_0). In general, the molecules are in the ground state, however, when the light absorption by the molecule occur, an electron is promoted from the lower energy state S_0 to a higher energy excited state S_1. According to the Franck Condon principle, the promotion of the electron from one electronic level to another is made through a vertical transition, *i.e.* when the electron is promoted to the excited state does not go to the zero vibrational state but to a more energetic vibrational level (Figure 1. 13, A).[113,114] Then, through vibrational movements, the electron decays to the zero vibrational level of the excited state (Figure 1. 13, B) and, finally, returns to the ground state through, for example, a fluorescence process (Figure 1. 13, C).[115]

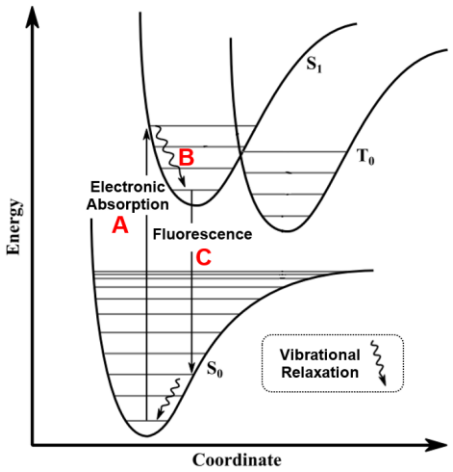

Figure 1. 13 | Potential curves diagram that shows a $s_0 \rightarrow s_1$ electronic transition according to Franck Condon principle (adapted from 116)

The energy of the absorbed photon by the molecule that allow the electron excitation must be equal to the energy difference between S_0-S_1 states, however, this transition can only be made keeping the initial spin state, *i.e.*, between two electronic states with the same electronic spin multiplicity (singlet → singlet).[114] The decay of the excited state to ground state can be done by several paths (Figure 1. 14). When the electron returns to the ground state through a $S_1 \rightarrow S_0$ transition with the emission of a photon, a *fluorescence* phenomenon is observed. This transition is highly allowed by spin. If the decay is made by the same type of transition but without the emission of a photon, it is an *internal conversion* (non-radioactive transition) where the electronic energy of the molecule is converted into vibrational energy that is then transferred to the medium as heat. The decay to the ground state can also be done through an intermediate state of different multiplicity, *i.e.*, through a transition $S_1 \rightarrow T_1 \rightarrow S_0$. In this case we have an *intersystem crossing* (non-radioactive transition) where the singlet state is converted into a triplet state. This triplet in turn goes into the ground state

without the emission of any photon. Finally, if the transition is $T_1 \rightarrow S_0$ with photon emission, a *phosphorescence* phenomenon is accomplished. This transition is highly forbidden by spin which leads to a much slower process and longer lifetime excited states comparing to fluorescence.[115] The mechanism of photon emission associated to a spontaneous fluorescence decay has a time period in nanoseconds scale. On the other hand, a phosphorescence decay process is several orders of magnitude slower than fluorescence, usually in a time scale of seconds or fractions of seconds. This seems to be related with a storage phenomenon where the energy is slowly released.[117]

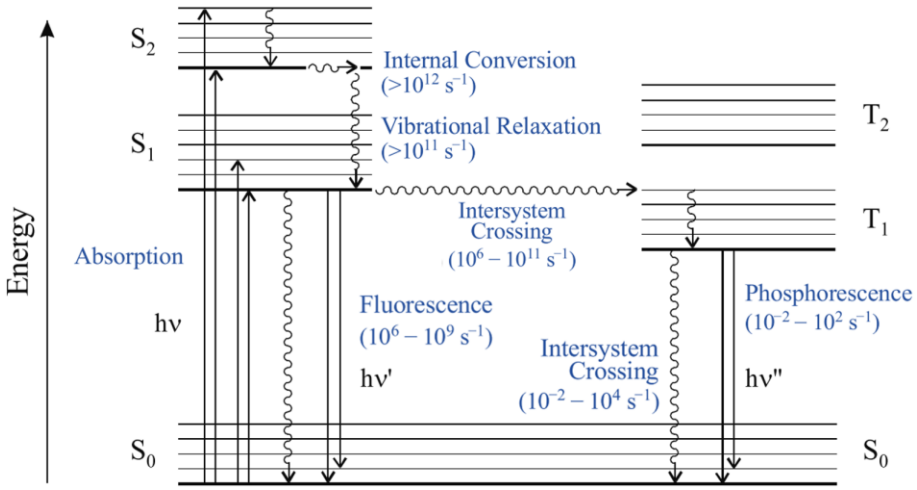

Figure 1. 14 | Jablonski diagram describing molecules electronic and vibrational levels and their transitions (adapted from 118)

Photoluminescent molecules can be described as a function of specific features such as the maximum value of absorption and emission spectra, quantum yield, lifetime, Stokes shift, brightness, and molar extinction coefficient.

For this thesis, it is important to define some of these parameters:

Quantum yield: Corresponds to one of the most important parameters of a luminescent molecule or material, it is a measure for the probe efficiency and can be defined as the ratio between the emitted and absorbed photons (Equation 1. 5).[115]

$$\Phi = \frac{\text{photons emitted}}{\text{photons absorbed}} \qquad \textbf{(Equation 1. 5)}$$

Specifically, fluorescence quantum yield equation can be also written as a function of rate constants associated to the deactivation mechanisms of the excited state (Equation 1. 6).[119]

$$\mathbf{\Phi_F} = \frac{\mathbf{k_r^s}}{\mathbf{k_r^s + k_{ic}^s + k_{isc}}} = \frac{\mathbf{k_r^s}}{\mathbf{k_r^s + k_{nr}^s}} \qquad \textbf{(Equation 1. 6)}$$

where k_r^S is the rate constant for radiative decay (transition $S_1 \rightarrow S_0$), k_{ic}^S is the rate constant for internal conversion ($transition\ S_1 \rightarrow S_0$) and k_{isc} is the constant for intersystem crossing. k_{ic}^S and k_{isc} are constants associated to non-radiative deactivation mechanisms (k_{nr}^s).

Lifetime: This parameter concerns to the average time that a luminescent molecule or material spends in the excited state before returning spontaneously to the ground state. This return step is made through the emission of a photon as already explained.[119]

Stokes shift: It concerns to the difference between the highest value of the absorption and emission spectra (Figure 1. 15). This difference between the absorption and emission spectra is typically due to the loss of some energy from the fluorophore when present in the excited state. This energy loss

occurs through molecular vibrations, and it is dissipated as heat. Thus, due to this, the emission always occurs at lower energy than absorption. It is important to acquire information about the excited state and the magnitude of this parameter is a direct method to evaluate the distortion level between the ground and the excited state of a molecule or material.[120]

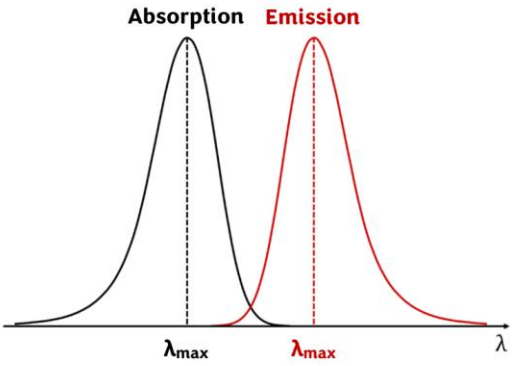

Figure 1. 15 | Stokes shift illustration (adapted from 121)

3.2. Birefringence

Refractive index of a sample is defined as the ratio between the light propagation speed in *vacuum* and the light propagation speed on that sample. The direction of a beam of light changes when it passes from a medium to another, both with different refractive indices.[122] Birefringence as a double refraction of light phenomenon occur in anisotropic materials, *i.e.*, materials where the refractive index depends on the linear polarization direction of the light regarding to its crystalline lattice orientation.[123] This specific property of these materials is related with the phenomenon where a polarized light beam is refracted and divided into two components (waves) when focuses on a birefringent sample (Figure 1. 16). The two waves (usually called by "ordinary" n_o and "extraordinary" n_e rays) exhibit

perpendicular vibration directions to each other and travel with different velocities generating a difference phase between them. This phase difference leads to an interference colours phenomenon that is the basis of birefringence imaging.[123–125]

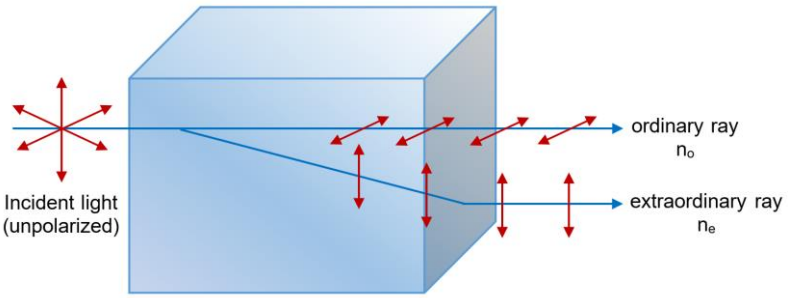

Figure 1. 16 | Scheme of birefringence phenomenon in an anisotropic material[126]

It is important to emphasize that birefringence is an important property inherent to the material and results from the difference between the two refraction indices.

4. Ionic Systems

4.1. Ionic liquids

Ionic liquids (ILs), defined as low melting organic salts (<100°C), have been shown an enormous potential of application in several areas of research. Back in the history, it is interesting to mention that the first synthesis of an IL, ethylammonium nitrate, was reported by Walden in 1914.[101,127–129] Since then, and mostly in the last 20 years, the publications and citations related with this class of organic salts have exponentially increased as can be seen in Figure 1. 17.

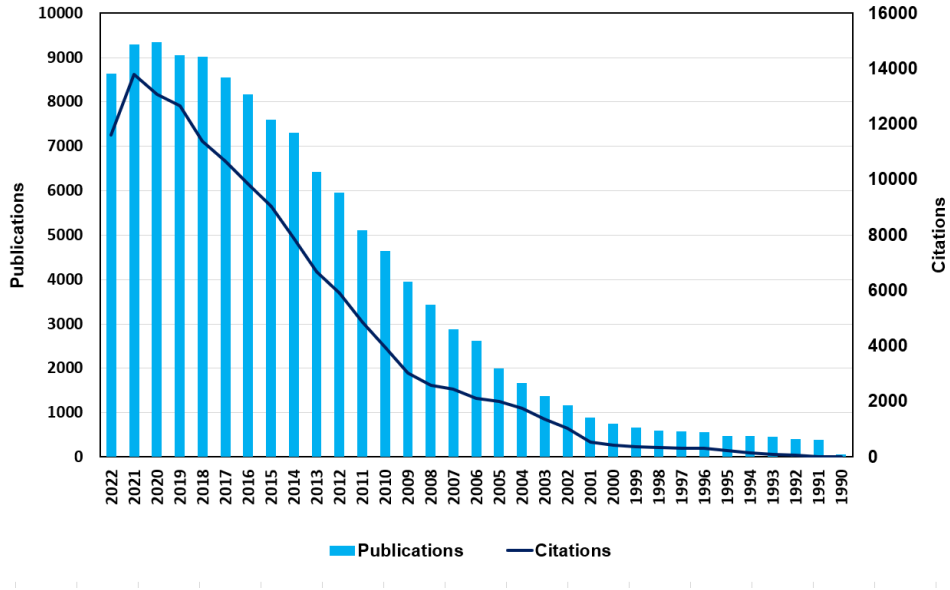

Figure 1. 17 | Publications and citations evolution over the last 30 years.[121]

Known by their peculiar properties, ionic liquids exhibit a negligible vapor pressure that allows their use in a wide range of temperatures and largely contributes to lower environmental pollution by reducing the emission of gases into the atmosphere.[130–136] In addition, many other important features such as high thermal and chemical stability, a wide electrochemical window, and a high ionic conductivity can be highlight.[137,138] The IL structure is composed by large organic cations, feature that distinguishes them from the inorganic salts, and by organic or inorganic anions. The large number of possible cation/anion combinations can tune the physical, chemical, and thermal properties of ILs. According to the desired applications, properties such as hydrophobicity, solvation capacity, polarity, viscosity, and density can be modulated. This ability allowed to increase the range of different ILs structures as well as their applications over the years.[127,139] Within the wide range of possible organic cation structures (Figure 1. 18), the most common

are based on alkylmethylimidazolium (a), tetra-alkylammonium (b), tetra-alkylphosphonium (c), alkylpyridinium (d), dialkylpyrrolidinium (e), trialkylsulfonium (f), alkylpyrazolium (g), alkylthiazolium (h) and alkylguanidinium (i) families.[129]

Room Temperature Ionic Liquids (RTILs) are described as a sub-class of ILs characterized by its liquid state at room temperature.[134,137] In order to obtain RTILs it is important to design cation/anion combinations possessing asymmetric ions as well as the charge displacement. In general, RTILs are particularly interesting for applications in several research areas including pharmaceutical industry.[129]

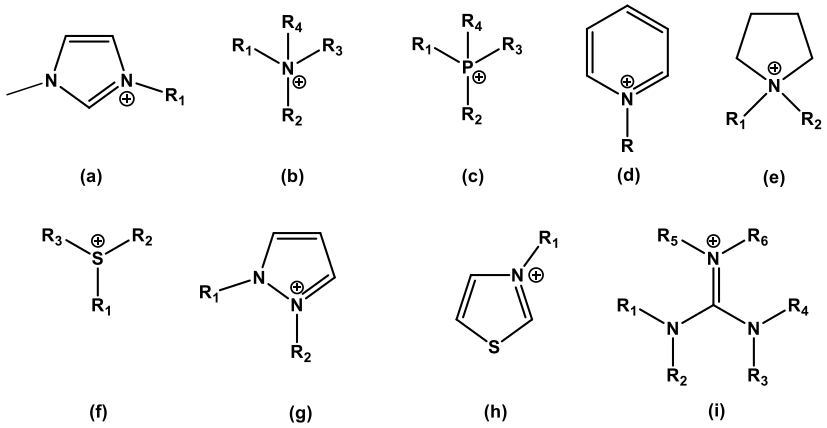

Figure 1. 18 | Common organic cations structures used in ILs design. [11]

Nowadays, the evolution of ILs and its peculiar properties allowed its organization in three different generations as indicated in Figure 1. 19. In the first generation, ILs were developed taking in account their physical properties such as melting point, density, viscosity, thermal stability, conductivity among others. Later, a second generation of ILs were considered according to physical and chemical properties including chemical reactivity, solvation, and electrochemical window, among others to the 1st

generation. More recent, a third generation of ILs have been reported by the combination of the previous chemical and physical properties with biological properties. This new generation arises from the incorporation of active pharmaceutical ingredient (API) structures in the IL formulation.[134] One of the main advantages of API-ILs are related with the possibility to improve the original drug solubility and bioavailability, drug delivery as well as biological activities. Moreover, the possibility to reduce the melting point associated to the pharmaceutical ingredient can transform crystalline drugs into amorphous and lead to the reduction of polymorphism phenomenon.[140]

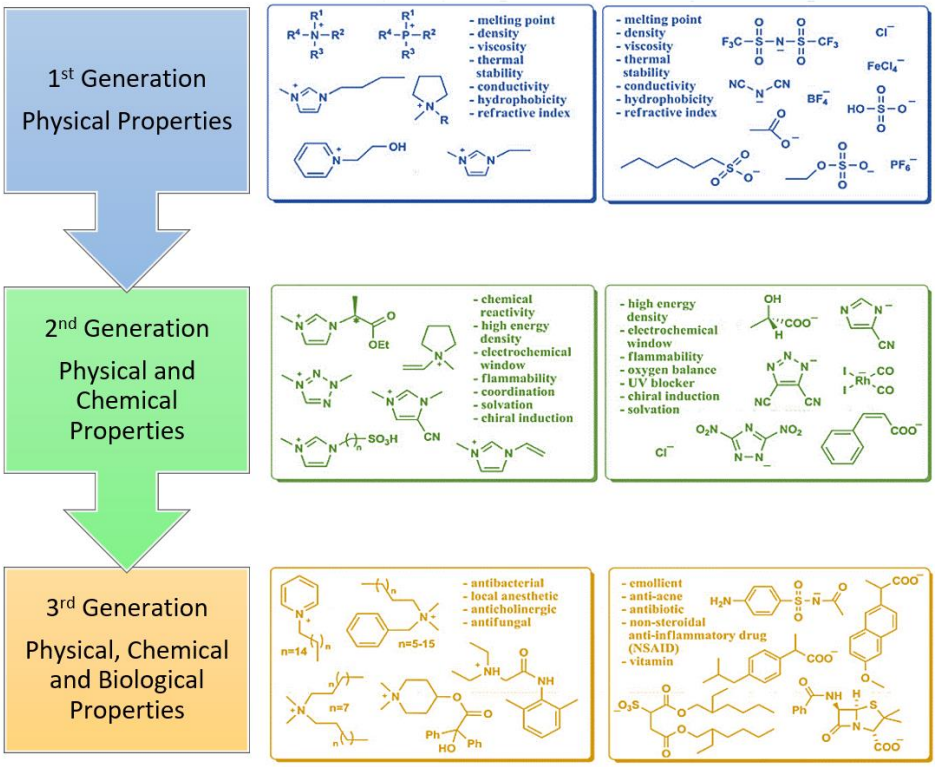

Figure 1. 19 | Ionic liquids generations. (adapted from 134)

Nevertheless, the potential application of ILs in pharmaceutical field it is not restricted to the development of API-ILs. It is also possible to use ILs as alternative solvents for the synthesis of APIs and for the discovery of new polymorphs according to the capability to promote a selective crystallization of APIs. Recent works reported the potential application of biocompatible ILs for API formulations (simple mixture of API and ILs) and to facilitate the drug delivery and specific administration to the body. Thus, ILs allied to pharmaceutical several development stages allows to overcome common problems associated to many drugs.[140–144]

4.1.1. Choline-based ILs

Discovered in 1862 by Adolph Strecker, this quaternary ammonium cation is classified as an essential nutrient for human health with important functions in human body such as being responsible for the correct maintenance of several organs or metabolic functions.[145–148] Choline intake from food was underestimated since it can be synthesized endogenously through the liver through a transferase enzyme (phosphatidylethanolamine N-methyltransferase), however, it was found that its biosynthesis did not produce an adequate amount for healthy maintenance of human metabolism. Thus, considering the gender and age of the population, in 1998 an adequate intake of choline was established by the Institute of Medicine Food and Nutrition Board.[149,150] This important nutrient can be found in two possible forms in the food (Figure 1. 20). The water-soluble structures include choline itself, a phosphorylated choline form (phosphocholine) and glycerophosphocholine scaffolds. Between lipid-soluble units, it is possible to find the two major components of cellular membranes, phosphatidylcholine and sphingomyelin which present distinct absorption and metabolism associated.[151]

(A) Water-soluble forms

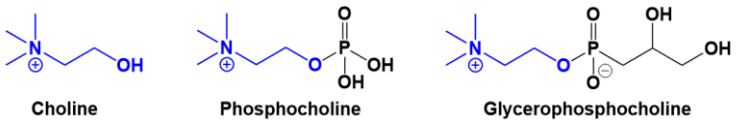

(B) Lipid-soluble forms

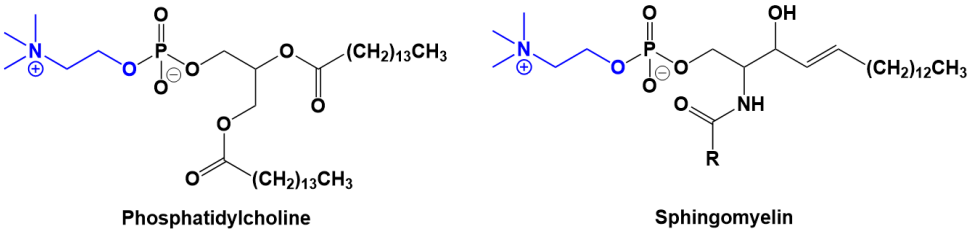

Figure 1. 20 | Structures of choline forms already found in food(adapted from 151)

Choline functions can be divided into four distinct synthetic pathways that leads to the formation of different important compounds as can be observed in Figure 1. 21. Through the formation of betaine, choline act as a source of methyl groups used in methionine cycle, an important step for several biochemical processes such as amino acids metabolism and cellular methylation.[152,153] Choline is one of the precursors of membrane phospholipids (phosphatidylcholine and sphingomyelin), the structural components of cell membranes involved in signal transduction between neurons. Moreover, it is essential for the synthesis of lipoproteins which are proteins responsible for lipids transport.[154] More specifically and in the context of this thesis, this nutrient can be used as a precursor to the synthesis of acetylcholine (ACh), a neurotransmitter with a broad range of important functions in the human body. Being essential for normal brain and muscles functioning, ACh is a signalling compound synthesized from two precursors, choline and acetyl-coenzyme A (acetyl-CoA), in the nerve cells by the enzyme choline acetyltransferase (ChAT). After the complete synthesis, this

chemical messenger is stored in vesicles and released from the terminal of a nerve cell to bind to a specific receptor present in another neuron surface. This process, called synapse, allows the change of information between the two neurons and it is essential to a healthy brain function. The loss of communication between neurons due to the degeneration of functional synaptic process contributes to the loss of important cognitive functions. Therefore, this neuronal network failure is one of the key points of Alzheimer's disease and cholinergic drugs (pharmaceutical compounds with a direct action on the receptor for acetylcholine, see section 1.2) are reported as one of the therapeutic strategies currently used in this disorder.[152,155–157] Additionally, Choline can be also metabolized to produce trimethylamine (TMA) and, subsequently, trimethylamine-N-oxide (TMAO) by flavin monooxygenases in the liver.[158,159]

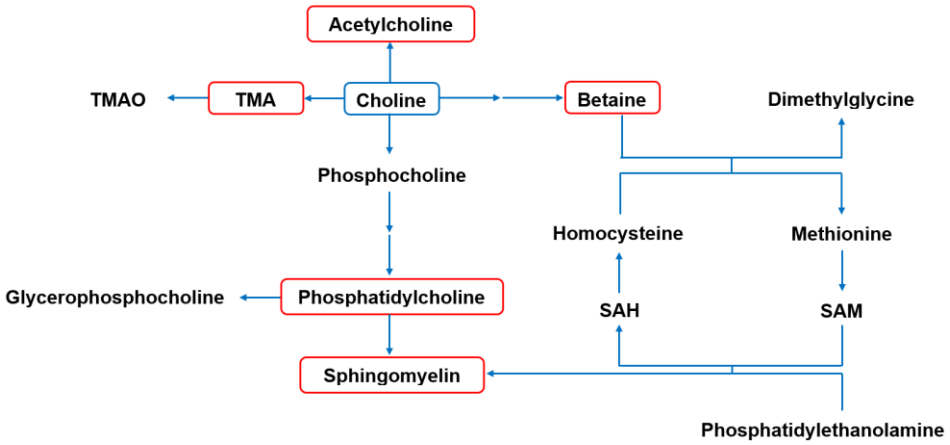

Figure 1. 21 | Synthetic pathways of choline metabolism. (adapted from 160)

Considering choline biological functions, it is evident that this nutrient plays an important role in human metabolism maintenance. Examples of choline *sources in the food include* eggs, liver, milk, and peanuts. It is well-

documented that choline deficiency in the human body can have serious biochemical consequences and, also, can result in several diseases such as fatty liver disease, liver and muscle damages and neurological disorders.[151,161] Taking into account the biological properties of choline, their use as organic cation in IL formulations has been largely explored. The reduced toxicity, low-cost and commercial availability of choline are additional factors for the interest to be considered. One of the major disadvantages of choline-based ILs is related to the tendency for crystallization.[162] The toxicity associated to this nutrient-based organic salts is highly dependent on cholinium cation structural modifications. The chemical changes including the introduction of alkyl substituents and the type of counter-ion mainly contribute for the intrinsic toxicity.[163]

4.1.2. Magnetic Ionic liquids

Magnetic Ionic Liquids (MILs) as a sub-class of low melting organic salts are composed by high-spin transition metals (d and f-blocks of the periodic table) and rare earth metals used as anions of the IL structure. These compounds combine the peculiar properties of ILs with the ability to respond to an external magnetic field. MILs were firstly described in 2004 by Hayashi and Hamaguchi by the synthesis of 1-Butyl-3-methylimidazolium tetrachloroferrate ([BMIM][$FeCl_4$]). After this first report, MILs have been attracting greater attention from the scientific community over the years due to their paramagnetic properties. Applications of MILs include their use in fluid-fluid separations, catalysis (with easy separation of MIL by magnetic manipulation and further recycling of the material), in desulfurization or microextraction processes, as probes for vesicles, in polymer chemistry, in microemulsions formulation, in CO_2 separation/capture procedures, in electrochemical devices and biological studies.[164–177] Also, due to their

paramagnetic properties, MILs as well as other systems such as magnetic nanoparticles, have been recently studied as potential contrast agents for Magnetic Resonance imaging (MRI) technique.[165] It is well-known that the higher toxicity associated to Gd (III) complexes is one of the major drawback of their application as contrast agents. In this context, the potential use of MILs can be a good alternative to the commercially available systems. The possibility to tune their properties and intrinsic toxicity by changing its cation and/or anion units is very attractive to be explored. Also, these organic salts are easily prepared and present highly chemical and thermal stability.[42,171,178]

4.2. Nanomaterials

Nano-based technology has been attained greater attention in the last few decades. This technology is defined *"as engineering and manufacturing of materials, devices, and systems at an incredibly small scale".*[179] The distinctive properties mostly associated to their size, shape, charge, and, also, to their surface area and reactivity, makes these nanomaterials (NMs) one of the most studied and potentially applied technology. The possibility of design their physical and chemical properties by changing their composition, has been allowing to increase substantially their applications range.[180,181] The industrial applications of nanomaterials include the cosmetics (*e.g.* hair care products, make-up formulation, anti-aging cosmetic products), as energy storage materials (*e.g.* hydrogen storage, lithium-ion batteries) and in automobiles production (*e.g.* surface glass coatings, fuel and oils additives). More recently, these materials have been also explored for biomedical applications. Figure 1. 22 illustrated some different types of nanomaterials used in medicine.[182]

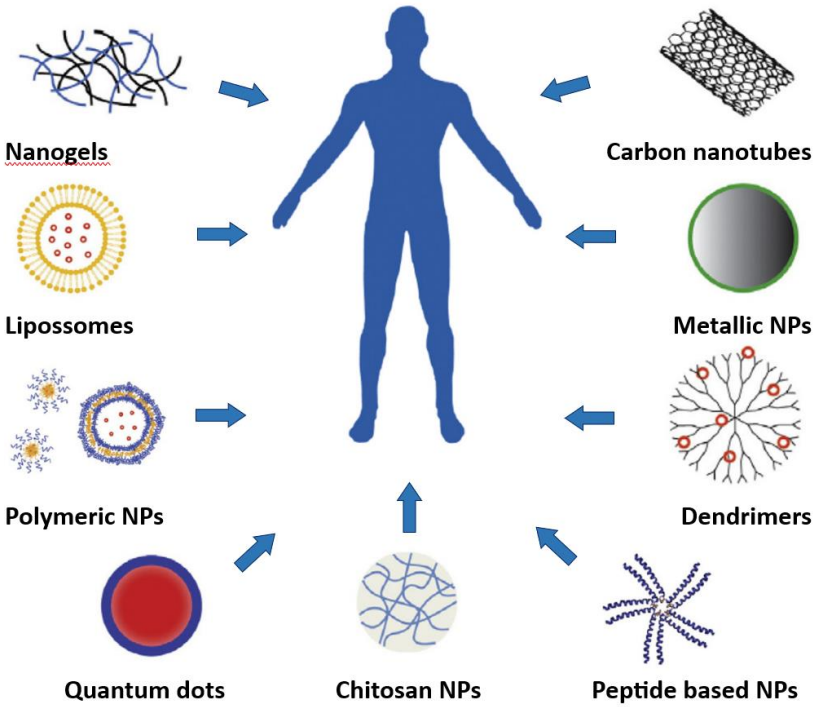

Figure 1. 22 | Different nanomaterials explored for biomedical applications (adapted from 182)

Nanomaterials are defined by ISO (International Organization for Standardization) as *"a material with any external dimension in the nanoscale or having internal structure or surface structure in the nanoscale; nanoscale is defined as the size range from approximately 1 nm to 100 nm".*[183] Today, there is a wide range of materials that are being used that can be included in this definition. Between them it is possible to find the nanospheres, nanorods, micelles and liposomes, among many others. In Figure 1. 23 are illustrated some of these nanomaterials.

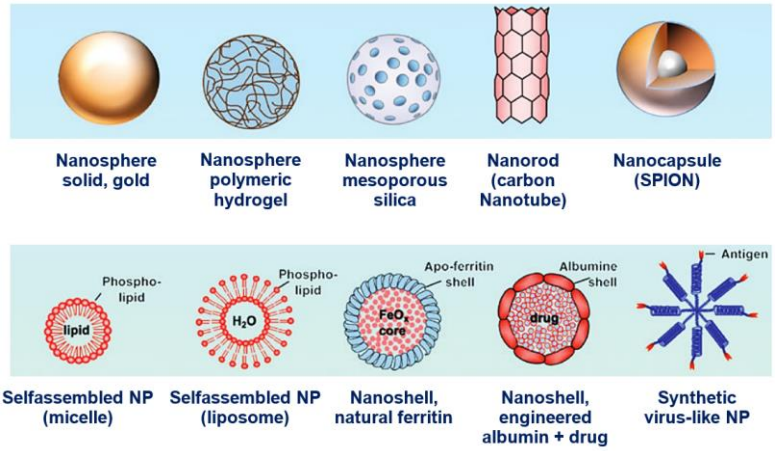

Figure 1. 23 | Schematic illustration of different nanomaterials.(adapted from 183)

Specifically, in this work, mesoporous silica nanoparticles are going to be more explored.

4.2.1. Mesoporous Silica Nanoparticles

Silica is recognized as safe material by FDA with application in cosmetics, as dietary supplement and in biomedical field including in the formulation of many different drugs and as a drug delivery carrier.[184–186] Silica-based nanomaterials, according to IUPAC (International Union of Pure and Applied Chemistry) can be divided into three classes according to their pore size: microporous (with diameters smaller than 2nm), mesoporous (with diameters in the range of 2 to 50 nm) and macroporous (with diameters values higher than 50 nm).[187] Specifically, mesoporous silica nanoparticles (MSNs) has received enormous attention as well as being the subject of several studies. This fact is mainly due to their unique properties such as high specific surface area, surface reactivity and tuneable pore size. It is, in fact, the porous structure as well as the possibility of varying the pore size that makes these nanoparticles an efficient system for biomedical applications (*e.g.* drug

delivery systems). The porous structure of silica NPs provides cavities that can be used to load guest molecules (bioactive compounds, proteins, metal complexes, among others) allowing their use as delivery vehicles for a drug-controlled release. Also, their surface can be functionalized due to the presence of silanol groups (Figure 1. 24). This functionalization can be useful to improve the accomplishment of nanoparticles functions.[188–191]

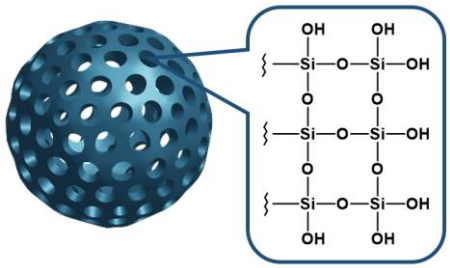

Figure 1. 24 | Silanol network of functionalized silica nanoparticles

Mesoporous silica is reported as an amorphous material possessing a more chaotic organization comparing to crystalline silica. This lack of organization contributes to the lower toxicity as well as easier excretion of this compound form. Amorphous silica-based nanoparticles are excreted in the urine after their hydrolytic degradation that gives rise to the biocompatible and water-soluble silicic acid. Also, when inhaled, due to their larger surface area and, consequently, to their higher solubility within the lung, this form of silica is quickly and easily cleared. Crystalline forms of silica, when inhaled initiate a progressive injury mechanism that can, eventually, end with the development of fibrosis. Additionally, porous amorphous silica, in opposition to nonporous materials, can be more rapidly degraded due to the presence of mesopores.[186,192]

Between the mesoporous materials can be distinguished several types of nanoparticles (Figure 1. 25), but two families represent the most prepared and studied types of nanoparticles: M41S (that includes Mobile Composition of Matter type, MCM-41 and MCM-48) and SBA (Santa Barbara Amorphous, SBA15).[187,193]

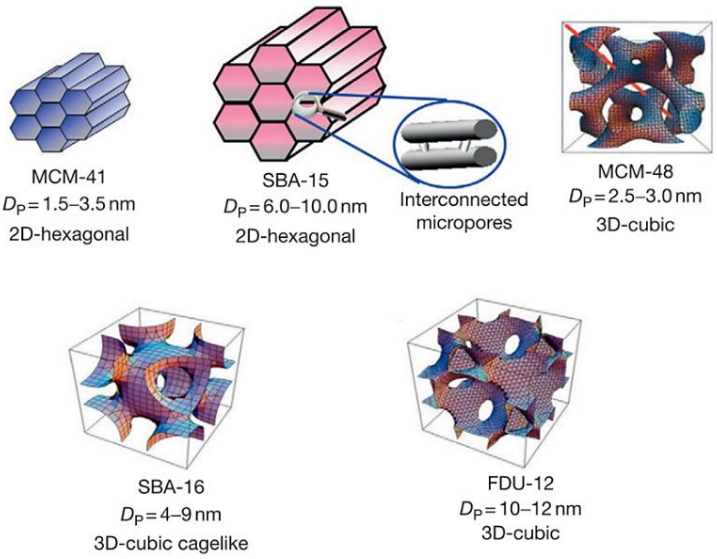

Figure 1. 25 | Examples of different types of nanoparticles (adapted from 194)

MSNs can be prepared by a supramolecular self-assembly mechanism using a surfactant in aqueous solution. The preparation process is indicated in Figure 1. 26. Surfactant molecules act as a template to generate the materials porosity and provides the required *"surface"* for the polymerization process that occurs by electrostatic and hydrogen bonding interactions. Polymerization is made through the hydrolysis of silica precursors followed by a condensation step at the hydrophilic surfactant interface. Finally, surfactant molecules are removed by calcination or solvent extraction and amorphous mesoporous silica nanoparticles are obtained.

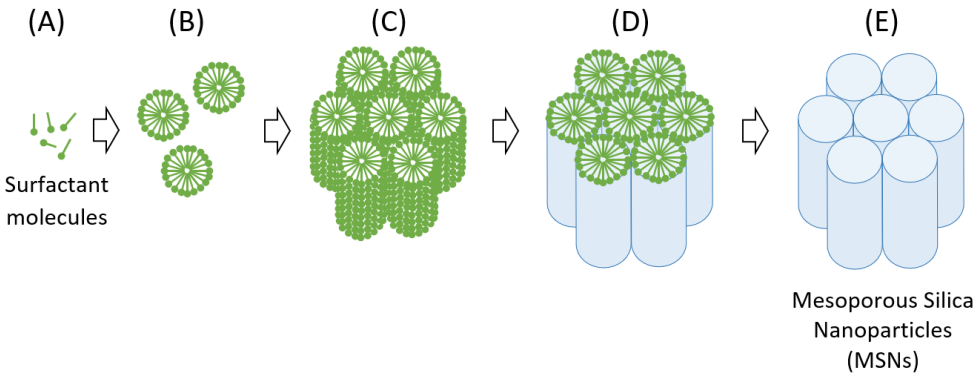

Figure 1. 26 | Illustration of the condensed synthetic procedure of MSNs preparation

Mesoporous materials are usually obtained with a spherical, rod or oval shape and large surface areas. Also, uniformly organized mesopores with large pore volumes can be attained.[193,195–197] Nanoparticles shape and pore size can be tuned by changing the synthesis conditions (*i.e.* stirring rate and temperature, among others) and surfactant alkyl chain size, respectively.

4.2.2. MSNs functionalization and metal complexation

After the preparation of the mesoporous silica nanoparticles, silanol groups presented in all nanoparticle structure (*i.e.*, inside the pores and in the external surface) can be functionalized. This functionalization can be performed through two methods described in Figure 1. 27: post-synthesis anchoring or one-pot co-condensation.[189]

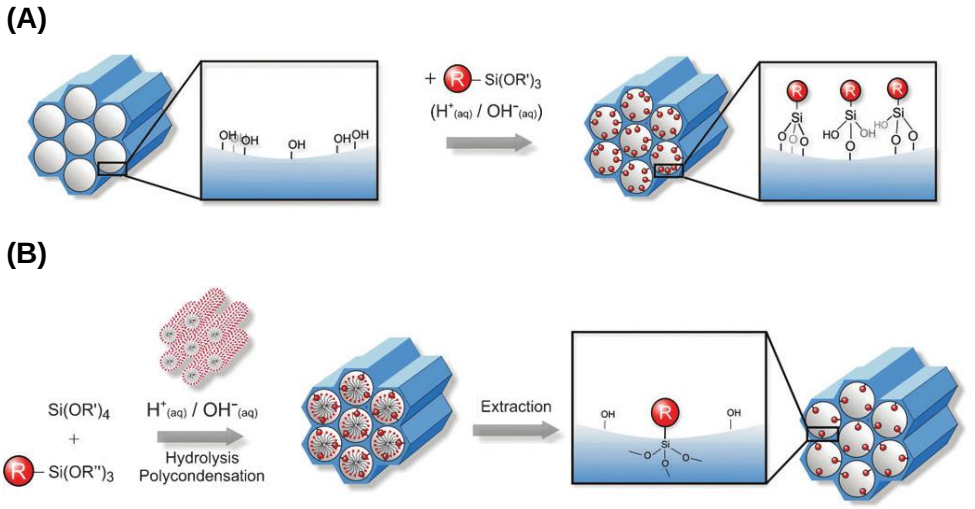

Figure 1. 27 | Functionalization methods: (a) Post-synthesis anchoring and (b) One-pot method (adapted from 198)

Post-synthesis anchoring method is mostly used in order to functionalize silica surface with different organic groups. A reaction between silanol groups and a trialkoxysilane is the bottom of this process whose advantage relies in the possibility of functionalizing either the pore or the external silica surface. The disadvantage of this method is related with the limited concentration of grafted organic groups and the heterogeneous distribution coverage of silica surface. Anchoring process results in a well-defined structure with a preserved morphology and, also, as a function of the selected alkoxysilane used in the reaction, allows to modulate properties such as the charge, hydrophobicity degree and/or textural features of the material. Additionally, due to the presence of the anchored functionalities, enables to perform secondary reactions and add organic molecules such as ligands or metal complexes. In one-pot co-condensation method, the introduction of the trialkoxysilane is performed simultaneously with the gel formation. Higher loadings percentage of organic functionalities and homogeneous distribution

on silica are the major advantages associated to this process. One-pot route can influence important properties of the structure of the desired materials such as its morphology, particle size and porosity. However, this method can lead to the major disadvantage of this functionalization route, the formation of materials with less ordered structure. Once the introduction of organic functionalities in the external and/or internal surface of silica walls, materials mesostructural order can be compromised. [189,194]

Within the mesoporous materials, MCM-41, MCM-48 and SBA family (SBA-15 and SBA-1), arises as the most used nanoparticles type to design nanomaterials that can be used as MRI probes. As already mentioned in section 2.2, paramagnetic MRI contrast agents are usually based on gadolinium chelates. In addition to the two methods described in Figure 25, chelating agents can also be introduced through reactions with functional groups previously incorporated into the nanoparticles surface.[189] Gadolinium can be inserted through a covalent conjugation where the metal is previously coordinated with the chelate molecule or by performing the complexation reaction after the introduction of chelate structure. [199]

References

(1) Cano, A.; Sánchez-López, E.; Ettcheto, M.; López-Machado, A.; Espina, M.; Souto, E. B.; Galindo, R.; Camins, A.; García, M. L.; Turowski, P. Current Advances in the Development of Novel Polymeric Nanoparticles for the Treatment of Neurodegenerative Diseases. *Nanomedicine* 2020, *15*, 1239–1261.

(2) Gao, H.-M.; Hong, J.-S. Why Neurodegenerative Diseases Are Progressive: Uncontrolled Inflammation Drives Disease Progression. *Trends Immunol.* 2008, *29* (8), 357–365.

(3) Brodal, P. *The Nervous System: Structure and Function*, 4th Ed.; Oxford University Press: New York, 2010.

(4) Fields, D. The Hidden Brain. *Sci. Am. Mind* 2011, *22*, 52–59.

(5) Mason, P. *Medical Neurobiology*; Oxford University Press: New York, 2011.

(6) Adejare, A. *Drug Discovery Approaches for the Treatment of Neurodegenerative Disorders: Alzheimer's Disease*; Academic Press - Elsevier, 2017.

(7) *World Health Organization*. Available online: https://www.who.int/. Last acessed: May 2021.

(8) Budson, A. E.; Solomon, P. R. *Memory Loss, Alzheimer's Disease, and Dementia*, 2nd Ed.; Elsevier Inc: China, 2016.

(9) Van Cauwenberghe, C.; Van Broeckhoven, C.; Sleegers, K. The Genetic Landscape of Alzheimer Disease: Clinical Implications and Perspectives. *Genet. Med.* 2016, *18* (5), 421–430.

(10) Atri, A. The Alzheimer's Disease Clinical Spectrum: Diagnosis and Management. *Med. Clin. North Am.* 2019, *103*, 263–293.

(11) Bishara, D.; Sauer, J.; Taylor, D. The Pharmacological Management of Alzheimer' s Disease. *Prog. Neurol. Psychiatry* 2015, 9–16.

(12) Wolfe, M. S. *The Molecular and Cellular Basis of Neurodegenerative Diseases*; Academic Press - Elsevier, 2018.

(13) Dugger, B. N.; Dickson, D. W. Pathology of Neurodegenerative Diseases. *Cold Spring Harb. Perspect. Biol.* 2016, *9*, a028035 (1-22).

(14) LaFerla, F. M.; Green, K. N.; Oddo, S. Intracellular Amyloid-β in Alzheimer's Disease. *Nat. Rev. Neurosci.* 2007, *8* (7), 499–509.

(15) Ryan, N. S.; Nicholas, J. M.; Weston, P. S. J.; Liang, Y.; Lashley, T.; Guerreiro, R.; Adamson, G.; Kenny, J.; Beck, J.; Chavez-gutierrez, L.; Strooper, B. De; Revesz, T.; Holton, J.; Mead, S.; Rossor, M. N.; Fox, N. C. Clinical Phenotype and Genetic Associations in Autosomal Dominant Familial Alzheimer ' s Disease : A Case Series. *Lancet Neurol.* 2016, *15* (13), 1326–1335.

(16) Hardy, J. Amyloid, the Presenilins and Alzheimer's Disease. *Trends Neurosci.* 1997, *20* (4), 154–159.

(17) Zheng, H.; Koo, E. H. Molecular Neurodegeneration The Amyloid Precursor Protein: Beyond Amyloid. *Mol. Neurodegener.* 2006, *1*, 5 (1-12).

(18) O'Brien, R.; Wong, P. Amyloid Precursor Protein Processing and Alzheimer's Disease. *Annu. Rev. Neurosci.* 2011, *1987*, 185–204.

(19) Thinakaran, G.; Koo, E. H. Amyloid Precursor Protein Trafficking, Processing, and Function. *J. Biol. Chem.* 2008, *283* (44), 29615–29619.

(20) Heppner, F. L.; Ransohoff, R. M.; Becher, B. Immune Attack: The Role of Inflammation in Alzheimer Disease. *Nat. Publ. Gr.* 2015, *16* (6), 358–372.

(21) Humpel, C. Identifying and Validating Biomarkers for Alzheimer's Disease.

Trends Biotechnol. 2011, *29* (1), 26–32.

(22) Chen, G. F.; Xu, T. H.; Yan, Y.; Zhou, Y. R.; Jiang, Y.; Melcher, K.; Xu, H. E. Amyloid Beta: Structure, Biology and Structure-Based Therapeutic Development. *Acta Pharmacol. Sin.* 2017, *38*, 1205–1235.

(23) Barage, S. H.; Sonawane, K. D. Amyloid Cascade Hypothesis: Pathogenesis and Therapeutic Strategies in Alzheimer's Disease. *Neuropeptides* 2015, *52*, 1–18.

(24) Guo, Y.; Wang, Q.; Chen, S.; Xu, C. Functions of Amyloid Precursor Protein in Metabolic Diseases. *Metabolism.* 2021, *115*, 154454.

(25) John, A.; Reddy, P. H. Synaptic Basis of Alzheimer's Disease: Focus on Synaptic Amyloid Beta, P-Tau and Mitochondria. *Ageing Res. Rev.* 2021, *65* (October 2020), 101208.

(26) Li, Y.; Sun, H.; Chen, Z.; Xu, H.; Bu, G.; Zheng, H. Implications of GABAergic Neurotransmission in Alzheimer's Disease. *Front. Aging Neurosci.* 2016, *8*, 1–12.

(27) Kaur, S.; DasGupta, G.; Singh, S. Altered Neurochemistry in Alzheimer's Disease: Targeting Neurotransmitter Receptor Mechanisms and Therapeutic Strategy. *Neurophysiology* 2019, *51* (4), 293–309.

(28) DaSilva, K. A.; Shaw, J. E.; McLaurin, J. Amyloid-β Fibrillogenesis: Structural Insight and Therapeutic Intervention. *Exp. Neurol.* 2010, *223*, 311–321.

(29) Buell, A. K. The Growth of Amyloid Fibrils: Rates and Mechanisms. *Biochem. J.* 2019, *476*, 2677–2703.

(30) H. Sack Jr., G. Pathophysiology of Amyloid Fibril Formation. *Amyloid Dis.* 2019, 1–11.

(31) Chiti, F.; Dobson, C. M. Protein Misfolding, Functional Amyloid, and Human Disease. *Annu. Rev. Biochem.* 2006, *75*, 333–366.

(32) Dovidchenko, N. V.; Leonova, E. I.; Galzitskaya, O. V. Mechanisms of Amyloid Fibril Formation. *Biochem.* 2014, *79*, 1515–1527.

(33) Iannuzzi, C.; Irace, G.; Sirangelo, I. The Effect of Glycosaminoglycans (GAGs) on Amyloid Aggregation and Toxicity. *Molecules* 2015, *20* (2), 2510–2528.

(34) Marsh, J.; Alifragis, P. Synaptic Dysfunction in Alzheimer's Disease: The Effects of Amyloid Beta on Synaptic Vesicle Dynamics as a Novel Target for Therapeutic Intervention. *Neural Regen. Res.* 2018, *13* (4), 616–623.

(35) He, Y.; Wei, M.; Wu, Y.; Qin, H.; Li, W.; Ma, X.; Cheng, J.; Ren, J.; Shen, Y.; Chen, Z.; Sun, B.; Huang, F. De; Shen, Y.; Zhou, Y. D. Amyloid β Oligomers Suppress Excitatory Transmitter Release via Presynaptic Depletion of Phosphatidylinositol-4,5-Bisphosphate. *Nat. Commun.* 2019, *10* (1), 1–18.

(36) Karisetty, B. C.; Bhatnagar, A.; Armour, E. M.; Beaver, M. Amyloid- β Peptide

Impact on Synaptic Function and Neuroepigenetic Gene Control Reveal New Therapeutic Strategies for Alzheimer ' s Disease. *Front. Mol. Neurosci.* 2020, *13*, 1–8.

(37) Kalhor, H. R.; Kamizi, M.; Akbari, J.; Heydari, A. Inhibition of Amyloid Formation by Ionic Liquids: Ionic Liquids Affecting Intermediate Oligomers. *Biomacromolecules* 2009, *10* (9), 2468–2475.

(38) Geerts, H.; Grossberg, G. T. Pharmacology of Acetylcholinesterase Inhibitors and N-Methyl-D-Aspartate Receptors for Combination Therapy in the Treatment of Alzheimer's Disease. *J. Clin. Pharmacol.* 2006, *46*, 8S-16S.

(39) Glynn-Servedio, B. E.; Ranola, T. S. AChE Inhibitors and NMDA Receptor Antagonists in Advanced Alzheimer's Disease. *Consult. Pharm.* 2017, *32*, 511–518.

(40) Nygaard, H. B. Current and Emerging Therapies for Alzheimer's Disease. *Clin. Ther.* 2013, *35* (10), 1480–1489.

(41) Atri, A. Effective Pharmacological Management of Alzheimer's Disease. *Am. J. Manag. Care* 2011, *17* (13), S346–S355.

(42) *Food and Drug Administration*. Available online: https://www.fda.gov/. Last acessed: July 2023.

(43) Valotassiou, V.; Malamitsi, J.; Papatriantafyllou, J.; Dardiotis, E.; Tsougos, I.; Psimadas, D.; Alexiou, S.; Hadjigeorgiou, G.; Georgoulias, P. SPECT and PET Imaging in Alzheimer's Disease. *Ann. Nucl. Med.* 2018, *32* (9), 583–593.

(44) Ulanova, M.; Poljak, A.; Wen, W.; Bongers, A.; Gloag, L.; Gooding, J.; Tilley, R.; Sachdev, P.; Braidy, N. Nanoparticles as Contrast Agents for the Diagnosis of Alzheimer's Disease: A Systematic Review. *Nanomedicine* 2020, *15* (7), 725–743.

(45) Vemuri, P.; Jack, C. R. Role of Structural MRI in Alzheimer's Disease. *Alzheimer's Res. Ther.* 2010, *2* (4), 23.

(46) Frisoni, G. B.; Fox, N. C.; Jack, C. R.; Scheltens, P.; Thompson, P. M. The Clinical Use of Structural MRI in Alzheimer Disease. *Nat. Rev. Neurol.* 2010, *6* (2), 67–77.

(47) Ramusino, M. C.; Garibotto, V.; Bacchin, R.; Altomare, D.; Dodich, A.; Assal, F.; Mendes, A.; Costa, A.; Tinazzi, M.; Morbelli, S. D.; Bauckneht, M.; Picco, A.; Dottorini, M. E.; Tranfaglia, C.; Farotti, L.; Salvadori, N.; Moretti, D.; Savelli, G.; Tarallo, A.; Nobili, F.; Parapini, M.; Cavaliere, C.; Salvatore, E.; Salvatore, M.; Boccardi, M.; Frisoni, G. B. Incremental Value of Amyloid-PET versus CSF in the Diagnosis of Alzheimer's Disease. *Eur. J. Nucl. Med. Mol. Imaging* 2020, *47* (2), 270–280.

(48) De Leon, M. J.; Desanti, S.; Zinkowski, R.; Mehta, P. D.; Pratico, D.; Segal, S.; Clark, C.; Kerkman, D.; Debernardis, J.; Li, J.; Lair, L.; Reisberg, B.; Tsui, W.; Rusinek, H. MRI and CSF Studies in the Early Diagnosis of Alzheimer's

Disease. *J. Intern. Med.* 2004, *256*, 205–223.

(49) Valotassiou, V.; Angelidis, G.; Psimadas, D.; Tsougos, I.; Georgoulias, P. In the Era of FDG PET, Is It Time for Brain Perfusion SPECT to Gain a Place in Alzheimer's Disease Imaging Biomarkers? *Eur. J. Nucl. Med. Mol. Imaging* 2020, 969–971.

(50) Waters, E. A.; Wickline, S. A. Contrast Agents for MRI. *Basic Res. Cardiol.* 2008, *103*, 114–121.

(51) Geraldes, C. F. G. C.; Laurent, S. Classification and Basic Properties of Contrast Agents for Magnetic Resonance Imaging. *Contrast Media Mol. Imaging* 2009, *4*, 1–23.

(52) Westbrook, C.; Kaut Roth, C.; Talbot, J. *MRI in Pactice*, 4th Ed.; Wiley Blackwell, 2011.

(53) Dale, B. M.; Brown, M. A.; Semelka, R. C. *MRI Basic Principles and Applications*, 5th Ed.; Wiley Blackwell, 2015.

(54) Chang, R.; Overby, J. *General Chemistry, The Essential Concepts*, 6th Ed.; McGraw-Hill: New York, 2011.

(55) Weishaupt, D.; Marincek, B. *Spin and the Nuclear Magnetic Resonance Phenomenon*, 2nd Ed.; Springer-Verlag Berlin Heidelberg, 2008.

(56) Buxton, R. B. *Introduction to Functional Magnetic Resonance Imaging*, 2nd Ed.; Cambridge University Press: New York, 2009.

(57) Brown, R. W.; Cheng, Y.-C. N.; Haacke, E. M.; Venkatesan, R. *MRI Physical Principles and Sequence Design*, 2nd Ed.; Wiley Blackwell, 2014.

(58) Westbrook, C. *At a Glance*, 3rd Ed.; John Wiley & Sons: Chichester, United Kingdom, 2016.

(59) Kuperman, V. *Magnetic Resonance Imaging Physical Principles and Applications*; Academic Press: United States of America, 2000.

(60) Wright, C.; Morris, D. M.; Baker, P. N.; Sci, B.; Crocker, I. P.; Gowland, P. A.; Parker, G. J.; Colin, P. Europe PMC Funders Group Magnetic Resonance Imaging Relaxation Time Measurements of the Placenta at 1.5 T. *Placenta* 2013, *32* (12), 1010–1015.

(61) Grover, V. P. B.; Tognarelli, J. M.; Crossey, M. M. E.; Cox, I. J.; Taylor-robinson, S. D.; Mcphail, M. J. W. Magnetic Resonance Imaging: Principles and Techniques: Lessons for Clinicians. *J. Clin. Exp. Hepatol.* 2015, *5* (3), 246–255.

(62) Constantinides, C. *The Basics Magnetic Resonance Imaging*; CRC Press, 2014.

(63) Westbrook, C.; Talbot, J. *MRI in Practice*; Wiley Blackwell, 2019.

(64) Bushong, S. C.; Clarke, G. D. *Magnetic Resonance Imaging - Physical and*

Biological Principles, 4th Ed.; Elsevier: United States of America, 2015.

(65) Claridge, T. D. W. *High-Resolution NMR Techniques in Organic Chemistry*, 3rd Ed.; Elsevier, 2016.

(66) Gunther, H. *NMR Spectroscopy - Basic Principles, Concepts and Applications in Chemistry*, 3rd Ed.; WILEY-VCH: Singapore, 2013.

(67) Bjørnerud, A. MR Contrast Agents. In *The Physics of Magnetic Resonance Imaging*; 2008; pp 129–153.

(68) Xiao, Y. D.; Paudel, R.; Liu, J.; Ma, C.; Zhang, Z. S.; Zhou, S. K. MRI Contrast Agents: Classification and Application (Review). *Int. J. Mol. Med.* 2016, *38*, 1319–1326.

(69) Wahsner, J.; Gale, E. M.; Rodríguez-Rodríguez, A.; Caravan, P. Chemistry of MRI Contrast Agents: Current Challenges and New Frontiers. *Chem. Rev.* 2019, *119* (2), 957–1057.

(70) De León-Rodríguez, L. M.; Martins, A. F.; Pinho, M. C.; Rofsky, N. M.; Sherry, A. D. Basic MR Relaxation Mechanisms and Contrast Agent Design. *J. Magn. Reson. Imaging* 2015, *42*, 545–565.

(71) Yon, M.; Billotey, C.; Marty, J. D. Gadolinium-Based Contrast Agents: From Gadolinium Complexes to Colloidal Systems. *Int. J. Pharm.* 2019, *569*, 118577.

(72) Baykara, M.; Ozcan, M.; Bilgen, M.; Kelestimur, H. Effects of Gadolinium and Gadolinium Chelates on Intracellular Calcium Signaling in Sensory Neurons. *Neurosci. Lett.* 2019, *707*, 134295.

(73) Sutresno, A.; Haryanto, F.; Viridi, S.; Arif, I. Influence Blocking by Gadolinium in Calcium Diffusion on Synapse Model: A Monte Carlo Simulation Study. *J. Biomed. Phys. Eng.* 2020, *10* (3), 251–260.

(74) Ramalho, J.; Ramalho, M. Gadolinium Deposition and Chronic Toxicity. *Magn. Reson. Imaging Clin. N. Am.* 2017, *25* (4), 765–778.

(75) Davies, J.; Siebenhandl-Wolff, P.; Tranquart, F.; Jones, P.; Evans, P. Gadolinium: Pharmacokinetics and Toxicity in Humans and Laboratory Animals Following Contrast Agent Administration. *Arch. Toxicol.* 2022, *96* (2), 403–429.

(76) Mochida, S. Presynaptic Calcium Channels. *Neurosci. Res.* 2018, *127*, 33–44.

(77) Rogosnitzky, M.; Branch, S. Gadolinium-Based Contrast Agent Toxicity: A Review of Known and Proposed Mechanisms. *BioMetals* 2016, *29* (3), 365–376.

(78) Dolphin, A. C.; Lee, A. Presynaptic Calcium Channels: Specialized Control of Synaptic Neurotransmitter Release. *Nat. Rev. Neurosci.* 2020, *21*, 213–229.

(79) Clough, T. J.; Jiang, L.; Wong, K. L.; Long, N. J. Ligand Design Strategies to Increase Stability of Gadolinium-Based Magnetic Resonance Imaging Contrast Agents. *Nat. Commun.* 2019, *10*, 1420 (1-14).

(80) *Drug development & delivery*. Available online: https://drug-dev.com/. Last acessed: January 2022.

(81) Hao, D.; Ai, T.; Goerner, F.; Hu, X.; Runge, V. M.; Tweedle, M. MRI Contrast Agents: Basic Chemistry and Safety. *J. Magn. Reson. Imaging* 2012, *36* (5), 1060–1071.

(82) Aime, S.; Barge, A.; Gianolio, E.; Pagliarin, R.; Silengo, L.; Tei, L. High Relaxivity Contrast Agents for MRI and Molecular Imaging. In *Molecular Imaging, An Essential Tool in Preclinical Research, Diagnostic Imaging, and Therapy*; Bogdanov Jr., A. A., Licha, K., Eds.; Springer-Verlag Berlin Heidelberg: Germany, 2005; pp 99–121.

(83) Tóth, É.; Helm, L.; Merbach, A. E. *Relaxivity of MRI Contrast Agents*; 2002.

(84) Raymond, K. N.; Pierre, V. C. Next Generation, High Relaxivity Gadolinium MRI Agents. *Bioconjug. Chem.* 2005, *16* (1), 3–8.

(85) Verwilst, P.; Park, S.; Yoon, B.; Kim, J. S. Recent Advances in Gd-Chelate Based Bimodal Optical/MRI Contrast Agents. *Chem. Soc. Rev.* 2015, *44*, 1791–1806.

(86) Rashid, H. U.; Yu, K.; Zhou, J. Lanthanide(III) Chelates as MRI Contrast Agents: A Brief Description. *J. Struct. Chem.* 2013, *54* (1), 223–249.

(87) Werner, E. J.; Datta, A.; Jocher, C. J.; Raymond, K. N. High-Relaxivity MRI Contrast Agents: Where Coordination Chemistry Meets Medical Imaging. *Angew. Chemie - Int. Ed.* 2008, *47*, 8568–8580.

(88) Angelovski, G. What We Can Really Do with Bioresponsive MRI Contrast Agents. *Angew. Chemie - Int. Ed.* 2016, *55*, 7038–7046.

(89) Botta, M. Second Coordination Sphere Water Molecules and Relaxivity of Gadolinium(III) Complexes: Implications for MRI Contrast Agents. *Eur. J. Inorg. Chem.* 2000, 399–407.

(90) Zhou, Z.; Yang, L.; Gao, J.; Chen, X. Structure–Relaxivity Relationships of Magnetic Nanoparticles for Magnetic Resonance Imaging. *Adv. Mater.* 2019, *31*, 1804567 (1-32).

(91) Cordeiro, R.; Beira, M. J.; Cruz, C.; Figueirinhas, J. L.; Corvo, M. C.; Almeida, P. L.; Rosatella, A. A.; Afonso, C. A. M.; Daniel, C. I.; Sebastião, P. J. Tuning the 1H NMR Paramagnetic Relaxation Enhancement and Local Order of [Aliquat]+-Based Systems Mixed with DMSO. *Int. J. Mol. Sci.* 2021, *22*, 706 (1-18).

(92) Pinheiro dos Santos, T. J.; Parambathu, A. V.; Fraenza, C. C.; Walsh, C.; Greenbaum, S. G.; Chapman, W. G.; Asthagiri, D.; Singer, P. M. Thermal and Concentration Effects on 1 H NMR Relaxation of Gd 3+ -Aqua Using MD

Simulations and Measurements. *Phys. Chem. Chem. Phys.* 2022, 27964–27975.

(93) Singer, P. M.; Parambathu, A. V.; Pinheiro Dos Santos, T. J.; Liu, Y.; Alemany, L. B.; Hirasaki, G. J.; Chapman, W. G.; Asthagiri, D. Predicting 1H NMR Relaxation in Gd3+-Aqua Using Molecular Dynamics Simulations. *Phys. Chem. Chem. Phys.* 2021, *23* (37), 20974–20984.

(94) Torrey, H. C. Nuclear Spin Relaxation by Translational Diffusion. *Phys. Rev.* 1953, *92* (4), 962–969.

(95) Freed, J. H. Dynamic Effects of Pair Correlation Functions on Spin Relaxation by Translational Diffusion in Liquids. II. Finite Jumps and Independent T 1 Processes. *J. Chem. Phys.* 1978, *68* (9), 4034–4037.

(96) Faux, D. A.; Istók, Ö.; Rahaman, A. A.; McDonald, P. J.; McKiernan, E.; Brougham, D. F. Nuclear Spin Relaxation in Aqueous Paramagnetic Ion Solutions. 2021, 1–39.

(97) Kumar, S.; Udgaonkar, J. B. Mechanisms of Amyloid Fibril Formation by Proteins. *Curr. Sci.* 2010, *98*, 639–656.

(98) Kaminski, C. F.; Schierle, G. S. K. Probing Amyloid Protein Aggregation with Optical Superresolution Methods : From the Test Tube to Models of Disease. *Neurophotonics* 2016, *3* (4), 041807.

(99) Nilsson, K. P. R. Small Organic Probes as Amyloid Specific Ligands - Past and Recent Molecular Scaffolds. *FEBS Lett.* 2009, *583* (16), 2593–2599.

(100) Reinke, A. A.; Gestwicki, J. E. Insight into Amyloid Structure Using Chemical Probes. *Chem. Biol. Drug Des.* 2011, *77* (6), 399–411.

(101) Brahmachari, G. *Green Synthetic Approaches for Biologically Relevant Heterocycles*; Elsevier Inc., 2015.

(102) Biancalana, M.; Koide, S. Molecular Mechanism of Thioflavin-T Binding to Amyloid Fibrils. *Biochim. Biophys. Acta - Proteins Proteomics* 2010, *1804*, 1405–1412.

(103) Howie, A. J.; Brewer, D. B. Optical Properties of Amyloid Stained by Congo Red: History and Mechanisms. *Micron* 2009, *40*, 285–301.

(104) Lau, S. K. Amyloid Staining. In *Basic and advanced laboratory techniques in histopathology and cytology*; Dey, P., Ed.; Springer: India, 2018; pp 109–112.

(105) Aliyan, A.; Cook, N. P.; Martí, A. A. Interrogating Amyloid Aggregates Using Fluorescent Probes. *Chem. Rev.* 2019, *119*, 11819–11856.

(106) Xu, M.; Ren, W.; Tang, X.; Hu, Y.; Zhang, H. Advances in Development of Fluorescent Probes for Detecting Amyloid-β Aggregates. *Acta Pharmacol. Sin.* 2016, *37*, 719–730.

(107) Li, M.; Zhao, C.; Yang, X.; Ren, J.; Xu, C.; Qu, X. In Situ Monitoring Alzheimer's Disease β-Amyloid Aggregation and Screening of Aβ Inhibitors

Using a Perylene Probe. *Small* 2013, *9* (1), 52–55.

(108) Liu, Y.; Pukala, T. L.; Musgrave, I. F.; Williams, D. M.; Dehle, F. C.; Carver, J. a. Gallic Acid Is the Major Component of Grape Seed Extract That Inhibits Amyloid Fibril Formation. *Bioorg. Med. Chem. Lett.* 2013, *23* (23), 6336–6340.

(109) Das, U.; Hariprasad, G.; Ethayathulla, A. S.; Manral, P.; Das, T. K.; Pasha, S.; Mann, A.; Ganguli, M.; Verma, A. K.; Bhat, R.; Chandrayan, S. K.; Ahmed, S.; Sharma, S.; Kaur, P.; Singh, T. P.; Srinivasan, A. Inhibition of Protein Aggregation: Supramolecular Assemblies of Arginine Hold the Key. *PLoS One* 2007, *2*, e1176.

(110) Lashuel, H. A.; Hartley, D. M.; Balakhaneh, D.; Aggarwal, A.; Teichberg, S.; Callaway, D. J. E. New Class of Inhibitors of Amyloid-?? Fibril Formation: Implications for the Mechanism of Pathogenesis in Alzheimer's Disease. *J. Biol. Chem.* 2002, *277* (45), 42881–42890.

(111) Branco, L. C.; Pina, F. Intrinsically Photochromic Ionic Liquids. *Chem. Commun. (Camb).* 2009, 6204–6206.

(112) Delgado, J. M.; Raymundo, A.; Vilarigues, M.; Branco, L. C.; Laia, C. A. T. Characterization of a Novel Intrinsic Luminescent Room-Temperature Ionic Liquid Based on [P6,6,6,14][ANS]. *Chem. - A Eur. J.* 2015, *21*, 726–732.

(113) Pina, F. Espectrofluorimetria. *Química* 1994, *54*, 1–5.

(114) Wardle, B. *Principles and Applications of Photochemistry*; John Wiley & Sons: Chichester, 2009.

(115) Lakowicz, J. R. *Principles of Fluorescence Spectroscopy*; Springer Science & Business Media: New York, 2006.

(116) Dejay, R. A. C. Polarization Portraits of Light- Harvesting Antennas : From Single Molecule Spectroscopy to Imaging, Faculty of Science, Lund University, 2014.

(117) Atkins, P.; Paula, J. de; Friedman, R. Fundamentals. In *Quanta, Matter, and Change, A molecular approach to physical chemistry*; W. H. Freeman and Company: China, 2009; pp 1–13.

(118) Montalti, M.; Credi, A.; Prodi, L.; Gandolfi, M. T. *Handbook of Photochemistry*, 3rd ed.; Taylor & Francis Group: Boca Raton, Florida, 2006.

(119) Valeur, B. *Molecular Fluorescence: Principles and Applications*; WILEY-VCH: Weinheim, 2001.

(120) *Photochemistry and Photophysics*; Vincenzo Balzani, Ceroni, P., Juris, A., Eds.; WILEY-VCH, 2014.

(121) *Web of Science*. Available online: https://www.webofscience.com/wos/woscc/basic-search. Last acessed: March 2023.

(122) Atkins, P., Paula, J. Molecular Spectroscopy. In *Physical Chemistry*; Oxford University Press, 2010; pp 417–486.

(123) Collins, S. P.; Dolbnya, I.; Palmer, B. A.; Edwards-Gau, G. R.; Morte-Ródenas, A.; Kariuki, B. M.; Lim, G. K.; Harris, K. D. M.; Joly, Y. X-Ray Birefringence in Highly Anisotropic Materials. *J. Phys. Conf. Ser.* 2013, *425*, 132015 (1-5).

(124) Mouquinho, A. I. M. New Polymeric Films for Smart Windows with Permanent Memory Effect, NOVA School of Science and Technology, PhD thesis, 2019.

(125) Koizumi, S.; Pernot, J.; Umezawa, H.; Suzuki, M. *Power Electronics Device Applications of Diamond Semiconductors*; Elsevier Ltd, 2018.

(126) *Openstax, The future of education*. Available online: https://openstax.org/books/university-physics-volume-3/pages/1-7-polarization. Last acessed: June 2023.

(127) Lei, Z.; Chen, B.; Koo, Y.-M.; MacFarlane, D. R. Introduction: Ionic Liquids. *Chem. Rev.* 2017, *117*, 6633–6635.

(128) Anastas, P. T. Origins and Early History of Green Chemistry. In *Advanced Green Chemistry: Part 1: Greener Organic Reactions and Processes*; Horváth, I. T., Malacria, M., Eds.; World Scientific, 2017; pp 1–17.

(129) Freemantle, M. *An Introduction to Ionic Liquids*; RSC Publishing, 2010.

(130) Plechkova, N. V.; Seddon, K. R. Applications of Ionic Liquids in the Chemical Industry. *Chem. Soc. Rev.* 2008, *37* (1), 123–150.

(131) Branco, L. C.; Rosa, J. N.; Moura Ramos, J. J.; Afonso, C. a. M. Preparation and Characterization of New Room Temperature Ionic Liquids. *Chem. - A Eur. J.* 2002, *8*, 3671–3677.

(132) Freire, M. G.; Ventura, S. P. M.; Santos, L. M. N. B. F.; Marrucho, I. M.; Coutinho, J. A. P. Evaluation of COSMO-RS for the Prediction of LLE and VLE of Water and Ionic Liquids Binary Systems. *Fluid Phase Equilib.* 2008, *268* (1–2), 74–84.

(133) Handy, S. T. *Ionic Liquids - Classes and Properties*; InTech: Rijeka, Croatia, 2011.

(134) Hough, W. L.; Smiglak, M.; Rodríguez, H.; Swatloski, R. P.; Spear, S. K.; Daly, D. T.; Pernak, J.; Grisel, J. E.; Carliss, R. D.; Soutullo, M. D.; Davis, J. H.; Rogers, R. D.; Davis, Jr., J. H.; Rogers, R. D.; Davis, J. H.; Rogers, R. D. The Third Evolution of Ionic Liquids: Active Pharmaceutical Ingredients. *New J. Chem.* 2007, *31* (8), 1429–1436.

(135) Wasserscheid, P.; Welton, T. *Ionic Liquids: Current State and Future Directions*; Shiflett, M. B., Scurto, A. M., Eds.; Oxford University Press, 2017.

(136) Gaune-escard, M.; Seddon, K. R. *Molten Salts and Ionic Liquids - Never the Twain?*; John Wiley & Sons: United States of America, 2010.

(137) Rogers, R. D.; Seddon, K. R. *Ionic Liquids IIIA: Fundamentals, Progress, Challenges, and Opportunities*, 1st Ed.; ACS Symposium Series, 2005.

(138) Plechkova, N. V.; Rogers, R. D.; Seddon, K. R.; Liquids, I.; Knowledge, F.; Series, A. C. S. S.; Society, A. C. *Ionic Liquids: From Knowledge to Application*; ACS Symposium Series: Washington, United States of America, 2009.

(139) Kadokawa, J. *Ionic Liquids - New Aspects for the Future*; InTech: Rijeka, Croatia, 2013.

(140) Pedro, S. N.; Freire, C. S. R.; Silvestre, A. J. D.; Freire, M. G. The Role of Ionic Liquids in the Pharmaceutical Field: An Overview of Relevant Applications. *Int. J. Mol. Sci.* 2020, *21*, 8298 (1-50).

(141) Lu, J.; Rohani, S. Polymorphism and Crystallization of Active Pharmaceutical Ingredients (APIs). *Curr. Med. Chem.* 2009, *16* (7), 884–905.

(142) Wu, X.; Zhu, Q.; Chen, Z.; Wu, W.; Lu, Y.; Qi, J. Ionic Liquids as a Useful Tool for Tailoring Active Pharmaceutical Ingredients. 2021, *338*, 268–283.

(143) Huang, W.; Wu, X.; Qi, J.; Zhu, Q.; Wu, W.; Lu, Y.; Chen, Z. Ionic Liquids : Green and Tailor-Made Solvents in Drug Delivery. *Drug Discov. Today* 2020, *25* (5), 901–908.

(144) Goto, M. Ionic Liquids as a Potential Tool for Drug Delivery Systems. *Medchemcomm* 2016, *7*, 1881–1897.

(145) Jr., J. W. E.; Macdonald, I. A.; Zeisel, S. H. *Present Knowledge in Nutrition*, 10th Ed.; Wiley Blackwell, 2012.

(146) Banfi, G.; Chan, C. P.; Chiesa, C.; Colombini, A.; Consoli, L.; Corrocher, R.; Coskun, M.; Csak, T.; Curtis, M. De; Delanghe, J. R.; Ferraro, F.; Girelli, D.; Grison, E.; Lanteri, P.; Lombardi, G.; Matinelli, N.; Natale, F.; Nielsen, O. H.; Olivieri, O.; Osborn, J. F.; Pacifico, L.; Petrasek, J.; Rainer, T. H.; Seidelin, J. B.; Speeckaert, M. M.; Seeckaert, R.; Szabo, G. *Advances in Clinical Chemistry*, 1st Ed.; Elsevier Inc., 2013.

(147) Blusztajn, J. K.; Slack, B. E.; Mellott, T. J. Neuroprotective Actions of Dietary Choline. *Nutrients* 2017, *9*, 815 (1-23).

(148) Zeisel, S. H. A Brief History of Choline. *Ann. Nutr. Metab.* 2012, *61*, 254–258.

(149) Zeisel, S. H.; Klatt, K. C.; Caudill, M. A. Nutrient Information. *Adv. Nutr.* 2018, *9*, 58–60.

(150) Wallace, T. C.; Blusztajn, J. K.; Caudill, M. A.; Klatt, K. C. The Underconsumed and Underappreciated Essential Nutrient. *Nutr. Today* 2018, *53* (6), 240–253.

(151) Wiedeman, A. M.; Barr, S. I.; Green, T. J.; Xu, Z.; Innis, S. M.; Kitts, D. D. Dietary Choline Intake: Current State of Knowledge across the Life Cycle. *Nutrients* 2018, *10*, 1513 (1-24).

(152) López-Cervantes, J.; Sánchez-Machado, D. I.; Campas-Baypoli, O. N.; Cantú-Soto, E. U.; Mora-López, G. S. de la. Influence of Other Nutrients (e.g., l-Arginine, Taurine, and Choline) on Liver Diseases. In *Influence of Nutrients, Bioactive Compounds, and Plant Extracts in Liver Diseases*; Alavian, S. M., Nabavi, S. M., Nabavi, S. F., Silva, A. S., Eds.; Academic Press - Elsevier: India, 2021; pp 193–208.

(153) Shen, W.; Gao, C.; Cueto, R.; Liu, L.; Fu, H.; Shao, Y.; Yang, W. Y.; Fang, P.; Choi, E. T.; Wu, Q.; Yang, X.; Wang, H. Homocysteine-Methionine Cycle Is a Metabolic Sensor System Controlling Methylation-Regulated Pathological Signaling. *Redox Biol.* 2020, *28*, 101322.

(154) Tayebati, S. K.; Amenta, F. Choline-Containing Phospholipids: Relevance to Brain Functional Pathways. *Clin. Chem. Lab. Med.* 2013, *51* (3), 513–521.

(155) Dowd, F. J.; Murrin, L. C.; Ralevic, V.; Scholar, E. M.; Summers, R. J.; Tew, K. D.; Wecker, L. *XPharm: The Comprehensive Pharmacology Reference*; Elsevier Inc., 2008.

(156) Laurent, G. J.; Shapiro, S. D. *Encyclopedia of Respiratory Medicine - Volume 1*; Elsevier Academic Press, 2006.

(157) Kashyap, G.; Bapat, D.; Das, D.; Gowaikar, R.; Amritkar, R. E.; Rangarajan, G.; Ravindranath, V.; Ambika, G. Synapse Loss and Progress of Alzheimer's Disease -A Network Model. *Sci. Rep.* 2019, *9* (1), 1–9.

(158) Zeisel, S. H.; DaCosta, K. A.; Youssef, M.; Hensey, S. Conversion of Dietary Choline to Trimethylamine and Dimethylamine in Rats: Dose-Response Relationship. *J. Nutr.* 1989, *119*, 800–804.

(159) Arias, N.; Arboleya, S.; Allison, J.; Kaliszewska, A.; Higarza, S. G.; Gueimonde, M.; Arias, J. L. The Relationship between Choline Bioavailability from Diet, Intestinal Microbiota Composition, and Its Modulation of Human Diseases. *Nutrients* 2020, *12*, 2340 (1-29).

(160) Artegoitia, V. M.; Middleton, J. L.; Harte, F. M.; Campagna, S. R.; De Veth, M. J. Choline and Choline Metabolite Patterns and Associations in Blood and Milk during Lactation in Dairy Cows. *PLoS One* 2014, *9*, e103412.

(161) Willett, W. C.; Giovannucci, E. *Epidemiology of Diet and Cancer Risk*, 11th Ed.; Ross, A. C., Caballero, B., Cousins, R. J., Tucker, K. L., Ziegler, T. R., Eds.; Lippincott Williams & Wilkins: China, 2014.

(162) Rosatella, A. A.; Siopa, F.; Frade, R. F. M.; Afonso, C. A. M. New Low Viscous Cholinium-Based Magnetic Ionic Liquids. *New J. Chem.* 2016, *40*, 3124–3129.

(163) Siopa, F.; Figueiredo, T.; Frade, R. F. M.; Neto, I.; Meirinhos, A.; Reis, C. P.; Sobral, R. G.; Afonso, C. A. M.; Rijo, P. Choline-Based Ionic Liquids : Improvement of Antimicrobial Activity. *Chem. Sel.* 2016, *1*, 5909–5916.

(164) O'Brien, J. T.; Firbank, M. J.; Davison, C.; Barnett, N.; Bamford, C.;

Donaldson, C.; Olsen, K.; Herholz, K.; Williams, D.; Lloyd, J. 18F-FDG PET and Perfusion SPECT in the Diagnosis of Alzheimer and Lewy Body Dementias. *J. Nucl. Med.* 2014, *55* (12), 1959–1965.

(165) Daniel, C. I.; Chávez, F. V.; Portugal, C. A. M.; Crespo, J. G.; Sebastiao, P. J. 1H NMR Relaxation Study of a Magnetic Ionic Liquid as a Potential Contrast Agent. *J. Phys. Chem. B* 2015, *119*, 11740–11747.

(166) Casado, N.; Zendegi, S.; Olmo, R. Del; Dominguez-Alfaro, A.; Forsyth, M. Tuning Electronic and Ionic Conductivities in Composite Materials for Electrochemical Devices. *ACS Appl. Polym. Mater.* 2021, *3*, 1777–1784.

(167) Stettner, T.; Balducci, A. Protic Ionic Liquids in Energy Storage Devices: Past, Present and Future Perspective. *Energy Storage Mater.* 2021, *40*, 402–414.

(168) Simões, M.; Pereira, A. R.; Simões, L. C.; Cagide, F.; Borges, F. Biofilm Control by Ionic Liquids. *Drug Discov. Today* 2021, *26* (6), 1340–1346.

(169) Nikfarjam, N.; Ghomi, M.; Agarwal, T.; Hassanpour, M.; Sharifi, E.; Khorsandi, D.; Ali Khan, M.; Rossi, F.; Rossetti, A.; Nazarzadeh Zare, E.; Rabiee, N.; Afshar, D.; Vosough, M.; Kumar Maiti, T.; Mattoli, V.; Lichtfouse, E.; Tay, F. R.; Makvandi, P. Antimicrobial Ionic Liquid-Based Materials for Biomedical Applications. *Adv. Funct. Mater.* 2021, *31*, 2104148 (1-27).

(170) Hayashi, S.; Hamaguchi, H. Discovery of a Magnetic Ionic Liquid [Bmim]FeCl4. *Chem. Lett.* 2004, *33* (12), 1590–1591.

(171) Gehlot, P. S.; Gupta, H.; Rathore, M. S.; Khatri, K.; Kumar, A. Intrinsic MRI Contrast from Amino Acid-Based Paramagnetic Ionic Liquids. *Mater. Adv.* 2020, *1* (6), 1980–1987.

(172) Li, L.; Huang, Y.; Yan, G.; Liu, F.; Huang, Z.; Ma, Z. Poly(3,4-Ethylenedioxythiophene) Nanospheres Synthesized in Magnetic Ionic Liquid. *Mater. Lett.* 2009, *63* (1), 8–10.

(173) Klee, A.; Prevost, S.; Kunz, W.; Schweins, R.; Kiefer, K.; Gradzielski, M. Magnetic Microemulsions Based on Magnetic Ionic Liquids. *Phys. Chem. Chem. Phys.* 2012, *14* (44), 15355–15360.

(174) He, M.; Liu, S.; Bai, L.; Liu, X. Propane/Propylene Separation and CO2 Capture in Magnetic Ionic Liquid [Bmim][FeCl4]. *Chem. Eng. Res. Des.* 2018, *137* (2012), 186–193.

(175) Clark, K. D.; Nacham, O.; Yu, H.; Li, T.; Yamsek, M. M.; Ronning, D. R.; Anderson, J. L. Extraction of DNA by Magnetic Ionic Liquids: Tunable Solvents for Rapid and Selective DNA Analysis. *Anal. Chem.* 2015, *87*, 1552–1559.

(176) Emaus, M. N.; Clark, K. D.; Hinners, P.; Anderson, J. L. Preconcentration of DNA Using Magnetic Ionic Liquids That Are Compatible with Real-Time PCR for Rapid Nucleic Acid Quantification. *Anal. Bioanal. Chem.* 2018, *410*, 4135–4144.

(177) Salama, A.; Hesemann, P. Recent Trends in Elaboration, Processing, and Derivatization of Cellulosic Materials Using Ionic Liquids. *ACS Sustain. Chem. Eng.* 2020, *8* (49), 17893–17907.

(178) Santos, E.; Albo, J.; Rosatella, A.; Afonso, C. A. M.; Irabien, A. Synthesis and Characterization of Magnetic Ionic Liquids (MILs) for CO2 Separation. *J. Chem. Technol. Biotechnol.* 2014, *89*, 866–871.

(179) Neves, A. R.; Reis, S. *Nanoparticles in Life Sciences and Biomedicine*; Pan Stanford Publishing Pte. Ltd: Singapore, 2018.

(180) Bundschuh, M.; Filser, J.; Lüderwald, S.; McKee, M. S.; Metreveli, G.; Schaumann, G. E.; Schulz, R.; Wagner, S. Nanoparticles in the Environment: Where Do We Come from, Where Do We Go To? *Environ. Sci. Eur.* 2018, *30*, 6 (1-17).

(181) Jeevanandam, J.; Barhoum, A.; Chan, Y. S.; Dufresne, A.; Danquah, M. K. Review on Nanoparticles and Nanostructured Materials: History, Sources, Toxicity and Regulations. *Beilstein J. Nanotechnol.* 2018, *9* (1), 1050–1074.

(182) Narain, R. *Polymer Science and Technology - Fundamentals and Applications*; Elsevier, 2020.

(183) Gubala, V.; Johnston, L. J.; Liu, Z.; Krug, H.; Moore, C. J.; Ober, C. K.; Schwenk, M.; Vert, M. Engineered Nanomaterials and Human Health: Part 1. Preparation, Functionalization and Characterization (IUPAC Technical Report). *Pure Appl. Chem.* 2018, *90* (8), 1283–1324.

(184) Fytianos, G.; Rahdar, A.; Kyzas, G. Z. Nanomaterials in Cosmetics: Recent Updates. *Nanomaterials* 2020, *10* (5), 1–16.

(185) Yang, Y. X.; Song, Z. M.; Cheng, B.; Xiang, K.; Chen, X. X.; Liu, J. H.; Cao, A.; Wang, Y.; Liu, Y.; Wang, H. Evaluation of the Toxicity of Food Additive Silica Nanoparticles on Gastrointestinal Cells. *J. Appl. Toxicol.* 2014, *34*, 424–435.

(186) Gisbert-Garzarán, M.; Vallet-Regí, M. Influence of the Surface Functionalization on the Fate and Performance of Mesoporous Silica Nanoparticles. *Nanomaterials* 2020, *10*, 916 (1-49).

(187) Jarmolińska, S.; Feliczak-Guzik, A.; Nowak, I. Synthesis, Characterization and Use of Mesoporous Silicas of the Following Types SBA-1, SBA-2, HMM-1 and HMM-2. *Materials (Basel).* 2020, *13* (19), 1–33.

(188) Hoang Thi, T. T.; Cao, V. Du; Nguyen, T. N. Q.; Hoang, D. T.; Ngo, V. C.; Nguyen, D. H. Functionalized Mesoporous Silica Nanoparticles and Biomedical Applications. *Mater. Sci. Eng. C* 2019, *99*, 631–656.

(189) Carniato, F.; Tei, L.; Botta, M. Gd-Based Mesoporous Silica Nanoparticles as MRI Probes. *Eur. J. Inorg. Chem.* 2018, 4936–4954.

(190) Manzano, M.; Vallet-Regí, M. Mesoporous Silica Nanoparticles for Drug Delivery. *Adv. Funct. Mater.* 2020, *30* (2), 3–5.

(191) Wang, Y.; Zhao, Q.; Han, N.; Bai, L.; Li, J.; Liu, J.; Che, E.; Hu, L.; Zhang, Q.; Jiang, T.; Wang, S.; Mpharm, Y. W.; Zhao, Q.; Han, N.; Mpharm, L. H. L. B.; Mpharm, J. L.; Mpharm, J. L.; Mpharm, E. C.; Mpharm, L. H. L. B.; Zhang, Q.; Jiang, T.; Wang, S. Mesoporous Silica Nanoparticles in Drug Delivery and Biomedical Applications. *Nanomedicine Nanotechnology, Biol. Med.* 2015, *11* (2), 313–327.

(192) O'Reilly, K. M. A.; Phipps, R. P.; Thatcher, T. H.; Graf, B. A.; Van Kirk, J.; Sime, P. J. Crystalline and Amorphous Silica Differentially Regulate the Cyclooxygenase-Prostaglandin Pathway in Pulmonary Fibroblasts: Implications for Pulmonary Fibrosis. *Am. J. Physiol. - Lung Cell. Mol. Physiol.* 2005, *288*, 1010–1016.

(193) Mehmood, A.; Ghafar, H.; Yaqoob, S.; Gohar, U. F.; Ahmad, B. Mesoporous Silica Nanoparticles: A Review. *J. Dev. Drugs* 2017, *6*, 1000174.

(194) Madrid, U. C. De; Tab, C. Ordered Mesoporous Silica Materials. 2011, 497–514.

(195) Bharti, C.; Gulati, N.; Nagaich, U.; Pal, A. K.; Gulati, N. Mesoporous Silica Nanoparticles in Target Drug Delivery System: A Review. *Int. J. Pharm. Investig.* 2015, *5*, 124–133.

(196) Issa, A. A.; Luyt, A. S. Kinetics of Alkoxysilanes and Organoalkoxysilanes Polymerization: A Review. *Polymers (Basel).* 2019, *11*, 537 (1-41).

(197) Asefa, T.; Tao, Z. Biocompatibility of Mesoporous Silica Nanoparticles. *Chem. Res. Toxicol.* 2012, *25*, 2265–2284.

(198) Hoffmann, F. Vitalising Porous Inorganic Silica Networks with Organic Functions—PMOs and Related Hybrid Materials. *Chem. Soc. rev.* 2011, *40*, 608–620.

(199) Bruckman, M. A.; Yu1, X.; Steinmetz, N. F. Engineering Gd-Loaded Nanoparticles to Enhance MRI Sensitivity via T1 Shortening. *Nanotechnology* 2013, *24*, 462001.

Chapter 2

Development of magnetic and luminescent ionic systems

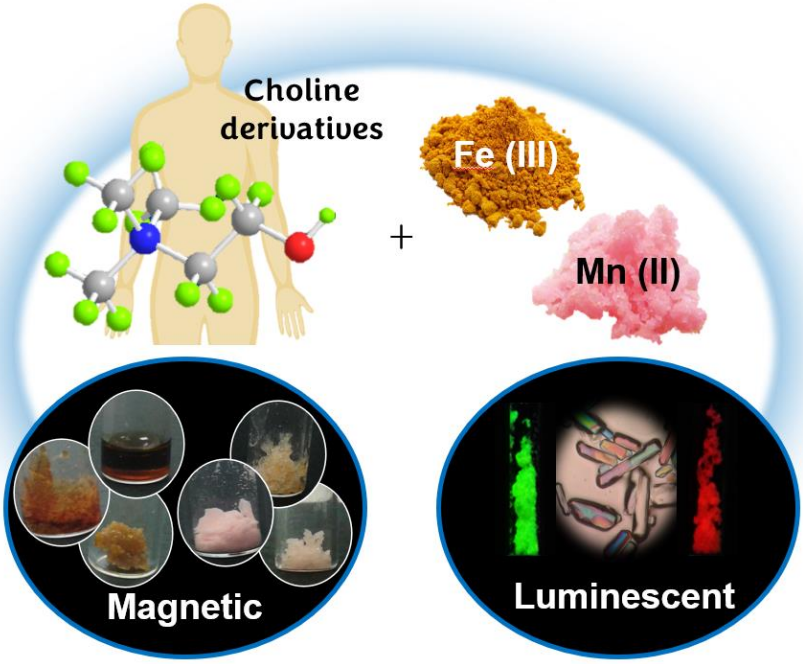

This chapter was adapted from the article “Synthesis and characterization of choline derivative salts incorporating magnetic metallic anions”, Andreia Forte, Sandra Gago, Celso Alves, Joana Silva, Joana Alves, Rui Pedrosa, César A. T. Laia, Isabel M. Marrucho, Luís C. Branco *(submitted for publication*).

Chapter 2

Development of magnetic and luminescent ionic systems

Abstract

Choline is an important nutrient involved in several essential functions of our body. Thus, a set of halogenated organic salts based on choline derivatives were developed from three low-cost amines using sustainable methodologies. These different choline derivative cations were combined with tetrachloroferrate ($FeCl_4$) and trichloromangate ($MnCl_3$) anions as to obtain task-specific magnetic ionic liquids and organic salts. All compounds were characterized by spectroscopic techniques and different physical or thermal properties such as the magnetic susceptibility for metal anion salts were evaluated. Compounds $[N_{1,1,2,C3OH}][FeCl_4]$ and $[N_{1,1,4,C3OH}][FeCl_4]$ were obtained as liquids at room temperature while the other organic salts possessed higher melting points. For both selected transition metals, the effective magnetic moment (μ_{eff}) was lower for long side or branched alkyl chains and in the presence of an additional ethanol group on the cation scaffold. Cytotoxicity assessment of chloride and manganese-based salts was performed to evaluate the biocompatibility of these compounds. Also, luminescence of manganese (II)-based salts was evaluated according to their, luminescence colour, quantum yield and lifetime decay. A correlation with salts structural features was performed.

1. Introduction

In the last years, Ionic Liquids (ILs) have been applied in many research fields due to their peculiar properties such as negligible volatility, high chemical and thermal stability, as well as the possibility to tune their physical-chemical properties by suitable cation-anion combinations. In general, room temperature ILs (RTILs) are largely applied as alternative solvents for

different research fields, such as organic synthesis, catalysis [1–3], as electrolytes for batteries and electrochemistry [3–5], analytical chemistry [6,7] and material science as lubricant fluids [8–10]. More recently, a third generation of ILs have been applied in pharmaceutical area incorporating an active principle ingredient (API-ILs) [11–13] as cation or anion. According to good solvation properties from ILs, they have been also reported to extract, stabilize and dissolve several organic, inorganic and polymeric compounds.[14] Due to the wide range of ILs applications, it became important to extend the toxicity studies of the different classes of ILs. Nowadays, it is important to mention that the type of IL cation and the size of their substituents has a greater effect in the IL toxicity comparing to the anion influence. Frequently the anion structure has a more relevant effect on the physical and chemical properties of the salt and even its impact on the toxicity is sometimes neglected. [15,16]

Choline is a quaternary ammonium cation with an ethanol group that can be synthesized endogenously or ingested through the diet, and it is necessary for important functions in the human body. The ethanol group from choline allows the reduction of the toxicity associated to tetraalkylammonium cations and increases the biocompatibility of these compounds. [17–19] In 2004, Hayashi and Hamaguchi reported the first magnetic IL based on tetrachloroferrate anion, [BMIM][$FeCl_4$].[20] Then, the same authors illustrated an unexpected strong response to a magnet at room temperature for two magnetic ILs containing tetrachloroferrate (III) ions, [BMIM][$FeCl_4$] and [C_nMIM][$FeCl_4$]. [21,22] In the last years, different magnetic ILs containing iron and other paramagnetic ions such as cobalt (II), manganese (II), cooper (I), ruthenium (III), gadolinium (III) and terbium (III) have gained greater attention.[23–27] These organic salts, as already mentioned in Chapter 1, can combine simultaneously ionic liquid properties as well as magnetic

properties, in particular their response to strong magnetic fields.[28,29] As discussed, magnetic IL applications were in the past frequently focused on catalysis and separation processes but, more recently, they are also being associated to a wider variety of applications such as electrochemical devices, as electrolytes and solvents in the polymerization of conducting polymers and as carrier liquid to produce magnetic fluids. Moreover, these magnetic salts have been investigated about their application in medical area, namely as contrast agents for magnetic resonance image (MRI).[23,30,31] Although being a topic under development, the common structures selected for the preparation of magnetic ionic liquids are still based in imidazolium, tetraalkylphosphonium and tetraalkylammonium cations. Thus, choline and its derivatives comparatively arise as a more biocompatible cation family. As an important part of human body metabolism, this nutrient can decrease the toxicity associated to the presence of metal anions in the final magnetic products and, also, increase the bioavailability of the magnetic organic salt.
Herein, different choline derivative salts combined with tetrachloroferrate (III) and trichloromanganese (II) were prepared and characterized. Physical and thermal properties of the prepared ILs and organic salts were performed. Furthermore, cytotoxicity of some compounds *in vitro* assays in four different cells was evaluated. Figure 2. 1 illustrates the chemical structure of the different prepared choline derivative salts.

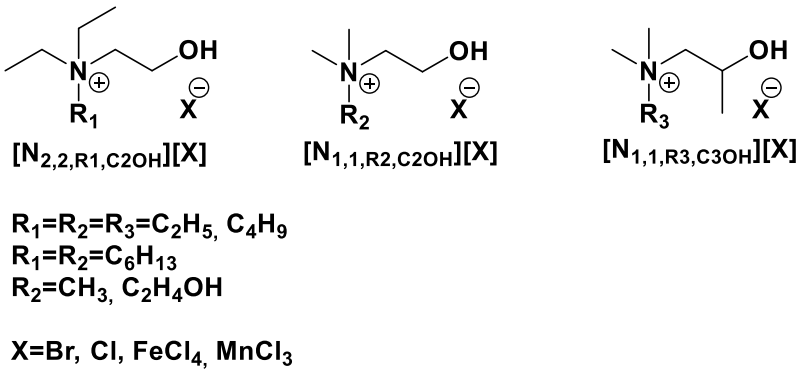

Figure 2. 1 | General scheme of biocompatible ILs and organic salts based on choline derivatives.

Additionally, during this work, it was possible to carry out a preliminary study related to manganese (II) salts and their luminescence properties. The use of more than one imaging technique simultaneously has been gaining over the last few decades an important role between the diagnosis tools studied and applied today. These multimodality imaging systems arise as a powerful tool that can improve important features such as the detection sensitivity and the accuracy of the clinical diagnostic.[32] Specifically, the combination of MRI with a fluorescence method can be useful to overcome these two techniques drawbacks. Although optical methods based on fluorescence properties necessarily require the preparation of specific materials and their response has a poor tissue penetration, their methodology it is single-cell sensitive and is particularly useful to perform fluorescence-guided surgeries.[33] Thus, fluorescence imaging can allow to overcome an important MRI limitation related with its low sensitivity. The combination of these two imaging methods can increase MRI sensitivity at cellular and subcellular levels.[34] Also, it is possible to obtain a low-cost combined methodology with non-radiative properties and an ultra-high spatial resolution.[35] Hence, manganese (II)-based complexes prepared in this work, were studied according to their

luminescence colour, quantum yield and lifetime decay. Also, a correlation with salts structural features was performed.

2. Results and Discussion

2.1. Synthesis and characterization of choline derivatives salts

Optimized alkylation methods from commercial and low-cost tertiary amines were performed for the preparation of a set of choline derivatives cations. To obtain these compounds, different alkyl chains (C_2, C_4 and C_6) and functionalized groups (alcohols) were introduced in the tertiary amines structures. The synthesis of these new ammonium salts was accomplished in ethanol under reflux for 48 h (Scheme 2. 1). It was used a slight excess of the alkyl halide in order to increase the amines quaternization yield. All synthesized organic cations were characterized by ^{1}H-NMR, FT-IR, and elemental analysis (C, H, N). The new cations structures were obtained in moderate to high yields (53-95%) except for [$N_{1,1,4,C3OH}$][Cl] salt (32%). The reduced yield observed in this case can be justified due to the lower reactivity of starting chloride alkylating agent as well as the presence of a secondary alcohol in the amine scaffold. Generally, these choline derivatives cations are hygroscopic and highly soluble in water, acetone and different alcohols. On the contrary, due to the presence of an ethanol group conferring a polar nature, these compounds show a very low solubility in other organic solvents such as dichloromethane, diethyl ether and alkanes. The relative purity obtained for the halogenated ammonium salts was evaluated by ^{1}H-NMR analysis by comparing the spectra and it revealed a high purity level (≥93%). Some physical and thermal properties of these organic salts, such as

physical state, melting and decomposition temperatures and densities (in the case of room temperature ILs) are indicated in Table 2. 1. The majority of the salts were obtained as solids at room temperature but $[N_{1,1,2,C3OH}][Cl]$ arises as a RTIL example. Additionally, $[N_{1,1,6,C2OH}][Br]$ and $[N_{1,1,2,C3OH}][Br]$ salts can be also included in the ionic liquids definition since they present melting points smaller than 100 ºC. For the remaining compounds, the melting temperatures were determined, however, in some cases, only decomposition temperatures were observed. Transition and decomposition temperatures can change according with the structural features of the organic cations. In general, the bromo-based salts possess higher melting points than the correspondent chloro-based salts. Also, as expected, longer alkyl chains in cation unit are associated to a decrease in the melting point or decomposition temperatures (e.g. $[N_{2,2,2,C2OH}][Br]$, $[N_{2,2,4,C2OH}][Br]$ and $[N_{2,2,6,C2OH}][Br]$) except for the cases of $[N_{1,1,2,C3OH}][Cl]$ and $[N_{1,1,4,C3OH}][Cl]$. When an additional ethanol group was introduced (e.g. $[N_{1,1,1,C2OH}][Cl]$ and $[N_{1,1,C2OH,C2OH}][Cl]$), it was not possible to determine the melting points of the salts but only its decomposition temperatures.

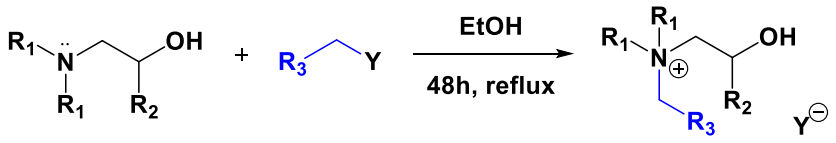

Scheme 2. 1 | Synthetic methodology for the preparation of biocompatible choline derivatives cations-based ionic liquids.

Table 2. 1 | Physical properties of halogen-based ionic liquids and organic salts based on Choline derivatives cations.

Organic Salt	PhysicalState	Yield (%)	Purity [a] (%)	Tm (Td) [b] (ºC)
$[N_{1,1,1,C2OH}][Cl]$	-	-	-	302 [d] [26]
$[N_{2,2,2,C2OH}][Br]$	Yellow Solid	93	>98	(221)
$[N_{2,2,2,C2OH}][Cl]$	Brown Solid	77	>99	(211)
$[N_{2,2,4,C2OH}][Br]$	Yellow Solid	61	99	90
$[N_{2,2,6,C2OH}][Br]$	Yellow Solid	53	93	55
$[N_{1,1,2,C2OH}][Br]$	White Solid	79	>99	(285)
$[N_{1,1,4,C2OH}][Cl]$	White Solid	75	>99	121
$[N_{1,1,6,C2OH}][Br]$	Yellow Solid	91	96	67 [d] [26]
$[N_{1,1,C2OH,C2OH}][Cl]$	White Solid	56	>99	(222)
$[N_{1,1,2,C3OH}][Br]$	Brown Solid	85	98	39
$[N_{1,1,2,C3OH}][Cl]$ [c]	Brown Liquid	79	>98	RTIL
$[N_{1,1,4,C3OH}][Cl]$	Yellow Solid	32	>99	108

[a] Purity obtained from ^{1}H-NMR spectroscopy. [b] Melting temperature (Tm) and decomposition temperature (Td) was determined on Electrothermal Melting Point Apparatus. [c] Density measurements were performed using a pycnometer at 20 ºC. The value obtained for $[N_{1,1,2,C3OH}][Cl]$ was 0.95g/ml. [d] Value obtained from the literature.

2.2. Synthesis and characterization of choline and derivatives-based magnetic salts

Different magnetic organic salts containing tetrachloroferrate (III) and trichloromanganese (II) anions and biocompatible choline derivative cations were prepared as described in Scheme 2. 2. When the ammonium counter-ion is chloride anion, the magnetic salt is synthesized through a direct complexation reaction with a metal chloride salt (Scheme 2. 2, Method 1). However, if the ammonium starting material was bromide-based on, it was necessary to change the bromide anion to a chloride anion by using an ionic exchange resin (Scheme 2. 2, Method 2) and then perform the complexation

reaction. These reactions were made without any additional purification steps.

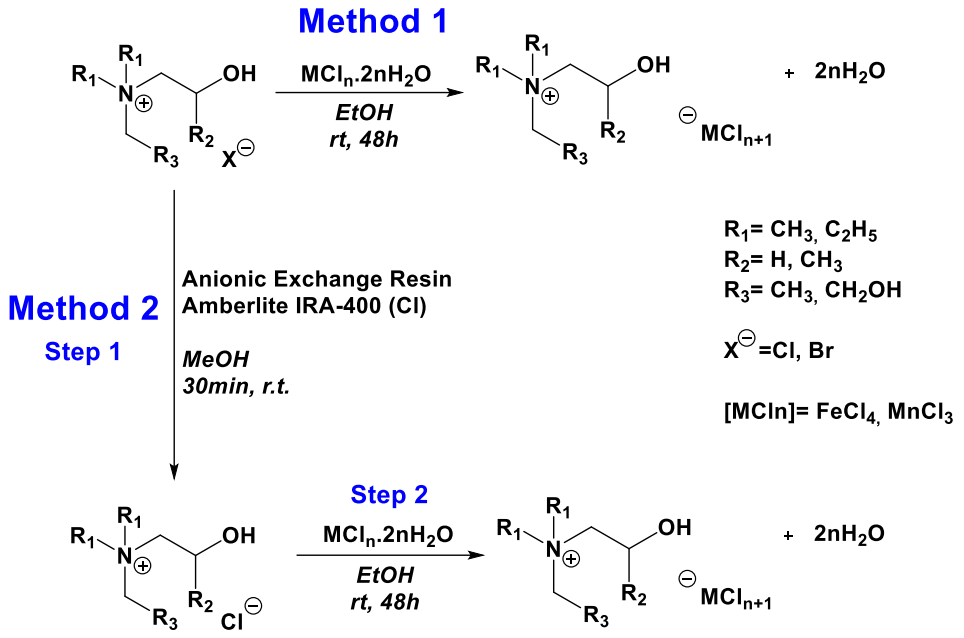

Scheme 2. 2 | Synthetic methodology from the preparation of magnetic organic salts based on Fe (III) and Mn (II).

The synthesized magnetic organic salts and their thermal properties are summarized in Table 2. 2. Almost all compounds showed to be solids. As an exception we can find $[N_{1,1,2,C3OH}][FeCl_4]$ and $[N_{1,1,4,C3OH}][FeCl_4]$ which resulted in brown liquids. Regarding the solid products, $[N_{1,1,4,C2OH}][FeCl_4]$ is presented as an example of an IL (melting point lower than 100 ºC). With the increase of the carbon atoms number and, with the increase of the structure asymmetry, it was possible to see a decrease in the melting point or decomposition temperatures. Also, for the majority of these compounds, iron

(III) based compounds presented a smaller melting or decomposition temperatures when compared with the manganese (II)-based compounds. The only exception is related with [$N_{1,1,1,C2OH}$] cation scaffold.

Table 2. 2 | Physical properties of iron (III) and manganese (II) magnetic ionic liquids and organic salts.

Organic Salt	Physical State	Tm (Td) [(a)] (ºC)
[$N_{1,1,1,C2OH}$][$FeCl_4$]	Brown Solid	>250
[$N_{1,1,1,C2OH}$][$MnCl_3$]	Pink Solid	(233)
[$N_{1,1,4,C2OH}$][$FeCl_4$]	Brown Solid	36
[$N_{1,1,4,C2OH}$][$MnCl_3$]	Pink Solid	(191)
[$N_{1,1,C2OH,C2OH}$][$FeCl_4$]	Brown Solid	192
[$N_{1,1,C2OH,C2OH}$][$MnCl_3$]	Pink Solid	(205)
[$N_{1,1,2,C3OH}$][$FeCl_4$] [(b)]	Brown liquid	RTIL
[$N_{1,1,2,C3OH}$][$MnCl_3$]	Yellow Solid	(203)
[$N_{1,1,4,C3OH}$][$FeCl_4$] [(b)]	Brown liquid	RTIL
[$N_{1,1,4,C3OH}$][$MnCl_3$]	Yellow Solid	132

[(a)] Melting temperature (Tm) and decomposition temperature (Td) was determined on Electrothermal Melting Point Apparatus. [(b)] Density measurements were performed using a pycnometer at 20 ºC. The value obtained for [$N_{1,1,2,C3OH}$][$FeCl_4$] and [$N_{1,1,4,C3OH}$][$FeCl_4$] were 1.23g/mL and 1.06g/mL, respectively.

2.3. Magnetic moment

In order to quantify the response of these new magnetic organic salts based on Fe (III) and Mn (II) to an applied external magnetic field, the mass magnetic susceptibility was measured, and the effective magnetic moment (μ_{eff}) was determined. The results are summarized in Table 2. 3. Fe (III) and Mn (II) are transition metals included in d-block elements of periodic table. These can present a distinct tendency to form coordination complexes or

complex ions with ligands. If we have a tetrahedral complex and knowing that chloride is a weak ligand, we have a smaller splitting between the d-orbitals and the electrons fill all orbitals before being paired. Thus, we are in the presence of a metal with a paramagnetic behaviour which means that in the presence of an external magnetic field these complexes are attracted by the field and in the absence of this field, they organize again randomly.[23] Fe (III) arises in this work as a well-known metal anion, with a more optimized synthetic process of organic salts when compared with other metals and as a inexpensive starting material. On the other hand, manganese (II) emerged as an alternative to Gd (III)-based contrast agents formulation (GdCAs). GdCAs advantages such as kinetic inertness, high-speed clearance, and satisfactory elimination by via hepatic/renal/hepatobiliary makes them the primary choice in diagnosis applications, however, as exposed in Chapter 1, Gd (III) presents a toxicity problem associated to its similarity with Ca^{2+} ionic radius. Also, the lower kinetic stability of GdCAs when the metal is coordinated with acyclic ligands have been shown to be a problem. Besides its essential role in human health maintenance, Mn (II) has several advantages that make it capable of enhancing T_1 contrast. Between them it is possible to highlight its rapid water exchange, a high relaxation time, its five unpaired electrons in d orbitals and its efficient elimination from the living system. Drawbacks associated to this metal-based CAs are usually related with its kinetic lability, the cytotoxic effect when the metal is presented in higher concentrations in the human organism and more complex synthetic procedures.[36,37] Being the magnetic susceptibility an important parameter to evaluate the ability of a compound to act as a CAs by enhancing T_1 contrast, the effective magnetic moments were determined (Table 2. 3) in order to evaluate the effect of (1) the interaction between the metal with choline or its derivatives cations as well as the effect associated to (2) the introduction of

a new chloride ligand after complexation reactions in the magnetic properties of these organic salts. The μ_{eff} values obtained are close to the range values already reported in the literature for other materials based on these two metals as can be seen in Figure 2. 2 (red dashed lines).[38–49] Specifically, comparing choline-based magnetic salt, the value obtained for $[N_{1,1,1,C2OH}][FeCl_4]$ (5.93MB) is close to the value reported in the literature (5.92MB).[50] Thus, the metal seems to preserve its magnetic properties when compared with already reported materials. In general, Fe (III)-based salts showed to have smaller μ_{eff} than compounds based on Mn (II).

Table 2. 3 | Magnetic susceptibility and effective magnetic moments of magnetic organic salts based on Fe (III) and Mn (II).

Cation	Anion	$10^{-6}.\chi_g$ (c.g.s) [(a)]	μ_{eff} (MB) [(b)]
$[N_{1,1,1,C2OH}]$	$[FeCl_4]$	49.30 ± 6.06	5.93 ± 0.37 5.92 [(c)]
	$[MnCl_3]$	53.74 ± 0.77	5.82 ± 0.04
$[N_{1,1,4,C2OH}]$	$[FeCl_4]$	36.76 ± 0.26	5.48 ± 0.02
	$[MnCl_3]$	44.81 ± 0.08	5.72 ± 0.01
$[N_{1,1,C2OH,C2OH}]$	$[FeCl_4]$	36.04 ± 0.34	5.55 ± 0.03
	$[MnCl_3]$	40.82 ± 2.15	5.35 ± 0.14
$[N_{1,1,2,C3OH}]$	$[FeCl_4]$	39.12 ± 0.54	5.53 ± 0.04
	$[MnCl_3]$	52.91 ± 0.75	6.07 ± 0.04
$[N_{1,1,4,C3OH}]$	$[FeCl_4]$	34.01 ± 0.22	5.37 ± 0.02
	$[MnCl_3]$	42.19 ± 0.29	5.67 ± 0.02

[(a)] Magnetic susceptibility (χ_g) measure by a Sherwood magnetic susceptibility balance. (b) Effective magnetic moment (μ_{eff}) obtained using the magnetic susceptibility and the equation $\mu_{eff} = 2.828\sqrt{X_g.T}$. (c) Value obtained from the literature [50].

From results exposed in Table 2. 3, we can set a standard behaviour of μ_{eff} values obtained that diverge with the structural features of the cation. For

both metals, when the side alkyl chain increases, the μ_{eff} decreases and the same tendency is observed when a branch is introduced in the cation structure (Figure 2. 2). Finally, when an additional ethanol group is introduced the μ_{eff} decreases.

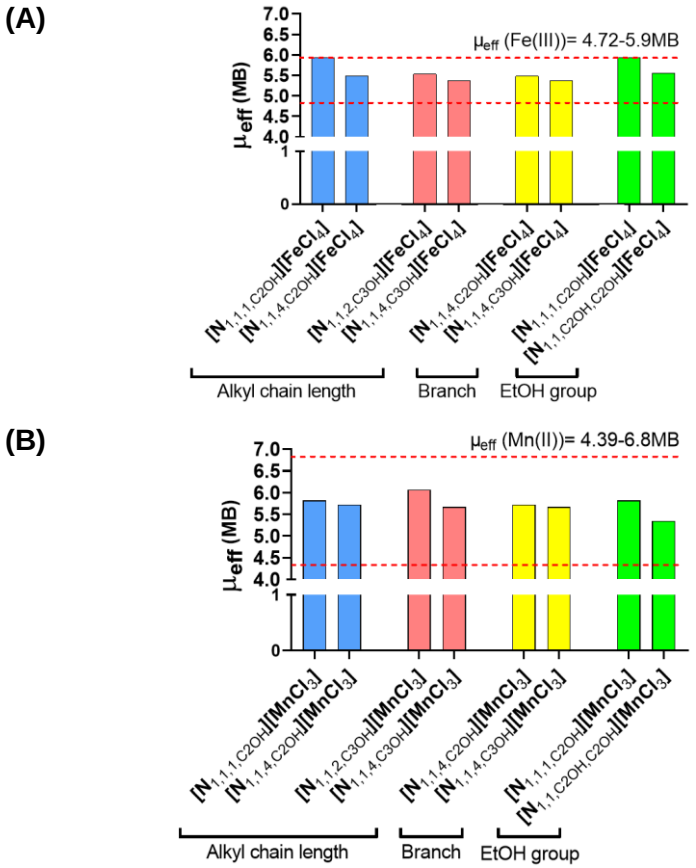

Figure 2. 2 | Variation of μ_{eff} with the structural properties of the cation for (A) iron (III) and (B) manganese (II) based organic salts.

2.4. Cytotoxicity studies

Cytotoxicity of choline derivative salts based on chloride and manganese metal complex anions was evaluated on 3T3 (murine, fibroblasts), 293T (human, epithelial cells from kidney) and in two *in vitro* human tumoral cellular models, HepG2 (liver cancer) and Caco-2 (colon cancer), after treatment at maximum concentration of 100 µg/ mL for 24 h. The cells viability was estimated by the MTT assay and the results presented in Figure 2. 3 and Figure 2. 4.

2.4.1. Choline Chloride derivative salts

The effects of choline derivative salts based on chloride anion on the studied cells' viability are shown in Figure 2. 3. It is possible to observe that the majority of the compounds did not induce any cytotoxicity on the 3T3, 293T and HepG2 cell lines when compared to the control situation. As an exception to this behaviour, it is possible to highlight the compound $[N_{2,2,2,C2OH}][Cl]$ that significantly reduced the viability of HepG2 (79.37% of viable cells) without affect the viability of 3T3 and 293T normal cells. In Caco-2 cells, compounds showed a different cytotoxic effect. Between the six compounds, only $[N_{1,1,4,C2OH}][Cl]$ did not significantly reduce the cells viability when compared with the control situation.

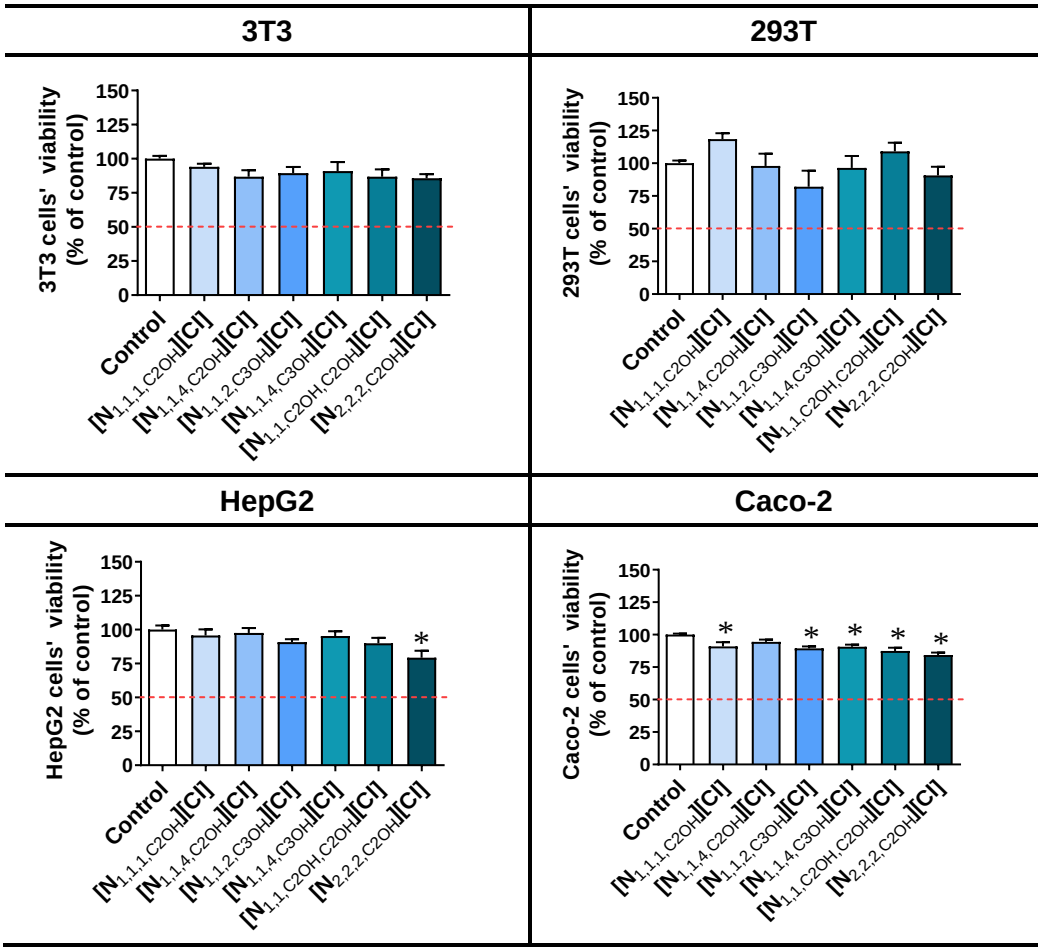

Figure 2. 3 | Cytotoxicity of choline chloride derivative salts (100 µg/mL) on 3T3, 293T, HepG2 and Caco-2 cells after treatment for 24h. Values represent mean ± standard error of the mean (SEM) of at least three independent experiments carried out in triplicate. Symbols represent significant differences (ANOVA, Dunnett's test, *p* - value < 0.05) when compared to: *control.

2.4.2. Manganese (II)-based salts

The effects of choline derivative salts based on manganese on studied cells' viability are shown in Figure 2. 4. Regarding to manganese-based salts, as can be seen, it is possible to observe a different behaviour for 3T3 and 293T cell lines than for the previous compounds. Almost all compounds significantly reduced the viability of normal cells when compared with the control treatment. Among all compounds, only $[N_{1,1,4,C2OH}][MnCl_3]$ did not induce cytotoxicity in 293T cells. Concerning the effect of these magnetic salts in HepG2 tumoral cells, as depicted above the $[N_{1,1,C2OH,C2OH}][MnCl_3]$ and $[N_{2,2,2,C2OH}][MnCl_3]$ presented cell viability values of 115.44% and 118.57%, respectively, which can indicate that these magnetic salts enhanced the mitochondrial activity. $[N_{1,1,4,C2OH}][Cl]$ salt was the only example that significantly reduced Caco-2 cells' viability when compared with the control situation. Comparing the cytotoxicity effects of these salts in normal and tumoral cells, most of these compounds seemed to induce a more marked effect on the cell viability of normal cells than in tumoral cells.

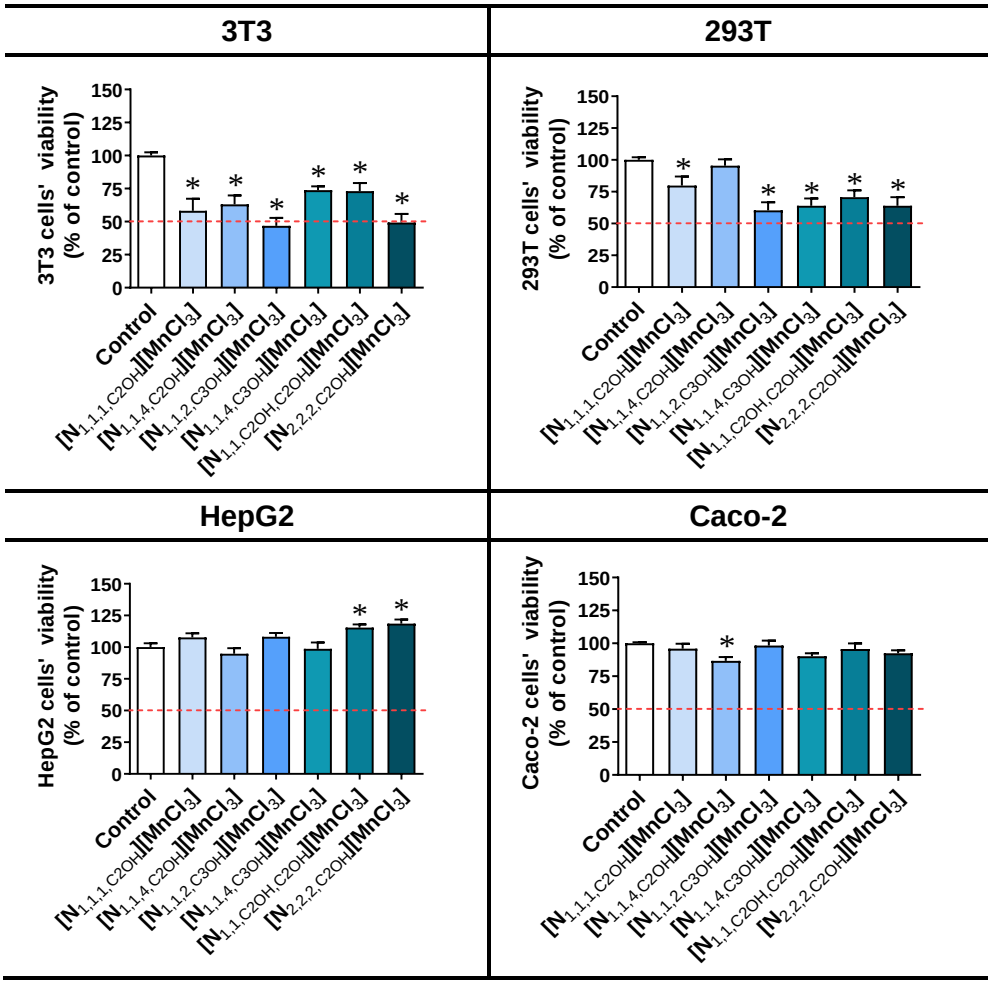

Figure 2. 4 | Cytotoxicity of manganese-based salts salts (100 µg/mL) on 3T3, 293T, HepG2 and Caco-2 cells after treatment for 24h. Values represent mean ± standard error of the mean (SEM) of at least three independent experiments carried out in triplicate. Symbols represent significant differences (ANOVA, Dunnett's test, *p* - value < 0.05) when compared to: *control.

2.5. Manganese (II) luminescence properties

As mentioned above, a set of choline derivative cations were prepared and used in further complexation reactions with metal transition manganese (II) in order to obtain choline-based magnetic organic salts. Additionally, in the present section, the synthesis of magnetic salts based on an example of a tetra-alkylammonium ($[N_{2,2,2,2}][MnCl_3]$), and two other cation families is reported. All synthesized Mn (II)-based organic salts proved to be efficient photoluminescent compounds emitting red and/or green light according to the metal coordination.

Table 2. 4 summarizes the thermal results obtained for $[N_{2,2,2,2}][MnCl_3]$ and choline derivative salts (previously reported in the present chapter, section 2.2). All compounds were obtained as solids (pink or yellow) and only for $[N_{1,1,4,C3OH}][MnCl_3]$ and $[N_{2,2,2,2}][MnCl_3]$ it was possible to measure the melting point transition. Also, the synthesized powders under ambient and 365nm UV light are shown on Table 2. 4. From the ammonium family salts, choline derivative compounds display a red photoluminescence (PL). On the other hand, tetra-alkylammonium $[N_{2,2,2,2}][MnCl_3]$ display a strong green emission. From the literature, and previous reported studies from other authors, manganese (II) red and green PL are associated to MnX_6^{4-} octahedral and MnX_4^{2-} tetrahedral type coordination, respectively. According to the reactions schemes planned for this work (Scheme 2. 3) and their cation:anion proportion of the synthetic method, Mn (II)-based complex anions should be coordinated with three chloride ligands and, eventually, one water molecule. Thus, the coordination number and their correlation with PL compounds must be clarified. Another interesting fact is that the only example of this green emission was obtained from an oxygen-free cation. Therefore, this feature could be one of the assets associated to this phenomenon.

Table 2. 4 | Physical, thermal and luminescence results obtained for ammonium cation family.

Compound	Physical State	Tm (Td) [(a)] (ºC)	Photographs of compounds powders under (A) ambient and (B) UV light (365nm)	
			(A)	(B)
$[N_{1,1,1,C2OH}][MnCl_3]$	Pink Solid	(233)		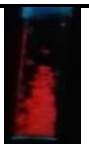
$[N_{1,1,4,C2OH}][MnCl_3]$	Pink Solid	(191)		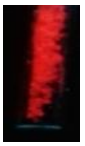
$[N_{1,1,2,C3OH}][MnCl_3]$	Yellow Solid	(203)	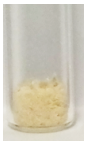	
$[N_{1,1,4,C3OH}][MnCl_3]$	Yellow Solid	132		
$[N_{1,1,C2OH,C2OH}][MnCl_3]$	Pink Solid	(205)		
$[N_{2,2,2,2}][MnCl_3]$	Pale Yellow Solid	212		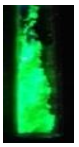

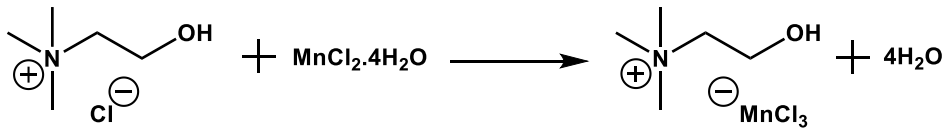

Scheme 2. 3 | Reactional scheme of the synthesis of $[N_{1,1,1,C2OH}][MnCl_3]$

In order to obtain organic salts based on other cation families, during this work, five examples of phosphonium and imidazolium cations were also used to prepare a set of an additional Mn (II)-based magnetic salts. The prepared salts and their thermal properties are summarized in Table 2. 5. It was observed that these compounds continue to show the same oxygen dependence for red light emission than the one verified for choline derivative salts. All compounds were again obtained as solids with melting point higher than 100 ºC. The single exception was $[C_2MIM][MnCl_3]$ salt where the transition temperature was 71 ºC. Thus, this is an example of an ionic liquid by definition.

Table 2. 5 | Luminescence results from phosphonium and imidazolium cations under the UV light at 366nm

	Compound	Physical State	Tm (Td) [(a)] (ºC)	Photographs of compounds powders under (A) ambient and (B) UV light (365nm)	
				(A)	(B)
Phosphonium	**$[P_{C1OH,C1OH,C1OH,C1OH}][MnCl_3]$**	Pink Solid	195		
	$[P_{4,4,4,4}][MnCl_3]$	Yellow Solid	148		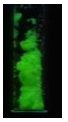
Imidazolium	**$[C_2OHMIM][MnCl_3]$**	Pink Solid	128	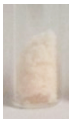	
	$[C_2OHDMIM][MnCl_3]$	Pink Solid	n.d.		
	$[C_2MIM][MnCl_3]$	Yellow Solid	71	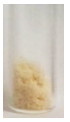	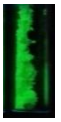

2.5.1. Single-crystal X-Ray crystallography

In collaboration with Single Crystal X-ray Crystallography service from FCT NOVA, this section shows the obtained crystallographic structures of three prepared compounds. In order to confirm the crystalline structure of $[N_{1,1,1,C2OH}][MnCl_3]$ salt, to determine the complex geometry and to understand the origin of the red light emission, crystals were prepared and

single crystal x-ray crystallography performed. The symmetry space group is *Pna*2_1 with Z=4. With an orthorhombic crystal system, the unit cell dimension is a = 16.8451(9) Å, b = 8.3549(4) Å and c = 7.4374(4) Å with α=β=γ=90º. The crystallographic image of the asymmetric unit of this magnetic salt (Figure 2. 5) confirmed, as suspected, that the oxygen atom influences the complex coordination number. In fact, this element act as one of the metal ligands as well as the expected chloride atoms.

.

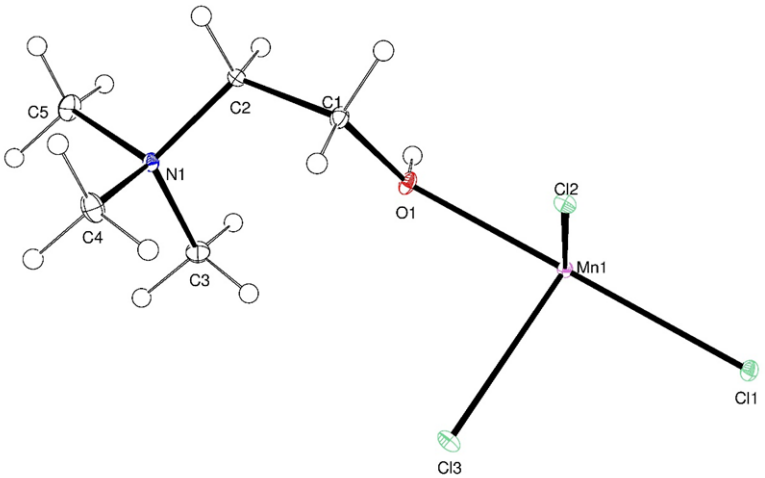

Figure 2. 5 | Perspective view of the asymmetric unit of the crystal structure of $[N_{1,1,1,C2OH}][MnCl_3]$ (polymeric structure).

More information about this compound rearrangement can be taken from the packing diagram of the polymeric structure of the crystal (Figure 2. 6). From this crystallographic image, it is possible to observe that the coordination system associated to crystalline structure of this salt is an octahedral geometry although a symmetry centre cannot be defined. This is in agreement and consistent with the red-light emission and our previous knowledge about Mn (II) coordination chemistry. Thus, as can be seen, the metal is six coordinated with the expected chloride atoms, the oxygen from

cation scaffold and, additionally, it is possible to find chloride bridges between two manganese atoms. The polymeric structure is as well supported by hydrogen bonds between the hydrogen (from -OH group) and chloride atoms (O…Cl 3.0589(2), H…Cl 2.22, O–H…Cl 175º, symmetry operation: -*x*,-*y*,-1/2+*z*).

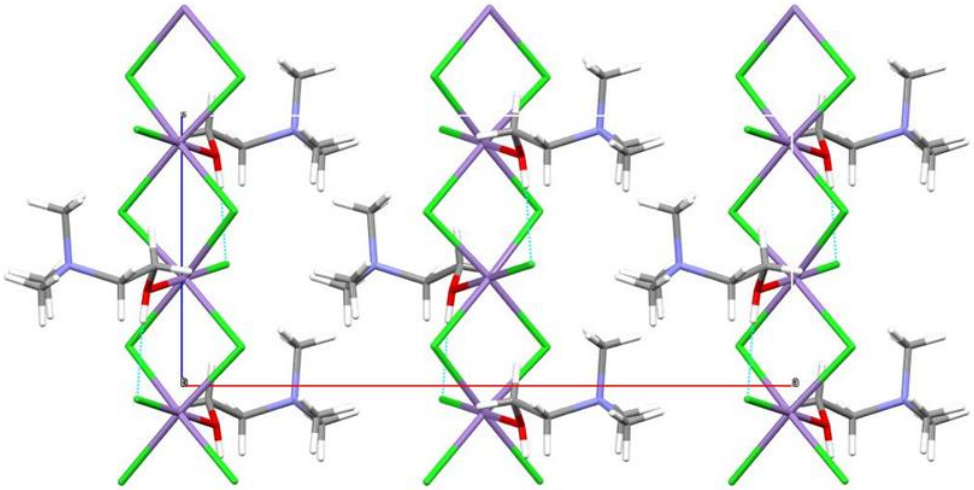

Figure 2. 6 | Packing diagram viewed down the *b* axis of the polymeric structure of $[N_{1,1,1,C2OH}][MnCl_3]$ crystal

Additionally to the previous study, crystals of $[N_{1,1,C2OH,C2OH}][MnCl_3]$ were also prepared. This compound structure allows to conclude about the effect of the presence of an additional ethanol group (and thus, the presence of two oxygen atoms) in the cation scaffold. For this magnetic salt, the symmetry space group obtained is $P2_1$ with Z=2. The crystal system attained in this case is monoclinic with the unit cell dimension of a = 8.4105(8) Å, b = 9.0674(9) Å and c = 22.428(2) Å, α=γ=90º and β=100.576(3)º. Figure 2. 7 (A) represents the obtained diagram of the title compound and, as can be seen, the metal has (similarly to $[N_{1,1,1,C2OH}][MnCl_3]$) an octahedral

coordination. Moreover, the coordination between the oxygen atom from the cation and the metal is maintained. However, for $[N_{1,1,C2OH,C2OH}][MnCl_3]$, the crystal structure presents a second oxygen-metal bond. This means that, in addition to the chloride ligands, the metal is coordinated with two oxygens atoms from two different cations. Similarly to $[N_{1,1,1,C2OH}][MnCl_3]$, hydrogen bonds stabilizing the crystalline structure of $[N_{1,1,C2OH,C2OH}][MnCl_3]$ salt could be also identified (Figure 2. 7 (B) and Table SI 10 – supplementary information).

(A)

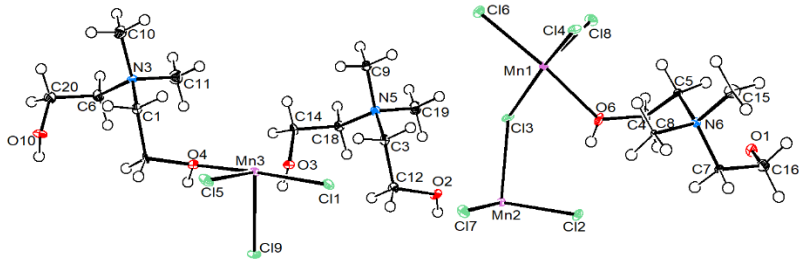

(B)

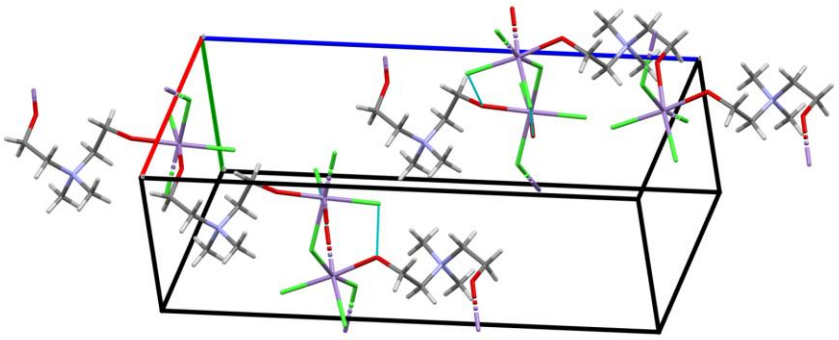

Figure 2. 7 | (A) ORTEP-3 diagram of the compound $[N_{1,1,1,C2OH}][MnCl_3]$ using 50% level ellipsoids; (B) packing diagram showing intramolecular hydrogen bonds (represented by dashed light-blue lines)**.**

Crystals of $[N_{2,2,2,2}][MnCl_3]$ were also prepared. The resolution of this compound structure allows to take conclusions about the effect of the absence of the ethanol group, namely the absence of the oxygen atom, in the cation scaffold. For this magnetic salt, the symmetry space group obtained was P21/n with Z=4. The crystal system attained in this case is monoclinic with the unit cell dimension of a = 16.5514(10) Å, b = 9.6164(6) Å and c = 16.7356(10) Å, α=γ=90º and β=116.967(2)º. Figure 2. 8 (A) and (B) represent the obtained diagram of the compound $[N_{2,2,2,2}][MnCl_3]$ and the packing diagram where can be seen that the molecule structural rearrangement is different from the previous structures showed in this section. In this crystal structure, unlike the expected, the metal manganese (II) is coordinated with four chloride atoms, *i.e.*, shows a tetrahedral coordination. Furthermore, according to this structure, since the metal anion is coordinated with four ligands, its charge will be -2. Consequently, as can be seen, we have two cations' scaffolds for one metal anion.

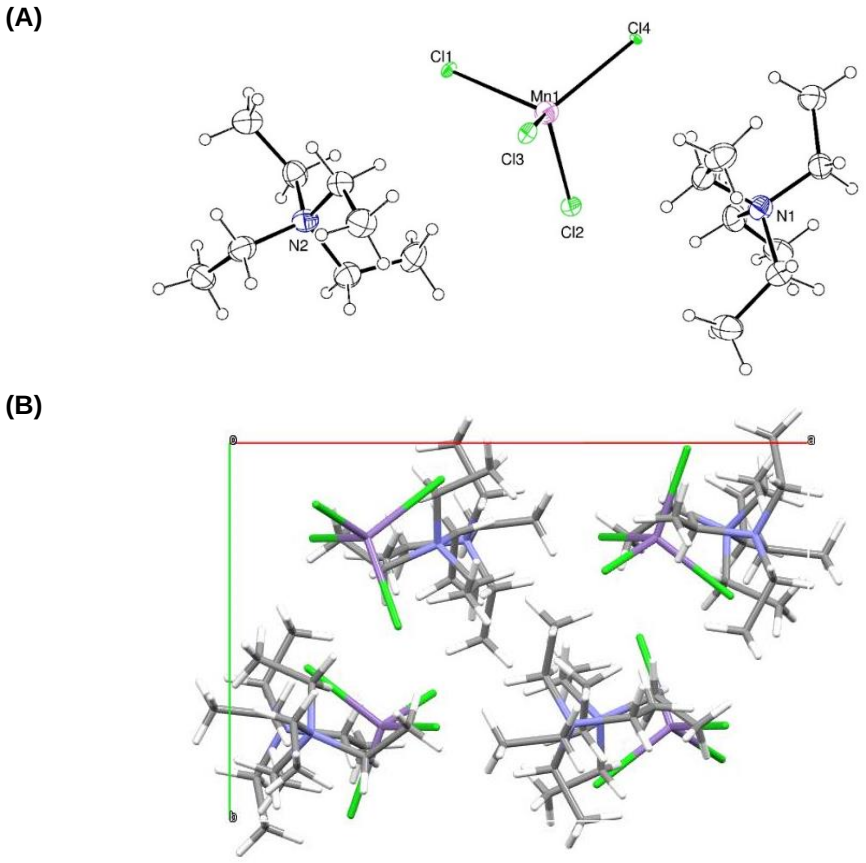

Figure 2. 8 | (A) diagram of the title compound; (B) packing diagram.

2.5.2. Luminescence properties

For all Mn (II)-based PL compounds, their luminescence quantum yield was measured in their powder's form using the absolute method. The lifetime decay was determined through Phosphorescence Decay. In Figure 2. 9, 2D spectra for $[N_{2,2,2,2}][MnCl_3]$ (Figure 2. 9 A)) and $[N_{1,1,1,C2OH}][MnCl_3]$ (Figure 2. 9 (B)) can be observed. As expected, and taking into account their emission light color under the UV lamp, compounds showed a peak emission wavelength of 640 nm (red) and 525 nm (green) for $[N_{1,1,1,C2OH}][MnCl_3]$ and

$[N_{2,2,2,2}][MnCl_3]$, respectively. Regarding to the excitation spectra, $[N_{2,2,2,2}]$-based compound presented one peak in the visible light range (450 nm) while the choline derivative compound showed three peaks at 420, 450 and 520 nm. This result seems to indicate the presence of crystal polymorphism, *i.e.*, the presence of more than one crystalline structure. From the 2D spectra it was possible to determine the excitation and emission target wavelengths to study the PL salts (supplementary information, Table SI 15). 2D spectra of all compounds can be seen in supplementary information (Figure SI 43-51).

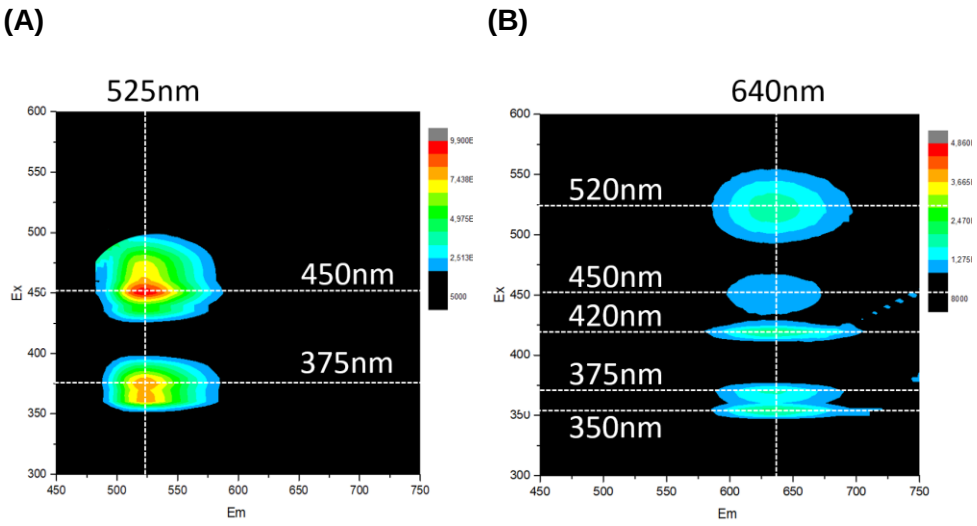

Figure 2. 9 | 2D spectra of (A) $[N_{2,2,2,2}][MnCl_3]$ and (B) $[N_{1,1,1,C2OH}][MnCl_3]$.

Luminescence quantum yield and phosphorescence lifetime decay were measured for two excitation wavelengths in choline-derivative compounds (420-430nm and 515-540nm). For the tetraalkylammonium salt, only one wavelength value was used (450nm). In this chapter, the results related with

the first excitation wavelength in visible light range (420-430nm) will be analyzed for all compounds.

Quantum yield and lifetime results obtained for the compounds are summarized in Table 2.6. Also, in this table can be found the Stokes shift calculated from excitation and emission spectra, as well as the radiative (k_r) and non-radiative (k_{nr}) constants determined through Equation 2. 1 and Equation 2. 2.

$$k_r = \frac{\Phi}{\tau} \qquad \textbf{(Equation 2. 1)}$$

$$k_{nr} = \frac{k_r}{\Phi} - k_r \qquad \textbf{(Equation 2. 2)}$$

Where k_r is the rate constant for radiative decay; k_{nr} is the rate constant for non-radiative deactivation mechanism; Φ is the quantum yield; and τ is the lifetime decay.

The results obtained for 515-540nm wavelength range, can be found in the supplementary information (Table SI 16).

As will be explained later in this discussion, the mechanism responsible for the deactivation of the excited state of the prepared salts is phosphorescence, as expected. The quantum yield of a PL compound can be defined as the product of quantum yields associated to all internal processes included in the pathway of the excited molecule to the ground state.

From choline derivative salts, $[N_{1,1,4,C2OH}][MnCl_3]$ showed to have the highest quantum yield (12.8%). On the contrary, the magnetic organic salt based on $[N_{1,1,2,C3OH}]$ cation, presented the lowest quantum yield. In fact, it was not possible to calculate this parameter for this salt since its 2D spectra does not show any peak within the range of wavelengths studied (Figure SI 44). Thus,

the quantum yield is considered smaller than 0.5%. Tetralkylammoniumm salt, $[N_{2,2,2,2}][MnCl_3]$, arises as the compound with the highest quantum yield, not only from ammonium family but also from all compounds (72.2%). Observing the values obtained for each synthesized salt, it is possible to establish a possible standard behaviour related with the cation structure and its effect on quantum yields. For all compounds, higher alkyl chains can be associated to an increase of quantum yields (e.g. $[N_{1,1,1,C2OH}][MnCl_3]$ – 4.7% and $[N_{1,1,4,C2OH}][MnCl_3]$ – 12.8 %). On the contrary, the branch presence tends to decrease the luminescence quantum yield of these magnetic salts (e.g. $[N_{1,1,4,C2OH}][MnCl_3]$ – 12.81% and $[N_{1,1,4,C3OH}][MnCl_3]$ – 2.5%. Finally, for choline derivative salts, the presence of an additional ethanol group does not show a substantial difference in quantum yield values (*e.g.* $[N_{1,1,1,C2OH}][MnCl_3]$ – 4.7% and $[N_{1,1,C2OH,C2OH}][MnCl_3]$ – 4.7%). Even so, the introduction of a second ethanol group slightly reduces the quantum yield. Phosphonium cation family results showed an higher value of quantum yield for the compound without ethanol groups (e.g. $[P_{C2OH,C2OH,C2OH,C2OH}][MnCl_3]$ – 3.6% and $[P_{4,4,4,4}][MnCl_3]$ – 4.5%). In agreement, for imizadolium cations, the presence of an ethanol group results in an decrease of quantum yield (e.g. $[C_2MIM][MnCl_3]$ – 18.5% and $[C_2OHMIM][MnCl_3]$ – 5.53%). With the presence of an acidic proton in the imidazolium ring the quantum yield also decreases (e.g. $[C_2OHMIM][MnCl_3]$ – 5.5% and $[C_2OHDMIM][MnCl_3]$ – 2.3%). As a common point between the families of cations, it can be highlighted the fact that cations based on alkyl side groups, have higher quantum yields when compared to cations of the same families but whose structure has at least one side group with oxygen in its constitution.

Table 2. 6 | Luminescence properties of manganese (II) ammonium, phosphonium and imidazolium salts

[Cation]	λ (nm)	ϕ (%)	τ (ms)	k_r (ms^{-1})	k_{nr} (ms^{-1})	Stokes shift (eV)
Ammonium						
[$N_{1,1,1,C2OH}$]	420	4.7	1.16	0.04	0.82	0.48
[$N_{1,1,4,C2OH}$]	420	12.8	0.95	0.13	0.2	0.44
[$N_{1,1,2,C3OH}$]	–	<0.5	–	–	–	–
[$N_{1,1,4,C3OH}$]	425	2.5	1.0	0.02	0.98	0.42
[$N_{1,1,C2OH,C2OH}$]	420	4.7	0.79	0.06	1.21	0.38
[$N_{2,2,2,2}$]	450	72.2	2.63	0.27	0.1	0.33
Phosphonium						
[$P_{C1OH,C1OH,C1OH,C1OH}$]	420	3.6	0.4	0.09	2.41	0.36
[$P_{4,4,4,4}$]	450	4.5	0,.2	0.14	2.99	0.51
Imidazolium						
[C_2OHMIM]	420	5.5	0.95	0.06	0.99	0.52
[C_2OHDMIM]	430	2.3	0.23	0.10	4.25	0.42
[C_2MIM]	450	18.5	0.49	0.38	1.66	0.42

Lifetime decays achieved for all compounds are within the order of magnitude of milliseconds. These phenomena can indicate that the return to the ground state is performed by a slower process, i.e., by a mechanism whose excited states have a higher lifetime. This deactivation process is, as mentioned in Chapter 1, called by phosphorescence. The determination of different decay rate constants (radiative and non-radiative mechanisms) are dependent of the lifetimes and quantum yields measurements, as specified

in Equation 2. 1 and Equation 2. 2. As can be seen, k_{nr} values are much higher than kr for almost all compounds. This means that the return of the molecule in the excited state to the ground state is made mostly by non-radiative transitions. As an exception arises $[N_{2,2,2,2}][MnCl_3]$ salt where it can be observed that k_r is higher than k_{nr}. Regarding to Stokes shift, the difference between the salts excitation and emission spectra is in the range of 0.33-0.52 eV. As defined, higher values of Stokes shift imply a more distorted geometry of the excited state compared with the ground state. Therefore, the set of values achieved in this work indicates that these compounds have a significant difference between the geometry of the molecule in the excited state (in this case, in the triplet state) regarding to the lower energy state (ground state).

2.5.3. Manganese (II) transitions

When the metal is in the absence of a magnetic field, all the electron orbitals present the same energy levels and are called degenerate orbitals. However, when the metal is coordinated with a set of ligands, these orbitals acquire different energies, and they separate into two different energy levels. The energy difference between the orbitals is often called ligand-field splitting parameter (Δ). The magnitude of this value depends on the ligand and metal nature. As weak-field ligands according to spectrochemical series, chloride (-Cl) and hydroxide (-OH) give rise to low-energy transitions and, thus, a high spin system is obtained. With a small ligand-field splitting parameter, the system requires lower energy light to perform the transitions and, consequently, longer wavelength values associated to those transitions are achieved. Specifically, divalent manganese ion has a d^5 electronic configuration with a $^4T_1 \rightarrow {}^6A_1$ transition associated to the crystal field strength. This fact and the dependence relation of the crystal field strength

with the chemical structure of the ligand and complex coordination number, makes manganese (II)-based complexes good candidates to explore their photophysical properties. According to Aufbau principle and Hund's rule, the orbitals filling is made from lower to higher energy orbitals and in order to have the highest number of unpaired electrons. Thus, in this specific case where the ligands produce a smaller crystal field splitting, the electrons from d5 metal complex can be organized in an octahedral and tetrahedral geometry as schematized in Figure 2. 10.

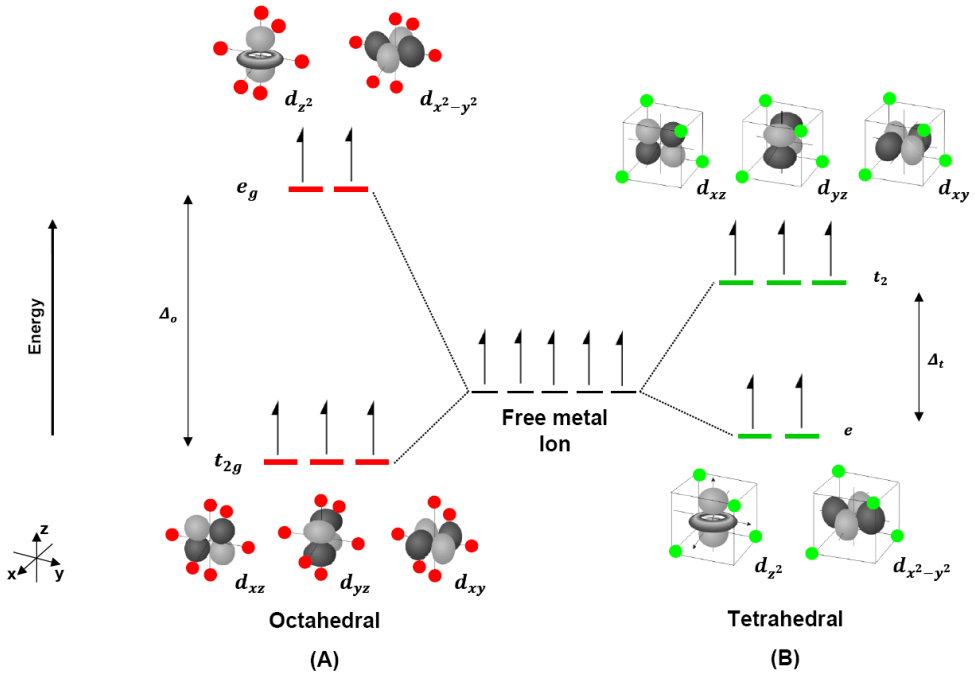

Figure 2. 10 | Splitting diagram of the degenerate d-orbitals due to an (A) octahedral ligand field and (A) tetrahedral ligand field.

Figure 2. 11 (A) illustrates the excitation and emission spectra of $[N_{1,1,1,C2OH}][MnCl_3]$ and $[N_{2,2,2,2}][MnCl_3]$ at ambient conditions. Crystal field transitions associated to Mn (II) in both coordination systems were identified

in the spectra. The origin of the green and red light emissions associated to tetrahedral and octahedral geometries, respectively, can be observed in Tanabe-Sugano diagram for Mn^{2+} (Figure 2. 11 (B)).

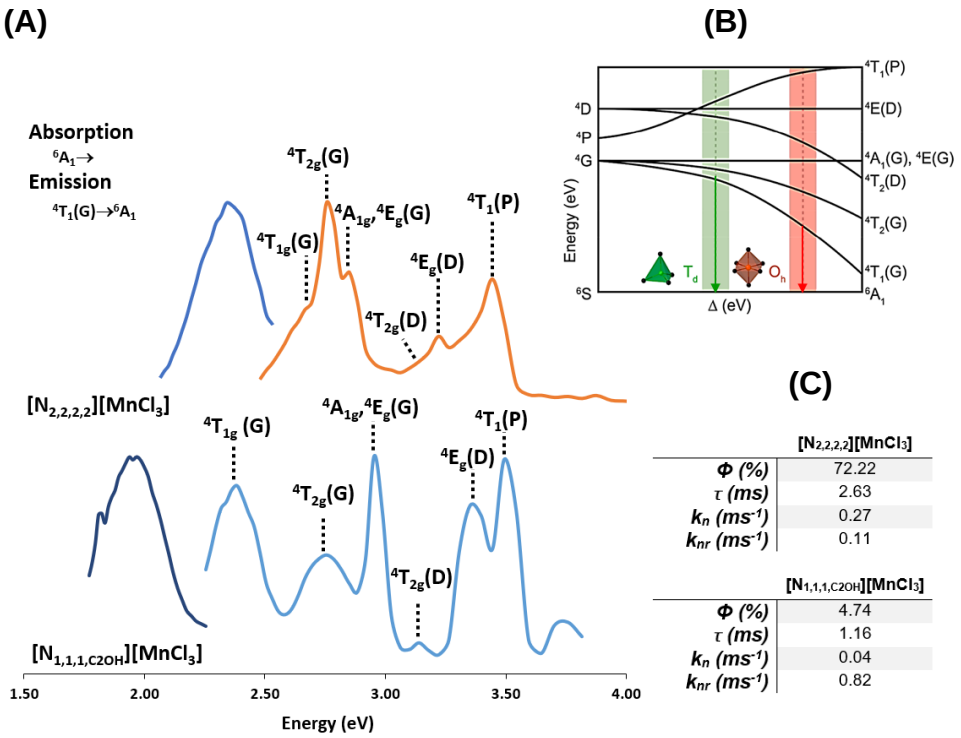

	$[N_{2,2,2,2}][MnCl_3]$
Φ (%)	72.22
τ (ms)	2.63
k_n (ms^{-1})	0.27
k_{nr} (ms^{-1})	0.11

	$[N_{1,1,1,C2OH}][MnCl_3]$
Φ (%)	4.74
τ (ms)	1.16
k_n (ms^{-1})	0.04
k_{nr} (ms^{-1})	0.82

Figure 2. 11 | (A) Excitation and corresponding emission spectra of $[N_{2,2,2,2}][MnCl_3]$ and $[N_{1,1,1,C2OH}][MnCl_3]$; (B) Tanabe-Sugano diagram for Mn (II); (C) Summarized luminescence properties results obtained for $[N_{2,2,2,2}][MnCl_3]$ and $[N_{1,1,1,C2OH}][MnCl_3]$.

As can be seen, the transition $^4T_2(G)\rightarrow{}^6A_1$ is the responsible for the green and red luminescence of Mn (II)-based compounds. As expected, $[N_{2,2,2,2}][MnCl_3]$ presents an emission peak with maximum on 530 nm (2,34 eV, green light) and 630 nm (1.97eV, red light) for $[N_{1,1,1,C2OH}][MnCl_3]$. This difference between the green and red luminescence is mainly caused by the

weaker crystal field associated to tetrahedral geometry of Mn (II)-based salt. As observed in Figure 2. 10, tetrahedral coordination implies a smaller crystal field splitting (and thus, lower energy difference) when compared with octahedral geometry. $[N_{2,2,2,2}][MnCl_3]$ salt presents an higher lifetime decay (2.63ms) when compared with choline derivative compound (1.16ms), Figure 2. 11(C). This difference seems to indicate the occurrence of more forbidden transitions for tetraalkylammonium cation and, consequently, an increase in the residence time of the molecule in the excited state. Also, these two salts showed to have different prevalence regarding to the type of transitions. Although the mechanism of deactivation of the excited state of this molecule presents radiative and non-radiative transitions, $[N_{2,2,2,2}][MnCl_3]$ presents an higher radiative transitions incidence ($k_r>k_{nr}$). On the contrary, $[N_{1,1,1,C2OH}][MnCl_3]$ has a much higher value of non-radiative transitions. Moreover, for this compound, k_r value is almost zero. Thus, considering the Equation 2. 2 and taking into account the value of k_r ($k_r\approx0$), it can be concluded that the quantum yield for $[N_{1,1,1,C2OH}][MnCl_3]$ is mostly dependent of the k_{nr} constant. Being these two parameters inversely proportional, a higher k_{nr} value is associated to a smaller quantum yield. This relation is in agreement to the results obtained for the two magnetic salts. Even though for the salt $[N_{2,2,2,2}][MnCl_3]$ the radiative constant is not zero and has some weight in relation to the quantum yield, its higher k_{nr} value can be related with its higher quantum yield.

Observing the excitation spectra of all compounds organized by their cation families (Figure 2. 12), it is possible to conclude that Mn (II) transitions are more well-defined for cations with oxygen in their structure. $[C_2OHDMIM]$ (Figure 2. 12 (C)) arises as an exception. This can be related with the acidic proton of this imidazolium scaffold. Specifically, for choline derivative salts (Figure 2. 12 (A)), it is possible to identify three transitions ($^4T_{2g}$ (G), $^4T_{2g}$ (D),

^4E (D), $^4T_1$ (P)) whose intensity, shape, and energy value changes with cations different structural features. So, the prohibition level associated to these transitions seems to be related with the cation structure.

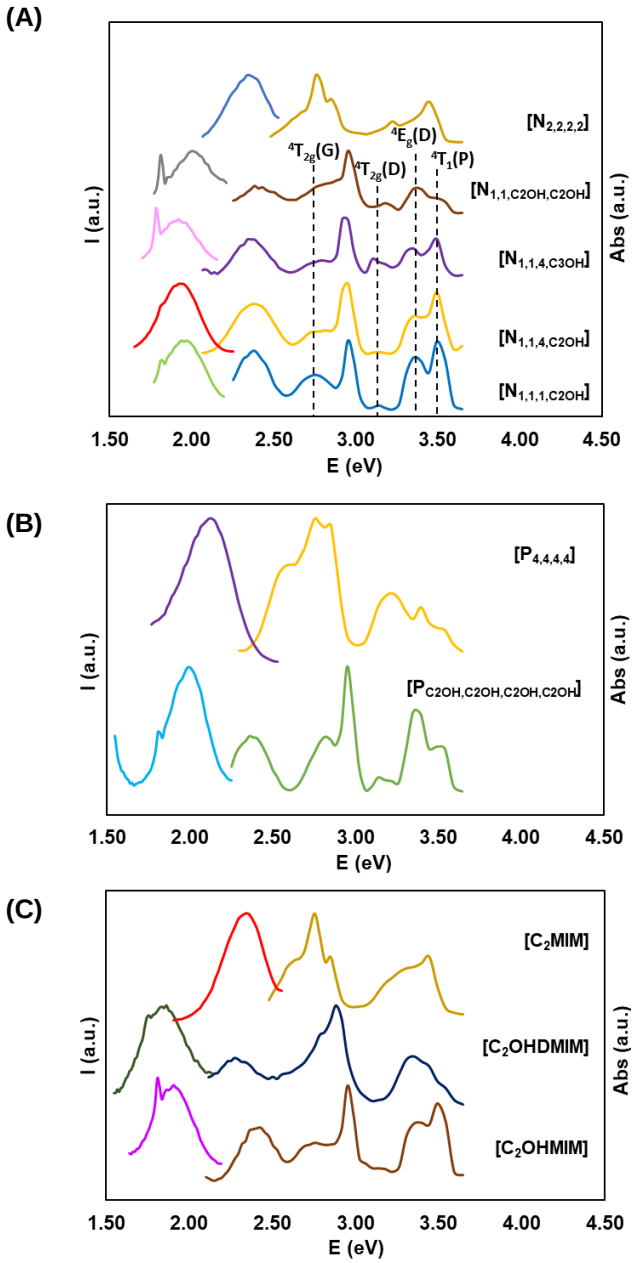

Figure 2. 12 | Excitation and emission spectra of (A) ammonium, (B) phosphonium and (C) imidazolium-based salts.

An additional preliminary study was also made in order to compare the luminescence quantum yield of the same compound in its powder and crystal forms (Figure 2. 13). From these results it is possible to see that the spectra from the two forms of $[N_{1,1,1,C2OH}][MnCl_3]$ salt are identical. The exception emerges from $^4T_{2g}$ (D) transition (more allowed in the powder form). Also, the quantum yield increases from 4.74% (powder) to 10.95% when the salt is in the crystal form.

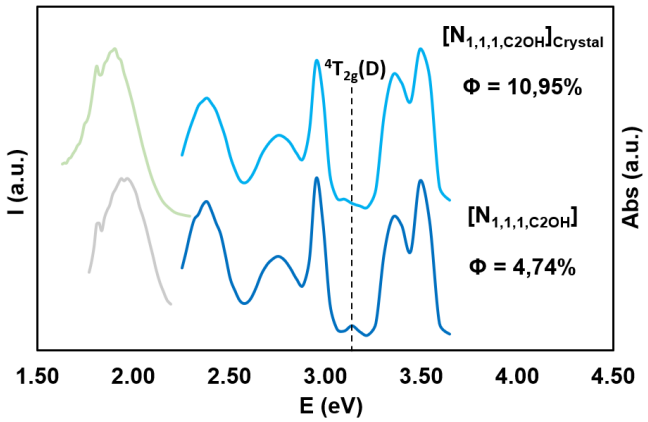

Figure 2. 13 | Excitation and emission spectra of $[N_{1,1,1,C2OH}][MnCl_3]$ in its powder and crystal forms.

3. Conclusions

A set of magnetic organic salts based on choline derivative cation family and transition metals iron (III) and manganese (II) were synthesized using sustainable synthetic methodologies. It was possible to obtain two examples of MILs, $[N_{1,1,2,C3OH}][FeCl_4]$ and $[N_{1,1,4,C3OH}][FeCl_4]$. Effective magnetic moments were determined and a standard behaviour dependent on the cation magnetic salt was defined. Choline chloride derivative salts and

manganese-based products were also tested for their cytotoxicity in four different cells lines. Overall, chloride-based salts, did not induce any cytotoxicity in normal and tumoral cells. On the other hand, almost all manganese-based compounds seemed to induce cytotoxic effects in normal cells. Specifically, all synthesized Mn (II) salts proved in this work to be efficient photoluminescent compounds emitting red and/or green light according to the metal coordination. In order to confirm the crystalline structure, to clarify the metal coordination and the corresponding emission colour, some particular salts ($[N_{1,1,1,C2OH}][MnCl_3]$, $[N_{1,1,C2OH,C2OH}][MnCl_3]$ and $[N_{2,2,2,2}][MnCl_3]$) were selected to prepare crystals and perform their evaluation by single crystal x-ray crystallography. Also, all compounds were studied according to their luminescence colour, quantum yield (absolute method) and lifetime decay (phosphorescence decay). From the obtained results, it was possible to set a correlation between the salts structural features and their luminescence properties. From all the prepared salts, the compounds that displayed the highest quantum yield were $[N_{1,1,4,C2OH}][MnCl_3]$ (from choline-derivative salts - 12.8%) and $[N_{2,2,2,2}][MnCl_3]$ (72.2%). Lifetime decay results seems to indicate that the deactivation of the excited state of all prepared salts is performed through a phosphorescence process. Additionally, it was possible to perform a comparison between the quantum yield of the same salt in its powder (4.74%) and crystal form (10.95%).

4. Experimental Section

4.1. General Remarks

All commercial organic solvents were used as supplied from Sigma-Aldrich in analytical purity grade. Commercially available reagents were purchased

from different chemical companies and then used as received. ^{1}H and ^{19}F-NMR were recorded on a Bruker AMX400 spectrometer. Chemical shifts are reported downfield in parts per million using D_2O, CD_3OD and $(CD_3)_2SO$ as deuterated solvents. Fourier transform infrared spectroscopy (FT-IR) spectra were carried out on a Bruker Tensor 27. Elemental analysis (C, H, N, analyzer) of each synthesized organic salt was performed by Laboratório de Análises at LAQV-REQUIMTE. For the salts which were solid at room temperature the melting point determination was performed using a Stuart Scientific Melting Point SMP1. The density of choline derivatives organic salts was determined using a pycnometer. The measurements were performed in duplicate and the average value is reported. All measurements were taken at 20 ºC.

4.2. Synthesis and characterization of choline derivatives salts

***N,N,N-Triethyl-N-hydroxyethylammonium bromide [$N_{2,2,2,C2OH}$][Br]*:** N,N-Diethyl-N-(2-hydroxyethyl)amine (5.00g, 42.66mmol) and ethanol were added to a round-bottomed flask. The resulting solution was placed in an ice bath and then slowly was added 1-bromo-ethane (5.12g, 46.95 mmol) under constant stirring. The reaction mixture was heated under reflux for 48 h after which the solvent was evaporated. The resulting solid was washed with diethyl ether and hexane and then dried under vacuum to give the product [$N_{2,2,2,C2OH}$][Br] as a pale yellow solid (8.98g, 93%). ^{1}H NMR (400 MHz, D_2O) δ(ppm) = 5.27 (t, 1H), 3.77 (m, 2H), 3.30 (m, 8H), 1.18 (t, $^{3}J(H,H)$=7.0 Hz, 9H). FT-IR (NaCl), $\tilde{\upsilon}$ = 3416, 2987, 1643, 1485, 1398, 1163, 1081 cm^{-1}. Elemental analysis calcd (%) for $C_8H_{20}BrNO$ (226.19 g mol^{-1}): C 42.48, N 6.19, H 8.93; found: C 42.27, N 6.13, H 8.61.

***N,N,N-Triethyl-N-hydroxyethylammonium chloride [$N_{2,2,2,C2OH}$][Cl]*:** [$N_{2,2,2,C2OH}$][Br] (2.5g, 11.05mmol) and methanol were added to a round-bottomed flask. Ionic exchange resin (IRA 400-Cl) was added to the resulting solution. The reaction mixture was under stirring for 30 minutes after which the resin was filtered. The solvent was then evaporated and the resulting solid was dried under vacuum to give the product [$N_{2,2,2,C2OH}$][Cl] as a brown solid (1.55g, 77%). ^{1}H NMR (400 MHz, D_2O δ (ppm) = 3.89 (m, 2H), 3.28 (q, ^{3}J(H,H)=7.6 Hz, 8H), 1.19 (t, ^{3}J(H,H)=6.8 Hz, 9H). FT-IR (NaCl), $\bar{\upsilon}$ = 3224 , 2980, 1637, 1487, 1395, 1162, 1062 cm^{-1}. Elemental analysis calcd (%) for $C_8H_{20}ClNO.1.5H_2O$ (208.77 g mol^{-1}): C 46.02, N 6.71, H 11.13; found: C 45.88, N 6.63, H 11.34

***N-butyl-N,N-diethyl-N-hydroxyethylammonium bromide [$N_{2,2,4,C2OH}$][Br]*:** The same procedure was followed as that described above for [$N_{2,2,2,C2OH}$][Br]: N,N-diethyl-N-(2-hydroxyethyl)amine (4.00g; 34.10mmol) and 1-bromo-butane (5.14g; 37.50mmol) were used. The product [$N_{2,2,4,C2OH}$][Br] (5.32g; 61%) was obtained as a yellow solid. ^{1}H NMR (400 MHz, D2O): δ (ppm) = 3.91 (m, 2H), 3.32 (q, ^{3}J(H,H)= 7.1 Hz, 6H), 3.20 (m, 2H), 1.61 (m, 2H), 1.31 (m, 2H), 1.21 (t, ^{3}J(H,H)=7.0Hz, 6H), 0.88 (t, ^{3}J(H,H)=7.4Hz, 3H), FT-IR (KBr), $\bar{\upsilon}$ = 3414, 2965, 1641, 1466, 1396, 1157, 1083 cm^{-1}. Elemental analysis calcd (%) for $C_{10}H_{24}BrNO.0.3H_2O$ (259.66 g mol^{-1}): C 46.25, N 5.40, H 9.57; found: C 46.41, N 5.60, H 9.91.

***N,N-diethyl-N-hexyl-N-hydroxyethylammonium bromide [$N_{2,2,6,C2OH}$][Br]*:** The same procedure was followed as that described above for [$N_{2,2,2,C2OH}$][Br]: N,N-diethyl-N-(2-hydroxyethyl)amine (1.00g; 8.53mmol) and 1-bromo-hexane (1.55g; 9.38mmol) were used. The product [$N_{2,2,6,C2OH}$][Br] (1.80g; 75%) was obtained as a yellow solid. ^{1}H NMR (400MHz, CD_3OD): δ

(ppm) = 3.96 (m, 2H), 3.85 (t, -OH), 3.47 (m, 6H), 3.17 (m, 2H), 1.74 (m, 2H), 1.41 (m, 6H), 1.34 (m, 6H), 0.95 (t, $^{3}J(H,H)$=7.0 Hz, 3H). FT-IR (KBr), $\bar{\upsilon}$ = 3316, 2927, 1630, 1465, 1396, 1155, 1082 cm^{-1}. Elemental analysis calcd (%) for $C_{12}H_{28}BrNO.0.8H_2O$ (296.73 g mol^{-1}): C 48.57, N 4.72, H 10.08; found: C 48.55, N 4.95, H 10.71.

***N-ethyl-N-hydroxyethyl-N,N-dimethylammonium bromide [$N_{1,1,2,C2OH}$][Br]*:** The same procedure was followed as that described above for [$N_{2,2,2,C2OH}$][Br]: N-(2-hydroxyethyl)-N,N-dimethylamine (1.00g; 11.20mmol) and 1-bromo-ethane (1.35g; 12.30mmol) were used. The product [$N_{1,1,2,C2OH}$][Br] (1.76g; 79%) was obtained as a white solid. ^{1}H NMR (400MHz, CD_3OD): δ (ppm) = 3.99 (m, 2H), 3.50 (q, $^{3}J(H,H)$=7.2Hz, 2H), 3.48 (m, 2H), 3.16 (s, 6H), 1.38 (tt, $^{3}J(H,N)$=2.4 Hz, $^{3}J(H,H)$=7.2 Hz, 3H). FT-IR (KBr), $\bar{\upsilon}$ = 3417, 1639, 1481, 1129, 1082 cm^{-1}. Elemental analysis calcd (%) for $C_6H_{16}BrNO$ (198.13 g mol^{-1}): C 36.37, N 7.07, H 8.16; found: C 35.97, N 6.92, H 7.30.

***N-butyl-N-hydroxyethyl-N,N-dimethylammonium chloride [$N_{1,1,4,C2OH}$][Cl]*:** The same procedure was followed as that described above for [$N_{2,2,2,C2OH}$][Br]: N-(2-hydroxyethyl)-N,N-dimethylamine (2.00g, 22.40mmol) and 1-chloro-butane (2.28g, 24.60mmol) were used. The product [$N_{1,1,4,C2OH}$][Cl] (3.04g, 75%) was obtained as a white solid. ^{1}H NMR (400 MHz, $(CD_3)_2SO$) δ (ppm) = 5.67 (t, $^{3}J(H,H)$=4.8 Hz, 1H), 3.81 (m, 2H), 3.39 (m, 2H), 3.10 (s, 6H), 1.66 (m, 2H), 1,29 (m, 2H), 0,92 (t, $^{3}J(H,H)$=7.6 Hz, 3H). FT-IR (KBr), $\bar{\upsilon}$ = 3256 (O-H), 2965 (C-H_{alif}), 1634 (O-H), 1488, 1380, 1124, 1049 cm^{-1}. Elemental analysis calcd (%) for$C_8H_{20}ClNO.0.2H_2O$ (181.74 g mol^{-1}) calcd (%) for C 51.84, N 7.56, H 11.12; found: C 51.52, N 7.95, H 11.42.

***N-hexyl-N-hydroxyethyl-N,N-dimethylammonium bromide [$N_{1,1,6,C2OH}$][Br]*:** The same procedure was followed as that described above for [$N_{2,2,2,C2OH}$][Br]: N-(2-hydroxyethyl)-N,N-dimethylamine (1.00g; 11.20mmol) and 1-Bromo-hexane (2.03g; 12.30mmol) were used. The product [$N_{1,1,6,C2OH}$][Br] (2.58g; 91%) was obtained as a white gel. ^{1}H NMR (400MHz, CD_3OD): δ (ppm) = 3.99 (m, 2H), 3.49 (m, 2H), 3.42 (m, 2H, H1), 3.17 (s, 6H), 1.80 (m, 2H), 1.38 (m, 6H), 0.92 (t, ^{3}J(H,H)=7 Hz, 3H). FT-IR (NaCl), $\bar{\upsilon}$ = 3419, 2958, 1639, 1469, 1400, 1132, 1087 cm^{-1}. Elemental analysis calcd (%) for $C_{10}H_{24}BrNO.H_2O$ (272.27 g mol^{-1}): C 44.11, N 5.15, H 9.64; found: C 43.94, N 5.27, H 10.60.

***N,N-dihydroxyethyl-N,N-dimethylammonium chloride [$N_{1,1,C2OH,C2OH}$][Cl]*:** The same procedure was followed as that described above for [$N_{2,2,2,C2OH}$][Br]: N-(2-hydroxyethyl)-N,N-dimethylamine (2.00g; 22.44mmol) and 1-chloro-ethanol (1,99g; 24.68mmol) were used. The product [$N_{1,1,C2OH,C2OH}$][Cl] (2.12g; 56%) was obtained as a white solid. ^{1}H NMR (400 MHz, D_2O) δ (ppm) = 3.99 (m, 4H), 3.52 (t, ^{3}J(H,H)=5.2Hz, 4H), 3.15 (s, 9H). FT-IR (KBr), $\bar{\upsilon}$ = 3356, 2963, 1634, 1478, 1079 cm^{-1}. Elemental analysis calcd (%) for $C_6H_{18}ClNO_3$ (169.68 g mol^{-1}): C 42.47, N 8.26, H 9.52; found: C 42.36, N 8.17, H 10.17.

***N-ethyl-N-hydroxypropyl-N,N-dimethylammonium bromide [$N_{1,1,2,C3OH}$][Br]*:** The same procedure was followed as that described above for [$N_{2,2,2,C2OH}$][Br]: N-(2-hydroxypropyl)-N,N-dimethylamine (1.00g; 9.69mmol) and 1-bromo-ethane (1.16g; 10.66mmol) were used. The product [$N_{1,1,2,C3OH}$][Br] (1.76g; 85%) was obtained as a brown solid. ^{1}H NMR (400 MHz, D_2O): δ (ppm) =4.32 (m, 1H), 3.38 (m, 2H), 3.23 (d, ^{3}J(H,H)= 5.6 Hz, 2H), 3.03 (d, ^{3}J(H,H)= 4.8Hz, 6H), 1.26 (t, ^{3}J(H,H)=7.0 Hz, 3H), 1.16 (d,

^{3}J(H,H)=6.4 Hz, 3H). FT-IR (KBr), $\bar{\upsilon}$ = 3418, 2981, 1640, 1482, 1147, 1021 cm^{-1}. Elemental analysis calcd (%) for $C_7H_{18}BrNO.0.2H_2O$ (215.76 g mol^{-1}): C 38.96, N 6.49, H 8.61; found: C 38.83, N 6.70, H 8.89.

***N-ethyl-N-hydroxypropyl-N,N-dimethylammonium chloride [$N_{1,1,2,C3OH}$][Cl]*:** The same procedure was followed as that described above for [$N_{2,2,2,C2OH}$][Cl]: [$N_{1,1,2,C3OH}$][Br] (2.50g, 11.79mmol) and ionic exchange resin (IRA 400-Cl) were used. The product [$N_{1,1,2,C3OH}$][Cl] (1.56g, 79%) was obtained as a brown liquid. ^{1}H NMR (400 MHz, D_2O): δ (ppm) = 4.32 (m, 1H), 3.38 (m, 2H), 3.22 (d, ^{3}J(H,H)=5.6 Hz, 2H), 3.03 (d, ^{3}J(H,H)=4.0 Hz, 6H), 1.26 (t, ^{3}J(H,H)=6.8 Hz, 3H), 1.16 (d, ^{3}J=6.0 Hz, 3H). FT-IR (KBr), $\bar{\upsilon}$ = 3418, 2979, 1640, 1487, 1399, 1151, 1073 cm^{-1}. Elemental analysis calcd (%) for $C_7H_{18}ClNO.1.4H_2O$ (192.94 g mol^{-1}): C 43.57, N 7.26, H 10.89; found: C 43.27, N 7.82, H 10.51.

***N-butyl-N-hydroxypropyl-N,N-dimethylammonium chloride [$N_{1,1,4,C3OH}$][Cl]*:** The same procedure was followed as that described above for [$N_{2,2,2,C2OH}$][Br]: N-(2-hydroxypropyl)-N,N-dimethylamine (2.00g, 19.4mmol) and 1-chloro-butane (1.97, 21.30mmol) were used. The product [$N_{1,1,4,C3OH}$][Cl] (1.22g, 32%) was obtained as a yellow solid. ^{1}H NMR (400 MHz, D_2O) δ (ppm) = 4.30 (m, 1H), 3.29 (m, 2H), 3.23 (m, 2H), 3.03 (d, ^{3}J(H,H)=5.2Hz, 6H), 1.65 (m, 2H), 1.27 (m, 2H), 1.15 (d, ^{3}J(H,H)=6.4Hz, 3H), 0.84 (t, ^{3}J(H,H)=7.4Hz, 3H). FT-IR (KBr), $\bar{\upsilon}$ = 3353, 2967, 1637, 1484, 1377, 1149, 1076 cm^{-1}. Elemental analysis calcd (%) for $C_9H_{22}ClNO.0.1H_2O$ (197.57 g mol^{-1}): C 54.71, N 7.09, H 11.35; found: C 54.33, N 7.09, H 11.96.

4.3. Synthesis and characterization of magnetic complexes salts

General method: Chloride salt of choline derivative/phosphonium or imidazolium and ethanol were added to a round-bottomed flask. After the complete dissolution, the selected hydrated lanthanide salt ($FeCl_3$ or $MnCl_2$) were added under vigorous magnetic stirring at room temperature. The reaction mixture was stirring for 48 h and then the solvent was evaporated, and the product was dried under vacuum.

4.3.1. Iron (III)-based organic salts

N-butyl-N-hydroxyethyl-N,N-dimethylammonium tetrachloroferrate (III) [$N_{1,1,4,C2OH}$][$FeCl_4$]*: [$N_{1,1,4,C2OH}$][Cl] (0,50g; 3,42mmol); $FeCl_3.6H_2O$ (0,92g; 3.42mmol); Yield: quantitative; brown solid. FT-IR (KBr), $\bar{\upsilon}$ = 3415, 2960, 1627, 1477, 1379, 1131, 1087 cm^{-1}. Elemental analysis calcd (%) for $C_8H_{20}Cl_4FeNO.3H_2O$ (397.99 g mol^{-1}): C 24.14, N 3.52, H 6.59; found: C 24.27, N 3.38, H 6.14.

N,N-dihydroxyethyl-N,N-dimethylammonium tetrachloroferrate (III) [$N_{1,1,C2OH,C2OH}$][$FeCl_4$]*: [$N_{1,1,C2OH,C2OH}$][Cl] (0,25g; 1.48mmol); $FeCl_3.6H_2O$ (0,39g; 1.48mmol); Yield: quantitative; brown solid. FT-IR (KBr), $\bar{\upsilon}$ = 3386, 1635, 1474, 1079 cm^{-1}. Elemental analysis calcd (%) for $C_6H_{16}Cl_4FeNO_2$ (331.87 g mol^{-1}): C 21.71, N 4.22, H 4.87; found: C 22.18, N 4.23, H 5.13.

N-ethyl-N-hydroxypropyl-N,N-dimethylammonium tetrachloroferrate (III) [$N_{1,1,2,C3OH}$][$FeCl_4$]*: [$N_{1,1,2,C3OH}$][Cl] (0.25g; 1.50mmol); $FeCl_3.6H_2O$ (0,41g; 1.51mmol); Yield: quantitative; brown liquid. FT-IR (KBr), $\bar{\upsilon}$ = 3407, 2978, 1627, 1482, 1395, 1145, 1018 cm^{-1}. Elemental analysis calcd (%) for

$C_7H_{18}Cl_4FeNO.3.5H_2O$ (392.97 g mol^{-1}): C 21.39, N 3.57, H 6.43; found: C 20.91, N 3.35, H 5.65.

N-butyl-N-hydroxypropyl-N,N-dimethylammonium tetrachloroferrate (III) [$N_{1,1,4,C3OH}$][$FeCl_4$]*: [$N_{1,1,4,C3OH}$][Cl] (0.26g, 1.30mol); $FeCl_3.6H_2O$ (0.35g, 1.30mol); Yield: quantitative; brown liquid. FT-IR (KBr), $\bar{\upsilon}$ = 3545, 2971, 1616, 1476, 1386, 1141, 1071 cm^{-1}. Elemental analysis calcd (%) for $C_9H_{22}Cl_4FeNO$ (357.96 g mol^{-1}): C 30.20, N 3.91, H 6.21; found: C 30.44, N 3.91, H 6.27.

N,N,N-triethyl-N-hydroxyethylammonium tetrachloroferrate (III) [$N_{1,1,1,C2OH}$][$FeCl_4$]*: [$N_{1,1,1,C2OH}$][Cl] (0.50g, 3.60mol); $FeCl_3.6H_2O$ (0.97g, 3.59mol); Yield: quantitative; pink solid. FT-IR (KBr), $\bar{\upsilon}$ = 3556, 2960, 1607, 1470, 1337, 1131, 1082 cm^{-1}. Elemental analysis calcd (%) for $C_5H_{14}Cl_4FeNO$ (301.84 g mol^{-1}): C 19.89, N 4.64, H 4.68; found: C 19.67, N 4.50, H 4.64.

4.3.2. Manganese (II)-based organic salts

N-butyl-N-hydroxyethyl-N,N-dimethylammonium trichloromanganate (II) [$N_{1,1,4,C2OH}$][$MnCl_3$]*: [$N_{1,1,4,C2OH}$][Cl] (0.50g, 3.43mmol); $MnCl_2.4H_2O$ (0.68g, 3.44mmol); Yield: quantitative; pink solid. FT-IR (KBr), $\bar{\upsilon}$ = 3440, 2964, 1615, 1469, 1383, 1172, 1086 cm^{-1}. Elemental analysis calcd (%) for $C_8H_{20}Cl_3MnNO.3H_2O$ (361.64 g mol^{-1}): C 26.57, N 3.87, H 7.26; found: C 26.40, N 3.73, H 6.68.

N,N-dihydroxyethyl-N,N-dimethylammonium trichloromanganate (II) [$N_{1,1,C2OH,C2OH}$][$MnCl_3$]*: [$N_{1,1,C2OH,C2OH}$][Cl] (0.25g, 1.49mmol); $MnCl_2.4H_2O$ (0.30g, 1.50mmol); Yield: quantitativ; yellow solid. FT-IR (KBr), $\bar{\upsilon}$ = 3366,

1627, 1472, 1328, 1126, 1073 cm^{-1}. Elemental analysis calcd (%) for $C_6H_{16}Cl_3MnNO_2$ (295.52 g mol^{-1}): C 24.38, N 4.74, H 5.47; found: C 24.35, N 4.61, H 5.40.

N-ethyl-N-hydroxypropyl-N,N-dimethylammonium trichloromanganate (II) [$N_{1,1,2,C3OH}$][$MnCl_3$]*: [$N_{1,1,2,C3OH}$][Cl] (0.25g, 1.49mmol); $MnCl_2.4H_2O$ (0.30g, 1.50mmol); Yield: quantitative; yellow solid. FT-IR (KBr), $\bar{\upsilon}$ = 3424, 2973, 1626, 1484, 1374, 1148, 1021 cm^{-1}. Elemental analysis calcd (%) for $C_7H_{18}Cl_3MnNO.2.5H_2O$ (338.60 g mol^{-1}): C 24.83, N 4.14, H 6.86; found: C 24.78, N 4.04, H 6.09.

N-butyl-N-hydroxypropyl-N,N-dimethylammonium trichloromanganate (II) [$N_{1,1,4,C3OH}$][$MnCl_3$]*: [$N_{1,1,4,C3OH}$][Cl] (0.26g, 1.31mol); $MnCl_2.4H_2O$ (0.27g, 1.30mol); Yield: quantitative; yellow solid. FT-IR (KBr), $\bar{\upsilon}$ = 3425, 2967, 1633, 1485, 1398, 1148, 1011 cm^{-1}. Elemental analysis calcd (%) for $C_9H_{22}Cl_3MnNO.0.1H_2O$ (321.61 g mol^{-1}): C 33.61, N 4.36, H 6.91; found: C 33.25, N 4.45, H 7.36.

N,N,N-triethyl-N-hydroxyethylammonium trichloromanganate (II) [$N_{1,1,1,C2OH}$][$MnCl_3$]*: [$N_{1,1,1,C2OH}$][Cl] (0.51g, 3.62mol); $MnCl_2.4H_2O$ (0.71g, 3.61mol); Yield: quantitative; pink solid. FT-IR (KBr), $\bar{\upsilon}$ = 3423, 1474, 1134, 1081 cm^{-1}. Elemental analysis calcd (%) for $C_5H_{14}Cl_3MnNO$ (265.49 g mol^{-1}): C 22.62, N 5.28, H 5.33; found: C 22.39, N 4.99, H 4.93.

Tetraethylammonium trichloromanganate (II) [$N_{2,2,2,2}$][$MnCl_3$]*: $N_{2,2,2,2}$][Cl] (0.50g, 2.38mmol); $MnCl_2.4H_20$ (0.47g, 2.38mmol); Yield: quantitative; yellow solid. **FTIR** (KBr), $\bar{\upsilon}$ = 3415, 2983, 1622, 1474, 1398, 1180, 1040, 880,

789 cm^{-1}. **Elemental analysis** calcd (%) for $C_8H_{20}Cl_3MnN$. $2H_2O$ (327.58 g mol^{-1}): C 29.33, N 4.28, H 7.38; found: C 29.14, N 4.15, H 6.82.

Tetrahydroxymethylphosphonium trichloromanganate (II) [$P_{OH,OH,OH,OH}$][$MnCl_3$]: [$P_{OH,OH,OH,OH}$][Cl] (0.31g, 1.33mmol); $MnCl_2.4H_2O$ (0.26g, 1.33mmol); Yield: quantitative; pink solid; FTIR (KBr), $\bar{\upsilon}$ = 3354, 2909, 1623, 1416, 1300, 1189, 1044, 920 cm^{-1}. Elemental analysis calcd (%) for $C_4H_{12}Cl_3O_4MnP$ (316.42 $g.mol^{-1}$): C 15.18, H 3.83; found: C 15.70, H 3.80.

Tetrabutylphosphonium trichloromanganate (II) [$P_{4,4,4,4}$][$MnCl_3$]: [$P_{4,4,4,4}$][Cl] (0.25g, 0.85mmol); $MnCl_2.4H_2O$ (0.17g, 0.85mmol); Yield: quantitative; yellow solid; FTIR (KBr), $\bar{\upsilon}$ = 3448, 2962-2871, 1642, 1463, 1407, 1382, 1315, 1237, 1099, 1007, 970, 918, 812, 720 cm^{-1}. Elemental analysis calcd (%) for $C_{16}H_{36}Cl_3MnP.2.5H_2O$ (465.83 $g.mol^{-1}$): C 40.88, H 8.19; found: C 41.25, H 8.19.

1-(2-hydroxyethyl)-3-methylimidazolium trichloromanganate (II) [C_2OHMIM][$MnCl_3$]: [C_2OHMIM][Cl] (0.26g, 1.57mmol); $MnCl_2.4H_2O$ (0.31g, 1.57mmol); Yield: quantitative; pink solid; FTIR (KBr), $\bar{\upsilon}$ = 3385, 1625, 1575, 1455, 1167, 1060, 832, 749, 650 cm^{-1}. Elemental analysis calcd (%) for $C_6H_{12}Cl_3MnN_2O$ (289.49 $g.mol^{-1}$): C 24.89, N 9.68, H 4.19; found: C 25.34, N 9.65, H 4.05.

1-(2-hydroxyethyl)-2,3-dimethylimidazolium trichloromanganate (II) [C_2OHDMIM][$MnCl_3$]: [C_2OHDMIM][Cl] (0.25g, 1.43mmol); $MnCl_2.4H_2O$ (0.28g, 1.42mmol); Yield: quantitative; pink solid; FTIR (KBr), $\bar{\upsilon}$ = 3386, 1622, 1575, 1449, 1167, 1058, 835, 749, 650 cm^{-1}. Elemental analysis calcd (%)

for $C_7H_{13}Cl_3MnN_2O$ (302.51 g.mol^{-1}): C 27.79, N 9.26, H 4.34; found: C 27.24, N 8.95, H 3.76.

1-ethyl-3-methylimidazolium trichloromanganate (II) [C_2MIM][$MnCl_3$]: [C_2MIM][Cl] (0.25g, 1.71mmol); $MnCl_2.4H_2O$ (0.34g, 1.70mmol); Yield: quantitative; yellow solid; FTIR (KBr), $\bar{\upsilon}$ = 3404, 3113, 2987, 1623, 1587, 1469, 1336, 1173, 1089, 956, 825, 732, 645, 619 cm^{-1}. Elemental analysis calcd (%) for $C_6H_{12}Cl_3MnN_2.1.5H_2O$ (300.52 g.mol^{-1}): C 23.98, N 9.32, H 5.04; found: C 23.84, N 8.98, H 5.38.

4.4. Magnetic moment determination

The Mass Susceptibility χ_g of compounds was determined using a Magnetic Susceptibility Balance at the room temperature (20 ºC), from Sherwood Scientific. The effective magnetic moment (μ_{eff}) values were obtained by using the following Equation 2.3, Equation 2.4 and Equation 2.5.

$$\chi_g = \frac{C.l.(R-R_0)}{10^9.m} \qquad \textbf{(Equation 2. 3)}$$

Where C is the constant of calibration balance (= 1.14), l is length of the sample (cm), R is the reading for the tube with the sample, R_0 is the empty tube reading and m is mass of the sample (g).

$$\chi_m = \chi_g.M_w \qquad \textbf{(Equation 2. 4)}$$

Where χ_m is the molar susceptibility and Mw is the molecular weight of the compound.

$$\mu_{eff} = 2,828\sqrt{\chi_m.T} \qquad \textbf{(Equation 2. 5)}$$

Where μeff is the effective magnetic moment and T is the measurement temperature (in Kelvin, T (°C) + 273).

4.5. Cytotoxicity studies

Cytotoxic activity of compounds was studied on 3T3, Caco-2, HepG2 and 293T cells previously acquired from DSMZ biobank. Cells were cultured in Dulbecco´s Modified Eagle´s medium: Nutrient Mix F-12 (DMEM/F-12) (Merck, Germany), in Minimum Essential Medium (MEM) (Merck, Germany), in RPMI medium (Sigma-Aldrich, USA), and in Dulbecco´s Modified Eagle´s medium (Merck, Germany), respectively, supplemented with 10% fetal bovine serum) (Hyclone, UK), 100 IU/mL penicillin, and 100 μg/mL streptomycin (Merck, Germany). For subculture, 3T3 (fibroblasts), Caco-2 (colon adenocarcinoma), HepG2 (hepatocellular carcinoma) and 293T (embryonal kidney) cells were dissociated using trypsin-EDTA (Sigma, USA), split in an 1:5, 1:3, 1:3 and 1:6 ratio, respectively, and seeded into Petri dishes with 25 cm^2 of growth area. Cells were maintained in a humidified atmosphere (95%), with 5% CO_2, at 37 °C. Cytotoxicity was evaluated on 3T3, Caco-2, HepG2 and 293T cells' viability after cells reached total confluence on 96-well plates. Cells were treated with samples at 100 μg/mL for 24 h and their effects were assessed using MTT (Sigma, Germany), a colorimetric assay based on the conversion of tetrazolium salts to blue formazan products by active mitochondria in viable cells. Results were expressed as percentage of control (%).

Data and statistical analysis was performed using one-way analysis of variance (ANOVA) with Dunnett's multiple comparison of group means to determine significant differences relatively to the control treatment. Results are presented as mean ± standard error of the mean (SEM). Differences were considered significant at a level of 0.05 (p - value < 0.05). Calculations

were performed using GraphPad v5.1 (GraphPad Software, La Jolla, CA, USA) software.

4.6. Single Crystal X-Ray Cristallography

A crystal of $[N_{1,1,1,C2OH}][MnCl_3]$, $[N_{1,1,C2OH,C2OH}][MnCl_3]$ and $[N_{2,2,2,2}][MnCl_3]$ suitable for single-crystal X-ray analysis was selected, covered with Fomblin (polyfluoro ether oil) and mounted on a nylon loop. The data was collected at 110(2) K on a Bruker D8 Venture diffractometer equipped with a Photon 100 CMOS detector and an Oxford Cryostem Cooler, using graphite monochromated Mo-Kα radiation (λ= 0.71073 Å). The data was processed using the APEX3 suite software package, which includes integration and scaling (SAINT), absorption corrections (SADABS [51]) and space group determination (XPREP). Structure solution and refinement were done using direct methods with the programs SHELXT 2018/2 and SHELXL-2018/3 [52,53] inbuilt in APEX and WinGX-Version 2021.3 [54] software packages. All non-hydrogen atoms were refined anisotropically and the hydrogen atoms were inserted in idealized positions and allowed to refine riding on the parent carbon atom. The molecular diagrams were drawn with ORTEP [3] or Mercury [55]. Crystal and structure refinement data are given in supplementary information.

Acknowledgements

This work was supported by Fundação para a Ciência e a Tecnologia through projects (PEst-C/LA0006/2013, PTCD/CTM-NAN/120658/2010, two contracts under Investigador FCT (L. C. Branco and I. M. Marrucho), a doctoral fellowship Andreia Forte (PD/BD/109625/2015), by the Portuguese

Foundation for Science and Technology (FCT) through the strategic project UID/MAR/04292/2020 granted to MARE—Marine and Environmental Sciences Centre and Solchemar company. This work was also supported by the Associate Laboratory for Green Chemistry- LAQV which is financed by national funds from FCT/MCTES (UID/QUI/50006/2019). The X-ray infrastructure was financed by FCT-MCTES through project RECI/BBB-BEP/0124/2012. The NMR spectrometers are part of The National NMR Facility, supported by FCT/MCTES (RECI/BBB-BQB/0230/2012).

References

(1) Qureshi, Z. S.; Deshmukh, K. M.; Bhanage, B. M. Applications of Ionic Liquids in Organic Synthesis and Catalysis. *Clean Technol. Environ. Policy* 2014, *16*, 1487–1513.

(2) Zhao, D.; Wu, M.; Kou, Y.; Min, E. Ionic Liquids: Applications in Catalysis. *Catal. Today* 2002, *74*, 157–189.

(3) Zhang, P.; Jiang, Z.; Cui, Y.; Xie, G.; Jin, Y.; Guo, L.; Catalysis, I.; Key, S.; Technology, G. C.; Engineering, C. Catalytic Performance of Ionic Liquid for Dehydrochlorination Reaction: Excellent Activity and Unparalled Stability. *Appl. Catal. B Environ.* 2019, *255*, 117757 (1-10).

(4) Singh, V. V.; Nigam, A. K.; Batra, A.; Boopathi, M.; Singh, B.; Vijayaraghavan, R. Applications of Ionic Liquids in Electrochemical Sensors and Biosensors. *Int. J. Electrochem.* 2012, 1–19.

(5) Sakaebe, H.; Matsumoto, H.; Tatsumi, K. Application of Room Temperature Ionic Liquids to Li Batteries. *Electrochim. Acta* 2007, *53*, 1048–1054.

(6) Liu, J.-F.; Jönsson, J. A.; Jiang, G.-B. Application of Ionic Liquids in Analytical Chemistry. *Trends Anal. Chem.* 2005, *24* (1), 20–27.

(7) Sun, P.; Armstrong, D. W. Ionic Liquids in Analytical Chemistry. *Anal. Chim. Acta* 2010, *661*, 1–16.

(8) Bermúdez, M. D.; Jiménez, A.-E.; Sanes, J.; Carrión, F.-J. Ionic Liquids as

Advanced Lubricant Fluids. *Molecules* 2009, *14*, 2888–2908.

(9) Kamimura, H.; Kubo, T.; Minami, I.; Mori, S. Effect and Mechanism of Additives for Ionic Liquids as New Lubricants. *Tribol. Int.* 2007, *40*, 620–625.

(10) Gong, X.; Li, L. Nanometer-Thick Ionic Liquids as Boundary Lubricants. *Adv. Eng. Mater.* 2017, *1700617*, 1700617 (1-13).

(11) Ferraz, R.; Branco, L. C.; Prudêncio, C.; Noronha, J. P.; Petrovski, Ž. Ionic Liquids as Active Pharmaceutical Ingredients. *ChemMedChem* 2011, *6*, 975–985.

(12) Marrucho, I. M.; Branco, L. C.; Rebelo, L. P. N. Ionic Liquids in Pharmaceutical Applications. *Annu. Rev. Chem. Biomol. Eng.* 2014, *5*, 527–547.

(13) Kadokawa, J. *Ionic Liquids - New Aspects for the Future*; InTech: Rijeka, Croatia, 2013.

(14) Sadat Rajabi, M.; Moniruzzaman, M.; Azmi Bustam, M.; Lotfi, M. Recent Advances of Ionic Liquids in Extarction of Biologically Active Compounds: A Review. *Am. J. Chem.* 2015, *5* (3A), 7–12.

(15) Frade, R. F. M.; Simeonov, S.; Rosatella, A. A.; Siopa, F.; Afonso, C. A. M. Toxicological Evaluation of Magnetic Ionic Liquids in Human Cell Lines. *Chemosphere* 2013, *92*, 100–105. https://doi.org/10.1016/j.chemosphere.2013.02.047.

(16) Frade, R. F.; Afonso, C. A. Impact of Ionic Liquids in Environment and Humans: An Overview. *Hum. Exp. Toxicol.* 2010, *29* (12), 1038–1054.

(17) Buchman, A. L. The Addition of Choline to Parenteral Nutrition. *Gastroenterology* 2009, *137*, S119–S128.

(18) Azevedo, A. M. O.; Costa, S. P. F.; Dias, A. F. V; Marques, A. H. O.; Pinto, P. C. A. G.; Bica, K.; Ressmann, A. K.; Passos, M. L. C.; Araújo, A. R. T. S.; Reis, S.; Saraiva, M. L. M. F. S. Anti-Inflammatory Choline Based Ionic Liquids: Insights into Their Lipophilicity, Solubility and Toxicity Parameters. *J. Mol. Liq.* 2017, *232*, 20–26.

(19) Siopa, F.; Figueiredo, T.; Frade, R. F. M.; Neto, I.; Meirinhos, A.; Reis, C. P.; Sobral, R. G.; Afonso, C. A. M.; Rijo, P. Choline-Based Ionic Liquids :

Improvement of Antimicrobial Activity. *Chem. Sel.* 2016, *1*, 5909–5916.

(20) Hayashi, S.; Hamaguchi, H. Discovery of a Magnetic Ionic Liquid [Bmim]FeCl4. *Chem. Lett.* 2004, *33* (12), 1590–1591.

(21) Pedro, I. de; Rojas, D. P.; Albo, J.; Luis, P.; Irabien, A.; Blanco, J. A.; Rodríguez, J. Long-Range Magnetic Ordering in Magnetic Ionic Liquid: Emim. *J. Phys. Condens. Matter* 2010, *22*, 296006 (1-4).

(22) Hayashi, S.; Saha, S.; Hamaguchi, H. A New Class of Magnetic Fluids: Bmim[FeCl4] and Nbmim[FeCl4] Ionic Liquids. *IEEE Trans. Magn.* 2006, *42* (1), 12–14.

(23) Santos, E.; Albo, J.; Irabien, A. Magnetic Ionic Liquids: Synthesis, Properties and Applications. *RSC Adv.* 2014, *4*, 40008–40018.

(24) Branco, A.; Branco, L. C.; Pina, F. Electrochromic and Magnetic Ionic Liquids. *Chem. Commun.* 2011, *47*, 2300–2302.

(25) Del Sesto, R. E.; McCleskey, T. M.; Burrell, A. K.; Baker, G. A.; Thompson, J. D.; Scott, B. L.; Wilkes, J. S.; Williams, P. Structure and Magnetic Behavior of Transition Metal Based Ionic Liquids. *Chem. Commun.* 2008, 447–449.

(26) Rosatella, A. A.; Siopa, F.; Frade, R. F. M.; Afonso, C. A. M. New Low Viscous Cholinium-Based Magnetic Ionic Liquids. *New J. Chem.* 2016, *40*, 3124–3129.

(27) Pereira, C. C. L.; Dias, S.; Coutinho, I.; Leal, J. P.; Branco, L. C. Europium(III) Tetrakis(β -Diketonate) Complex as an Ionic Liquid: A Calorimetric and Spectroscopic Study. *Inorg. Chem.* 2013, *52*, 3755–3764.

(28) Krieger, B. M.; Lee, H. Y.; Emge, T. J.; Wishartb, J. F.; Castner, E. W.; Jr. Physical Chemistry of Ionic Liquids. *Phys. Chem. Chem. Phys.* 2010, *12*, 8919–8925.

(29) Santos, E.; Albo, J.; Rosatella, A.; Afonso, C. A. M.; Irabien, A. Synthesis and Characterization of Magnetic Ionic Liquids (MILs) for CO2 Separation. *J. Chem. Technol. Biotechnol.* 2014, *89*, 866–871.

(30) Rodríguez-Arco, L.; Gómez-Ramírez, A.; Durán, J. D. G.; López-López, M. T. New Perspectives for Magnetic Fluid-Based Devices Using Novel Ionic Liquids as Carriers. In *Smart Actuation and Sensing Systems*; Berselli, G.,

Vertechy, R., Vassura, G., Eds.; IntechOpen, 2012; pp 445–464.

(31) Giernoth, R. Task-Specific Ionic Liquids. *Angew. Chemie - Int. Ed.* 2010, *49*, 2834–2839.

(32) Lee, S. Y.; Jeon, S. I.; Jung, S.; Chung, I. J.; Ahn, C. H. Targeted Multimodal Imaging Modalities. *Adv. Drug Deliv. Rev.* 2014, *76*, 60–78.

(33) Yuan, D.; Ding, L.; Sun, Z.; Li, X. MRI / Fluorescence Bimodal Amplification System for Cellular GSH Detection and Tumor Cell Imaging Based on Manganese Dioxide Nanosheet. *Sci. Rep.* 2018, *8*, 1747 (1-9).

(34) Han, C.; Xie, T.; Wang, K.; Jin, S.; Li, K.; Dou, P.; Yu, N.; Xu, K. Development of Fluorescence/MR Dual-Modal Manganese-Nitrogen-Doped Carbon Nanosheets as an Efficient Contrast Agent for Targeted Ovarian Carcinoma Imaging. *J. Nanobiotechnology* 2020, *18*, 175 (1-15).

(35) Zhan, Y.; Zhan, W.; Li, H.; Xu, X.; Cao, X.; Zhu, S.; Liang, J.; Chen, X. In Vivo Dual-Modality Fluorescence and Magnetic Resonance Imaging-Guided Lymph Node Mapping with Good Biocompatibility Manganese Oxide Nanoparticles. *Molecules* 2017, *22*, 2208 (1-13).

(36) Kálmán, F. K.; Kálmán, F. K.; Nagy, V.; Váradi, B.; Garda, Z.; Molnár, E.; Trencsényi, G.; Kiss, J.; Même, S.; Même, W.; Tóth, É.; Tircsó, G. Mn(II)-Based MRI Contrast Agent Candidate for Vascular Imaging. *J. Med. Chem.* 2020, *63*, 6057–6065.

(37) Anbu, S.; Hoffmann, S. H. L.; Carniato, F.; Kenning, L.; Price, T. W.; Prior, T. J.; Botta, M.; Martins, A. F.; Stasiuk, G. J. Magnetic Resonance Imaging A Single-Pot Template Reaction Towards a Manganese-Based T1 Contrast Agent Research Articles. *Angew.Chem. Int. Ed.* 2021, *60*, 10736–10744.

(38) Çapan, A.; Uruş, S.; Sönmez, M. Ru(III), Cr(III), Fe(III) Complexes of Schiff Base Ligands Bearing Phenoxy Groups: Application as Catalysts in the Synthesis of Vitamin K3. *J. Saudi Chem. Soc.* 2018, *22*, 757–766.

(39) Pogány, L.; Moncol, J.; Pavlik, J.; Mazúr, M.; Šalitroš, I. High-Spin Mononuclear Iron(III) Complexes with Pentadentate Schiff Base Ligands: Structural Analysis and Magnetic Properties. *Chempluschem* 2019, *84*, 358–367.

(40) Wang, G. X.; Yin, J.; Li, J.; Yin, Z. B.; Zhang, W. X.; Xi, Z. Synthesis and Characterization of Manganese(II) Complexes Supported by Cyclopentadienyl-Phosphine Ligands. *Inorg. Chem. Front.* 2019, *6*, 428–433.

(41) Al-Wasidi, A. S.; Naglah, A. M.; Refat, M. S.; El-Megharbel, S. M.; Kalmouch, A.; Moustafa, G. O. Synthesis, Spectroscopic Characterization and Antimicrobial Studies of Mn(II), Co(II), Ni(II), Cr(III) and Fe(III) Melatonin Drug Complexes. *Egypt. J. Chem.* 2020, *63* (4), 1469–1481.

(42) Sarangi, A. K.; Mahapatra, B. B.; Sethy, S. K. Synthesis and Characterization of Tetranuclear Metal Complexes with an Octadentate Azodye Ligand. *Chem. Africa* 2018, *1*, 17–28.

(43) Gaber, M.; El-Ghamry, H. A.; Fathalla, S. K. Synthesis, Structural Identification, DNA Interaction and Biological Studies of Divalent Mn, Co and Ni Chelates of 3-Amino-5-Mercapto-1,2,4-Triazole Azo Ligand. *Appl. Organomet. Chem.* 2020, *34*, e5678 (1-12).

(44) Waheed, E. J.; Farhan, M. A.; Hameed, G. F. Synthesis and Characterization of New Manganese(II), Cobalt(II), Cadmium(II) and Mercury(II) Complexes with Ligand [N-(3-Acetylphenylcarbamothioyl)-2-Chloroacetamide] and Their Antibacterial Studies. *J. Phys. Conf. Ser.* 2019, *1234*, 012096 (1-11).

(45) Yousef, T. A.; Abu El-Reash, G. M.; Abu AL-Zahab, M.; Safaan, M. A. A. Physicochemical Investigations, Biological Studies of the Cr(III), Mn(II), Fe(III), Co(II), Ni(II), Cu(II), Zn(II), Cd(II), Hg(II) and UO2(VI) Complexes of Picolinic Acid Hydrazide Derivative: A Combined Experimental and Computational Approach. *J. Mol. Struct.* 2019, *1197*, 564–575.

(46) Hassoon, A. A.; Harrison, R. G.; Nawar, N.; Smith, S. J.; Mostafa, M. M. Synthesis, Single Crystal X-Ray, Spectroscopic Characterization and Biological Activities of Mn2+, Co2+, Ni2+ and Fe3+ Complexes. *J. Mol. Struct.* 2020, *1203*, 127240 (1-13).

(47) Earnshaw, B. A.; King, E. A. Transition Metal-Schiff's Base Complexes. Part IV. Investigations of Some Iron(II) and Manganese(II) Systems. *J. Am. Chem. Soc.* 1968, 1048–1052.

(48) Asmussen, R. W.; Soling, H. The Magnetic Properties of Manganous

Complexes. *Acta Chem. Scand.* 1657, *11*, 1331–1339.

(49) Batra, G.; Mathur, P. Mononuclear and Binuclear Manganese(II) Complexes with Tridentate Bis-Benzimidazolyl Ligands. *Transit. Met. Chem.* 1994, *19*, 160–164.

(50) Pedro, I. de; García-Saiz, A.; González, J.; Ruiz de Larramendi, I.; Rojo, T.; Afonso, C. a M.; Simeonov, S. P.; Waerenborgh, J. C.; Blanco, J. a; Ramajo, B.; Fernández, J. R. Magnetic Ionic Plastic Crystal: Choline[FeCl4]. *Phys. Chem. Chem. Phys.* 2013, *15*, 12724–12733.

(51) Krause, L.; Herbst-Irmer, R.; Sheldrick, G. M.; Stalke, D. Comparison of Silver and Molybdenum Microfocus X-Ray Sources for Single-Crystal Structure Determination. *J. Appl. Crystallogr.* 2015, *48* (1), 3–10.

(52) Sheldrick, G. M. Crystal Structure Refinement with SHELXL. *Acta Crystallogr. Sect. C Struct. Chem.* 2015, *71* (Md), 3–8.

(53) Hübschle, C. B.; Sheldrick, G. M.; Dittrich, B. ShelXle: A Qt Graphical User Interface for SHELXL. *J. Appl. Crystallogr.* 2011, *44* (6), 1281–1284.

(54) Farrugia, L. J. WinGX and ORTEP for Windows: An Update. *J. Appl. Crystallogr.* 2012, *45* (4), 849–854.

(55) MacRae, C. F.; Sovago, I.; Cottrell, S. J.; Galek, P. T. A.; McCabe, P.; Pidcock, E.; Platings, M.; Shields, G. P.; Stevens, J. S.; Towler, M.; Wood, P. A. Mercury 4.0: From Visualization to Analysis, Design and Prediction. *J. Appl. Crystallogr.* 2020, *53*, 226–235.

Chapter 3

Development of Lanthanides-based ionic systems

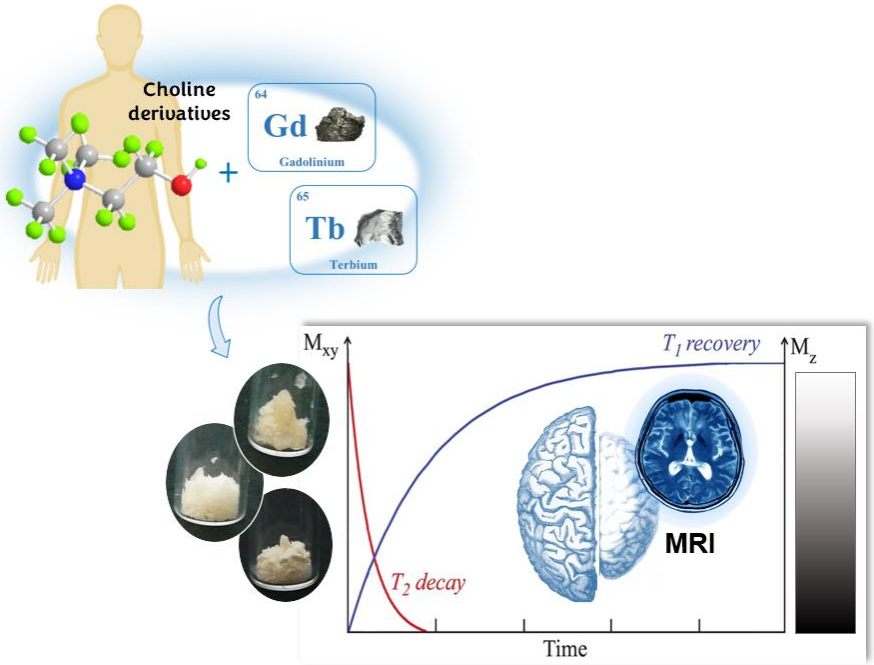

This chapter was adapted from the article “Lanthanides-based organic salts: Synthesis, characterization and cytotoxicity studies”, Andreia Forte, Sandra Gago, Celso Alves, Joana Silva, Joana Alves, Rui Pedrosa, César A. T. Laia, Isabel M. Marrucho, Luís C. Branco, 2023, Molecules, 28, 7152 (DOI: 10.3390/molecules28207152)

Chapter 3

Development of Lanthanides-based ionic systems

Abstract

The formulation of Magnetic Ionic Liquids (MILs) or organic salts based on lanthanides as anions have been explored in the last few years in order to evaluate their use in more bio-applications including imaging for clinical diagnosis. Specifically, the application of contrast agents in MRI can be useful due to the poor image contrast observed in some situations. Most of MRI contrast agents commercially available are formulated with Gd^{3+}, however, although its many advantages, this metal presents a high toxicity level due to several mechanisms of action including calcium channel inhibition. Thus, it has become of utmost importance to find viable and more biocompatible alternatives to the contrast agents already used in clinical practice. In this chapter, following the key concept of the Chapter 2, a set of choline family-based salts and two other different cation families were combined with gadolinium (III) and terbium (III) anions. Synthetic methodologies used were previously optimized and all organic salts were obtained as solids with melting temperatures higher than 100 ºC. Magnetic moment obtained for Gd (III) salts were, as expected, smaller than those obtained for Tb (III)-based compounds. The μ_{eff} attained for Gd (III) and Tb (III) magnetic salts are in the range of 6.55-7.30 MB and 8.22-9.34 MB, respectively. Also, similarly to the metals from previous chapter, it was possible to observe a correlation between the μ_{eff} values obtained for lanthanides and the structural features of the cation. Cytotoxicity of lanthanides-based salts was also evaluated and most of the prepared compounds did not induced cytotoxicity on 3T3, 293T, Caco2 and HepG2 cells.

1. Introduction

In last decades, Ionic liquids (ILs) as low melting organic salts have been studied and applied in a growing range of different areas.[1] Their negligible volatility, high chemical and thermal stability and wide electrochemical range can be highlighted but the significant advantage of these salts relies on the possibility to tune their physicochemical and/or biological properties by changing their formulation, i.e., through the suitable combination of specific organic cations and organic or inorganic anions units.[2–4] Currently, a new subclass of ILs, Magnetic Ionic Liquids (MILs) have attracted greater attention. MILs are composed by at least one paramagnetic element in the cation or anion and combine the properties of ILs and magnetic materials, in particular the response to a strong magnetic field.[5] Since their first report in 2004 by Hayashi and Hamaguchi, MILs have been largely explored in different research areas such as catalysis, separation processes and more recently in bio-applications.[6–9] Specifically, due to their magnetic and luminescence properties, metal complexes based on Lanthanides have been explored for their use in biomedical field, namely to apply in imaging diagnosis techniques. As mentioned in Chapter 1, MRI can provide images from the internal structures of human body with a good spatial resolution as well as an unlimited tissue penetration level. The image generated by this technique is based on proton relaxation rates from water molecules and proton densities in different tissues.[10] Although in some cases a poor image contrast can be observed, the addition of some compounds (contrast agents) can improve this limitation through the change of nuclear relaxation rate of water molecules.[11] MRI T_1-shortening agents are mainly composed by a paramagnetic metal-chelate structure with a particular focus in the reduction of longitudinal relaxation time of water molecules directly coordinated or in vicinity of the contrast agent. T_1 weighted image is one of the basic pulse

sequences used in MRI technique. This sequence allows to show the difference between the T_1 relaxation times of tissues.[12,13] In the 3D image of the longitudinal relaxation time of protons present in the tissues, it is possible to observe that short relaxation times appear bright comparing to longer relaxation times where the image is darker. Sometimes, this contrast difference can be enough to perform an adequate diagnostic, however, in some cases it is required the addition of a contrast agent in order to enhance this contrast. This compound induces a reduction of T_1 relaxation time, an hypersignal is attained and, as a consequence, a brighter image can be observed.[14,15] Most commercially available MRI contrast agents are formulated with gadolinium (III), Gd^{3+}. This metal is the preferential choice for T_1 contrast agents' formulation due to its seven unpaired electrons (the highest number for a metal ion) and its long electronic relaxation time. Owing to the combination of these properties, gadolinium ions induce the largest effect comparatively to other paramagnetic ions corresponding to the highest relaxation efficiency.[10,12,16] In general, the Lanthanides (Ln), or rare-earth metals, are characterized by the progressive filling of their 4f valence orbitals and for being highly paramagnetic due to their unpaired electrons. Particularly, in Gd (III) case, a higher magnetic moment, magnetic susceptibilities and electronic relaxation times is observed.[17–24] The use of this metal in the formulation of contrast agents for medical applications has its major drawback in Gd (III) toxicity due to several mechanisms of action including calcium channel inhibition.[12]

Herein, following the key concept of the previous chapter, a series of new magnetic organic salts based on different choline derivative cations combined with gadolinium (III) and terbium (III) anions were prepared and characterized. Additionally, examples of ammonium and phosphonium

cations were used for comparison. Figure 3. 1 illustrates the chemical structures of the prepared biocompatible magnetic organic salts.

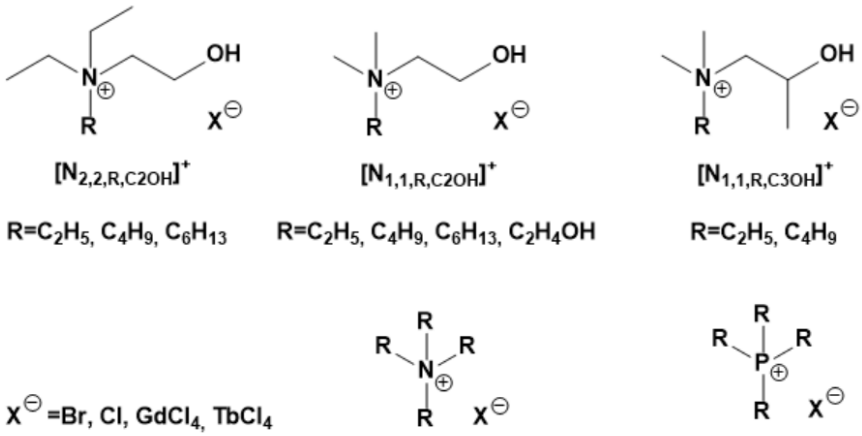

Figure 3. 1 | Structure of biocompatible organic salts synthesized in this work.

During this work it was possible to study all the prepared salts regarding to their toxicity and, additionally, it was even possible to carry out a relaxometry evaluation of two selected magnetic salts in order to assess about their applicability as MRI contrast agents.

2. Results and Discussion

2.1. Synthesis and characterization of magnetic salts

A set of choline derivative cations described in a previous work [25] were used to synthesize new magnetic salts based on two different lanthanides, gadolinium (III) and terbium (III). Due to their similar electronic configuration, Lanthanide's series show identical physical-chemical properties. Most of the metals from this family are paramagnetic elements due to their unpaired

electrons. This feature and their 4f electron configuration, makes them good candidates to use in metal complexes formulations. Over the years, the main choice to be applied in MRI contrast agents design is focused on trivalent cation Gd^{3+}. This metal presents several advantages such as the high number of unpaired electrons (seven electrons, the highest between lanthanides family), the high magnetic moment associated and the predisposition to form metal complexes with high stability.[26] Terbium (III) arises as an alternative since it possesses an higher magnetic moment than gadolinium (III) and it is also a strongly paramagnetic ion.[27]

The synthetic methodology used in this work in order to develop these novel lanthanide-based magnetic organic salts is summarized in Scheme 3. 1.

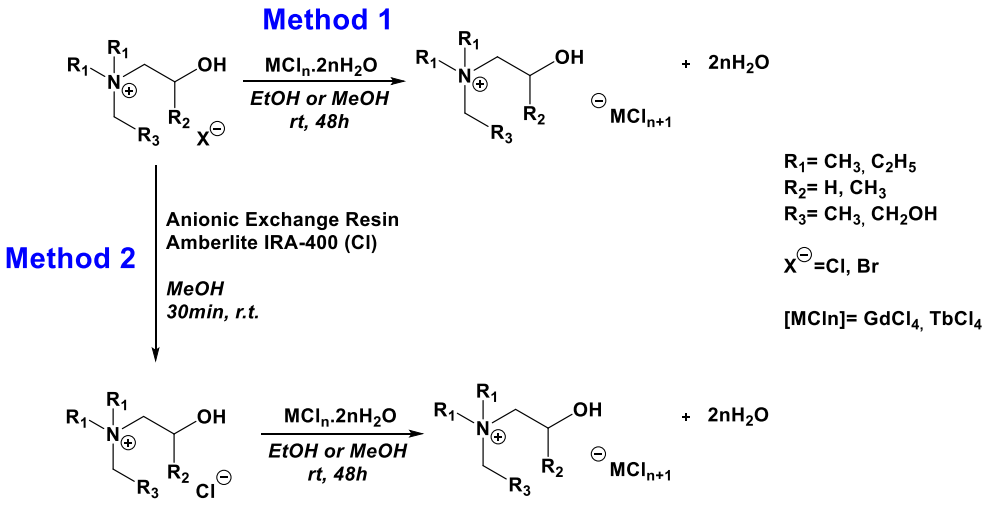

Scheme 3. 1 | Synthetic methodology adopted to develop lanthanides-based magnetic salts.

Beyond choline derivative cations, also other organic cations such as tetra-alkyl ammonium ($[N_{2,2,2,2}]$) and also two phosphonium cations ($[P_{OH,OH,OH,OH}]$

and [$P_{4,4,4,4}$]) were selected. As already described before, two synthetic methods were applied to obtain the metal-based organic salts: for the cases where the organic cation had a chloride as counter-ion, only the metal complexation reaction was performed but when this anion is bromide, it is required a previous step to convert this salt in the correspondent chloride ones. This synthetic step is accomplished by using an ionic exchange resin. It is important to emphasize that the complexation reactions were made in a single step procedure with no additional purification steps. The different families of magnetic salts were characterized according to their physical and thermal properties. The results are presented in Table 3. 1. All compounds were obtained as solids and most of them with transition temperatures (melting or decomposition) higher than 100 ºC. Due to their cation scaffold, most of the synthesized magnetic salts reveal a high hygroscopic nature. Choline derivatives-based salts are highly soluble in water and alcohols but present low solubility in apolar organic solvents.

Table 3. 1 | Physical properties of lanthanides-based organic salts.

Compound	Physical State	Tm [Td] [(a)] (ºC)
	Gd (III)	
$[N_{1,1,1,C2OH}][GdCl_4]$	White Solid	145
$[N_{1,1,4,C2OH}][GdCl_4]$	White Solid	[118]
$[N_{1,1,C2OH,C2OH}][GdCl_4]$	White Solid	Hygroscopic
$[N_{1,1,2,C3OH}][GdCl_4]$	Pale Yellow Solid	147
$[N_{1,1,4,C3OH}][GdCl_4]$	Yellow Solid	148
$[N_{2,2,2,C2OH}][GdCl_4]$	White Solid	[95]
$[N_{1,1,1,C2COOCH3}][GdCl_4]$	White Solid	152
$[N_{2,2,2,2}][GdCl_4]$	White Solid	114
$[P_{4,4,4,4}][GdCl_4]$	Yellow Solid	Hygroscopic
	Tb (III)	
$[N_{1,1,1,C2OH}][TbCl_4]$	White Solid	[114]
$[N_{1,1,4,C2OH}][TbCl_4]$	White Solid	[115]
$[N_{1,1,C2OH,C2OH}][TbCl_4]$	White Solid	Hygroscopic
$[N_{1,1,2,C3OH}][TbCl_4]$	Pale Yellow Solid	139
$[N_{1,1,4,C3OH}][TbCl_4]$	Yellow Solid	155
$[P_{OH,OH,OH,OH}][TbCl_4]$	White Solid	146
$[N_{1,1,1,C2COOCH3}][TbCl_4]$	White Solid	142
$[N_{2,2,2,2}][TbCl_4]$	White Solid	110
$[P_{4,4,4,4}][TbCl_4]$	Yellow Solid	Hygroscopic

One of the basis of lanthanides chemistry and applications is related with their luminescence. This important property arises from forbidden 4f-4f electronic transitions and results in narrow line widths associated to long lifetimes. These properties makes these elements attractive for several

optical applications.[28] It is expectable that Gd (III) and Tb (III) complexes own similar chemical features as well as biodistribution profiles.[29] However, the visual observation apparently suggest that Tb (III)-based compounds present a more intense luminescent behaviour than gadolinium (III) salts. This can be useful for further bio-applications. The visual observation of these compounds seems to indicate a green light emission that can be explored in the future. In Table 3. 2 can be seen some images from prepared Tb (III)-based organic salts under (A) white light and (B) UV light (366nm).

Table 3. 2 | Images from prepared Tb (III)-based organic salts under (A) white light and (B) UV light (366nm).

Compound	$[N_{1,1,1,C2OH}]$	$[N_{1,1,4,C2OH}]$	$[N_{1,1,C2OH,C2OH}]$	$[N_{1,1,2,C3OH}]$	$[N_{1,1,4,C3OH}]$	$[P_{OH,OH,OH,OH}]$	$[P_{4,4,4,4}]$
(A)							
(B)							

2.2. Magnetic moment

Since magnetic properties are one of the major important features of contrast agents, magnetic susceptibility of the prepared lanthanide-based magnetic organic salts was measured. The effective magnetic moment (μ_{eff}) of these compounds was also determined. All results are summarized in Table 3. 3. It is important to note that, as expected, the μ_{eff} values found for Gd (III) salts

are smaller than correspondent Tb (III) compounds. The μ_{eff} obtained for Gd (III) magnetic salts are in a range of 6.55-7.30 MB. $[N_{1,1,1,C2OH}][GdCl_4]$, $[N_{1,1,2,C3OH}][GdCl_4]$ and $[N_{1,1,4,C3OH}][GdCl_4]$ salts showed the highest magnetic moments in the case of Gd (III) series. Regarding to Tb (III)-based salts, the values obtained are in a range of 8.22-9.34 MB. In general, the values are comparatively lower than those corresponding to the free metal. This observation can be justified by metal-ligand coordination as well as the possible interaction with the organic cation. Even so, Tb (III)-based salts presented very high μ_{eff} and, also, these are higher than those obtained for Gd (III). Thus, although their magnetic properties can be affected with the coordination and salt formulation, Tb (III) seems to maintain higher values of magnetic moments. More recently, the interest in this metal-based compounds has increased significantly, however, there are still few studies using Tb complexes for magnetic applications

Regarding to choline derivative salts, the results showed a standard behaviour of μ_{eff} values that depend on cation structural features. The correlation between the organic cation scaffold and the values obtained seems to be the same for both metals (Figure 3. 2). Thus, when the side alkyl chain increases, the μ_{eff} decreases. The same trend is observed when a branch is introduced in the cation structure. Finally, when an additional ethanol group is introduced, the μ_{eff} decreases. This behaviour was already found for another two metals, Fe (III) and Mn (II).

Table 3. 3 | Magnetic susceptibility and effective magnetic moments of magnetic organic salts based on Gd (III) and Tb (III).

Compound	$10^{-6}.\chi_g$ (c.g.s) [(a)]	μ_{eff} (MB) [(b)]
Gd (III)		
Gd (III) free ion	-	7.94 [30]
$[N_{1,1,1,C2OH}]$ $[GdCl_4]$	55.78	7.30
$[N_{1,1,4,C2OH}]$ $[GdCl_4]$	45.48	6.93
$[N_{1,1,C2OH,C2OH}]$ $[GdCl_4]$	45.25	6.82
$[N_{1,1,2,C3OH}]$ $[GdCl_4]$	51.24	7.24
$[N_{1,1,4,C3OH}]$ $[GdCl_4]$	47.83	7.22
$[N_{2,2,2,C2OH}]$ $[GdCl_4]$	40.61	6.55
$[N_{1,1,1,C2COOCH3}][GdCl_4]$	n.d.	n.d.
$[N_{2,2,2,2}]$ $[GdCl_4]$	n.d.	n.d.
$[P_{4,4,4,4}]$ $[GdCl_4]$	37.45	7.04
Tb (III)		
Tb (III) free ion	-	9.72 [31]
$[N_{1,1,1,C2OH}]$ $[TbCl_4]$	82.41	8.90
$[N_{1,1,4,C2OH}]$ $[TbCl_4]$	82.23	9.34
$[N_{1,1,C2OH,C2OH}]$ $[TbCl_4]$	65.59	8.22
$[N_{1,1,2,C3OH}]$ $[TbCl_4]$	72.21	8.61
$[N_{1,1,4,C3OH}]$ $[TbCl_4]$	58.45	7.99
$[P_{OH,OH,OH,OH}]$ $[TbCl_4]$	59.29	8.01
$[N_{1,1,1,C2COOCH3}][TbCl_4]$	n.d.	n.d.
$[N_{2,2,2,2}]$ $[TbCl_4]$	n.d.	n.d.
$[P_{4,4,4,4}]$ $[TbCl_4]$	56.50	8.66

[(a)] Magnetic susceptibility (χ_g) measure by a Sherwood magnetic susceptibility balance. (b) Effective magnetic moment (μ_{eff}) obtained using the magnetic susceptibility and the equation $\mu eff=2.828\sqrt{\mathbf{XgT}}$. n.d. not determined.

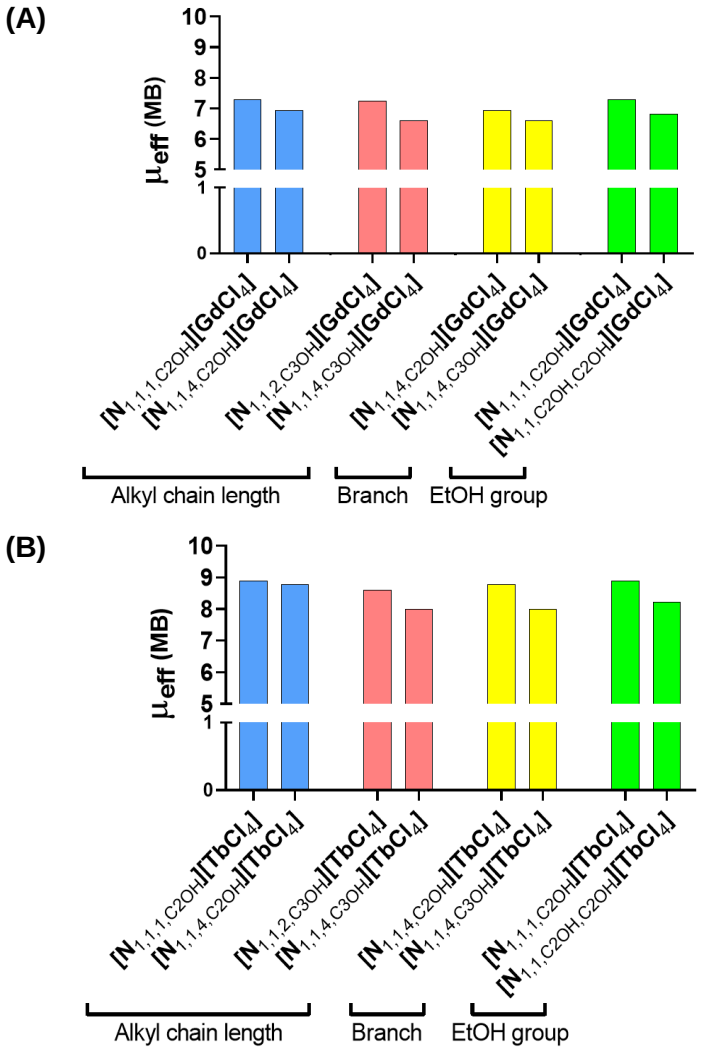

Figure 3. 2 | Variation of μ_{eff} with the cation structural properties for (A) Gd (III) and (B) Tb (III)-based magnetic organic salts.

2.3. Cytotoxicity of lanthanides-based salts

Cytotoxicity of lanthanides-based prepared salts (100 µg/ mL) was evaluated on 3T3, 293T, Caco-2, and HepG2 cells after 24 h treatment. The effects of

synthesized organic salts on studied cells' viability were estimated by the MTT assay and the results are displayed in Figure 3. 3 and Figure 3. 4, according to the cells´ nature (normal or carcinogenic). From the obtained results, can be emphasize that most of the tested compounds did not induced cytotoxicity on 3T3, 293T, Caco2 and HepG2 cells. Even so, some exceptions can be highlighted: Gd (III) based compounds induced a more marked effect in the 3T3 cells' viability than for the remaining cell lines. $[N_{1,1,1,C2OH}][GdCl_4]$, $[N_{1,1,4,C2OH}][GdCl_4]$, $[N_{1,1,1,C2COOH}][GdCl_4]$, $[N_{2,2,2,2}][GdCl_4]$ and $[P_{4,4,4,4}][GdCl_4]$ salts significantly reduced the cells' viability in a range of 16.17 to 32.28% when compared with the control. For the same cellular model, Tb (III) based salts $[N_{1,1,4,C2OH}][TbCl_4]$, $[P_{OH,OH,OH,OH}][TbCl_4]$ and $[P_{4,4,4,4}][TbCl_4]$ also decreased 3T3 cells' viability in 19.77%, 81.22%, and 25.08%, respectively. For 293T cells, a different behaviour could be observed: from all synthesized magnetic compounds, $[N_{1,1,1,C2OH}][TbCl_4]$, $[N_{2,2,2,2}][GdCl_4]$, $[N_{2,2,2,2}][TbCl_4]$, $[N_{1,1,1,C2COOCH3}][GdCl_4]$ and $[N_{1,1,1,C2COOCH3}][TbCl_4]$ presented a percentage of cells' viability higher than 100% when compared with the control situation. Thus, these compounds seem to increase the mitochondrial activity.

$[P_{OH,OH,OH,OH}][TbCl_4]$ was the only example that exhibited a cytotoxic effect in 293T cells (63.95% of viable cells) when compared to the control situation. Regarding to tumoral cells, the prepared compounds revealed a smaller cytotoxic effect comparing to normal cells. For Caco-2 cells, only $[N_{1,1,4,C3OH}][TbCl_4]$ and $[P_{OH,OH,OH,OH}][TbCl_4]$ induced a significant reduction of viability in 19.06% and 57.10%, respectively, comparing to control situation. Finally, $[N_{2,2,2,2}][GdCl_4]$, $[P_{4,4,4,4}][GdCl_4]$, $[N_{1,1,4,C3OH}][TbCl_4]$, $[N_{2,2,2,2}][TbCl_4]$ and $[P_{OH,OH,OH,OH}][TbCl_4]$ salts decreased significantly the viability of HepG2 cells comparing to control situation. In this case, a cells' viability range of 25.80 to 81.96% was observed.

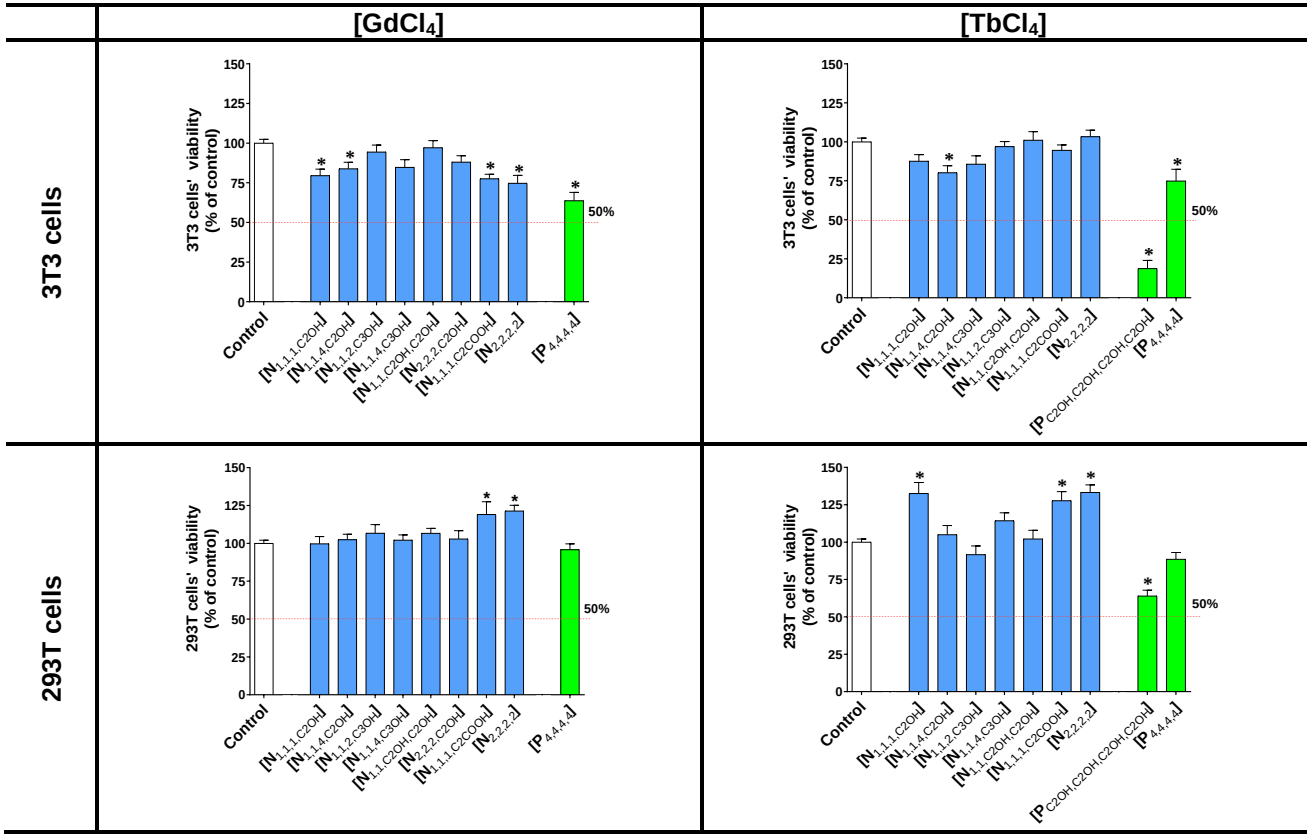

Figure 3. 3 | Cytotoxicity of Gd (III) and Tb (III) based organic salts (100 µg/ mL) on 3T3 and 293T cells' viability after treatment for 24 h. Values represent mean ± standard error of the mean (SEM) of at least three independent experiments carried out in triplicate. Symbols represent significant differences (ANOVA, Dunnett's test, $p < 0.05$) when compared to: *control.

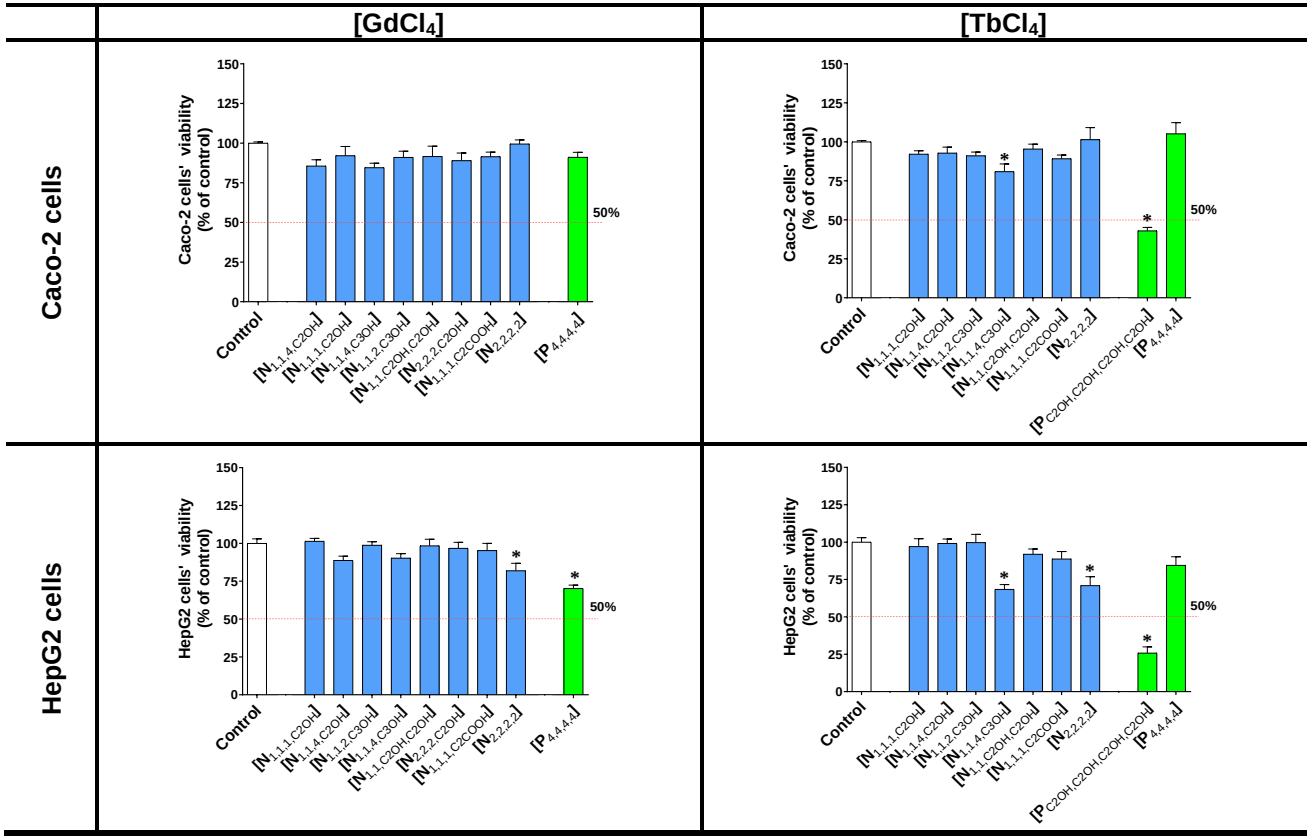

Figure 3. 4 | Cytotoxicity of Gd (III) and Tb (III) based organic salts (100 µg/ mL) on HepG2 and Caco-2 cells' viability after treatment for 24 h. Values represent mean ± standard error of the mean (SEM) of at least three independent experiments carried out in triplicate. Symbols represent significant differences (ANOVA, Dunnett's test, $p < 0.05$) when compared to: *control.

2.4. T_1 and T_2 Relaxation studies

Over the years, several studies have been developed in order to increase the magnetic field strength of MRI scanners commercially available while maintaining the safety characteristics for the patient. Thus, although the standard MRI is equipped with a magnetic field of 1.5T, there are already several examples of apparatus whose magnetic field is 3 and 7T.[32–34] More recently some preliminary results of the first human images obtained at a new high-field equipment (9.4T) have been reported. From this study, it was possible to confirm the safe applicability of this high magnetic field as a diagnostic method to obtain images of the human head.[35] Although there are some issues to review and overcome, these high field scanners present as their main advantage the greater signal-to-noise ratio which results in other two important benefits, the higher spatial resolution as well as the possibility to operate at reduced acquisition times.[33,35] Simultaneously, developing new safe contrast agents that can be applied to a wide range of field strengths is also important. This allows not only to take greater advantage of the standard scanner used in clinical practice but also to be applied in higher field scanners. T_1 agents prove to be an excellent choice due to some intrinsic properties and advantages. Between them can be found their positive image contrast, the possibility to reduce the acquisition times as well as the ability to remain stable when stored at room temperature.[33] Therefore, over the years many efforts have been made in order to develop new contrast agents for MRI. As mentioned before, these are predominantly based on gadolinium (III) chelates structures. Although alternatives to Gd (III) are currently being studied, the design of novel compounds is mostly performed through the modification of ligands' structural features.[36] Recalling the commercial contrast agents' structures presented in Chapter 1 (section 2.2), they can be organized by the nature of their ligands (macrocyclic or linear) and their

charge (ionic or non-ionic). Particularly, most of the ionic structures commercially available for MRI have in their formulation the same cation scaffold, n-methylglucamine (Figure 3. 5). The exception arises with the now discontinued contrast agent, Ablavar®, formulated in the trisodium salt monohydrate form.

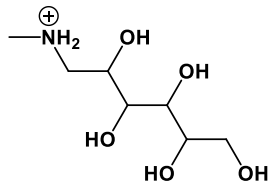

Figure 3. 5 | Structure of the *N*-methylglucamine cation used in the formulation of ionic contrast agents.

Following this idea, the choline family can be applied as an alternative to the cations already used in commercial CAs. Thus, as detailed in the previous subsections in this chapter, a set of new magnetic organic salts based on the cholinium family combined with gadolinium (III) and terbium (III) lanthanides were prepared. After the toxicity studies where it was possible to observe a set of promising results, the applicability of the prepared salts as MRI contrast agents were also evaluated, in collaboration with Drª Marta C. Corvo (Cenimat), through relaxometry studies. Hence, from the prepared choline-based magnetic salts, two of these salts were selected to perform the relaxometry analysis. The structures of these salts can be observed in Figure 3. 6.

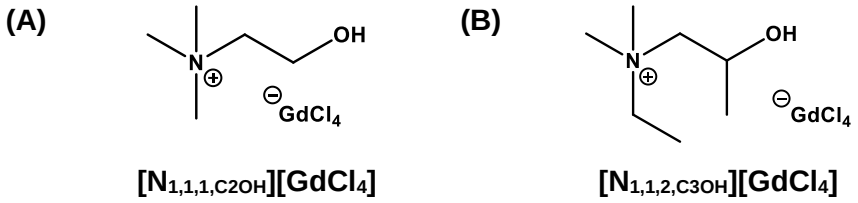

[$N_{1,1,1,C2OH}$][$GdCl_4$] **[$N_{1,1,2,C3OH}$][$GdCl_4$]**

Figure 3. 6 | Structure of selected choline-based organic salts used in relaxometry analysis: (A) *N*-hydroxyethyl-*N,N,N*-trimethylammonium tetrachlorogadolinate (III) [$N_{1,1,1,C2OH}$][$GdCl_4$] (B) *N*-ethyl-N-hydroxypropyl-*N,N*-dimethylammonium tetrachlorogadolinate (III), [$N_{1,1,2,C3OH}$][$GdCl_4$].

The cationic structure of the first selected compound is basically the well-known cholinium cation, [$N_{1,1,1,C2OH}$]. The second compound, [$N_{1,1,2,C3OH}$][$GdCl_4$], despite its similarity to choline, presents two main differences that can be highlighted: 1) an ethyl group directly attached to the nitrogen atom; and 2) a secondary alcohol as a result of the introduction of an additional -CH_3 group (branch). Regarding the metal anion, gadolinium (III)-based salts were chosen. Keeping in mind our interest in the evaluation of choline derivatives-based salts formulated with other metals (terbium (III) and, also, Manganese (II) from the previous chapter), since the approved MRI commercial CAs are based on gadolinium (III), only examples prepared with this metal were selected. Relaxivities r_1 and r_2 of compounds [$N_{1,1,1,C2OH}$][$GdCl_4$] and [$N_{1,1,2,C3OH}$][$GdCl_4$] were determined in aqueous solutions at 400 MHz (9.4T) and 37 ºC (309 K). The studies were conducted using the equipment Bruker Avance III 400 by measuring the effect of five different compound concentrations on longitudinal (T_1) and transversal (T_2) relaxation times of water. The concentrations used in this study are in the range of 0.05-1.00 mM. Longitudinal and transversal relaxation times were

obtained using an inversion recovery and Carr-Purcell-Meiboom-Gill sequences, respectively.

All the relaxation fitting results used to obtain T_1 and T_2 relaxation times and, consequently, the corresponding relaxivities values can be observed in the supplementary information (Figures S70-S89). Regarding the T_1 data, most concentrated solutions showed a mono-exponential behaviour. Nevertheless, when the concentration decreases (0.10 and 0.05 mM for $[N_{1,1,1,C2OH}][GdCl_4]$ and 0.05M for $[N_{1,1,2,C3OH}][GdCl_4]$), this behaviour changes and it is possible to observe the presence of a multi-exponential system. This variation can be related to the increase of water amount in salt solution and, consequently, the possibility of having an ion solvation phenomenon. From the obtained results, it is plausible to assume that, due to the low concentration of each salt and to the higher amount of the solution solvent, the water molecules can interact with the organic salts and stabilize their ions. Briefly, when the amount of solvent increases, the structure of the ionic liquid or organic salt can suffer an ion dissociation process (Figure 3. 7). When the solution has a high salt concentration, the ions are organized in a continuous network structure in the salt/solvent mixture (Figure 3. 7 (A)), however, when the solvent amount increases, this ordered structure gets distorted and collapses forming smaller species. Between these, it can be found the presence of ion pairs stabilized by induction, electrostatic and dispersion contributions (Figure 3. 7 (C)). [37,38] These structures can co-exist in three different forms: *1) as contact ion pairs (CIPs) where the cation and the anion share the same solvation shell (Figure 3. 7 (C)); 2) as solvent-shared ion pairs (SIPs) where the ions are separated by a single layer of solvent (Figure 3. 7 (D)); 3) and as solvent-separated ion pairs (2SIPs), the most solvated example of ion pair, where the ions are separated by two layers of solvent molecules Figure 3. 7 (E)).* For sufficient diluted solutions,

the solvation effect can stabilize the ions, avoid their proximity and lead, eventually, to a situation where the ions can exist as free species with no interaction between them (Figure 3. 7 (F)).[38,39] Thus, the solvent plays an active role in the salt dissociation, and ion pairs formation and/or, also, it can present a solvation effect that has an impact in both isolated ions and the formed ion pairs, according to the concentration of the IL.[39]

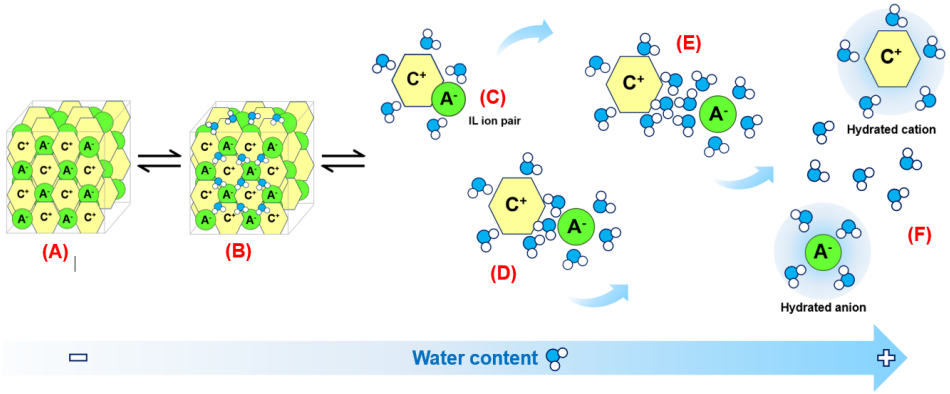

Figure 3. 7 | Schematic illustration of an IL aqueous solution. The ionic liquid is displayed in yellow and green (cations and anions, respectively) and the water molecules in blue and white (oxygen and hydrogen, respectively). Adapted from 39–41

By the observation of relaxation fitting results, the change of behaviour effect seems to be more evident for $[N_{1,1,1,C2OH}][GdCl_4]$ salt. Also, it is possible to verify that, for this choline cation-based salt, the behaviour seems to change at lower concentrations (0.10 mM). The formation of the ion pairs for these types of mixtures can be corroborated through several techniques since their presence can change the physical and chemical properties of the system. The most used method is the application of conductivity measurements, however, techniques based on other thermodynamic properties (e.g.

viscosity, density, vapor pressure, surface tension, among others), as well as spectroscopic measurements, can be applied.[38,42]

Regarding the T_2 relaxation time, both compounds presented a mono-exponential behaviour for all salts concentrations. Once obtained T_1 and T_2 values (supplementary information, Tables SI 17-19), the corresponding relaxivities were determined through application of Equation 3. 1, already mentioned in Chapter 1 (section 2.2). Figure 3. 9 (A) and (B) shows the plots of the relaxation rates as a function of compounds concentration and relaxivities r_1 and r_2 (indicated in each plot) were extracted from these plots through the curve slope.

$$\frac{1}{T_{i,obs}} = \frac{1}{T_{i,d}} + r_i[CA] \qquad \textbf{(Equation 3. 1)}$$

where $1/T_{i,obs}$ is the relaxation rate observed; $1/T_{i,d}$ is the relaxation rate in the absence of the paramagnetic ion; r_i (i=1,2) is the relaxivity, the specific concentration independent factor that characterizes the paramagnetic agent; and [CA] the paramagnetic ion/contrast agent concentration.

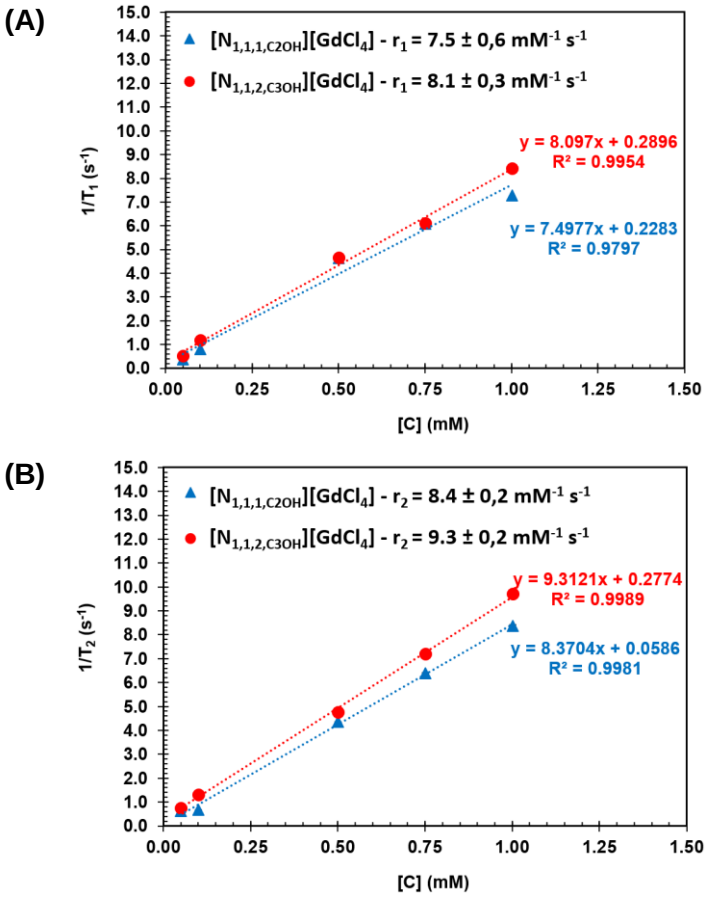

Figure 3. 8 | Relaxivity measurements of selected compounds at 9.4T: Relaxation rates (A) $1/T_1$ and (B) $1/T_2$ versus compounds concentration

As can be observed through the plots, both compounds present a good linear relation between salts concentration and relaxation rates with R-squared values of ≥0.98. By observation of the curves, this linearity appears to be slightly altered for the compound $[N_{1,1,1,C2OH}][GdCl_4]$ ($1/T_1$ vs [C]). This can be related to the more evident multi-exponential behaviour mentioned above.

2.4.1. Choline-based salts vs commercial contrast agents

As explained in Chapter 1 (section 2.2), the efficiency of an MRI contrast agent is defined by its relaxivity. This parameter allows to assess the information on how much a contrast agent can enhance the longitudinal ($r_1=1/T_1$) or transverse ($r_2=1/T_2$) water relaxation rate and, consequently, increase the tissue contrast. As mentioned, although gadolinium (III)-based CAs can increase both longitudinal and transverse relaxation rates, its major effect in the tissues relies on the reduction of T_1 relaxation time. Thus, it is important to evaluate the prepared salts according to their r_1 relaxivity. Knowing that r_1 relaxivity usually has an inverse proportion relation with the field strength, it can be assumed that in lower fields (such as those applied in clinical practice), the relaxivities can be higher than the ones obtained for 9.4 T.[33] Relaxivities r_1 and r_2 associated with each MRI commercial CA approved today as well as the two studied magnetic salts are presented in Table 3. 4. As can be seen, the values obtained with a 3T magnetic field strength show a broad range of relaxivities (4.1-19.0 mM^{-1} s^{-1} for r_1 and 4.6-34 mM^{-1} s^{-1} for r_2). Although the relaxometry studies were carried out using magnetic fields of different strengths, assuming that, as above explained, there is an inverse proportion relation between r_1 relaxivity and the field strength, it is possible to perform a rough comparison and take some conclusions about the r_1 relaxivities of both compound's sets. Comparing the results obtained for the salts prepared in this work with some contrast agents commercially available, the relaxivities r_1 associated with the choline-based magnetic salts are higher than the majority of the commercial contrast agents. Thus, it is expected that these values increase when subjected to a lower magnetic field (3T) and that the difference between choline salts and commercial agents also increases and becomes more evident. Considering

that MRI contrast agents' efficiency presents a linear relationship with their relaxivity, high relaxivities are correlated with a greater enhancement of the image contrast. Thus, from the relaxivities results obtained in this work and taking into account the comparison performed with the commercial contrast agents, it is possible to assume that the prepared choline-based magnetic salts should theoretically provide a high-enhancement effect.

Table 3. 4 | Relaxivity constants r_1 and r_2 of MRI commercial contrast agents and the two studied magnetic salts measured at 3T and 9.4T, respectively.

Compound	r_1 (mM^{-1} s^{-1})	r_2 (mM^{-1} s^{-1})	Ref
$[N_{1,1,1,C2OH}][GdCl_4]$	7.5	8.4	-
$[N_{1,1,2,C3OH}][GdCl_4]$	8.1	9.3	-
Magnevist®	3.7-3.9	5.2	43 (a)
Gadovist®	4.5-5.0	6.3-7.1	
ProHance®	3.7	5.7	
Multihance®	5.5-5.9	11.0-17.5	
Omniscan®	4,0	5,6	
Optimark®	4,5	5,9	
Eovist®	6,2	11.0	
Ablavar®	5.3	6.1	
Elucirem®	11.3	13.5	44 (b)

Relaxivities obtained in water at 37 ºC.
(a) the concentration range of 0.25-0.50mM.
(b) the concentration range of 0.5-5mM.

3. Conclusions

A set of Gd (III) and Tb (III)-based magnetic organic salts was prepared and characterized. Choline derivatives and other two organic cations were tested in metal complexation reactions in order to obtain new and more biocompatible magnetic organic salts for potential application as contrast agents for MRI. Gd (III) is the most common metal used in contrast agents'

formulation, but the high metal-free associated toxicity is reported as a significant limitation. Tb (III) complexes arises at this point as a good alternative for Gd (III) complexes due to the nature and magnetic properties of the metal. For choline derivative magnetic salts, a standard correlation between μ_{eff} of compounds and their organic cation structure is observed. Cytotoxic effect of the prepared compounds in four different cell lines was evaluated and no significant toxicity was observed for the majority of the prepared compounds for the studied cells. In order to evaluate the applicability of two selected salts as MRI contrast agents, relaxometry studies were performed. Results showed for both assessed salts a concentration-dependent behaviour for water longitudinal relaxation mechanism through the observation of a multi-exponential system in more diluted solutions. This phenomenon can be compatible with an ion solvation process, and thus, with the formation of ion pairs. On the contrary, for all concentrations, transversal relaxation fitting results showed a mono-exponential system. Relaxivities r_1 from prepared salts and from commercial contrast agents could be compared. Results indicated that choline-based magnetic salts presented higher relaxivities r_1 than most of the contrast agents applied today in MRI.

4. Experimental Section

4.1. General remarks

All commercial organic solvents were used as supplied from Sigma-Aldrich in analytical purity grade. Commercially available reagents were purchased from different chemical companies and then used as received. Fourier transform infrared spectroscopy (FT-IR) spectra were carried out on a Bruker

Tensor 27. Elemental analysis (C, H, N, analyzer) of each synthesized organic salt was performed by Laboratório de Análises at LAQV-REQUIMTE. For the salts which were solid at room temperature the melting point determination was performed using a Stuart Scientific Melting Point SMP1.

4.2. Synthesis of metal-complexed salts

General method: Choline chloride derivative salt (as indicated in Figure 1) and ethanol were added to a round-bottomed flask. After the complete dissolution, the selected hydrated lanthanide salt ($GdCl_3$ or $TbCl_3$) were added under vigorous magnetic stirring at room temperature. The reaction mixture was stirring for 48 h and then the solvent was evaporated, and the product was dried under vacuum.

4.2.1. Gadolinium (III)-based organic salts

N-hydroxyethyl-N,N,N-trimethylammonium tetrachlorogadolinate (III) [$N_{1,1,1,C2OH}$][$GdCl_4$]: [$N_{1,1,1,C2OH}$][Cl] (0.21g, 1.50 mmol); $GdCl_3.6H_2O$ (0.55g, 1.49mmol); Yield: quantitative; white solid; FT-IR (KBr), $\bar{\upsilon}$ = 3355, 1627, 1476, 1280, 1200, 1132, 1081, 955 cm^{-1}. Elemental analysis calcd (%) for $C_5H_{14}Cl_4GdNO.2.8H_2O$ (453.50 $g.mol^{-1}$): C 13.24, N 3.09, H 4.32; found: C 12.79, N 2.92, H 4.14.

N-butyl-N-hydroxyethyl-N,N-dimethylammonium tetrachlorogadolinate (III) [$N_{1,1,4,C2OH}$][$GdCl_4$]: [$N_{1,1,4,C2OH}$][Cl] (0.20g, 1.35mmol); $GdCl_3.6H_2O$ (0.50g, 1.36mmol); Yield: quantitative; white solid; FT-IR (KBr), $\bar{\upsilon}$ = 3363, 2964, 1627, 1468, 1084, 975, 921 cm^{-1}. Elemental analysis calcd (%) for $C_8H_{20}Cl_4GdNO.0.5H_2O$ (454.35 $g.mol^{-1}$): C 21.15, N 3.08, H 4.67; found: C 21.32, N 3.02, H 5.50.

N-butyl-N-hydroxyethyl-N,N-dimethylammonium tetrachlorogadolinate (III) [$N_{1,1,4,C3OH}$][$GdCl_4$]: [$N_{1,1,4,C3OH}$][Cl] (0.26g, 1.32mmol); $GdCl_3.6H_2O$ (0.49g, 1.32mmol); Yield: quantitative; yellow solid; FT-IR (KBr), $\bar{\upsilon}$ = 3375, 2967, 1635, 1508, 1148, 1071, 993, 890 cm^{-1}. Elemental analysis calcd (%) for $C_9H_{22}Cl_4GdNO.0.5H_2O$ (468.38 $g.mol^{-1}$): C 23.08, N 2.99, H 4.96; found: C 22.59, N 3.07, H 4.90.

N-ethyl-N-hydroxypropyl-N,N-dimethylammonium tetrachlorogadolinate (III) [$N_{1,1,2,C3OH}$][$GdCl_4$]: [$N_{1,1,2,C2OH}$][Cl] (0.17g, 1.04mmol); $GdCl_3.6H_2O$ (0.38g, 1.03mmol); Yield: quantitative; yellow solid; FT-IR (KBr), $\bar{\upsilon}$ = 3334, 1635, 1476, 1410, 1144, 1083, 1023, 977 cm^{-1}. Elemental analysis calcd (%) for $C_7H_{18}Cl_4GdNO.3.5H_2O$ (494.38 $g.mol^{-1}$): C 17.01, N 2.83, H 5.11; found: C 16.67, N 2.67, H 4.42.

N,N-dihydroxyethyl-N,N-dimethylammonium tetrachlorogadolinate (III) [$N_{1,1,C2OH,C2OH}$][$GdCl_4$]: [$N_{1,1,C2OH,C2OH}$][Cl] (0.25g, 1.48mmol); $GdCl_3.6H_2O$ (0.55g, 1.47mmol); Yield: quantitative; white solid; FT-IR (KBr), $\bar{\upsilon}$ = 3357, 1631, 1477, 1078, 957 cm^{-1}. Elemental analysis calcd (%) for $C_6H_{16}Cl_4GdNO_2.0.5H_2O$ (442.29 $g.mol^{-1}$): C 16.29, N 3.17, H 3.88; found: C 16.30, N 2.80, H 4.33.

N,N,N-triethyl-N-hydroxyethylammonium tetrachlorogadolinate (III) [$N_{2,2,2,C2OH}$][$GdCl_4$]: [$N_{2,2,2,C2OH}$][Cl] (0.21g, 1.14mmol); $GdCl_3.6H_2O$ (0.42g, 1.13mmol); Yield: quantitative; white solid; FT-IR (KBr), $\bar{\upsilon}$ = 3471, 1635, 1477, 1402, 1156, 1081, 924 cm^{-1}. Elemental analysis calcd (%) for $C_8H_{20}Cl_4GdNO.3.5H_2O$ (508.41 $g.mol^{-1}$): C 18.90, N 2.76, H 5.36; found: C 18.76, N 2.30, H 4.64.

(2-Acetoxyethyl)-N,N,N-trimethylammonium tetrachlorogadolinate (III) [$N_{1,1,1,C2COOCH3}$][$GdCl_4$]: [$N_{1,1,1,C2COOCH3}$][Cl] (0.26g, 1.46mmol); $GdCl_3.6H_2O$

(0.54g, 1.46mmol); Yield: quantitative; white solid; FT-IR (KBr), $\bar{\upsilon}$ = 3384, 1721, 1637, 1478, 1401, 1254, 1051, 954, 669 cm^{-1}. Elemental analysis calcd (%) for $C_7H_{16}Cl_4GdNO.2.5H_2O$ (490.34 $g.mol^{-1}$): C 17.15, N 2.86, H 4.33; found: C 16.95, N 2.76, H 4.8.

Tetraethylammonium tetrachlorogadolinate (III) $[N_{2,2,2,2}][GdCl_4]$: $[N_{2,2,2,2}][Cl]$ (0.26g, 1.41mmol); $GdCl_3.6H_2O$ (0.53g, 1.42mmol); Yield: quantitative; white solid; FT-IR (KBr), $\bar{\upsilon}$ = 3379, 1628, 1488, 1142, 1396, 1175, 1057, 1002, 787, 635 cm^{-1}. Elemental analysis calcd (%) for $C_8H_{20}Cl_4GdN.0.25H_2O$ (433.85 $g.mol^{-1}$): C 21.15, N 3.23, H 4.77; found: C 21.66, N 3.07, H 5.14.

Tetrabutylphosphonium tetrachlorogadolinate (III) $[P_{4,4,4,4}][GdCl_4]$: $[P_{4,4,4,4}][Cl]$ (0.25g, 0.85mmol); $GdCl_3.6H_2O$ (0.32g, 0.85mmol); Yield: quantitative; yellow solid; FT-IR (KBr), $\bar{\upsilon}$ = 3375, 2960-2873, 1625, 1464, 1232, 1095, 1003, 968, 908 cm^{-1}. Elemental analysis calcd (%) for $C_{16}H_{36}Cl_4GdP.4.5H_2O$ (639.63 $g.mol^{-1}$): C 30.04, H 7.11; found: C 30.34, H 7.75.

4.2.2. Terbium (III)-based organic salts

N-hydroxyethyl-N,N,N-trimethylammonium tetrachloroterbate (III) $[N_{1,1,1,C2OH}][TbCl_4]$: $[N_{1,1,1,C2OH}][Cl]$ (0.21g, 1.50 mmol); $TbCl_3.6H_2O$ (0.57g, 1.50mmol); Yield: quantitative; white solid; FT-IR (KBr), $\bar{\upsilon}$ = 3380, 1628, 1476, 1081, 1047, 955 cm^{-1} . Elemental analysis calcd (%) for $C_5H_{14}Cl_4NOTb.2.3H_2O$ (446.38 $g.mol^{-1}$): C 13.45, N 3.14, H 4.21; found: C 13.14, N 2.99, H 4.67.

N-butyl-N-hydroxyethyl-N,N-dimethylammonium tetrachloroterbate (III) $[N_{1,1,4,C2OH}][TbCl_4]$: $[N_{1,1,4,C2OH}][Cl]$ (0.30g, 2.06mmol); $TbCl_3.6H_2O$ (0.77g, 2.07 mmol); Yield: quantitative; white solid; FT-IR (KBr), $\bar{\upsilon}$ = 3370, 2965-

2876, 1633, 1486, 1131, 1084, 1051, 976, 920 cm^{-1}. Elemental analysis calcd (%) for $C_8H_{20}Cl_4NOTb.2.5H_2O$ (492.07 $g.mol^{-1}$): C 19.53, N 2.85, H 5.13; found: C 19.53, N 2.74, H 5.03.

N-butyl-N-hydroxyethyl-N,N-dimethylammonium tetrachloroterbate (III) [$N_{1,1,4,C3OH}$][$TbCl_4$]: [$N_{1,1,4,C3OH}$][Cl] (0.26g, 1.32mmol); $TbCl_3.6H_2O$ (0.49g, 1.31mmol); Yield: quantitative; yellow solid; FT-IR (KBr), $\bar{\upsilon}$ = 3346, 2967-2877, 1628, 1485, 1288, 1148, 1072, 993, 891 cm^{-1}. Elemental analysis calcd (%) for $C_9H_{22}Cl_4NOTb.2H_2O$ (497.09 $g.mol^{-1}$): C 21.74, N 2.82, H 5.28; found: C 22.15, N 2.85, H 6.00.

N-ethyl-N-hydroxypropyl-N,N-dimethylammonium tetrachloroterbate (III) [$N_{1,1,2,C3OH}$][$TbCl_4$]: [$N_{1,1,2,C2OH}$][Cl] (0.25g, 1.49mmol); $TbCl_3.6H_2O$ (0.56g, 1.49mmol); Yield: quantitative; yellow solid; FT-IR (KBr), $\bar{\upsilon}$ = 3357, 1633, 1485, 1148, 1114, 1088, 1020, 980 cm^{-1}. Elemental analysis calcd (%) for $C_7H_{18}Cl_4NOTb.4H_2O$ (505.07 $g.mol^{-1}$): C 16.65, N 2.77, H 5.20; found: C 16.60, N 2.70, H 4.43.

N,N-dihydroxyethyl-N,N-dimethylammonium tetrachloroterbate (III) [$N_{1,1,C2OH,C2OH}$][$TbCl_4$]: [$N_{1,1,C2OH,C2OH}$][Cl] (0.25g, 1.48mmol); $TbCl_3.6H_2O$ (0.55g, 1.47mmol); Yield: quantitative; white solid; FT-IR (KBr), $\bar{\upsilon}$ = 3371, 1639, 1479, 1076, 959 cm^{-1}. Elemental analysis calcd (%) for $C_6H_{16}Cl_4NO_2Tb$ (434.96 $g.mol^{-1}$): C 16.57, N 3.22, H 3.72; found: C 16.25, N 3.04, H 3.64.

(2-Acetoxyethyl)-N,N,N-trimethylammonium tetrachloroterbate (III) [$N_{1,1,1,C2COOCH3}$][$TbCl_4$]: [$N_{1,1,1,C2COOCH3}$][Cl] (0.25g, 1.39mmol); $TbCl_3.6H_2O$ (0.54g, 1.45mmol); Yield: quantitative; white solid; FT-IR (KBr), $\bar{\upsilon}$ = 3396, 1636, 1478, 1401, 1255, 1133, 1083, 1052, 954, 643 cm^{-1}. Elemental analysis calcd (%) for $C_7H_{16}Cl_4NOTb.2.5H_2O$ (492.02 $g.mol^{-1}$): C 17.09, N 2.85, H 4.31; found: C 17.16, N 3.39, H 4.54.

Tetraethylammonium tetrachloroterbate (III) [$N_{2,2,2,2}$][$TbCl_4$]: [$N_{2,2,2,2}$][Cl] (0.26g, 1.41mmol); $TbCl_3.6H_2O$ (0.53g, 1.42mmol); Yield: quantitative; white solid; FT-IR (KBr), $\bar{\upsilon}$ = 3384, 1636, 1486, 1399, 1175, 1002, 786, 670 cm^{-1}. Elemental analysis calcd (%) for $C_8H_{20}Cl_4NTb.H_2O$ (449.04 $g.mol^{-1}$): C 21.40, N 3.12, H 4.95; found: C 21.04, N 2.94, H 4.77.

Tetrahydroxymethylphosphonium tetrachloroterbate (III) [$P_{OH,OH,OH,OH}$][$TbCl_4$]: [$P_{OH,OH,OH,OH}$][Cl] (0.25g, 1.31mmol); $TbCl_3.6H_2O$ (0.50g, 1.31mmol); Yield: quantitative; white solid; FT-IR (KBr), $\bar{\upsilon}$ = 3384, 1637, 1400, 1048, 670 cm^{-1}. Elemental analysis calcd (%) for $C_4H_{12}Cl_4O_4PTb.4.5H_2O$ (536.95 $g.mol^{-1}$): C 8.95, H 3.95; found: C 9.31, H 4.34.

Tetrabutylphosphonium tetrachloroterbate (III) [$P_{4,4,4,4}$][$TbCl_4$]: [$P_{4,4,4,4}$][Cl] (0.25g, 0.86mmol); $TbCl_3.6H_2O$ (0.33g, 0.87mmol); Yield: quantitative; yellow solid; FT-IR (KBr), $\bar{\upsilon}$ = 3355, 2961-2872, 1629, 1465, 1408, 1232, 1095, 967, 904 cm^{-1}. Elemental analysis calcd (%) for $C_{16}H_{36}Cl_4PTb.4H_2O$ (632.30 $g.mol^{-1}$): C 30.39, H 7.03; found: C 31.15, H 7.58.

4.3. Magnetic moment determination

The Mass Susceptibility χ_g of compounds was determined using a Magnetic Susceptibility Balance at the room temperature (20 ºC), from Sherwood Scientific. The effective magnetic moment (μ_{eff}) values were obtained by using the following Equation 3. 2, Equation 3. 3 and Equation 3. 4.

$$\chi_g = \frac{C.l.(R-R_0)}{10^9.m} \quad \textbf{(Equation 3. 2)}$$

Where C is the constant of calibration balance (= 1.14), l is length of the sample (cm), R is the reading for the tube with the sample, R_0 is the empty tube reading and m is mass of the sample (g).

$$\chi_m = \chi_g . M_w \qquad \textbf{(Equation 3. 3)}$$

Where χ_m is the molar susceptibility and Mw is the molecular weight of the compound.

$$\mu_{eff} = 2,828\sqrt{\chi_m . T} \qquad \textbf{(Equation 3. 4)}$$

Where μeff is the effective magnetic moment and T is the measurement temperature (in Kelvin, T (°C) + 273).

4.4. Cytotoxicity

3T3, Caco-2, HepG2 and 293T cell lines were previously acquired from DSMZ biobank. Cells were cultured according to the supplier's instructions. 3T3 cells were cultured in Dulbecco´s Modified Eagle´s medium: Nutrient Mix F-12 (DMEM/F-12) (Merck, Germany), Caco-2 cells were cultivated in Minimum Essential Medium (MEM) (Merck, Germany), HepG2 cells were grown in RPMI medium (Sigma-Aldrich, USA), and 293T cells were cultivated in Dulbecco´s Modified Eagle´s medium (Merck, Germany). All mediums were supplemented with 10% serum bovine fetal (Hyclone, UK), 100 IU/mL penicillin, and 100 μg/mL streptomycin (Merck, Germany).

For subculture, 3T3 cells, Caco-2 cells, HepG2 cells, and 293T cells were dissociated by the means of trypsin-EDTA treatment (Sigma, USA), split in a 1:5, 1:3, 1:3, 1:6 ratio, respectively, and seeded into Petri dishes with 25 cm2

of growth area. Cells were maintained in humidified atmosphere, 5% CO_2 and 37°C.

Cytotoxicity of lanthanides-based prepared salts was evaluated on 3T3, Caco-2, HepG2 and 293T cells' viability after cells reached total confluence on 96-well plates. Cells were treated with salts at 100 µg/ mL for 24 h. Effects were estimated by the means of MTT (Sigma, Germany) colorimetric assay based on the conversion of tetrazolium salts to blue formazan products by active mitochondria. Results were expressed in percentage of control (%).

Data and statistical analysis: Results are presented as mean ± standard error of the mean (SEM). At least three independent experiments were carried out in triplicate. Statistical analysis was performed using one-way analysis of variance (ANOVA) with Dunnett's multiple comparison of group means to determine significant differences relatively to control treatment. Differences were considered statistically significant at a level of 0.05 (p - value < 0.05). Calculations were performed using GraphPad v5.1 (GraphPad Software, La Jolla, CA, USA) software.

4.5. Relaxometric measurements

Longitudinal (T_1) and transversal (T_2) relaxation times from a set of prepared aqueous solutions with a concentration range of 0.05-1.00mM were performed at 37 ºC by using a nuclear magnetic resonance spectrometer, Bruker Avance III 400, operating at 400.15 MHz for ^1H, equipped with a diffusion probe Bruker DiffBB. The T_1 and T_2 values were determined using the inversion recovery and the Carr−Purcell−Meiboom−Gill (CPMG) sequencies, respectively.

Acknowledgements

This work was supported by Fundação para a Ciência e a Tecnologia through projects (PEst-C/LA0006/2013, PTCD/CTM-NAN/120658/2010, two contracts under Investigador FCT (L. C. Branco and I. M. Marrucho), a doctoral fellowship Andreia Forte (PD/BD/109625/2015), through the strategic project UID/MAR/04292/2020 granted to MARE—Marine, through the project PTNMR (ROTEIRO/0031/2013; PINFRA/22161/2016), and Solchemar company.

References

(1) Welton, T. Ionic Liquids: A Brief History. *Biophys. Rev.* 2018, *10*, 691–706.

(2) Ferraz, R.; Branco, L. C.; Marrucho, I. M.; Araújo, J. M. M.; Rebelo, L. P. N.; Da Ponte, M. N.; Prudêncio, C.; Noronha, J. P.; Petrovski, E. Development of Novel Ionic Liquids Based on Ampicillin. *Medchemcomm* 2012, *3*, 494–497.

(3) Amde, M.; Liu, J.; Pang, L. Environmental Application, Fate, Effects and Concerns of Ionic Liquids: A Review. *Environ. Sci. Technol.* 2015, *49*, 12611–12627.

(4) Mallakpour, S.; Dinari, M. Ionic Liquids as Green Solvents: Progress and Prospects. In *Green Solvents II - Properties and Applications of Ionic Liquids*; Mohammad, A., Inamuddin, Eds.; Springer: Dordrecht, 2012.

(5) Clark, K. D.; Nacham, O.; Purslow, J. A.; Pierson, S. A.; Anderson, L. Magnetic Ionic Liquids in Analytical Chemistry: A Review. *Anal. Chim. Acta* 2016, *934*, 9–21. https://doi.org/10.1016/j.aca.2016.06.011.

(6) Luo, A. M.; Shao, Y.; Zhang, K. J.; Wang, Y. W.; Peng, Y. Syntheses of Three Terbium Complexes as Fluorescent Probes and Their Application on the PH Detection of Routine Urine Test. *Chinese Chem. Lett.* 2017, *28*, 2009–2013.

(7) Daniel, C. I.; Chávez, F. V.; Portugal, C. A. M.; Crespo, J. G.; Sebastiao, P. J. 1H NMR Relaxation Study of a Magnetic Ionic Liquid as a Potential Contrast Agent. *J. Phys. Chem. B* 2015, *119*, 11740–11747.

(8) Rodríguez-Arco, L.; Gómez-Ramírez, A.; Durán, J. D. G.; López-López, M. T. New Perspectives for Magnetic Fluid-Based Devices Using Novel Ionic Liquids as Carriers. In *Smart Actuation and Sensing Systems*; Berselli, G., Vertechy, R., Vassura, G., Eds.; InTech, 2012; pp 445–464.

(9) Hayashi, S.; Hamaguchi, H. Discovery of a Magnetic Ionic Liquid [Bmim]FeCl4. *Chem. Lett.* 2004, *33* (12), 1590–1591.

(10) Lacerda, S.; Tóth, É. Lanthanide Complexes in Molecular Magnetic Resonance Imaging and Theranostics. *ChemMedChem* 2017, *12*, 883–894.

(11) Caravan, P.; Esteban-Gómez, D.; Rodríguez-Rodríguez, A.; Platas-Iglesias, C. Water Exchange in Lanthanide Complexes for MRI Applications. Lessons Learned over the Last 25 Years. *Dalt. Trans.* 2019, *48*, 11161–11180.

(12) De León-Rodríguez, L. M.; Martins, A. F.; Pinho, M. C.; Rofsky, N. M.; Sherry, A. D. Basic MR Relaxation Mechanisms and Contrast Agent Design. *J. Magn. Reson. Imaging* 2015, *42*, 545–565.

(13) Westbrook, C. *At a Glance*, 3rd Ed.; John Wiley & Sons: Chichester, United Kingdom, 2016.

(14) Verwilst, P.; Park, S.; Yoon, B.; Kim, J. S. Recent Advances in Gd-Chelate Based Bimodal Optical/MRI Contrast Agents. *Chem. Soc. Rev.* 2015, *44*, 1791–1806.

(15) Xiao, Y. D.; Paudel, R.; Liu, J.; Ma, C.; Zhang, Z. S.; Zhou, S. K. MRI Contrast Agents: Classification and Application (Review). *Int. J. Mol. Med.* 2016, *38*, 1319–1326.

(16) Cotton, S. *Lanthanide and Actinide Chemistry*; 2006. https://doi.org/10.1002/0470010088.

(17) Bettencourt-Dias, A. de. Introduction to Lanthanide Ion Luminescence. In *Luminescence of Lanthanide Ions in Coordination Compounds and Nanomaterials*; Bettencourt-Dias, A. de, Ed.; John Wiley & Sons: India, 2014; pp 1–48.

(18) Leonard, J. P.; Nolan, C. B.; Stomeo, F.; Gunnlaugsson, T. Photochemistry and Photophysics of Coordination Compounds: Lanthanides. *Top. Curr. Chem.* 2007, *281*, 1–43.

(19) Bünzli, J.-C. G. Review: Lanthanide Coordination Chemistry: From Old Concepts to Coordination Polymers. *J. Coord. Chem.* 2014, *67* (23–24), 3706–3733. https://doi.org/10.1080/00958972.2014.957201.

(20) Tang, J.; Zhang, P. A Basis for Lanthanide Single-Molecule Magnets. In *Lanthanide Single Molecule Magnets*; Springer-Verlag Berlin Heidelberg: Heidelberg, 2015; pp 1–39.

(21) Peters, J. A.; Huskens, J.; Raber, D. J. Lanthanide Induced Shifts and Relaxation Rate Enhancements. *Prog. Nucl. Magn. Reson. Spectrosc.* 1996, *28*, 283–350.

(22) Dong, H.; Du, S.; Zheng, X.; Lyu, G.; Sun, L.; Li, L.; Zhang, P.; Zhang, C.; Yan, C. Lanthanide Nanoparticles : From Design toward Bioimaging and Therapy. *Chem. Rev.* 2015, *115*, 10725–10815.

(23) Teo, R. D.; Termini, J.; Gray, H. B. Lanthanides: Applications in Cancer Diagnosis and Therapy. *J. Med. Chem.* 2016, *59*, 6012–6024.

(24) Cotton, S. Electronic and Magnetic Properties of the Lanthanides. In *Lanthanide and Actinide Chemistry*; Woolins, D., Crabtree, B., Atwood, D., Meyer, G., Eds.; John Wiley & Sons: Chippenham, England, 2006; pp 61–87.

(25) Forte, A.; Gago, S.; Alves, C.; Silva, J.; Rosa, J.; Pedrosa, R.; Laia, C. A. T.; Marrucho, I. M.; Branco, L. C. Unpublished Research. 2020.

(26) Werner, E. J.; Datta, A.; Jocher, C. J.; Raymond, K. N. High-Relaxivity MRI Contrast Agents: Where Coordination Chemistry Meets Medical Imaging. *Angew. Chemie - Int. Ed.* 2008, *47*, 8568–8580.

(27) Viswanathan, S.; Kovacs, Z.; Green, K. N.; Ratnakar, S. J.; Sherry, A. D. Alternatives to Gadolinium-Based Metal Chelates for Magnetic Resonance Imaging. *Chem. Rev.* 2010, *110*, 2960–3018.

(28) Murugesu, M.; Schelter, E. J. Not Just Lewis Acids: Preface for the Forum on New Trends and Applications for Lanthanides. *Inorg. Chem.* 2016, *55*, 9951–9953.

(29) Nghia, N. T.; Tinet, E.; Ettori, D.; Beilvert, A.; Pavon-Djavid, G.; Maire, M.; Ou, P.; Tualle, J. M.; Chaubet, F. Gadolinium/Terbium Hybrid

Macromolecular Complexes for Bimodal Imaging of Atherothrombosis. *J. Biomed. Opt.* 2017, *22* (7), 076004 (1-8).

(30) Sitharaman, B.; Jacobson, B. D.; Wadghiri, Y. Z.; Bryant, H.; Frank, J. The Magnetic, Relaxometric, and Optical Properties of Gadolinium-Catalyzed Single Walled Carbon Nanotubes The Magnetic, Relaxometric, and Optical Properties of Gadolinium-Catalyzed Single Walled Carbon Nanotubes. *J. Appl. Phys.* 2013, *113*, 134308 (1-7).

(31) Gould, C. A.; Mcclain, K. R.; Yu, J. M.; Groshens, T. J.; Furche, F.; Harvey, B. G.; Long, R. Synthesis and Magnetism of Neutral, Linear Metallocene Complexes of Terbium(II) and Dysprosium(II). *J. Am. Chem. Soc.* 2019, *141*, 12967–12973.

(32) Cho, A. MRI for All. *Science (80-.).* 2023, *379*, 748–751.

(33) Caravan, P.; Farrar, C. T.; Frullano, L.; Uppal, R. Influence of Molecular Parameters and Increasing Magnetic Field Strength on Relaxivity of Gadolinium- and Manganese-Based T1 Contrast Agents. *Contrast Media Mol. Imaging* 2009, *4* (2), 89–100.

(34) Hagberg, G. E.; Scheffler, K. Effect of R1 and R2 Relaxivity of Gadolinium-Based Contrast Agents on the T1-Weighted MR Signal at Increasing Magnetic Field Strengths. *Contrast Media Mol. Imaging* 2013, *8*, 456–465.

(35) Vaughan, T.; Delabarre, L.; Snyder, C.; Tian, J.; Akgun, C.; Shrivastava, D.; Liu, W.; Olson, C.; Adriany, G.; Strupp, J.; Andersen, P.; Gopinath, A.; Moortele, P. Van De; Garwood, M. 9.4T Human MRI Preliminary Results. *Magn. Reson. Imaging* 2006, *56* (6), 1274–1282.

(36) Runge, V. M.; Heverhagen, J. T. *The Physics of Clinical MR Taught Through Images*, 5th Ed.; Springer: Cham, Switzerland, 2015.

(37) Fong-Padrón, C.; Cabaleiro-Lago, E. M.; Rodríguez-Otero, J. Water Interaction with Ion Pairs from Ionic Liquids. Computational Study and Performance Assessment of Several Common Functionals. *Chem. Phys. Lett.* 2014, *593*, 181–188.

(38) Nordness, O.; Brennecke, J. F. Ion Dissociation in Ionic Liquids and Ionic Liquid Solutions. *Chem. Rev.* 2020, *120* (23), 12873–12902.

(39) Silva, W.; Zanatta, M.; Ferreira, A. S.; Corvo, M. C.; Cabrita, E. J. Revisiting Ionic Liquid Structure-property Relationship: A Critical Analysis. *Int. J. Mol. Sci.* 2020, *21* (20), 1–37.

(40) Ma, C.; Laaksonen, A.; Liu, C.; Lu, X.; Ji, X. The Peculiar Effect of Water on Ionic Liquids and Deep Eutectic Solvents. *Chem. Soc. Rev.* 2018, *47* (23), 8685–8720.

(41) Rodenbücher, C.; Wippermann, K.; Korte, C. Atomic Force Spectroscopy on Ionic Liquids. *Appl. Sci.* 2019, *9* (11).

(42) Katoh, R.; Hara, M.; Tsuzuki, S. Ion Pair Formation in [Bmim]I Ionic Liquids. *J. Phys. Chem. B* 2008, *112* (48), 15426–15430.

(43) Rohrer, M.; Bauer, H.; Mintorovitch, J.; Requardt, M.; Weinmann, H. J. Comparison of Magnetic Properties of MRI Contrast Media Solutions at Different Magnetic Field Strengths. *Invest. Radiol.* 2005, *40* (11), 715–724.

(44) Robic, C.; Port, M.; Rousseaux, O.; Louguet, S.; Fretellier, N.; Catoen, S.; Factor, C.; Le Greneur, S.; Medina, C.; Bourrinet, P.; Raynal, I.; Idée, J. M.; Corot, C. Physicochemical and Pharmacokinetic Profiles of Gadopiclenol: A New Macrocyclic Gadolinium Chelate With High T1 Relaxivity. *Invest. Radiol.* 2019, *54*, 475–484.

Chapter 4

Mesoporous Silica Nanoparticles with Manganese and Lanthanides ionic systems

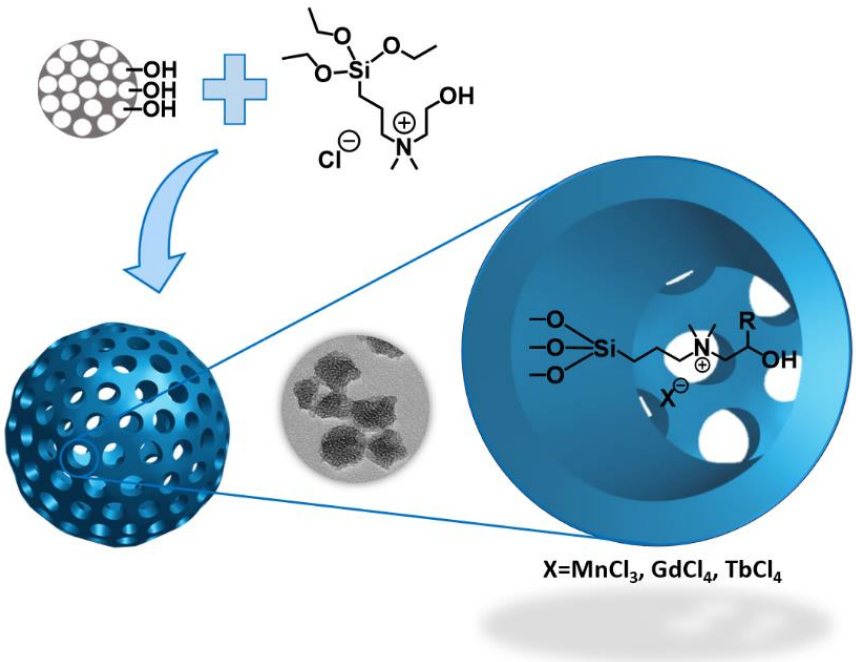

This chapter was adapted from the article “Manganese and Lanthanides based ionic liquids functionalized in Mesoporous silica nanoparticles: synthesis, characterization and cytotoxicity studies”, Andreia Forte, Sandra Gago, Manuela Ribeiro Carrott, Peter Carrott, Celso Alves, Fernando Teodoro, Rui Pedrosa, Isabel Marrucho and Luis Branco, 2021, Dalton Trans., 50, 8588-8599 (DOI: 10.1039/d1dt00605c).

Chapter 4

Mesoporous Silica Nanoparticles with Manganese and Lanthanides ionic systems

Abstract

Several organic salts based on the combination of two different choline derivative cations and $MnCl_3^-$, $GdCl_4^-$ and $TbCl_4^-$ as anions were immobilized in mesoporous silica nanoparticles (MSNs) by a two-step synthetic method. Firstly, MSNs were functionalized with choline derivative cations with chloride anions and then the metals were incorporated by the reaction of the chloride with the respective metal chloride salts. These nanomaterials were fully characterized by different characterization techniques such as ^{1}H-NMR, FT-IR, elemental analysis, TEM, TGA, N_2 adsorption, XRD and DLS. These characterization data were important to confirm the successful functionalization of the nanomaterials and to access their textural properties and colloidal stability. The final materials were also characterized by ICP-MS that indicated the metal contents. The cytotoxicity profile was evaluated in four different cell lines (3T3, 293T, HepG2 and Caco-2), which shows some relevant differences between the metal organic salts and their immobilized analogues.

1. Introduction

Nanotechnology has attracted great attention in the last few years due to the possibility to produce a wide range of nanomaterials with different properties and compositions.[1] Among these nano-materials, Mesoporous Silica Nanoparticles (MSNs) have been widely explored due to their properties such as high chemical stability, high specific surface area, tuneable particle and pore sizes, and narrow pore size distribution. The biocompatibility of MSNs and the possibility of functionalizing them with specific molecules either on the internal surface of their pores or on the external particle surface

are their major advantages.[2–4] Ionic Liquids (ILs) are a class of compounds that has attracted interest from academic and industrial communities in the last few years.[5] They are usually defined as organic salts completely composed of ions with a melting point below 100 °C. One of the main features of these salts is the possibility of tuning their physical-chemical properties by applying different combinations of cation and anion scaffolds. This ability can create a large variety of IL structures for different applications.[6,7] Recently, a new class of these task-specific salts known as Magnetic ILs (MILs) has been explored. These materials that combine simultaneously ionic liquid properties and magnetic properties, in particular, the response to strong magnetic fields, were firstly reported by Hayashi and Hamaguchi in 2004.[8,9] MILs have abroad range of applications in chemical reactions and separation processes, in electrochemical and medical devices, as solvents in the polymerization of conducting polymers and as carrier liquids to produce magnetic fluids.[10,11] More recently, these magnetic salts, as well as other systems such as magnetic nanoparticles, have been studied as potential contrast agents for Magnetic Resonance imaging (MRI) technique.[12] MILs containing iron as well as other paramagnetic ions including transition metals, such as cobalt (II), manganese (II) and some lanthanides, such as gadolinium (III) and terbium (III), have been reported.[10,13–16] However, their toxicity is a matter of concern. Several MILs based on choline derivative structures as cations and paramagnetic metal based anions have been explored to modulate their toxicity.[15,17] Choline is a quaternary ammonium cation with a hydroxyethyl group that plays a critical role in the human body system. This essential nutrient needed for the synthesis of the acetylcholine neurotransmitter plays a fundamental role in cell membrane signalling among other important functions, and can be synthesized endogenously or acquired through diet.[18] The hydroxyethyl group present in the choline

structure is one of the reasons associated with the low toxicity of these compounds.[19] In this work, magnetic organic salts immobilized in MSNs, based on two different choline derivative structures as cations and $[MnCl_3]^-$, $[GdCl_4]^-$ and $[TbCl_4]^-$ as anions, were prepared.

2. Results and discussion

2.1. Synthesis of magnetic organic salts based on choline derivatives

Using optimized alkylation methods, a set of choline derivative cations were synthesized from three different amines. From these compounds, two selected chloride-based organic salts, $[N_{1,1,4,C2OH}][Cl]$ and $[N_{1,1,4,C3OH}][Cl]$, were used to carry outmetal complexation reactions with two different lanthanides, gadolinium (III) and terbium (III), and one transition metal, manganese (II), in order to obtain organic salts, as illustrated in Scheme 4. 1.

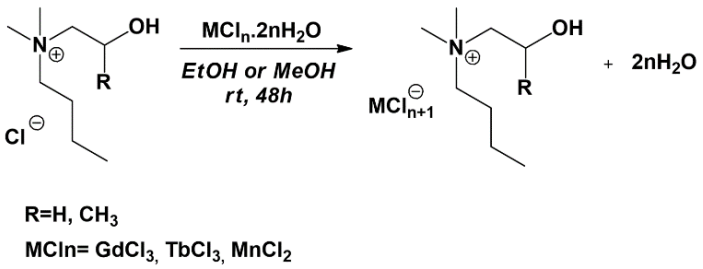

Scheme 4. 1 | Schematic synthetic step of the magnetic organic salts based on choline derivative cations.

Some physical properties of these metal organic salts such as their physical state and thermal properties (melting and decomposition temperatures) were evaluated (Table 4. 1).

Table 4. 1 | Physical and thermal properties of magnetic organic salts

Cation	Anion	Physical State	Tm [Td] [(a)] (ºC)
$[N_{1,1,4,C2OH}]$	$[GdCl_4]$	White Solid	[118]
	$[TbCl_4]$	White Solid	[115]
	$[MnCl_3]$	Pink Solid	[191]
$[N_{1,1,4,C3OH}]$	$[GdCl_4]$	Yellow Solid	148
	$[TbCl_4]$	Yellow Solid	155
	$[MnCl_3]$	Yellow Solid	132

[(a)] Melting temperature (Tm) and decomposition temperature (Td) was determined on Electrothermal Melting Point Apparatus

All compounds were obtained as solids materials with transition temperatures higher than 100°C. For $[N_{1,1,4,C3OH}]$ based salts, no melting point was found and only decomposition temperatures could be measured. Typically, organic salts based on biocompatible choline derivatives showed low toxicity. However, their combination with metals can increase this parameter. When coordinated with a large linear molecule, the metal toxicity is reduced since the metal is trapped. In this work, metal organic salts were immobilized in MSNs and the impact of this immobilization in their toxicity profile was evaluated.

2.2. Synthesis and functionalization of MSNs

Two sets of mesoporous silica nanoparticles functionalized with magnetic organic salts were developed. The optimized synthetic methodology to obtain these materials comprises four major steps as shown in Scheme 4. 2.

Alkoxysilane precursors Si-DMAE and Si-DMAP, analogues of [$N_{1,1,4,C2OH}$] and [$N_{1,1,4,C3OH}$] cations with a small difference of a propyl chain instead of a butyl chain (see Scheme 4. 1 and Scheme 4. 2), were synthesized by performing two amine alkylation reactions between (3-chloropropyl)triethoxysilane and two different amines, 2-dimethylaminoethanol (DMAE) or 1-dimethylamino-2-propanol (DMAP). Mesoporous silica nanoparticles precursors, MSN-A and MSN-B, were prepared based on a well-established methodology already described in the literature.[20] The CTAB surfactant was used as a template and its removal was performed using acidic ethanol in order to reduce nano-particle aggregation. Then, the surface silanol groups were functionalized with alkoxysilane derivates to obtain MSN-Si-DMAE and MSN-Si-DMAP containing choline derivatives as cations and chloride as anions. Finally, MSNs containing $[MnCl_3]^-$, $[GdCl_4]^-$ and $[TbCl_4]^-$ anions were obtained by the reaction of the chloride ions with the corresponding metal chlorides. These final materials were characterized by several techniques: ^{1}H-NMR (proton nuclear magnetic resonance), FT-IR (Fourier transform infrared), EA (elemental analysis), ICP-MS (inductively coupled plasma mass spectrometry), XRF (X-Ray Fluorescence), TEM (transmission electron microscopy), TGA (thermogravimetric analysis), N_2 adsorption, XRD (X-ray diffraction) and DLS (dynamic light scattering).

The successful functionalization of MSNs with choline derivatives was confirmed by ^{1}H-NMR (Figure 4. 1), FT-IR (Supplementary Information, Figure SI 90-91 and Table SI 20) and elemental analysis. To obtain solution ^{1}H-NMR spectra of MSN-Si-DMAE and MSN-Si-DMAP, the silica matrix was destroyed according to a method described in the literature.[21] The peaks obtained for MSN-Si-DMAE and MSN-Si-DMAP were assigned to the protons of organic salts in Figure 4. 1 (A) and (B), respectively.

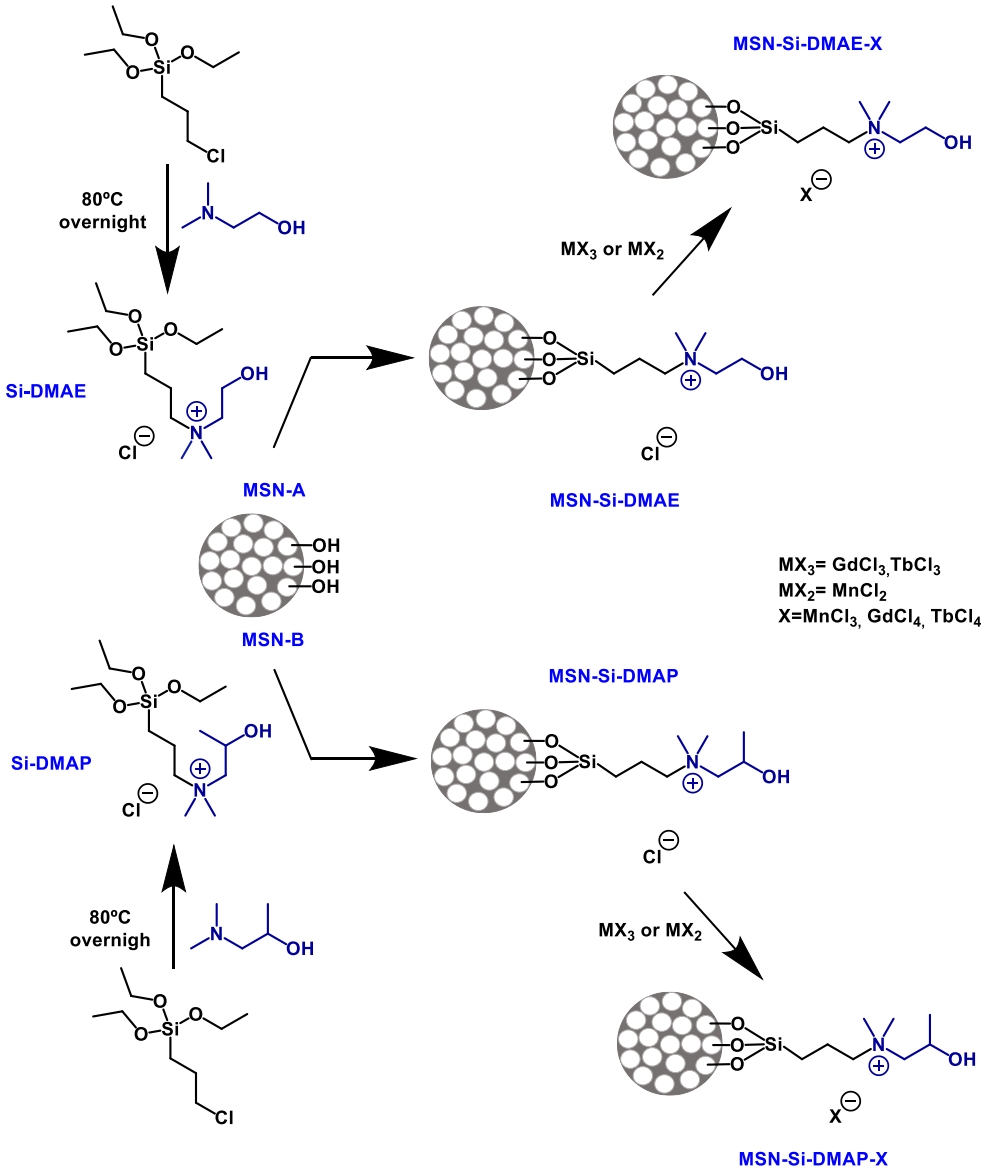

Scheme 4. 2 | Schematic illustration of the silica mesoporous nanoparticles preparation process.

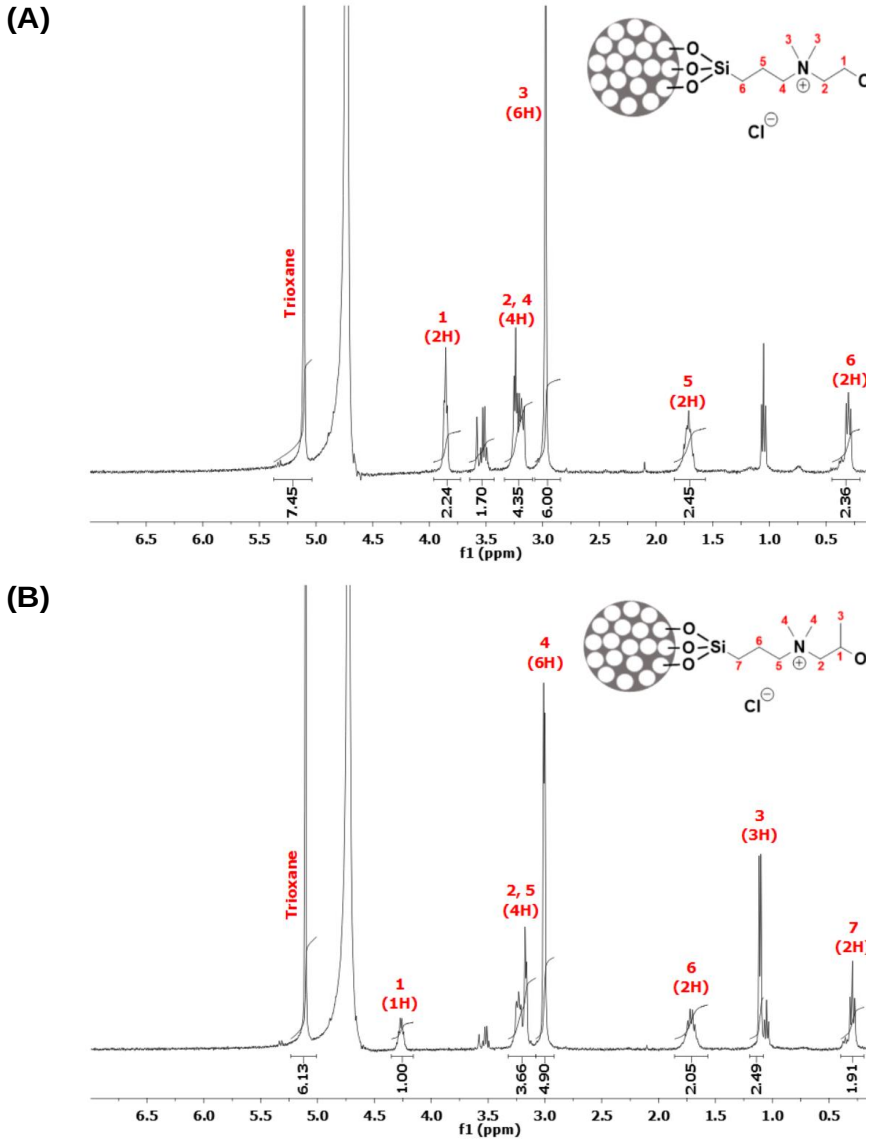

Figure 4. 1 | ^{1}H-NMR spectra for (A) MSN-Si-DMAE and (B) MSN-Si-DMAP

FT-IR spectra of functionalized materials (SI, Figures SI 89-90 and Table SI 4) clearly show the typical silica absorption bands at 1095 cm^{-1} for MSN-A and 1092 cm^{-1} for MSN-B and, also, the presence of Si-DMAE and Si-DMAP chloride salts could be confirmed by the bands associated with C–H bonding

vibrations at 1477 cm^{-1} and 1400 cm^{-1} for MSN-Si-DMAE and 1479 cm^{-1} and 1400 cm^{-1} for MSN-Si-DMAP.

Elemental analysis indicates 1.50 mmol g^{-1} of cation for MSN-Si-DMAE and 1.45 mmol g^{-1} of cation for MSN-Si-DMAP (Table 4. 2).

Table 4. 2 | Cations and metals loadings based on elemental analysis and ICP-MS results.

	Cation (mmol/g)	**Metal (mmol/g)**
MSN-Si-DMAE	1.50	-
MSN-Si-DMAE-Gd	1.50	0.07
MSN-Si-DMAE-Tb	1.35	0.09
MSN-Si-DMAE-Mn	1.47	0.19
MSN-Si-DMAP	1.45	-
MSN-Si-DMAP-Gd	1.42	0.03
MSN-Si-DMAP-Tb	1.31	0.02
MSN-Si-DMAP-Mn	1.43	0.04

Metal complexation reactions efficiency of the final materials was evaluated by XRF and ICP-MS. From XRF spectra it was possible to identify characteristic fluorescent X-rays specific for the three target metals and confirm the complexation success (Figure 4. 2, Figures SI 91-93 and Table SI 5 in SI). Also, in all spectra it is possible to identify peaks associated to silica and chloride elements.

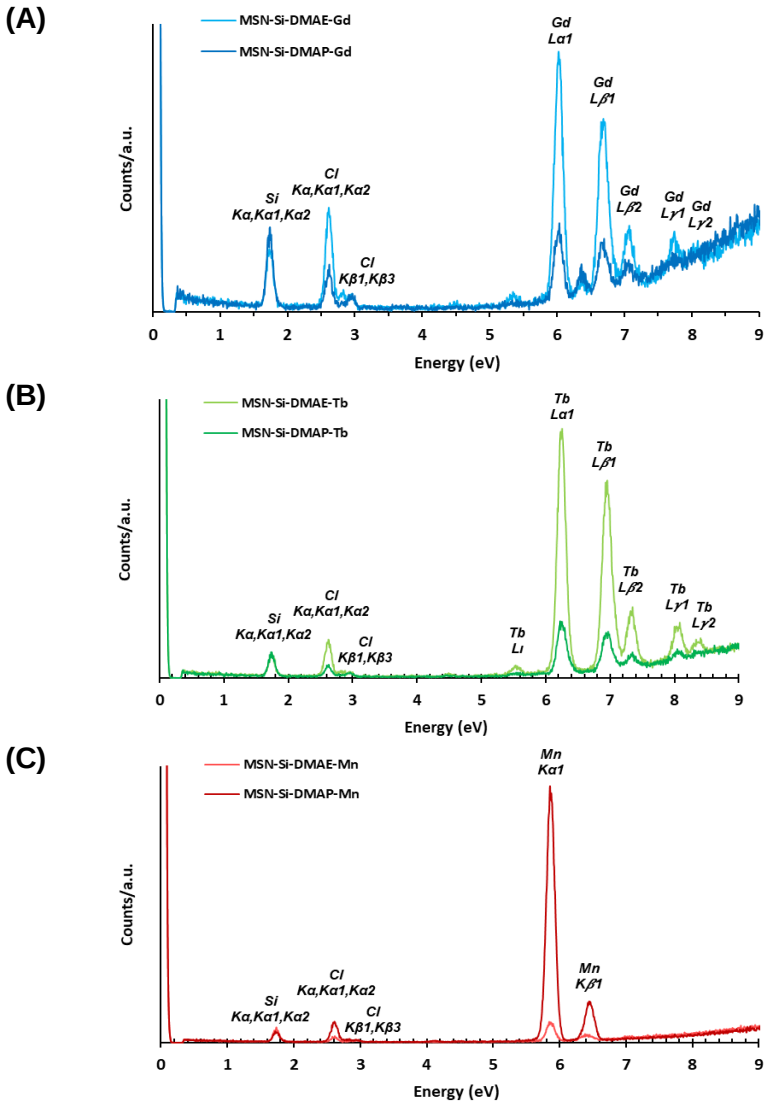

Figure 4. 2 | μ-EDXRF spectra obtained for (A) MSN-Si-DMEA-Gd and MSN-Si-DMPA-Gd; (B) MSN-Si-DMEA-Tb and MSN-Si-DMPA-Tb; (C) MSN-Si-DMEA-Mn and MSN-Si-DMPA-Mn

ICP-MS results show that metal loadings range from 0.02 mmol g^{-1} to 0.19 mmol g^{-1} (Table 4. 2). Higher metal loadings were achieved for the Si-DMAE

cation which can be related steric effects resulting from the presence of a secondary alcohol in the Si-DMAP cation. Another important piece of information that can be taken from these results is the incomplete complexation reactions between the chloride ions and the metal chlorides. The metal values in percentage per cation unit are in the range of 2.25–13.18%, which means that the majority of the cations are in the MSN structure with chloride as counter ions. These results are supported by XRF results.

The overall amount of loaded organic cations in nanoparticles, which by elemental analysis is around 20% (in mass) for MSN-Si-DMAE and 21% for MSN-Si-DMAP, was confirmed by thermogravimetric analysis. TGA curves, presented in Figure 4. 3 for all studied materials, indicate a 2 to 4% mass loss between 80 and 200 °C, which can be justified by the release of water.

TGA curves of MSN-Si-DMAE and MSN-Si-DMAP, presented in Figure 4. 3 (A) and (B) respectively, are similar and show two main mass changes, the first between 200 °C and 290 °C that corresponds to 9% mass loss and another in the 330–500 °C range. Between 200 °C and 500 °C, 20% mass loss for MSN-Si-DMAE and 21.9% for MSN-Si-DMAP were obtained, which is consistent with the content of organic cations obtained by elemental analysis. Regarding MSN-Si-DMAE-X and MSN-Si-DMAP-X and the first step, the same behavior of their precursors could be found for most materials and the mass loss is also 9%, although for some materials slightly higher temperatures are required to obtain the same mass loss. Considering now the second mass change, it occurs at higher temperatures than for MSN-Si-DMAE and MSN-Si-DMAP materials. The observed displacements to higher temperatures are due to the presence of metal complexes and their interactions with the organic cations.

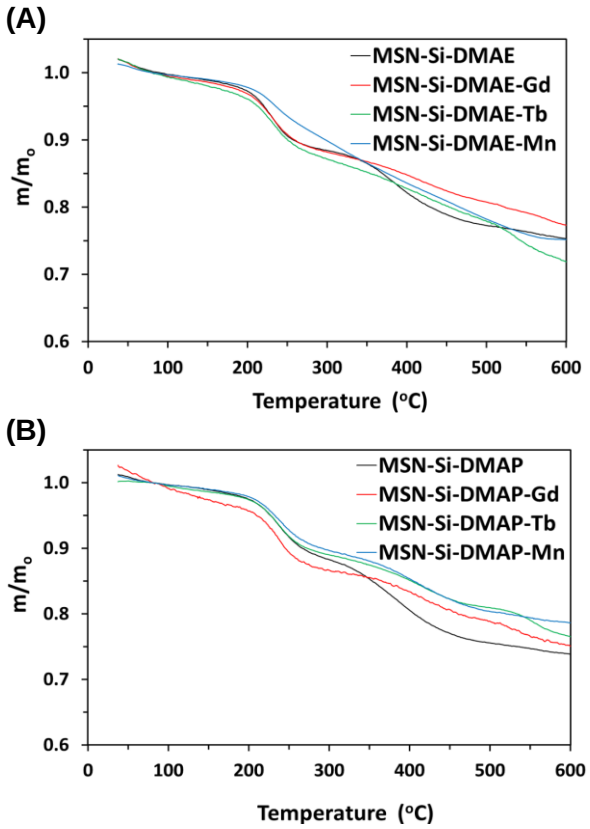

Figure 4. 3 | Thermogravimetric analysis of (A) MSN-Si-DMAE and MSN-Si-DMAE-X; (B) MSN-Si-DMAP and MSN-Si-DMAP-X (m_o is the mass at 80°C)

2.3. Characterization by transmission electron microscopy, nitrogen adsorption at 77 K and X-ray diffraction

The prepared nanoparticles were characterized according to their morphology and particle size. MSN-A, MSN-B and all metal-based nanoparticles were analyzed by transmission electron microscopy (TEM). Nanoparticle images and the average diameter values obtained from TEM can be seen in Figure 4. 4.

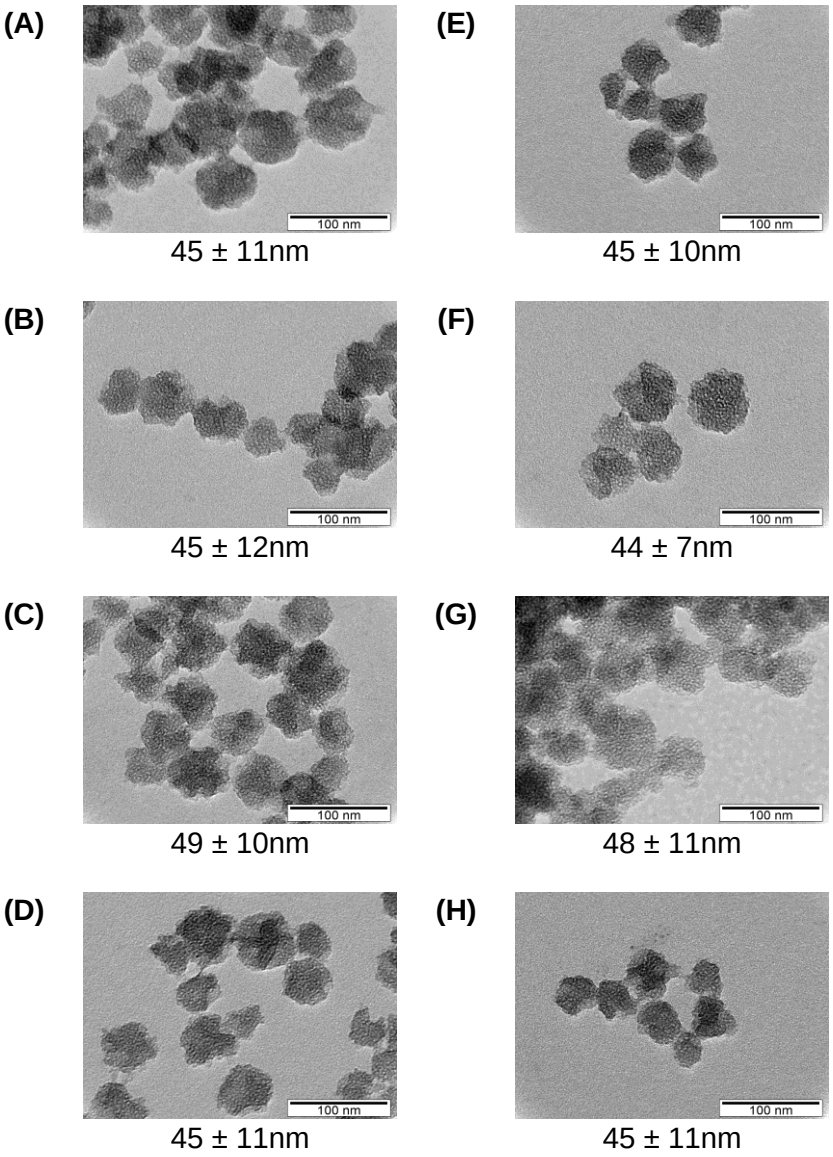

Figure 4. 4 | Transmission electron microscopy images and mean diameter ± SD of (A) MSN-A; (B) MSN-Si-DMAE-Gd; (C) MSN-Si-DMAE-Tb; (D) MSN-Si-DMAE-Mn; (E) MSN-B; (F) MSN-Si-DMAP-Gd; (G) MSN-Si-DMAP-Tb; (H) MSN-Si-DMAP.

The images show monodisperse nanoparticles with spherical shapes and some aggregation. All nanoparticles presented similar particle average diameter values. Even so, it is possible to observe that Si-DMAE-based materials have a very slightly larger diameter than Si-DMAP-based materials. N_2 adsorption–desorption isotherms determined at 77 K on silica nanoparticles MSN-A and MSN-B are presented respectively in Figure 4. 5 (A) and (B), together with the representative adsorption–desorption isotherms for each material after functionalization. Considering that no differences could be seen in this scale for the functionalized materials, adsorption isotherms are shown in another scale in the figures on the right for all the functionalized materials. The N_2 adsorption–desorption isotherms were analysed by the BET method using the criteria recommended by Rouquerol et al.[22], and subsequently endorsed by IUPAC,[23] and by NLDFT using the Quantachrome software ASiQwin. The results are summarized in Table 4. 3.

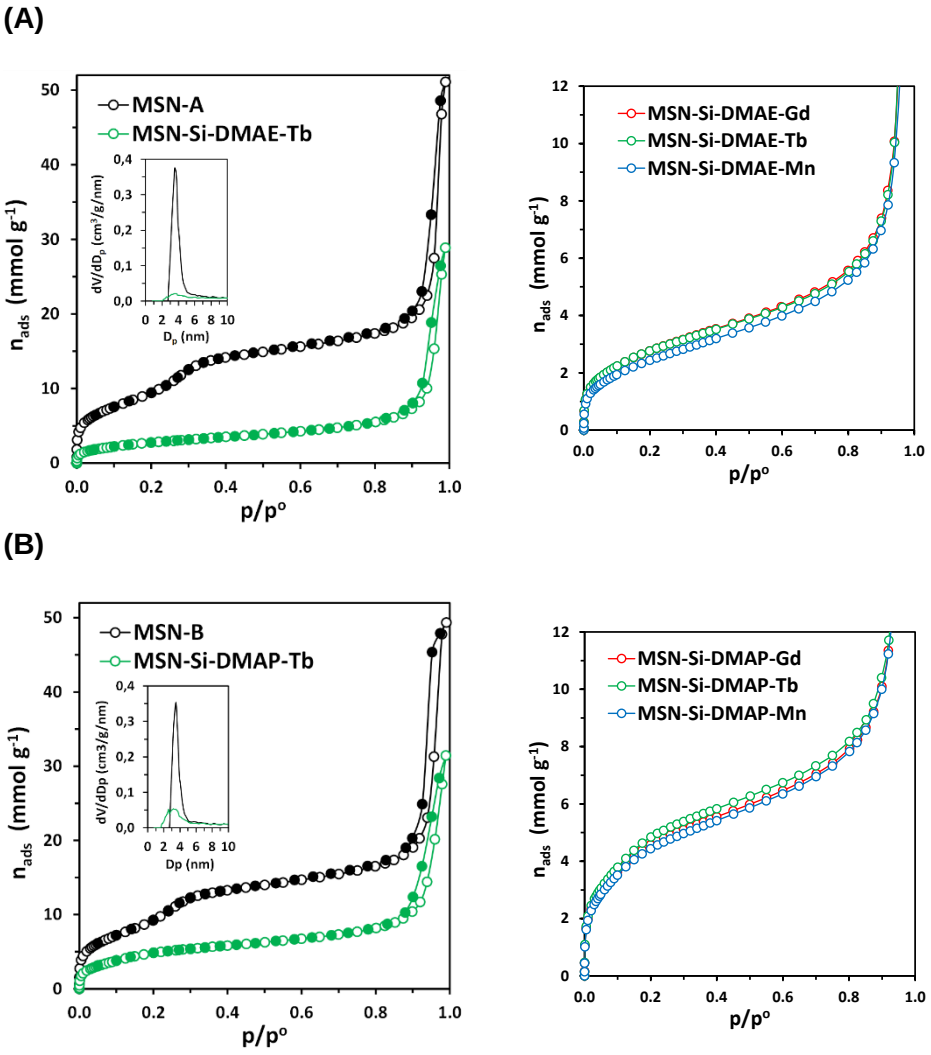

Figure 4. 5 | Nitrogen adsorption isotherms determined at 77 K on (A) MSN-A and MSN-Si-DMAE-X; (B) MSN-B and MSN-Si-DMAP-X. NLDFT pore size distributions are inserted into figures on the left

Table 4. 3 | Textural characteristics of the mesoporous silica nanoparticles obtained by analysis of the N_2 adsorption isotherms determined at 77 K.

Sample	A_{BET} (m^2 g^{-1})	D_p (nm)	V_p (cm^3 g^{-1})
MSN-A	743	3.54	0.44
MSN-Si-DMAE-Gd	228	3.54	0.08
MSN-Si-DMAE-Tb	228	3.54	0.08
MSN-Si-DMAE-Mn	200	3.78	0.07
MSN-B	719	3.54	0.39
MSN-Si-DMAP-Gd	382	3.18	0.14
MSN-Si-DMAP-Tb	400	3.18	0.15
MSN-Si-DMAP-Mn	371	3.18	0.13

A_{BET} – specific surface area obtained by the BET method in the p/p^o range 0.045-0.12 for all; D_p - pore diameter obtained from the NLDFT pore size distributions; V_p – cumulative pore volume corresponding to 8 nm obtained from the NLDFT pore size distributions

As can be seen in Figure 4. 5, the isotherms obtained on MSN-A and MSN-B are type IV of the IUPAC classification,[23] with a well-defined step associated with filling of cylindrical mesopores by capillary condensation. The pore size distributions, inserted into the figures on the left, show that the pore diameter is reasonably uniform in both silica materials. The nitrogen adsorption–desorption isotherms on the nanoparticles are reversible up to a high pressure, and values above 0.9 show a hysteresis cycle that is usually obtained on materials with small size spherical nanoparticles and is associated with capillary condensation in voids between particles. The functionalization did not affect the shape of the hysteresis cycle which was found to be similar for all materials. Regarding the nitrogen adsorption and condensation in the uniform mesopores, a reduction in the adsorbed amounts was observed for all the functionalized materials. As expected, functionalized materials present smaller values of specific surface areas and

pore volumes, and a decrease in the pore size distributions when compared to the starting materials MSN-A and MSN-B. For the materials with the same organic cation, no significant differences were found for different metals. Nevertheless, the nanomaterials with lanthanides have slightly larger specific surface areas and pore volumes in both series. When the materials with different organic cations and the same metal are compared, larger values can be observed for MSN-Si-DMAP-X materials. It is noticeable in the nitrogen adsorption isotherms on MSN-Si-DMAP-X that a pore filling step is still perceptible and displaced to a lower relative pressure due to the decrease of pore size as obtained from NLDFT. Regarding MSN-Si-DMAE-Gd and MSN-Si-DMAE-Tb, the mean pore size is maintained, while in the case of MSN-Si-DMAE-Mn the slightly larger mean pore size results from the disappearance of pores of smaller size as found in the pore size distribution. All the nitrogen adsorption results are consistent with the smaller %metal/cation found, in each series, for lanthanides in comparison with Mn, and the smaller %metal/cation for all metals found for MSN-Si-DMAP-X. Thus, more space in pores is available since the chloride counterions occupy a smaller volume than the metal complexes. As can be seen in Figure 4. 6, the X-ray diffraction patterns of MSN-A and MSN-B have a main peak in the low-angle region at around 2° (2θ), and another with a much lower intensity at around 4° (2θ), indicating some ordering of the pores with a reasonably uniform pore size. The main peak is broader, less intense and corresponds to ad-spacing larger than those usually obtained for MCM-41 and MCM-48 silicas with similar average pore diameters, consistent with a less ordered arrangement of the pores inside such small nanoparticles. All the functionalized materials present a broad peak also at around 2° (2θ), although with a lower intensity than those of the starting silica materials, indicating that some ordered mesopores remain after functionalization.

Consistent with the nitrogen adsorption studies and the smaller %metal/cation in MSN-Si-DMAP-X, the peak is slightly better resolved and more intense for MSN-Si-DMAP-X materials than for MSN-Si-DMAE-X.

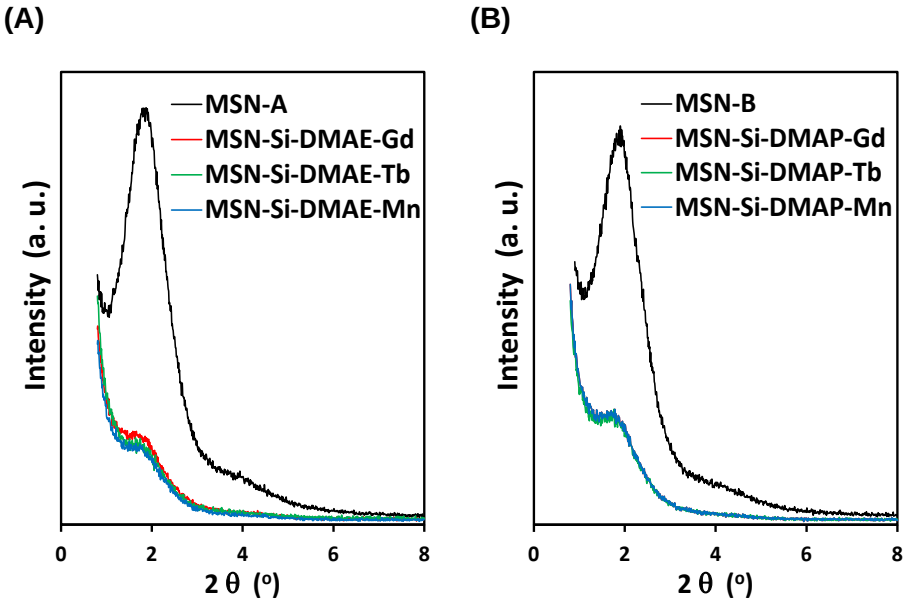

Figure 4. 6 | X-ray diffraction patterns of (A) MSN-A and MSN-Si-DMAE-X; (B) MSN-B and MSN-Si-DMAP-X.

2.4. Nanoparticles Colloidal Stability

The prepared MSNs, before and after functionalization, were suspended in water by sonication and their colloidal stability was monitored by dynamic light scattering (DLS). Hydrodynamic diameter and zeta potential values were measured for all nanomaterials and the results are summarized in Table 4. 4.

Table 4. 4 | Hydrodynamic diameter and zeta potential of the final materials obtained in water by DLS (mean ±SD).

	Average Hydrodynamic diameter (nm)	Polydispersity index (PDI)	Zeta Potential (mV)	pH
MSN-A	204 ± 28.30	0.38 ± 0.04	-9.90 ± 3.12	5.07
MSN-Si-DMAE	107 ± 2.63	0.35 ± 0.03	+49.46 ± 1.72	4.65
MSN-Si-DMAE-Gd	110 ± 0.76	0.29 ± 0.02	+43.16 ± 1.62	4.04
MSN-Si-DMAE-Tb	123 ± 2.52	0.40 ± 0.03	+46.40 ± 1.36	4.06
MSN-Si-DMAE-Mn	125 ± 0.76	0.34 ± 0.03	+45.06 ± 1.77	4.00
MSN-B	193 ± 1.89	0.42 ± 0.06	-5.36 ± 2.21	4.15
MSN-Si-DMAP	135 ± 1.82	0.33 ± 0.08	+59.16 ± 1.24	4.17
MSN-Si-DMAP-Gd	125 ± 5.60	0.37 ± 0.05	+48.10 ± 1.08	3.93
MSN-Si-DMAP-Tb	137 ± 0.61	0.34 ± 0.12	+43.76 ± 1.72	4.06
MSN-Si-DMAP-Mn	149 ± 2.84	0.42 ± 0.12	+49.58 ± 1.21	4.00

As can be seen, hydrodynamic diameters are in the range of 107–204 nm, with an average polydispersity index of 0.36. As is well known, smaller nanoparticles have a higher surface energy which makes the particles more prone to aggregate, in order to lower the energy of the system.[24] According to TEM images, the prepared nanoparticles have an average size in the range of 45–49 nm. Their small size can lead to an aggregation phenomenon, proved by their hydrodynamic diameter values obtained by DLS measurements. Non-functionalized nanoparticles MSN-A and MSN-B have much higher values of hydrodynamic diameters than functionalized materials. This effect can be related to a major tendency to aggregate. These materials also presented a negative zeta potential (−9.90 mV and−5.36 mV) due to the negatively charged terminal silanol groups present at the nanoparticle surface and the pH used in this study. When MSN-A and MSN-

B are functionalized with DMAE and DMAP structures, the values of hydrodynamic diameters decrease, and their zetapotential values change from negative to positive due to the positive charge associated with choline derivative scaffolds. When metal complexes are introduced in the nanoparticles, slightly lower values of zeta potentials are obtained. Higher values of hydrodynamic diameters and zeta potentials were obtained for MSN-Si-DMAP and MSN-Si-DMAP-X nanoparticles. High zeta potential values obtained for all prepared nanoparticles indicate the high colloidal stability of these materials in water suspensions. Moreover, PDI values indicate that these materials are monodisperse which is in correlation with the TEM results.

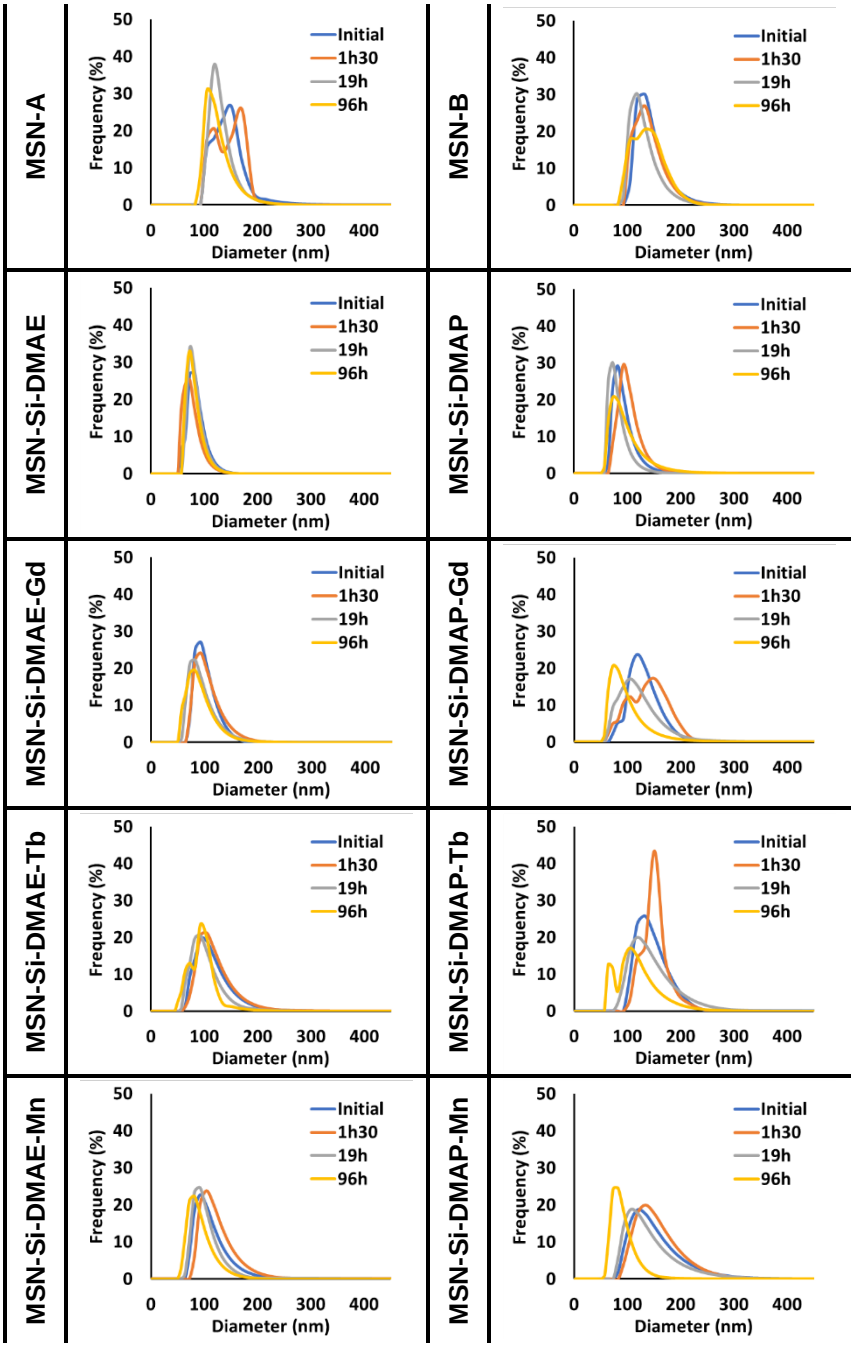

Figure 4. 7 | Time evolution of hydrodynamic diameter distributions of prepared nanoparticles suspensions in water.

It can be observed (Figure 4. 7) that colloidal suspensions with DMAE-based nanoparticles are more stable than those with DMAP-based nanoparticles. Also, the shape and value of hydrodynamic diameter curves are maintained for DMAE-based nanomaterials. This can be related to the presence of a secondary alcohol in the DMAP structure since the presence of a branched structure is usually responsible for the decrease of attractive forces between molecules. Also, the presence of metal complexes seems to have some effect on the stability of the nanoparticles. As can be observed, MSN-Si-DMAE-X and MSN-Si-DMAP-X present hydrodynamic diameter distribution curves with a tendency to change significantly over time. In contrast, MSN-Si-DMAE and MSN-Si-DMAP have distribution curves with more conserved shapes and values. This effect seems to be more evident for DMAP-based nanoparticles. These conclusions are in agreement with the results obtained for hydrodynamic diameters and zeta potentials.

2.5. Cytotoxicity

The cytotoxic effects of magnetic organic salts and the pre-pared mesoporous silica nanoparticles were evaluated on 3T3, 293T, HepG2 and Caco-2 cells after 24 h of treatment. All compounds were tested at a maximum concentration of 100 μg mL^{-1}. The cell viability was estimated by the MTT assay and the results are presented in the following sections.

2.5.1. Choline derivatives magnetic organic salts

The effects of two choline derivative salts with chloride and metal complexes as anions on the studied cell viability are presented in Figure 4. 8. The starting metal chlorides were also studied. It is possible to observe that the majority of the compounds did not induce any cytotoxicity on the cell lines studied compared to the control. Even so, there are some exceptions that

can be highlighted. Manganese-based salts, $[N_{1,1,4,C2OH}][MnCl_3]$ and $[N_{1,1,4,C3OH}][MnCl_3]$, as well as $MnCl_2{\cdot}4H_2O$, reduced significantly the viability of 3T3 cells (63.00%, 73.76% and 67.21% of viable cells, respectively) compared with the control. In 293Tcells, when compared with control, only the synthesized salt $[N_{1,1,4,C3OH}][MnCl_3]$ and $MnCl_2{\cdot}4H_2O$ was observed to significantly reduce the cell viability in more than 35% and 40%,respectively. For these cells, some prepared compounds and also gadolinium and terbium chlorides presented cell viabilities higher than 100%, which can suggest that these magnetic salts may enhance the mitochondrial activity. $[N_{1,1,4,C3OH}][TbCl_4]$ salt was the only prepared compound that significantly reduced the viability of HepG2 and Caco-2 cells compared with the control. Also, $GdCl_3{\cdot}6H_2O$ and $MnCl_2{\cdot}4H_2O$ induced a reduction effect on Caco-2 cell viability when com-pared with the control. In general, the compounds based on cations $[N_{1,1,4,C2OH}]$ and $[N_{1,1,4,C3OH}]$ exhibited similar behaviors.

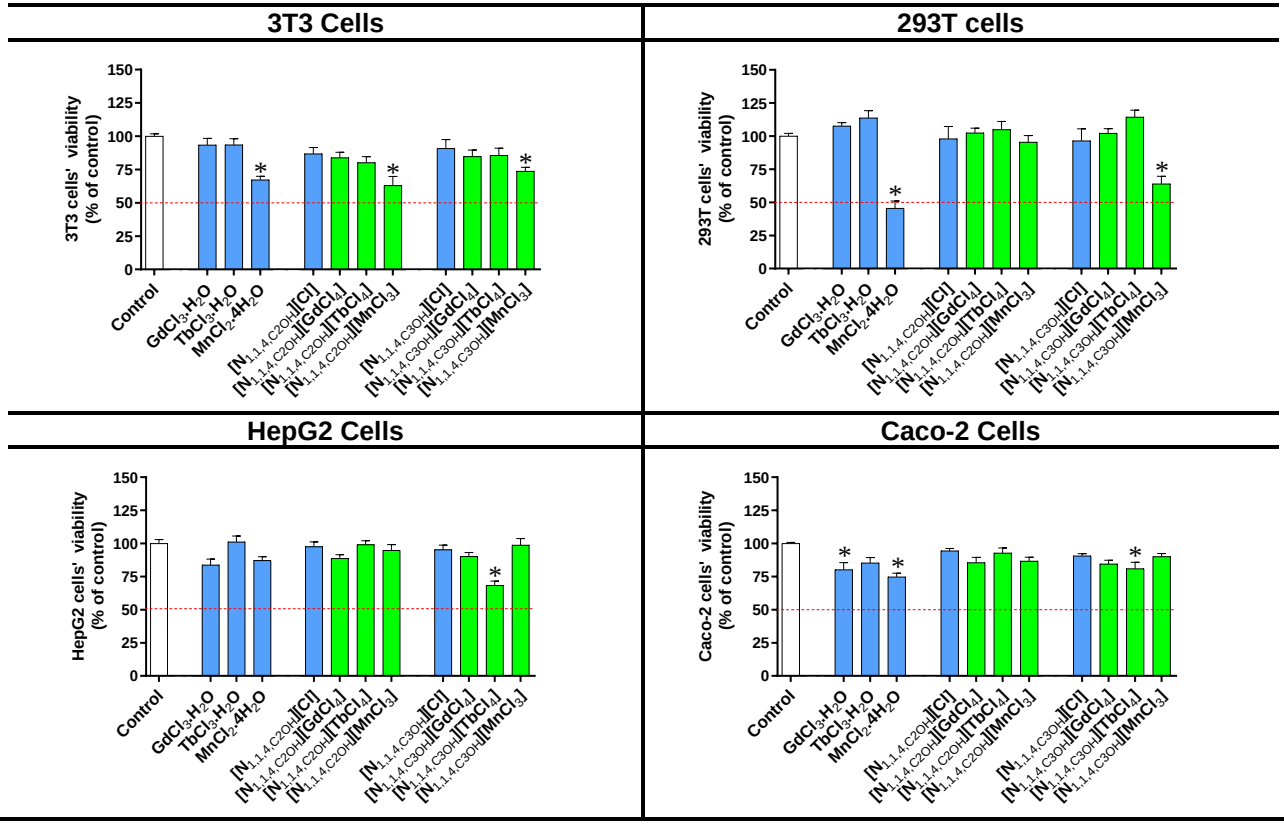

Figure 4. 8 | Cytotoxicity of magnetic organic salts (100 µg/ mL) on 3T3, 293T, HepG2 and Caco-2 cells after treatment for 24 h. Values represent mean ± standard error of the mean (SEM) of at least three independent experiments carried out in triplicate. Symbols represent significant differences (ANOVA, Dunnett's test, $p < 0.05$) when compared to: *control.

2.5.2. Mesoporous Silica Nanoparticles

The effects of all the prepared nanoparticles on the studied cell viability are shown in Figure 4. 9. Concerning the prepared nanomaterials, the cytotoxicities of the two sets of nanoparticles based on DMAE and DMAP scaffolds and their precursors were evaluated. In 3T3 cells, for the first set of materials, it is possible to observe that the nanoparticles before and after functionalization, MSN-A and MSN-Si-DMAE, significantly reduce the cell viability in more than 20% (79.96% and 72.32% of viable cells, respectively) when compared with the control. Regarding the metal-based materials, only MSN-Si-DMAE-Tb was observed to reduce the cell viability in these cell lines. Regarding the second set of nanoparticles, MSN-B was also observed to reduce the cell viability (52.11% of viable cells) and all metal-based materials were observed to be responsible for a significant reduction of cell viability compared to the control. In this case, a range of 77.65–83.09% of viable cells was achieved. In 293T cells, among the DMAE set, only MSN-A presented a significant reduction of cell viability in almost 30% in comparison to the control. For the DMAP set, almost all induced a reduction in the cell viability, with the exceptions being Si-DMAP and MSN-Si-DMAP-Tb. DMAE-based materials and their precursors do not seem to have any effect on HepG2 cells. MSN-B, MSN-Si-DMAP-Gd and MSN-Si-DMAP-Tb, in contrast, induced cell viability reductions of 46.05%, 27.85% and22.5%, respectively, compared to the control. Finally, almost all induced cytotoxicity in Caco-2 cells (70.50–87.88% of viable cells) and only MSN-A and Si-DMAE did not exhibit a cytotoxic effect. As can be seen, DMAP-based materials and their precursors seem to induce a more marked effect on cell viability than DMAE-based materials.

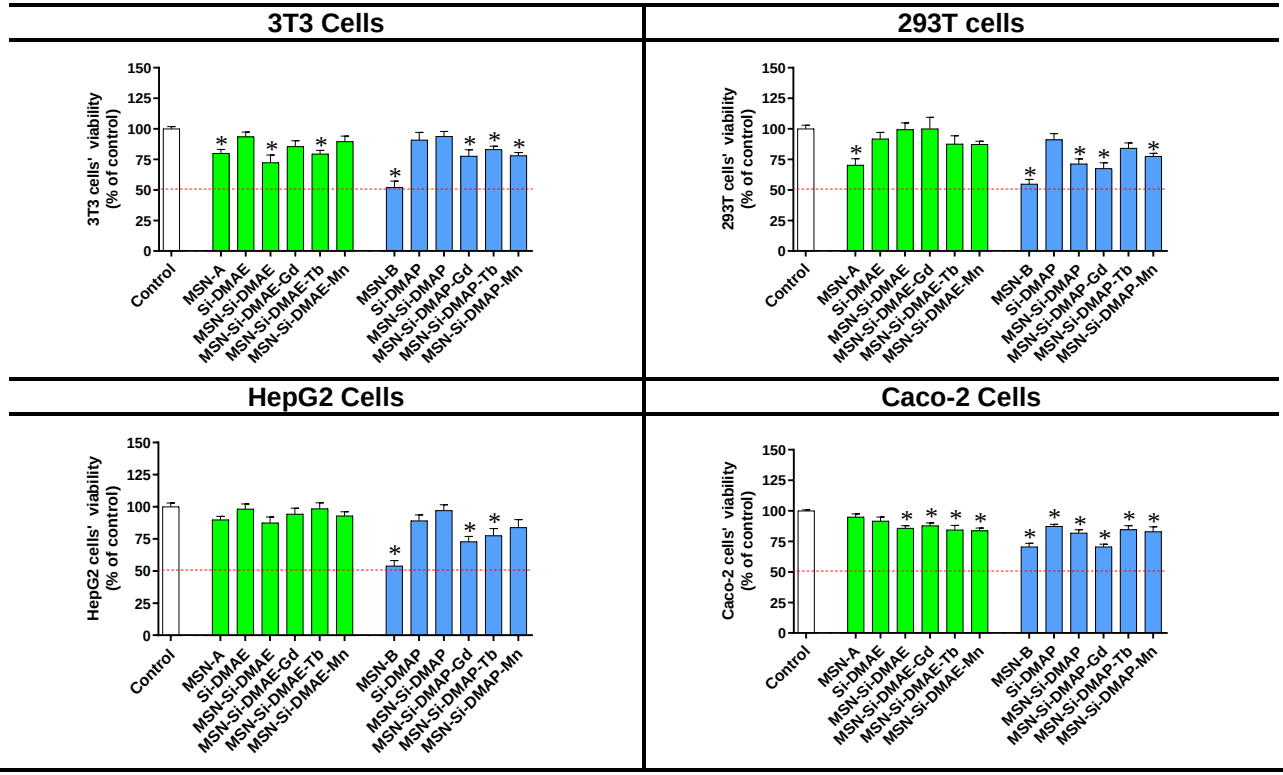

Figure 4. 9 | Cytotoxicity of prepared mesoporous silica nanoparticles (100 µg/ mL) on 3T3, 293T, HepG2 and Caco-2 cells after treatment for 24 h. Values represent mean ± standard error of the mean (SEM) of at least three independent experiments carried out in triplicate. Symbols represent significant differences (ANOVA, Dunnett's test, $p < 0.05$) when compared to: *control.

2.5.3. Choline derivatives magnetic organic salts vs MSNs containing magnetic organic salts analogues

A final comparison between the cytotoxicities of metal organic salts and their analogues immobilized in mesoporous silica nanoparticles is summarized in Figure 4. 10 and Figure 4. 11. In general, no significant differences could be found between metal organic salts and their analogues immobilized in MSNs. Only a few examples can be highlighted in 3T3, 293T and Caco-2 cells. In 3T3 cells, only $[N_{1,1,4,C2OH}][MnCl_3]$ and MSN-Si-DMAE-Mn showed significant differences. In this case, the immobilized analogue exhibited a smaller cytotoxic effect compared with the metal organic salt. In 293T cells, two pairs ($[N_{1,1,4,C3OH}][GdCl_4]$/MSN-Si-DMAP-Gd and $[N_{1,1,4,C3OH}][TbCl_4]$/MSN-Si-DMAP-Tb) displayed significant differences between the effect of the two systems in cell viability. For both, the nanoparticles presented a higher cytotoxic effect than the metal organic salts. In Caco-2 cells, MSN-Si-DMAP-Gd nano-particles induced a higher cytotoxic effect than $[N_{1,1,4,C3OH}][GdCl_4]$ in cell viability.

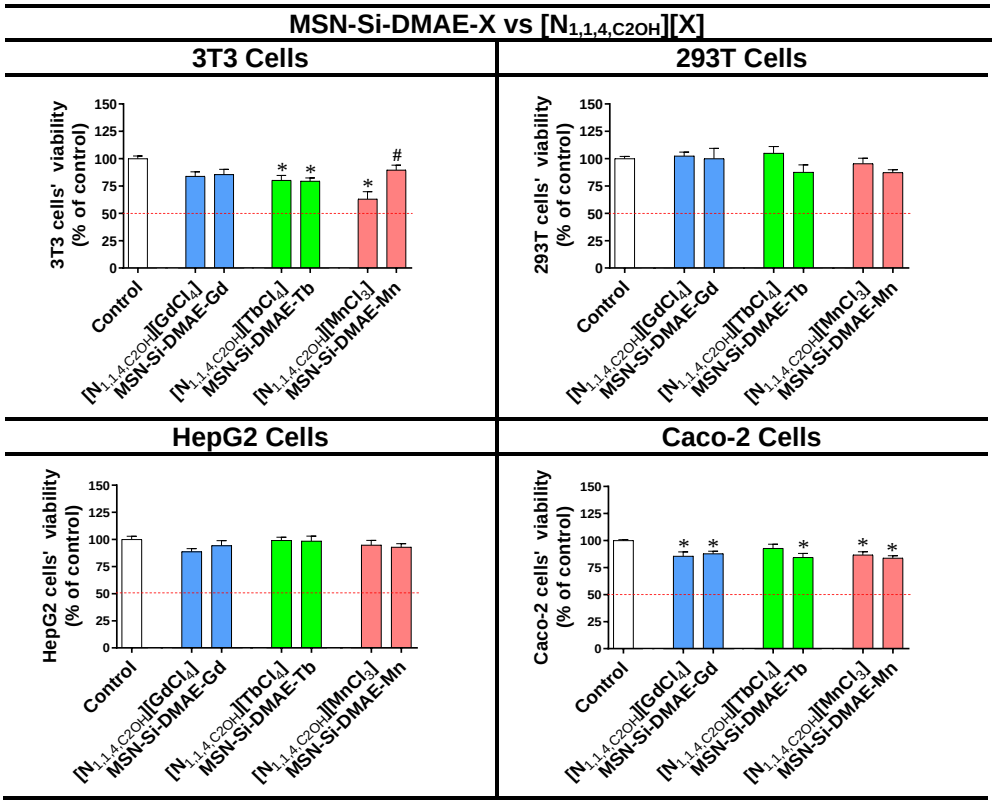

Figure 4. 10 | Cytotoxicity of choline derivative magnetic salts (100 µg/ mL) on 3T3, 293T, HepG2 and Caco-2 cells after treatment for 24 h. Values represent mean ± standard error of the mean (SEM) of at least three independent experiments carried out in triplicate. Symbols represent significant differences (ANOVA, Dunnett's test, $p < 0.05$) when compared to: *control, #$[N_{1,1,4,C2OH}][MnCl_3]$, δ$[N_{1,1,4,C3OH}][GdCl_4]$, α$[N_{1,1,4,C3OH}][TbCl_4]$.

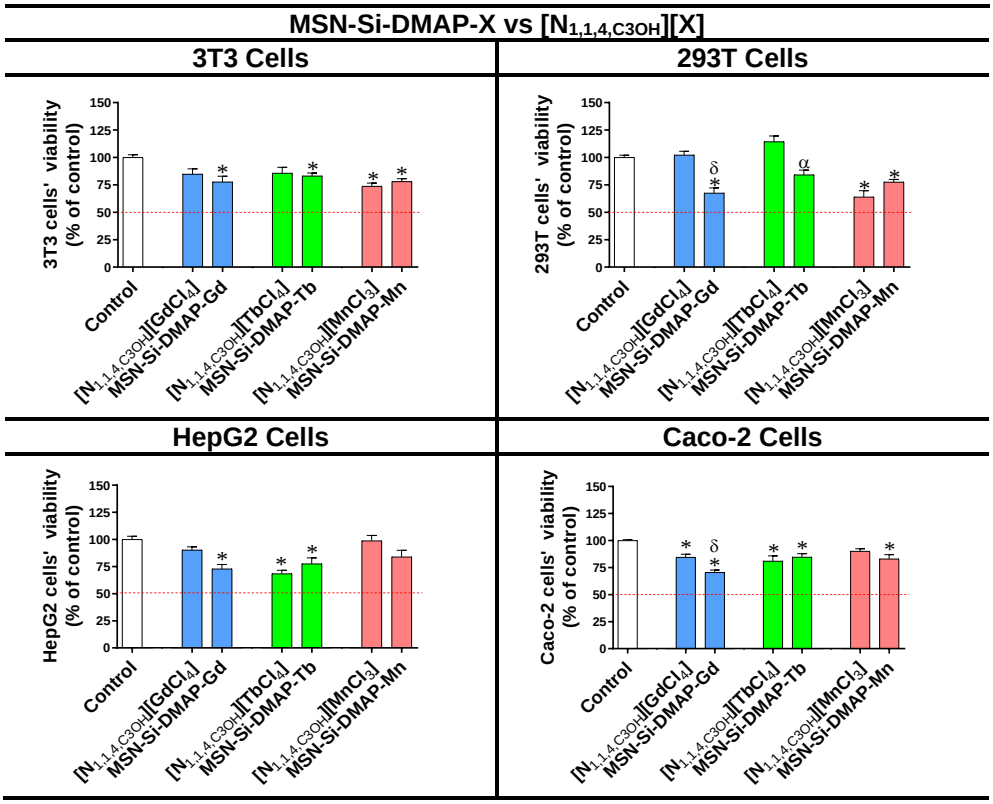

Figure 4. 11 | Cytotoxicity of choline derivative magnetic salts (100 µg/ mL) on 3T3, 293T, HepG2 and Caco-2 cells after treatment for 24 h. Values represent mean ± standard error of the mean (SEM) of at least three independent experiments carried out in triplicate. Symbols represent significant differences (ANOVA, Dunnett's test, $p < 0.05$) when compared to: *control, #[$N_{1,1,4,C2OH}$][$MnCl_3$], δ[$N_{1,1,4,C3OH}$][$GdCl_4$], α[$N_{1,1,4,C3OH}$][$TbCl_4$].

3. Conclusions

Magnetic organic salts based on the combination of two choline derivatives cations [$N_{1,1,4,C2OH}$] and [$N_{1,1,4,C3OH}$] with the anionic metal complexes [MnCl3], [$GdCl_4$] and [$TbCl_4$] were synthesized. In order to reduce the eventual toxicity associated to the metal complex presence, their analogues were immobilized

in MSNs. All materials were characterized by different techniques that confirmed the successful functionalization of MSNs with the cations [$N_{1,1,4,C2OH}$] and [$N_{1,1,4,C3OH}$]. Elemental analysis indicated 1.50 mmol/g of [$N_{1,1,4,C2OH}$] in MSN-Si-DMAE and 1.45 mmol/g of [$N_{1,1,4,C3OH}$] in MSN-Si-DMAP. For the final materials with the presence of $MnCl_3^-$, $GdCl_4^-$ and $TbCl_4^-$ as counter ions the ICP-MS results showed metal loadings in the range of 0.02-0.19 mmol/g with higher values for Si-DMAE cation, which can be related to possible steric effects resulting from the presence of a secondary alcohol in the Si-DMAP cation.

Cytotoxicity studies of the magnetic organic salts and their immobilized analogues were performed in four different cells 3T3, Caco-2, HepG2 and 293T. In general, the cytotoxic effect of the two cations is similar but there are relevant differences between the metal organic salts and their immobilized analogues. In the case of 3T3 cells, MSN-Si-DMAE-Mn exhibited a smaller cytotoxic effect than the corresponding metal organic salt. The system MSN-Si-DMAP-Gd presented higher cytotoxic effect than [$N_{1,1,4,C3OH}$][$GdCl_4$] in the case of 293T and Caco-2 cells and the same effect is observed for the MSN-Si-DMAP-Tb in the case of 293T cells.

Some of these magnetic organic salts and nanomaterials can be interesting for further applications for biological detection or as contrast agents for magnetic resonance imaging (MRI). NMR relaxation studies will be performed in order to evaluate their potential as MRI agents.

4. Experimental Section

4.1. Chemicals

All reagents used in the synthesis of magnetic salts and preparation of nanoparticles, namely, Pluronic F 127 (BASF), *n*-cetyltrimethylammonium bromide (CTAB, $((C_{16}H_{33})N(CH_3)_3)Br$, Sigma-Aldrich), triethanolamine (TEA, $N(C_2H_5O)_3$, Alfa Aesar), tetraethyl orthosilicate (TEOS, $Si(OC_2H_5)_4$, Aldrich,98%), (3-chloropropyl)triethoxysilane ($Cl(CH_2)_3Si(OCH_3)_3$, TCI,>97%), N,N-dimethyl(N-2-hydroxyethyl)amine (Aldrich), N,N-dimethyl(N-2-hydroxypropyl)amine (Aldrich), gadolinium (III) chloride hexa-hydrate ($GdCl_3 \cdot 6H_2O$, Alfa Aesar), terbium (III) chloride hexahyhdrate ($TbCl_3 \cdot 6H_2O$, Aldrich, trace metal basis), manganese (II) chloride tetrahydrate ($MnCl_2 \cdot 4H_2O$, Alfa Aesar) and 1-chloro-butane (Sigma-Aldrich, 99%) were purchased from chemical suppliers and used without further purification.

4.2. Synthesis of magnetic organic salts

Synthetic general procedure: The metal chloride hydrated ($MCl_n.2nH_2O$) was added to an ethanolic solution of choline derivative salt ($[N_{1,1,4,C2OH}][Cl]$ or $[N_{1,1,4,C3OH}][Cl]$) under constant stirring. The reaction mixture was stirred at room temperature for 48h and then the solvent was evaporated. The final solid was dried under vacuum.

N-butyl-N-hydroxyethyl-N,N-dimethylammonium tetrachlorogadolinate (III) $[N_{1,1,4,C2OH}][GdCl_4]$: $[N_{1,1,4,C2OH}][Cl]$ (0.20 g, 1.35 mmol); $GdCl_3.6H_2O$ (0.50 g, 1.36 mmol); Yield: quantitative; white solid; FTIR (KBr), $\bar{\upsilon}$ = 3425, 2964-2878, 1625, 1475, 1083, 920 cm^{-1}. Elemental analysis calcd (%) for

$C_8H_{20}NOGdCl_4.0.5H_2O$ (454.35 g.mol^{-1}): C 21.15, N 3.08, H 5.67; found: C 21.32, N 3.02, H 5.50.

N-butyl-N-hydroxypropyl-N,N-dimethylammonium tetrachlorogadolinate (III) [$N_{1,1,4,C3OH}$][$GdCl_4$]: [$N_{1,1,4,C3OH}$][Cl] (0.26 g, 1.32 mmol); $GdCl_3.6H_2O$ (0.49 g, 1.30 mmol) Yield: quantitative; yellow solid; FTIR (KBr), $\bar{\upsilon}$ = 3351, 1634, 1476, 1081, 960 cm^{-1}. Elemental analysis calcd (%) for $C_9H_{22}NOGd\ Cl_4.0.5H_2O$ (468.38 g.mol^{-1}): C 23.08, N 2.99, H 4.96; found: C 22.59, N 3.07, H 4.90.

N-butyl-N-hydroxyethyl-N,N-dimethylammonium tetrachloroterbate (III) [$N_{1,1,4,C2OH}$][$TbCl_4$]: [$N_{1,1,4,C2OH}$][Cl] (0.30 g, 2.06 mmol); $TbCl_3.6H_2O$ (0.77 g, 2.07 mmol); Yield: quantitative; white solid; FTIR (KBr), $\bar{\upsilon}$ = 3370, 2965-2876, 1633, 1486, 1131, 1084, 1051, 976, 920 cm^{-1}. Elemental analysis calcd (%) for $C_8H_{20}NOTbCl_4.2.5H_2O$ (492.28 g.mol^{-1}): C 19.53, N 2.85, H 5.13; found: C 19.53, N 2.74, H 5.03.

N-butyl-N-hydroxypropyl-N,N-dimethylammonium tetrachloroterbate (III) [$N_{1,1,4,C3OH}$][$TbCl_4$]: [$N_{1,1,4,C3OH}$][Cl] (0.26 g, 1.32 mmol); $TbCl_3.6H_2O$ (0.46 g, 1.24 mmol); Yield: quantitative; yellow solid; FTIR (KBr), $\bar{\upsilon}$ = 3379, 2971, 1636, 1476, 1143-1077, 990, 947 cm^{-1}. Elemental analysis calcd (%) for $C_9H_{22}NOTbCl_4.2H_2O$ (497.09 g.mol^{-1}): C 21.74, N 2.82, H 5.28; found: C 22.15, N 2.85, H 6.00.

N-butyl-N-hydroxyethyl-N,N-dimethylammonium trichloromanganese (II) [$N_{1,1,4,C2OH}$][$MnCl_3$]: [$N_{1,1,4,C2OH}$][Cl] (0.50 g, 3.43 mmol); $MnCl_2.4H_2O$ (0.68 g, 3.44 mmol); Yield: quantitative; pink solid; FTIR (KBr), $\bar{\upsilon}$ = 3440 2964, 1615, 1469, 1086, 977, 922 cm^{-1}. Elemental analysis calcd (%) for

$C_8H_{20}NOMnCl_3.3H_2O$ (361.64 g.mol^{-1}): C 26.57, N 3.87, H 7.26; found: C 26.40, N 3.73, H 6.68.

N-butyl-N-hydroxypropyl-N,N-dimethylammonium trichloromanganase (II) [$N_{1,1,4,C3OH}$][$MnCl_3$]: [$N_{1,1,4,C3OH}$][Cl] (0.26 g, 1.31 mmol); $MnCl_2.4H_2O$ (0.27 g, 1.30 mmol); Yield: quantitative; yellow solid; FTIR (KBr), $\bar{\upsilon}$ = 3425, 2967, 1633, 1485, 1148, 1011, 994, 908 cm^{-1}. Elemental analysis calcd (%) for $C_9H_{22}NOMnCl_3.H_2O$ (321.61 g.mol^{-1}): C 33.61, N 4.36, H 6.91; found: C 33.25, N 4.45, H 7.36.

3.3. Synthesis of Mesoporous Silica Nanoparticles (MSNs)

3.3.1. Synthesis of MSNs

MSNs used in this work were prepared based on a previously reported method described by Bouchoucha [20]. CTAB (1.33 g), F-127 (5.36 g) and TEA (31.3 g) were added to a Teflon vessel and were dissolved in ethanol absolute (114 mL) and water (250 mL). The final solution was placed under constant stirring overnight. TEOS (5.12 mL) was then added at room temperature under vigorous constant stirring and left for 1 min. The mixture was then left under static conditions. After 24h, ethanol (200 mL) was added and the colloidal solution was centrifuged (18 000 rpm for 15 minutes). The final product was washed with water twice and then dried overnight at 70 ºC. Finally, in order to extract the surfactant, the nanoparticles were mixed with acidic ethanol (0.1 M) and placed under constant stirring and reflux overnight. The final nanoparticles were washed with ethanol three times and dried overnight at 70 ºC (MSN-A - 1.51 g and MSN-B - 2.04g). $FTIR_{MSN-A}$ (KBr): $\bar{\upsilon}$ = 3448, 2959-2925, 1637, 1400, 1089, 965 cm^{-1}. $FTIR_{MSN-B}$ (KBr): $\bar{\upsilon}$ = 3449, 2926, 1637, 1400, 1088, 965 cm^{-1}.

3.3.2. Synthesis of precursors Si-DMAE and Si-DMAP

General procedure: (3-chloropropyl)triethoxysilane and the selected amine (DMAE or DMAP) were added to a round-bottomed flask. The reaction mixture was stirred for 24h at 80 °C. The final mixture was then washed with diethyl ether and dried under vacuum to give the final product.

Si-DMAE: (3-chloropropyl)triethoxysilane (4.05 mL); DMAE (1.69 mL); Yield: 4.78g, 86%; ^{1}H-NMR (400MHz, $CD_3(SO)_2$): δ (ppm) = 3.78 (m, 8H), 3.39 (m, 4H), 3.09 (s, 6H), 1.71 (m, 2H), 1.16 (m, 9H), 0.52 (m, 2H).

Si-DMAP: (3-chloropropyl)triethoxysilane (1.18 mL); DMAP (2.8 mL); Yield: 2.76 g, 83%; ^{1}H-NMR (400MHz, $CDCl_3$): δ (ppm) = 4.54 (m, 1H), 3.83 (q, 3J(H,H)=6.8 Hz, 6H), 3.55 (m, 4H), 3.39 (d, 3J(H,H)=5.2 Hz, 6H), 1.87 (m, 2H), 1.31 (d, 3J(H,H)=6.0 Hz, 9H), 1.23 (t, 3J(H,H)=7.0 Hz, 2H), 0.64 (m, 2H).

3.3.3. MSNs functionalization with Si-DMAE and Si-DMAP precursors

General procedure: Prepared MSNs (MSN-A and MSN-B) and ethanol (20mL) were added to a round-bottomed flask. To the resultant suspension was added the precursor (Si-DMAE or Si-DMAP). The reaction was placed under reflux with a constant stirring for 24h at 100 °C. The reaction mixture was centrifuged (5000 rpm, 15 minutes) and then washed with ethanol four times. Finally, the final product was dried overnight at 80 °C to give the final product.

MSN-Si-DMAE: MSN-A (1.015 g); Si-DMAE (0.950 g); MSN-Si-DMAE (1.29 g); ^{1}H-NMR (400MHz, D_2O+NaOH): δ (ppm) = 3.86 (t, ^{3}J(H,H)=5.6 Hz, 2H), 3.21 (m, 4H), 2.97 (s, 6H), 1.70 (m, 2H), 0.28 (m, 2H); FTIR (KBr): $\bar{\upsilon}$ = 3422,

2970, 1638, 1477, 1400, 1095, 959 cm^{-1}. Elemental analysis (%) found: C 11.35, N 2.30, H 2.34.

MSN-Si-DMAP: MSN-B (1.032 g); Si-DMAP (1.002 g); Yield: MSN-Si-DMAP (1.21 g). ^{1}H-NMR (400MHz, D_2O+NaOH): δ (ppm) = 4.27 (m, 1H), 3.23 (m, 2H), 3.17 (m, 2H), 3.01 (s, 6H), 1.70 (m, 2H), 1.10 (d, 3J(H,H)=6.4 Hz, 3H), 0.29 (m, 2H). FTIR (KBr): $\bar{\upsilon}$ = 3422, 2920, 1637, 1479, 1400, 1092, 958 cm^{-1}. Elemental analysis (%) found: C 12.15, N 2.28, H 2.71.

3.3.4. Synthesis of supported metal organic salts analogues

General procedure: Functionalized materials (MSN-Si-DMAE and MSN-Si-DMAP) and ethanol were added to a flask. To the resultant suspension, $MCl_n.2nH_2O$ was added. The reaction mixture was stirred at room temperature for one week and then the product was washed with ethanol (three times). Finally, the solid was dried overnight at 80 °C to give the final product.

MSN-Si-DMAE-Gd: MSN-Si-DMAE (0.401g); $GdCl_3.6H_2O$ (0.511 g); Yield: MSN-Si-DMAE-Gd (0.380 g). Elemental analysis (%) found: C 11.85, N 2.24, H 1.99, Gd 1.05.

MSN-Si-DMAE-Tb: MSN-Si-DMAE (0.407 g); $TbCl_3.6H_2O$ (0.526 g); MSN-Si-DMAE-Tb (0.420 g); Anal. Found (%) found: C 10.40, N 2.04, H 2.27, Tb 1.44.

MSN-Si-DMAE-Mn: MSN-Si-DMAE (0.401 g); $MnCl_2.4H_2O$ (0.281 g); MSN-Si-DMAE-Mn (0.440 g). Elemental analysis (%) found: C 11.41, N 2.22, H 2.46, Mn 1.07.

MSN-Si-DMAP-Gd: MSN-Si-DMAP (0.397 g); $GdCl_3.6H_2O$ (0.545 g); MSN-Si-DMAP-Gd (0.262 g). Elemental analysis (%) found: C 12.58, N 2.15, H 2.68, Gd 0.50.

MSN-Si-DMAP-Tb: MSN-Si-DMAP (0.362 g); $TbCl_3.6H_2O$ (0.536 g); MSN-Si-DMAP-Tb (0.305 g). Elemental analysis (%) found: C 11.45, N 2.00, H 2.68, Tb 0.38.

MSN-Si-DMAP-Mn: MSN-Si-DMAP (0.364 g); $MnCl_2.4H_2O$ (0.236 g); MSN-Si-DMAP-Mn (0.255 g). Elemental analysis (%) found: C 12.25, N 2.23, H 2.11, Mn 0.22.

3.4. Nanoparticles characterization

Proton nuclear magnetic resonance spectra were performed using a Bruker AMX400 system (400, 13 MHz). Data are indicated in the following order: solvent, chemical shift, spin multiplicity (s, singlet; t, triplet; m, multiplet), coupling constant (Jin Hz), and relative intensity (proton numbers). Fourier Transform infrared spectra were recorded on a Bruker tensor27 system using the KBr pellet method under ambient conditions. The carbon, hydrogen, and nitrogen contents of the functionalized silica nanoparticles were obtained with a EuroVector EuroEA300 elemental analyser. Thermogravimetric analysis (TGA) was performed on a PerkinElmer STA6000system with a heating rate of 10 °C min^{-1} and under a 20 $mLmin^{-1}$ flow of He. Transmission electron microscopy (TEM) images were obtained using a Hitachi H-8100 microscope with thermionic emission (LaB6) and an acceleration voltage of 200kV at MicroLAb (Instituto Superior Técnico). The average size of the nanoparticles was determined by manual counting using the Image J software. The samples were supported on carbon-coated copper grids and

the digital image acquisition was performed with a CCD MegaView II bottom-mounted camera. Nitrogen adsorption–desorption isotherms at 77 K were determined on a Quantachrome Autosorb iQ system, using helium and nitrogen of 99.999% purity. Prior to the adsorption measurements, the samples were outgassed for 8 hat 180 °C (unmodified silica nanoparticles) or 80 °C (functionalized materials), with a heating rate of 1 °C min^{-1}. The X-ray diffraction (XRD) measurements were carried out on a BrukerAXS-D8 Advance powder diffractometer, using CuKα radiation (40 kV, 30 mA), with a step size of 0.01° (2θ) and 5 s per step. The particle size and zeta potential were measured using a Horiba SZ-100 system. X-ray fluorescence studies were performed on a μ-XRF spectrometer ArtTAX 800, Bruker, operating with a molybdenum (Mo) X-ray source and focusing polycapillary lens and electro-thermally cooled xFlash (Si drift) detector.

3.5. Cytotoxicity studies

The cell lines (3T3, 293T, HepG2, and Caco-2) were previously acquired from DSMZ biobank. 3T3, Caco-2, HepG2 and 293Tcells were cultured in Dulbecco's modified Eagle's medium: Nutrient Mix F-12 (DMEM/F-12) (Merck, Germany), in Minimum Essential Medium (MEM) (Merck, Germany), in RPMI medium (Sigma-Aldrich, USA), and in Dulbecco's modified Eagle's medium (Merck, Germany), respectively, supplemented with 10% FBS (Hyclone, UK), 100 IU mL^{-1} penicillin, and 100 μgmL^{-1} streptomycin (Merck, Germany), and maintained under a humidified atmosphere (95%) with 5% CO_2 at 37 °C. The cytotoxic effects of compounds (100 μgmL^{-1}; 24 h) on cell viability were evaluated after they reached total confluence on 96-well plates. The effects were estimated by the MTT assay (Sigma, Germany) and the results are expressed in percentage of control (%). Data are presented as mean ± standard error of the mean (SEM) and

statistical analysis was performed using one-way analysis of variance (ANOVA) with Dunnett's multiple comparisons of group means to determine significant differences relative to the control treatment. Differences were considered significant at a level of 0.05 (p-value < 0.05). The calculations were performed using the GraphPad v5.1 (GraphPad Software, La Jolla, CA, USA) software.

Acknowledgements

This work was supported by National Funds through FCT/MCTES – Portuguese Foundation for Science and Technology within the scope of the projects UID/QUI/0619/2019, UIDB/50006/2020 (LAQV-REQUIMTE) and UIDB/00100/2020, UID/MAR/04292/2020 (MARE—Marine and Environmental Sciences Centre). Also, doctoral fellowship to Andreia Forte (PD/BD/109625/2015) and Solchemar company. The NMR spectrometers are part of The National NMR Facility, supported by FCT/MCTES (RECI/BBB-BQB/0230/2012). Authors also thank to Prof. Madalena Dionísio and Dr. Natália Correia for support with the DSC analysis.

References

(1) Vivero-Escoto, J. L. *Silica Nanoparticles, Preparation, Properties and Uses*; Nova Science Publishers, Inc.: New York, 2012.

(2) Mehmood, A.; Ghafar, H.; Yaqoob, S.; Gohar, U. F.; Ahmad, B. Mesoporous Silica Nanoparticles: A Review. *J. Dev. Drugs* 2017, *6*, 1000174.

(3) Yamamoto, E.; Kuroda, K. Colloidal Mesoporous Silica Nanoparticles. *Bull. Chem. Soc. Jpn* 2016, *89*, 501–539. https://doi.org/10.1246/bcsj.20150420.

(4) Bharti, C.; Gulati, N.; Nagaich, U.; Pal, A. K.; Gulati, N. Mesoporous Silica Nanoparticles in Target Drug Delivery System: A Review. *Int. J. Pharm. Investig.* 2015, *5*, 124–133.

(5) Aparicio, S.; Atilhan, M.; Karadas, F. Thermophysical Properties of Pure Ionic Liquids : Review of Present Situation. *Ind. Eng. Chem. Res.* 2010, *49*, 9580–9595.

(6) Kadokawa, J. *Ionic Liquids - New Aspects for the Future*; InTech: Rijeka, Croatia, 2013.

(7) Lei, Z.; Chen, B.; Koo, Y.-M.; MacFarlane, D. R. Introduction: Ionic Liquids. *Chem. Rev.* 2017, *117*, 6633–6635.

(8) Nie, L. rong; Yao, S.; Dong, B.; Li, X. lu; Song, H. Synthesis, Characterization and Physical Properties of Novel Cholinium-Based Organic Magnetic Ionic Liquids. *J. Mol. Liq.* 2017, *240*, 152–161. https://doi.org/10.1016/j.molliq.2017.05.044.

(9) Hayashi, S.; Hamaguchi, H. Discovery of a Magnetic Ionic Liquid [Bmim]FeCl4. *Chem. Lett.* 2004, *33* (12), 1590–1591.

(10) Santos, E.; Albo, J.; Irabien, A. Magnetic Ionic Liquids: Synthesis, Properties and Applications. *RSC Adv.* 2014, *4*, 40008–40018.

(11) Rodríguez-Arco, L.; Gómez-Ramírez, A.; Durán, J. D. G.; López-López, M. T. New Perspectives for Magnetic Fluid-Based Devices Using Novel Ionic Liquids as Carriers. In *Smart Actuation and Sensing Systems*; Berselli, G., Vertechy, R., Vassura, G., Eds.; IntechOpen, 2012; pp 445–464.

(12) Daniel, C. I.; Chávez, F. V.; Portugal, C. A. M.; Crespo, J. G.; Sebastiao, P. J. 1H NMR Relaxation Study of a Magnetic Ionic Liquid as a Potential Contrast Agent. *J. Phys. Chem. B* 2015, *119*, 11740–11747.

(13) Branco, A.; Branco, L. C.; Pina, F. Electrochromic and Magnetic Ionic Liquids. *Chem. Commun.* 2011, *47*, 2300–2302.

(14) Del Sesto, R. E.; McCleskey, T. M.; Burrell, A. K.; Baker, G. A.; Thompson, J. D.; Scott, B. L.; Wilkes, J. S.; Williams, P. Structure and Magnetic Behavior of Transition Metal Based Ionic Liquids. *Chem. Commun.* 2008, 447–449.

(15) Rosatella, A. A.; Siopa, F.; Frade, R. F. M.; Afonso, C. A. M. New Low Viscous Cholinium-Based Magnetic Ionic Liquids. *New J. Chem.* 2016, *40*, 3124–3129.

(16) Pereira, C. C. L.; Dias, S.; Coutinho, I.; Leal, J. P.; Branco, L. C. Europium(III) Tetrakis(β -Diketonate) Complex as an Ionic Liquid: A Calorimetric and Spectroscopic Study. *Inorg. Chem.* 2013, *52*, 3755–3764.

(17) Frade, R. F. M.; Simeonov, S.; Rosatella, A. A.; Siopa, F.; Afonso, C. A. M. Toxicological Evaluation of Magnetic Ionic Liquids in Human Cell Lines. *Chemosphere* 2013, *92*, 100–105.

(18) Zeisel, S. H.; Da Costa, K. A. Choline: An Essential Nutrient for Public Health. *Nutr. Rev.* 2009, *67*, 615–623.

(19) Siopa, F.; Figueiredo, T.; Frade, R. F. M.; Neto, I.; Meirinhos, A.; Reis, C. P.;

Sobral, R. G.; Afonso, C. A. M.; Rijo, P. Choline-Based Ionic Liquids : Improvement of Antimicrobial Activity. *Chem. Sel.* 2016, *1*, 5909–5916.

(20) Bouchoucha, M.; Côté, M. F.; C-Gaudreault, R.; Fortin, M. A.; Kleitz, F. Size-Controlled Functionalized Mesoporous Silica Nanoparticles for Tunable Drug Release and Enhanced Anti-Tumoral Activity. *Chem. Mater.* 2016, *28*, 4243–4258.

(21) Crucho, C. I. C.; Baleizão, C.; Farinha, J. P. S. Functional Group Coverage and Conversion Quantification in Nanostructured Silica by 1H NMR. *Anal. Chem.* 2017, *89*, 681–687.

(22) Rouquerol, F.; Rouquerol, J.; Sing, K. *Adsorption by Powders and Porous Solids*; Academic Press: London, United Kingdom, 1999.

(23) Thommes, M.; Kaneko, K.; Neimark, A. V.; Olivier, J. P.; Rodriguez-Reinoso, F.; Rouquerol, J.; Sing, K. S. W. Physisorption of Gases, with Special Reference to the Evaluation of Surface Area and Pore Size Distribution (IUPAC Technical Report). *Pure Appl. Chem.* 2015, *87*, 1051–1069. https://doi.org/10.1515/pac-2014-1117.

(24) Capco, D. G.; Chen, Y. *Nanomaterial, Impacts on Cell Biology and Medicine*; Springer Netherlands: Dordrecht, 2014.

Chapter 5

Development of novel organic salts based on Thioflavin T and Congo Red units for amyloid staining

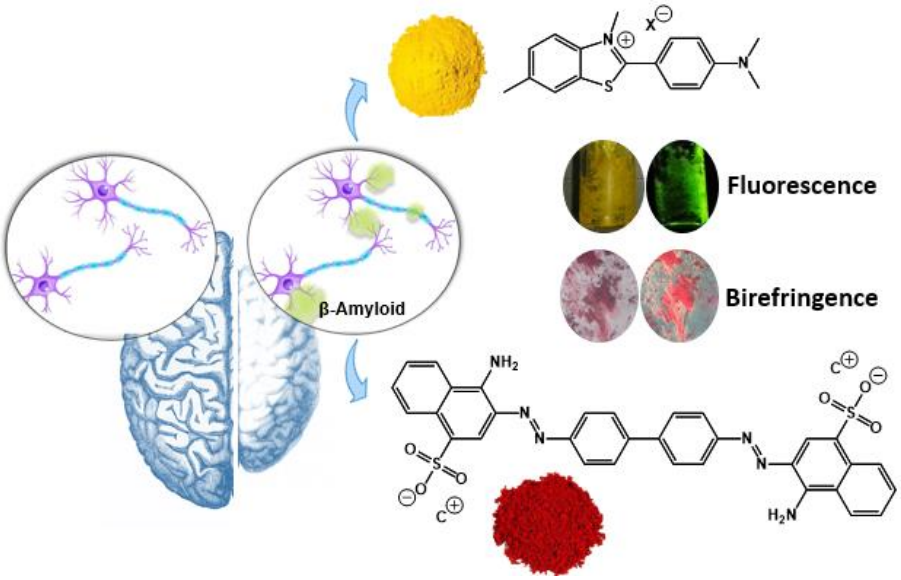

Chapter 5

Development of novel organic salts based on Thioflavin T and Congo Red units for amyloid staining

Abstract

Affecting a high percentage of people worldwide, Alzheimer's disease is one of the most common neurodegenerative disorders. This form of dementia, and many others similar, is characterized by the deposition of insoluble protein aggregates commonly known by amyloid fibrils in the brain. The discovery of new fluorescent probes as efficient tools to detect and follow these aggregates formation process is significantly relevant in order to elucidate the molecular mechanisms associated to protein aggregation as well as to obtain an early and accurate clinical diagnosis and therapeutics of neurodegenerative disorders. Over the years, some conventional fluorescent probes for protein aggregation detection have been tested. The standard method relies in the use of two well-known probes, Thioflavin T (ThT) molecule as fluorescent probe and congo red (CR) dye due to its birefringence. In this chapter, different organic salts based on ThT and CR scaffolds were prepared and characterized according to their physical, thermal, fluorescence and birefringence properties.

1. Introduction

Neurodegenerative diseases (ND) are incurable and highly incapacitating diseases characterized by the progressive degeneration and death of neural tissues.[1,2] *Affecting millions of people worldwide, neurodegenerative diseases arise as one of the most debilitating illnesses with a substantial social, economic, and health impact. These disorders are, in our days, the fourth leading cause of death and have been shown over the years the ability to affect both patient's cognitive and physical skills.*[3] According to World Health Organization, it is estimated that almost 50 million people have dementia worldwide and it is expected that this number triple by 2050.[4] One

of the main problems associated with this type of pathologies, is the fact that they are detected at a late stage where the therapeutic options and efficiency are less effective.[5] As mentioned in the thesis introduction, the formation of amyloid-based fibrils are one of the most important hallmarks of many neurodegenerative disorders such as Alzheimer's Disease (AD).[1,6] Thus, this protein aggregates has been considered an important biomarker for the detection of earlier disease and also a therapeutic target for AD. Specifically, there are many studies based on the development of new methodologies to detect this biomarker. These protein aggregates can be readily detected *in vitro* and in different tissues such as cerebrospinal fluid (CSF) through the use of Thioflavin T probe (Figure 5. 1).[7] This is a small organic dye whose fluorescence intensity increases upon binding to amyloid structure.[8] Over the years, this has been the most used method to monitor amyloid fibrils development, however, this dye showed some drawbacks related with its poor sensitivity to detect the less complex structures of fibril formation process.[7] Also, from the literature, it is already known that ionic compounds, namely ionic liquids, have potential ability to stabilize proteins, and more specifically, amyloid earlier structures.[9–11] Knowing that the detection of these less complex units can be determinant for the discovery of AD in more prior stages of the disease, it became important from a mechanistic and a pharmaceutical point of view to develop novel ionic compounds capable of detect and, ideally, stabilize the initial structures of amyloid fibrils formation.

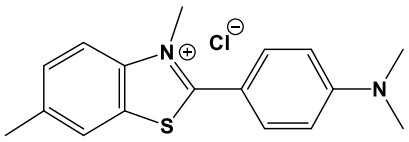

Figure 5. 1 | Structure of Thioflavin T dye.

Beyond ThT, Congo red (CR) dye has been also used in the detection of amyloid aggregates. As can be seen in Figure 5. 2, this symmetrical dye discovered in 1883 by the chemist Paul Böttiger is structurally composed by a hydrophobic central biphenyl group connected to two flanked charged naphthalene rings through diazo units. Each naphthalene unit possesses an amino and a sulphate group that comprise the hydrophilic moiety of CR scaffold.[12–14]

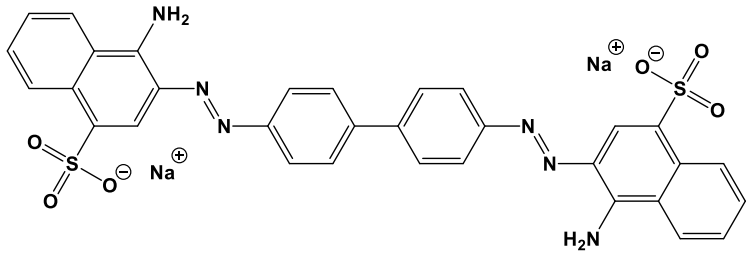

Figure 5. 2 | Structure of Congo red optical dye

Being widely applied for more than 100 years this well-known dye becomes one of the most used amyloid-specific dyes for staining aggregates deposits in tissues and *in vitro*.[15,16] Amyloid monitorization by congo red is based on its characteristic birefringence. This optical property concerns to the ability of some materials appear bright when subject to a crossed polariser.[17] Also used to stain different materials such as cellulose paper and cotton, when bounded to amyloid fibrils, congo red showed to have an yellow-green birefringence color that allows to perform the diagnostic of these protein aggregates.[16] One of the major disadvantages of this probe is related with its low sensitivity.[18] To perform an accurate confirmation of amyloid fibrils with this dye, the tissue sections need to have a specific thickness that allows to visualize the birefringence phenomenon.[16] Also, the high toxicity associated to this probe can be a limiting parameter.

This part of the work aims to the development of different low-melting organic salts and task-specific ionic liquids based on based on ThT and CR scaffolds combined with appropriate counter-ions in order to obtain the desired salts in high yields and purity levels. The adequate selection of counter-ions can be relevant for the improvement of intrinsic fluorescent or birefringence properties for potential bio-applications.

2. Results and discussion

2.1. Thioflavin T-based ionic salts

2.1.1. Counter-ions and synthetic procedures

Synthetic methodologies were developed in order to obtain ThT-based fluorescent probes. To perform the reactions, a set of counter-ions (Figure 5. 3) were selected according to some important factors such as their potential effect in Aβ aggregation process, their use in pharmaceutical area, their function in human metabolism and/or their biocompatibility. Many of these counter-ions were a challenge since they present some characteristics that influence the reactions conditions. According to the anion structure, nature and chemical behaviour, different procedures were followed.

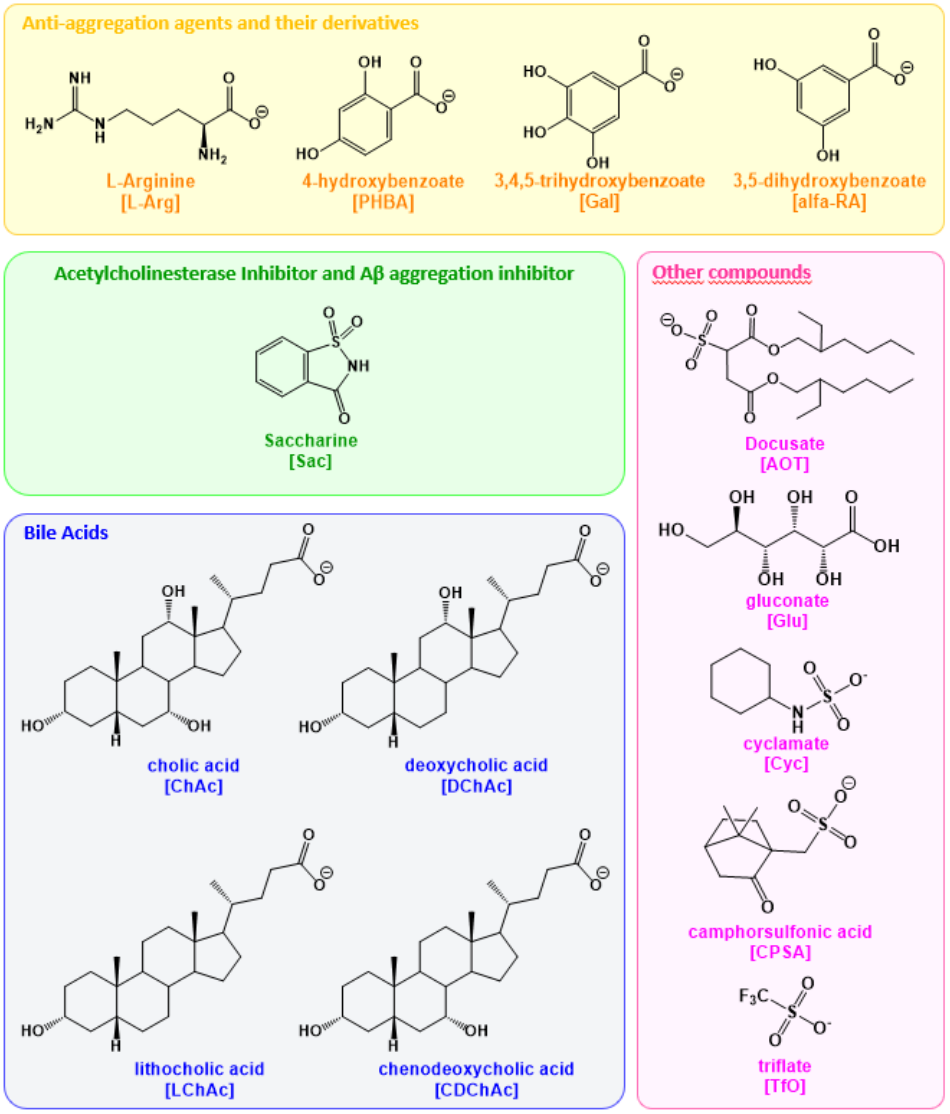

Figure 5. 3 | ThT counter-ions structures.

A. Ionic exchange synthetic procedure

The first synthetic approach used in this work was based on an ionic exchange reaction where the Thioflavin T halide form reacts with a sodium, potassium or lithium salt (Scheme 5. 1). From this reaction, two products are

formed, the main product composed by Thioflavin T cation unit and the chosen counter-ion and, also, an inorganic salt as a by-product. The secondary product is then removed by precipitation and filtration to purify the desired ThT-based organic salt. Selected counter-ions included docusate [AOT], triflate [OTf], dicyanamide [DCA], bistriflimide [NTf_2], sacharine [Sac], gluconate [Glu] and cyclamate [Cyc]. Methanol was selected as solvent for the reactions performed at room temperature for 24 h (Scheme 5. 1). Prepared organic salts were characterized by ^{1}H-NMR, elemental analysis (C, H, N), thermal properties and luminescence quantum yield.

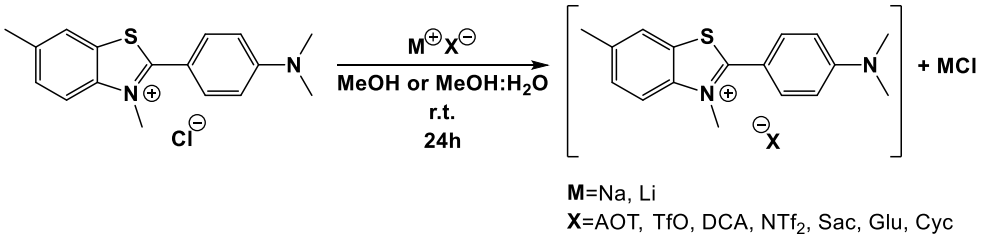

Scheme 5. 1 | General synthetic procedure of ionic exchange reactions.

Table 5. 1 summarizes all the prepared ThT organic salts as well as their physical and thermal properties.

Table 5. 1 | Prepared novel organic salts based on ThT unit through ionic exchange synthetic methodology.

Compound	η (%)	Purity (%) [(a)]	Physical state	Tm [Td] (ºC) [(b)]
[ThT][Cl]	-	-	Yellow Solid	212
[ThT][AOT]	72	99	Yellow Gel	RTIL [275]
[ThT][TfO]	54	92	Yellow Solid	155 [>300]
[ThT][Sac]	38	99	Yellow Solid	203.5

[(a)] Purity obtained from ^{1}H-NMR spectroscopy.
[(b)] Melting (Tm) were determined on Electrothermal Melting Point Apparatus and DSC (for [ThT][Sac]).

From this synthetic approach, the compounds were obtained in moderate (54 and 72%) to low (38% for [ThT][Sac]) yields according to the difficulty in the purification steps. Almost all compounds were obtained as solids, except for [ThT][AOT] (yellow gel), and with high purity levels (≥92%). According to the achieved melting and decomposition temperatures, all compounds present values above 100 ºC. Still, it was possible to reduce the melting points comparing to starting material ([ThT][Cl]) of at least three compounds. [ThT][AOT] arises as an example of room temperature ionic liquid (RTIL).

B. Ionic exchange resin synthetic procedure

The second approach used to prepare the salts consisted in the reaction between a carboxylic acid-based compound and Thioflavin T in its hydroxide form. To perform these reactions, it was selected the following acids: gallic acid [Gal], L-arginine [Arg], gluconic acid [Glu], *p*-hydroxybenzoic acid [PHBA] and 3,5-Dihydroxybenzoic acid [α-RA]. [ThT][OH] preparation was made from the corresponding chloride salt using a hydroxide exchange resin (Scheme 5. 2, Step 1). In this step, the resin was applied in two distinct ways: 1) through the use of a packed column where the Thioflavin T solution (in water, ethanol and/or methanol) was eluted and then collected and 2)

through slow stirring in ThT-solution before filtration. In both methods, an acid-base neutralization reaction is performed by the addition of the collected hydroxide solution to another solution of the selected carboxylic acid-based compound (Scheme 5. 2, step 2).

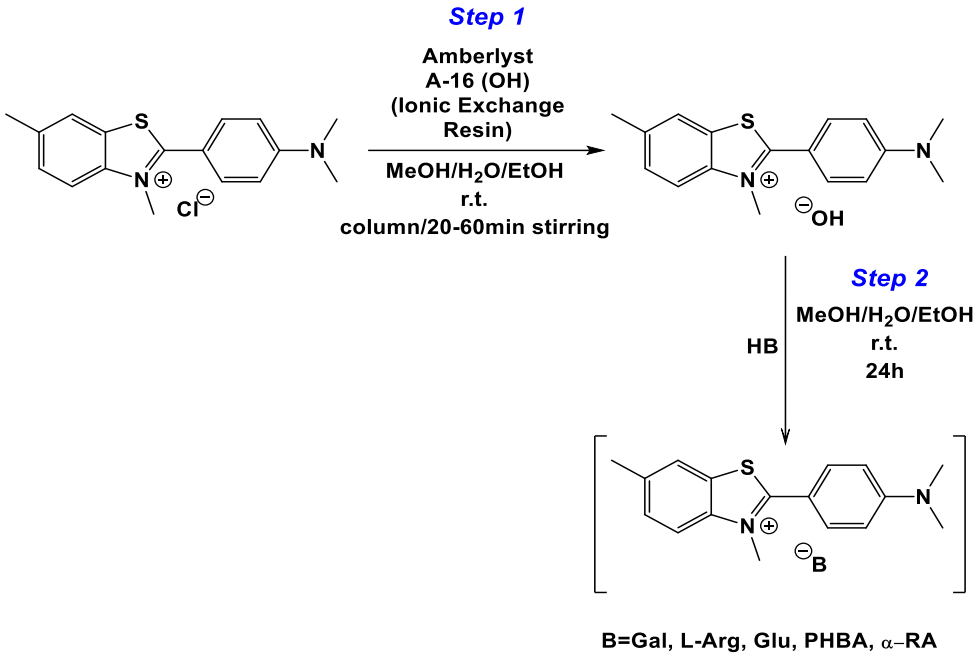

Scheme 5. 2 | General synthetic procedure of ionic exchange resin methodology.

This method presents the advantage of being halide species free since all chloride anions are immobilized in the resin through the replacement with hydroxide anions that becomes the counter-ion of Thioflavin T. However, during the work, it was possible to verify that ThT cation decomposes in the resin. This was the main reason to explore two different approaches using the resin. The main idea would be to change ThT residence time in the resin, however, in any of the applied techniques (even with a short residence time in the resin), the cation decomposed.

C. Acid-base synthetic procedure

A third approach was applied to prepare ThT-based compounds. In this methodology the main goal was to neutralize the selected carboxylic or sulfonic acid-based compounds and then perform an ionic exchange reaction with ThT-chloride form. This method allows to use Thiflavin T cation without any previous manipulation to change its counter-ion which reduces the decomposition risk and, also, enables the use of the first and successful synthetic approach. For these reactions, Tht-selected counter-ions were: gallic acid [Gal], L-arginine [Arg], , *p*-hydroxybenzoic acid [PHBA], 3,5-Dihydroxybenzoic acid [α-RA], cholic acid [ChAc], deoxycholic acid [DChAc], lithocholic acid [LChAc], chenodeoxycholic acid [CDChAc] and camphorsulfonic acid [CPSA]. These compounds were firstly neutralized through the use of sodium hydroxide in order to prepare their sodium salts (Scheme 5. 3, Method 1, Step 1). After this neutralization reaction, the novel salts were used to perform ionic exchange reactions with ThT halide form (Scheme 5. 3, Step 2).

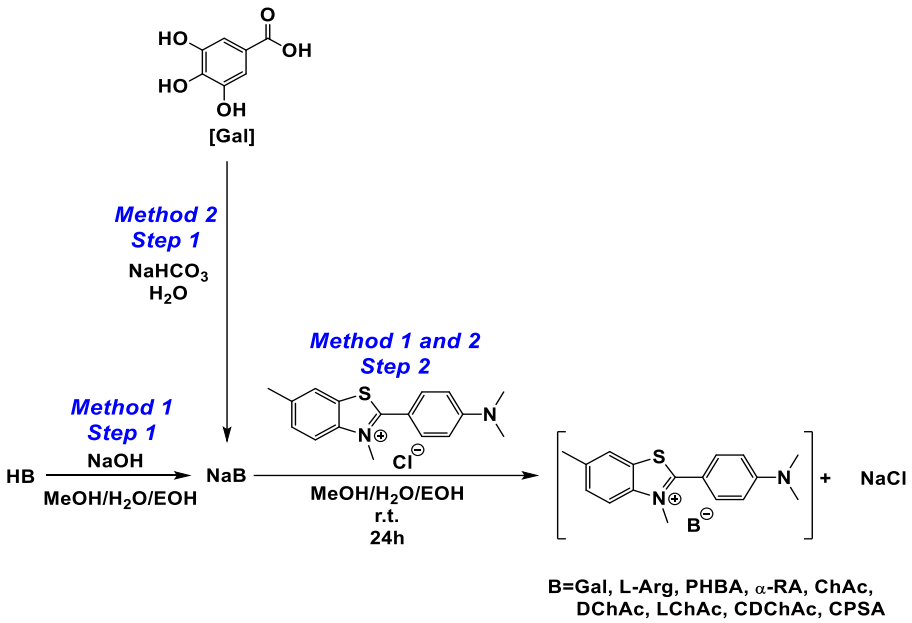

Scheme 5. 3 | General synthetic procedure of acid-base synthetic approach.

From the selected acids, it was possible to obtain the final desired products with [PHBA], [α-RA], [ChAc], [LChAc] and [CPSA]. Table 5. 2 summarizes all the prepared ThT organic salts obtained by acid-base synthetic approach as well as their physical and thermal properties.

Table 5. 2 | Prepared novel organic salts based on ThT unit through acid-base synthetic approach.

Compound	η (%)	Purity (%) [(a)]	Physical state	Tm (ºC)
[ThT][Cl]	-	-	Yellow Solid	212
[ThT][PHBA]	36	99	Yellow Solid	200.7 [(b)]
[ThT][α-RA]	34	n.d.	Yellow Solid	n.d.
[ThT][ChAc]	56	n.d.	Orange Solid	n.d.
[ThT][CPSA]	63	99	Orange Solid	n.d.

η - reaction yield. Tm - melting temperature. n.d. – not determined.
[(a)] Purity obtained from ^{1}H-NMR spectroscopy.
[(b)] Melting temperature (Tm) determined by DSC.

All compounds were obtained with medium yields (45-63%) with the exception of [ThT][PHBA] (36%) and [ThT][αRA] (34%). The reduced value associated to these products can be related with the purification method used in the synthesis. Both final products precipitated in the reaction solvent and washing purification steps were needed. All compounds were obtained as solids. From selected counter-ions, gallic acid and arginine would be the most interesting compounds due to their potential as anti-aggregation agents.[13,19–23] L-arginine is an essential amino acid with many important functions in human body. It is already established that amino acids can be present as zwitterionic species in aqueous solution within a range of pH (Figure 5. 4). This fact is the major difficulty of perform synthesis with this compound. Several optimization processes (by changing reactions conditions) were made to the synthetic approach used, however, it was not possible to achieve to the final product.

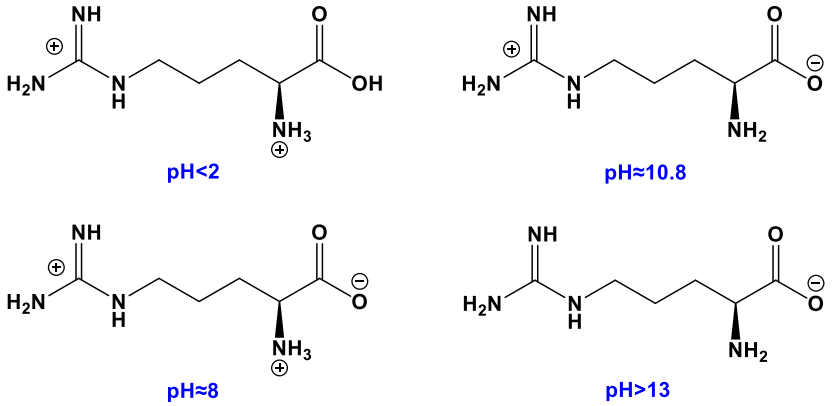

Figure 5. 4 | L-Arginine structures according to medium pH. (adapted from [24])

Regarding to gallic acid, the main problem associated to this antioxidant compound is related with the possibility to form radicals as a function of the reaction medium pH and, also, the possibility to hydroxyl groups reacts with sodium hydroxide to form the phenoxide specie due to their acidic nature (Figure 5. 5).

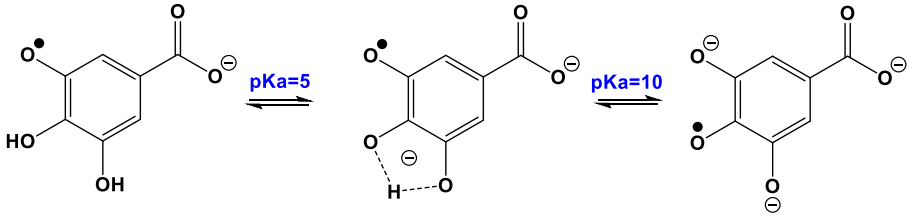

Figure 5. 5 | Free radicals' structure as a result of gallic acid oxidation. (adapted from [25])

Thus, to overcome these problems and as an alternative to Method 1, a secondary synthetic methodology where sodium hydroxide is replaced for sodium carbonate ($NaHCO_3$) was used in order to obtain the sodium salt form of this important triphenolic compound (Scheme 5. 3, Method 2, Step 1). This optimization process is still ongoing.

2.1.2. Amyloid fibrils formation and ThT fluorescence

As mentioned already, the standard method to follow amyloid fibrils formation *in vitro* is based on ThT fluorescence. In this work, it was possible to optimize the formation and monitorization of fibrillation process using Lysozyme from chicken egg white. This protein is frequently used as a model since it is very similar to human lysozyme. Fibrils were prepared based on a well-stablished methodology already described in the literature by Silva et al.[26] Figure 5. 6 illustrates the schematic procedure of fibrils production process.

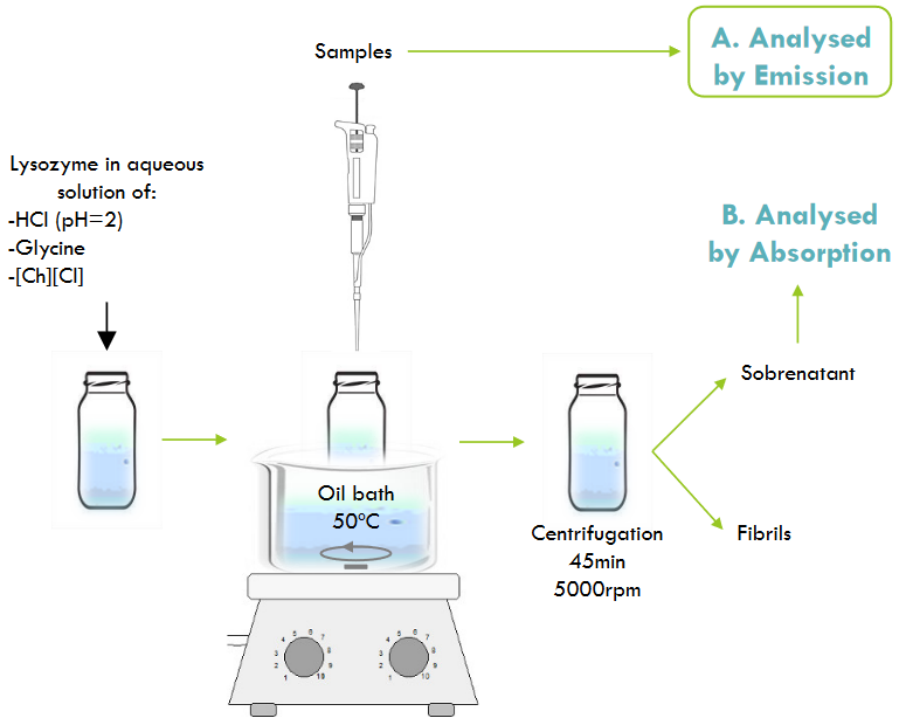

Scheme 1

Figure 5. 6 | Schematic procedure of Lysozyme from chicken egg white fibrils formation.

Fibrils formation methodology was carried out with lysozyme in aqueous buffer solution of HCl (pH=2) with glycine and choline chloride to promote protein fibrillation.[27] The samples were incubated at 50 ºC under constant stirring and samples were taken at specific times. Figure 5. 7 shows (A) the emission spectra of each sample and (B) ThT fluorescence intensity as a function of time. As expected, ThT fluorescence increases with time and fibrils formation. As detailed in Chapter 1 (section 3), due to the rotation of benzothiazole-aniline bond and a self-quenching process, a decrease of fluorescence intensity associated to ThT molecule can be observed. With the growth of fibrils formation and, thus, the increase of β-sheet structure, ThT fluorescence increases. In this optimization process, after approximately 90 minutes, fibrils formation reaches to an equilibrium. These studies are in progress and the main goal is to follow fibrils formation in the presence of prepared compounds. It is important to understand if the formation process of the protein aggregates can be influenced (increases or decreases) by the presence of the different compounds. This allows to conclude about the inhibitory or stabilization effect of ThT-based organic salts in the aggregation process. To do this, a conversion ratio between the initial protein (native state) and the fibrils presented in the final solution must be determined. This conversion can be achieved by UV spectroscopy and by the application of a calibration curve that allows determining protein and aggregates concentration.

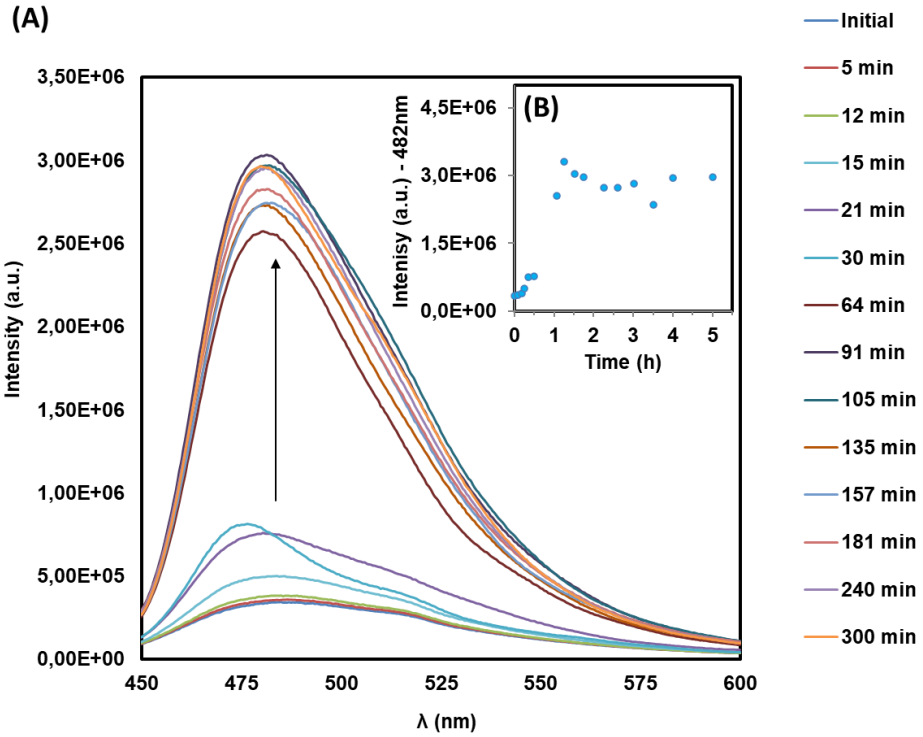

Figure 5. 7 | (A) Emission spectra of each taken sample; (B) ThT fluorescence intensity described as a function of time for HEWL fibrils.

2.2. Congo red-based ionic salts

2.2.1. Counter-ions and synthetic procedures

As to ThT-based reactions, there are not yet many reported studies in the literature related with synthetic methodologies using congo red moiety to obtain organic salts. The majority of the described methodologies are related with the change of congo red structure by the addition of different groups for example. Thus, during this work it was necessary to perform the planning and optimization of compounds preparation processes based on this probe. The main difficulty of this part of the work was the low solubility of CR in

several organic solvents, its stability, and the fact that it has a very large structure where the two sodium atoms are well protected, making it difficult to replace them with other selected cations. To perform the reactions, a set of counter-ions shown in Figure 5. 8, were selected according to their biocompatibility, toxicity, and solubility.

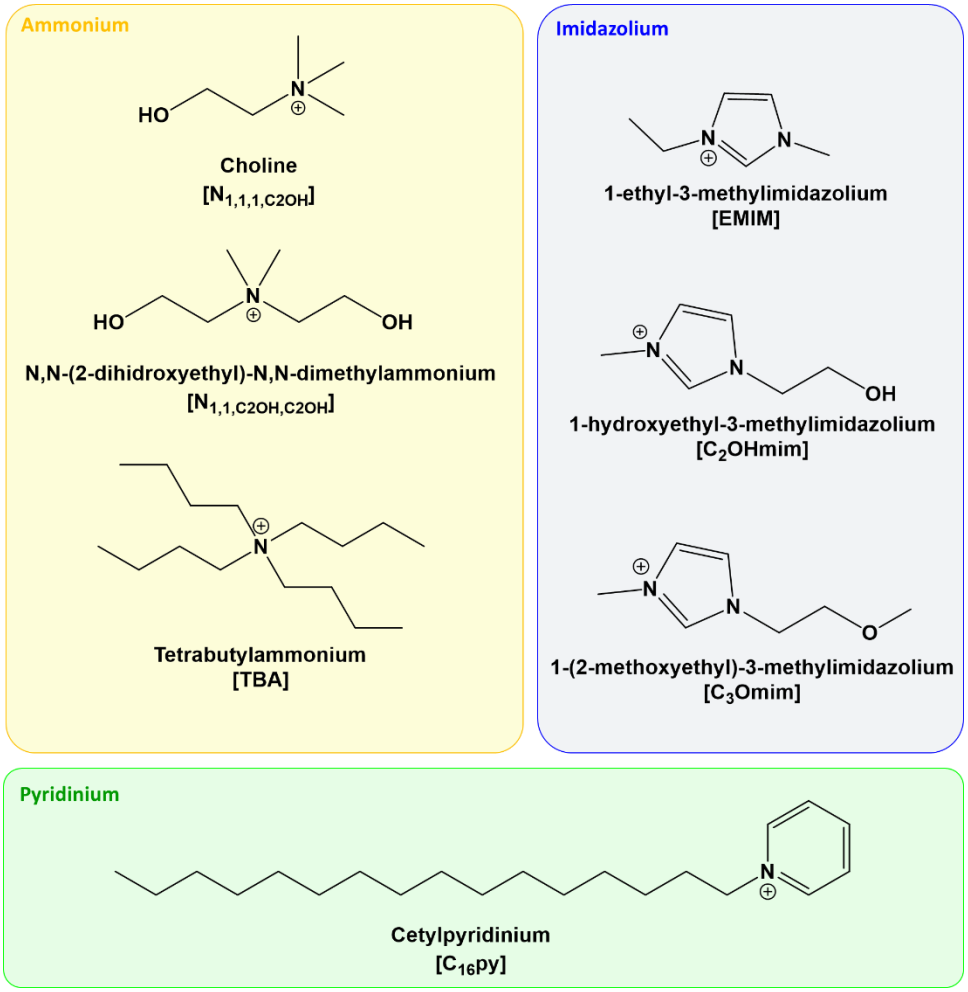

Figure 5. 8 | Congo Red counter-ions structures.

A. Ionic exchange methodology

As usually in organic salts preparation, the first synthetic approach used was based on an ionic exchange reaction. This methodology was previously explained in chapter 6.1 (section 4.1). As mentioned, from this reaction is expected to obtain two products as a result of the ionic exchange reaction between the two involved salts. The main product is the novel organic salt based on congo red anion unit and the chosen counter-ion and, also, an inorganic salt that arises in this process as a by-product. Selected counter-ions used included choline [$N_{1,1,1,C2OH}$], N,N-dihydroxyethyl-N,N-dimethylammonium [$N_{1,1,C2OH,C2OH}$], 1-(2-methoxyethyl)-3-methylimidazolium [C_3OMIM] and 1-hydroxyethyl-3-methylimidazolium [C_2OHMIM]. Initially, the synthetic procedure was accomplished in a MeOH:H_2O mixture under room temperature for 24 h (Scheme 5. 4, Method 1).

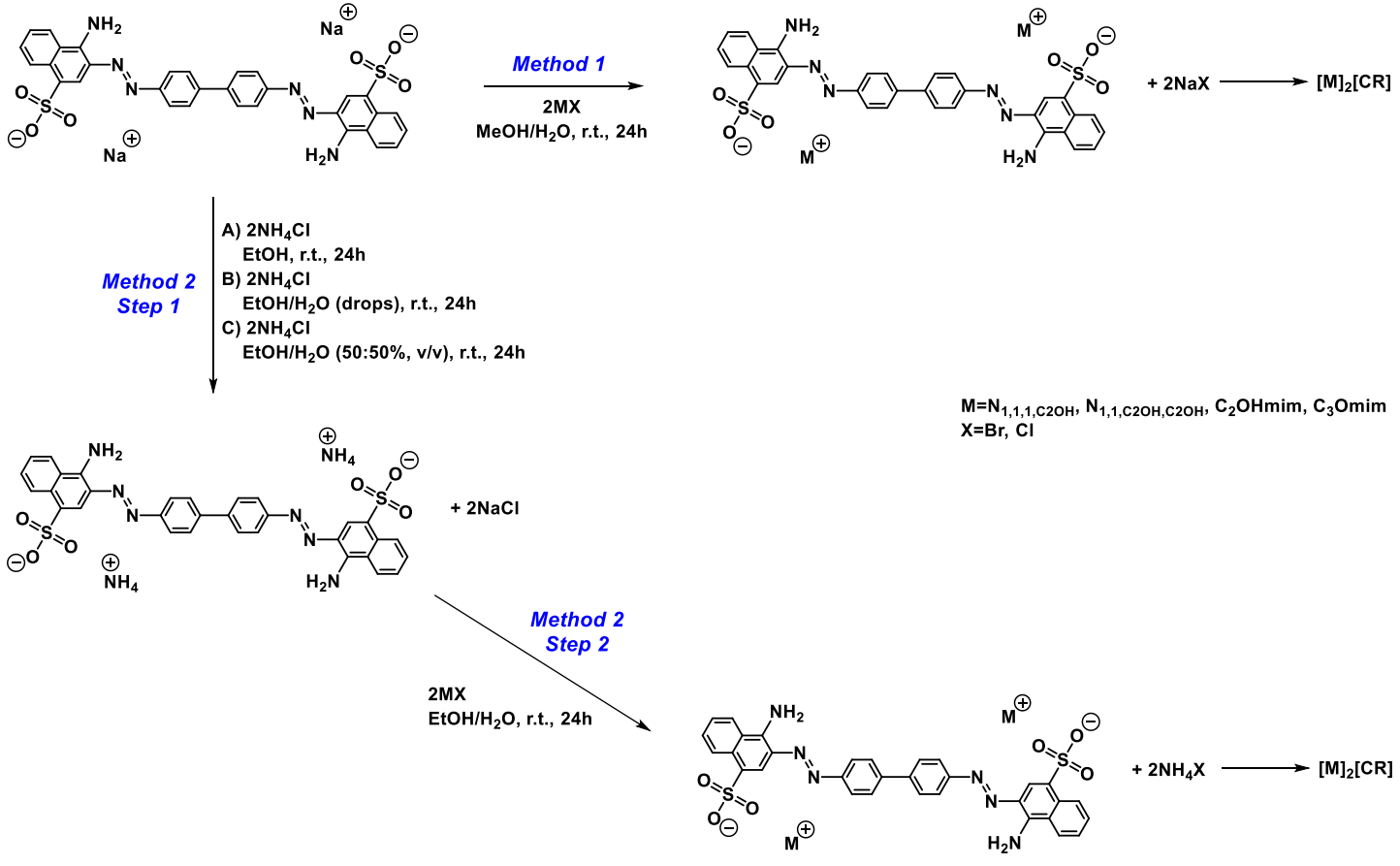

Scheme 5. 4 | Synthetic methodology based on ionic exchange reaction.

Any of the proposed salts were obtained with this synthetic method. All performed reactions resulted in an organic salt with a cation:anion proportion different from the expected 2:1. Thus, two conditions were verified in the execution of this method, an excess of selected cation amount and a loss of CR during the purification process. Both conditions can be justified by the reduced solubility of CR-sodium salt. Sodium atoms are not being all exchange by the selected cations during the reaction. Therefore, at the end of the reaction time a mixture of four different species can be probably verified (Scheme 5. 5).

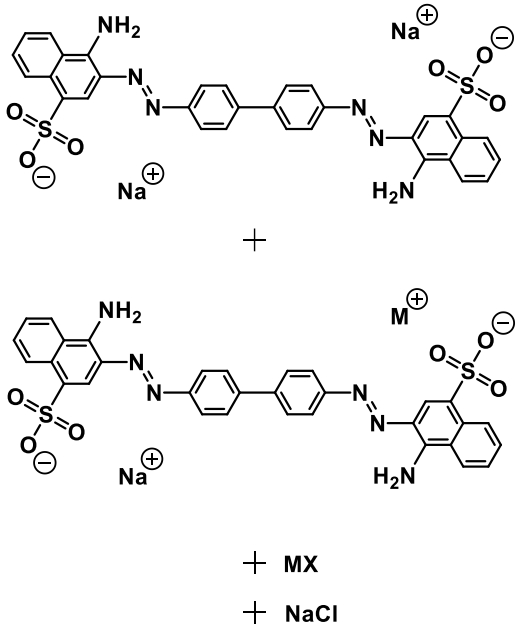

Scheme 5. 5 | Structure of final species presented in the reaction medium.

Due to the reduced solubility of CR-sodium salt an incomplete reaction can be probably verified. In this case, $[Na]_2[CR]$ as well as NaCl produced during the reaction, are lost in the purification process (filtration) leading to a final mixture with the selected cation in excess.

In order to increase the solubility of CR and, also, to facilitate the exchange of sodium atoms, a second procedure was applied (Scheme 5. 4, Method 2). The main idea was to change sodium atoms for ammonium (smaller than selected cations) and, with this change, increase CR solubility leading to an easier exchange of ammonium cations by the selected structures. Reactional solvent was optimized in order to increase CR dissolution. This synthetic method did not result in the expected final products due to the inefficient exchange of sodium for ammonium cations.

B. Ionic exchange resin method

A second synthetic approach used to prepare the salts consists in the reaction between the protonated-CR dye and the selected compounds in their hydroxide form. Selected counter-ions used with this method included choline [$N_{1,1,1,C2OH}$], N,N-dihydroxyethyl-N,N-dimethylammonium [$N_{1,1,C2OH,C2OH}$], tetrabutylammonium [$N_{4,4,4,4}$], 1-ethyl-3-methylimidazolium [C_2MIM], 1-(2-methoxyethyl)-3-methylimidazolium [C_3OMIM], 1-hydroxyethyl-3-methylimidazolium [C_2OHMIM] and cetylpyridinium [$C_{16}py$]. Congo red protonated specie could be obtained by the use of an ionic exchange resin where the sodium atoms remain immobilized in the resin through the replacement with protons (Scheme 5. 6, Step 1). This initial step has, however, an important limitation related with the amount of solvents necessary to perform the exchange between sodium and protons atoms. Due to Congo red limited solubility very high volumes of water and ethanol are required. Beyond the problem associated to volume itself, there is still the much higher consumption of energy needed to evaporate the solvents. At the same time of this synthetic step, the selected compounds needed to complete the reactions are also passed through an exchange resin where halogen anions are immobilized in the resin through the replacement with

hydroxide anions (Scheme 5. 6, Step 2). Finally, a neutralization reaction is performed to give the pure final products without the necessity to perform any purification procedure.

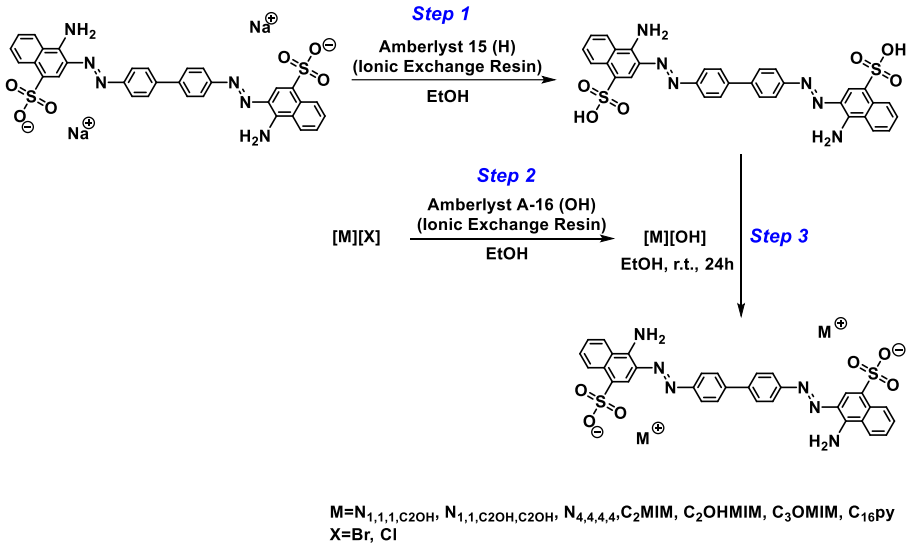

Scheme 5. 6 | Synthetic approach based on ionic exchange resin.

Due to the low stability of CR-acidic form, the separation of the resin was carried out through a decantation process. In Table 5. 3 it is possible to see the summarized results obtained. Regarding to the synthesis related with the preparation of $[N_{4,4,4,4}]_2[CR]$ and $[C_{16}pyr]_2[CR]$ salts, it was verified by ^{1}H-NMR the presence of approximately 20% of cation excess when compared with anion scaffold for both compounds.

Table 5. 3 | Prepared novel organic salts based on CR unit through ionic exchange synthetic methodology.

	Purity (%) [(a)]	Physical state	Tm [Td] (ºC) [(b)]
$[Na]_2[CR]$	-	Red Solid	>360
$[N_{1,1,1,C2OH}]_2[CR]$	>90	Dark Red Solid	>250
$[N_{1,1,C2OH,C2OH}]_2[CR]$	>90	Dark Red Solid	>250
$[C_2MIM]_2[CR]$	94	Green Solid	n.d.
$[C_2OHMIM]_2[CR]$	>90	Dark Red Solid	175.2
$[C_3OMIM]_2[CR]$	>90	Red Solid	n.d.

[(a)] Purity obtained from ^{1}H-NMR spectroscopy.
[(b)] Melting temperatures (Tm) were determined on Electrothermal Melting Point Apparatus and DSC (for $[C_2OHMIM]_2[CR]$).

All compounds were obtained as solids with high purity levels. As can be seen, for compounds whose transition temperatures were evaluated, it was possible to reduce the melting point when compared with the starting material ($[Na]_2[CR]$).

2.2.2. Birefringence evaluation

Some products were also evaluated about their birefringence properties (Figure 5. 9) since this is the method used to detect amyloid plaques with Congo Red. All compounds showed to maintain this ability through the observation of their bright color under cross-polarized light in the absence of amyloid plaques. Future studies must be made in the presence of amyloid aggregates.

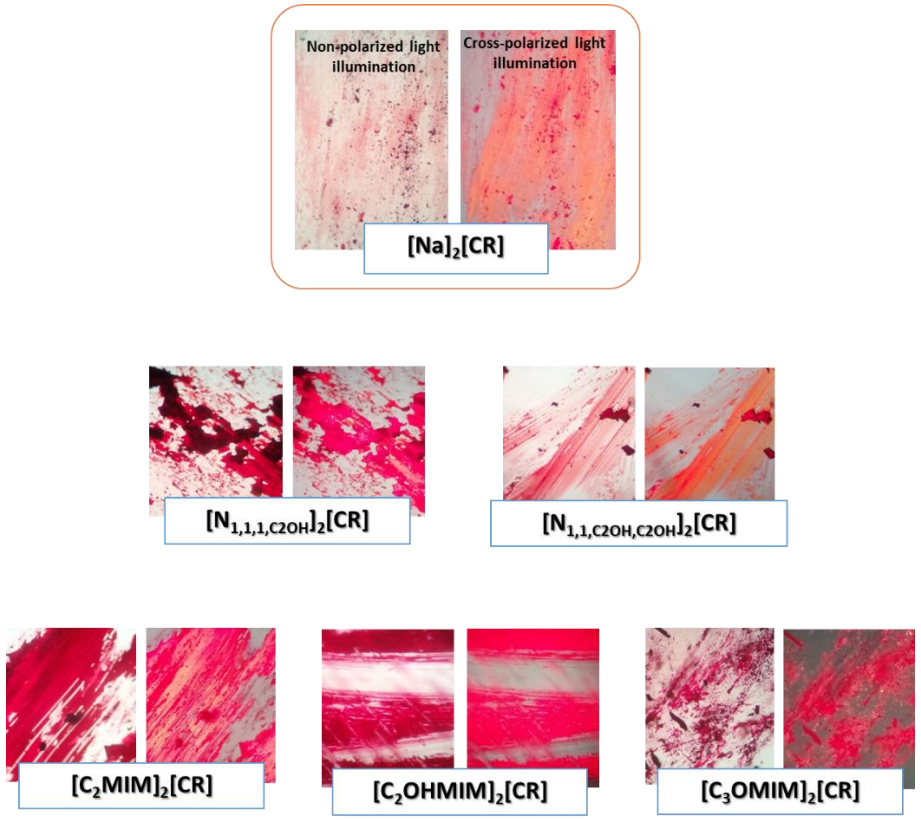

Figure 5. 9 | Synthesized CR-based compounds birefringence.

3. Conclusions

A set of Thioflavin T and Congo red-based compounds were prepared. Synthetic methodologies used in salts formulation were a major challenge and still need to be optimized, however, an huge step was reached with this work. Several methods were experimented according to the used probe. Obtained ThT-based salts were prepared essentially by two methods, ionic exchange reactions and acid-base synthetic approach. All prepared ionic compounds were characterized by ^{1}H-NMR and elemental analysis. Also, their thermal properties were evaluated. All compounds were obtained as

solids in small to moderate yields (36-72%) and with high purity levels (≥92% for all synthetized salts).

Regarding to congo red salts, a methodology based on ionic exchange reactions was firstly applied, however, this procedure seems to be unsuitable to this compound. This can be probably related with this probe structural size and rigidity. Thus, during this work it was possible to find an alternative methodology that allowed the preparation of salts based on this dye. This method is based on an acid-base reaction and still needs to be improved in order to overcome congo red low stability problem and, also, in order to achieve to a method more sustainable and effective. Nevertheless, this initial optimization work it is an important step in the chemistry of congo red reactions. All prepared compounds were characterized by ^{1}H-NMR, elemental analysis and about their thermal features. All compounds were obtained as solids in small to moderate yields (32-63%) and with a high purity level (>90% for all synthetized salts). Finally, CR-based salts were characterized according to their birefringence. It was possible to observe by cross polarization that all CR-based salts maintained this important property after counter-ion change.

4. Experimental Section

4.1. General Remarks

All commercial organic solvents were used as supplied from Sigma-Aldrich in analytical purity grade. Commercially available reagents were purchased from different chemical companies and almost all used as received. Thioflavin T (tech. 75%, alfa aesar) was purified through dissolution in ethanol and filtration of precipitated impurities. ^{1}H, ^{13}C and ^{19}F-NMR were recorded on a Bruker AMX400 spectrometer. Chemical shifts are reported

downfield in parts per million using CD_3OD and $(CD_3)_2SO$ as deuterated solvents. Elemental analysis (C, H, N, analyzer) of each synthesized organic salt was performed by Laboratório de Análises at LAQV-REQUIMTE. For the salts which were solid at room temperature, the melting point determination was performed using a Stuart Scientific Melting Point SMP1 and/or Differential Scanning Calorimetry (DSC). ThT fluorescence measurements were performed in solution and using a SPEX Fluorolog-3 Model FL3-22 spectrofluorimeter.

4.2. Synthetic methodologies and characterization

4.2.1. Synthesis and characterization of Thioflavin T-based probes

2-[4-(Dimethylamino)phenyl]-3,6-dimethylbenzothiazolium docusate [ThT][AOT]: [ThT][Cl] (0.30g; 0.94mmol) and methanol were added to a round-bottomed flask. To the resulting solution was added [Na][AOT] (0.46g; 1.04mmol) under constant stirring. The reaction mixture was stirring at room temperature for 24h after which time the solvent was evaporated. The mixture was redissolved in acetone and the precipitated was filtered. The solvent was again evaporated, and the compound dried under vacuum. The product [ThT][AOT] (0.48g, 72%) was obtained as a yellow gel. ^{1}H NMR (400 MHz, $(CD_3)_2SO$) δ 8.15 (m, 2H), 7.82 (d, J^3 *(H,H)* = 9.0 Hz, 2H), 7.71 (d, J^3 *(H,H)* = 8.2 Hz, 1H), 6.98 (d, J^3 *(H,H)* = 9.1 Hz, 2H), 4.22 (s, 3H), 3.88 (s, 4H), 3.61 (dd, J^3 *(H,H)* = 11.6, 3.5 Hz, 1H), 3.12 (s, 6H), 2.87 (m, 1H), 2.80 (dd, J^3 *(H,H)* = 17.2, 3.5 Hz, 1H), 1.48 (s, 2H), 1.23 (s, 16H), 0.84 (m, 12H). ^{13}C NMR (100 MHz, DMSO) δ 173.13, 171.54, 168.84, 154.14, 141.44, 138.55, 132.70, 131.02, 128.62, 123.78, 117.03, 112.47, 111.43, 66.62, 66.55, 66.51, 61.91, 38.63, 34.61, 31.15, 30.21, 30.09, 30.03, 28.80, 22.88, 21.45, 14.38, 14.35, 11.28, 11.25, 11.21. Elemental analysis calcd (%) for

$C_{37}H_{56}N2O7S2.4H_2O$ (777.15): C 57.18, N 3.61, H 8.32; found: C 57.26, N 4.3, H 6.96.

2-[4-(Dimethylamino)phenyl]-3,6-dimethylbenzothiazolium triflate [ThT][OTf]: [ThT][Cl] (0.50g; 1.57mmol) and methanol were added to a round-bottomed flask. To the resulting solution was added [Na][OTf] (0.32g; 1.88mmol) under constant stirring. The reaction mixture was stirring at room temperature for 24h after which time the solvent was evaporated. The mixture was redissolved in acetone and the precipitated was filtered. The solvent was again evaporated, and the compound dried under vacuum. The product [ThT][OTf] (0.37g, 54%) was obtained as a yellow solid. ^{1}H NMR (400 MHz, $(CD_3)_2SO$) δ 8.16 (m, 13H), 7.83 (d, J^3 *(H,H)* = 9.1 Hz, 12H), 7.72 (d, J^3 *(H,H)* = 8.5 Hz, 7H), 6.99 (d, J^3 *(H,H)* = 9.1 Hz, 12H), 4.23 (s, 20H), 3.13 (s, 37H), 2.84 (s, 2H), 2.68 (s, 3H), 2.54 (s, 20H), 2.34 (s, 5H). ^{19}F NMR (376 MHz, DMSO) δ -77.76. Elemental analysis calcd (%) for $C_{18}H_{19}N_2O_3S_2.4H_2O$ (504.59): C 42.84, N 5.55, H 5.40; found: C 42.83, N 5.17, H 3.63.

2-[4-(Dimethylamino)phenyl]-3,6-dimethylbenzothiazolium saccharin [ThT][Sac]: [ThT][Cl] (0.30g; 0.95mmol) and methanol:H_2O (25:75%) were added to a round-bottomed flask. To the resulting solution was added [Na][Sac] (0.21g; 1.14mmol) under constant stirring. The reaction mixture was stirring at room temperature for 24h after which it was visible a precipitated. The mixture was filtered and the solid washed with water and then dried under vacuum. The product [ThT][Sac] (0.16g, 38%) was obtained as a yellow solid. ^{1}H NMR (400 MHz, $(CD_3)_2SO$) δ 8.15 (m, 2H), 7.83 (d, J^3 *(H,H)* = 8.9 Hz, 2H), 7.72 (d, J^3 *(H,H)* = 8.4 Hz, 1H), 7.64 (m, 1H), 7.58 (m, 3H), 6.98 (d, J^3 *(H,H)* = 9.0 Hz, 2H), 4.23 (s, 3H), 3.13 (s, 6H), 2.54 (s, 3H).

Elemental analysis calcd (%) for $C_{24}H_{23}N_3O_3S_2.0.5H_2O$ (474.63): C 60.73, N 8.86, H 5.11; found: C 60.31, N 8.56, H 4.99

2-[4-(Dimethylamino)phenyl]-3,6-dimethylbenzothiazolium 4-Hydroxybenzoate [ThT][PHBA]: 4-Hydroxybenzoate (0.09g; 0.63mmol) and H_2O were added to a round-bottomed flask. To the resulting solution was added NaOH (1.25mL) under constant stirring. The reaction mixture was stirring at room temperature for 1h. A solution of [ThT][Cl] (0.20g, 0.63mmol) and MeOH:H_2O was then added to the previous solution. The mixture was stirring at room temperature for 24h after which it was observed the presence of a precipitated. The solid was filtered, washed with distilled H_2O and the final product dried under vacuum. The product [ThT][PHBA] (0.09g, 36%) was obtained as a yellow solid. ^{1}H NMR (400 MHz, CD_3OD) δ 8.01 (m, 2H), 7.82 (m, 4H), 7.72 (d, J^3 *(H,H)* = 8.5 Hz, 1H), 7.01 (d, J^3 *(H,H)* = 8.9 Hz, 2H), 6.72 (d, J^3 *(H,H)* = 8.4 Hz, 2H), 4.30 (s, 3H), 3.19 (s, 6H), 2.61 (s, 3H). Elemental analysis calcd (%) for $C_{24}H_{24}N2O3S.2.5H_2O$ (465.61): C 61.91, N 6.02, H 6.29; found: C 62.34, N 5.86, H 5.90. Elemental analysis calcd (%) for $C_{24}H_{24}N_2O_4S.H_2O$ (454.58): C 63.41, N 6.16, H 5.78; found: C 62.89, N 5.91, H 5.66.

2-[4-(Dimethylamino)phenyl]-3,6-dimethylbenzothiazolium 3,5-Dihydroxybenzoate [ThT][α-RA]: 3,5-Dihydroxybenzoic acid (0.10g; 0.63mmol) and H_2O were added to a round-bottomed flask. To the resulting solution was added NaOH (1.26mL) under constant stirring. The reaction mixture was stirring at room temperature for 1h. A solution of [ThT][Cl] (0.20g, 0.63mmol) and EtOH was then added to the previous solution. The mixture was stirring at room temperature for 24h after which it was observed the presence of a precipitated. The solid was filtered, washed with distilled

H_2O and the final product dried under vacuum. The product [ThT][α-RA] (0.09g, 34%) was obtained as a yellow solid. ^{1}H NMR (400 MHz, $(CD_3)_2SO$ δ 9.02 (m, -OH), 8.13 (m, 2H), 7.82 (d, J^3 *(H,H)* = 7.2 Hz, 2H), 7.71 (d, J^3 *(H,H)* = 6.8 Hz, 1H), 6.98 (d, J^3 *(H,H)* = 7.2 Hz, 2H), 6.73 (s, 2H), 6.14 (s, 1H), 4.22 (s, 3H), 3.12 (S,6H), 2.54 (S, 3H). Elemental analysis calcd (%) for $C_{24}H_{24}N_2O_4S.H_2O$ (454.58): C 63.41, N 6.16, H 5.78; found: C 62.89, N 5.91, H 5.66.

2-[4-(Dimethylamino)phenyl]-3,6-dimethylbenzothiazolium cholate [ThT][ChAc]: Cholic acid (0.19g; 0.47mmol) and a mixture ethanol:H_2O were added to a round-bottomed flask. To the resulting solution was added NaOH (0.94mL) under constant stirring. The reaction mixture was stirring at room temperature overnight. A solution of [ThT][Cl] (0.15g, 0.47mmol) and EtOH was then added to the previous solution and the mixture was stirring at room temperature for 24h. The solvent was evaporated and the solid redissolved in a mixture of CH_2Cl_2:EtOH (CH_2Cl_2 in large excess). The mixture was filtered and the final product dried under vacuum. The product [ThT][ChAc] (0.17g, 52%) was obtained as a yellow solid. ^{1}H NMR (400 MHz, $(CD_3)_2SO$ δ 8.16 (m, 2H), 7.83 (d, J^3 *(H,H)* = 8.8 Hz, 2H), 7.72 (d, J^3 *(H,H)* = 8.4 Hz, 1H), 6.99 (d, J^3 *(H,H)* = 9.2 Hz, 2H), 4.23 (s, 3H), 3.13 (S,6H), 2.55 (S, 3H), 0.59 (s,3H). Elemental analysis calcd (%) for $C_{41}H_{58}N_2O_5S.4.5H_2O$ (772.16): C 63.77, N 3.63, H 8.76; found: C 63.39, N 4.11, H 7.97.

2-[4-(Dimethylamino)phenyl]-3,6-dimethylbenzothiazolium camphorsulfonate [ThT][CPSA]: Camphorsulfonic acid (0.11g; 0.45mmol) and ethanol were added to a round-bottomed flask. To the resulting solution was added NaOH (0.90mL) under constant stirring. The reaction mixture was stirring at room temperature overnight. A solution of [ThT][Cl] (0.14g,

0.45mmol) and EtOH was then added to the previous solution and the mixture was stirring at room temperature for 24h. The solvent was evaporated and the solid redissolved in a mixture of CH_2Cl_2:EtOH (CH_2Cl_2 in large excess). The mixture was filtered and the final product dried under vacuum. The product [ThT][CPSA] (0.14g, 59%) was obtained as a yellow solid. ^{1}H NMR (400 MHz, $(CD_3)_2SO$) δ 8.16 (m, 2H), 7.83 (d, J^3 *(H,H)* = 9.0 Hz, 2H), 7.71 (d, J^3 *(H,H)* = 8.4 Hz, 1H), 6.98 (d, J^3 *(H,H)* = 9.0 Hz, 2H), 4.23 (s, 3H), 3.13 (s, 6H), 2.86 (m, 1H), 2.70 (m, 1H), 2.54 (s, 3H), 2.36 (m, 1H), 2.24 (dt, J^3 *(H,H)* = , 1H), 1.93 (t, J^3 *(H,H)* = 4.3 Hz, 1H), 1.79 (m, 2H), 1.26 (q, J^3 *(H,H)* = 9.4 Hz, 2H), 1.06 (m, 3H), 0.74 (s, 3H). Elemental analysis calcd (%) for $C_{27}H_{34}N_2O_4S_2.6H_2O$ (568.81): C 57.01, N 4.93, H 7.10; found: C 56.85, N 4.74, H 6.76

4.2.2. Synthesis and characterization of Congo red-based probes

3,3'-((1E,1'E)-[1,1'-biphenyl]-4,4'-diylbis(diazene-2,1-diyl))bis(4-aminonaphthalene-1-sulfonic acid) [H]$_2$[CR]: Congo red (0.5g, 0.72mmol) was dissolved in a water/ethanol mixture (ethanol in large excess) and the ionic exchange resin Amberlyst 15 (H) was added to the solution. The prepared mixture was then slowly stirred for 30 mins at room temperature after which was decanted, and the solution evaporated. The final product was dried under vacuum to give the product $[H_2]_2$[CR] as a blue solid (0.28g, 59%). ^{1}H NMR (400 MHz,$(CD_3)_2SO$) δ(ppm) = 8.75 (d, J^3 *(H,H)* = 8.2 Hz, 2H), 8.46 (d, J^3 *(H,H)* = 8.2 Hz, 2H), 8.32 (s, 2H), 8.12 (d, J^3 *(H,H)* = 8.5 Hz, 4H), 7.97 (d, J^3 *(H,H)* = 8.5 Hz, 4H), 7.64 (t, J^3 *(H,H)* = 7.6 Hz, 2H), 7.53 (t, J^3 *(H,H)* = 7.4 Hz, 2H).

Synthetic general procedure for congo red-based salts: Selected organic cations in chloride or bromide form ($[N_{1,1,1,C2OH}][Cl]$, $[N_{1,1,C2OH,C2OH}][Cl]$, $[C_2OHMIM][Cl]$, $[C_3OMIM][Cl]$, $[C_2MIM][Br]$, $[C_{16}Pyr][Cl]$) were dissolved in water and passed through an anion exchange resin Amberlite IRA-400-OH. The prepared hydroxide cation aqueous solution was then slowly added to protonated congo red previously prepared and dissolved in ethanol. The mixture was stirred at room temperature overnight after which water and ethanol were evaporated. The final products were dried under vacuum.

Di-N,N,N-triethyl-N-hydroxyethylammonium 4-amino-3-[4-[4-(1-amino-4-sulfonato-naphthalen-2-yl)diazenylphenyl]phenyl]diazenyl-naphthalene-1-sulfonate **$[N_{1,1,1,C2OH}]_2[CR]$:** $[N_{1,1,1,C2OH}][Cl]$ (0.02 g, 0.16 mmol); $[H]_2[CR]$ (0.05 g, 0.08 mmol); Yield: quantitative; red solid; ^{1}H-NMR (400 MHz, $(CD_3)_2SO$) δ 8.77 (d, J^3 *(H,H)* = 8.4 Hz, 2H), 8.45 (d, J^3 *(H,H)* = 8.1 Hz, 2H), 8.32 (s, 2H), 8.12 (d, J^3 *(H,H)* = 8.4 Hz, 4H), 7.98 (d, J^3 *(H,H)* = 8.5 Hz, 4H), 7.73 (s, 4H), 7.60 (t, J^3 *(H,H)* = 7.7 Hz, 2H), 7.51 (t, J^3 *(H,H)* = 7.5 Hz, 2H), 5.32 (s, 2H), 3.83 (s, 4H), 3.10 (s, 18H). Elemental analysis calcd (%) for $C_{42}H_{54}N_8O_{10}Cl_2.4H_2O$ (937.98 g.mol^{-1}): C 53.78, N 11.95, H 6.25; found: C 53.33, N 11.51, H 5.93.

Di-N,N-dihydroxyethyl-N,N-dimethylammonium 4-amino-3-[4-[4-(1-amino-4-sulfonato-naphthalen-2-yl)diazenylphenyl]phenyl]diazenyl-naphthalene-1-sulfonate **$[N_{1,1,C2OH,C2OH}]_2[CR]$:** $[N_{1,1,C2OH,C2OH}][Cl]$ (0.02 g, 0.126 mmol); $[H]_2[CR]$ (0.04 g, 0.06 mmol); Yield: quantitative; dark red solid; ^{1}H-NMR (400 MHz, $(CD_3)_2SO$) δ 8.77 (d, J^3 *(H,H)* = 8.5 Hz, 2H), 8.45 (d, J^3 *(H,H)* = 8.3 Hz, 2H), 8.32 (s, 2H), 8.13 (d, J^3 *(H,H)* = 8.1 Hz, 4H), 7.98 (d, J^3 *(H,H)* = 8.4 Hz, 4H), 7.73 (s, 4H), 7.60 (t, J^3 *(H,H)* = 5.4 Hz, 2H), 7.51 (t, J = 7.5 Hz, 2H), 5.28 (s, 4H), 3.84 (s, 8H), 3.46 (s, 8H), 3.12 (s, 12H). Elemental

analysis calcd (%) for $C_{44}H_{54}N_8O_{10}S_2.6H_2O$ (1034.08 g.mol^{-1}): C 51.10, N 10.84, H 6.45; found: C 50.65, N 10.39, H 5.54.

***Di*-1-(2-hydroxyethyl)-3-methylimidazolium *4-amino-3-[4-[4-(1-amino-4-sulfonato-naphthalen-2-yl)diazenylphenyl]phenyl]diazenyl-naphthalene-1-sulfonate* [C_2OHMIM]$_2$[CR]:** [C_2OHMIM][Cl] (0.02 g, 0.13 mmol); [H]$_2$[CR] (0.04 g, 0.06 mmol); Yield: quantitative; dark red solid; ^{1}H-NMR (400 MHz, $(CD_3)_2SO$) δ 9.08 (s, 2H), 8.77 (d, J^3 *(H,H)* = 8.3 Hz, 2H), 8.45 (d, J^3 *(H,H)* = 8.4 Hz, 2H), 8.32 (s, 2H), 8.12 (d, J^3 *(H,H)* = 8.4 Hz, 4H), 7.98 (d, J = 8.4 Hz, 4H), 7.70 (d, J^3 *(H,H)* = 12.1 Hz, 8H), 7.60 (t, J^3 *(H,H)* = 7.5 Hz, 2H), 7.51 (t, J^3 *(H,H)* = 7.4 Hz, 2H), 5.20 (s, 2H), 4.21 (m, 4H), 3.86 (s, 6H), 3.71 (s, 4H). Elemental analysis calcd (%) for $C_{44}H_{44}N_{10}O_8S_2.6.5H_2O$ (1029.01 g.mol^{-1}): C 51.35, N 13.62, H 5.59; found: C 50.58, N 12.72, H 4.59.

***4-amino-3-[4-[4-(1-amino-4-sulfonato-naphthalen-2-yl)diazenylphenyl]phenyl]diazenyl-naphthalene-1-sulfonate* [C_3OMIM]$_2$[CR]:** [C_3OMIM][Cl] (0.03 g, 0.15 mmol); [H]$_2$[CR] (0.05 g, 0.08 mmol); Yield: quantitative; red solid; ^{1}H-NMR (400 MHz, $(CD_3)_2SO$) δ 9.09 (s, 2H), 8.78 (d, J^3 *(H,H)* = 8.3 Hz, 2H), 8.46 (d, J^3 *(H,H)* = 8.0 Hz, 2H), 8.33 (s, 2H), 8.13 (d, J^3 *(H,H)* = 8.2 Hz, 4H), 7.98 (d, J^3 *(H,H)* = 8.3 Hz, 4H), 7.71 (d, J^3 *(H,H)* = 12.8 Hz, 4H), 7.61 (t, J^3 *(H,H)* = 7.4 Hz, 2H), 7.51 (t, J^3 *(H,H)* = 7.3 Hz, 2H), 4.34 (m, 4H), 3.86 (s, 6H), 3.71 – 3.62 (m, 4H), 3.25 (s, 6H). Elemental analysis calcd (%) for $C_{46}H_{48}N_{10}O_8S_2.7.5H_2O$ (1075.09 g.mol^{-1}): C 51.39, N 13.03, H 5.92; found: C 51.08, N 12.57, H 5.56.

***Di*-1-ethyl-3-methylimidazolium *4-amino-3-[4-[4-(1-amino-4-sulfonato-naphthalen-2-yl)diazenylphenyl]phenyl]diazenyl-naphthalene-1-sulfonate* [C_2MIM]$_2$[CR]:** [C_2MIM][Cl] (0.18 g, 0.28 mmol); [H]$_2$[CR] (0.09 g,

0.46 mmol); Yield: quantitative; green solid; ^{1}H NMR (400 MHz, $(CD_3)_2SO$) δ 9.11 (s, 2H), 8.78 (d, J^3 *(H,H)* = 8.4 Hz, 2H), 8.45 (d, J^3 *(H,H)* = 8.0 Hz, 2H), 8.32 (s, 2H), 8.13 (d, J^3 *(H,H)* = 8.5 Hz, 4H), 7.98 (d, J^3 *(H,H)* = 8.5 Hz, 4H), 7.78 (s, 4H), 7.69 (s, 4H), 7.60 (t, J^3 *(H,H)* = 7.4 Hz, 2H), 7.51 (t, J^3 *(H,H)* = 7.2 Hz, 2H), 4.17 (q, J^3 *(H,H)* = 7.2 Hz, 4H), 3.84 (s, 6H), 1.41 (t, J^3 *(H,H)* = 7.3 Hz, 6H). Elemental analysis calcd (%) for $C_{44}H_{44}N_{10}O_6S_2.6.5H_2O$ (997.01 g.mol^{-1}): C 53.00, N 14.05, H 5.77; found: C 53.58, N 12.22, H 5.33.

Acknowledgments

This work was supported by Fundação para a Ciência e a Tecnologia through projects (PEst-C/LA0006/2013, PTCD/CTM-NAN/120658/2010, two contracts under Investigador FCT (L. C. Branco and I. M. Marrucho), a doctoral fellowship Andreia Forte (PD/BD/109625/2015), by the Portuguese Foundation for Science and Technology (FCT) through the strategic project UID/MAR/04292/2020 granted to MARE—Marine and Environmental Sciences Centre and Solchemar company.

References

(1) Dugger, B. N.; Dickson, D. W. Pathology of Neurodegenerative Diseases. *Cold Spring Harb. Perspect. Biol.* 2016, *9*, a028035 (1-22).

(2) Zhou, J.; Jangili, P.; Son, S.; Ji, M. S.; Won, M.; Kim, J. S. Fluorescent Diagnostic Probes in Neurodegenerative Diseases. *Adv. Mater.* 2020, *32*, 2001945 (1-43).

(3) Rai, M.; Yadav, A.; Ingle, A. P.; Reshetilov, A.; Blanco-Prieto, M. J.; Feitosa; M., C. Neurodegenerative Diseases: The Real Problem and Nanobiotechnological Solutions. In *Nanobiotechnology in Neurodegenerative Diseases*; Rai, M., Yadav, A., Eds.; Springer, 2019; pp 1–18.

(4) *World Health Organization*. available online: https://www.who.int/. Last acessed: December 2021.

(5) Cano, A.; Sánchez-López, E.; Ettcheto, M.; López-Machado, A.; Espina, M.;

Souto, E. B.; Galindo, R.; Camins, A.; García, M. L.; Turowski, P. Current Advances in the Development of Novel Polymeric Nanoparticles for the Treatment of Neurodegenerative Diseases. *Nanomedicine* 2020, *15*, 1239–1261.

(6) Sweeney, P.; Park, H.; Baumann, M.; Dunlop, J.; Frydman, J.; Kopito, R.; McCampbell, A.; Leblanc, G.; Venkateswaran, A.; Nurmi, A.; Hodgson, R. Protein Misfolding in Neurodegenerative Diseases: Implications and Strategies. *Transl. Neurodegener.* 2017, *6*, 6 (1-13).

(7) Hanczyc, P.; Fita, P. Laser Emission of Thioflavin T Uncovers Protein Aggregation in Amyloid Nucleation Phase. *ACS Photonics* 2021, *8*, 2598–2609.

(8) Sebastiao, M.; Quittot, N.; Bourgault, S. Thioflavin T Fluorescence to Analyse Amyloid Formation Kinetics: Measurement Frequency as a Factor Explaining Irreproducibility. *Anal. Biochem.* 2017, *532*, 83–86.

(9) Takekiyo, T.; Yoshimura, Y. Suppression and Dissolution of Amyloid Aggregates Using Ionic Liquids. *Biophys. Rev.* 2018, *10*, 853–860.

(10) Weingärtner, H.; Cabrele, C.; Herrmann, C. How Ionic Liquids Can Help to Stabilize Native Proteins. *Phys. Chem. Chem. Phys.* 2012, *14*, 415–426.

(11) Pillai, V. V. S.; Benedetto, A. Ionic Liquids in Protein Amyloidogenesis: A Brief Screenshot of the State-of-the-Art. *Biophys. Rev.* 2018, *10*, 847–852.

(12) Yakupova, E. I.; Bobyleva, L. G.; Vikhlyantsev, I. M.; Bobylev, A. G. Congo Red and Amyloids: History and Relationship. *Biosci. Rep.* 2019, *39*, BSR20181415.

(13) Girych, M.; Gorbenko, G.; Maliyov, I.; Trusova, V.; Mizuguchi, C.; Saito, H.; Kinnunen, P. Combined Thioflavin T-Congo Red Fluorescence Assay for Amyloid Fibril Detection. *Methods Appl. Fluoresc.* 2016, *4*, 034010.

(14) Frid, P.; Anisimov, S. V.; Popovic, N. Congo Red and Protein Aggregation in Neurodegenerative Diseases. *Brain Res. Rev.* 2007, *53*, 135–160.

(15) Khurana, R.; Uversky, V. N.; Nielsen, L.; Fink, A. L. Is Congo Red an Amyloid-Specific Dye? *J. Biol. Chem.* 2001, *276*, 22715–22721.

(16) *Current Clinical Pathology: Amyloid and Related Disorders*; Picken, M. M., Dogan, A., Herrera, G. A., Eds.; Springer Science & Business Media: New York, 2012.

(17) Howie, A. J.; Brewer, D. B. Optical Properties of Amyloid Stained by Congo Red: History and Mechanisms. *Micron* 2009, *40*, 285–301.

(18) El-Meanawy, A.; Mueller, C.; Iczkowski, K. A. Improving Sensitivity of Amyloid Detection by Congo Red Stain by Using Polarizing Microscope and Avoiding Pitfalls. *Diagn. Pathol.* 2019, *14*, 57 (1-7).

(19) Mamsa, S. S. A.; Meloni, B. P. Arginine and Arginine-Rich Peptides as

Modulators of Protein Aggregation and Cytotoxicity Associated With Alzheimer's Disease. *Front. Mol. Neurosci.* 2021, *14* (October), 1–19.

(20) Das, U.; Hariprasad, G.; Ethayathulla, A. S.; Manral, P.; Das, T. K.; Pasha, S.; Mann, A.; Ganguli, M.; Verma, A. K.; Bhat, R.; Chandrayan, S. K.; Ahmed, S.; Sharma, S.; Kaur, P.; Singh, T. P.; Srinivasan, A. Inhibition of Protein Aggregation: Supramolecular Assemblies of Arginine Hold the Key. *PLoS One* 2007, *2*, e1176.

(21) Mori, T.; Koyama, N.; Yokoo, T.; Segawa, T.; Maeda, M.; Sawmiller, D.; Tan, J.; Town, T. Gallic Acid Is a Dual a/b-Secretase Modulator That Reverses Cognitive Impairment and Remediates Pathology in Alzheimer Mice. *J. Biol. Chem.* 2020, *295* (48), 16251–16266.

(22) Liu, Y.; Pukala, T. L.; Musgrave, I. F.; Williams, D. M.; Dehle, F. C.; Carver, J. A. Gallic Acid Is the Major Component of Grape Seed Extract That Inhibits Amyloid Fibril Formation. *Bioorganic Med. Chem. Lett.* 2013, *23* (23), 6336–6340.

(23) Konar, M.; Bag, S.; Roy, P.; Dasgupta, S. Gallic Acid Induced Dose Dependent Inhibition of Lysozyme Fibrillation. *Int. J. Biol. Macromol.* 2017, *103*, 1224–1231.

(24) Rajendran, S. Corrosion Behaviour of Carbon Steel in Isoelectric Point and Nearly Neutral Aqueous Medium by L – Arginine and Zinc Ion as a Synergist. *Int. J. Nano Corros. Sci. Eng.* 2016, *3*, 415–427.

(25) Eslami, A. C.; Pasanphan, W.; Wagner, B. A.; Buettner, G. R. Free Radicals Produced by the Oxidation of Gallic Acid: An Electron Paramagnetic Resonance Study. *Chem. Cent. J.* 2010, *4*, 15 (1-4).

(26) Silva, N. H. C. S.; Pinto, R. J. B.; Freire, C. S. R.; Marrucho, I. M. Production of Lysozyme Nanofibers Using Deep Eutectic Solvent Aqueous Solutions. *Colloids Surfaces B Biointerfaces* 2016, *147*, 36–44.

(27) Silva, N. H. C. S.; Pinto, R. J. B.; Martins, M. A.; Ferreira, R.; Correia, I.; Freire, C. S. R.; Marrucho, I. M. Ionic Liquids as Promoters of Fast Lysozyme Fibrillation. *J. Mol. Liq.* 2018, *272*, 456–467.

Chapter 6

Conclusions
and
Future work

Affecting millions of people worldwide, neurodegenerative diseases are defined as incurable and highly incapacitating diseases that are characterized by the progressive loss of structure and function of nerve cells (neurons). Among the several diseases that can be included in this category (i.e. Parkinson's or Huntington's diseases, amyotrophic lateral sclerosis), Alzheimer's disease emerges as the most common form of dementia. In addition to the massive problems associated to the patient loss of life quality and impairment of mental and physical abilities, one of the main problems associated to this type of pathologies, is the fact that they are only detected at a late stage where the treatment options are less effective. Thus, this thesis was focused on the development of ionic systems for early detection of neurodegenerative diseases. The followed strategy consisted of two distinct paths as illustrated in Scheme 6. 1.

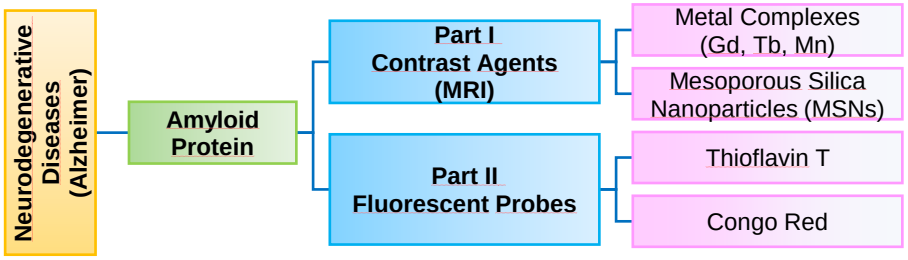

Scheme 6. 1 | Scheme of the followed strategy in the thesis.

A. Synthesis and characterization of novel ionic contrast agents

The first pathway consisted in the preparation of a set of potential contrast agents for MRI diagnosis technique. During this part of the work, it was possible to synthesize a set of magnetic ionic liquids or organic salts based on the choline cation and its derivatives (Figure 6. 1). These structures were prepared from commercial and low-cost tertiary amines using optimized

alkylation methods. Thus, different alkyl chains (C_2, C_4 and C_6) and functionalized groups (alcohols) were introduced in the tertiary amines structures to obtain the desired choline derivative cations.

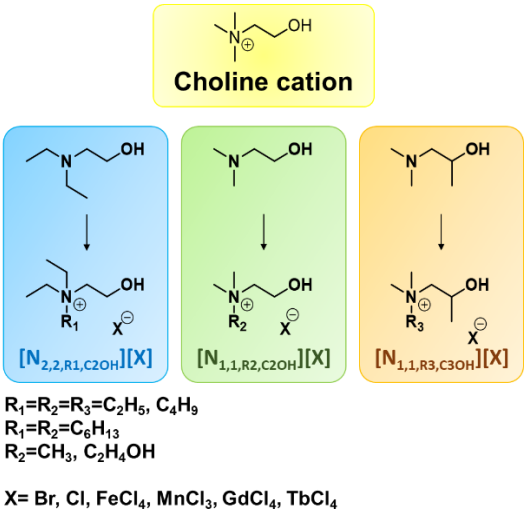

Figure 6. 1 | General scheme of biocompatible ILs and organic salts based on choline derivatives.

Cholinium family was selected in order to increase the biocompatibility of the salts due to its small cytotoxicity and extremely important functions in the human body. The main idea of using this organic cation scaffold was to reduce the toxicity associated to the presence of metal anions in the final magnetic products as well as to increase the bioavailability of the magnetic organic salt. All synthesized choline derivative organic cations were structurally characterized by ^{1}H-NMR, FTIR, and elemental analysis (C, H, N). Most of the halogenated compounds were obtained as solids and as a high relative purity product (≥93% determined by ^{1}H-NMR). $[N_{1,1,6,C2OH}][Br]$ and $[N_{1,1,2,C3OH}][Cl]$ salts are presented in this work as examples of RTILs. Further complexation reactions, to introduce the metals in the organic salt

formulation were also performed. Once obtained the cation structures (chloride salts), the transition metals such as iron (III) and manganese (II); and lanthanides such as gadolinium (III) and terbium (III), were selected to be combined to organic cations through complexation reactions. All compounds were characterized according to their physical, thermal, and magnetic properties. Three examples of MILs, $[N_{1,1,4,C2OH}][FeCl_4]$, $[N_{1,1,2,C3OH}][FeCl_4]$ and $[N_{1,1,4,C3OH}][FeCl_4]$ were obtained. $[N_{1,1,2,C3OH}][FeCl_4]$ and $[N_{1,1,4,C3OH}][FeCl_4]$ salts arise also as two examples of RTILs. All Mn (II), Gd (III) and Tb (III) based salts resulted in solid products with melting temperatures higher than 100 ºC. Despite a significant reduction of the melting point (comparing to choline chloride and metals), the prepared salts are not included in ionic liquids definition (melting point lower than 100 ºC). Effective magnetic moments were also determined for all prepared salts, and it was possible to establish a standard behavior between this magnetic property and the cation structural features. Cytotoxic effect of the prepared compounds (halogen and metal-based salts) was evaluated in four different cell lines, normal (3T3 and 293T) and tumoral (Caco-2 and HepG2). In general, chloride-based salts did not induce any cytotoxicity in normal and tumoral cells while in the case of metal-based salts, most of the compounds did not present any cytotoxicity for the studied cells.

Two gadolinium (III)-based magnetic salts, $[N_{1,1,1,C2OH}][GdCl_4]$ and $[N_{1,1,2,C3OH}][GdCl_4]$, were selected to carried out a preliminary study that allowed to evaluate their applicability as MRI contrast agents through determination of their relaxivities r_1 and r_2. The study was conducted in aqueous solutions at 400 MHz (9.4 T), 37 ºC (309 K) and by measuring the effect of five different compounds concentrations (0.05-1.00mM) on longitudinal (T_1) and transversal (T_2) relaxation times of water. From the observation of T_1 relaxation fitting results, it was possible to verify a

concentration-dependent change in the system behaviour. The increase of water amount, i.e., with the reduction of compounds concentration, a change from a mono-exponential to a multi-exponential system could be verified. This behaviour can be related with an ion solvation mechanism where the organized structure of the organic salt is broken and smaller species such as ion pairs or, in more diluted solutions, isolated hydrated ions are formed and stabilized by the solvent. Further conductivity measurements or another equivalent method should be performed in order to check the formation of the ion pairs. T_2 relaxation fitting results showed a mono-exponential behaviour for all salts concentrations. Once obtained the relaxivity constants r_1 and r_2, and assuming the theory that relates the inverse proportion relation between r_1 relaxivity and the field strength, it was possible to perform a rough comparison between the prepared salts and some commercial contrast agents. In this context, choline-based magnetic salts presented higher r_1 relaxivities than most of the contrast agents commercially available which can lead to the theoretical conclusion that prepared salts can provide an high-enhancement effect.

Additionally, all manganese (II)-based salts (choline derivatives, tetraethylammonium and two additional families, phosphonium and imidazolium) showed to be photoluminescent compounds with the emission colour (red and green) directly associated to the metal coordination type (MnX_6^{4-} for octahedral and MnX_4^{2-} for tetrahedral systems, respectively). Single crystal x-ray crystallography was performed to confirm the crystalline structure of the salts $[N_{1,1,1,C2OH}][MnCl_3]$, $[N_{1,1,C2OH,C2OH}][MnCl_3]$ and $[N_{2,2,2,2}][MnCl_3]$ and to determine the complex geometry. Luminescence of all manganese (II)-based salts was evaluated according to their quantum yield (absolute method) and lifetime decay (phosphorescence decay). Excitation spectra showed the presence of crystal polymorphism for compounds with

the presence of oxygen in their cation structure. It was also possible to correlate the salts quantum yield and their structural features. $[N_{1,1,4,C2OH}][MnCl_3]$ exhibited the highest quantum yield (12.8%) from choline derivative salts. On the other hand, $[N_{2,2,2,2}][MnCl_3]$ arises as the compound with the highest quantum yield (72.2%) from all prepared salts. Lifetime decays indicated us that the deactivation mechanism of compounds in the excited state is accomplished through a phosphorescence process. In this part of the work, it was possible to identify the crystal field transitions associated to Mn (II) in both coordination systems and to conclude that they are, in general, more well-defined for cations with oxygen in their structure. Finally, a preliminary study was also made in order to compare the luminescence quantum yield of the same compound, $[N_{1,1,1,C2OH}][MnCl_3]$, in its powder and crystal forms. Although the excitation spectra are very similar ($^4T_{2g}$ (D) transition emerges as the exception), it is important to highlight that compound quantum yield increases from 4.74% (powder) to 10.95% in its crystal form.

When coordinated with a large linear molecule, the metal toxicity is reduced since the metal is trapped. In this work, metal organic salts prepared possess a small size ligand, which can lead to an increase of their toxicity. In order to evaluate the toxicity of the prepared magnetic organic salts due to the small size ligand (chloride) and to compare with a different and safe system, the analogues of two selected choline derivatives cations ($[N_{1,1,4,C2OH}]$ and $[N_{1,1,4,C3OH}]$) were immobilized in mesoporous silica nanoparticles (MSNs). It is important to emphasize about the possibility to modulate the MILs toxicity combining the organic salts and nanoparticle systems. All prepared nanomaterials were completely characterized by different techniques: ^{1}H-NMR (proton nuclear magnetic resonance), FT-IR (Fourier transform infrared), EA (elemental analysis), ICP-MS (inductively coupled plasma

mass spectrometry), XRF (X-Ray Fluorescence), TEM (transmission electron microscopy), TGA (thermogravimetric analysis), N_2 adsorption, XRD (X-ray diffraction) and DLS (dynamic light scattering). These techniques allowed to elucidate about the features of nanomaterials structure, to confirm the effective functionalization of MSNs with the selected cations as wells as the presence of the desired metal anions. It was possible to verify that the cation:anion (metal complex) proportion obtained in the final materials was not the expected 1:1. Thus, in the future, MSNs based ionic liquids should be optimized using an alternative synthetic methodology. Once the correct proportion between elements in the metallic complex is guaranteed, it is required to evaluate their magnetic properties as well as the functionality of gadolinium (III)-based materials as MRI contrast agents. These relaxivities results can be compared with the results obtained for choline derivative salts already studied in this work. Moreover, it is important to extend the relaxometry studies to other materials already prepared with manganese (II) and terbium (III) for both systems. As performed for non-functionalized salts, cytotoxicity studies of the immobilized analogues were performed in the same four cells lines (3T3, Caco-2, HepG2 and 293T). In general, it was not possible to distinguish a cytotoxic effect between the two cations, however, from the evaluation of the two systems it was possible to observe some specific differences between the metal organic salts and their immobilized analogues.

In the future work, it would be interested to develop iron oxide nanoparticles (IONPs) functionalized with the same cations already described in order to compare their magnetic properties and their effectiveness as contrast agent for MRI.

B. Synthesis and characterization of novel amyloid-specific dyes

For second pathway of the thesis (Scheme 6. 1), the main objective was focused on the preparation a set of novel ionic compounds capable of being applied as amyloid-specific dyes for staining aggregates deposits and, ideally, to stabilize the initial structures of amyloid fibrils formation. Thus, two commercial available probes, thioflavin T and congo red, were used as starting materials to achieve to these new ionic probes (Figure 6. 2). Several synthetic methodologies were applied in order to obtain the desired salts.

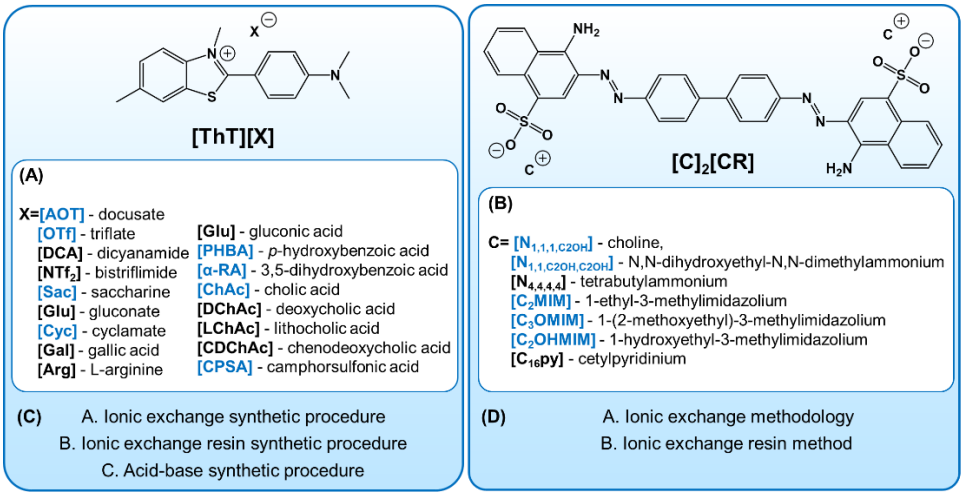

Figure 6. 2 | (A) ThT and **(B)** CR selected counter-ions and **(C, D)** respective synthetic methodologies adopted in this work. Acronyms identified with blue colour correspond to the compounds obtained through the methods used in this work.

Nevertheless, the preparation of ionic amyloid-specific dyes was reached using different counter-ions as illustrated in Figure 6. 2 (A) and (B).

ThT-based salts were prepared by three distinct methods, through ionic exchange reactions, ionic exchange resin procedure and acid-base synthetic approach (Figure 6. 2 (C)). From these three methodologies, the ionic

exchange resin was the only one that did not result in any of the desired products since ThT appears to decompose in the resin. All prepared salts (in blue on Figure 6. 2 (A)) were characterized by ^{1}H-NMR, elemental analysis and thermal analysis. ThT-organic salts were obtained as solids with a high purity level (>90% determined by ^{1}H-NMR).

ThT detection method is based on its fluorescence properties. This probe presents a self-quenching ability exhibited for the free state structure. When bounded to the amyloid aggregates, the rotation associated to the bond between benzothiazole and aniline units is blocked and ThT fluorescence increases. During this work, it was possible to optimize the formation and monitorization of fibrillation process using Lysozyme from chicken egg white. It was possible to observe that fibrils formation (without the presence of any of the synthesized organic salts) reaches to an equilibrium state after approximately 90 minutes.

Regarding to CR-based salts, two synthetic procedures were applied (Figure 6. 2 (D)). Ionic exchange reactions proved to be unsuitable to perform chemical reactions with this compound. This limitation can be justify by the size of CR structure. Alternatively, an ion exchange resin was used to change sodium ions from Congo red salt by H^{+} followed by an acid-base reaction with the hydroxide forms of the selected counter-ions. This method still needs to be improved in order to overcome Congo red low stability issue and, to achieve a more sustainable and effective synthetic process. Prepared compounds (in blue on (Figure 6. 2 (B)) were characterized by ^{1}H-NMR, elemental analysis and thermal analysis. All CR-based salts were obtained as solids with a high purity level (>90% determined by ^{1}H-NMR).

According to CR intrinsic birefringence, it is possible to detect amyloid aggregates through the observation of their bright color change under cross-polarized light in the absence/presence of amyloid plaques. In general, all

CR-based salts maintained this important property in the absence of amyloid plaques after counter-ion change.

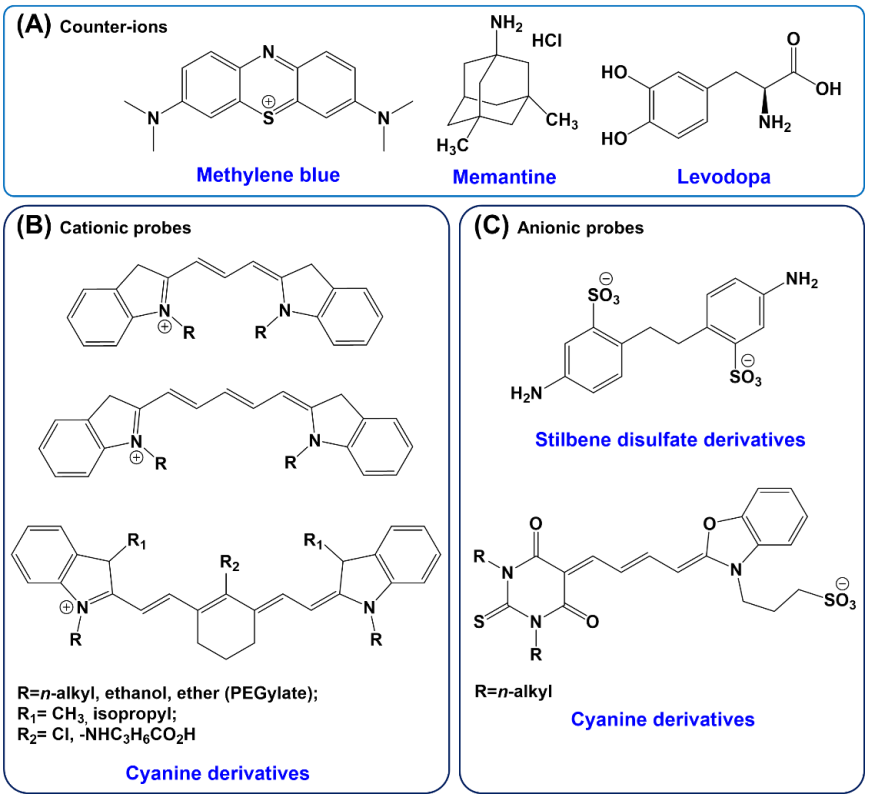

Figure 6. 3 | Structures of (A) important counter-ions to be used in the preparation of new probes; (B) Cationic and (C) anionic probes as possible alternatives.

Complementary fluorescence (ThT) and birefringence (CR) studies of the prepared ThT and CR-based organic probes in the presence of amyloid fibrils are in progress.

Taking advantage of the previous experience about the development of alternative ionic organic probes for amyloid staining, it would be possible to design new salts for ThT and CR probes based on different counter-ions

(Figure 6. 3 (A)). These ions can be selected for a dual-function: 1) a significant role in the inhibition of amyloid oligomerization (e.g. methylene blue) and/or 2) using drugs already tested for neurodegenerative diseases (e.g. memantine and levodopa).

For other side, it would be also possible to explore new fluorescent probes such as cyanine and stilbene as alternatives to ThT and CR (Figure 6. 3 (B) and (C)).

Supplementary Information

Supplementary Information

Chapter 2

1. Structural characterization of biocompatible choline derivatives organic salts (^{1}H-NMR and FT-IR)

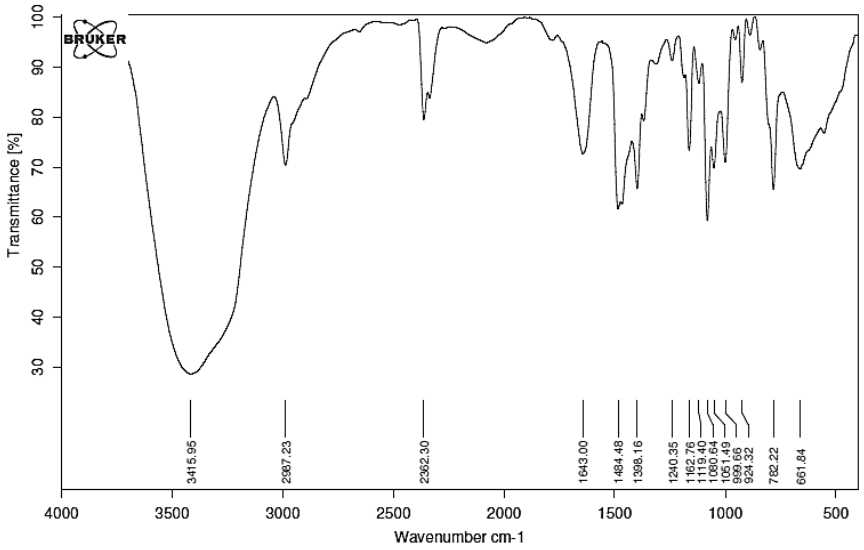

Figure SI 1 | FT-IR spectra of [$N_{2,2,2,C2OH}$][Br].

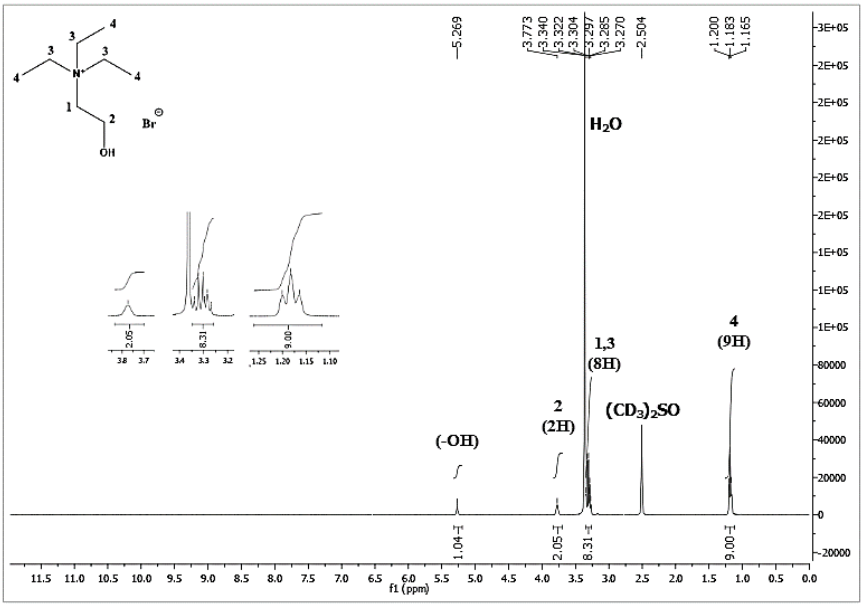

Figure SI 2 | ^{1}H-NMR spectra of [$N_{2,2,2,C2OH}$][Cl] in $(CD_3)_2SO$.

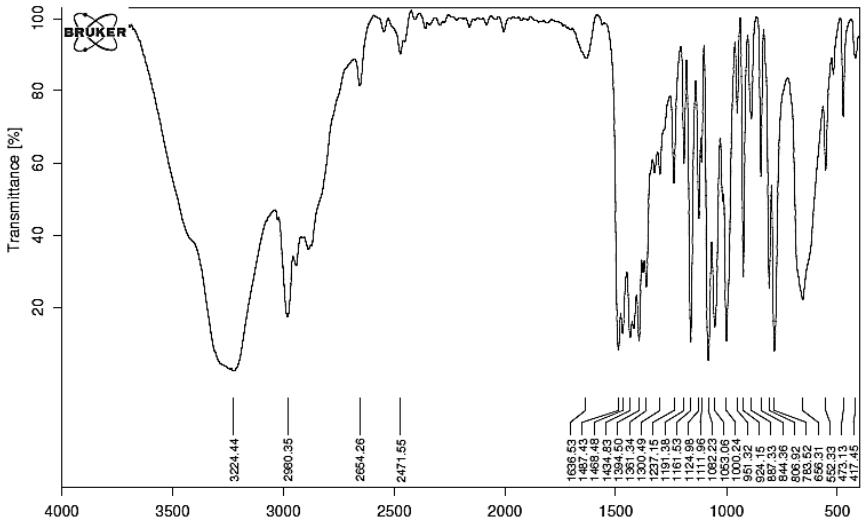

Figure SI 3 | FT-IR spectra of $[N_{2,2,2,C2OH}][Cl]$.

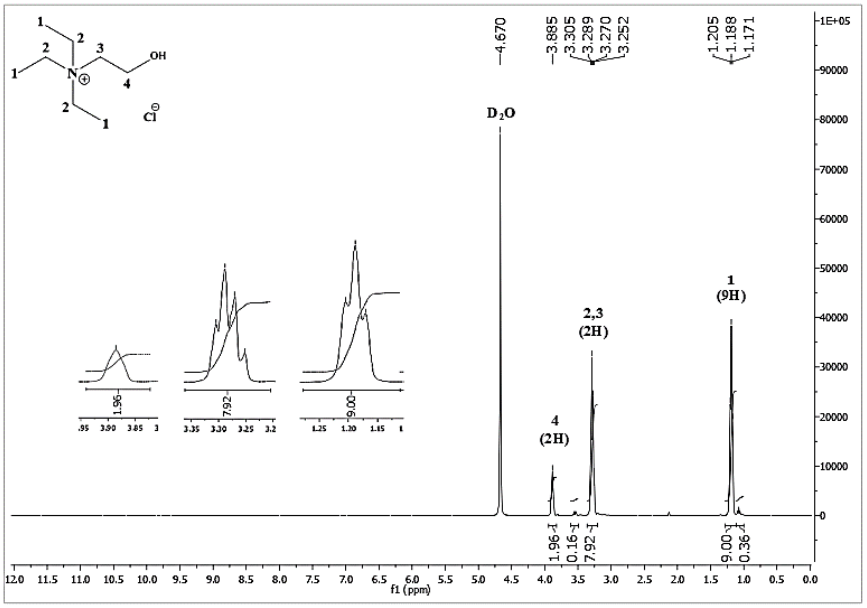

Figure SI 4 | ^{1}H-NMR spectra of $[N_{2,2,2,C2OH}][Cl]$ in D_2O.

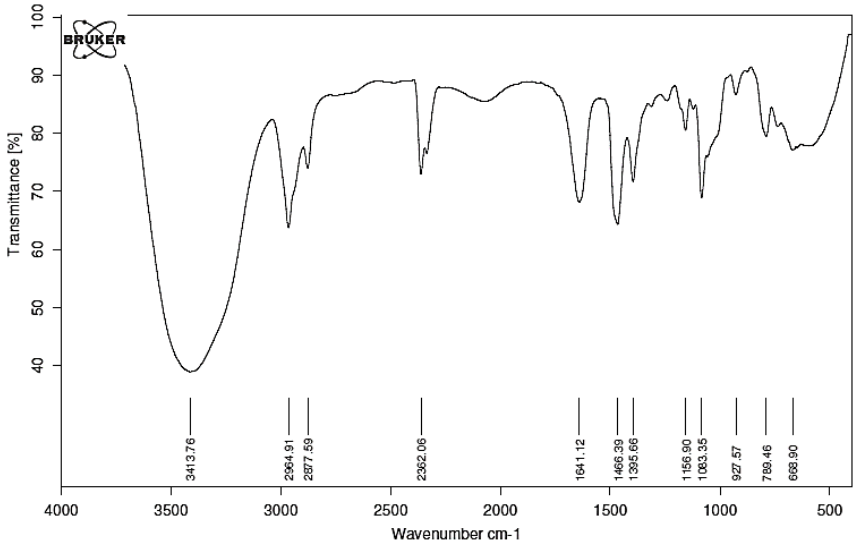

Figure SI 5 | FT-IR spectra of $[N_{2,2,4,C2OH}][Br]$.

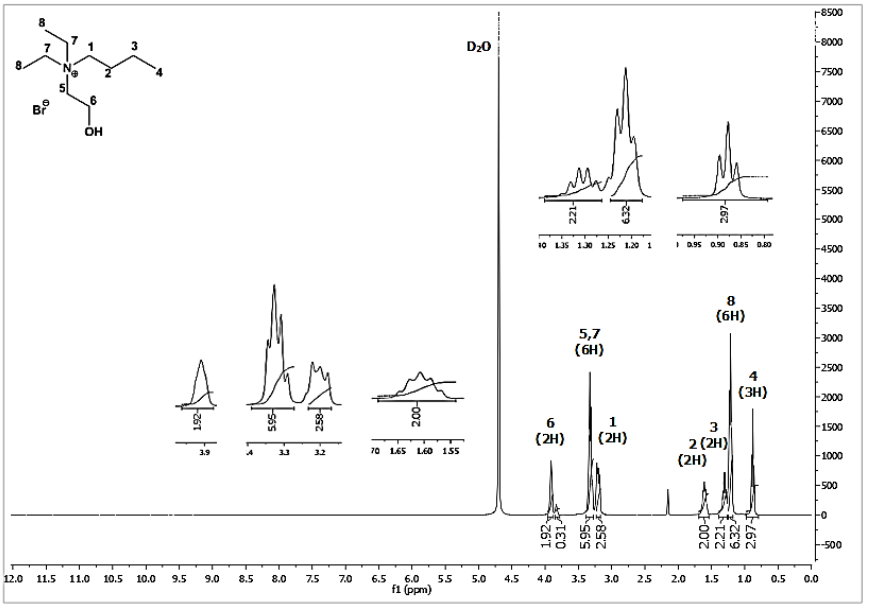

Figure SI 6 | ^{1}H-NMR spectra of $[N_{2,2,4,C2OH}][Cl]$ in D_2O.

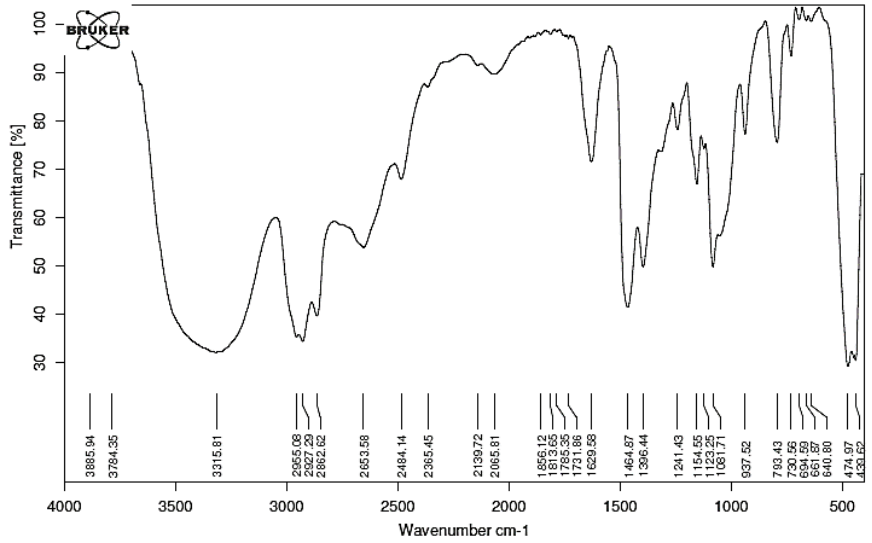

Figure SI 7 | FT-IR spectra of [$N_{2,2,6,C2OH}$][Br].

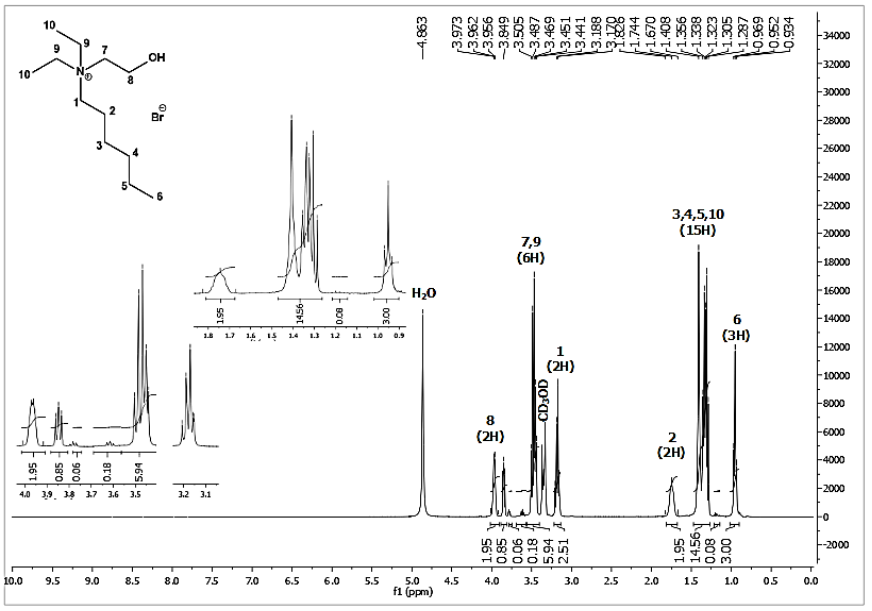

Figure SI 8 | ^{1}H-NMR spectra of [$N_{2,2,6,C2OH}$][Br] in CD_3OD.

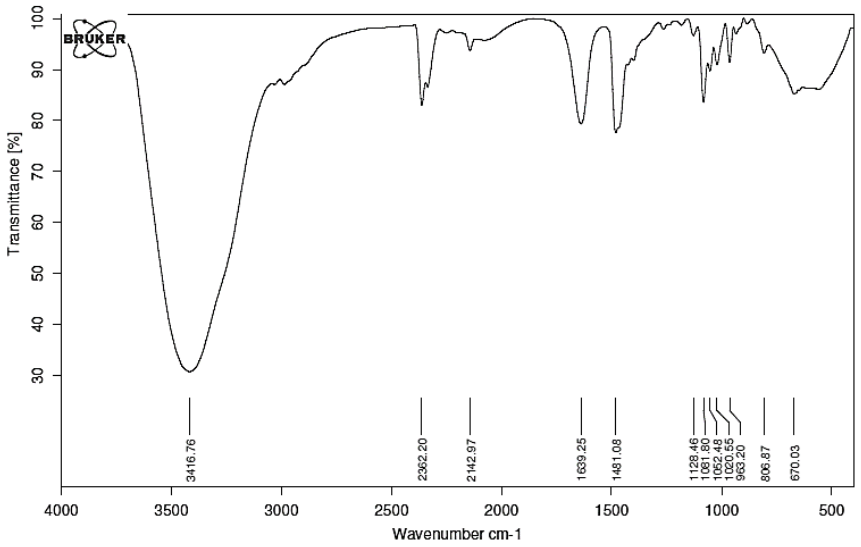

Figure SI 9 | FT-IR spectra of [$N_{1,1,2,C2OH}$][Br].

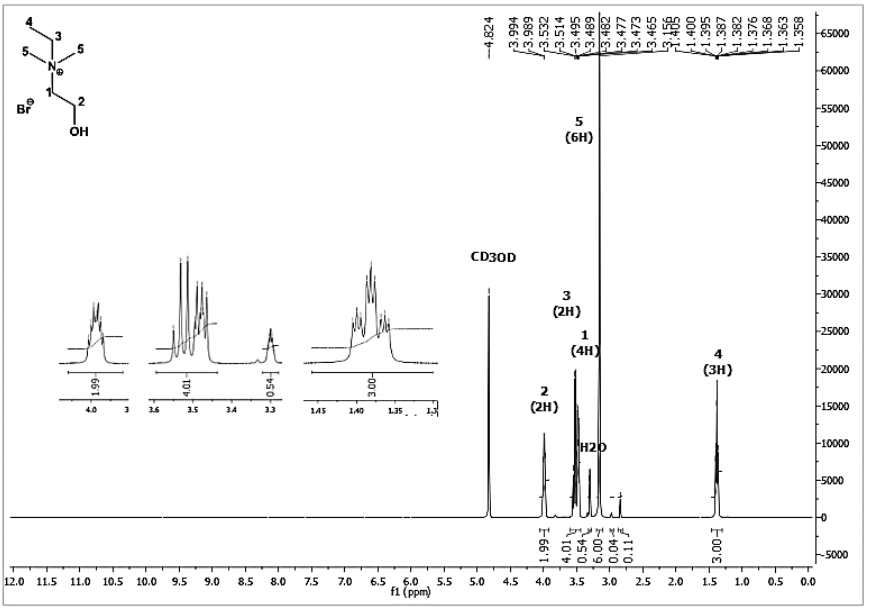

Figure SI 10 | ^{1}H-NMR spectra of [$N_{1,1,2,C2OH}$][Br] in CD_3OD.

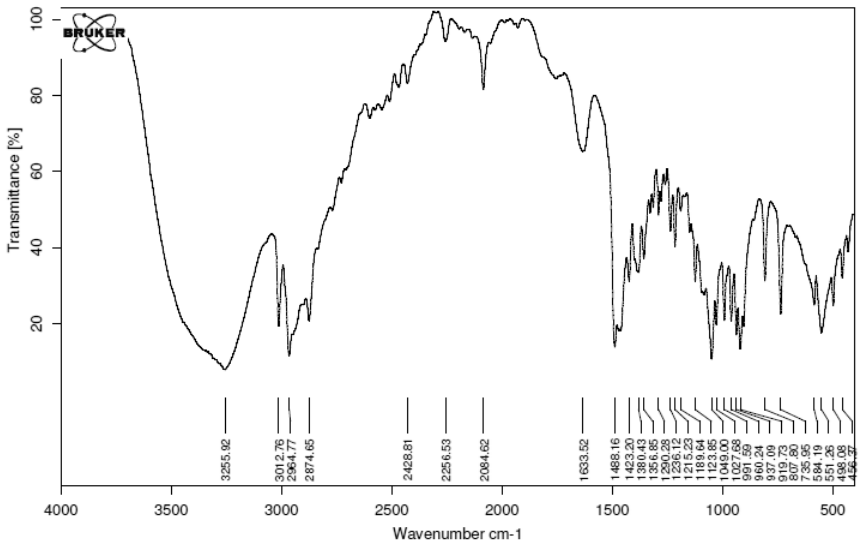

Figure SI 11 | FT-IR spectra of [$N_{1,1,4,C2OH}$][Cl].

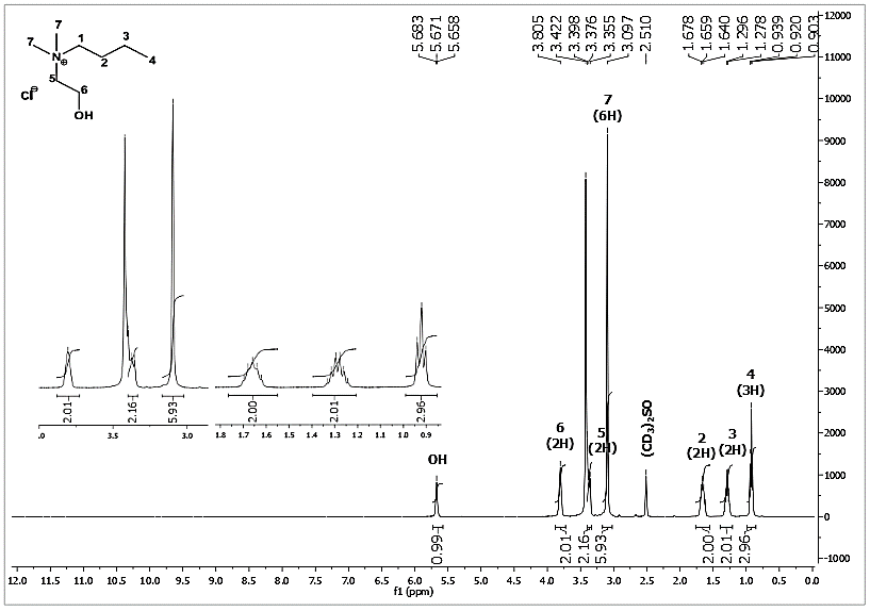

Figure SI 12 | ^{1}H-NMR spectra of [$N_{1,1,4,C2OH}$][Cl] in $(CD_3)_2SO$.

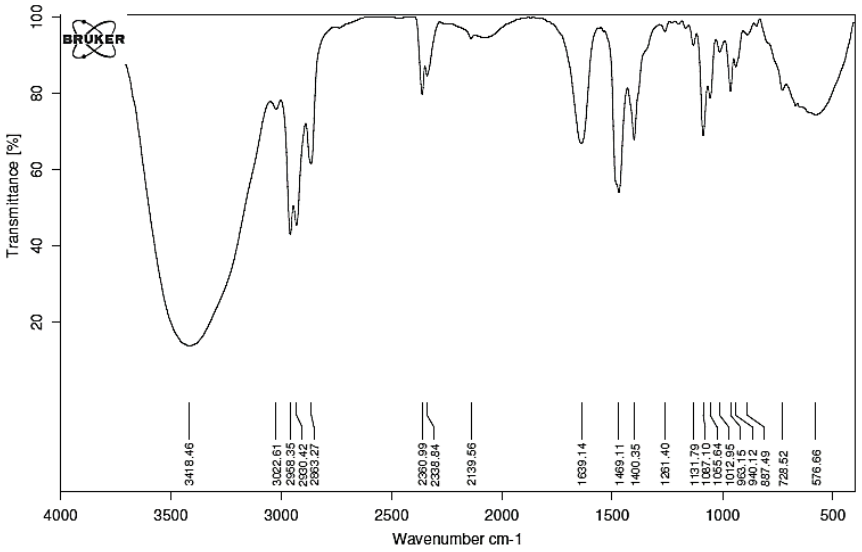

Figure SI 13 | FT-IR spectra of [$N_{1,1,6,C2OH}$][Br].

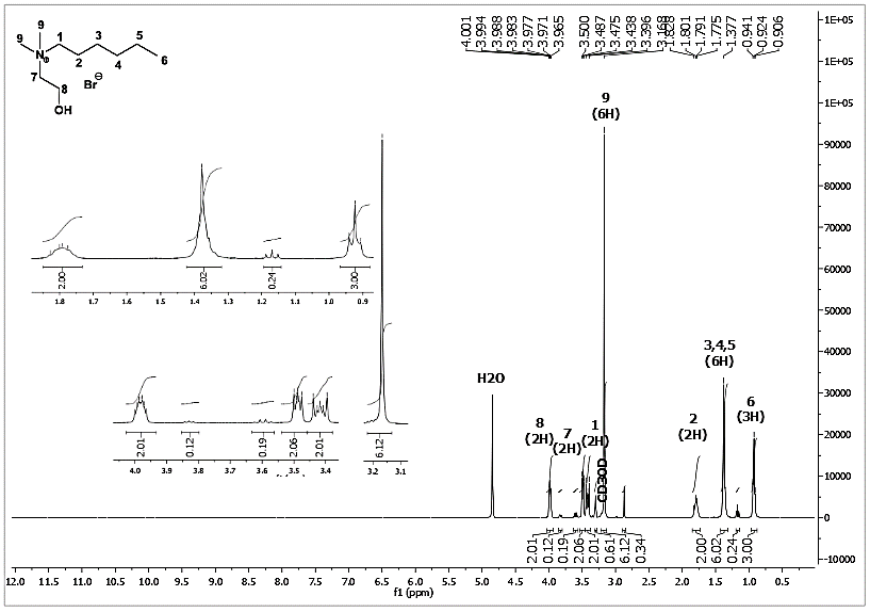

Figure SI 14 | ^{1}H-NMR spectra of [$N_{1,1,6,C2OH}$][Br] in CD_3OD.

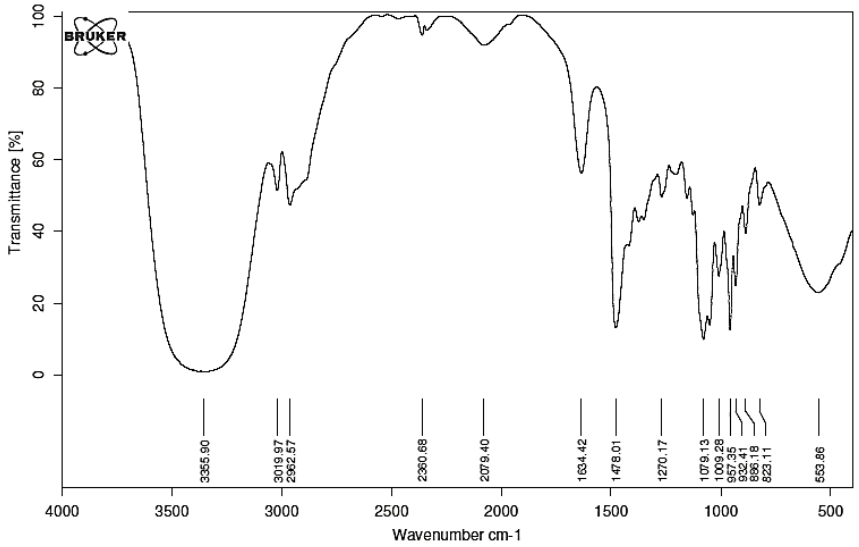

Figure SI 15 | FT-IR spectra of [$N_{1,1,C2OH,C2OH}$][Cl].

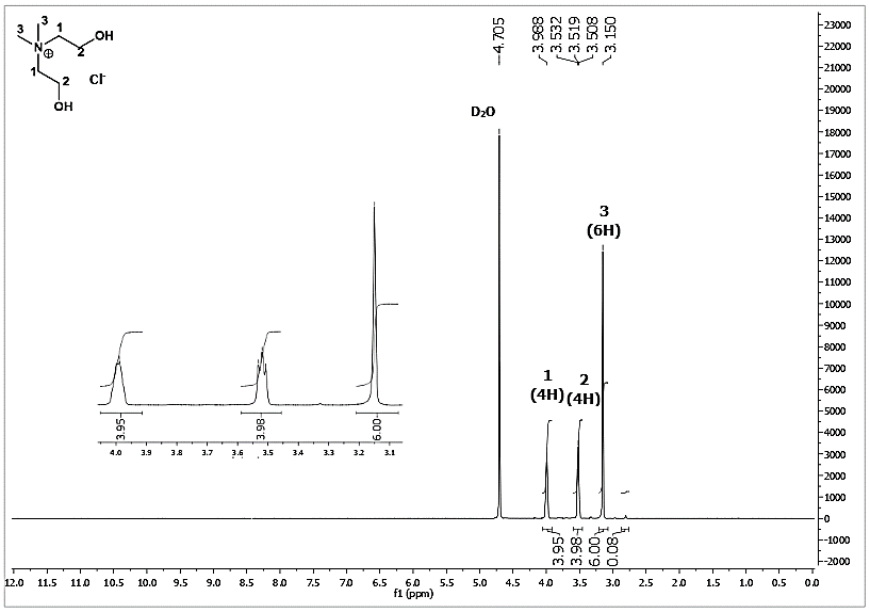

Figure SI 16 | ^{1}H-NMR spectra of [$N_{1,1,C2OH,C2OH}$][Cl] in D_2O.

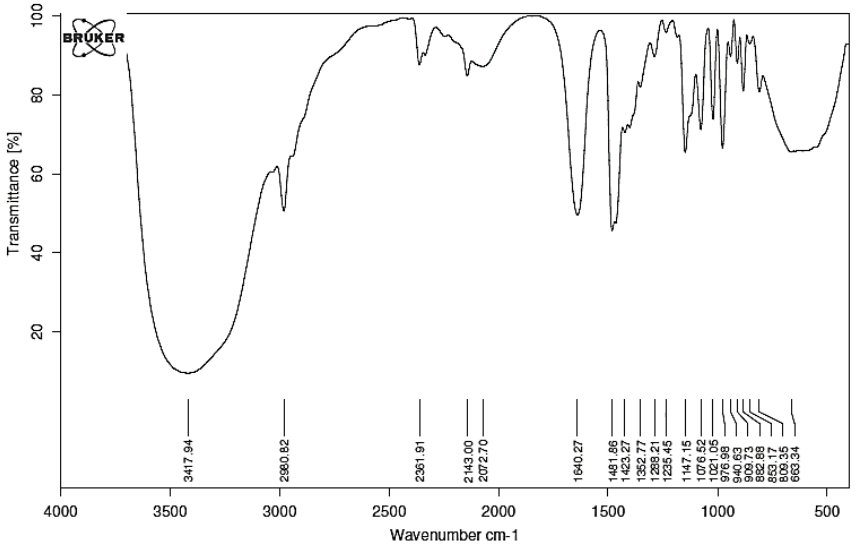

Figure SI 17 | FT-IR spectra of [$N_{1,1,2,C3OH}$][Br].

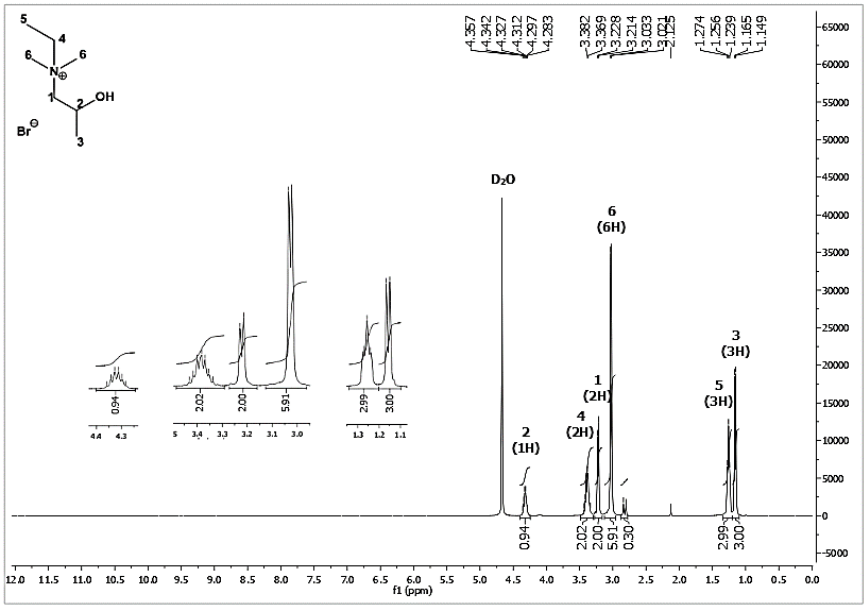

Figure SI 18 | ^{1}H-NMR spectra of [$N_{1,1,2,C3OH}$][Br] in D_2O.

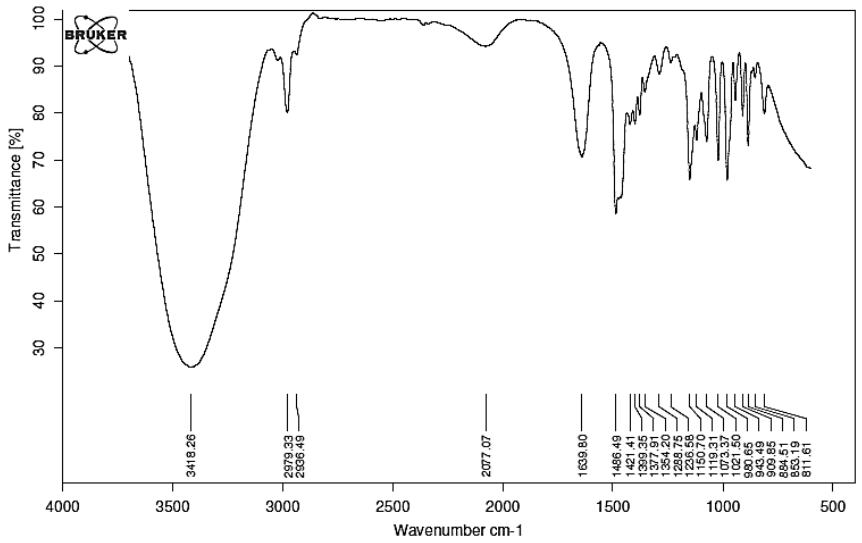

Figure SI 19 | FT-IR spectra of $[N_{1,1,2,C3OH}][Cl]$.

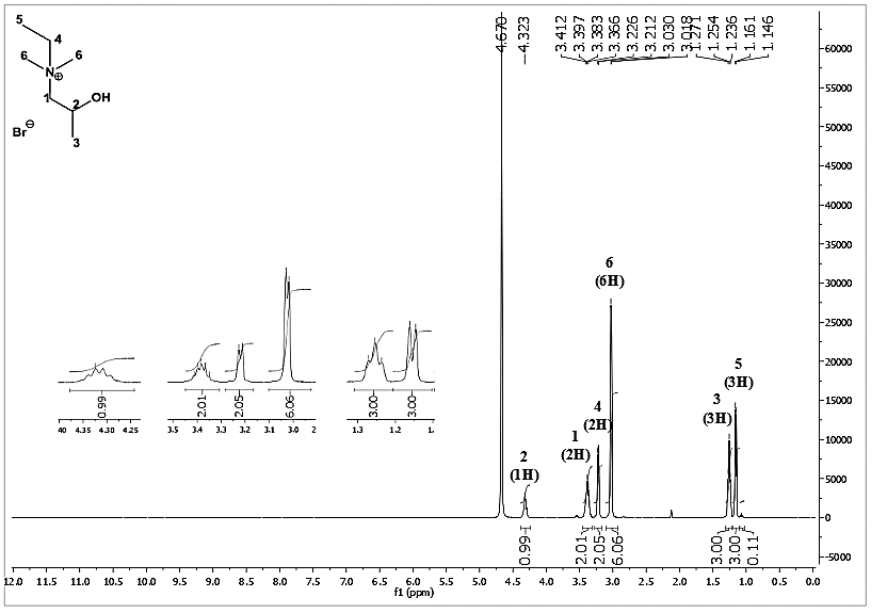

Figure SI 20 | ^{1}H-NMR spectra of $[N_{1,1,2,C3OH}][Cl]$ in D_2O.

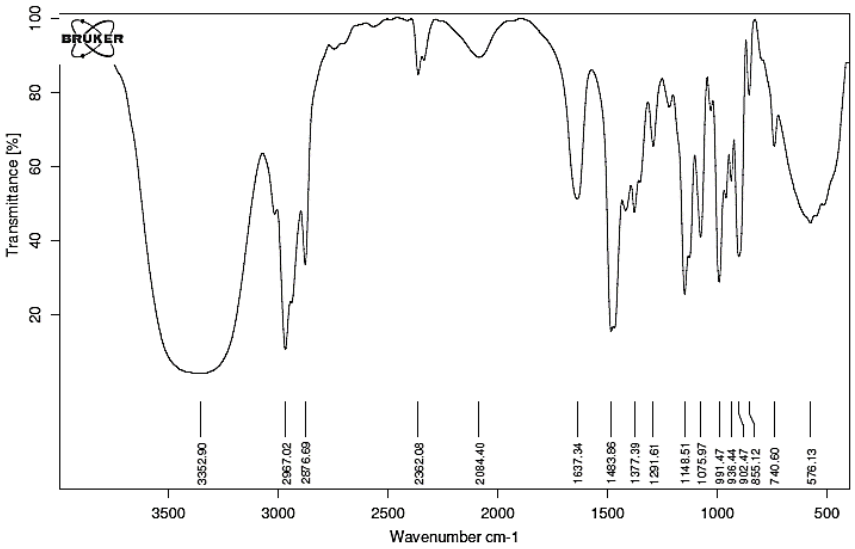

Figure SI 21 | FT-IR spectra of [$N_{1,1,4,C3OH}$][Cl].

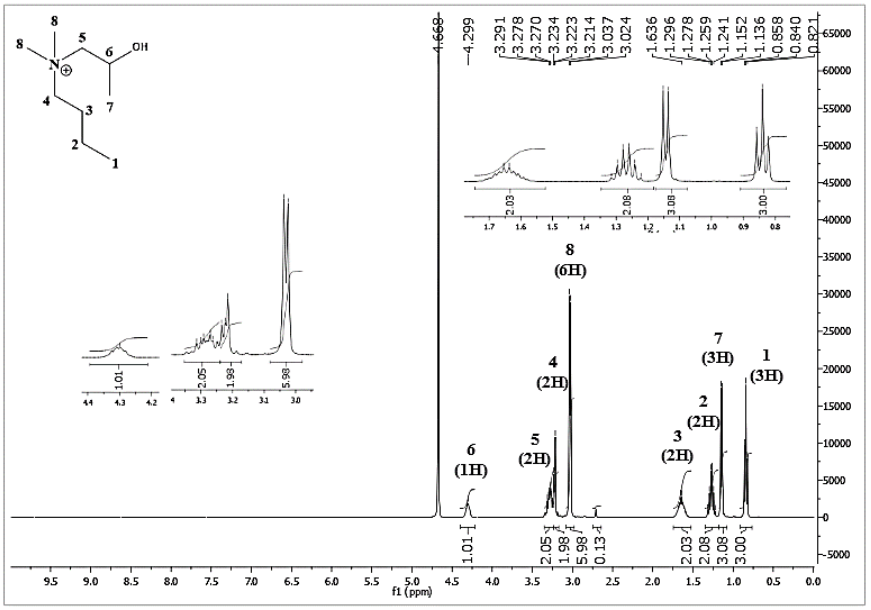

Figure SI 22 | ^{1}H-NMR spectra of [$N_{1,1,4,C3OH}$][Cl] in D_2O.

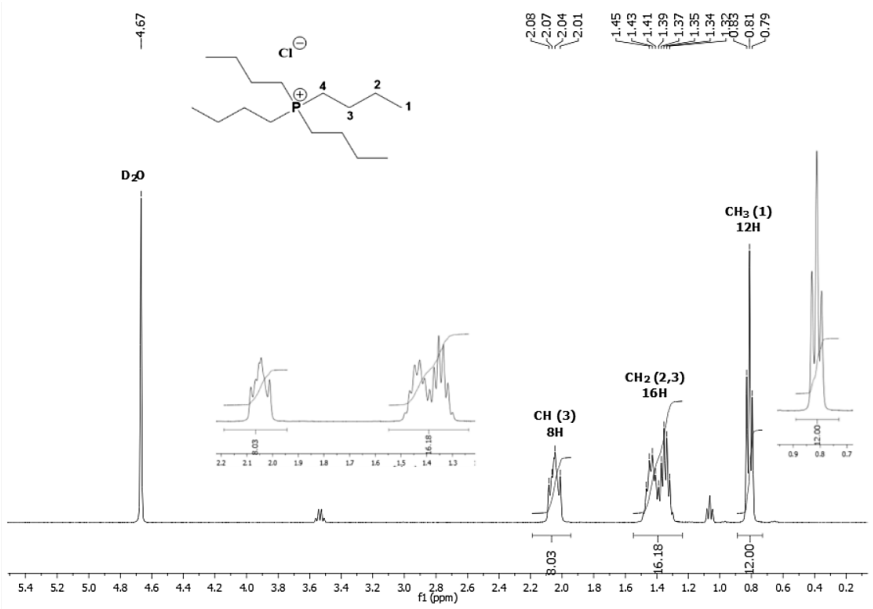

Figure SI 23 | ^{1}H-NMR spectra of $[P_{4,4,4,4}][Cl]$ in D_2O.

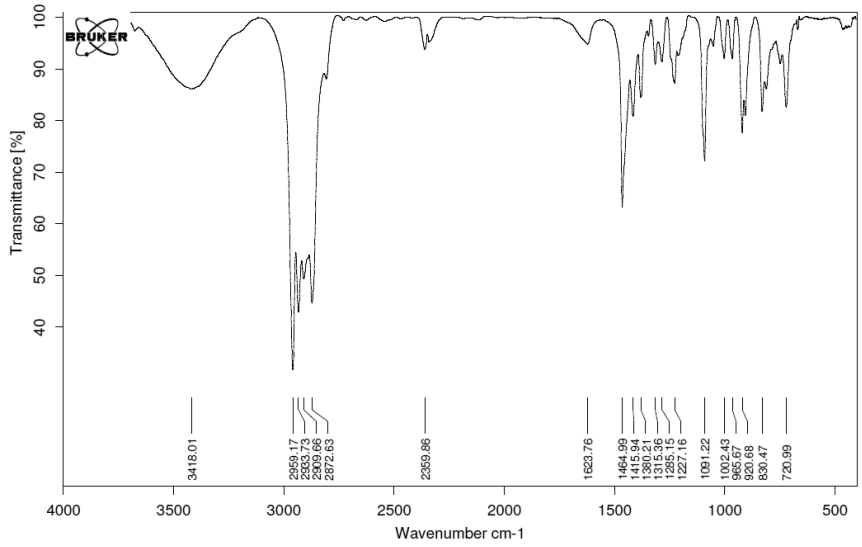

Figure SI 24 | FT-IR spectra of $[P_{4,4,4,4}][Cl]$.

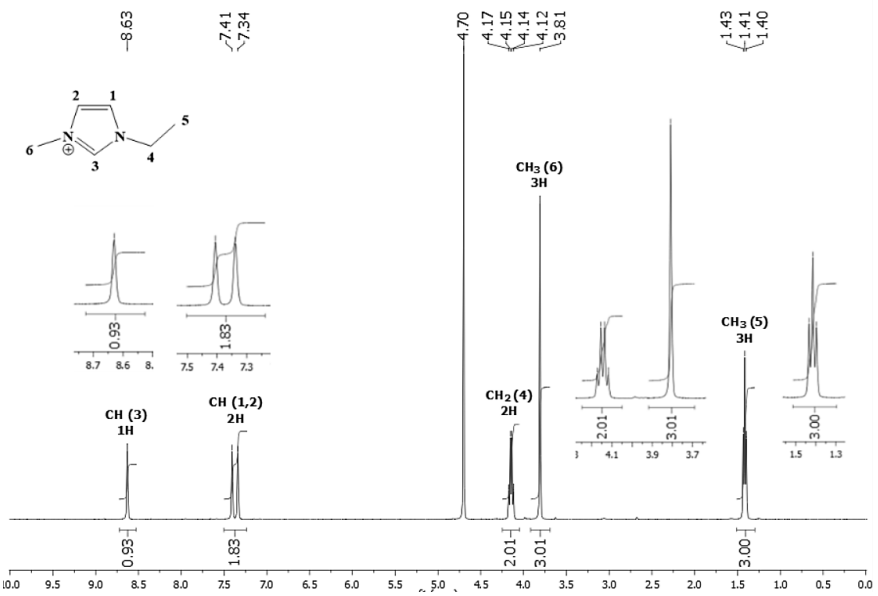

Figure SI 25 | ^{1}H-NMR spectra of [C_2MIM][Cl] in D_2O.

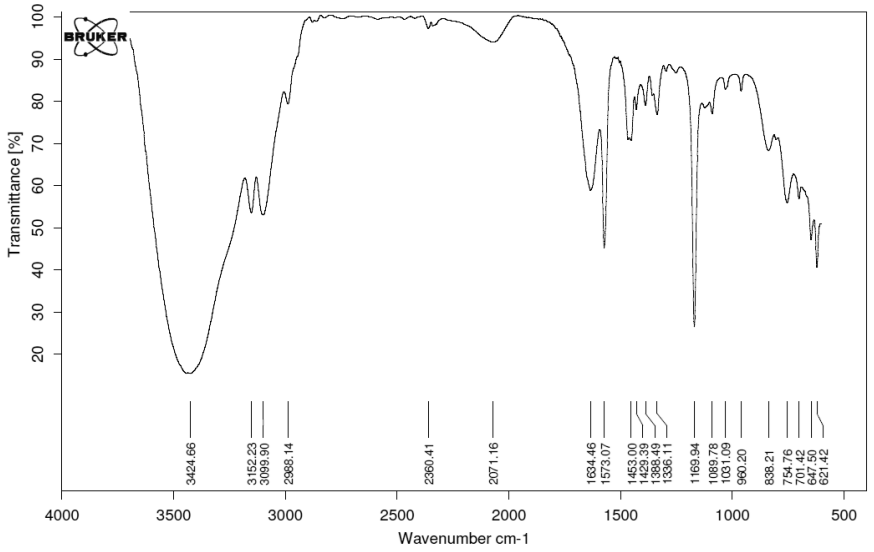

Figure SI 26 | FT-IR spectra of [C_2MIM][Cl].

2. Structural characterization of magnetic organic salts (FT-IR)

2.1. Iron (III)-based magnetic salts

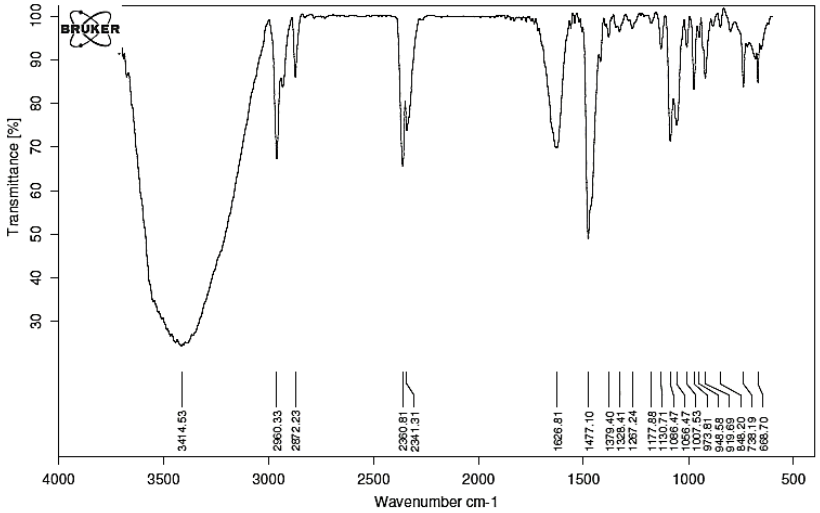

Figure SI 27 | FT-IR spectra of $[N_{1,1,4,C2OH}][FeCl_4]$.

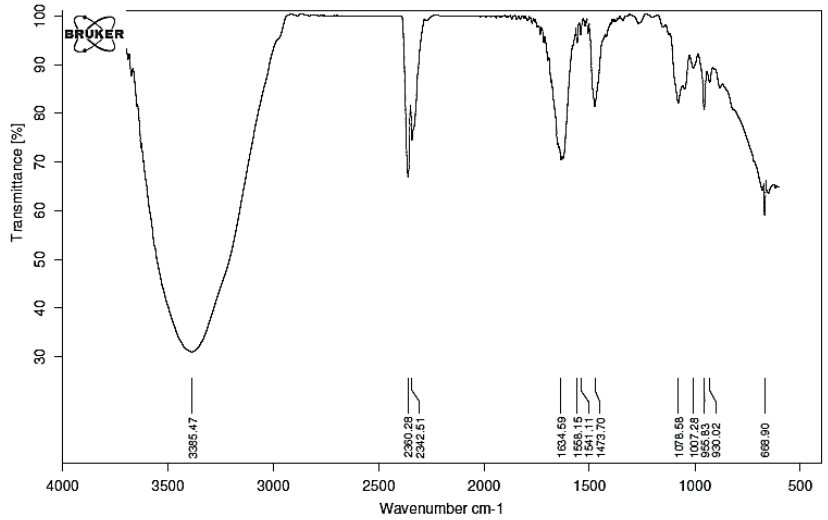

Figure SI 28 | FT-IR spectra of $[N_{1,1,C2OH,C2OH}][FeCl_4]$.

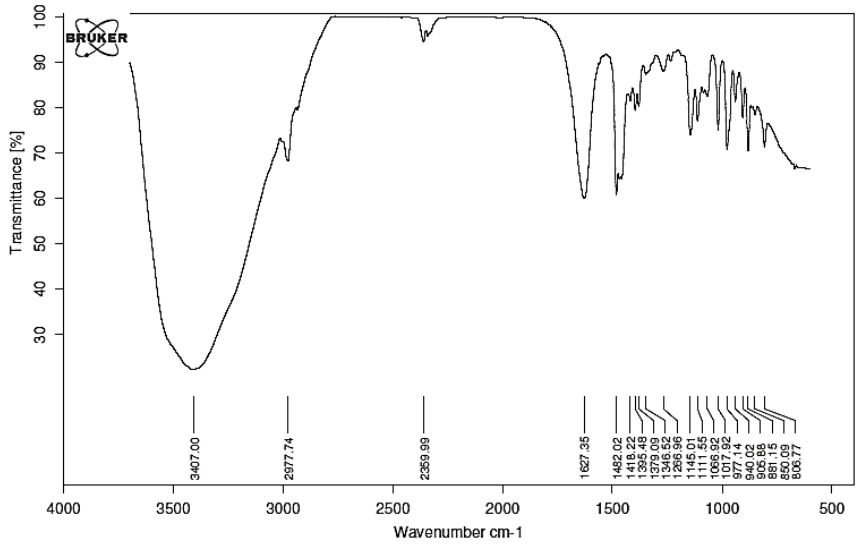

Figure SI 29 | FT-IR spectra of $[N_{1,1,2,C3OH}][FeCl_4]$.

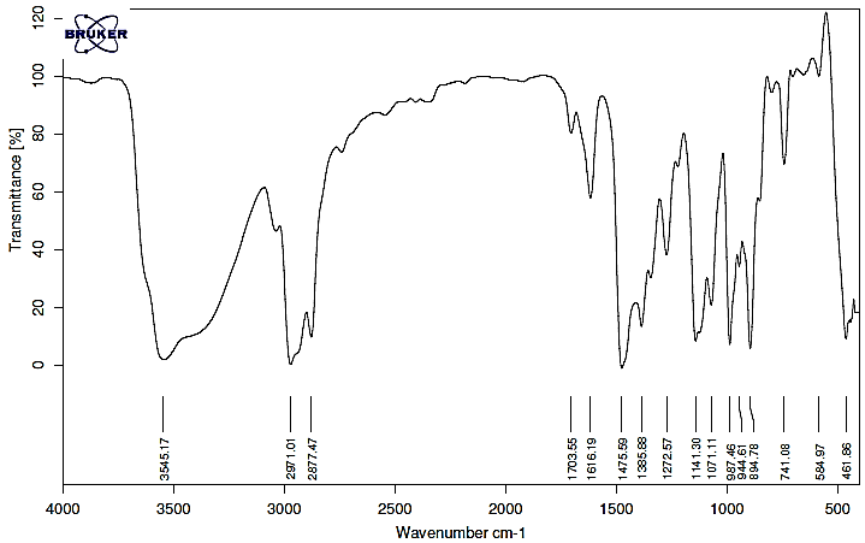

Figure SI 30 | FT-IR spectra of $[N_{1,1,4,C3OH}][FeCl_4]$.

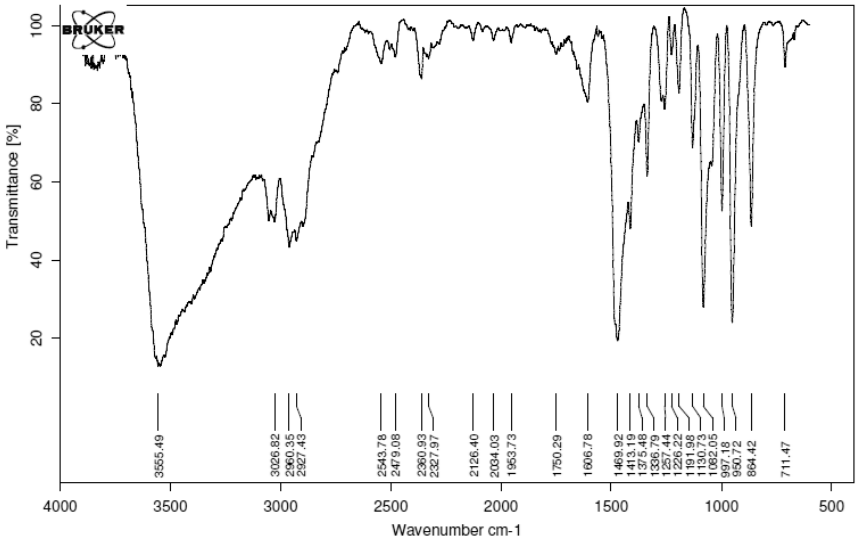

Figure SI 31 | FT-IR spectra of $[N_{1,1,1,C2OH}][FeCl_4]$.

2.2. Manganese (II)-based magnetic salts

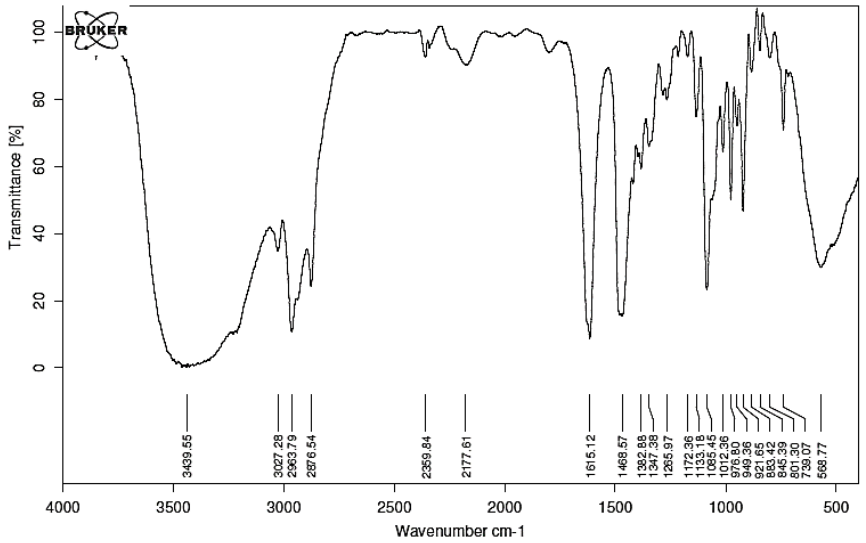

Figure SI 32 | FT-IR spectra of $[N_{1,1,4,C2OH}][MnCl_3]$.

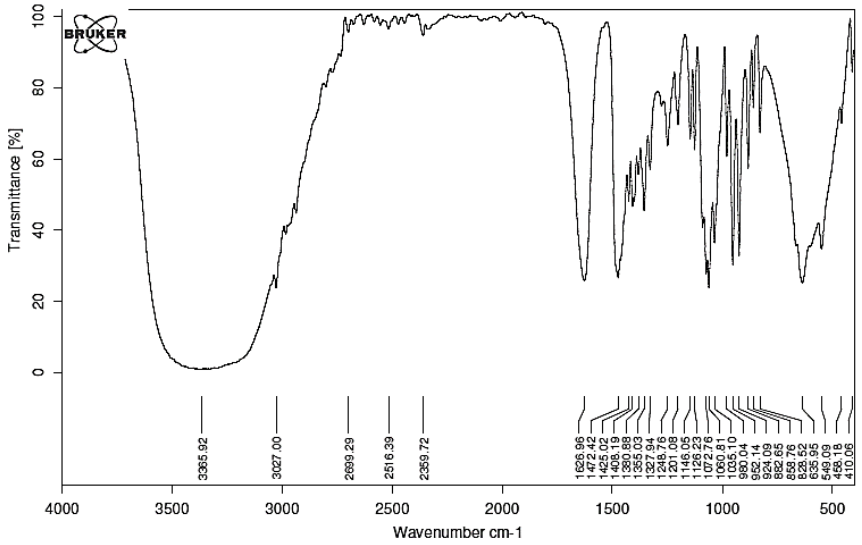

Figure SI 33 | FT-IR spectra of $[N_{1,1,C2OH,C2OH}][MnCl_3]$.

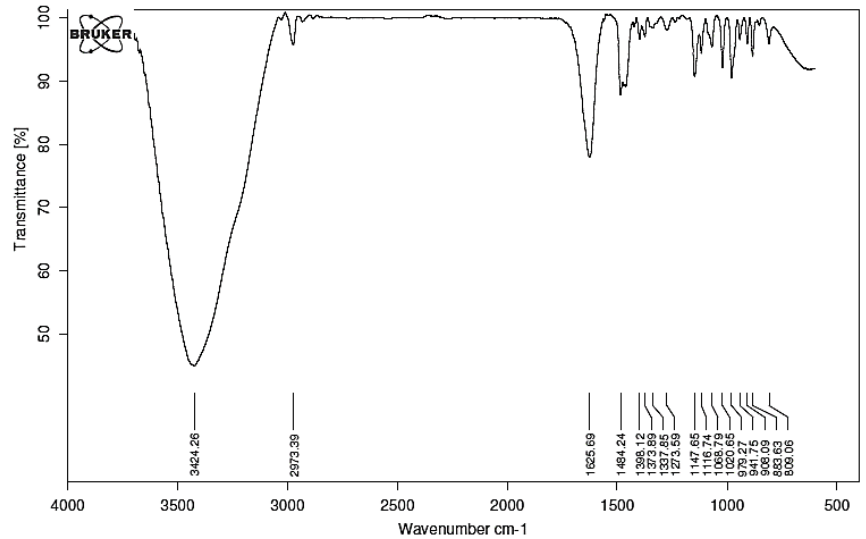

Figure SI 34 | FT-IR spectra of $[N_{1,1,2,C3OH}][MnCl_3]$.

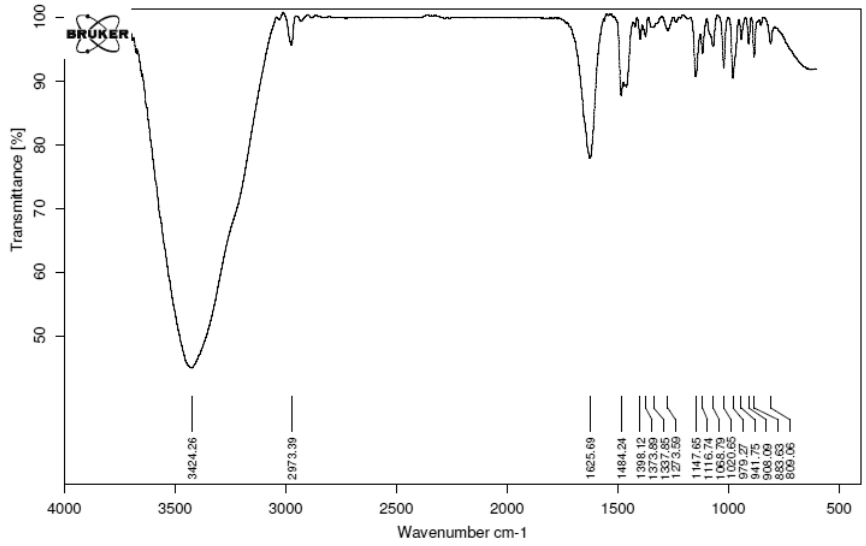

Figure SI 35 | FT-IR spectra of $[N_{1,1,4,C3OH}][MnCl_3]$.

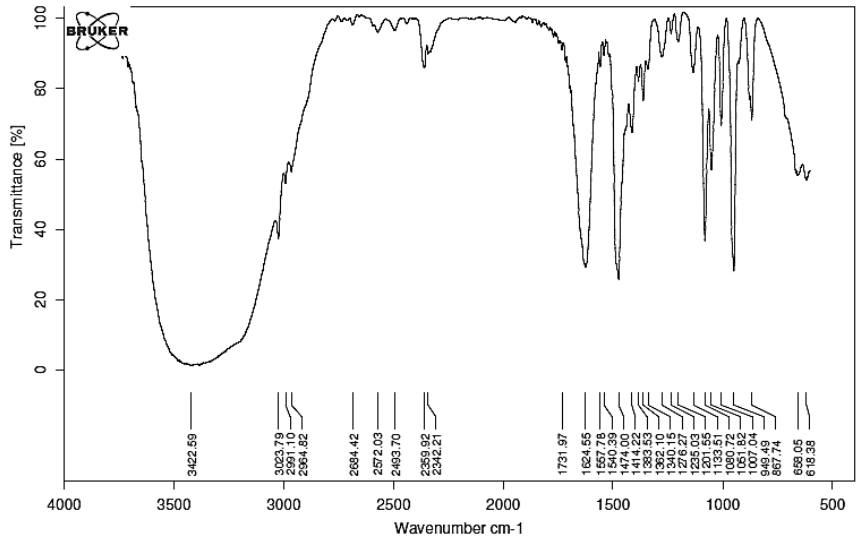

Figure SI 36 | FT-IR spectra of $[N_{1,1,1,C2OH}][MnCl_3]$.

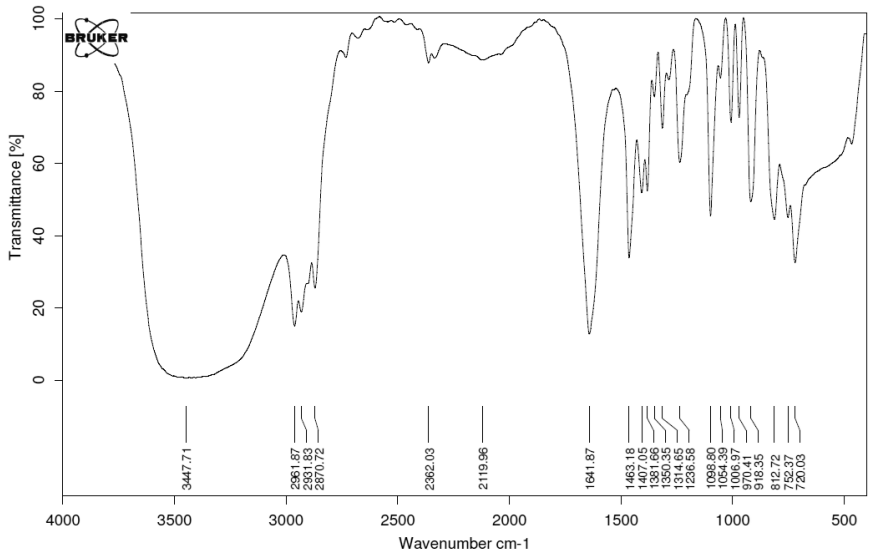

Figure SI 37 | FT-IR spectra of $[P_{4,4,4,4}][MnCl_3]$.

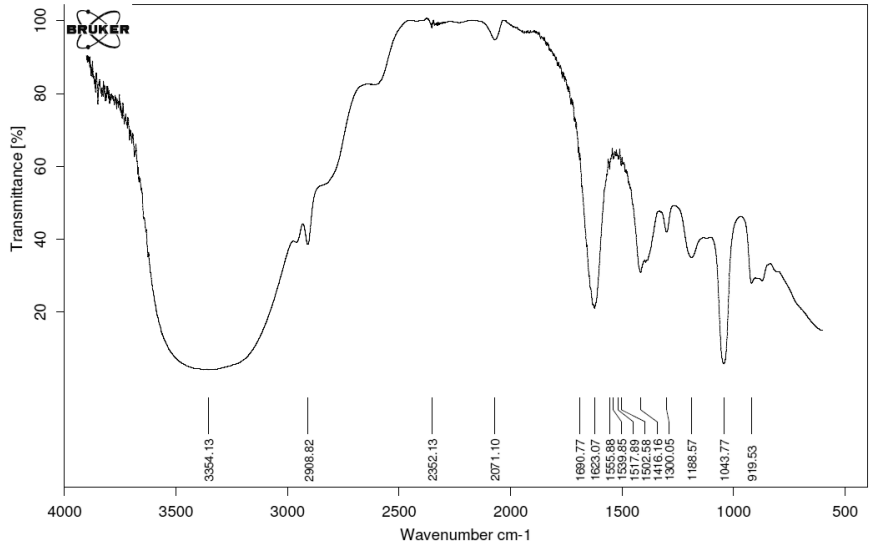

Figure SI 38 | FT-IR spectra of $[P_{C2OH,C2OH,C2OH,C2OH}][MnCl_3]$.

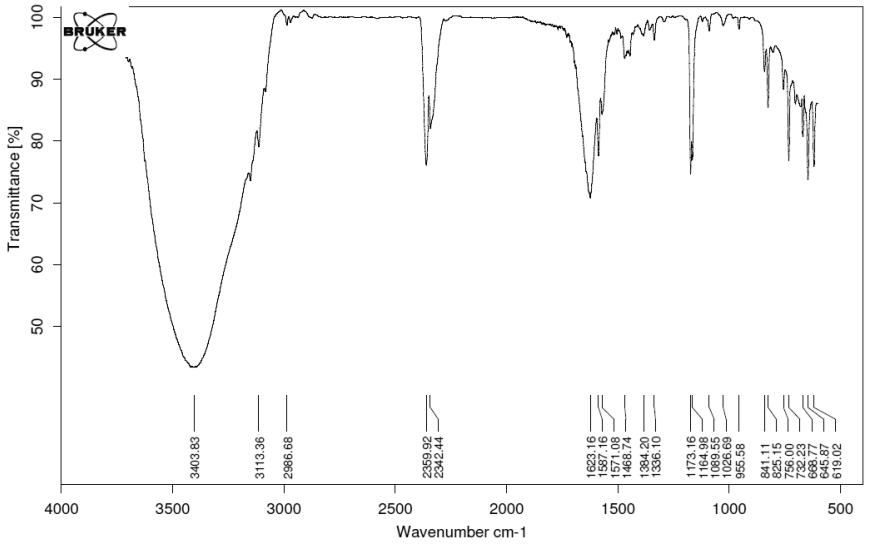

Figure SI 39 | FT-IR spectra of [C_2MIM][$MnCl_3$].

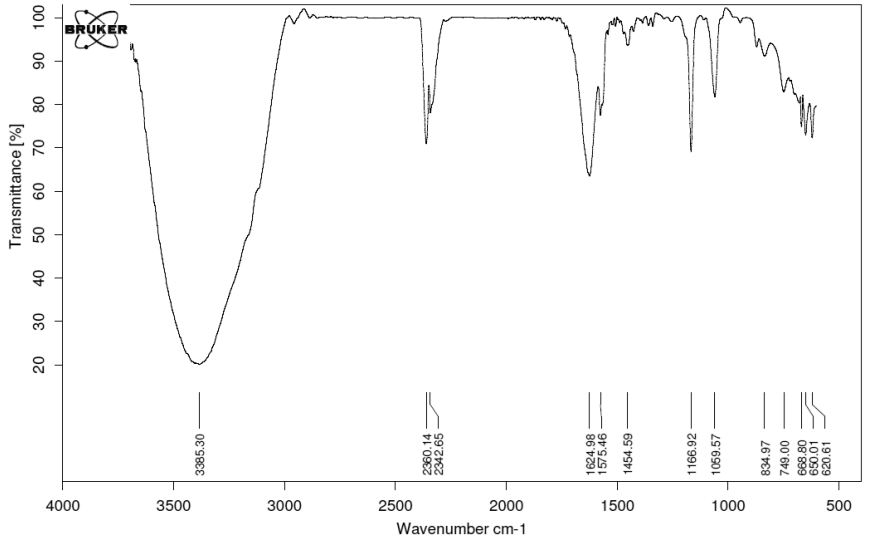

Figure SI 40 | FT-IR spectra of [C_2OHMIM][$MnCl_3$].

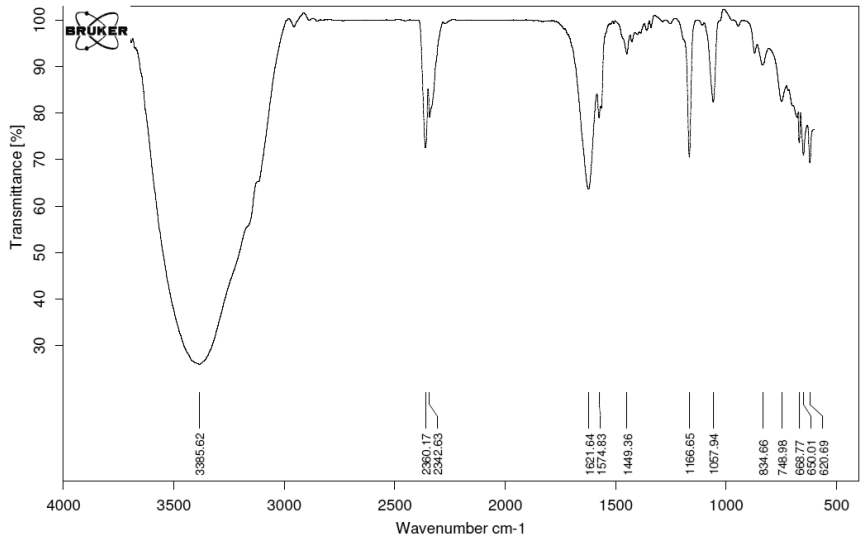

Figure SI 41 | FT-IR spectra of $[C_2OHDMIM][MnCl_3]$.

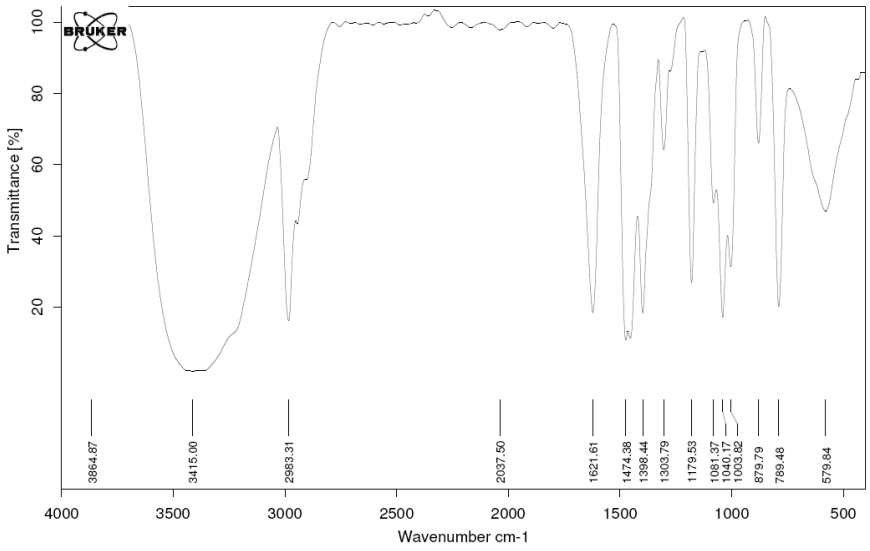

Figure SI 42 | FT-IR spectra of $[N_{2,2,2,2}][MnCl_3]$.

3. Single crystal x-ray crystallography

3.1. Single crystal X-ray analysis of $[N_{1,1,1,C2OH}][MnCl_3]$

Table SI 1 | Crystal data and structure refinement for the title compound.

Empirical formula	C5 H14 Cl3 Mn N O	
Formula weight	265.46	
Temperature	110(2) K	
Wavelength	0.71073 Å	
Crystal system	Orthorhombic	
Space group	Pna21	
Unit cell dimensions	a = 16.8451(9) Å	α= 90°.
	b = 8.3549(4) Å	β= 90°.
	c = 7.4374(4) Å	γ= 90°.
Volume	1046.73(9) $Å^3$	
Z	4	
Density (calculated)	1.685 Mg/m^3	
Absorption coefficient	1.977 mm^{-1}	
Crystal size	0.05 x 0.05 x 0.05 mm^3	
Reflections collected	15667	
Independent reflections	1864 [R(int) = 0.0263]	
Completeness to theta = 25.69°	99.7 %	
Refinement method	Full-matrix least-squares on F^2	
Data / restraints / parameters	1864 / 1 / 107	
Goodness-of-fit on F^2	1.134	
Final R indices [I>2sigma(I)]	R1 = 0.0144, wR2 = 0.0345	
R indices (all data)	R1 = 0.0148, wR2 = 0.0346	
Absolute structure parameter	0.010(12)	
Largest diff. peak and hole	0.185 and -0.447 $e.Å^{-3}$	

Table SI 2 | Atomic coordinates (x 10^4) and equivalent isotropic displacement parameters ($Å^2$x 10^3) for the title compound. U(eq) is defined as one third of the trace of the orthogonalized U^{ij} tensor.

	x	y	z	U(eq)
Mn(1)	5046(1)	4843(1)	3989(1)	6(1)
Cl(2)	5867(1)	6142(1)	6467(1)	8(1)
Cl(3)	4014(1)	4279(1)	6429(1)	10(1)
Cl(1)	5729(1)	2235(1)	4492(1)	9(1)
O(1)	4433(1)	7153(1)	3530(2)	10(1)
N(1)	3155(1)	9823(1)	4460(2)	9(1)
C(1)	4566(1)	8640(2)	4444(2)	11(1)
C(2)	4009(1)	9959(2)	3847(2)	11(1)
C(4)	3092(1)	9983(2)	6459(3)	16(1)
C(5)	2704(1)	11176(2)	3622(2)	16(1)
C(3)	2786(1)	8267(2)	3887(2)	15(1)

Table SI 3 | Bond lengths [Å] and angles [°] for the title compound.

Mn(1)-O(1)	2.2145(10)	O(1)-Mn(1)-Cl(2)	89.62(3)
		Cl(1)-Mn(1)-Cl(2)	90.742(14)
Mn(1)-Cl(1)	2.4928(4)	O(1)-Mn(1)-Cl(3)	87.33(3)
Mn(1)-Cl(2)	2.5477(4)	Cl(1)-Mn(1)-Cl(3)	92.633(14)
Mn(1)-Cl(3)	2.5562(4)	Cl(2)-Mn(1)-Cl(3)	86.222(15)
Mn(1)-Cl(2)#1	2.5610(4)	O(1)-Mn(1)-Cl(2)#1	83.54(3)
Mn(1)-Cl(3)#1	2.5828(5)	Cl(1)-Mn(1)-Cl(2)#1	96.095(14)
Cl(2)-Mn(1)#2	2.5611(4)	Cl(2)-Mn(1)-Cl(2)#1	173.151(9)
Cl(3)-Mn(1)#2	2.5828(5)	Cl(3)-Mn(1)-Cl(2)#1	93.021(14)
O(1)-C(1)	1.4338(17)	O(1)-Mn(1)-Cl(3)#1	85.68(3)
O(1)-H(1)	0.84(2)	Cl(1)-Mn(1)-Cl(3)#1	94.351(14)
N(1)-C(4)	1.496(2)	Cl(2)-Mn(1)-Cl(3)#1	94.537(14)
N(1)-C(5)	1.4979(18)	Cl(3)-Mn(1)-Cl(3)#1	172.964(10)
N(1)-C(3)	1.5022(18)	Cl(2)#1-Mn(1)-Cl(3)#1	85.390(15)
N(1)-C(2)	1.5135(18)	Mn(1)-Cl(2)-Mn(1)#2	93.828(11)
C(1)-C(2)	1.5149(19)	Mn(1)-Cl(3)-Mn(1)#2	93.108(11)
C(1)-H(1A)	0.9900	C(1)-O(1)-Mn(1)	127.52(9)
C(1)-H(1B)	0.9900	C(1)-O(1)-H(1)	112.4(13)
C(2)-H(2A)	0.9900	Mn(1)-O(1)-H(1)	108.7(13)
C(2)-H(2B)	0.9900	C(4)-N(1)-C(5)	108.10(12)
C(4)-H(4A)	0.9800	C(4)-N(1)-C(3)	109.31(12)
C(4)-H(4B)	0.9800	C(5)-N(1)-C(3)	109.02(12)
C(4)-H(4C)	0.9800	C(4)-N(1)-C(2)	111.08(12)
C(5)-H(5A)	0.9800	C(5)-N(1)-C(2)	107.40(12)
C(5)-H(5B)	0.9800	C(3)-N(1)-C(2)	111.82(11)
C(5)-H(5C)	0.9800	O(1)-C(1)-C(2)	113.22(12)
C(3)-H(3A)	0.9800	O(1)-C(1)-H(1A)	108.9
C(3)-H(3B)	0.9800	C(2)-C(1)-H(1A)	108.9
C(3)-H(3C)	0.9800	O(1)-C(1)-H(1B)	108.9
O(1)-Mn(1)-Cl(1)	179.63(3)	C(2)-C(1)-H(1B)	108.9

H(1A)-C(1)-H(1B)	107.7	N(1)-C(5)-H(5A)	109.5
N(1)-C(2)-C(1)	116.52(12)	N(1)-C(5)-H(5B)	109.5
N(1)-C(2)-H(2A)	108.2	H(5A)-C(5)-H(5B)	109.5
C(1)-C(2)-H(2A)	108.2	N(1)-C(5)-H(5C)	109.5
N(1)-C(2)-H(2B)	108.2	H(5A)-C(5)-H(5C)	109.5
C(1)-C(2)-H(2B)	108.2	H(5B)-C(5)-H(5C)	109.5
H(2A)-C(2)-H(2B)	107.3	N(1)-C(3)-H(3A)	109.5
N(1)-C(4)-H(4A)	109.5	N(1)-C(3)-H(3B)	109.5
N(1)-C(4)-H(4B)	109.5	H(3A)-C(3)-H(3B)	109.5
H(4A)-C(4)-H(4B)	109.5	N(1)-C(3)-H(3C)	109.5
N(1)-C(4)-H(4C)	109.5	H(3A)-C(3)-H(3C)	109.5
H(4A)-C(4)-H(4C)	109.5	H(3B)-C(3)-H(3C)	109.5
H(4B)-C(4)-H(4C)	109.5		

Symmetry transformations used to generate equivalent atoms:

#1 -x+1,-y+1,z-1/2

#2 -x+1,-y+1,z+1/

Table SI 4 | Torsion angles [°] for the title compound.

O(1)-Mn(1)-Cl(2)-Mn(1)#2	96.53(3)
Cl(1)-Mn(1)-Cl(2)-Mn(1)#2	-83.404(13)
Cl(3)-Mn(1)-Cl(2)-Mn(1)#2	9.185(11)
Cl(2)#1-Mn(1)-Cl(2)-Mn(1)#2	93.05(14)
Cl(3)#1-Mn(1)-Cl(2)-Mn(1)#2	-177.828(14)
O(1)-Mn(1)-Cl(3)-Mn(1)#2	-98.90(3)
Cl(1)-Mn(1)-Cl(3)-Mn(1)#2	81.470(14)
Cl(2)-Mn(1)-Cl(3)-Mn(1)#2	-9.100(11)
Cl(2)#1-Mn(1)-Cl(3)-Mn(1)#2	177.719(14)
Cl(3)#1-Mn(1)-Cl(3)-Mn(1)#2	-105.54(13)
Cl(1)-Mn(1)-O(1)-C(1)	171(100)
Cl(2)-Mn(1)-O(1)-C(1)	0.74(12)
Cl(3)-Mn(1)-O(1)-C(1)	86.98(12)
Cl(2)#1-Mn(1)-O(1)-C(1)	-179.68(12)
Cl(3)#1-Mn(1)-O(1)-C(1)	-93.84(12)
Mn(1)-O(1)-C(1)-C(2)	-177.05(9)
C(4)-N(1)-C(2)-C(1)	65.72(16)
C(5)-N(1)-C(2)-C(1)	-176.27(13)
C(3)-N(1)-C(2)-C(1)	-56.71(18)
O(1)-C(1)-C(2)-N(1)	72.51(18)

Table SI 5 | Hydrogen bonds for the title compound [Å and °].

D-H	d(D-H)	d(H..A)	<DHA	d(D..A)	A
O1-H1	0.843	2.218	174.92	3.059	Cl1 [-x+1, -y+1, z-1/2]

3.2. Single crystal X-ray analysis of $[N_{1,1,C2OH,C2OH}][MnCl_3]$

Table SI 6 | Crystal data and structure refinement for the title compound.

Empirical formula	C18 H47 Cl9 Mn3 N3 O6	
Formula weight	885.45	
Temperature	110(2) K	
Wavelength	0.71073 Å	
Crystal system	Monoclinic	
Space group	P 21	
Unit cell dimensions	a = 8.4105(8) Å	□= 90°.
	b = 9.0674(9) Å	□= 100.576(3)°.
	c = 22.428(2) Å	□ = 90°.
Volume	1681.3(3) Å3	
Z	2	
Density (calculated)	1.749 Mg/m3	
Absorption coefficient	1.862 mm-1	
F(000)	904	
Crystal size	0.400 x 0.200 x 0.160 mm3	
Theta range for data collection	2.785 to 25.347°.	
Index ranges	-10<=h<=10, -10<=k<=10, -27<=l<=27	
Reflections collected	20269	
Independent reflections	5564 [R(int) = 0.0402]	
Completeness to theta = 25.242°	94.5 %	
Refinement method	Full-matrix least-squares on F2	
Data / restraints / parameters	5564 / 148 / 368	
Goodness-of-fit on F2	1.330	
Final R indices [I>2sigma(I)]	R1 = 0.0495, wR2 = 0.1377	
R indices (all data)	R1 = 0.0681, wR2 = 0.1411	
Absolute structure parameter	0.078(9)	
Extinction coefficient	n/a	
Largest diff. peak and hole	0.276 and -0.301 e.Å-3	

Table SI 7 | Atomic coordinates (x 10^4) and equivalent isotropic displacement parameters ($Å^2$x 10^3) for the title compound. U(eq) is defined as one third of the trace of the orthogonalized U^{ij} tensor.

	x	y	z	U(eq)
C(1)	4757(18)	3864(19)	-1761(7)	9(3)
C(3)	8088(18)	3874(19)	1564(7)	9(3)
C(4)	9050(20)	7441(19)	4831(7)	10(3)
C(5)	8573(17)	8852(18)	5092(6)	5(3)
C(6)	6584(19)	2710(19)	-2421(7)	12(4)
C(7)	6758(18)	7689(17)	5759(6)	5(3)
C(8)	5599(17)	8765(17)	4769(6)	3(2)
C(9)	9850(20)	5404(17)	1089(7)	11(4)
C(10)	6530(20)	5403(19)	-2249(8)	15(4)
C(11)	7730(20)	3730(20)	-1438(7)	17(4)
C(12)	7656(19)	2442(18)	1842(7)	10(3)
C(14)	8726(17)	2709(19)	309(7)	9(3)
C(15)	6810(20)	10388(17)	5585(8)	13(4)
C(16)	7932(19)	7690(20)	6356(7)	12(4)
C(17)	4289(19)	2434(19)	-1504(7)	10(4)
C(18)	9929(19)	2711(18)	915(7)	10(4)
C(19)	11070(19)	3760(20)	1903(7)	16(4)
C(20)	5412(18)	2714(19)	-3016(7)	12(4)
N(3)	6364(15)	3905(16)	-1971(5)	7(3)
N(5)	9715(15)	3906(16)	1360(6)	9(3)
N(6)	6941(14)	8902(15)	5307(5)	7(3)
O(1)	9537(13)	7240(13)	6299(5)	11(2)
O(2)	8507(13)	2237(13)	2444(5)	10(2)
O(3)	7128(13)	2266(14)	367(5)	11(2)
O(4)	5176(13)	2236(13)	-882(5)	11(2)
O(6)	8156(14)	7244(15)	4219(5)	11(3)
O(10)	3783(13)	2265(12)	-2967(5)	9(2)
Cl(1)	4046(5)	4000(5)	960(2)	10(1)

Cl(2)	7379(5)	4000(5)	4294(2)	10(1)
Cl(3)	9448(5)	5506(4)	3129(2)	10(1)
Cl(4)	7210(5)	10505(4)	3537(2)	10(1)
Cl(5)	1910(5)	3980(5)	-567(2)	13(1)
Cl(6)	9290(4)	8997(5)	2373(2)	10(1)
Cl(7)	5244(5)	3979(5)	2765(2)	12(1)
Cl(8)	11426(5)	8980(5)	3900(2)	13(1)
Cl(9)	3878(5)	508(4)	203(2)	10(1)
Mn(1)	8742(3)	8156(3)	3363(1)	7(1)
Mn(2)	7925(3)	3157(3)	3303(1)	7(1)
Mn(3)	4593(3)	3154(3)	-30(1)	7(1)

Table SI 8 | Bond lengths [Å] and angles [°].

C(1)-C(17)	1.50(2)	C(9)-H(9C)	0.9800
C(1)-N(3)	1.511(19)	C(10)-N(3)	1.51(2)
C(1)-H(1A)	0.9900	C(10)-H(10A)	0.9800
C(1)-H(1B)	0.9900	C(10)-H(10B)	0.9800
C(3)-C(12)	1.51(2)	C(10)-H(10C)	0.9800
C(3)-N(5)	1.520(19)	C(11)-N(3)	1.505(19)
C(3)-H(3A)	0.9900	C(11)-H(11A)	0.9800
C(3)-H(3B)	0.9900	C(11)-H(11B)	0.9800
C(4)-O(6)	1.449(19)	C(11)-H(11C)	0.9800
C(4)-C(5)	1.49(2)	C(12)-O(2)	1.420(18)
C(4)-H(4A)	0.9900	C(12)-H(12A)	0.9900
C(4)-H(4B)	0.9900	C(12)-H(12B)	0.9900
C(5)-N(6)	1.536(18)	C(14)-O(3)	1.431(18)
C(5)-H(5A)	0.9900	C(14)-C(18)	1.54(2)
C(5)-H(5B)	0.9900	C(14)-H(14A)	0.9900
C(6)-C(20)	1.51(2)	C(14)-H(14B)	0.9900
C(6)-N(3)	1.51(2)	C(15)-N(6)	1.497(19)
C(6)-H(6A)	0.9900	C(15)-H(15A)	0.9800
C(6)-H(6B)	0.9900	C(15)-H(15B)	0.9800
C(7)-C(16)	1.51(2)	C(15)-H(15C)	0.9800
C(7)-N(6)	1.523(19)	C(16)-O(1)	1.438(19)
C(7)-H(7A)	0.9900	C(16)-H(16A)	0.9900
C(7)-H(7B)	0.9900	C(16)-H(16B)	0.9900
C(8)-N(6)	1.498(17)	C(17)-O(4)	1.467(18)
C(8)-H(8A)	0.9800	C(17)-H(17A)	0.9900
C(8)-H(8B)	0.9800	C(17)-H(17B)	0.9900
C(8)-H(8C)	0.9800	C(18)-N(5)	1.51(2)
C(9)-N(5)	1.50(2)	C(18)-H(18A)	0.9900
C(9)-H(9A)	0.9800	C(18)-H(18B)	0.9900
C(9)-H(9B)	0.9800	C(19)-N(5)	1.513(19)

C(19)-H(19A)	0.9800	C(17)-C(1)-H(1A)	108.1
C(19)-H(19B)	0.9800	N(3)-C(1)-H(1A)	108.1
C(19)-H(19C)	0.9800	C(17)-C(1)-H(1B)	108.1
C(20)-O(10)	1.453(18)	N(3)-C(1)-H(1B)	108.1
C(20)-H(20A)	0.9900	H(1A)-C(1)-H(1B)	107.3
C(20)-H(20B)	0.9900	C(12)-C(3)-N(5)	116.0(13)
O(1)-Mn(2)#1	2.312(11)	C(12)-C(3)-H(3A)	108.3
O(2)-Mn(2)	2.234(11)	N(5)-C(3)-H(3A)	108.3
O(2)-H(20)	0.84(3)	C(12)-C(3)-H(3B)	108.3
O(3)-Mn(3)	2.300(11)	N(5)-C(3)-H(3B)	108.3
O(3)-H(30)	0.88(19)	H(3A)-C(3)-H(3B)	107.4
O(4)-Mn(3)	2.219(11)	O(6)-C(4)-C(5)	110.4(13)
O(4)-H(40)	0.84(3)	O(6)-C(4)-H(4A)	109.6
O(6)-Mn(1)	2.228(11)	C(5)-C(4)-H(4A)	109.6
O(6)-H(600)	0.71(17)	O(6)-C(4)-H(4B)	109.6
O(10)-Mn(1)#2	2.293(11)	C(5)-C(4)-H(4B)	109.6
O(10)-H(100)	0.87(3)	H(4A)-C(4)-H(4B)	108.1
Cl(1)-Mn(3)	2.471(4)	C(4)-C(5)-N(6)	117.8(14)
Cl(2)-Mn(2)	2.472(4)	C(4)-C(5)-H(5A)	107.9
Cl(3)-Mn(2)	2.552(4)	N(6)-C(5)-H(5A)	107.9
Cl(3)-Mn(1)	2.553(5)	C(4)-C(5)-H(5B)	107.9
Cl(4)-Mn(1)	2.556(4)	N(6)-C(5)-H(5B)	107.8
Cl(4)-Mn(2)#3	2.556(5)	H(5A)-C(5)-H(5B)	107.2
Cl(5)-Mn(3)	2.470(4)	C(20)-C(6)-N(3)	116.6(13)
Cl(6)-Mn(1)	2.471(4)	C(20)-C(6)-H(6A)	108.2
Cl(7)-Mn(2)	2.469(5)	N(3)-C(6)-H(6A)	108.1
Cl(8)-Mn(1)	2.471(4)	C(20)-C(6)-H(6B)	108.1
Cl(9)-Mn(3)	2.551(4)	N(3)-C(6)-H(6B)	108.1
Cl(9)-Mn(3)#2	2.559(4)	H(6A)-C(6)-H(6B)	107.3
		C(16)-C(7)-N(6)	117.4(12)
C(17)-C(1)-N(3)	116.9(14)	C(16)-C(7)-H(7A)	107.9

N(6)-C(7)-H(7A)	107.9	O(2)-C(12)-H(12B)	109.0
C(16)-C(7)-H(7B)	107.9	C(3)-C(12)-H(12B)	109.0
N(6)-C(7)-H(7B)	107.9	H(12A)-C(12)-H(12B)	107.8
H(7A)-C(7)-H(7B)	107.2	O(3)-C(14)-C(18)	113.4(12)
N(6)-C(8)-H(8A)	109.5	O(3)-C(14)-H(14A)	108.9
N(6)-C(8)-H(8B)	109.5	C(18)-C(14)-H(14A)	108.9
H(8A)-C(8)-H(8B)	109.5	O(3)-C(14)-H(14B)	108.9
N(6)-C(8)-H(8C)	109.5	C(18)-C(14)-H(14B)	108.9
H(8A)-C(8)-H(8C)	109.5	H(14A)-C(14)-H(14B)	107.7
H(8B)-C(8)-H(8C)	109.5	N(6)-C(15)-H(15A)	109.5
N(5)-C(9)-H(9A)	109.5	N(6)-C(15)-H(15B)	109.5
N(5)-C(9)-H(9B)	109.5	H(15A)-C(15)-H(15B)	109.5
H(9A)-C(9)-H(9B)	109.5	N(6)-C(15)-H(15C)	109.5
N(5)-C(9)-H(9C)	109.5	H(15A)-C(15)-H(15C)	109.5
H(9A)-C(9)-H(9C)	109.5	H(15B)-C(15)-H(15C)	109.5
H(9B)-C(9)-H(9C)	109.5	O(1)-C(16)-C(7)	113.0(13)
N(3)-C(10)-H(10A)	109.5	O(1)-C(16)-H(16A)	109.0
N(3)-C(10)-H(10B)	109.5	C(7)-C(16)-H(16A)	109.0
H(10A)-C(10)-H(10B)	109.5	O(1)-C(16)-H(16B)	109.0
N(3)-C(10)-H(10C)	109.5	C(7)-C(16)-H(16B)	109.0
H(10A)-C(10)-H(10C)	109.5	H(16A)-C(16)-H(16B)	107.8
H(10B)-C(10)-H(10C)	109.5	O(4)-C(17)-C(1)	110.3(12)
N(3)-C(11)-H(11A)	109.5	O(4)-C(17)-H(17A)	109.6
N(3)-C(11)-H(11B)	109.5	C(1)-C(17)-H(17A)	109.6
H(11A)-C(11)-H(11B)	109.5	O(4)-C(17)-H(17B)	109.6
N(3)-C(11)-H(11C)	109.5	C(1)-C(17)-H(17B)	109.6
H(11A)-C(11)-H(11C)	109.5	H(17A)-C(17)-H(17B)	108.1
H(11B)-C(11)-H(11C)	109.5	N(5)-C(18)-C(14)	116.6(12)
O(2)-C(12)-C(3)	112.8(13)	N(5)-C(18)-H(18A)	108.2
O(2)-C(12)-H(12A)	109.0	C(14)-C(18)-H(18A)	108.2
C(3)-C(12)-H(12A)	109.0	N(5)-C(18)-H(18B)	108.1

C(14)-C(18)-H(18B)	108.1	C(7)-N(6)-C(5)	113.1(12)
H(18A)-C(18)-H(18B)	107.3	C(16)-O(1)-Mn(2)#1	132.7(10)
N(5)-C(19)-H(19A)	109.5	C(12)-O(2)-Mn(2)	128.2(10)
N(5)-C(19)-H(19B)	109.5	C(12)-O(2)-H(20)	115(10)
H(19A)-C(19)-H(19B)	109.5	Mn(2)-O(2)-H(20)	105(10)
N(5)-C(19)-H(19C)	109.5	C(14)-O(3)-Mn(3)	133.3(10)
H(19A)-C(19)-H(19C)	109.5	C(14)-O(3)-H(30)	102(10)
H(19B)-C(19)-H(19C)	109.5	Mn(3)-O(3)-H(30)	112(10)
O(10)-C(20)-C(6)	113.8(13)	C(17)-O(4)-Mn(3)	128.2(9)
O(10)-C(20)-H(20A)	108.8	C(17)-O(4)-H(40)	95(10)
C(6)-C(20)-H(20A)	108.8	Mn(3)-O(4)-H(40)	124(10)
O(10)-C(20)-H(20B)	108.8	C(4)-O(6)-Mn(1)	127.8(10)
C(6)-C(20)-H(20B)	108.8	C(4)-O(6)-H(600)	104(10)
H(20A)-C(20)-H(20B)	107.7	Mn(1)-O(6)-H(600)	110(10)
C(11)-N(3)-C(10)	107.9(13)	C(20)-O(10)-Mn(1)#2	133.7(9)
C(11)-N(3)-C(1)	110.1(12)	C(20)-O(10)-H(100)	100(10)
C(10)-N(3)-C(1)	107.8(13)	Mn(1)#2-O(10)-H(100)	117(10)
C(11)-N(3)-C(6)	106.6(12)	Mn(2)-Cl(3)-Mn(1)	127.74(18)
C(10)-N(3)-C(6)	109.7(12)	Mn(1)-Cl(4)-Mn(2)#3	127.46(18)
C(1)-N(3)-C(6)	114.6(13)	Mn(3)-Cl(9)-Mn(3)#2	127.54(16)
C(9)-N(5)-C(18)	110.8(12)	O(6)-Mn(1)-O(10)#4	82.4(4)
C(9)-N(5)-C(19)	107.8(12)	O(6)-Mn(1)-Cl(8)	91.1(3)
C(18)-N(5)-C(19)	107.7(12)	O(10)#4-Mn(1)-Cl(8)	173.4(3)
C(9)-N(5)-C(3)	106.2(13)	O(6)-Mn(1)-Cl(6)	175.5(4)
C(18)-N(5)-C(3)	114.1(13)	O(10)#4-Mn(1)-Cl(6)	94.2(3)
C(19)-N(5)-C(3)	110.1(12)	Cl(8)-Mn(1)-Cl(6)	92.33(15)
C(15)-N(6)-C(8)	108.0(12)	O(6)-Mn(1)-Cl(3)	85.7(4)
C(15)-N(6)-C(7)	110.5(11)	O(10)#4-Mn(1)-Cl(3)	79.8(3)
C(8)-N(6)-C(7)	108.8(11)	Cl(8)-Mn(1)-Cl(3)	99.11(16)
C(15)-N(6)-C(5)	107.0(12)	Cl(6)-Mn(1)-Cl(3)	90.94(15)
C(8)-N(6)-C(5)	109.3(10)	O(6)-Mn(1)-Cl(4)	88.9(4)

O(10)#4-Mn(1)-Cl(4)	84.0(3)	Cl(2)-Mn(2)-Cl(4)#6	90.93(15)
Cl(8)-Mn(1)-Cl(4)	96.59(16)	Cl(3)-Mn(2)-Cl(4)#6	163.75(18)
Cl(6)-Mn(1)-Cl(4)	93.60(15)	O(4)-Mn(3)-O(3)	82.3(4)
Cl(3)-Mn(1)-Cl(4)	163.46(18)	O(4)-Mn(3)-Cl(5)	91.2(3)
O(2)-Mn(2)-O(1)#5	82.3(4)	O(3)-Mn(3)-Cl(5)	173.5(3)
O(2)-Mn(2)-Cl(7)	90.9(3)	O(4)-Mn(3)-Cl(1)	175.4(3)
O(1)#5-Mn(2)-Cl(7)	173.2(3)	O(3)-Mn(3)-Cl(1)	94.1(3)
O(2)-Mn(2)-Cl(2)	175.5(3)	Cl(5)-Mn(3)-Cl(1)	92.31(15)
O(1)#5-Mn(2)-Cl(2)	94.2(3)	O(4)-Mn(3)-Cl(9)	85.5(3)
Cl(7)-Mn(2)-Cl(2)	92.42(15)	O(3)-Mn(3)-Cl(9)	80.1(3)
O(2)-Mn(2)-Cl(3)	89.1(3)	Cl(5)-Mn(3)-Cl(9)	99.00(15)
O(1)#5-Mn(2)-Cl(3)	84.6(3)	Cl(1)-Mn(3)-Cl(9)	90.98(15)
Cl(7)-Mn(2)-Cl(3)	96.45(16)	O(4)-Mn(3)-Cl(9)#4	89.2(3)
Cl(2)-Mn(2)-Cl(3)	93.45(15)	O(3)-Mn(3)-Cl(9)#4	84.0(3)
O(2)-Mn(2)-Cl(4)#6	85.6(3)	Cl(5)-Mn(3)-Cl(9)#4	96.49(15)
O(1)#5-Mn(2)-Cl(4)#6	79.5(3)	Cl(1)-Mn(3)-Cl(9)#4	93.39(15)
Cl(7)-Mn(2)-Cl(4)#6	98.99(16)	Cl(9)-Mn(3)-Cl(9)#4	163.72(12)

Symmetry transformations used to generate equivalent atoms:

#1 -x+2,y+1/2,-z+1 #2 -x+1,y-1/2,-z #3 x,y+1,z

#4 -x+1,y+1/2,-z #5 -x+2,y-1/2,-z+1 #6 x,y-1,z

Table SI 9 | Torsion angles [°] for the title compound.O(6)-C(4)-C(5)-N(6) 76.2(16)

N(5)-C(3)-C(12)-O(2)	75.6(17)	C(12)-C(3)-N(5)-C(18)	56.2(17)
N(6)-C(7)-C(16)-O(1)	-72.4(18)	C(12)-C(3)-N(5)-C(19)	-65.0(17)
N(3)-C(1)-C(17)-O(4)	77.2(16)	C(16)-C(7)-N(6)-C(15)	-57.6(17)
O(3)-C(14)-C(18)-N(5)	-71.3(18)	C(16)-C(7)-N(6)-C(8)	-176.0(12)
N(3)-C(6)-C(20)-O(10)	-71.2(18)	C(16)-C(7)-N(6)-C(5)	62.4(17)
C(17)-C(1)-N(3)-C(11)	-66.4(18)	C(4)-C(5)-N(6)-C(15)	176.2(13)
C(17)-C(1)-N(3)-C(10)	176.2(12)	C(4)-C(5)-N(6)-C(8)	-67.1(16)
C(17)-C(1)-N(3)-C(6)	53.8(17)	C(4)-C(5)-N(6)-C(7)	54.2(16)
C(20)-C(6)-N(3)-C(11)	-176.3(13)	C(7)-C(16)-O(1)-Mn(2)#1	135.7(11)
C(20)-C(6)-N(3)-C(10)	-59.8(17)	C(3)-C(12)-O(2)-Mn(2)	82.3(15)
C(20)-C(6)-N(3)-C(1)	61.6(18)	C(18)-C(14)-O(3)-Mn(3)	136.2(12)
C(14)-C(18)-N(5)-C(9)	-59.1(17)	C(1)-C(17)-O(4)-Mn(3)	82.7(14)
C(14)-C(18)-N(5)-C(19)	-176.8(13)	C(5)-C(4)-O(6)-Mn(1)	84.0(15)
C(14)-C(18)-N(5)-C(3)	60.7(17)	C(6)-C(20)-O(10)-Mn(1)#2	135.7(12
C(12)-C(3)-N(5)-C(9)	178.6(13)		

Symmetry transformations used to generate equivalent atoms:

#1 -x+2,y+1/2,-z+1 #2 -x+1,y-1/2,-z #3 x,y+1,z

#4 -x+1,y+1/2,-z #5 -x+2,y-1/2,-z+1 #6 x,y-1,z

Table SI 10 | Hydrogen bonds for the title compound [Å and °].

D-H...A	d(D-H)	d(H...A)	d(D...A)	<(DHA)
C(3)-H(3B)...Cl(1)	0.99	2.64	3.423(15)	136.2
C(3)-H(3B)...O(3)	0.99	2.50	3.030(19)	113.0
C(3)-H(3A)...Cl(3)	0.99	2.96	3.788(16)	141.9
C(4)-H(4A)...Cl(2)#1	0.99	2.91	3.567(17)	124.6
C(4)-H(4A)...Cl(8)	0.99	2.84	3.442(17)	120.2
C(1)-H(1A)...Cl(9)#4	0.99	2.92	3.777(16)	145.0
C(1)-H(1B)...Cl(6)#2	0.99	2.64	3.431(16)	136.6
C(5)-H(5A)...Cl(4)	0.99	2.93	3.776(15)	144.5
C(5)-H(5B)...Cl(2)#1	0.99	2.64	3.434(15)	136.9
C(5)-H(5B)...O(1)	0.99	2.55	3.052(18)	111.0
C(6)-H(6A)...Cl(6)#7	0.99	2.73	3.644(17)	154.1
C(7)-H(7A)...Cl(2)#8	0.99	2.75	3.658(15)	152.3
C(8)-H(8A)...Cl(4)	0.98	2.77	3.652(15)	149.8
C(8)-H(8B)...Cl(2)#8	0.98	2.65	3.559(14)	154.5
C(8)-H(8C)...O(6)	0.98	2.46	3.004(19)	114.5
C(9)-H(9B)...Cl(9)#4	0.98	2.89	3.861(17)	170.5
C(9)-H(9C)...Cl(1)#9	0.98	2.98	3.812(17)	143.9
C(10)-H(10A)...Cl(6)#7	0.98	2.96	3.799(18)	144.7
C(10)-H(10C)...Cl(4)#2	0.98	2.89	3.861(18)	169.9
C(11)-H(11A)...Cl(6)#7	0.98	2.64	3.560(18)	156.2
C(11)-H(11B)...O(4)	0.98	2.44	3.00(2)	115.8
C(11)-H(11C)...Cl(9)#4	0.98	2.80	3.668(18)	148.1
C(12)-H(12A)...Cl(1)	0.99	2.94	3.594(16)	124.5
C(12)-H(12A)...Cl(7)	0.99	2.85	3.447(17)	119.6
C(14)-H(14A)...Cl(9)#4	0.99	2.69	3.411(17)	129.8
C(15)-H(15B)...Cl(3)#1	0.98	2.89	3.858(18)	171.2
C(16)-H(16A)...Cl(3)#1	0.99	2.71	3.432(17)	129.9
C(17)-H(17A)...Cl(5)	0.99	2.86	3.453(16)	119.0
C(17)-H(17A)...Cl(6)#2	0.99	2.91	3.565(16)	124.9
C(18)-H(18B)...Cl(1)#9	0.99	2.72	3.639(16)	153.7
C(19)-H(19A)...O(2)	0.98	2.41	3.00(2)	117.8
C(19)-H(19B)...Cl(3)	0.98	2.80	3.650(17)	145.6
C(19)-H(19C)...Cl(1)#9	0.98	2.65	3.567(17)	155.2
C(20)-H(20A)...Cl(4)#2	0.99	2.70	3.419(17)	129.3
C(1)-H(1A)...Cl(9)#4	0.99	2.92	3.777(16)	145.0
C(1)-H(1B)...O(10)	0.99	2.55	3.046(19)	110.8
C(1)-H(1B)...Cl(6)#2	0.99	2.64	3.431(16)	136.6
C(3)-H(3B)...O(3)	0.99	2.50	3.030(19)	113.0
C(3)-H(3B)...Cl(1)	0.99	2.64	3.423(15)	136.2

C(3)-H(3A)...Cl(3)	0.99	2.96	3.788(16)	141.9
C(4)-H(4A)...Cl(2)#1	0.99	2.91	3.567(17)	124.6
C(4)-H(4A)...Cl(8)	0.99	2.84	3.442(17)	120.2
C(5)-H(5A)...Cl(4)	0.99	2.93	3.776(15)	144.5
C(5)-H(5B)...O(1)	0.99	2.55	3.052(18)	111.0
C(5)-H(5B)...Cl(2)#1	0.99	2.64	3.434(15)	136.9
C(6)-H(6A)...Cl(6)#7	0.99	2.73	3.644(17)	154.1
C(7)-H(7A)...Cl(2)#8	0.99	2.75	3.658(15)	152.3
C(8)-H(8A)...Cl(4)	0.98	2.77	3.652(15)	149.8
C(8)-H(8B)...Cl(2)#8	0.98	2.65	3.559(14)	154.5
C(8)-H(8C)...O(6)	0.98	2.46	3.004(19)	114.5
C(9)-H(9B)...Cl(9)#4	0.98	2.89	3.861(17)	170.5
C(9)-H(9C)...Cl(1)#9	0.98	2.98	3.812(17)	143.9
C(10)-H(10A)...Cl(6)#7	0.98	2.96	3.799(18)	144.7
C(10)-H(10C)...Cl(4)#2	0.98	2.89	3.861(18)	169.9
C(11)-H(11A)...Cl(6)#7	0.98	2.64	3.560(18)	156.2
C(11)-H(11B)...O(4)	0.98	2.44	3.00(2)	115.8
C(11)-H(11C)...Cl(9)#4	0.98	2.80	3.668(18)	148.1
C(12)-H(12A)...Cl(1)	0.99	2.94	3.594(16)	124.5
C(12)-H(12A)...Cl(7)	0.99	2.85	3.447(17)	119.6
C(14)-H(14A)...Cl(9)#4	0.99	2.69	3.411(17)	129.8
C(15)-H(15B)...Cl(3)#1	0.98	2.89	3.858(18)	171.2
C(15)-H(15C)...Cl(2)#8	0.98	2.96	3.802(18)	144.0
C(16)-H(16A)...Cl(3)#1	0.99	2.71	3.432(17)	129.9
C(17)-H(17A)...Cl(5)	0.99	2.86	3.453(16)	119.0
C(17)-H(17A)...Cl(6)#2	0.99	2.91	3.565(16)	124.9
C(18)-H(18B)...Cl(1)#9	0.99	2.72	3.639(16)	153.7
C(19)-H(19A)...O(2)	0.98	2.41	3.00(2)	117.8
C(19)-H(19B)...Cl(3)	0.98	2.80	3.650(17)	145.6
C(19)-H(19C)...Cl(1)#9	0.98	2.65	3.567(17)	155.2
C(20)-H(20A)...Cl(4)#2	0.99	2.70	3.419(17)	129.3
O(2)-H(20)...Cl(6)#6	0.84(3)	2.23(7)	3.022(13)	158(16)
O(3)-H(30)...Cl(5)#2	0.88(19)	2.27(19)	3.099(13)	158(15)
O(4)-H(40)...Cl(1)#2	0.84(3)	2.18(3)	3.018(12)	175(17)
O(4)-H(40)...Cl(9)	0.84(3)	3.14(17)	3.248(12)	90(12)
O(6)-H(600)...Cl(2)	0.71(17)	2.33(18)	3.024(14)	168(19)

Symmetry transformations used to generate equivalent atoms:

#1 -x+2,y+1/2,-z+1 #2 -x+1,y-1/2,-z #3 x,y+1,z

#4 -x+1,y+1/2,-z #5 -x+2,y-1/2,-z+1 #6 x,y-1,z

#7 -x+2,y-1/2,-z #8 -x+1,y+1/2,-z+1 #9 x+1,y,z

3.3. Single crystal X-ray analysis of $[N_{2,2,2,2}][MnCl_3]$

Table SI 11 | Crystal data and structure refinement for the title compound.

Empirical formula	C16 H40 Cl4 Mn N2	
Formula weight	457.24	
Temperature	110(2) K	
Wavelength	0.71073 Å	
Crystal system	Monoclinic	
Space group	P21/n	
Unit cell dimensions	a = 16.5514(10) Å	α= 90°.
	b = 9.6164(6) Å	β= 116.967(2)°.
	c = 16.7356(10) Å	γ = 90°.
Volume	2374.1(3) Å3	
Z	4	
Density (calculated)	1.279 Mg/m3	
Crystal size	0.45 x 0.25 x 0.10 mm3	
Reflections collected	38079	
Independent reflections	4799 [R(int) = 0.0562]	
Goodness-of-fit on F2	0.803	
Final R indices [I>2sigma(I)]	R1 = 0.1190, wR2 = 0.3102	
R indices (all data)	R1 = 0.1329, wR2 = 0.3176	

Table SI 12 | Atomic coordinates ($x10^4$) and equivalent isotropic displacement parameters ($Å^2 x\ 10^3$) for the title compound. U(eq) is defined as one third of the trace of the orthogonalized U^{ij} tensor.

	x	y	z	U(eq)
Cl(1)	6433(1)	2520(2)	877(1)	43(1)
Cl(2)	7909(1)	4851(2)	-57(1)	38(1)
Mn(1)	7368(1)	2496(2)	70(1)	71(1)
Cl(3)	8653(1)	958(2)	919(1)	48(1)
Cl(4)	6490(2)	1621(3)	-1415(2)	60(1)
N(1)	9073(6)	2565(10)	-1770(7)	70(2)
N(2)	6402(7)	-2318(10)	1294(7)	71(2)
C(1)	9552(8)	3851(13)	-1818(8)	73(3)
C(2)	8083(9)	-2496(15)	1657(11)	85(4)
C(3)	9399(8)	1401(13)	-2162(8)	73(3)
C(4)	7354(8)	-1684(13)	1721(9)	75(3)
C(5)	5753(9)	-1287(14)	1371(9)	78(3)
C(6)	6421(10)	-3670(14)	1755(9)	82(3)
C(7)	6104(9)	-2622(15)	319(9)	80(3)
C(8)	5910(10)	-1037(16)	2334(10)	86(4)
C(9)	8914(10)	17(14)	-2286(9)	84(3)
C(10)	9381(10)	5157(14)	-1406(9)	83(3)
C(11)	9269(9)	2195(15)	-814(8)	79(3)
C(12)	10260(10)	2016(16)	-171(9)	85(4)
C(13)	5504(10)	-4306(15)	1476(10)	86(3)
C(14)	7685(9)	3030(14)	-3272(9)	82(3)
C(15)	8037(8)	2755(15)	-2296(9)	78(3)
C(16)	6166(11)	-1376(17)	-228(9)	91(4)

Table SI 13 | Bond lengths [Å] and angles [°] for the title compound.

Cl(1)-Mn(1)	2.474(2)	C(7)-C(16)	1.54(2)
Cl(2)-Mn(1)	2.480(2)	C(7)-H(7A)	0.9700
Mn(1)-Cl(4)	2.391(3)	C(7)-H(7B)	0.9700
Mn(1)-Cl(3)	2.447(3)	C(8)-H(8A)	0.9600
N(1)-C(1)	1.491(15)	C(8)-H(8B)	0.9600
N(1)-C(3)	1.516(15)	C(8)-H(8C)	0.9600
N(1)-C(11)	1.524(15)	C(9)-H(9A)	0.9600
N(1)-C(15)	1.542(15)	C(9)-H(9B)	0.9600
N(2)-C(7)	1.504(16)	C(9)-H(9C)	0.9600
N(2)-C(6)	1.504(17)	C(10)-H(10A)	0.9600
N(2)-C(5)	1.510(16)	C(10)-H(10B)	0.9600
N(2)-C(4)	1.531(16)	C(10)-H(10C)	0.9600
C(1)-C(10)	1.520(18)	C(11)-C(12)	1.509(19)
C(1)-H(1A)	0.9700	C(11)-H(11A)	0.9700
C(1)-H(1B)	0.9700	C(11)-H(11B)	0.9700
C(2)-C(4)	1.482(17)	C(12)-H(12A)	0.9600
C(2)-H(2A)	0.9600	C(12)-H(12B)	0.9600
C(2)-H(2B)	0.9600	C(12)-H(12C)	0.9600
C(2)-H(2C)	0.9600	C(13)-H(13A)	0.9600
C(3)-C(9)	1.519(18)	C(13)-H(13B)	0.9600
C(3)-H(3A)	0.9700	C(13)-H(13C)	0.9600
C(3)-H(3B)	0.9700	C(14)-C(15)	1.488(19)
C(4)-H(4A)	0.9700	C(14)-H(14A)	0.9600
C(4)-H(4B)	0.9700	C(14)-H(14B)	0.9600
C(5)-C(8)	1.529(19)	C(14)-H(14C)	0.9600
C(5)-H(5A)	0.9700	C(15)-H(15A)	0.9700
C(5)-H(5B)	0.9700	C(15)-H(15B)	0.9700
C(6)-C(13)	1.50(2)	C(16)-H(16A)	0.9600
C(6)-H(6A)	0.9700	C(16)-H(16B)	0.9600
C(6)-H(6B)	0.9700	C(16)-H(16C)	0.9600

Cl(4)-Mn(1)-Cl(3)	110.45(10)	N(1)-C(3)-H(3A)	108.3
Cl(4)-Mn(1)-Cl(1)	109.55(10)	C(9)-C(3)-H(3A)	108.3
Cl(3)-Mn(1)-Cl(1)	106.45(9)	N(1)-C(3)-H(3B)	108.3
Cl(4)-Mn(1)-Cl(2)	107.78(10)	C(9)-C(3)-H(3B)	108.3
Cl(3)-Mn(1)-Cl(2)	110.46(9)	H(3A)-C(3)-H(3B)	107.4
Cl(1)-Mn(1)-Cl(2)	112.16(9)	C(2)-C(4)-N(2)	117.1(10)
C(1)-N(1)-C(3)	106.6(9)	C(2)-C(4)-H(4A)	108.0
C(1)-N(1)-C(11)	112.6(10)	N(2)-C(4)-H(4A)	108.0
C(3)-N(1)-C(11)	109.5(9)	C(2)-C(4)-H(4B)	108.0
C(1)-N(1)-C(15)	110.6(9)	N(2)-C(4)-H(4B)	108.0
C(3)-N(1)-C(15)	111.3(9)	H(4A)-C(4)-H(4B)	107.3
C(11)-N(1)-C(15)	106.2(9)	N(2)-C(5)-C(8)	113.9(11)
C(7)-N(2)-C(6)	108.0(9)	N(2)-C(5)-H(5A)	108.8
C(7)-N(2)-C(5)	108.9(10)	C(8)-C(5)-H(5A)	108.8
C(6)-N(2)-C(5)	111.9(10)	N(2)-C(5)-H(5B)	108.8
C(7)-N(2)-C(4)	110.2(9)	C(8)-C(5)-H(5B)	108.8
C(6)-N(2)-C(4)	109.1(10)	H(5A)-C(5)-H(5B)	107.7
C(5)-N(2)-C(4)	108.7(9)	C(13)-C(6)-N(2)	114.2(11)
N(1)-C(1)-C(10)	116.6(10)	C(13)-C(6)-H(6A)	108.7
N(1)-C(1)-H(1A)	108.1	N(2)-C(6)-H(6A)	108.7
C(10)-C(1)-H(1A)	108.1	C(13)-C(6)-H(6B)	108.7
N(1)-C(1)-H(1B)	108.1	N(2)-C(6)-H(6B)	108.7
C(10)-C(1)-H(1B)	108.1	H(6A)-C(6)-H(6B)	107.6
H(1A)-C(1)-H(1B)	107.3	N(2)-C(7)-C(16)	114.6(11)
C(4)-C(2)-H(2A)	109.5	N(2)-C(7)-H(7A)	108.6
C(4)-C(2)-H(2B)	109.5	C(16)-C(7)-H(7A)	108.6
H(2A)-C(2)-H(2B)	109.5	N(2)-C(7)-H(7B)	108.6
C(4)-C(2)-H(2C)	109.5	C(16)-C(7)-H(7B)	108.6
H(2A)-C(2)-H(2C)	109.5	H(7A)-C(7)-H(7B)	107.6
H(2B)-C(2)-H(2C)	109.5	C(5)-C(8)-H(8A)	109.5
N(1)-C(3)-C(9)	115.9(10)	C(5)-C(8)-H(8B)	109.5

H(8A)-C(8)-H(8B)	109.5	H(12A)-C(12)-H(12C)	109.5
C(5)-C(8)-H(8C)	109.5	H(12B)-C(12)-H(12C)	109.5
H(8A)-C(8)-H(8C)	109.5	C(6)-C(13)-H(13A)	109.5
H(8B)-C(8)-H(8C)	109.5	C(6)-C(13)-H(13B)	109.5
C(3)-C(9)-H(9A)	109.5	H(13A)-C(13)-H(13B)	109.5
C(3)-C(9)-H(9B)	109.5	C(6)-C(13)-H(13C)	109.5
H(9A)-C(9)-H(9B)	109.5	H(13A)-C(13)-H(13C)	109.5
C(3)-C(9)-H(9C)	109.5	H(13B)-C(13)-H(13C)	109.5
H(9A)-C(9)-H(9C)	109.5	C(15)-C(14)-H(14A)	109.5
H(9B)-C(9)-H(9C)	109.5	C(15)-C(14)-H(14B)	109.5
C(1)-C(10)-H(10A)	109.5	H(14A)-C(14)-H(14B)	109.5
C(1)-C(10)-H(10B)	109.5	C(15)-C(14)-H(14C)	109.5
H(10A)-C(10)-H(10B)	109.5	H(14A)-C(14)-H(14C)	109.5
C(1)-C(10)-H(10C)	109.5	H(14B)-C(14)-H(14C)	109.5
H(10A)-C(10)-H(10C)	109.5	C(14)-C(15)-N(1)	115.4(10)
H(10B)-C(10)-H(10C)	109.5	C(14)-C(15)-H(15A)	108.4
C(12)-C(11)-N(1)	114.9(11)	N(1)-C(15)-H(15A)	108.4
C(12)-C(11)-H(11A)	108.5	C(14)-C(15)-H(15B)	108.4
N(1)-C(11)-H(11A)	108.5	N(1)-C(15)-H(15B)	108.4
C(12)-C(11)-H(11B)	108.5	H(15A)-C(15)-H(15B)	107.5
N(1)-C(11)-H(11B)	108.5	C(7)-C(16)-H(16A)	109.5
H(11A)-C(11)-H(11B)	107.5	C(7)-C(16)-H(16B)	109.5
C(11)-C(12)-H(12A)	109.5	H(16A)-C(16)-H(16B)	109.5
C(11)-C(12)-H(12B)	109.5	C(7)-C(16)-H(16C)	109.5
H(12A)-C(12)-H(12B)	109.5	H(16A)-C(16)-H(16C)	109.5
C(11)-C(12)-H(12C)	109.5	H(16B)-C(16)-H(16C)	109

Table SI 14 | Torsion angles [°] for the title compound.

C(3)-N(1)-C(1)-C(10)	-176.2(10)
C(11)-N(1)-C(1)-C(10)	-56.1(14)
C(15)-N(1)-C(1)-C(10)	62.6(14)
C(1)-N(1)-C(3)-C(9)	-172.9(10)
C(11)-N(1)-C(3)-C(9)	64.9(13)
C(15)-N(1)-C(3)-C(9)	-52.2(14)
C(7)-N(2)-C(4)-C(2)	-56.5(15)
C(6)-N(2)-C(4)-C(2)	61.9(14)
C(5)-N(2)-C(4)-C(2)	-175.8(12)
C(7)-N(2)-C(5)-C(8)	172.4(11)
C(6)-N(2)-C(5)-C(8)	53.1(14)
C(4)-N(2)-C(5)-C(8)	-67.5(13)
C(7)-N(2)-C(6)-C(13)	-67.6(13)
C(5)-N(2)-C(6)-C(13)	52.3(14)
C(4)-N(2)-C(6)-C(13)	172.6(11)
C(6)-N(2)-C(7)-C(16)	-172.5(11)
C(5)-N(2)-C(7)-C(16)	65.7(14)
C(4)-N(2)-C(7)-C(16)	-53.5(14)
C(1)-N(1)-C(11)-C(12)	-56.5(15)
C(3)-N(1)-C(11)-C(12)	62.0(14)
C(15)-N(1)-C(11)-C(12)	-177.7(12)
C(1)-N(1)-C(15)-C(14)	61.5(14)
C(3)-N(1)-C(15)-C(14)	-56.9(14)
C(11)-N(1)-C(15)-C(14)	-176.0(11)

4. Luminescence characterization of Manganese (II)-based salts

4.1. Excitation (λ_{exc}) and emission (λ_{em}) wavelength and 2D spectra

Table SI 15 | Excitation and emission wavelengths of manganese (II)-based salts.

Compound	λ_{em1}	λ_{exc1}	λ_{em2}	λ_{exc2}
$[N_{1,1,1,C2OH}][MnCl_3]$	630	420	635	525
$[N_{1,1,4,C2OH}][MnCl_3]$	640	420	645	520
$[N_{1,1,4,C3OH}][MnCl_3]$	645	425	635	525
$[N_{1,1,C2OH,C2OH}][MnCl_3]$	620	420	-	-
$[P_{C2OH,C2OH,C2OH,C2OH}][MnCl_3]$	620	420	625	525
$[N_{2,2,2,2}][MnCl_3]$				
$[N_{2,2,2,2}][MnCl_3]$				
$[P_{4,4,4,4}][MnCl_3]$	585	450	-	-
$[C_2OHMIM][MnCl_3]$	650	420	645	515
$[C_2OHDMIM][MnCl_3]$	665	430	690	540
$[C_2MIM][MnCl_3]$	530	450	-	-

Table SI 16 | Luminescence properties of manganese (II) ammonium, phosphonium and imidazolium salts obtained for 515-540nm wavelength range.

Compound	ϕ (%)	τ (ms)	k_r (ms^{-1})	k_{nr} (ms^{-1})	Stokes shift (eV)
$[N_{1,1,1,C2OH}][MnCl_3]$	4.29	1.17	0.04	0.82	0.44
$[N_{1,1,4,C2OH}][MnCl_3]$	12.38	0.94	0.13	0.93	0.46
$[N_{1,1,2,C3OH}][MnCl_3]$	-	-	-	-	-
$[N_{1,1,4,C3OH}][MnCl_3]$	2.93	0.96	0.03	1.01	0.41
$[N_{1,1,C2OH,C2OH}][MnCl_3]$	-	-	-	-	-
$[N_{2,2,2,2}][MnCl_3]$	-	-	-	-	-
$[P_{C1OH,C1OH,C1OH,C1OH}][\ MnCl_3]$	2.82	0.39	0.07	2.49	0.38
$[P_{4,4,4,4}][MnCl_3]$	-	-	-	-	-
$[C_2OHMIM][MnCl_3]$	3.97	0.95	0.04	1.01	0.49
$[C_2OHDMIM][MnCl_3]$	2.94	0.19	0.15	5.11	0.48
$[C_2MIM][MnCl_3]$	-	-	-	-	-

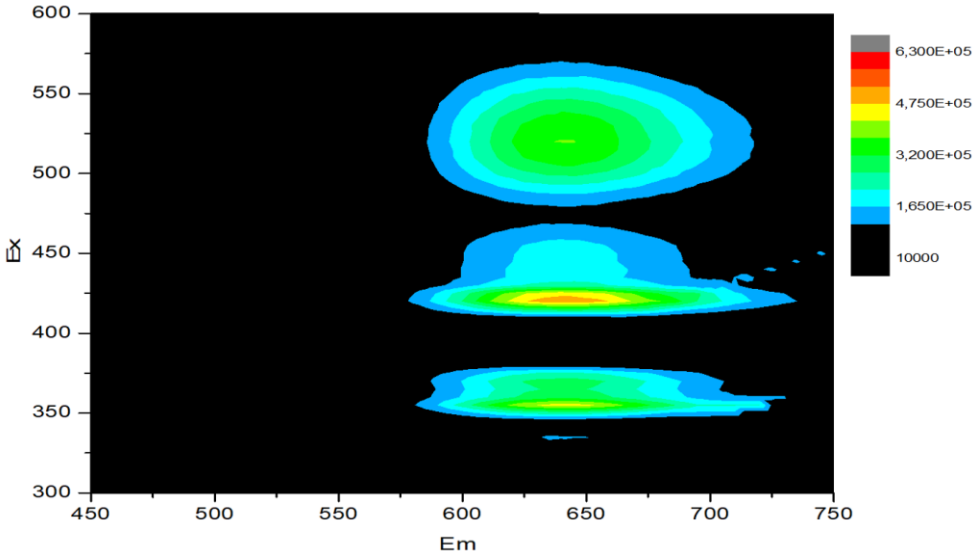

Figure SI 43 | 2D spectrum of $[N_{1,1,4,C2OH}][MnCl_3]$.

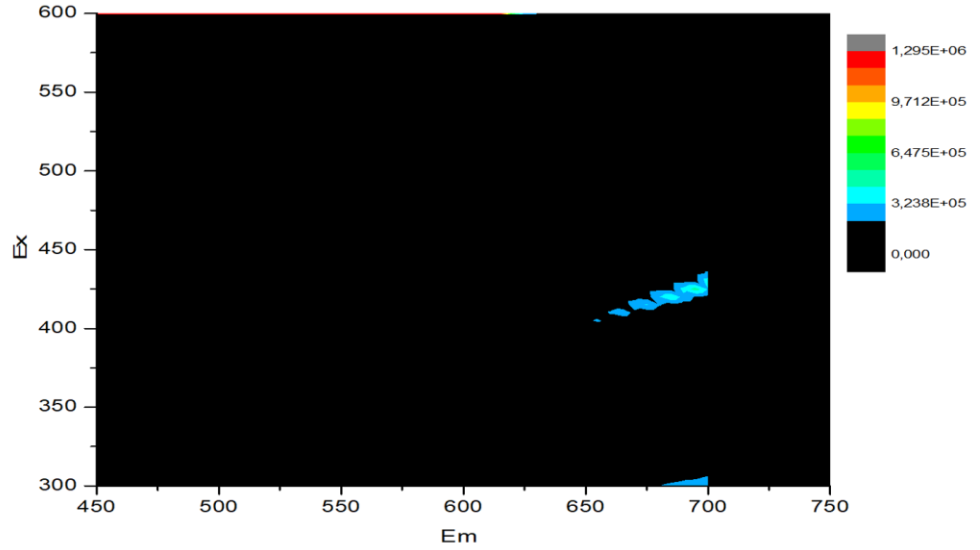

Figure SI 44 | 2D spectrum of $[N_{1,1,2,C3OH}][MnCl_3]$.

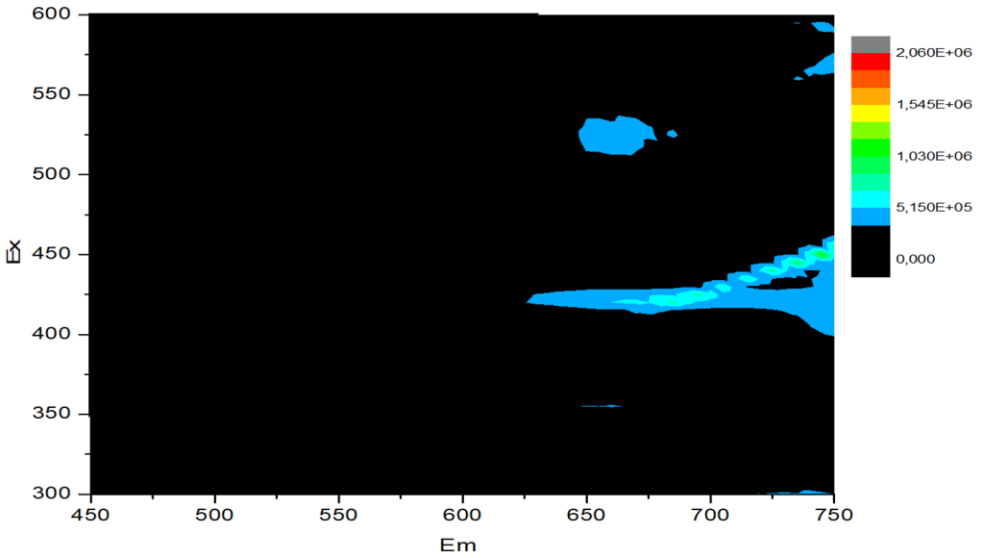

Figure SI 45 | 2D spectrum of $[N_{1,1,4,C3OH}][MnCl_3]$.

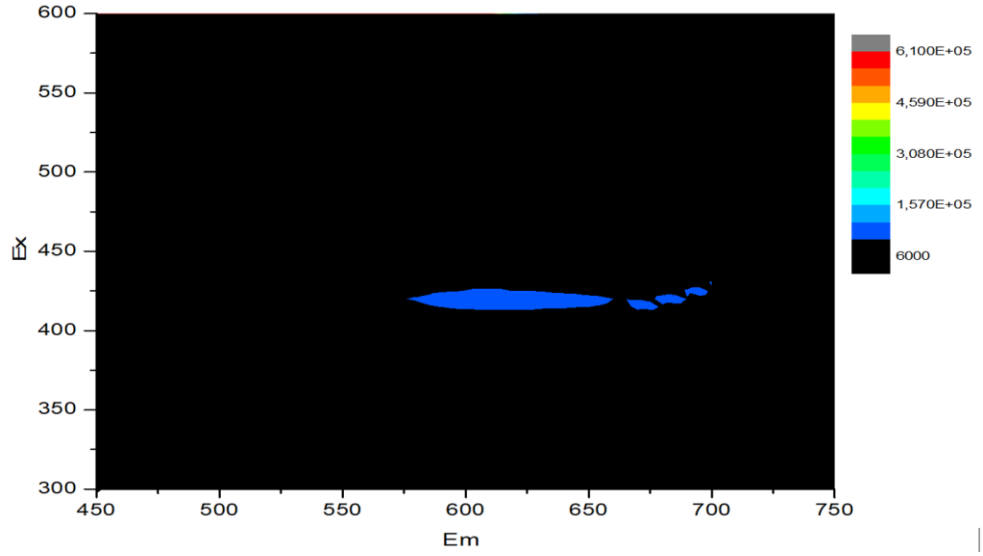

Figure SI 46 | 2D spectrum of $[N_{1,1,C2OH,C2OH}][MnCl_3]$.

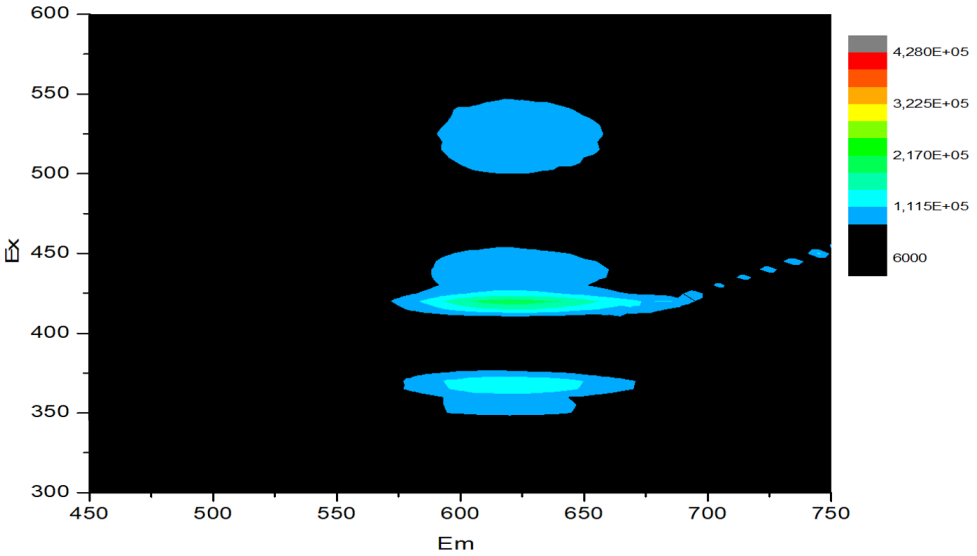

Figure SI 47 | 2D spectrum of $[P_{C2OH,C2OH,C2OH,C2OH}][MnCl_3]$.

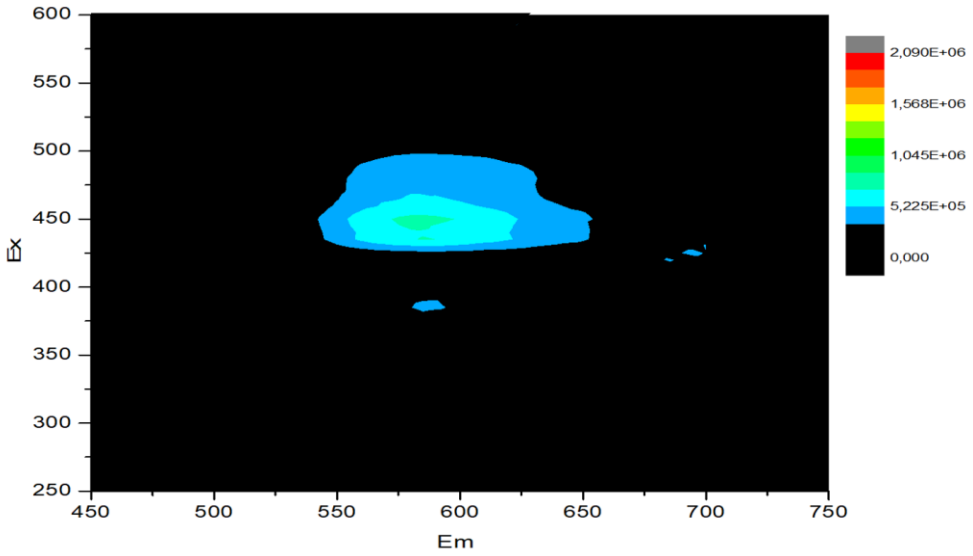

Figure SI 48 | 2D spectrum of $[P_{4,4,4,4}][MnCl_3]$.

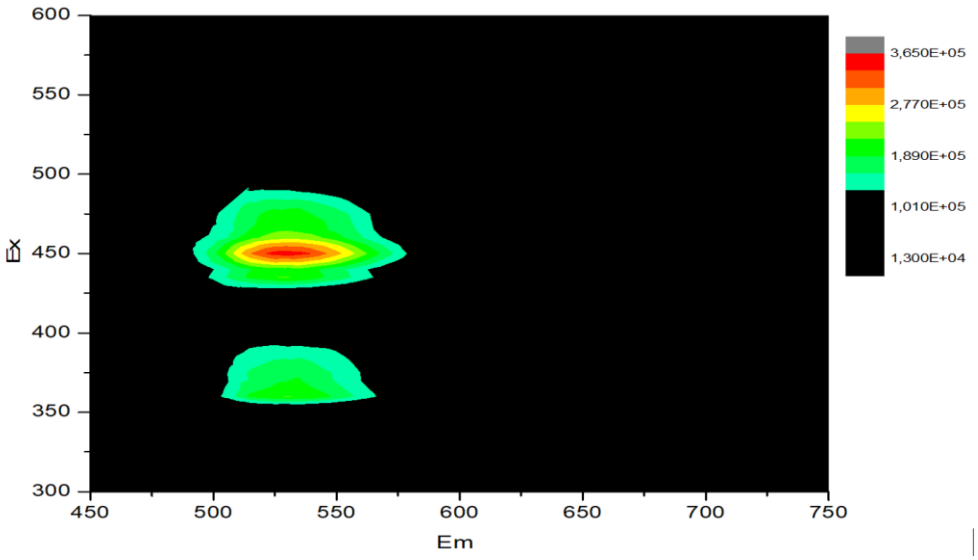

Figure SI 49 | 2D spectrum of [C_2MIM][$MnCl_3$].

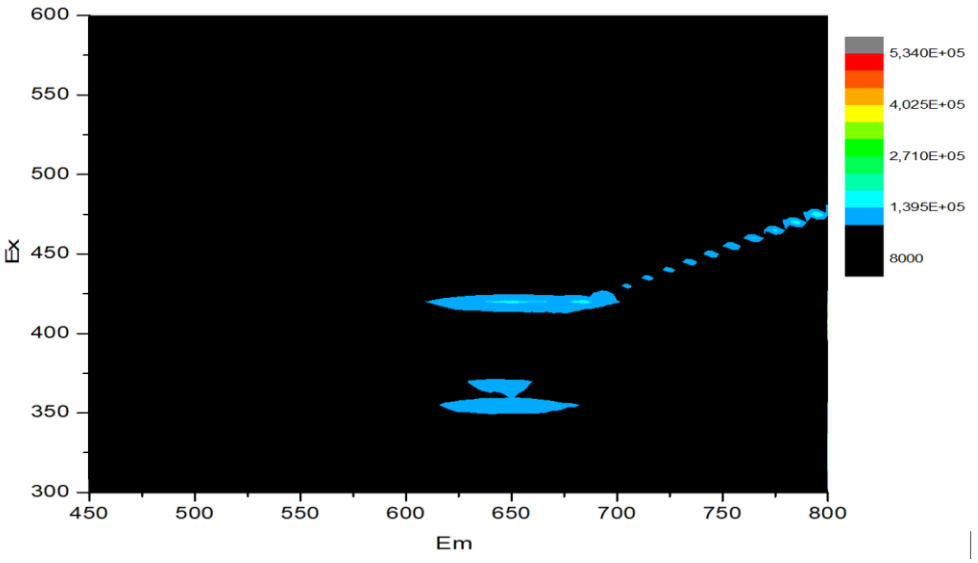

Figure SI 50 | 2D spectrum of [C_{2OHMIM}][$MnCl_3$].

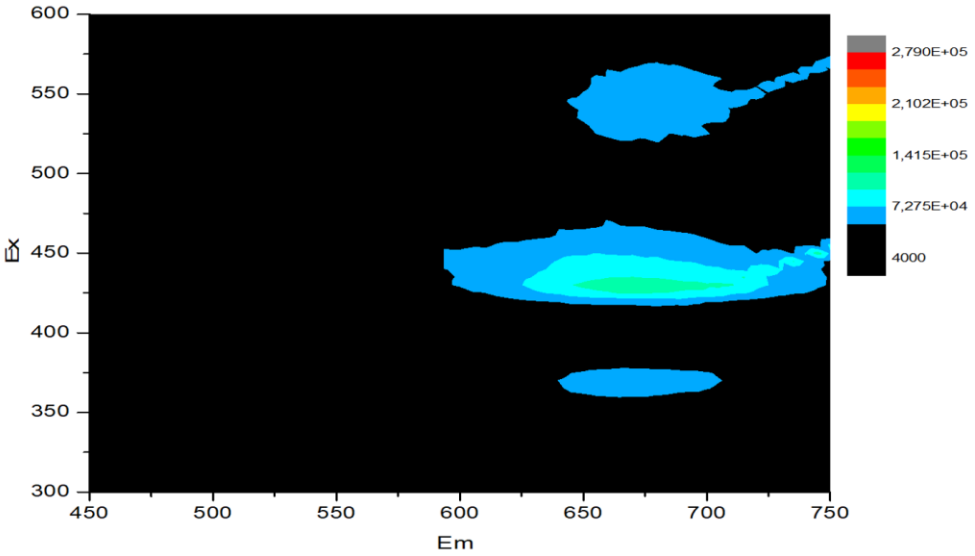

Figure SI 51 | 2D spectrum of [$C_{2OHDMIM}$][$MnCl_3$].

4.2. Lifetime decay curves

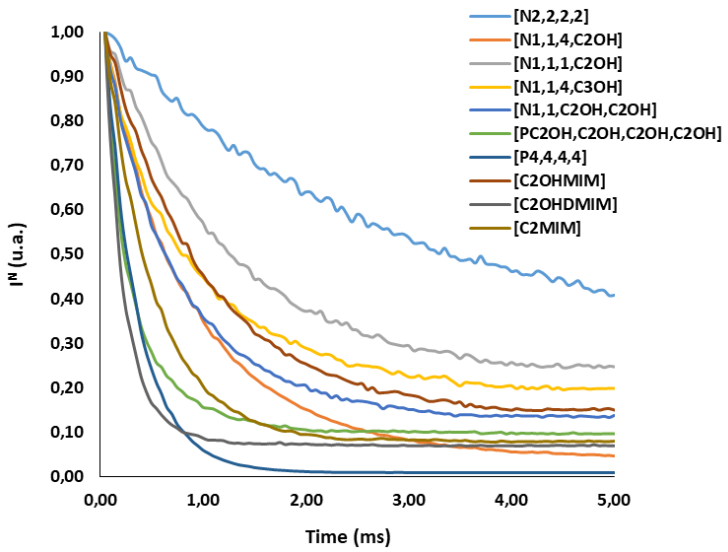

Figure SI 52 | Lifetime decay curves of manganese (II)-based organic salts.

Chapter 3

1. Structural characterization of magnetic organic salts (FT-IR)

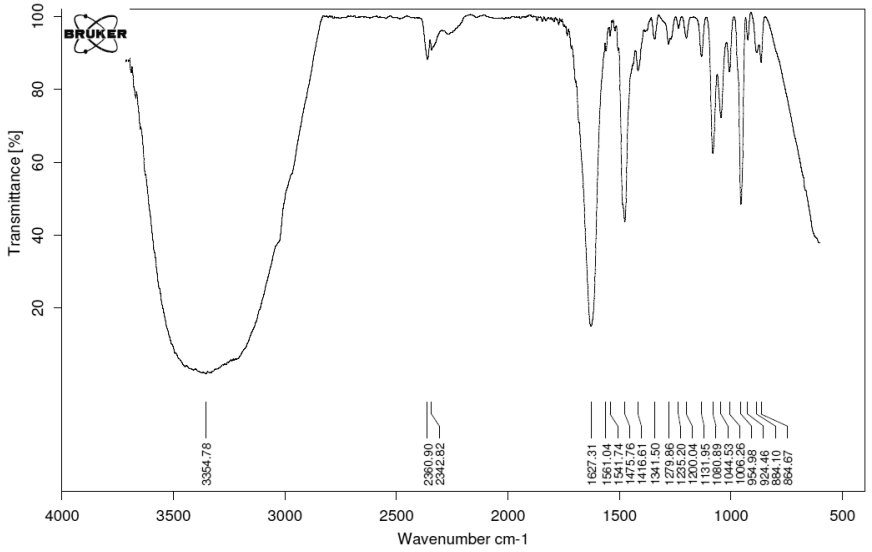

Figure SI 53 | FT-IR spectra of $[N_{1,1,1,C2OH}][GdCl_4]$.

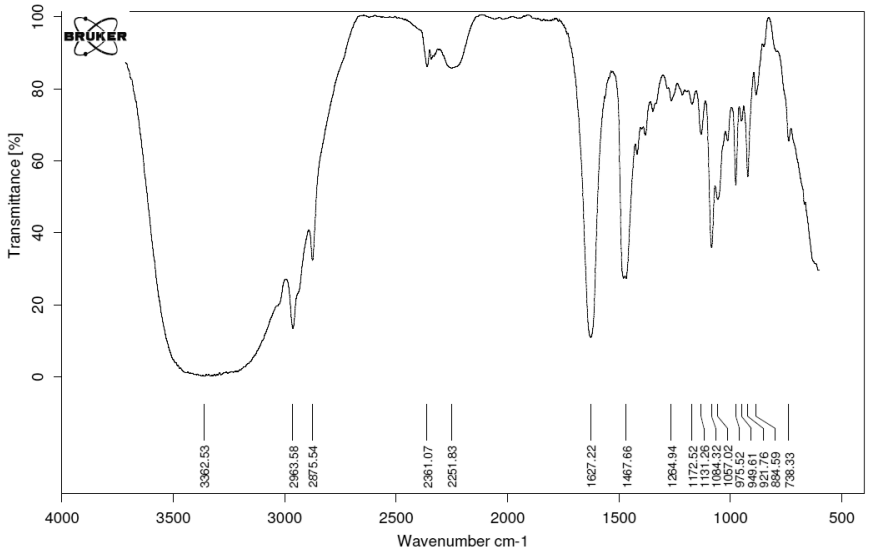

Figure SI 54 | FT-IR spectra of $[N_{1,1,4,C2OH}][GdCl_4]$.

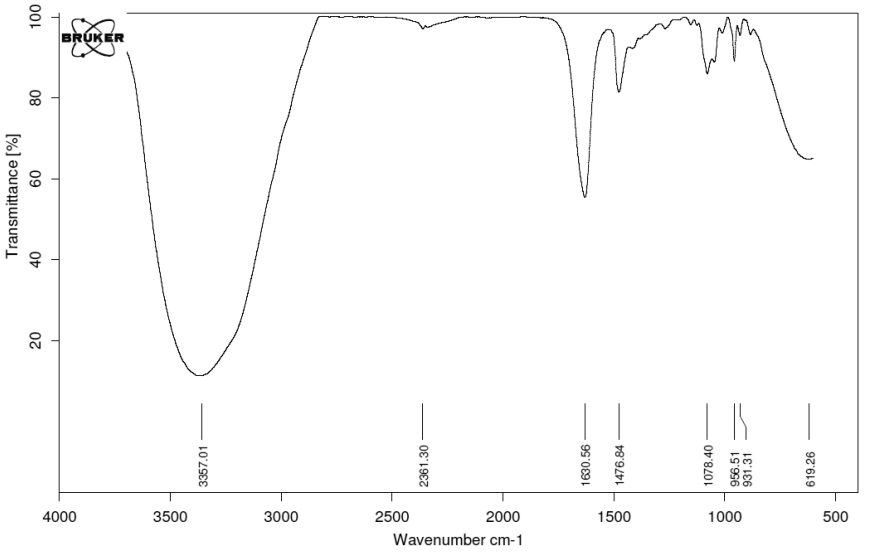

Figure SI 55 | FT-IR spectra of $[N_{1,1,C2OH,C2OH}][GdCl_4]$.

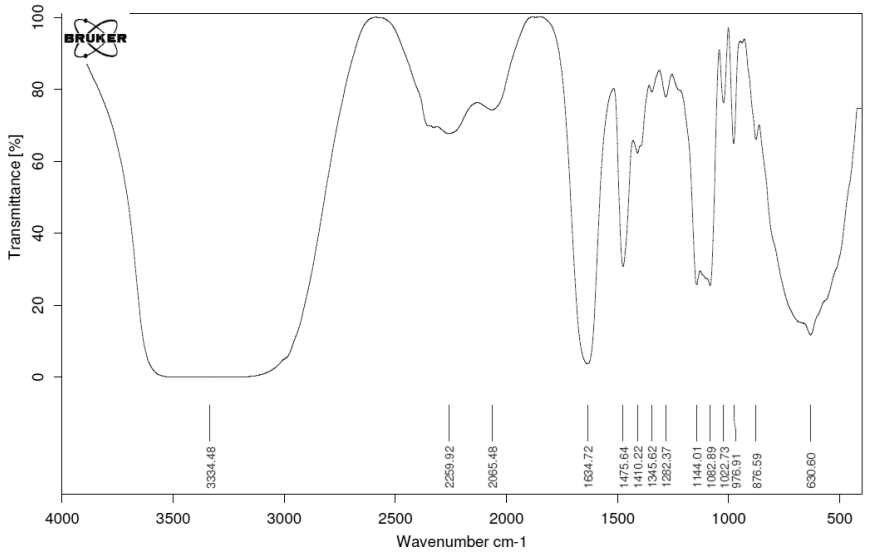

Figure SI 56 | FT-IR spectra of $[N_{1,1,2,C3OH}][GdCl_4]$.

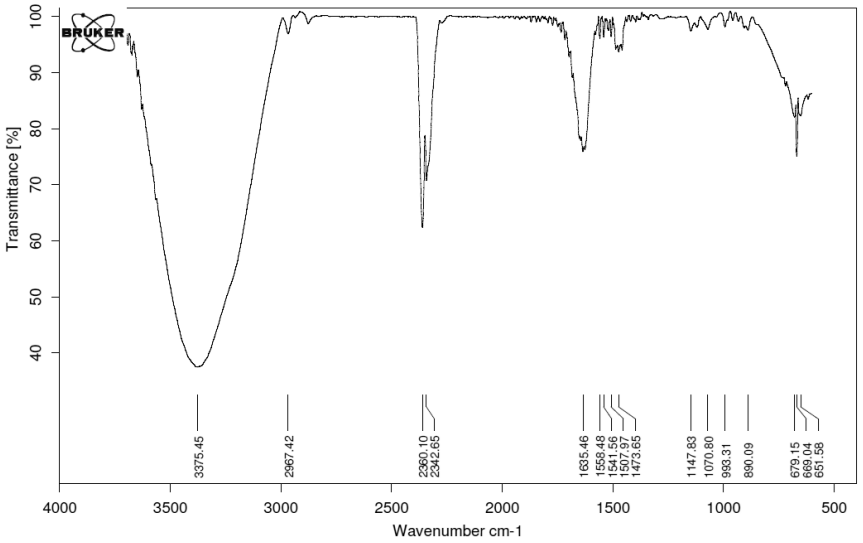

Figure SI 57 | FT-IR spectra of $[N_{1,1,4,C3OH}][GdCl_4]$.

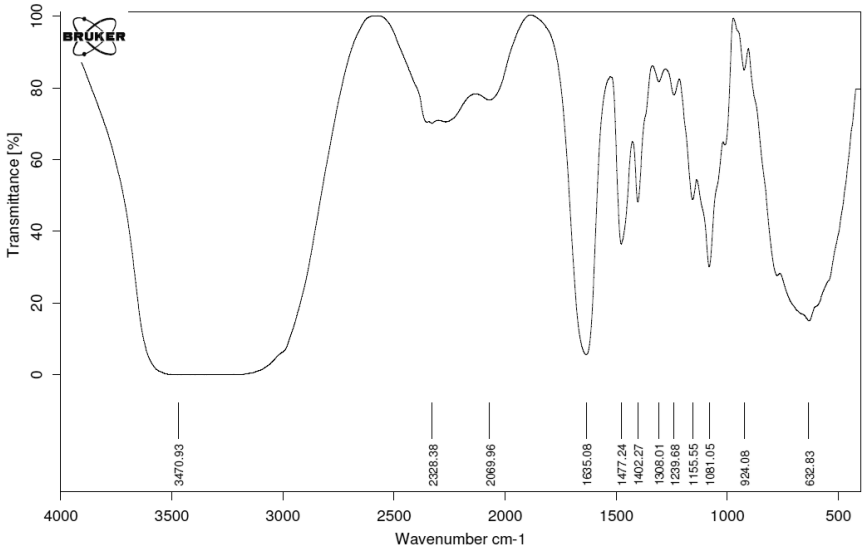

Figure SI 58 | FT-IR spectra of $[N_{2,2,2,C2OH}][GdCl_4]$.

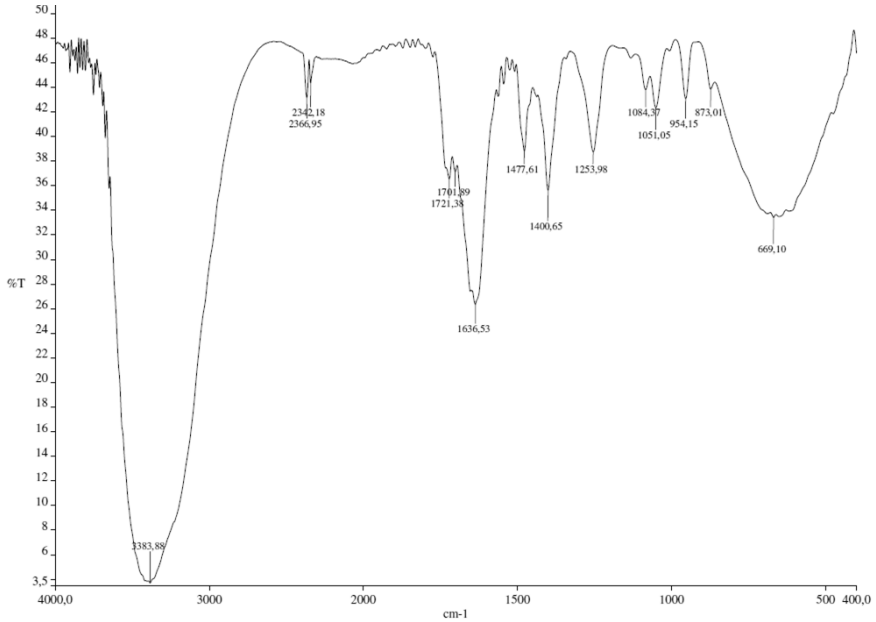

Figure SI 59 | FT-IR spectra of $[N_{1,1,1,C2COOCH3}][GdCl_4]$.

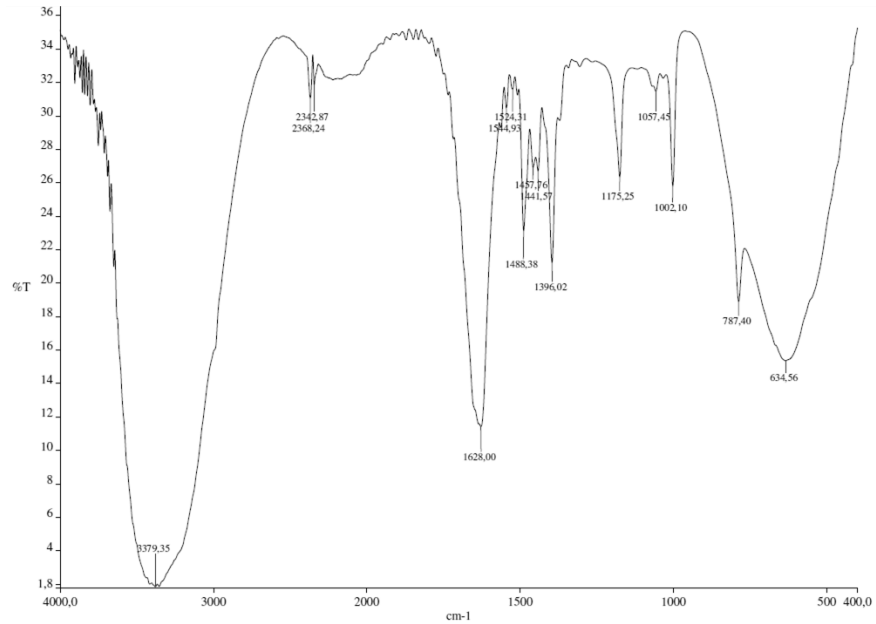

Figure SI 60 | FT-IR spectra of $[N_{2,2,2,2}][GdCl_4]$.

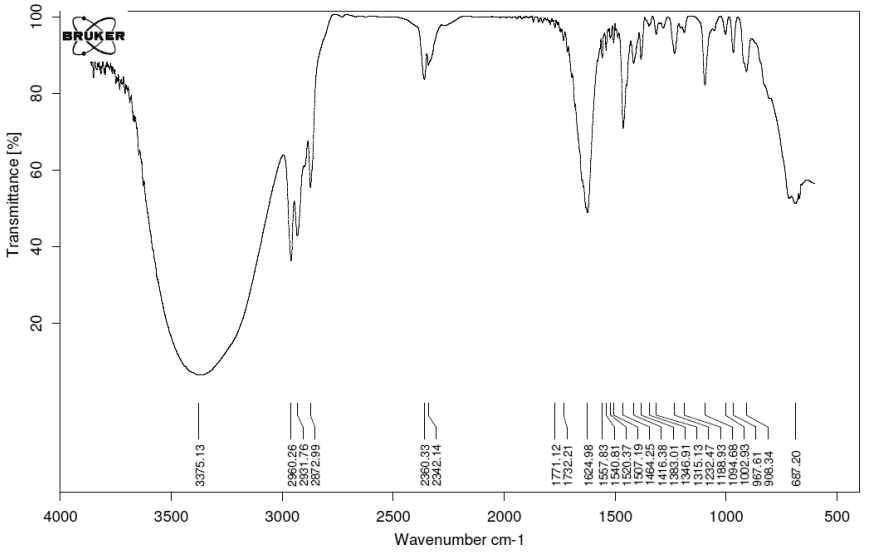

Figure SI 61 | FT-IR spectra of $[P_{4,4,4,4}][GdCl_4]$.

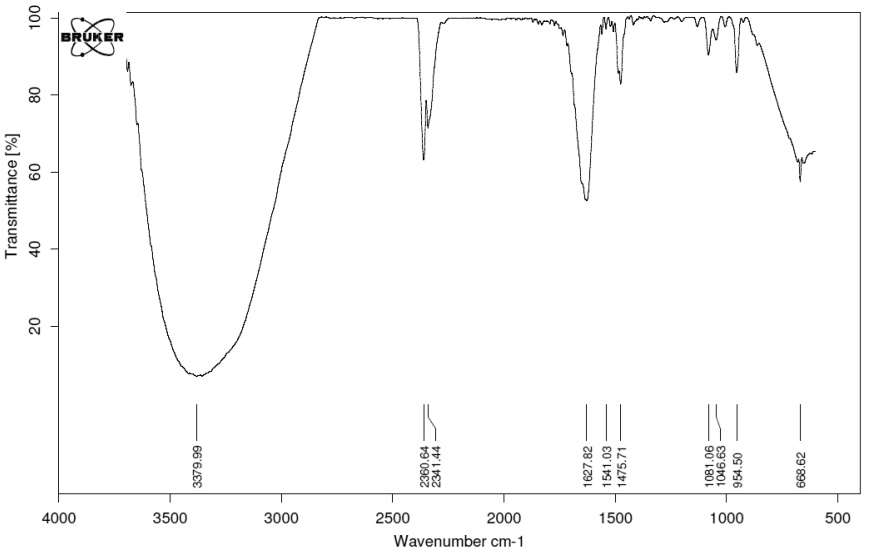

Figure SI 62 | FT-IR spectra of $[N_{1,1,1,C2OH}][TbCl_4]$.

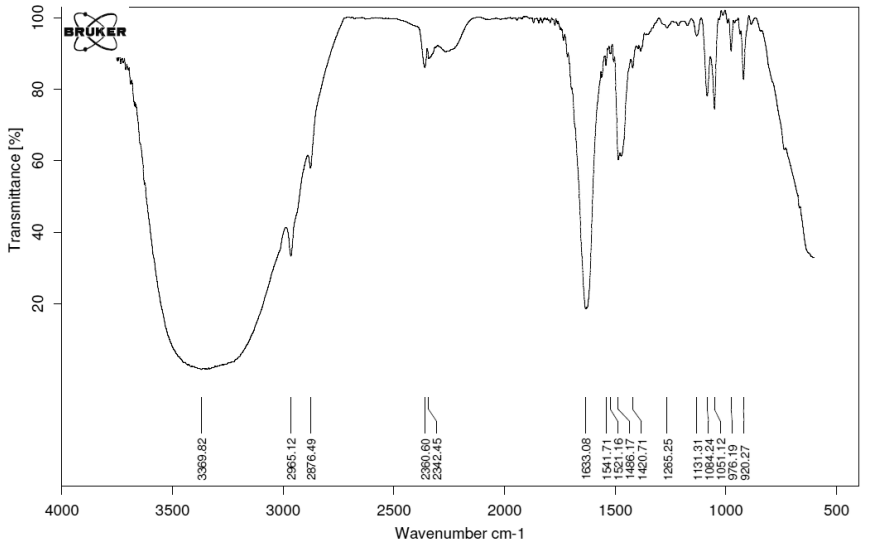

Figure SI 63 | FT-IR spectra of $[N_{1,1,4,C2OH}][TbCl_4]$.

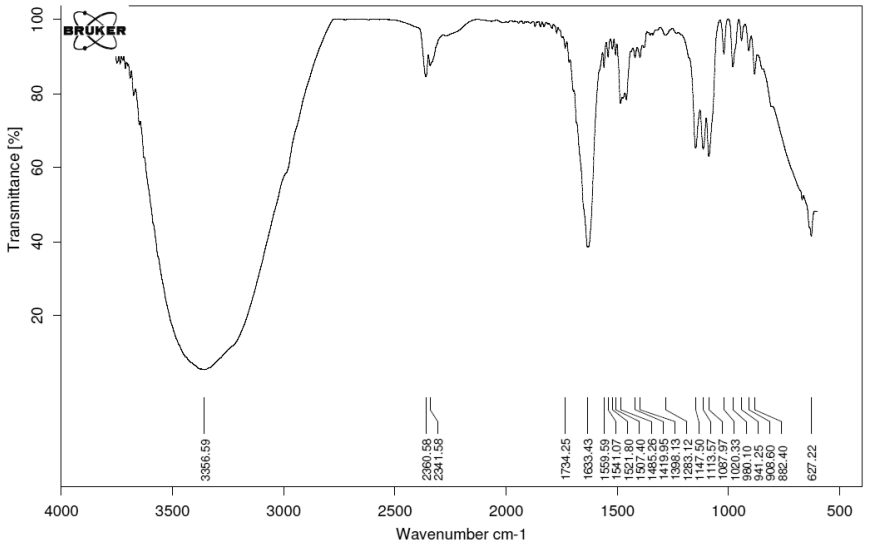

Figure SI 64 | FT-IR spectra of $[N_{1,1,2,C3OH}][TbCl_4]$.

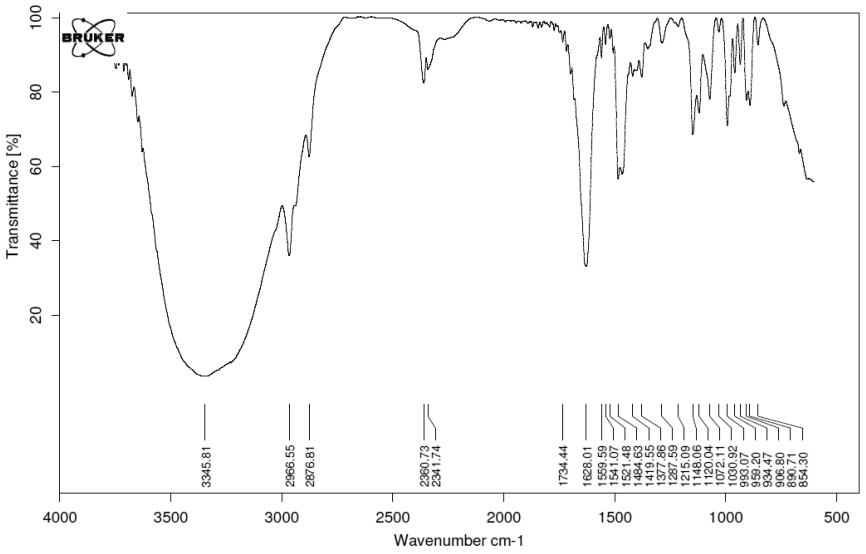

Figure SI 65 | FT-IR spectra of $[N_{1,1,4,C3OH}][TbCl_4]$.

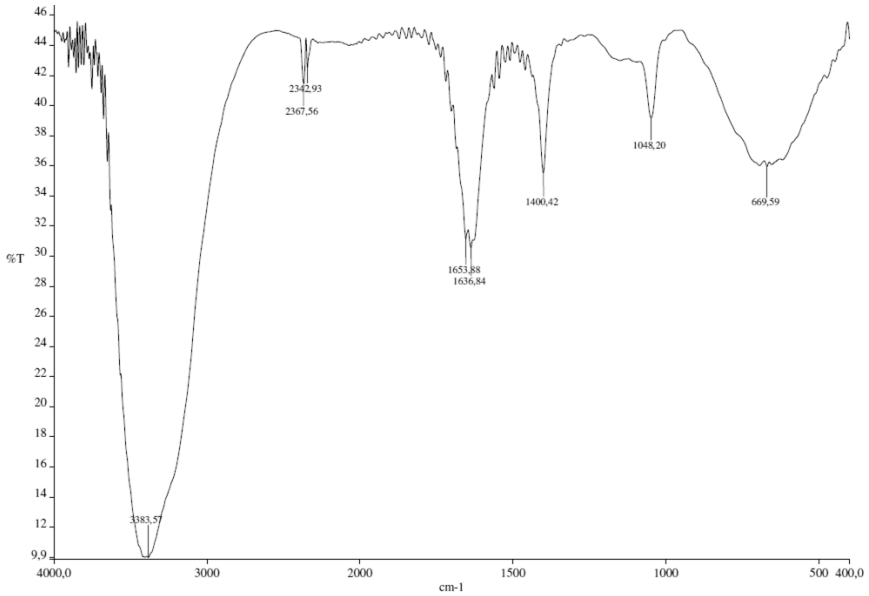

Figure SI 66 | FT-IR spectra of $[P_{C2OH,C2OH,C2OH,C2OH}][TbCl_4]$.

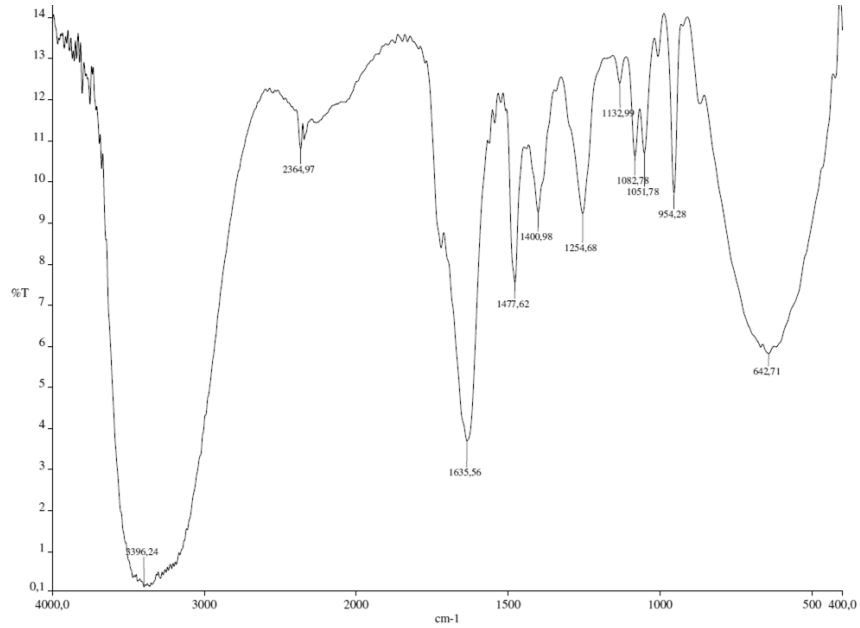

Figure SI 67 | FT-IR spectra of $[N_{1,1,1,C2COOCH3}][TbCl_4]$.

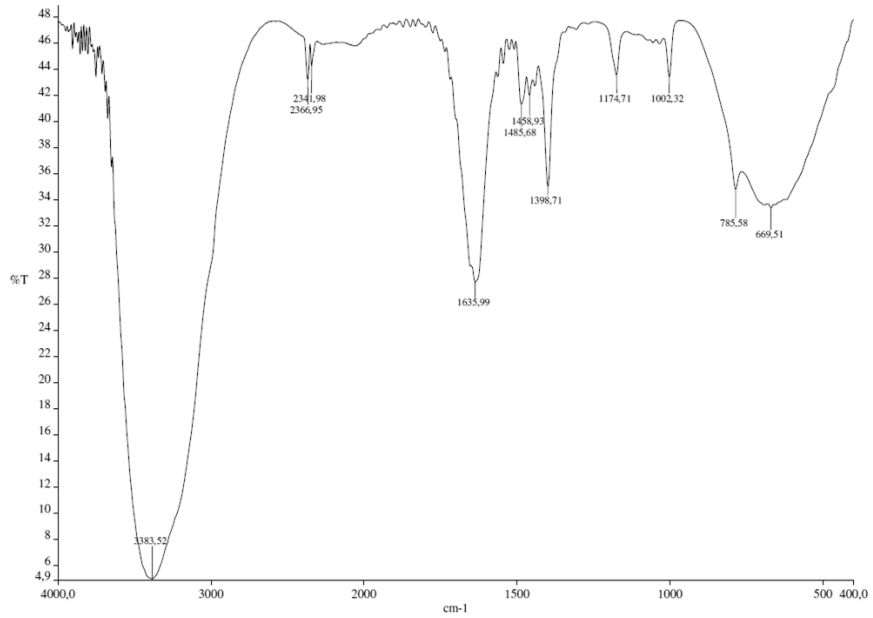

Figure SI 68 | FT-IR spectra of $[N_{2,2,2,2}][TbCl_4]$.

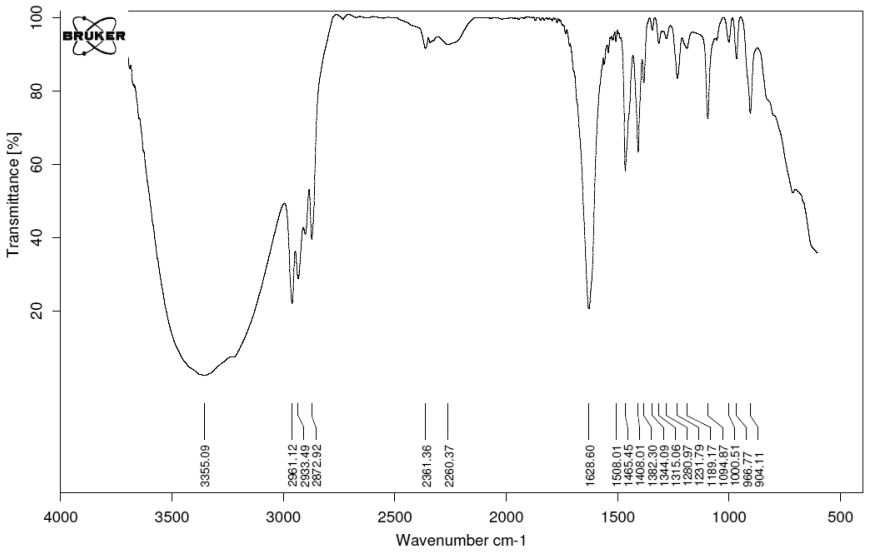

Figure SI 69 | FT-IR spectra of $[P_{4,4,4,4}][TbCl_4]$.

2. Relaxometric Studies of $[N_{1,1,1,C2OH}][GdCl_4]$ and $[N_{1,1,2,C3OH}][GdCl_4]$ salts

Table SI 17 | T_1 relaxation measurements (in triplicate) of selected choline-based magnetic salts measured at 9.4T.

$[N_{1,1,1,C2OH}][GdCl_4]$						
[C] (mM)	**T_1 A (s)**	**T_1 B (s)**	**T_1 C (s)**	**T_2 A (s)**	**T_2 B (s)**	**T_2 C (s)**
1,00	0.137	0.138	0.137	0.119	0.120	0.119
0,75	0.164	0.165	0.164	0.157	0.156	0.156
0,50	0.214	0.217	0.217	0.229	0.230	0.229
0,10	1.230	1.284	1.277	1.486	1.488	1.494
	0.157	0.080	0.175			
	0.565	0.050	1.717			
0,05	2.637	2.688	2.623	1.601	1.608	1.609
	0.067	0.081	0.075			
	0.114	0.116	0.103			

$[N_{1,1,2,C3OH}][GdCl_4]$						
[C] (mM)	**T_1 A (s)**	**T_1 B (s)**	**T_1 C (s)**	**T_2 A (s)**	**T_2 B (s)**	**T_2 C (s)**
1,00	0.119	0.119	0.119	0.103	0.103	0.103
0,75	0.164	0.163	0.163	0.138	0.139	0.139
0,50	0.215	0.215	0.213	0.210	0.210	0.210
0,10	0.845	0.844	0.848	0.751	0.758	0.765
0,05	1.866	1.947	2.029	1.332	1.328	1.324
	0.187	0.187	0.186			

Table SI 18 | Average T_1 relaxation measurements of selected choline-based magnetic salts measured at 9.4T and corresponding r_1 value.

Compound	[C] (mM)	T_1 (s) ± SD	$1/T_1$ (s^{-1}) ± SD	r_1 (mM^{-1} s^{-1})
$[N_{1,1,1,C2OH}][GdCl_4]$	1,00	0,138 ± 0,001	7,270 ± 0,041	7,5
	0,75	0,164 ± 0,000	6,091 ± 0,012	
	0,50	0,216 ± 0,001	4,636 ± 0,031	
	0,10	1,264 ± 0,029	0,791 ± 0,019	
	0,05	2,649 ± 0,034	0,377 ± 0,005	
$[N_{1,1,2,C3OH}][GdCl_4]$	1,00	0,119 ± 0,000	8,424 ± 0,012	8,1
	0,75	0,163 ± 0,000	6,122 ± 0,008	
	0,50	0,214 ± 0,001	4,664 ± 0,030	
	0,10	0,846 ± 0,002	1,182 ± 0,030	
	0,05	1,949 ± 0,079	0,514 ± 0,021	

$$\mathbf{M_{z_\tau} = M_0 . \left(1 - e^{-\frac{\tau}{T_1}}\right)} \quad \mathbf{(Equation\ SI\ 1)}$$

Table SI 19 | Average T_2 relaxation measurements of selected choline-based magnetic salts measured at 9.4T and corresponding r_2 value.

Compound	[C] (mM)	T_2 (s)	$1/T_2$ (s^{-1})	r_2 (mM^{-1} s^{-1})
$[N_{1,1,1,C2OH}][GdCl_4]$	1,00	0,119 ± 0,000	8,368 ± 0,023	8,4
	0,75	0,156 ± 0,000	6,396 ± 0,020	
	0,50	0,229 ± 0,000	4,357 ± 0,004	
	0,10	1,489 ± 0,004	0,671 ± 0,002	
	0,05	1,606 ± 0,004	0,623 ± 0,002	
$[N_{1,1,2,C3OH}][GdCl_4]$	1,00	0,103 ± 0,000	9,729 ± 0,041	9,3
	0,75	0,139 ± 0,000	7,207 ± 0,017	
	0,50	0,210 ± 0,000	4,757 ± 0,004	
	0,10	0,758 ± 0,007	1,319 ± 0,013	
	0,05	1,328 ± 0,004	0,753 ± 0,002	

$$\mathbf{M_{xy} = M_0 . e^{-\frac{\tau}{T_2}}} \quad \mathbf{(Equation\ SI\ 2)}$$

2.1. NMR T_1 relaxation time measurements of $[N_{1,1,1,C2OH}][GdCl_4]$ at different concentrations

2.1.1. [C]=1mM

(A)

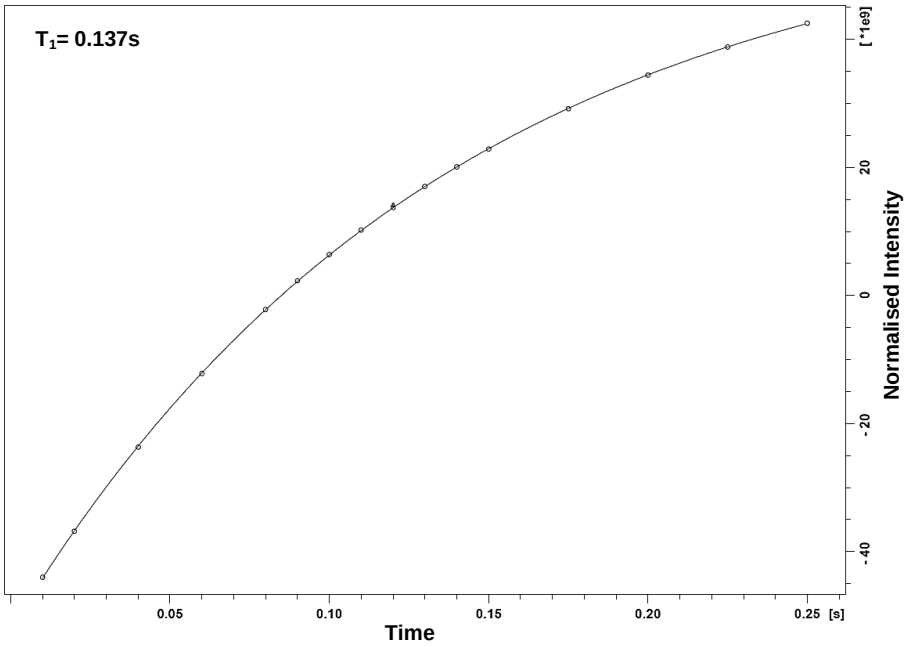

(B)

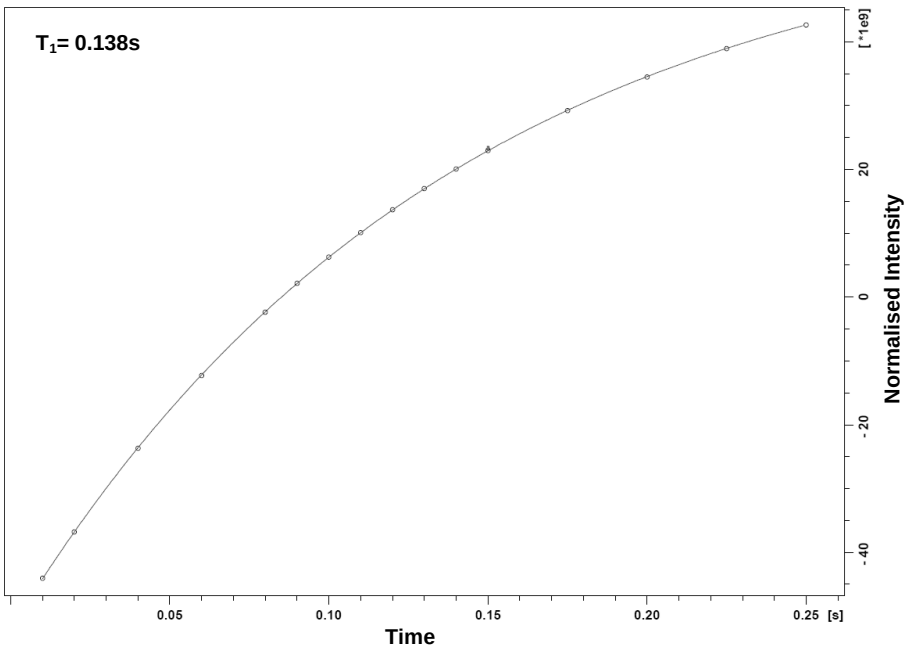

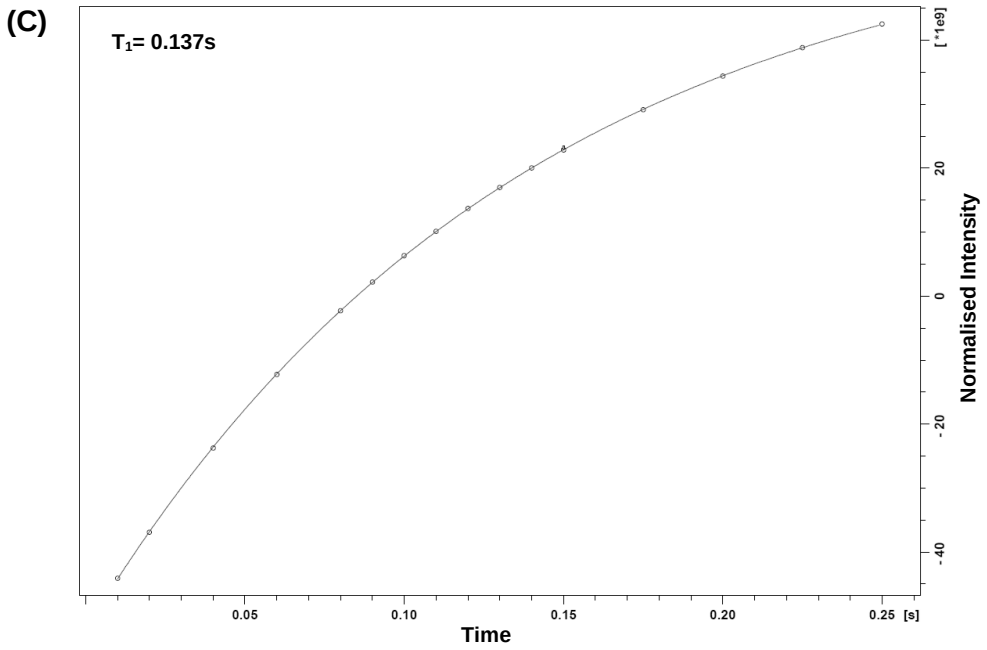

Figure SI 70 | T_1 saturation recovery curve for 1.00mM aqueous solution of $[N_{1,1,1,C2OH}][GdCl_4]$ at 37 ºC fitted with Equation SI 1.

2.1.2. [C]=0.75mM

(A)

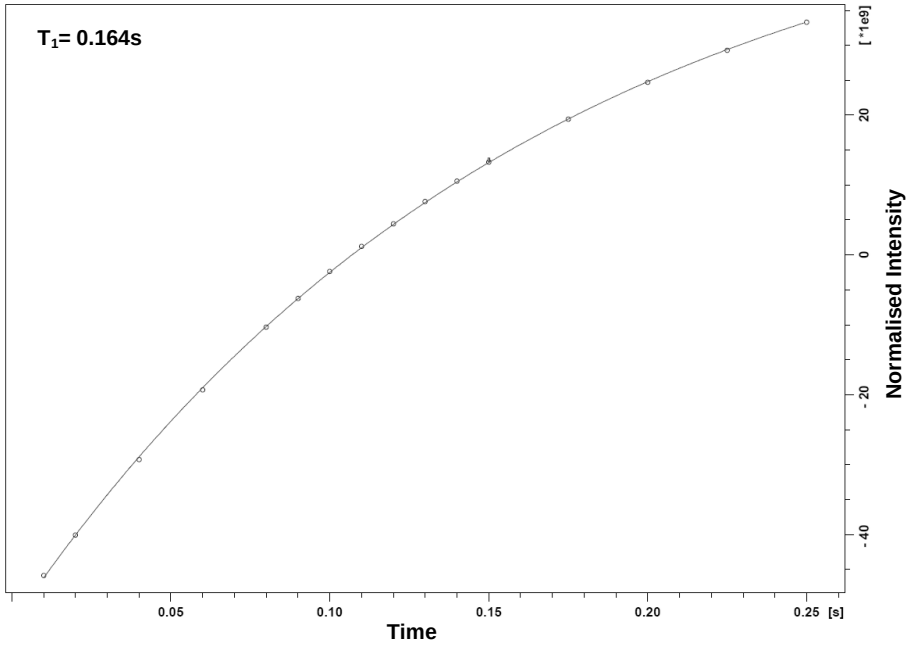

(B)

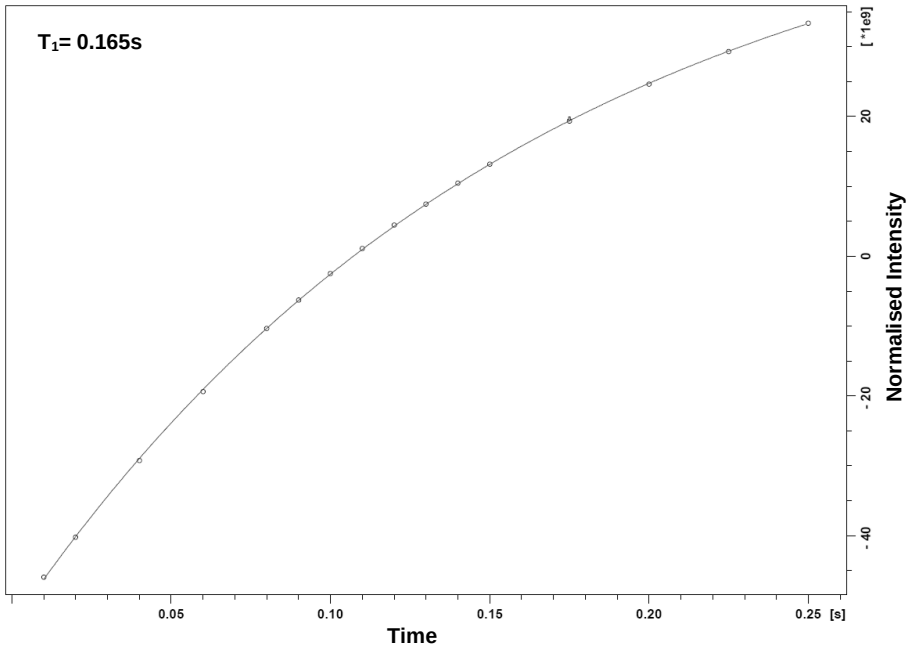

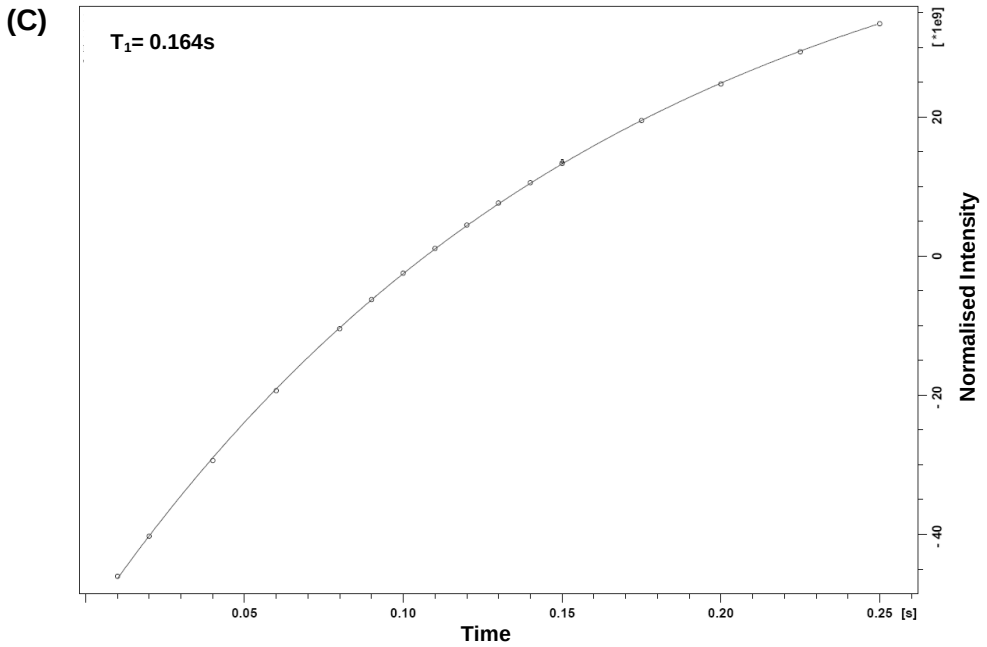

Figure SI 71 | T_1 saturation recovery curve for 0.75mM aqueous solution of $[N_{1,1,1,C2OH}][GdCl_4]$ at 37 ºC fitted with Equation SI 1.

2.1.3. [C]=0.50mM

(A)

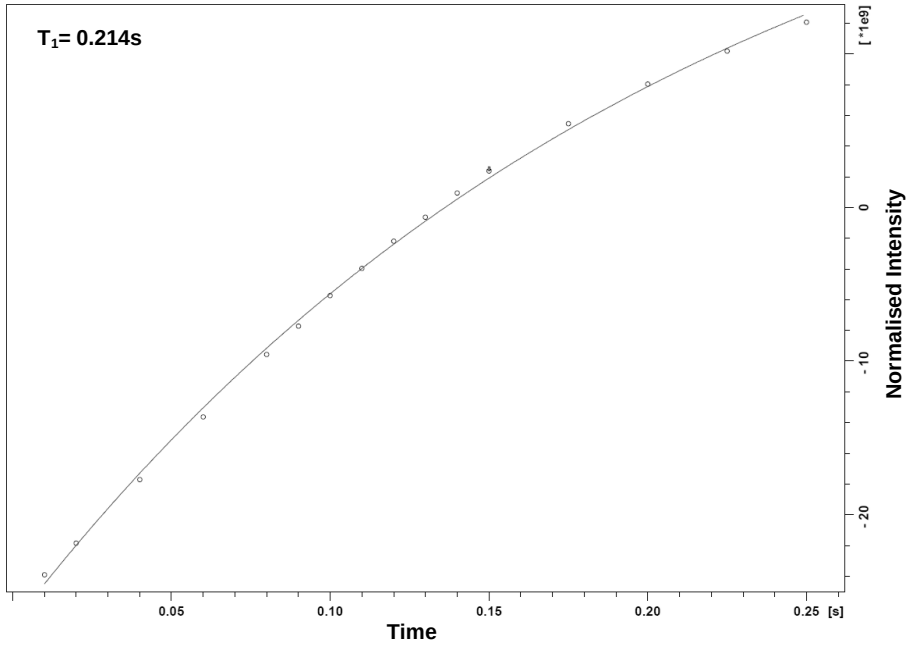

(B)

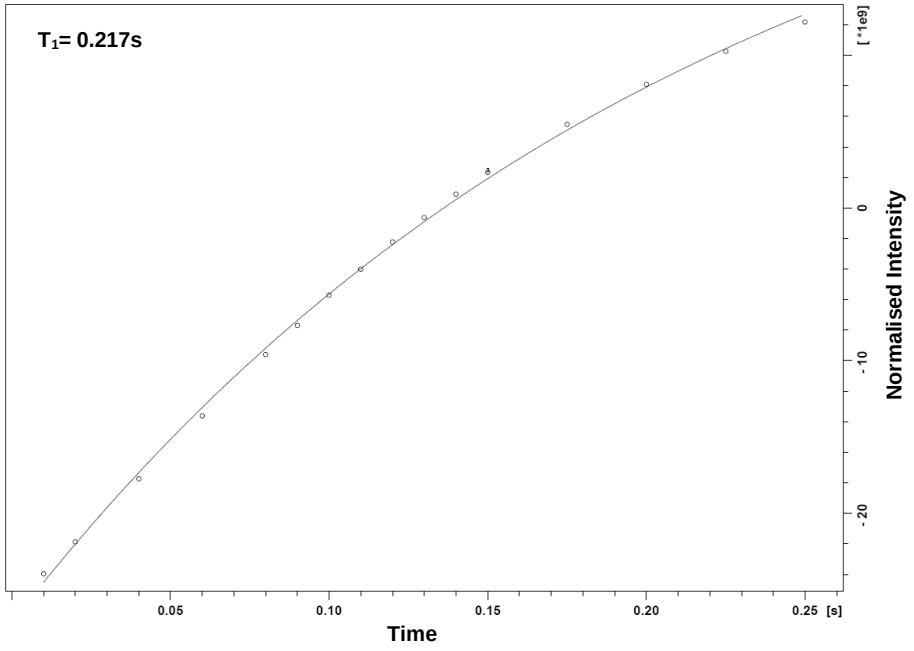

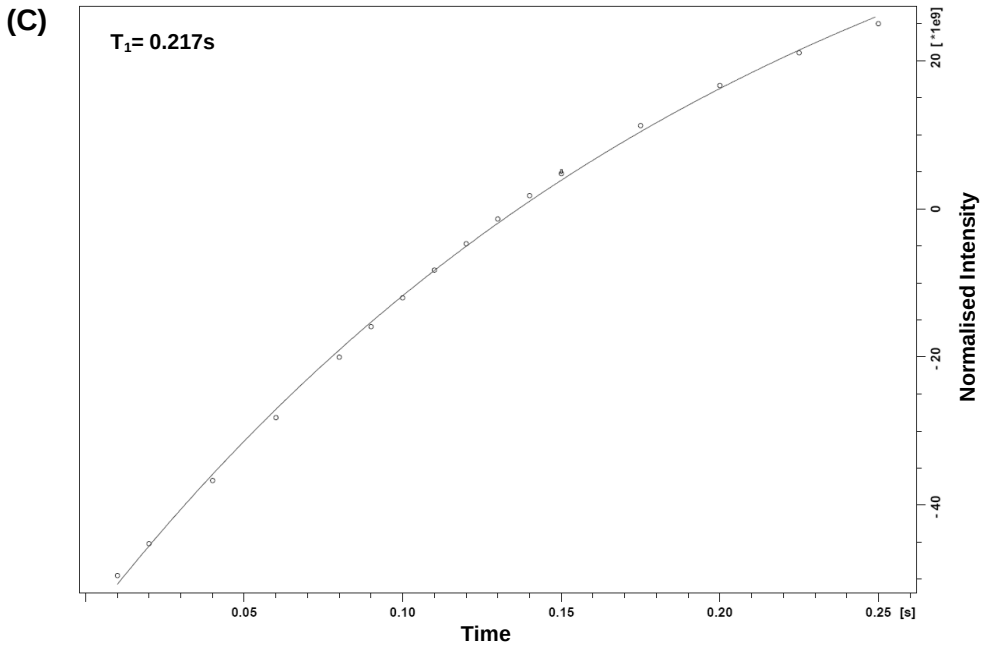

Figure SI 72 | T_1 saturation recovery curve for 0.50mM aqueous solution of $[N_{1,1,1,C2OH}][GdCl_4]$ at 37 ºC fitted with Equation SI 1.

2.1.4. [C]=0.10mM

(A)

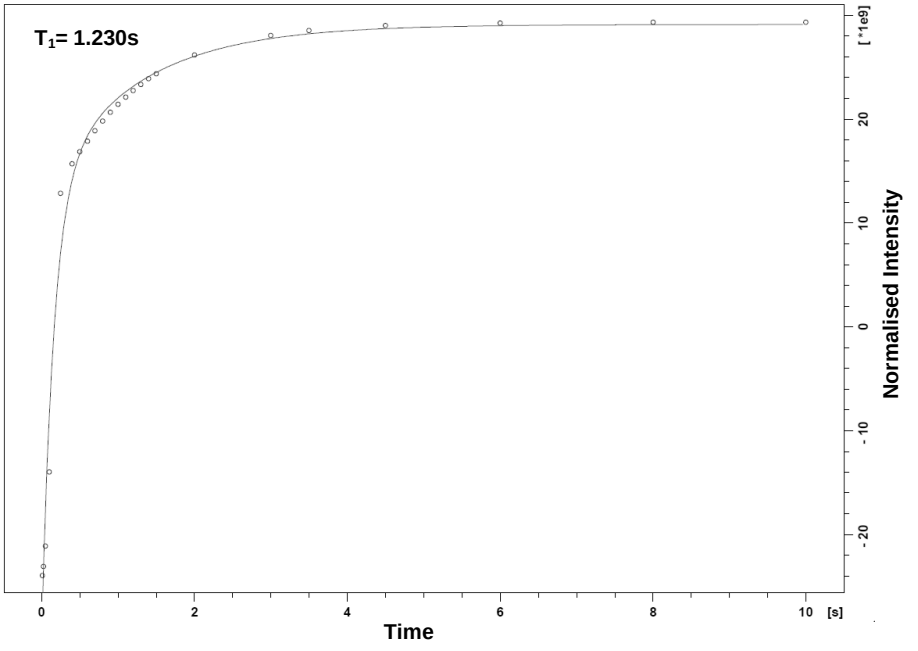

(B)

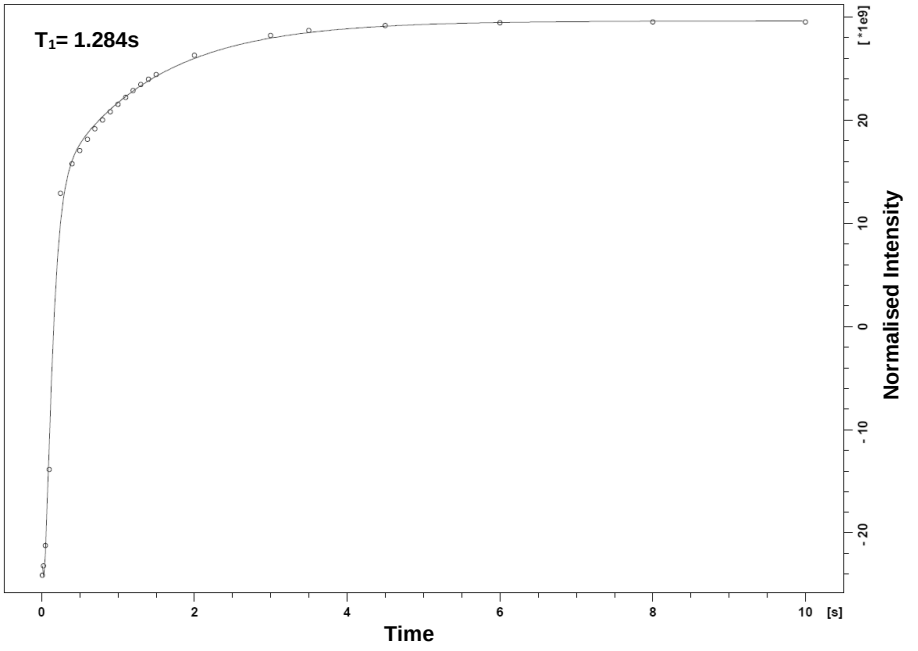

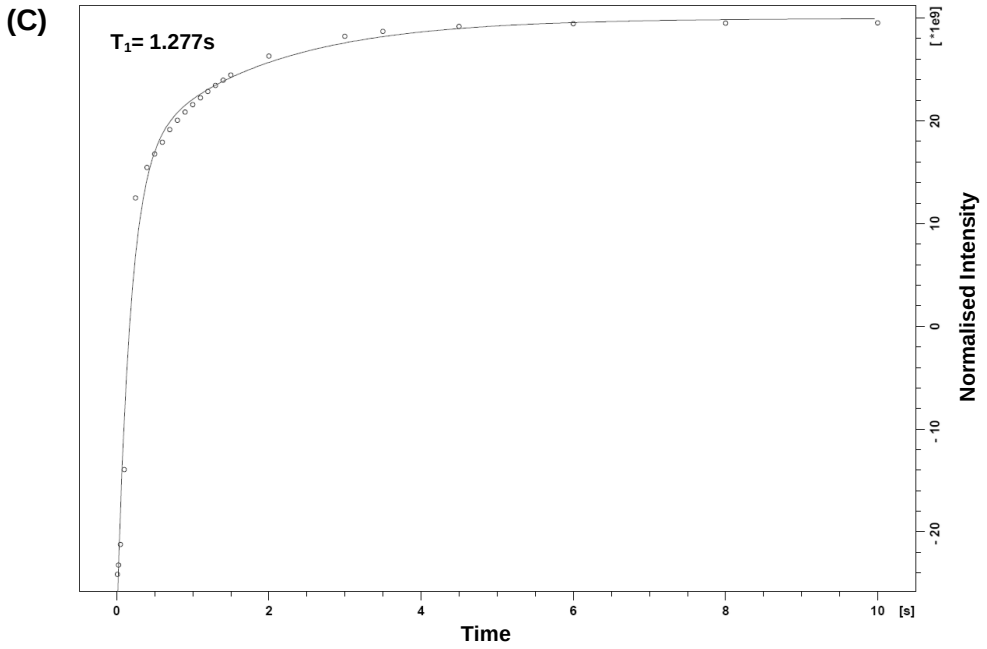

Figure SI 73 | T_1 saturation recovery curve for 0.10mM aqueous solution of $[N_{1,1,1,C2OH}][GdCl_4]$ at 37 ºC fitted with Equation SI 1.

2.1.5. [C]=0.05mM

(A)

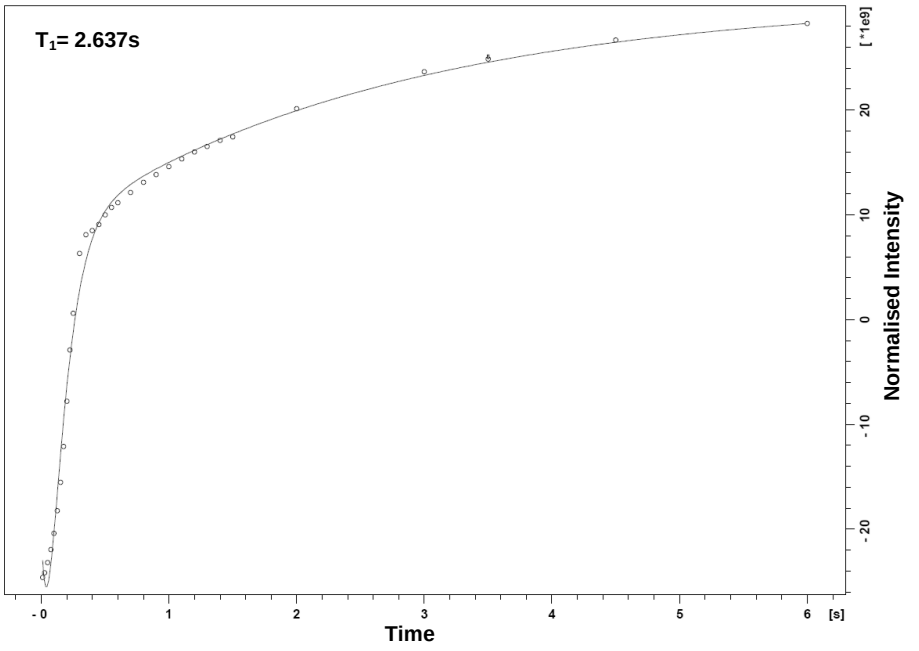

(B)

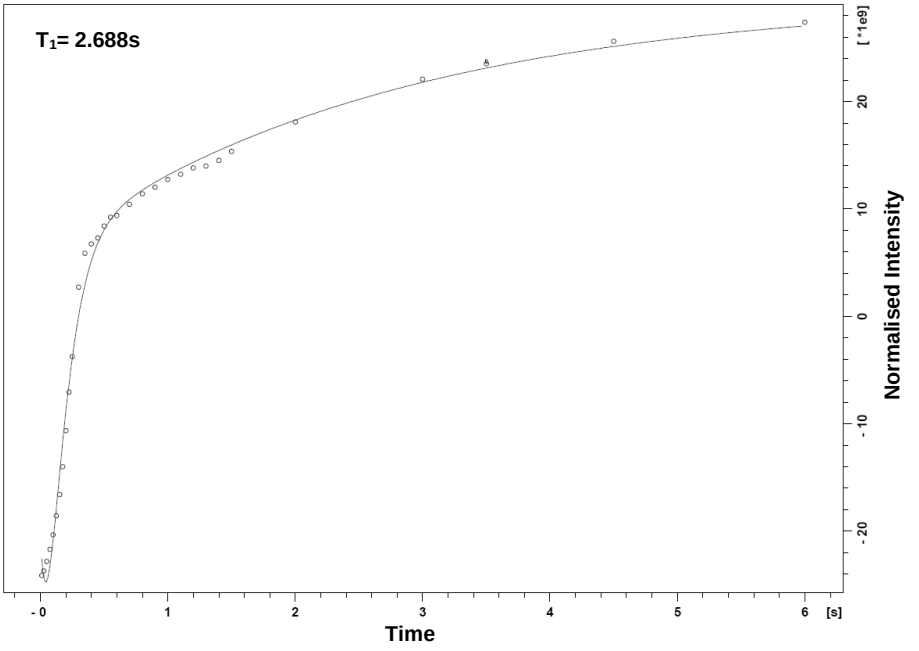

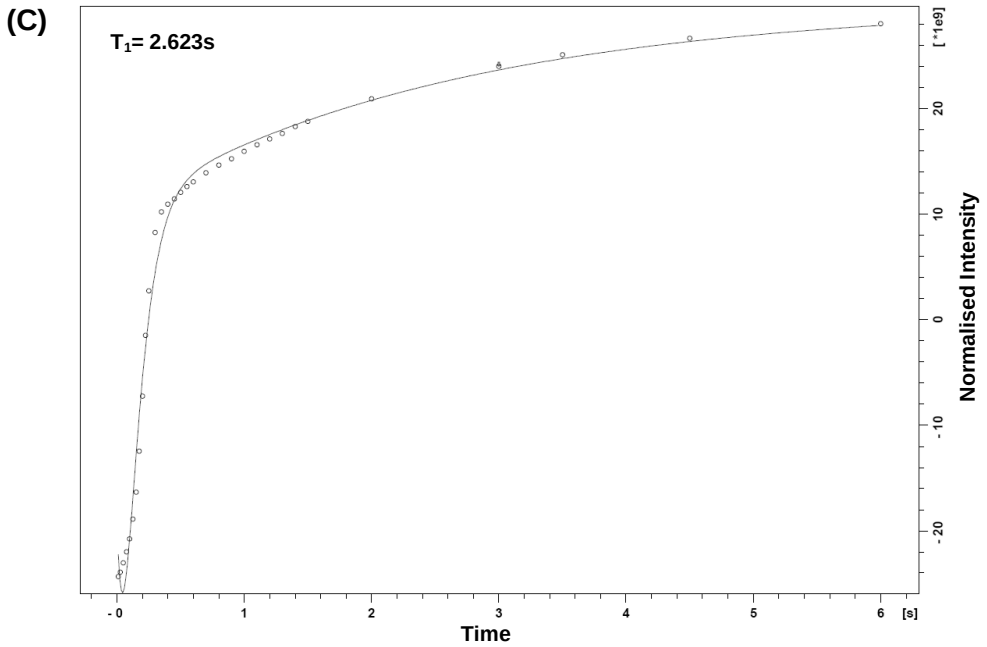

Figure SI 74 | T_1 saturation recovery curve for 0.05mM aqueous solution of $[N_{1,1,1,C2OH}][GdCl_4]$ at 37 ºC fitted with Equation SI 1.

2.2. NMR T_1 relaxation time measurements of $[N_{1,1,2,C3OH}][GdCl_4]$ at different concentrations

2.2.1. [C]=1.00mM

(A)

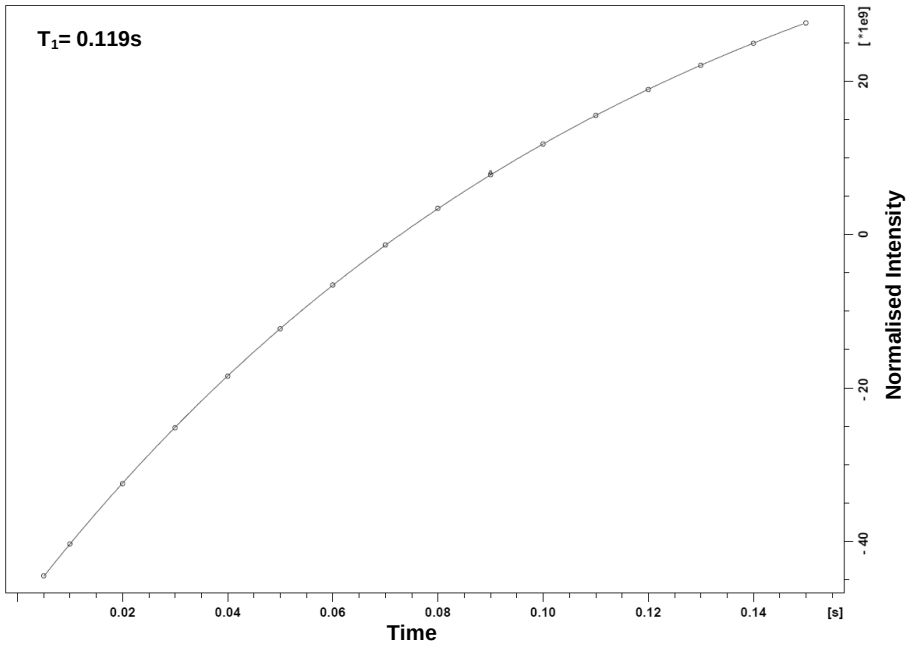

(B)

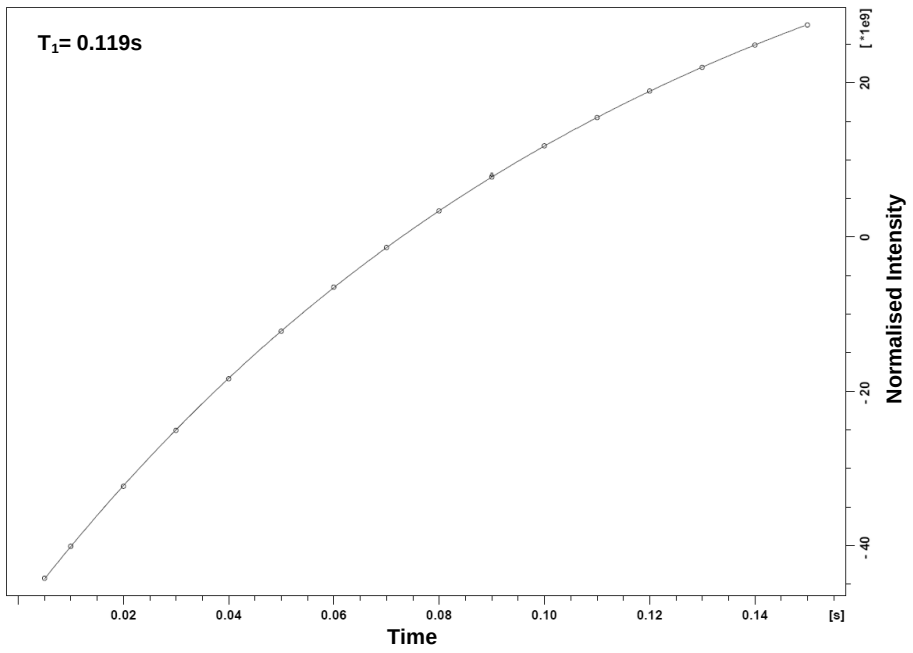

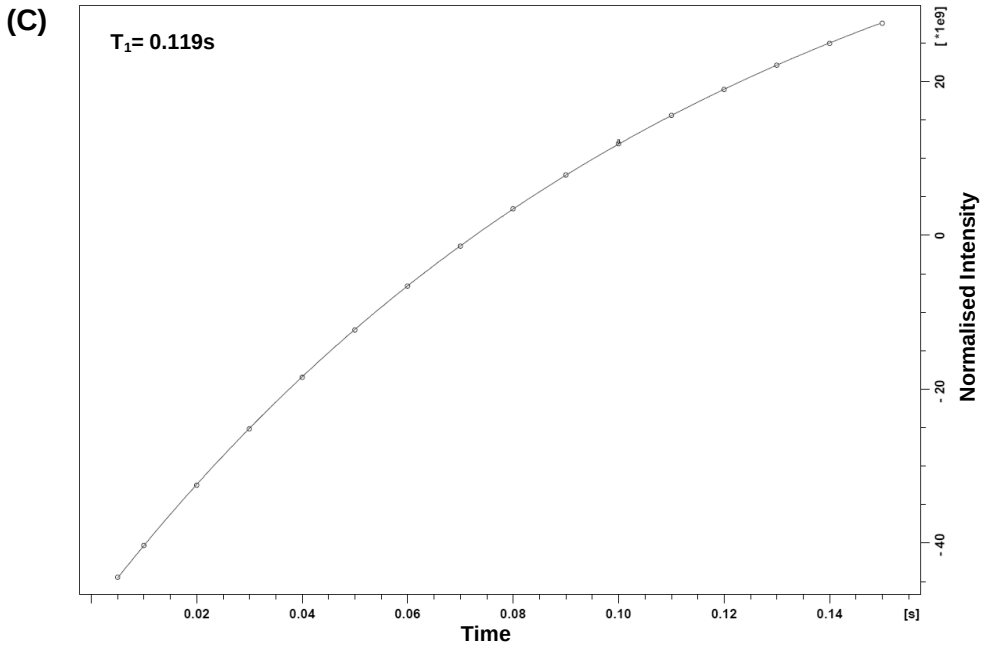

Figure SI 75 | T_1 saturation recovery curve for 1.00mM aqueous solution of $[N_{1,1,2,C3OH}][GdCl_4]$ at 37 ºC fitted with Equation SI 1.

2.2.2. [C]=0.75mM

(A)

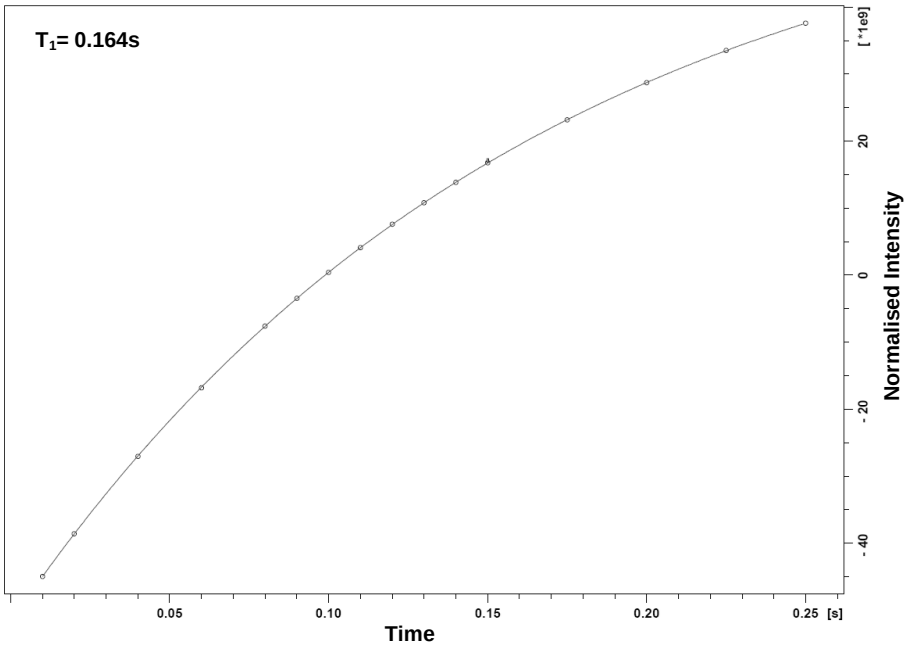

(B)

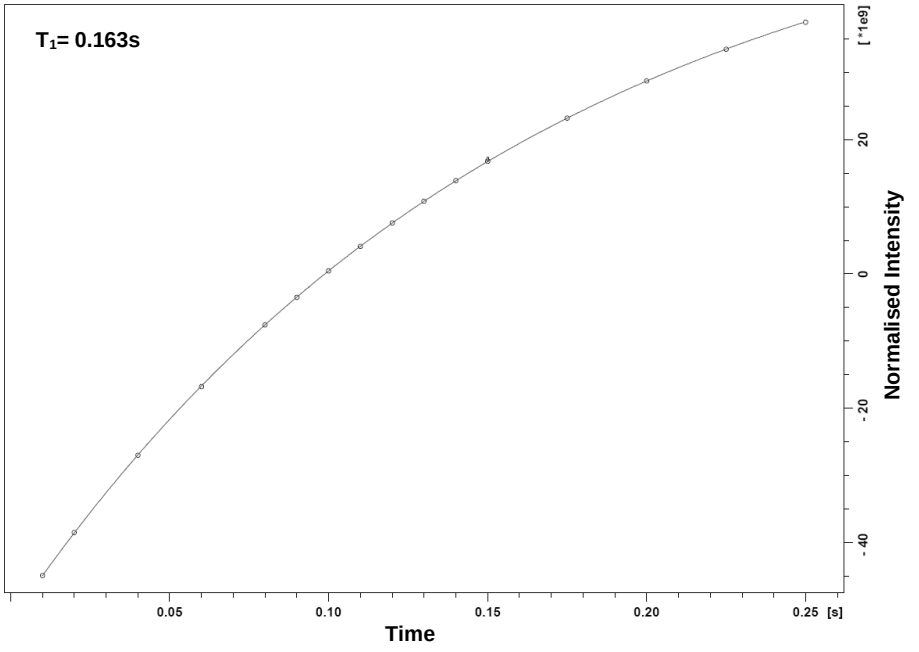

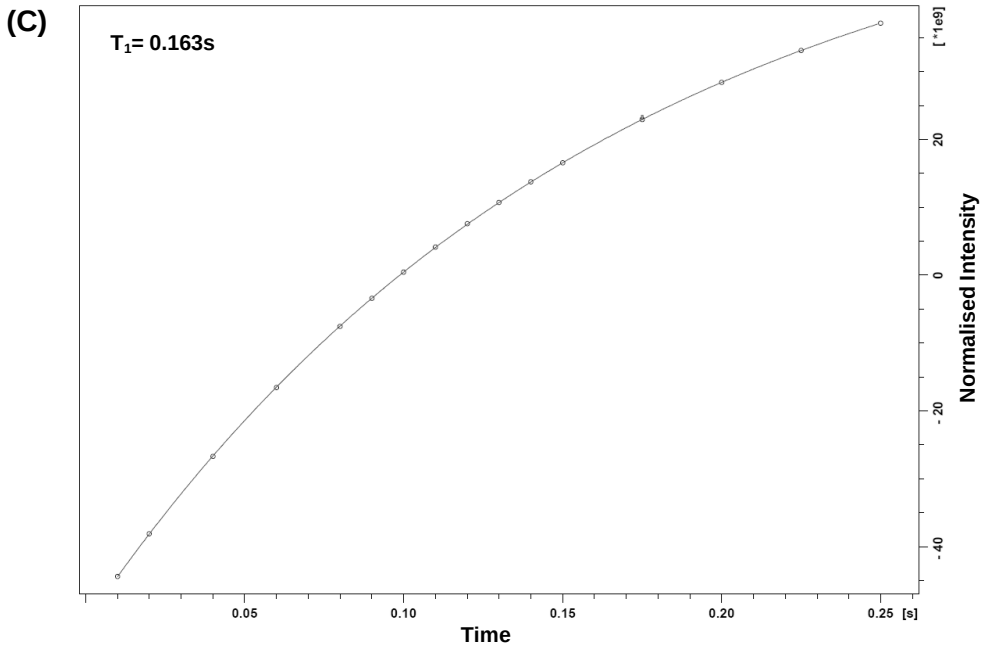

Figure SI 76 | T_1 saturation recovery curve for 0.75mM aqueous solution of $[N_{1,1,2,C3OH}][GdCl_4]$ at 37 ºC fitted with Equation SI 1.

2.2.3. [C]=0.50mM

(A)

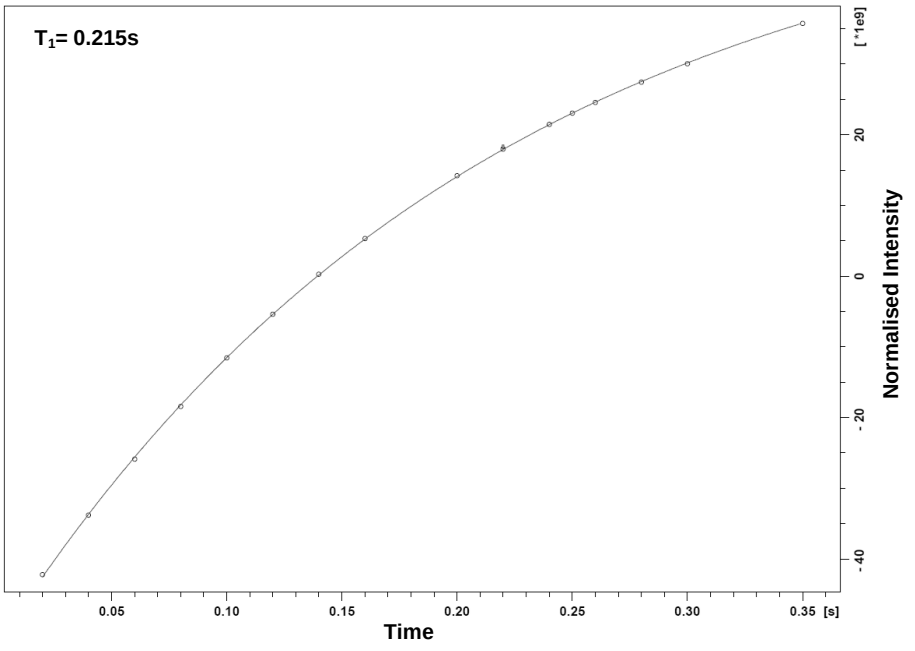

(B)

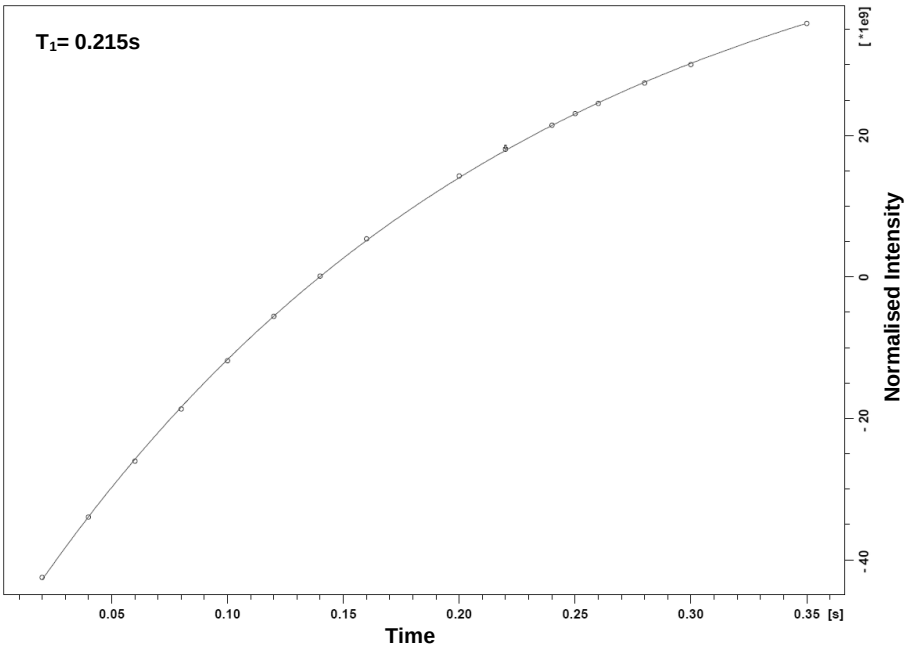

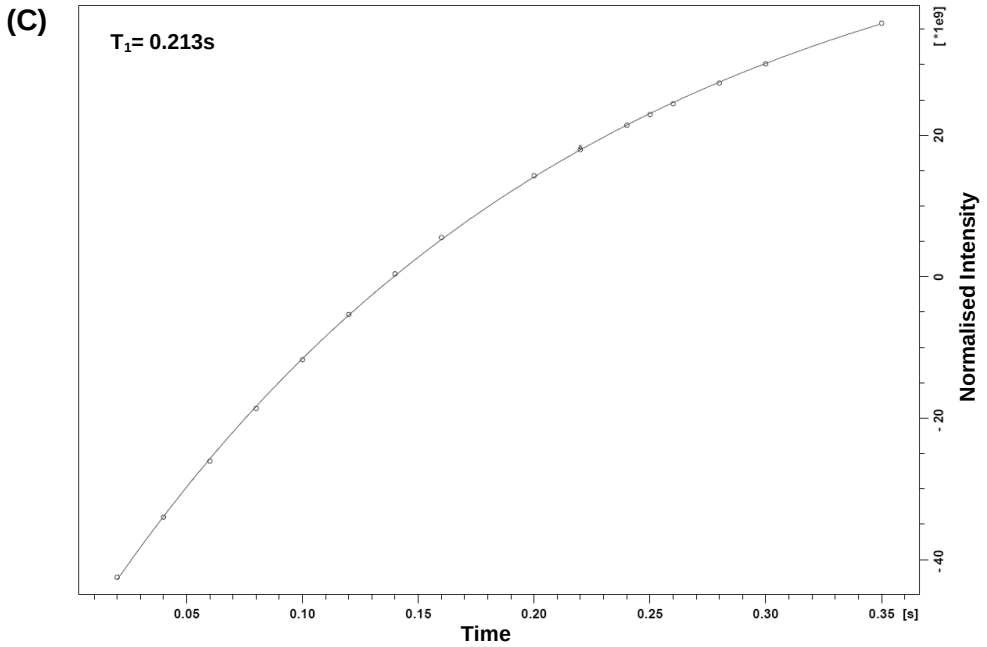

Figure SI 77 | T_1 saturation recovery curve for 0.50mM aqueous solution of $[N_{1,1,2,C3OH}][GdCl_4]$ at 37 ºC fitted with Equation SI 1.

2.2.4. [C]=0.10mM

(A)

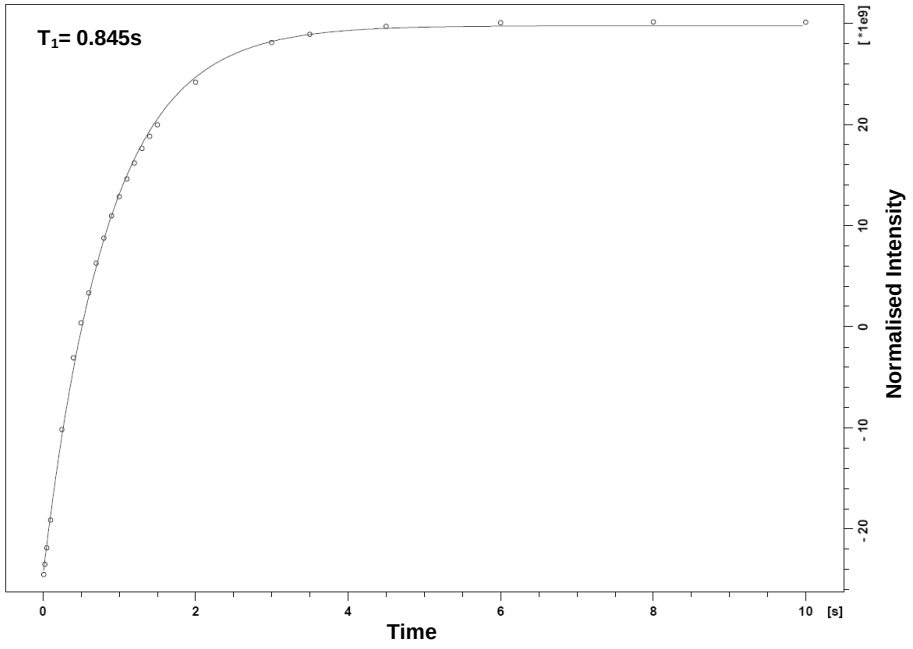

(B)

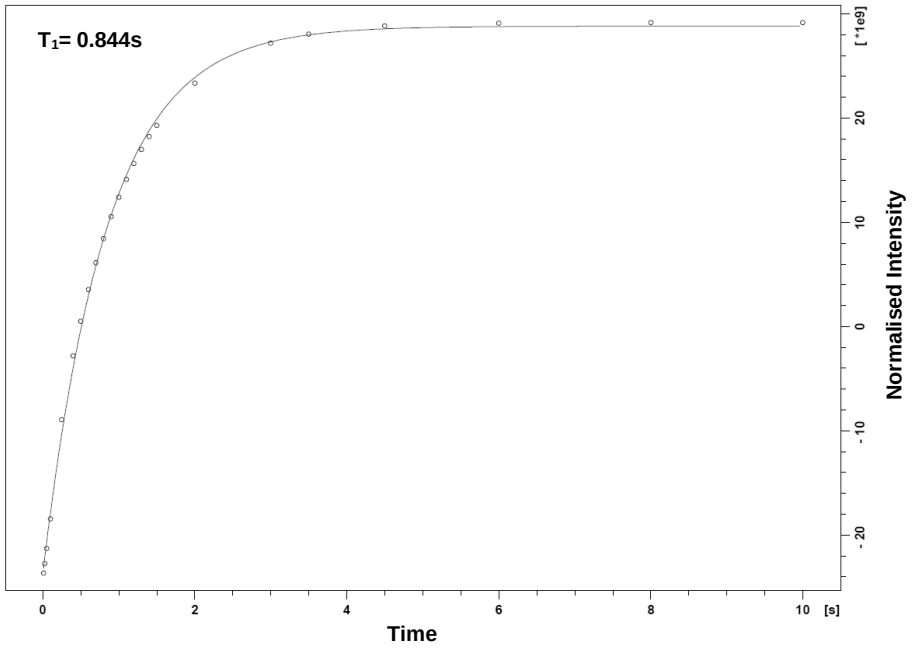

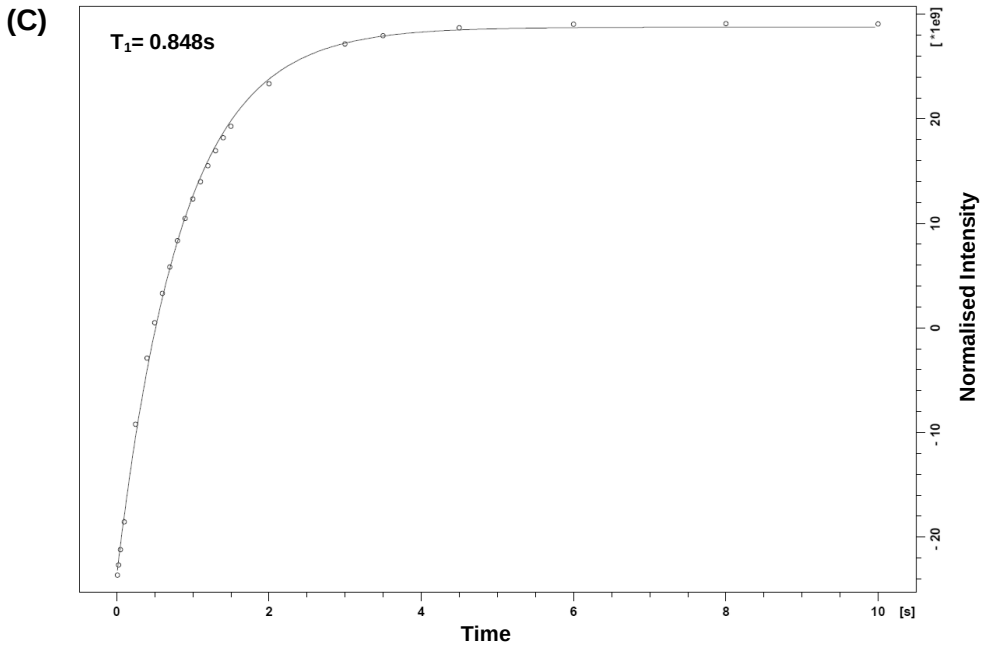

Figure SI 78 | T_1 saturation recovery curve for 0.10mM aqueous solution of $[N_{1,1,2,C3OH}][GdCl_4]$ at 37 ºC fitted with Equation SI 1.

2.2.5. [C]=0.05mM

(A)

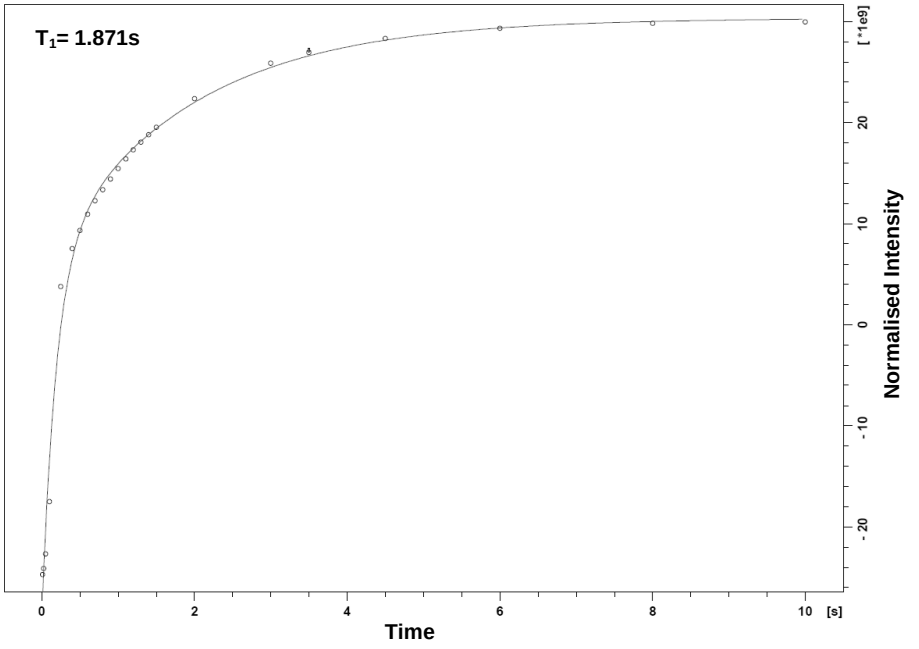

(B)

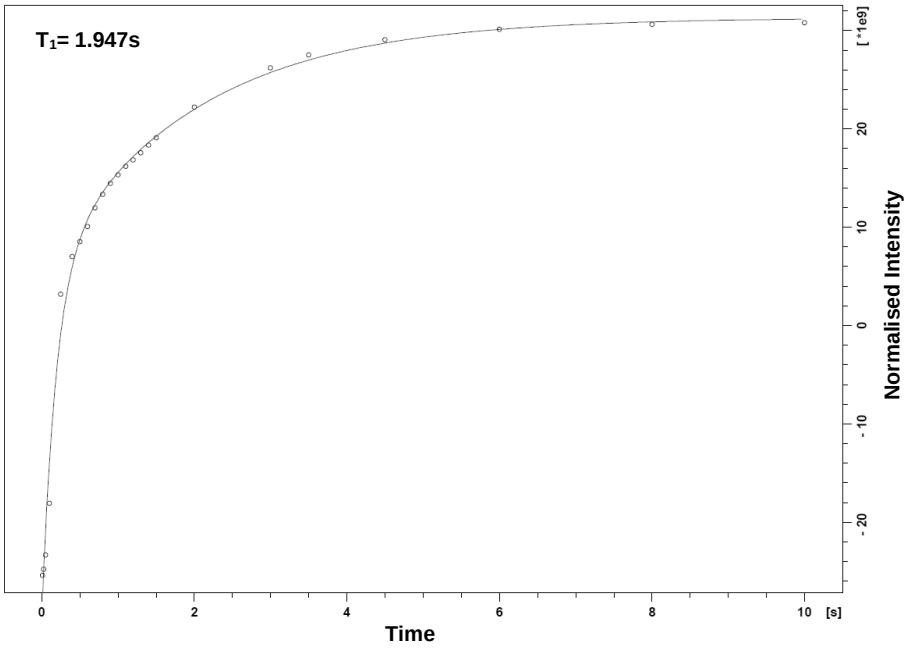

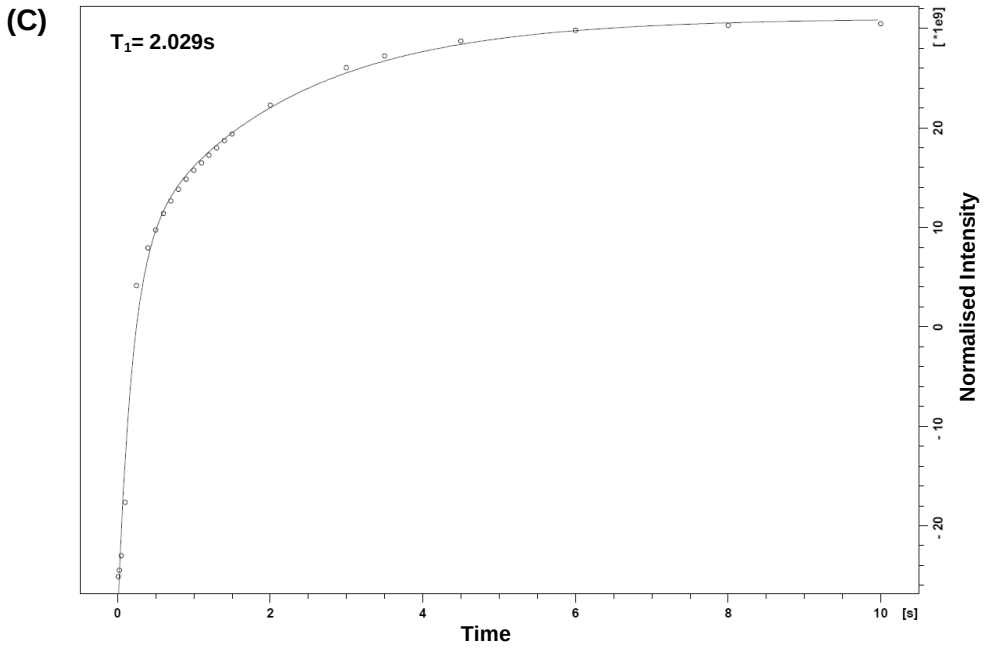

Figure SI 79 | T_1 saturation recovery curve for 0.05mM aqueous solution of $[N_{1,1,2,C3OH}][GdCl_4]$ at 37 ºC fitted with Equation SI 1.

2.3. NMR T_2 relaxation time measurements of $[N_{1,1,1,C2OH}][GdCl_4]$ at different concentrations

2.3.1. [C]=1.00mM

(A)

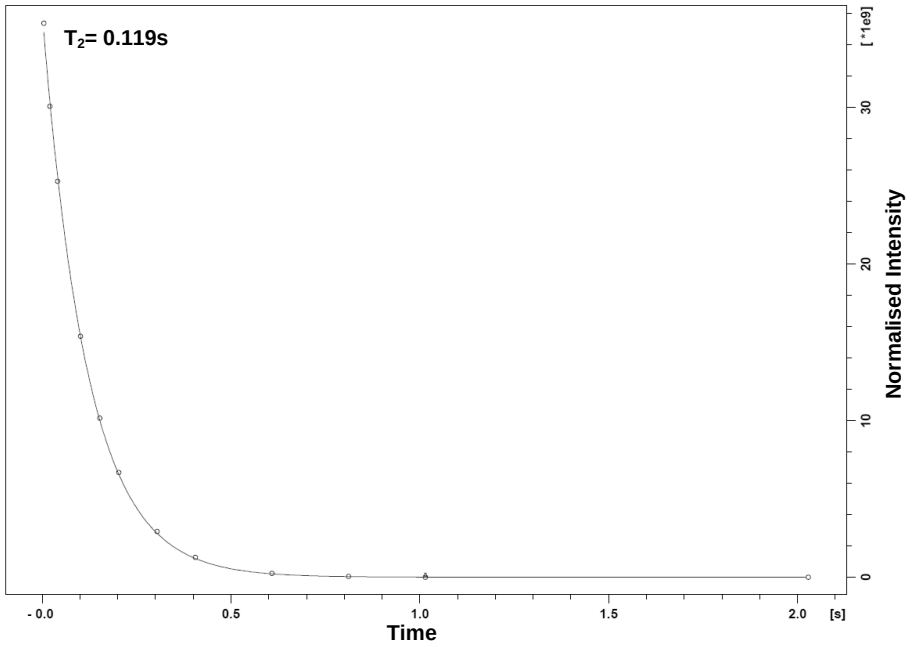

(B)

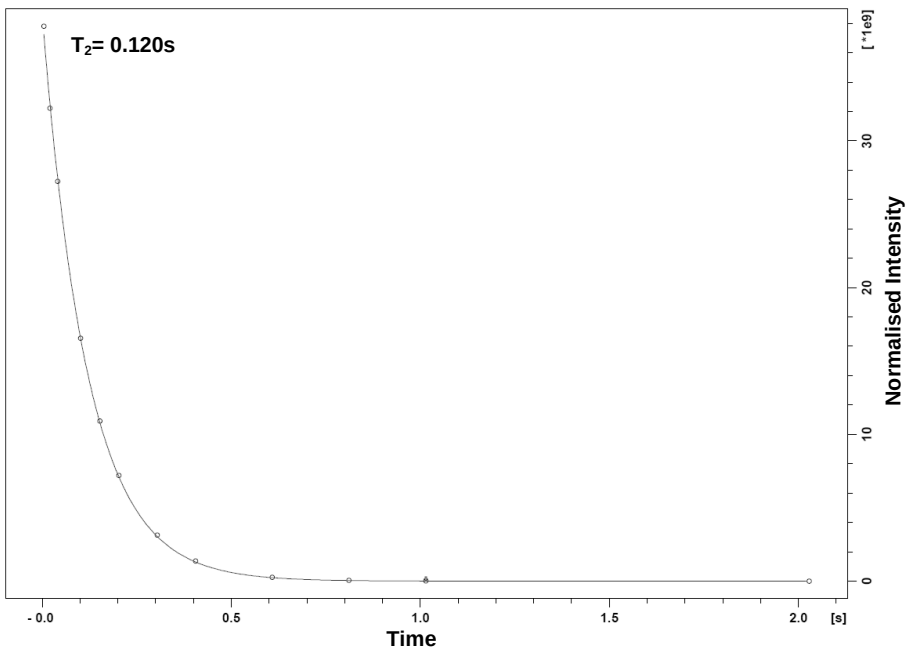

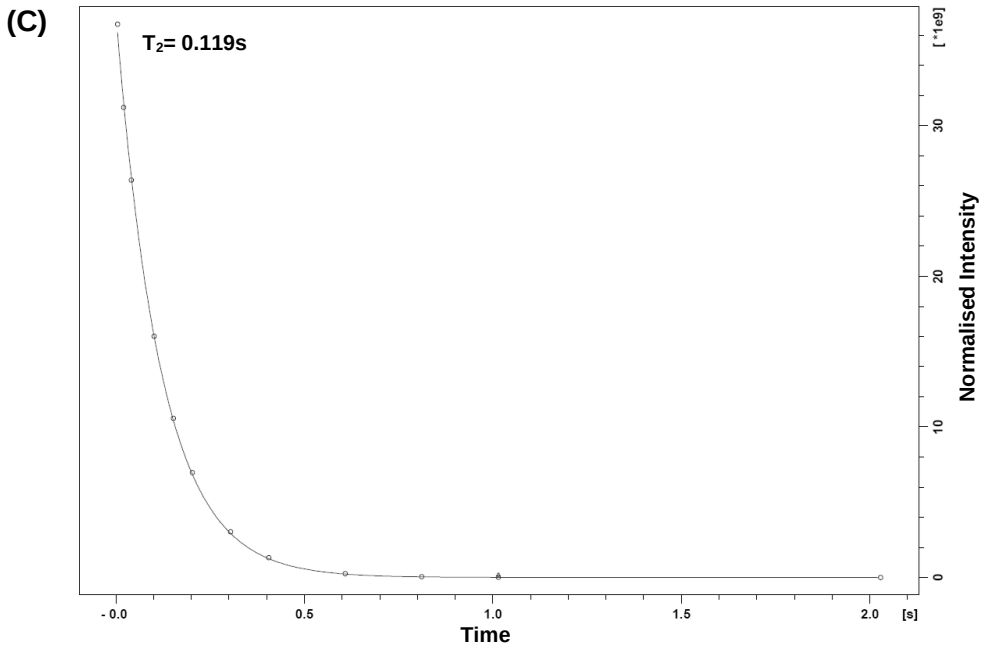

Figure SI 80 | T_2 CPMG decay curve for 1.00mM aqueous solution of $[N_{1,1,1,C2OH}][GdCl_4]$ at 37 ºC fitted with Equation SI 2.

2.3.2. [C]=0.75mM

(A)

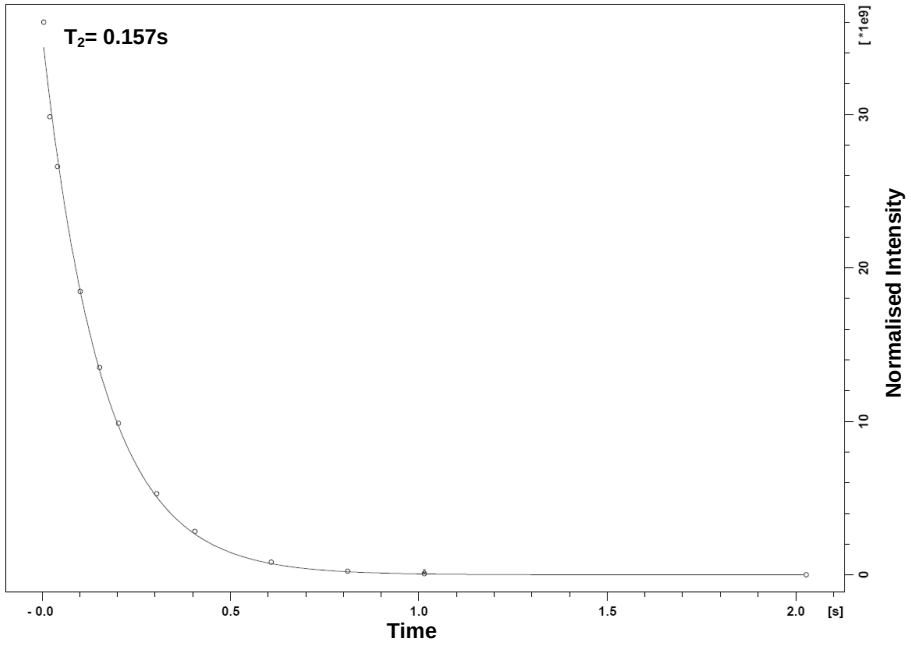

(B)

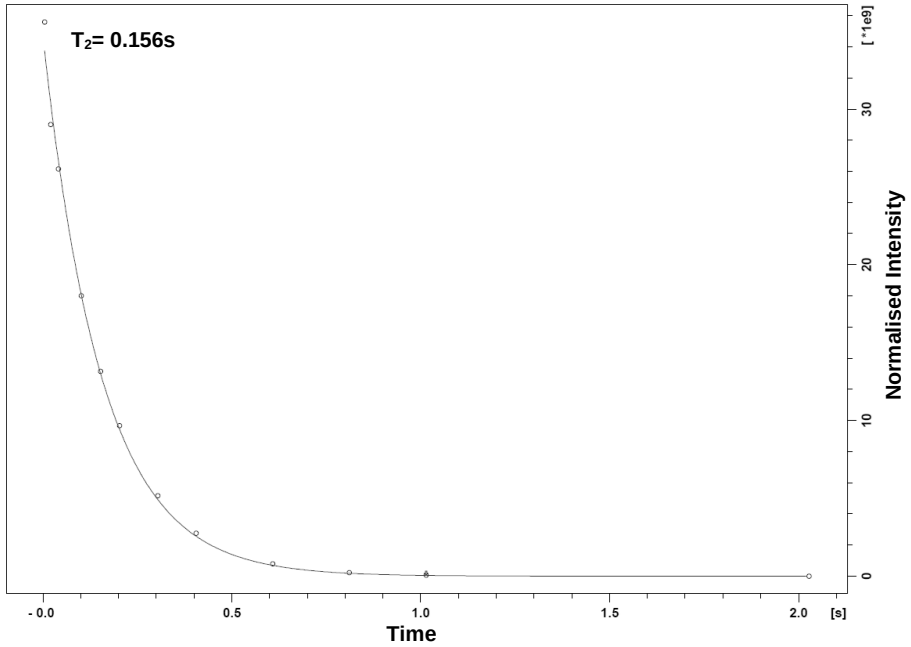

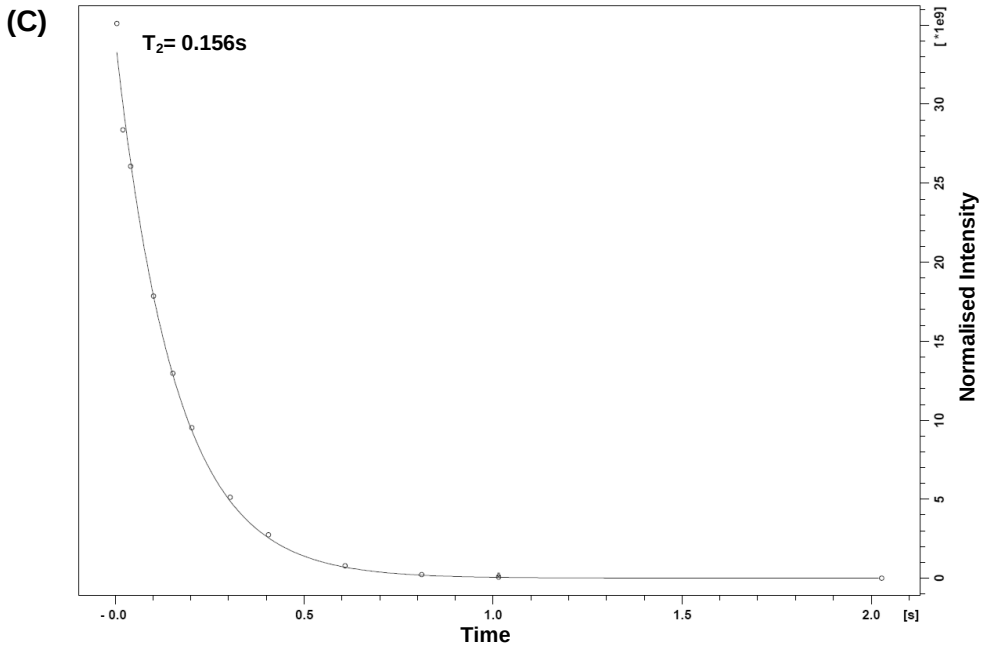

Figure SI 81 | T_2 CPMG decay curve for 0.75mM aqueous solution of $[N_{1,1,1,C2OH}][GdCl_4]$ at 37 ºC fitted with Equation SI 2.

2.3.3. [C]=0.50mM

(A)

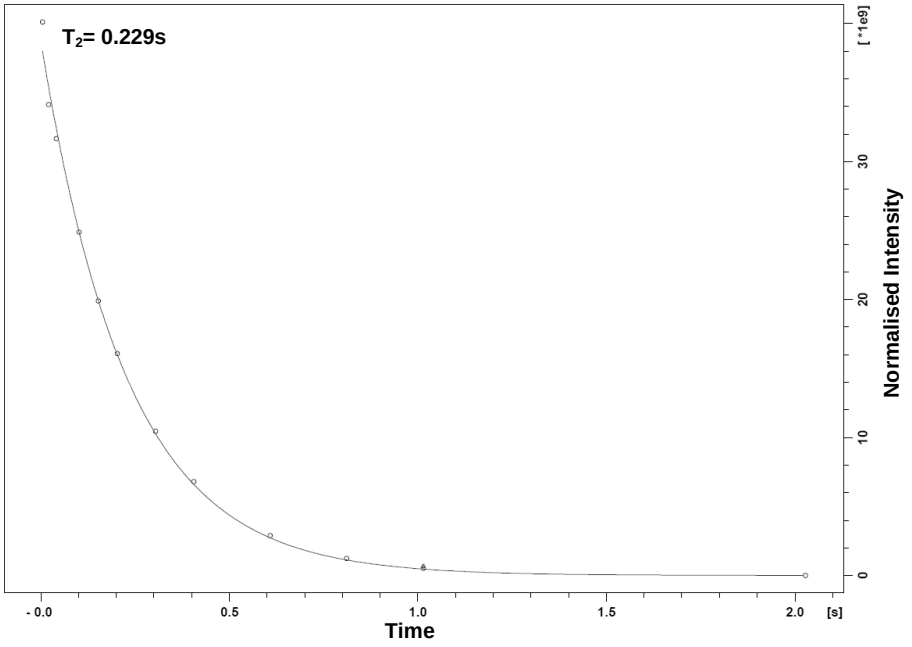

(B)

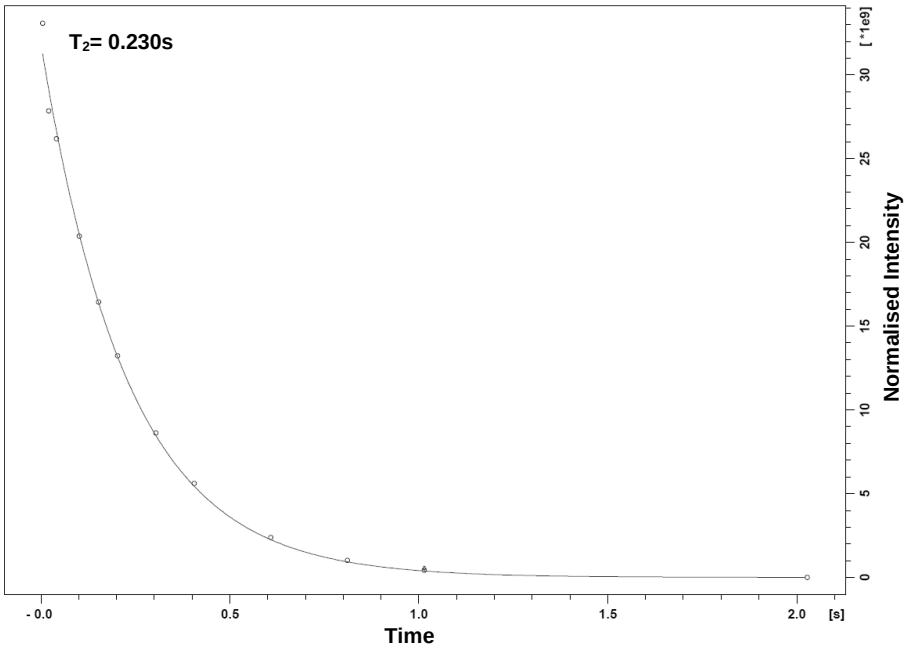

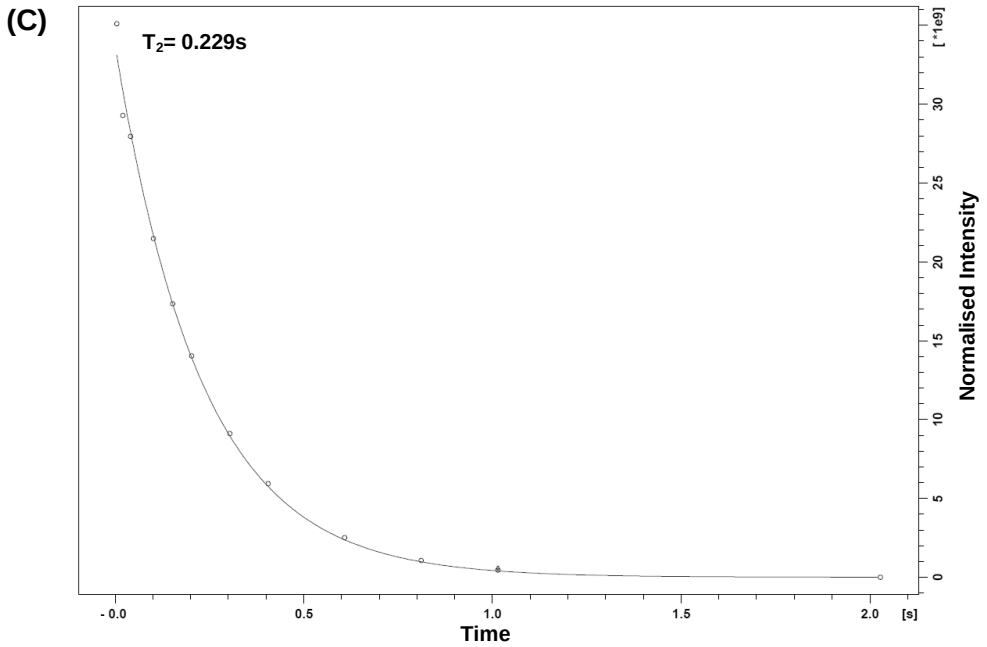

Figure SI 82 | T_2 CPMG decay curve for 0.50mM aqueous solution of $[N_{1,1,1,C2OH}][GdCl_4]$ at 37 ºC fitted with Equation SI 2.

2.3.4. [C]=0.10mM

(A)

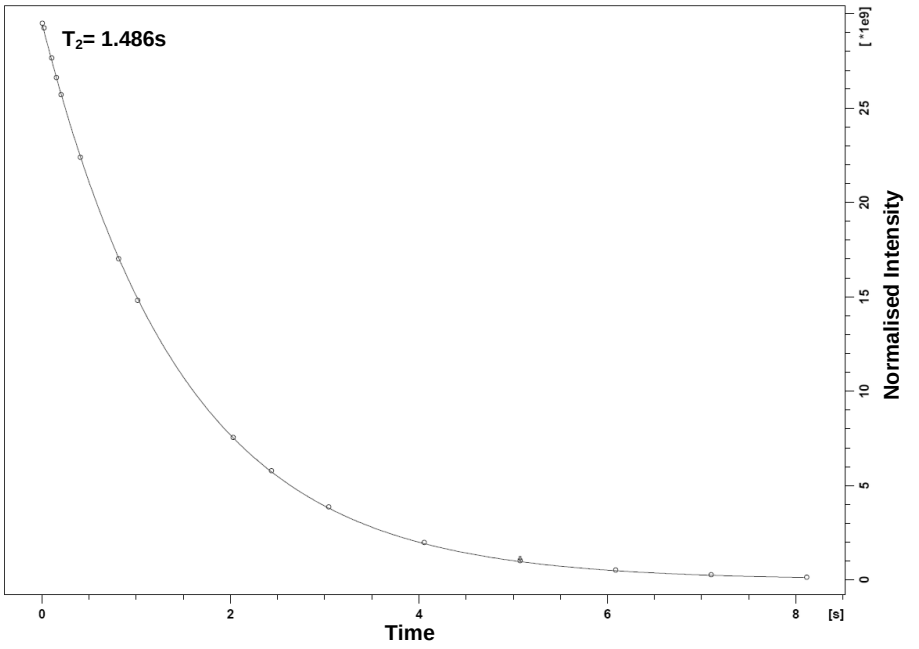

(B)

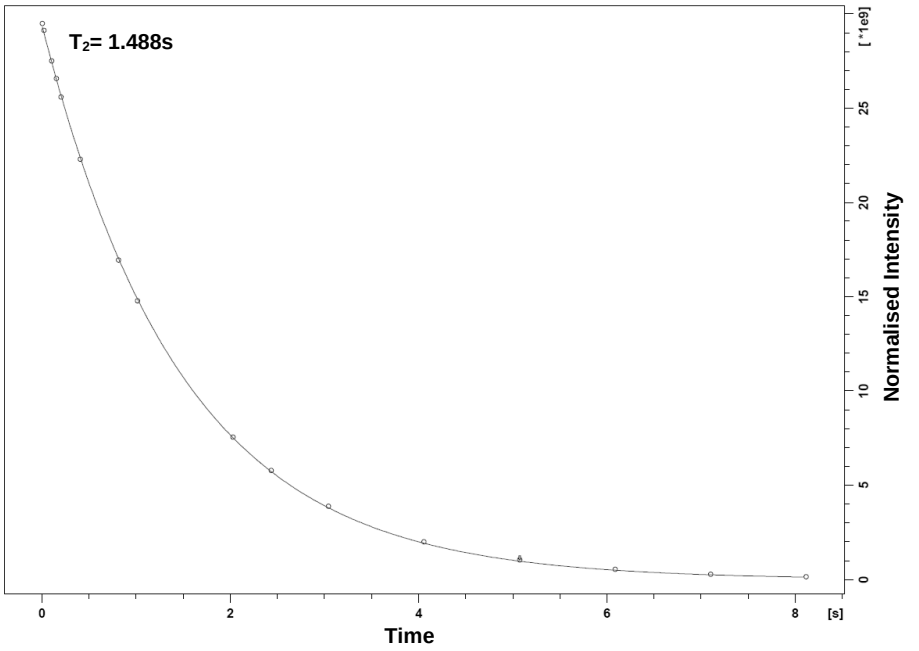

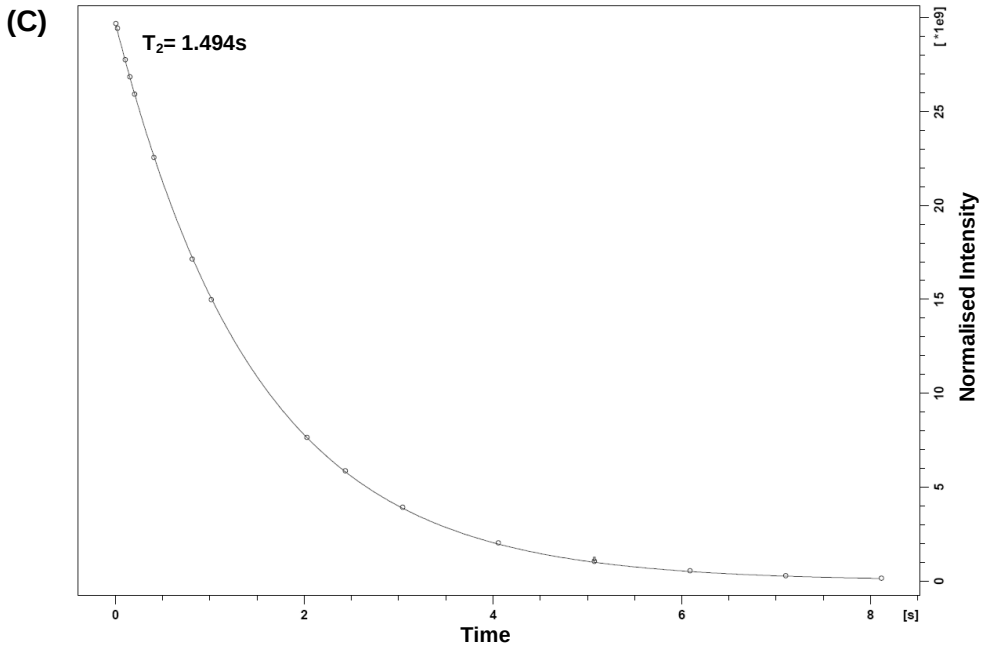

Figure SI 83 | T_2 CPMG decay curve for 0.10mM aqueous solution of $[N_{1,1,1,C2OH}][GdCl_4]$ at 37 ºC fitted with Equation SI 2.

2.3.5. [C]=0.05mM

(A)

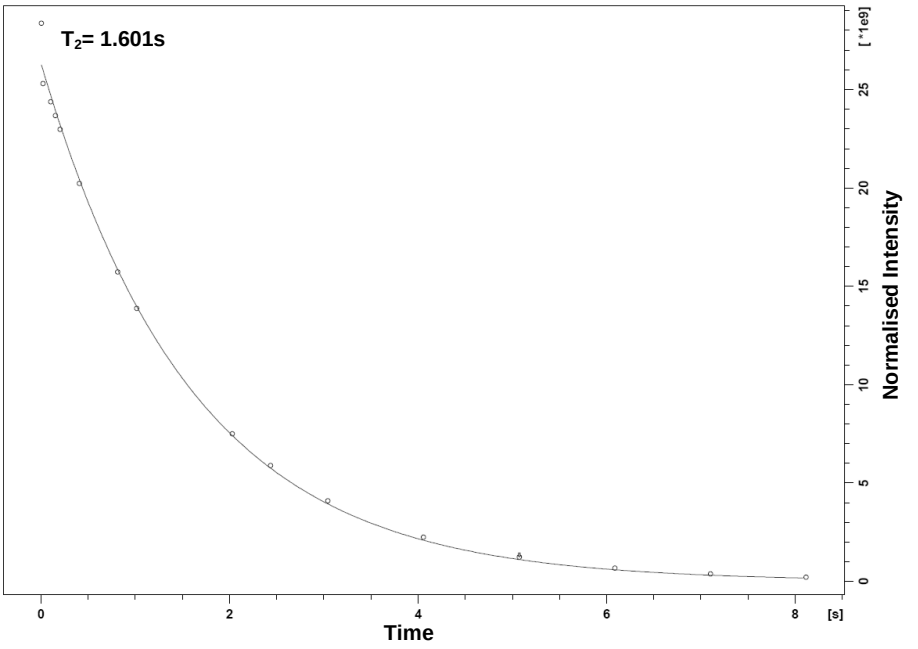

(B)

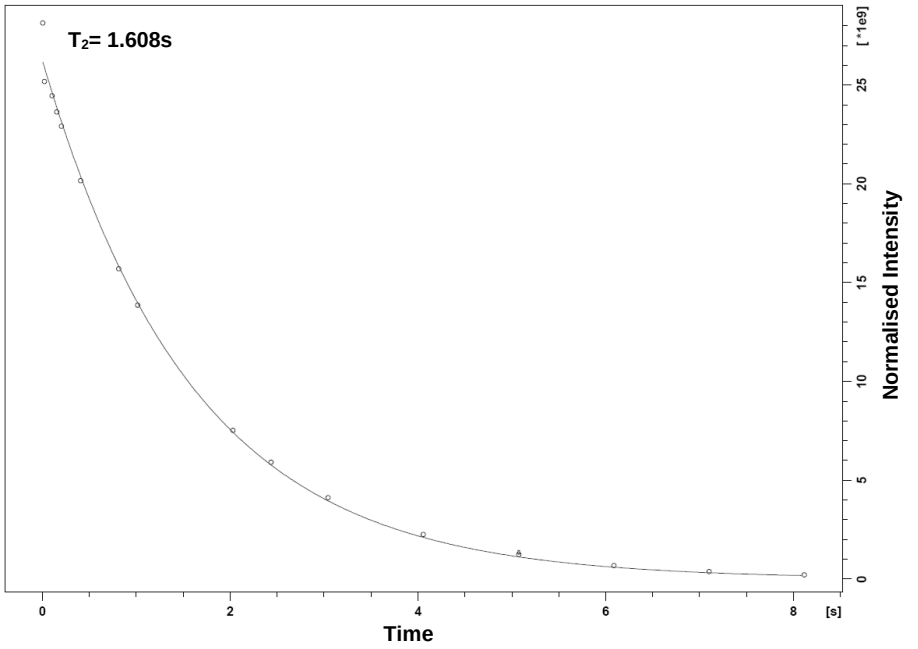

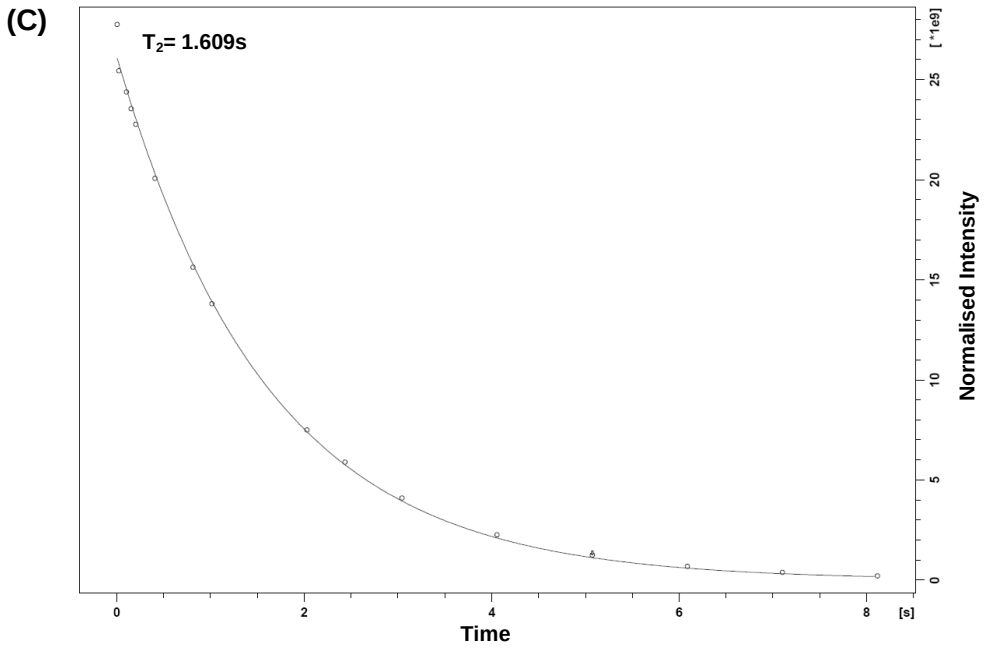

Figure SI 84 | T_2 CPMG decay curve for 0.05mM aqueous solution of $[N_{1,1,1,C2OH}][GdCl_4]$ at 37 ºC fitted with Equation SI 2.

2.4. NMR T_2 relaxation time measurements of $[N_{1,1,2,C3OH}][GdCl_4]$ at different concentrations

2.4.1. [C]=1.00mM

(A)

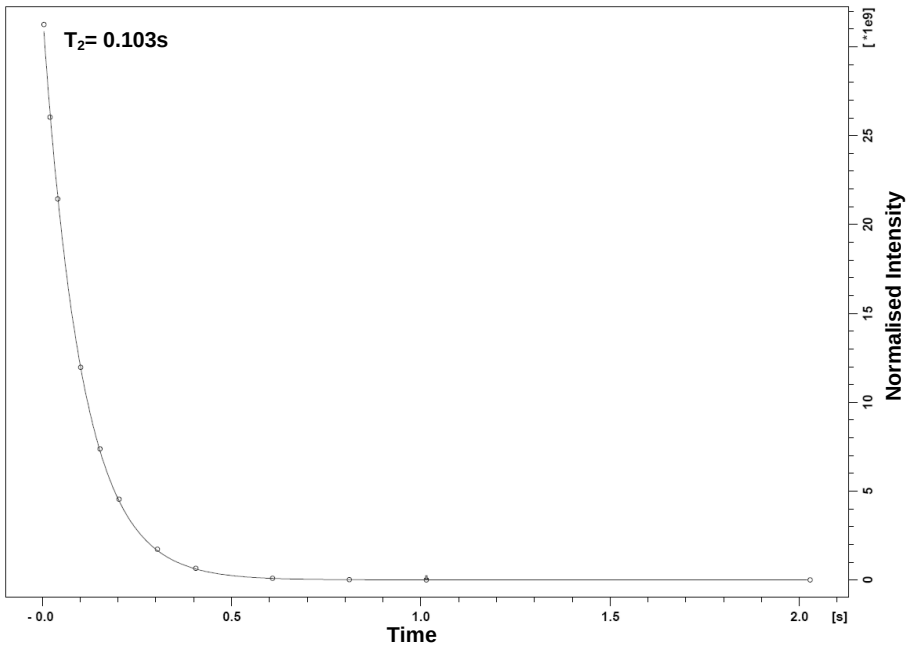

(B)

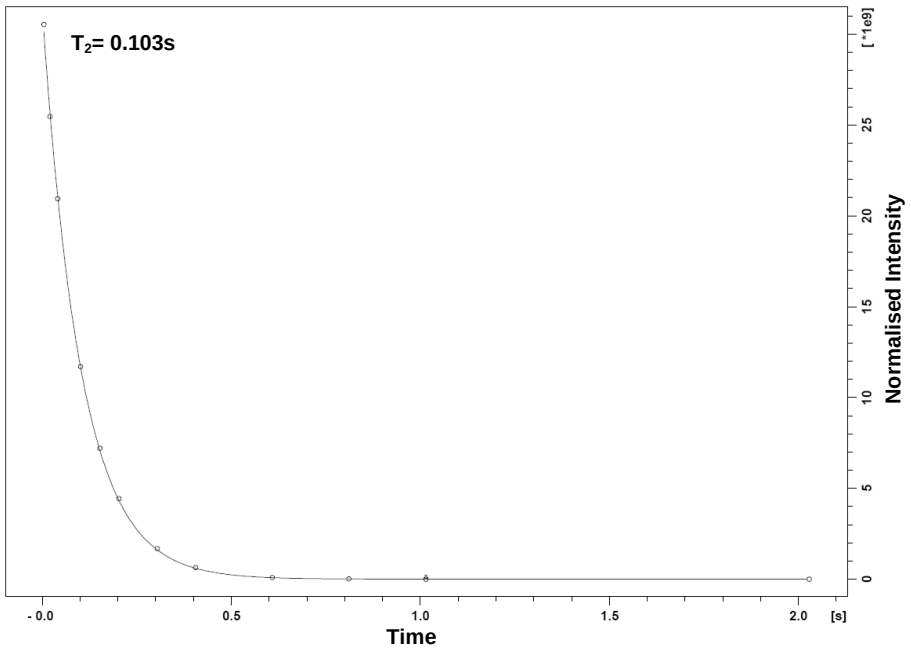

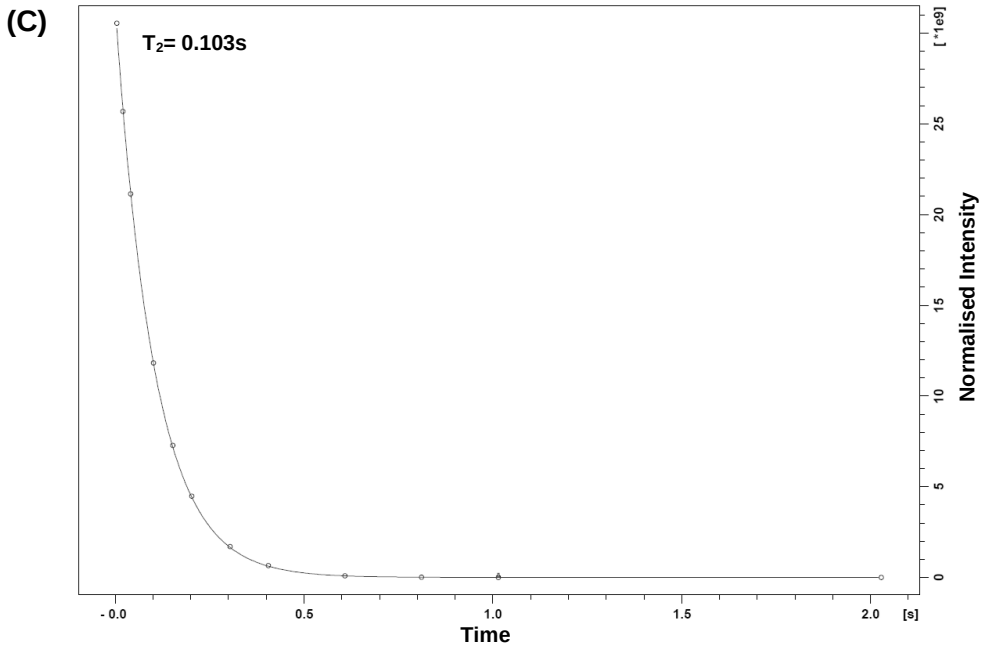

Figure SI 85 | T_2 CPMG decay curve for 1.00mM aqueous solution of $[N_{1,1,2,C3OH}][GdCl_4]$ at 37 ºC fitted with Equation SI 2.

2.4.2. [C]=0.75mM

(A)

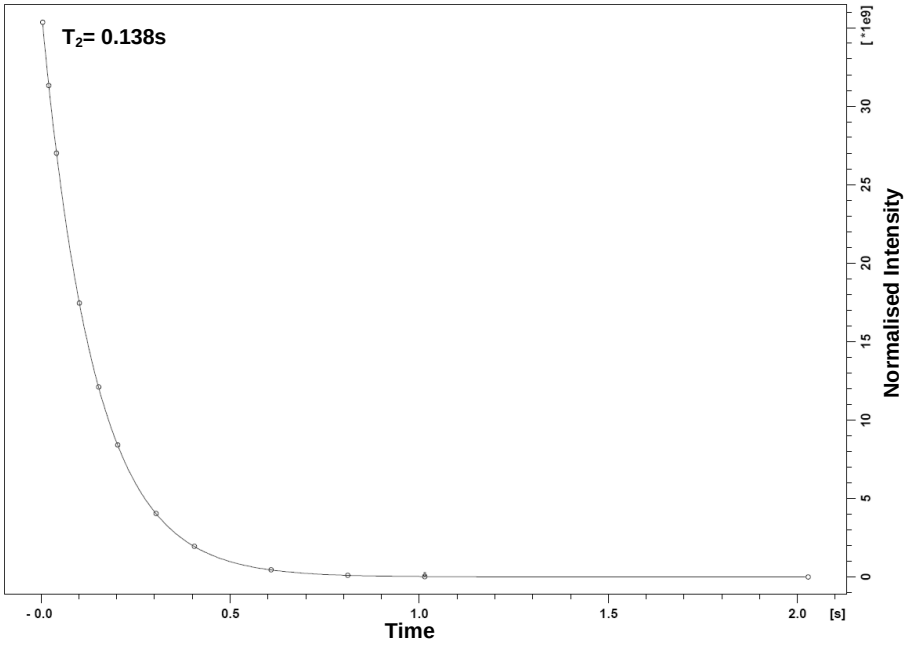

(B)

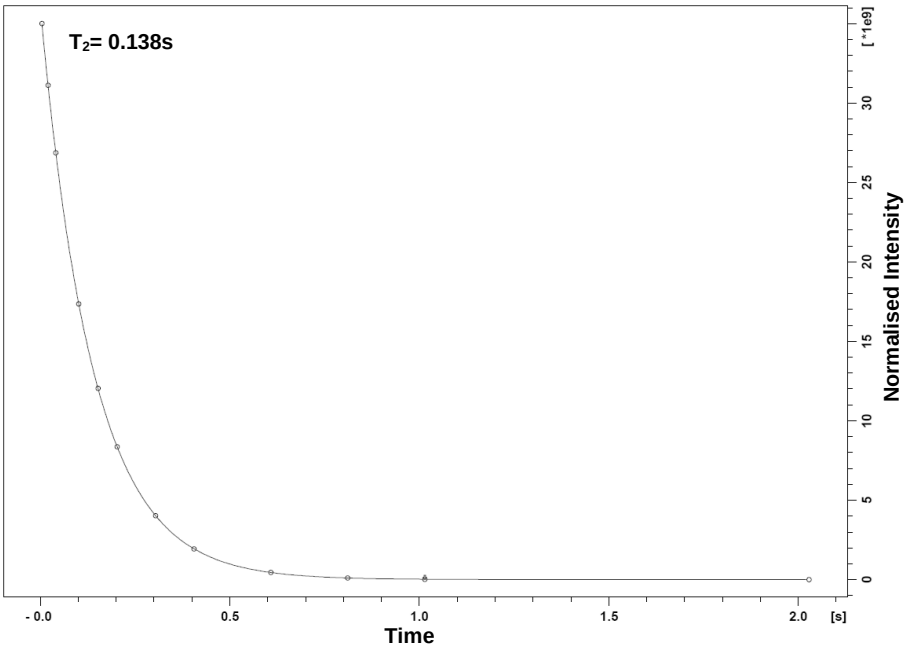

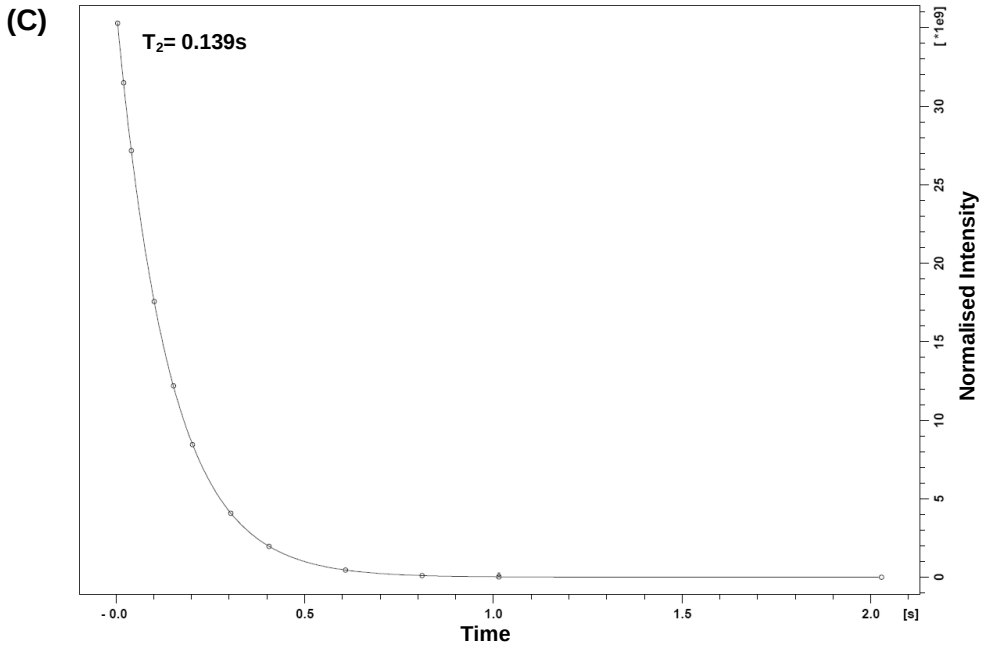

Figure SI 86 | T_2 CPMG decay curve for 0.75mM aqueous solution of $[N_{1,1,2,C3OH}][GdCl_4]$ at 37 ºC fitted with Equation SI 2.

2.4.3. [C]=0.50mM

(A)

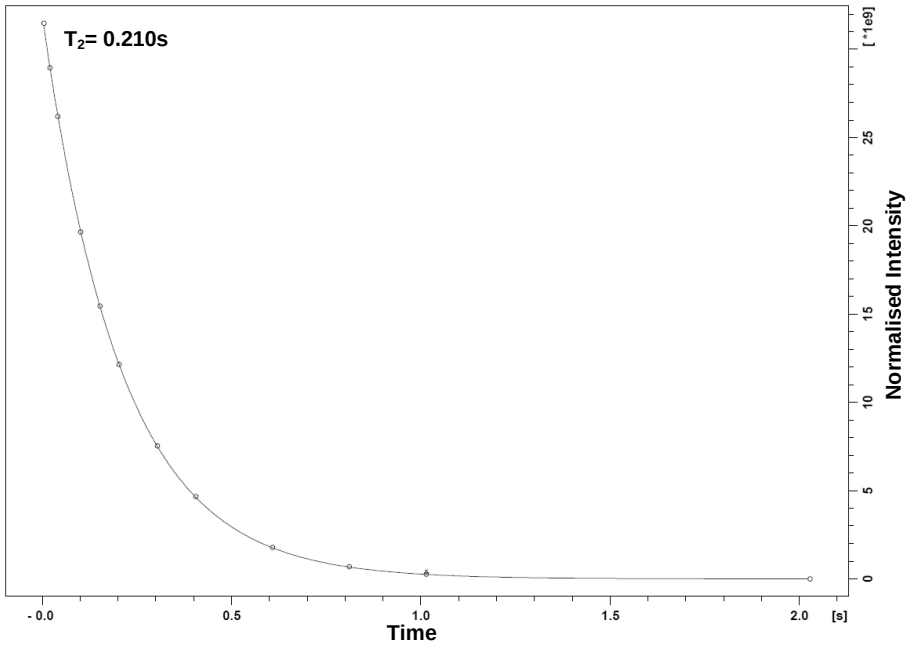

(B)

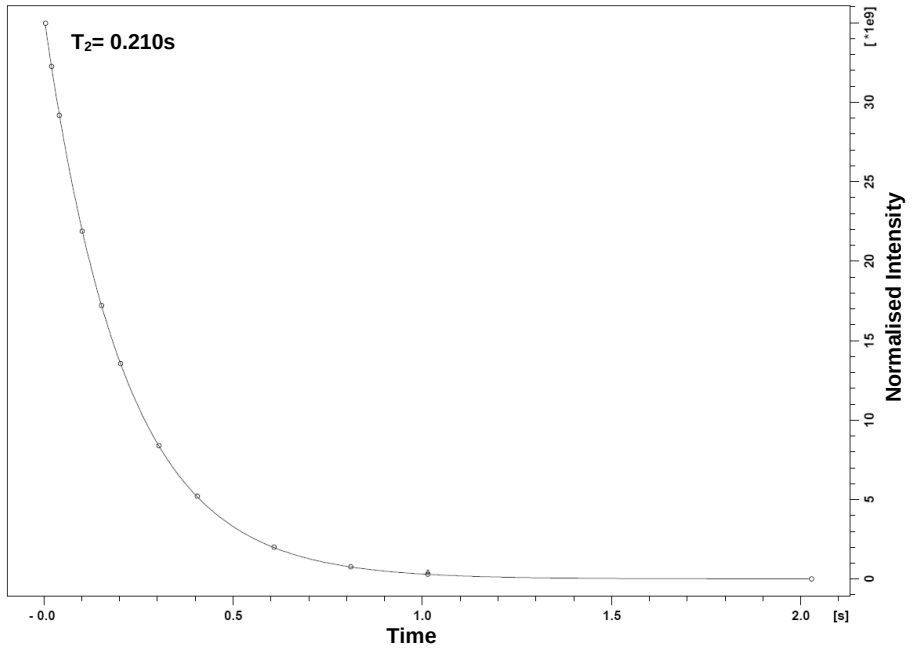

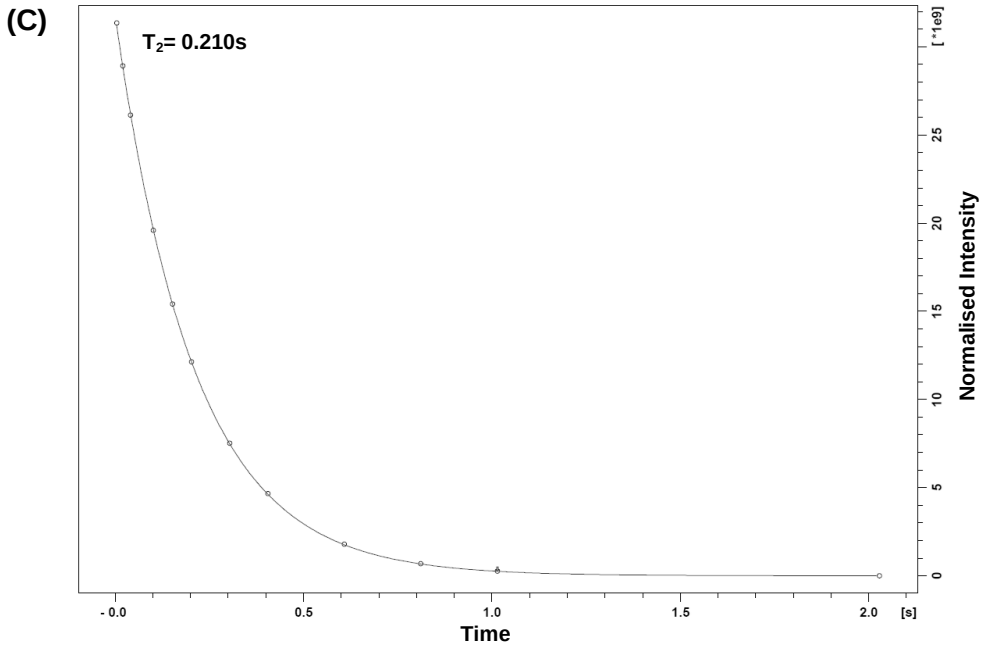

Figure SI 87 | T_2 CPMG decay curve for 0.50mM aqueous solution of $[N_{1,1,2,C3OH}][GdCl_4]$ at 37 ºC fitted with Equation SI 2.

2.4.4. [C]=0.10mM

(A)

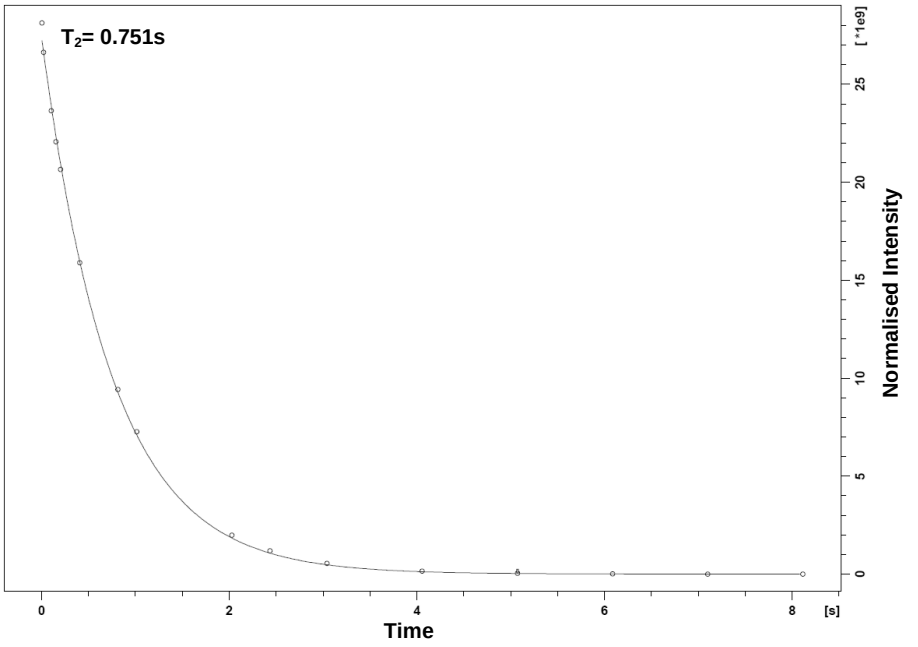

(B)

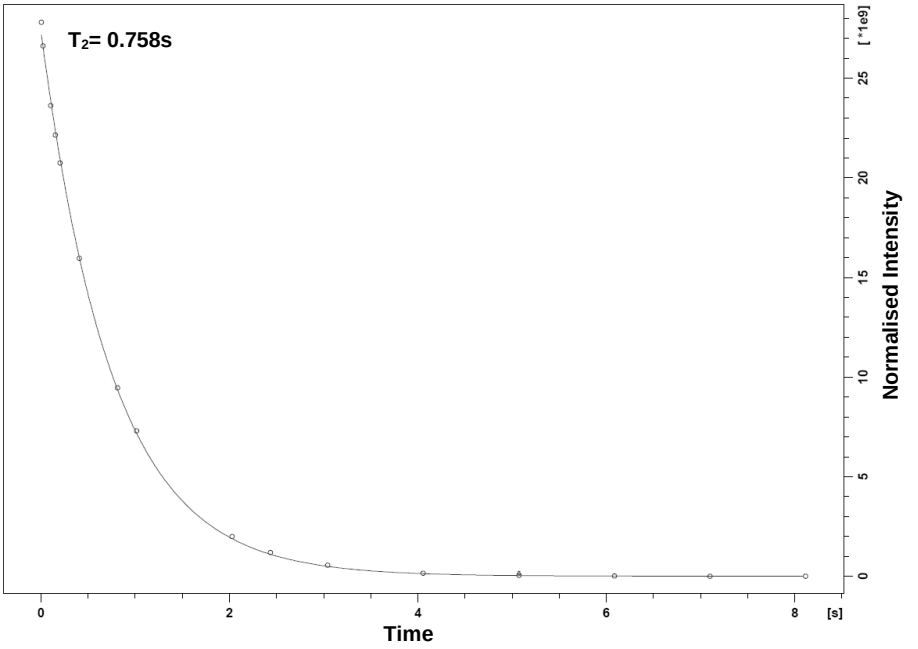

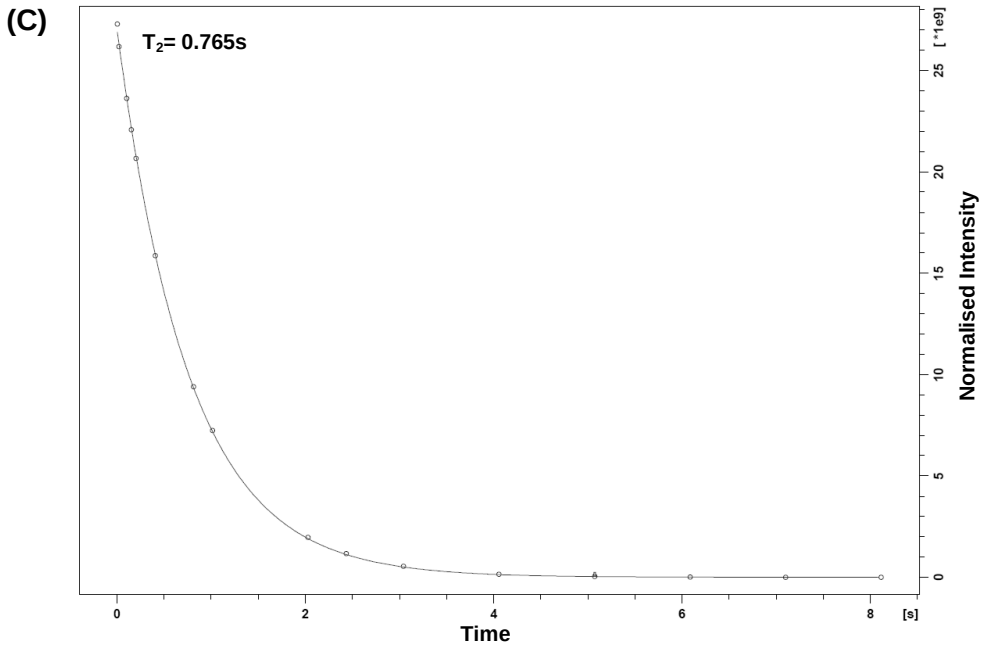

Figure SI 88 | T_2 CPMG decay curve for 0.10mM aqueous solution of $[N_{1,1,2,C3OH}][GdCl_4]$ at 37 ºC fitted with Equation SI 2.

2.4.5. [C]=0.05mM

(A)

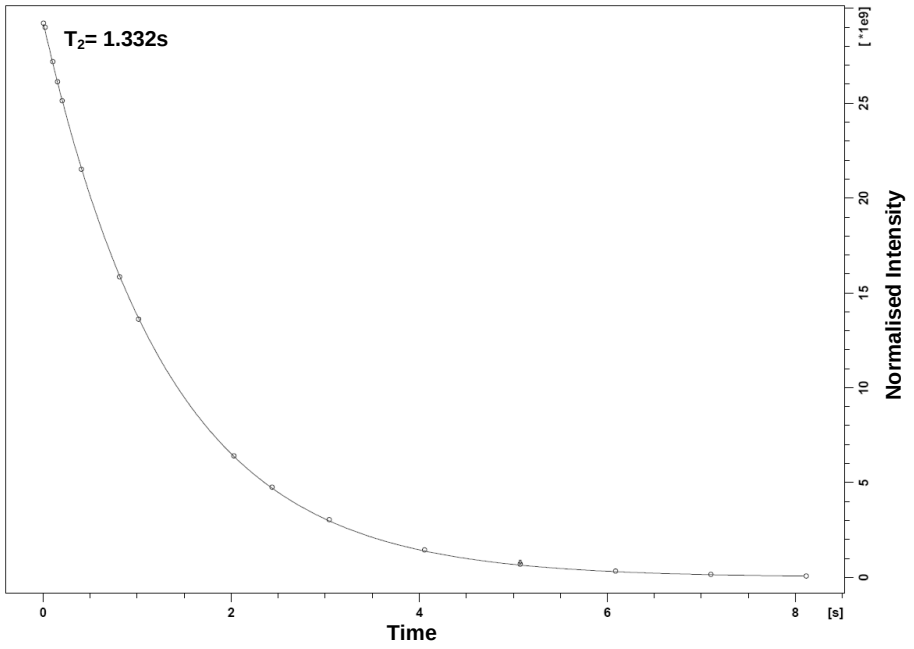

(B)

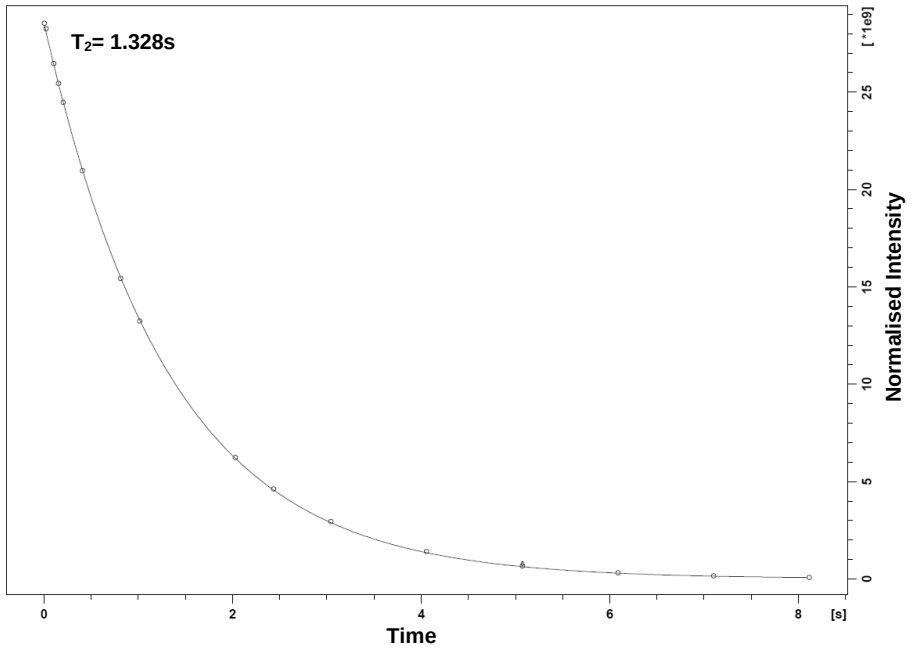

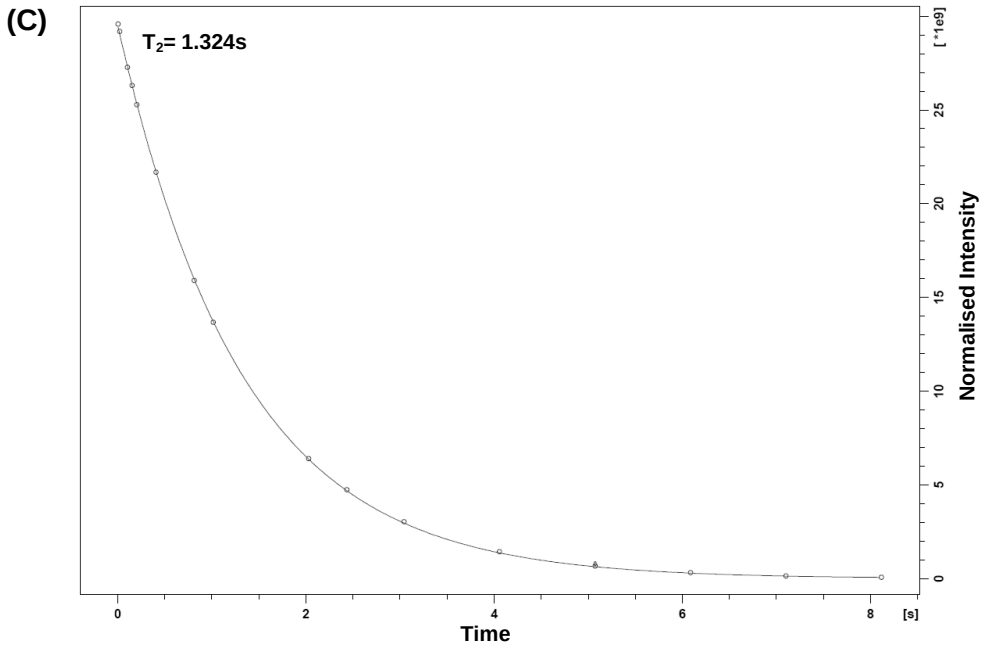

Figure SI 89 | T_2 CPMG decay curve for 0.05mM aqueous solution of $[N_{1,1,2,C3OH}][GdCl_4]$ at 37 ºC fitted with Equation SI 2.

Chapter 4

1. MSNs functionalization – Structural characterization (FT-IR)

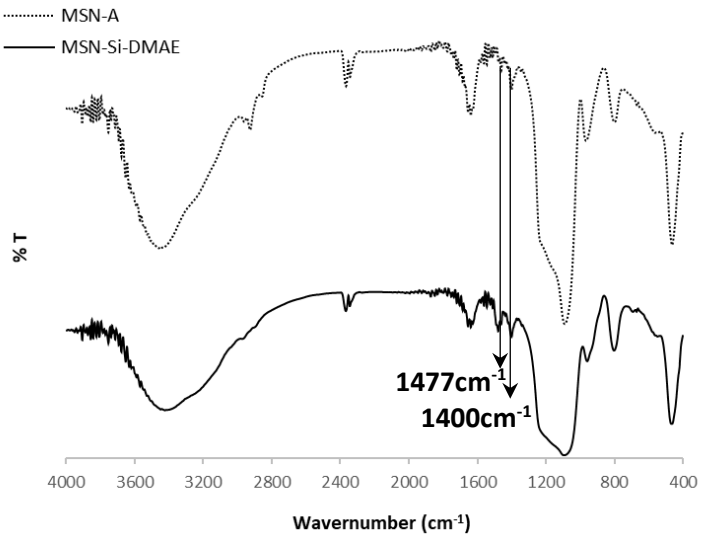

Figure SI 90 | FT-IR spectra for (A) MSN-A and (B) MSN-Si-DMAE.

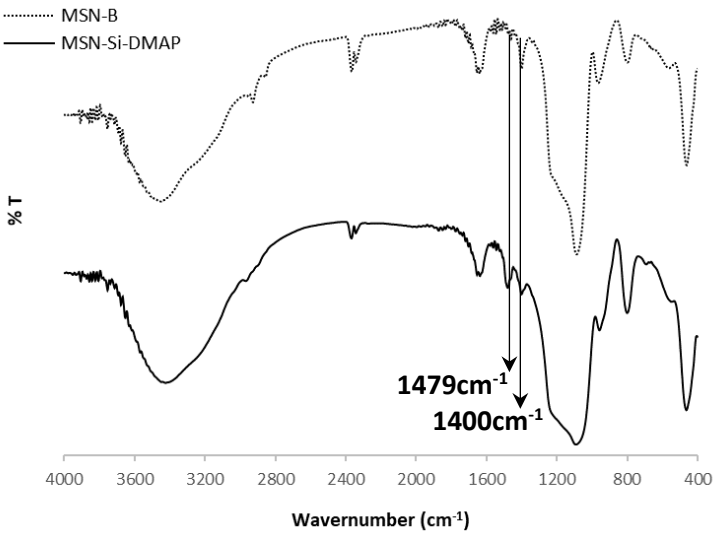

Figure SI 91 | FT-IR spectra for (A) MSN-B and (B) MSN-Si-DMAP.

Table SI 20 | FT-IR peaks assignments for MSN-A, MSN-B, MSN-B, MSN-Si-DMAE and MSN-Si-DMAP.

Assignment	MSNs	Frequency/cm^{-1}
***v* (OH) of free Si-OH or adsorbed water**	MSN-A	3448
	MSN-B	3449
	MSN-Si-DMAE	3422
	MSN-Si-DMAP	3422
***δ* (OH) of adsorbed water**	MSN-A	*1637*
	MSN-B	*1637*
	MSN-Si-DMAE	*1638*
	MSN-Si-DMAP	*1637*
v_{as} (Si-O-Si)	MSN-A	*1089*
	MSN-B	*1088*
	MSN-Si-DMAE	*1095*
	MSN-Si-DMAP	*1092*
***v* (Si-OH)**	MSN-A	965
	MSN-B	965
	MSN-Si-DMAE	*959*
	MSN-Si-DMAP	*958*
v_s (Si-O-Si)	MSN-A	*799*
	MSN-B	*799*
	MSN-Si-DMAE	*802*
	MSN-Si-DMAP	*800*
***δ* (O-Si-O)**	MSN-A	*463*
	MSN-B	*463*
	MSN-Si-DMAE	*467*
	MSN-Si-DMAP	*464*

2. Metal complexation reactions efficiency (XRF)

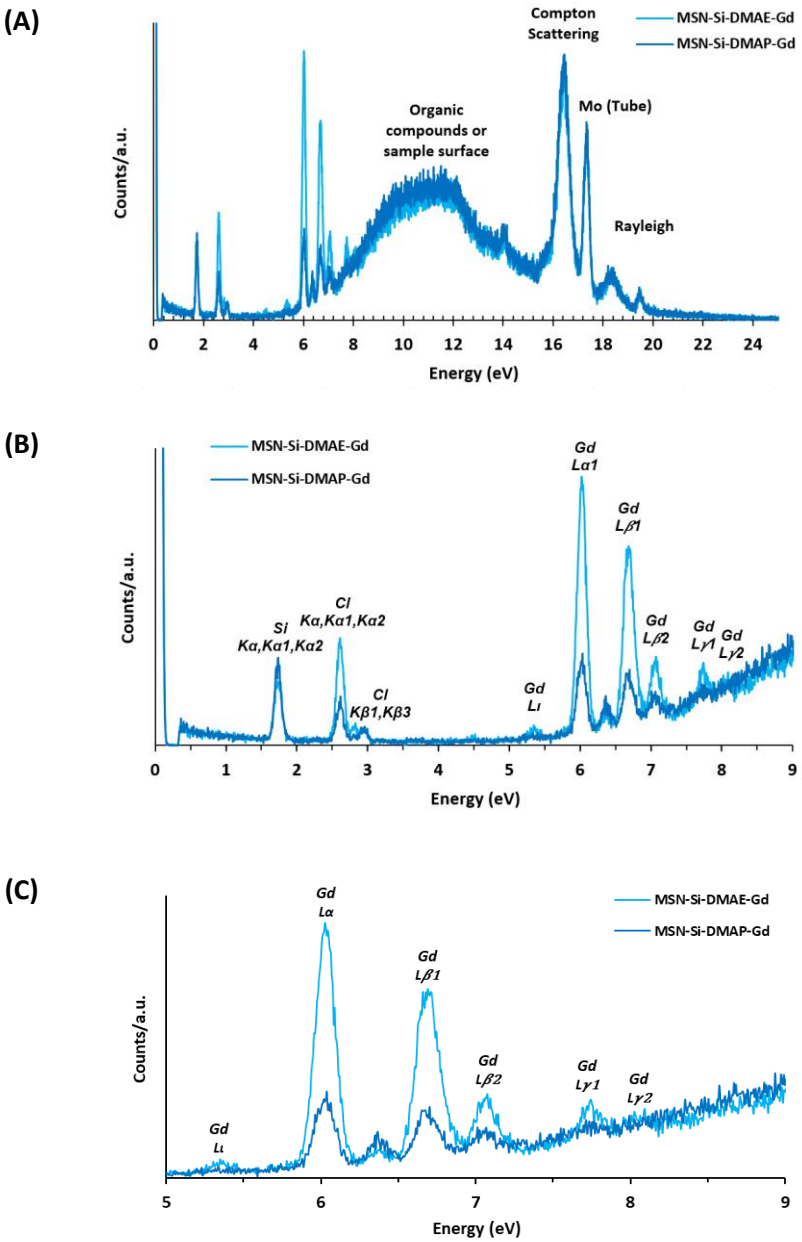

Figure SI 92 | μ-EDXRF spectra obtained for MSN-Si-DMEA-Gd (light blue) and for MSN-Si-DMAP-Gd (dark blue).

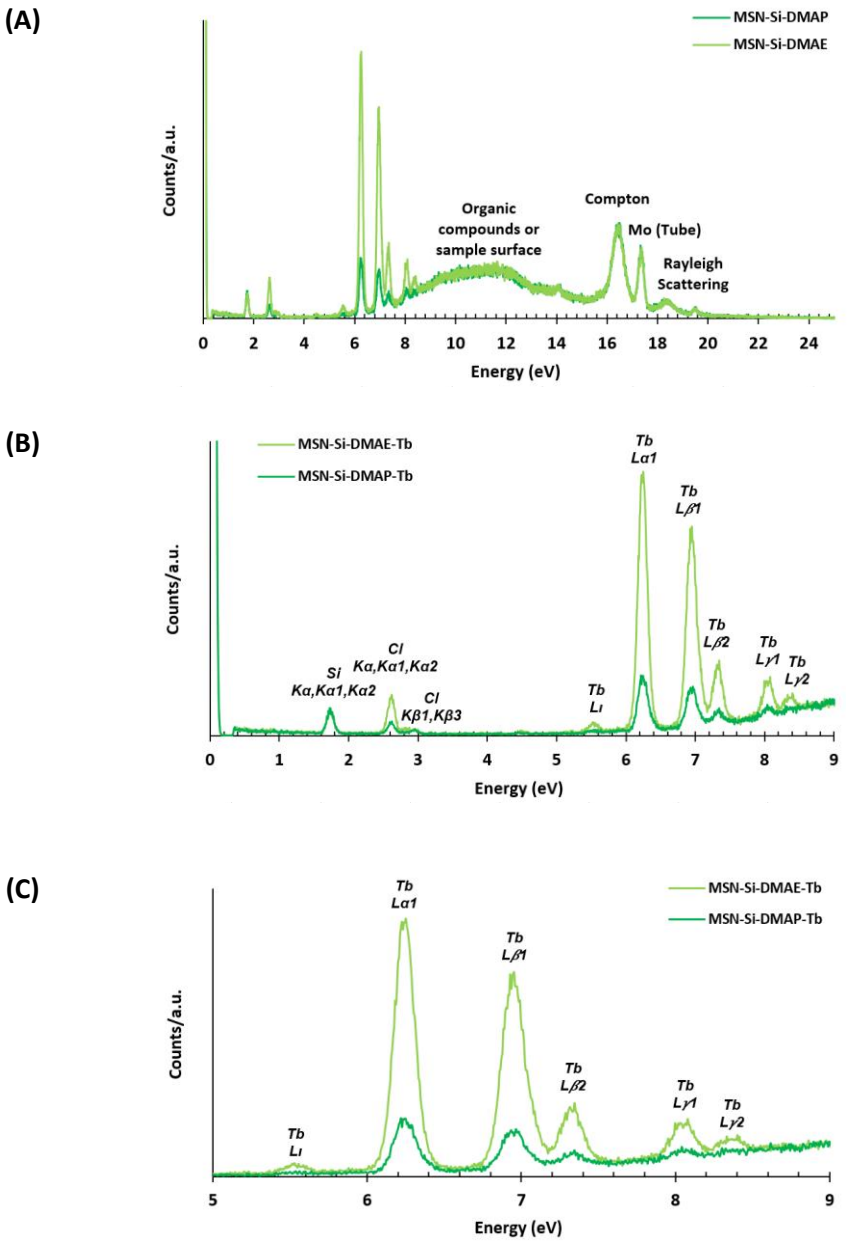

Figure SI 93 | μ-EDXRF spectra obtained for MSN-Si-DMEA-Tb (light green) and for MSN-Si-DMAP-Tb (dark green).

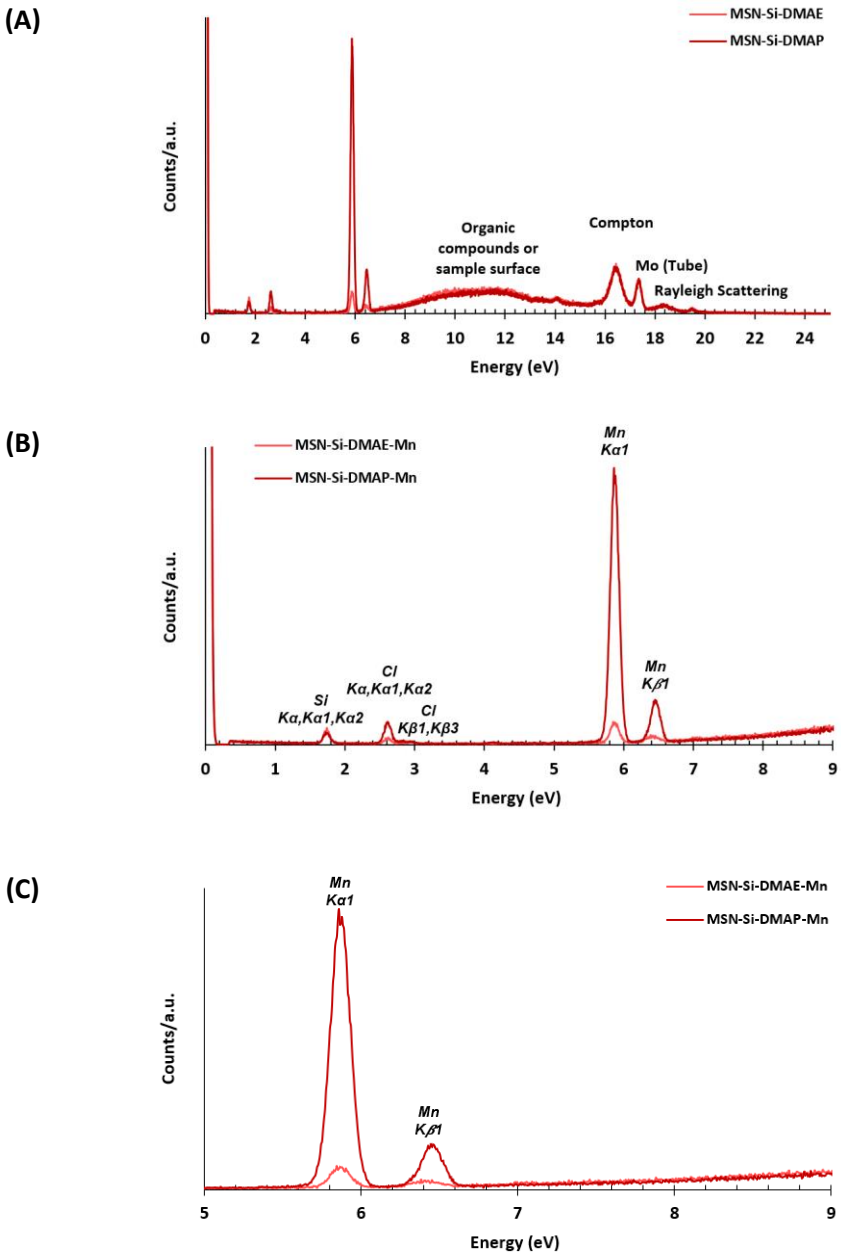

Figure SI 94 | μ-EDXRF spectra obtained for MSN-Si-DMEA-Mn (light red) and for MSN-Si-DMAP-Mn (dark red).

Table SI 21 | Characteristic X-ray energies of the prepared nanomaterials.

		MSN-Si-DMAE-Gd	MSN-Si-DMAP-Gd
		Energy (keV)	**Energy (keV)**
Si	***Kα,Kα1,Kα2***	1.75	1.74
Cl	***Kα,Kα1,Kα2***	2.61	2.62
	Kβ1,Kβ3	2.82	2.95
Gd	***Lı***	5.35	5.43
	Lα1	6.03	6.04
	Lβ1	6.69	6.67
	Lβ2	7.09	7.06
	Lγ1	7.73	7.74
	Lγ2	8.07	-
		MSN-Si-DMAE-Tb	**MSN-Si-DMAP-Tb**
		Energy (keV)	**Energy (keV)**
Si	***Kα,Kα1,Kα2***	1.75	1.73
Cl	***Kα,Kα1,Kα2***	2.61	2.61
	Kβ1,Kβ3	2.83	2.97
Tb	***Lı***	5.54	5.53
	Lα1	6.24	6.24
	Lβ1	6.94	6.99
	Lβ2	7.33	7.32
	Lγ1	8.05	8.07
	Lγ2	8.37	8.36
		MSN-Si-DMAE-Mn	**MSN-Si-DMAP-Mn**
		Energy (keV)	**Energy (keV)**
Si	***Kα,Kα1,Kα2***	1.74	1.74
Cl	***Kα,Kα1,Kα2***	2.61	2.61
	Kβ1,Kβ3	2.95	2.95
Mn	***Kα1***	5.87	5.87
	Kβ1	6.42	6.45

Chapter 5

1. Structural characterization of ThT-based probes (^{1}H-NMR)

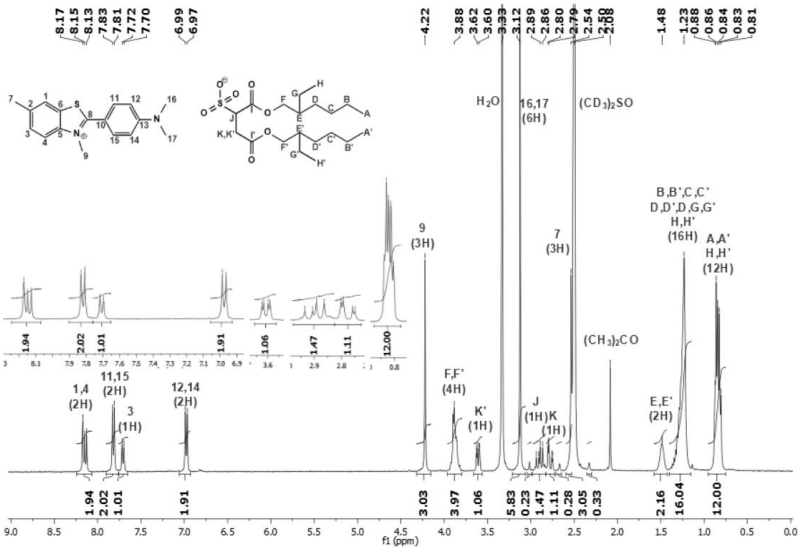

Figure SI 95 **|** ^{1}H-NMR spectra of [ThT][AOT] in $(CD3)_2SO$.

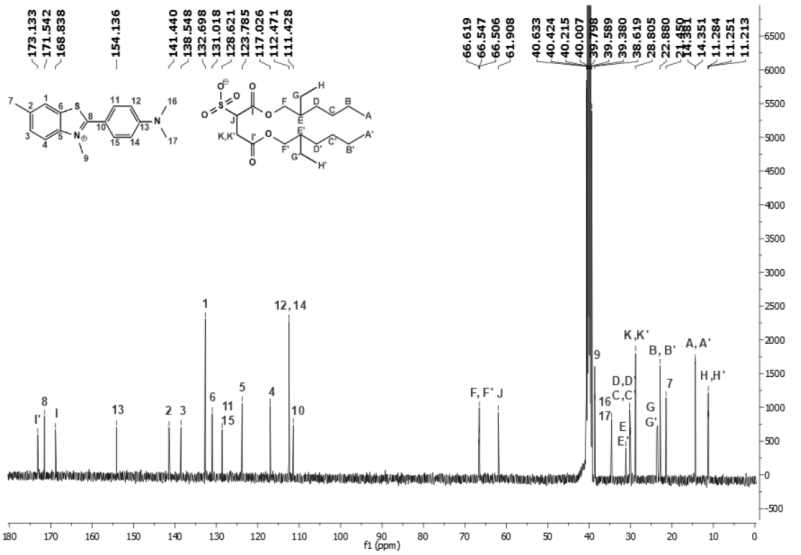

Figure SI 96 | ^{13}C-NMR spectra of [ThT][AOT] in $(CD3)_2SO$.

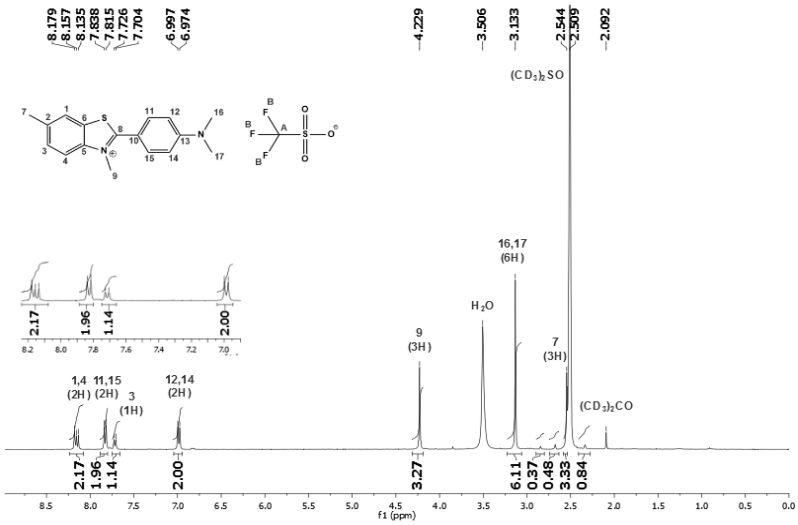

Figure SI 97 | ^{1}H-NMR spectra of [ThT][TfO] in $(CD3)_2SO$.

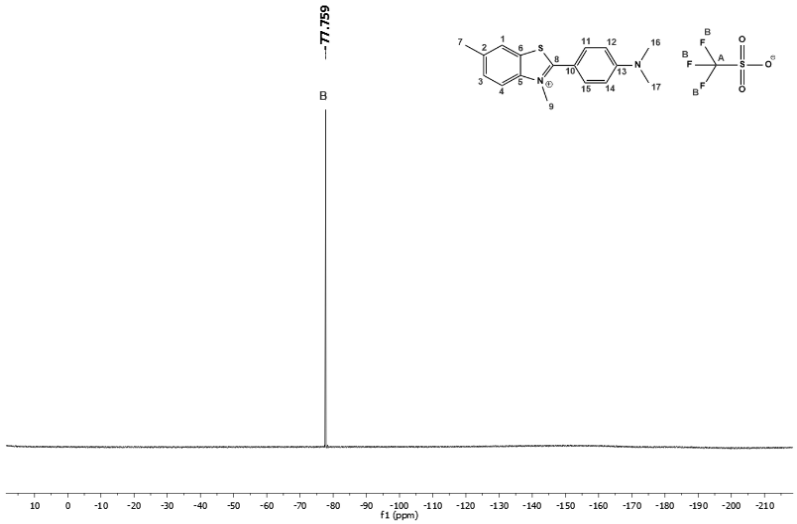

Figure SI 98 | ^{19}F-NMR spectra of [ThT][TfO] in $(CD3)_2SO$.

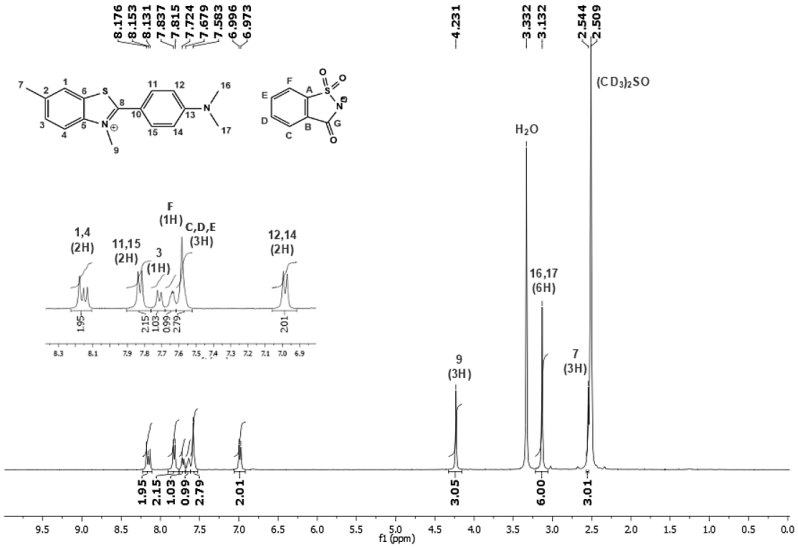

Figure SI 99 | ^{1}H-NMR spectra of [ThT][Sac] in $(CD3)_2SO$.

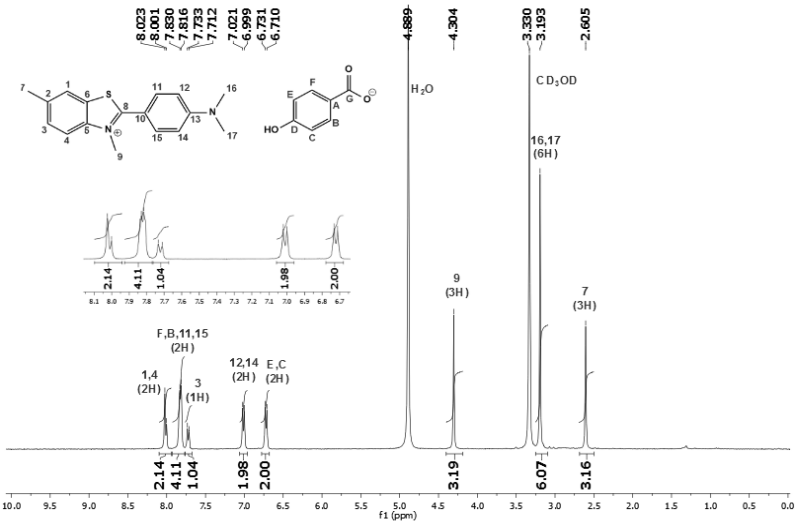

Figure SI 100 | ^{1}H-NMR spectra of [ThT][PHBA] in CD_3OD.

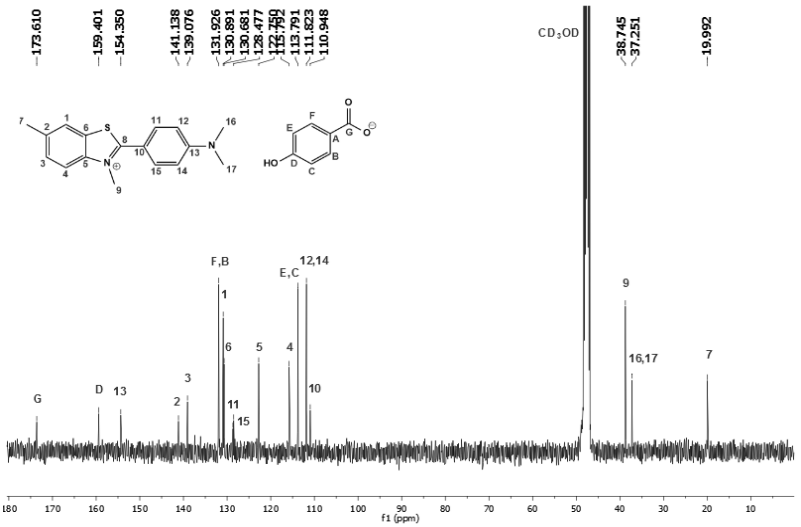

Figure SI 101 | ^{13}C-NMR spectra of [ThT][PHBA] in CD_3OD.

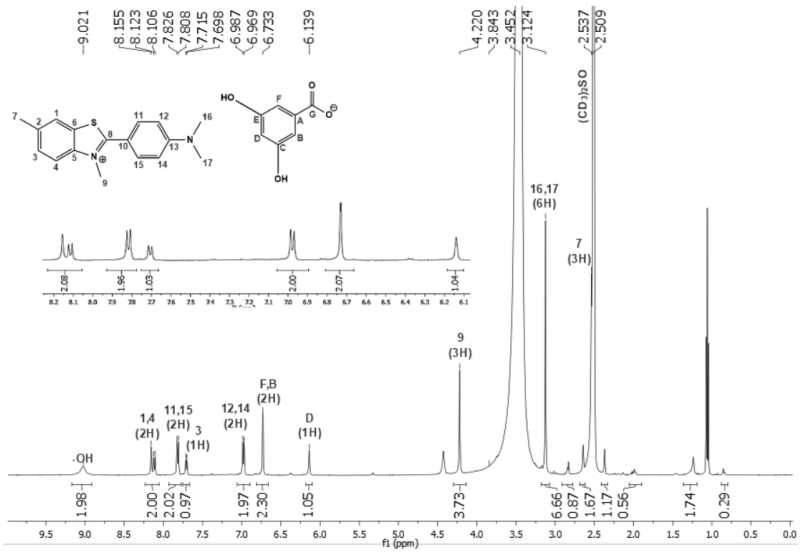

Figure SI 102 | ^{1}H-NMR spectra of [ThT][αRA] in $(CD3)_2SO$.

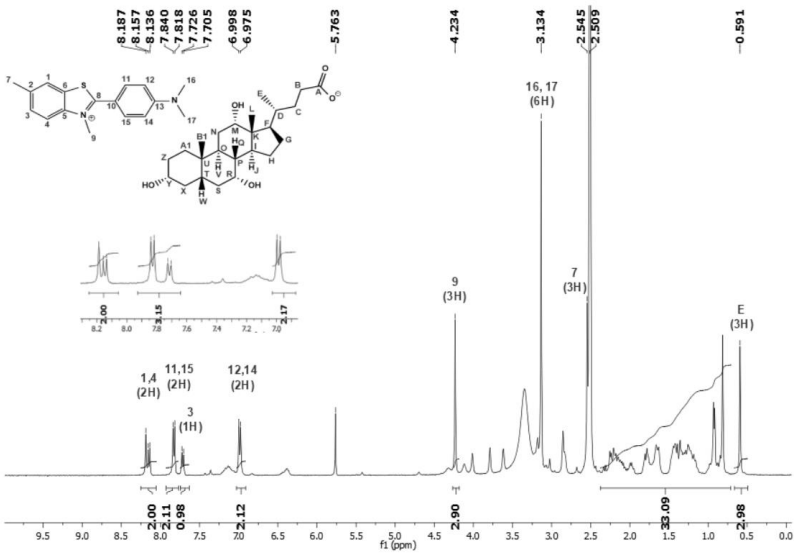

Figure SI 103 | ^{1}H-NMR spectra of [ThT][ChAc] in $(CD3)_2SO$.

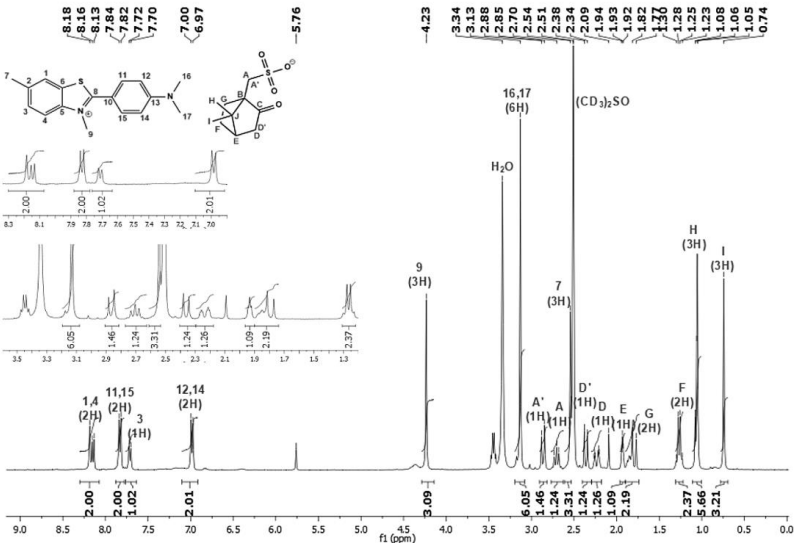

Figure SI 104 | ^{1}H-NMR spectra of [ThT][CPSA] in $(CD3)_2SO$.

2. Structural characterization of CR-based probes (^{1}H-NMR)

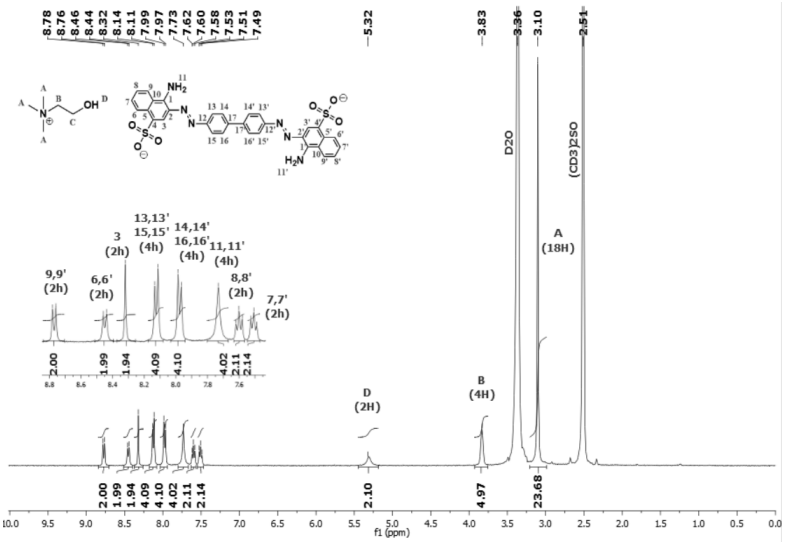

Figure SI 105 | ^{1}H-NMR spectra of $[N_{1,1,1,C2OH}]_2[CR]$ in $(CD3)_2SO$.

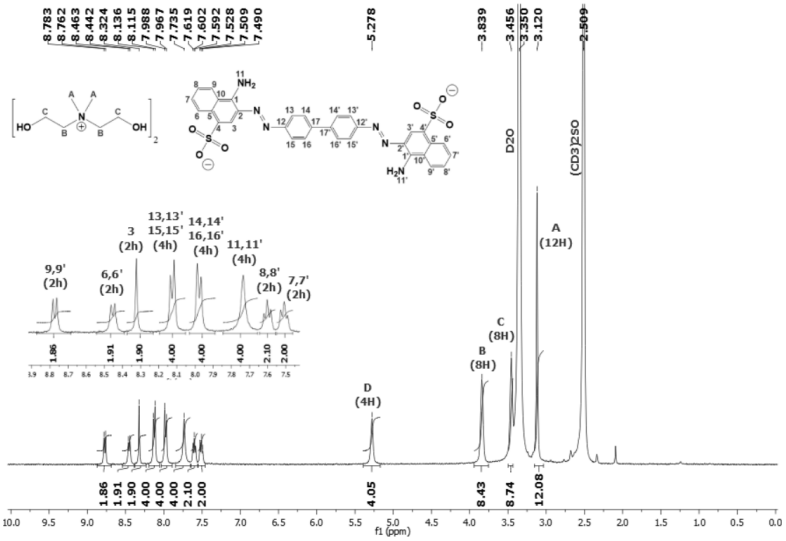

Figure SI 106 | ^{1}H-NMR spectra of $[N_{1,1,C2OH,C2OH}]_2[CR]$ in $(CD3)_2SO$.

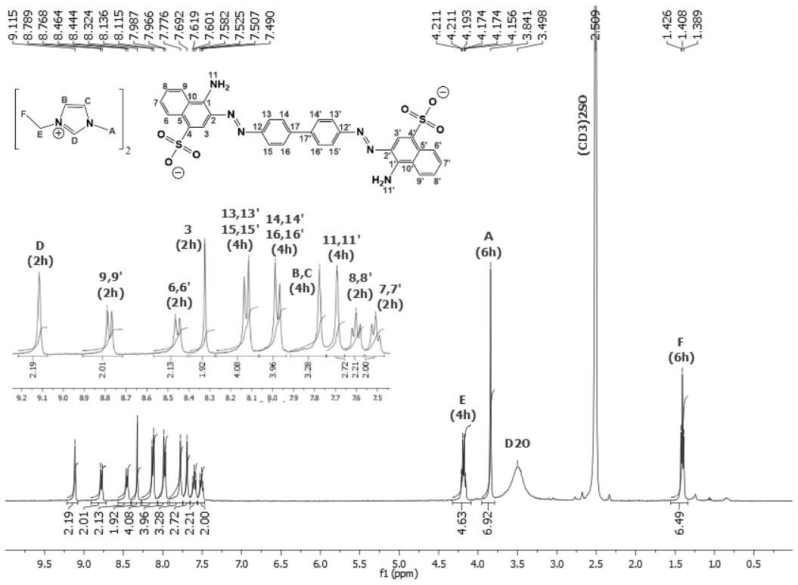

Figure SI 107 | ^{1}H-NMR spectra of $[C_2MIM]_2[CR]$ in $(CD3)_2SO$.

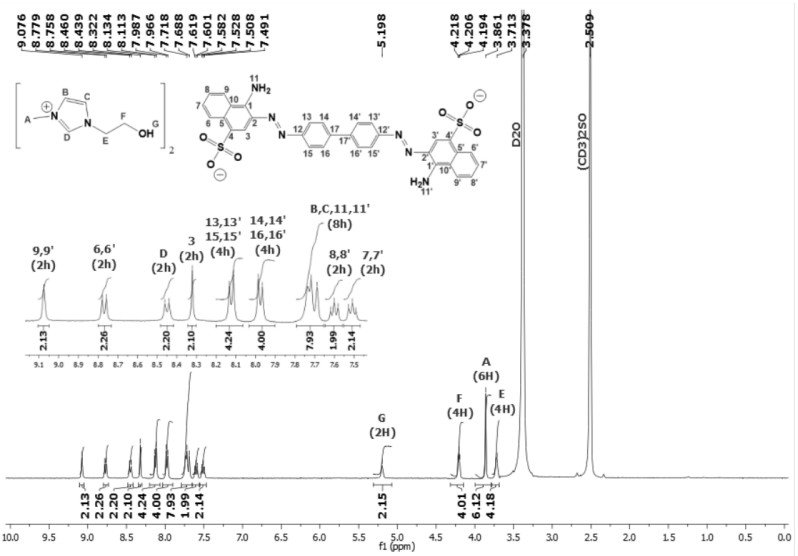

Figure SI 108 | ^{1}H-NMR spectra of $[C_2MIM]_2[CR]$ in $(CD3)_2SO$.

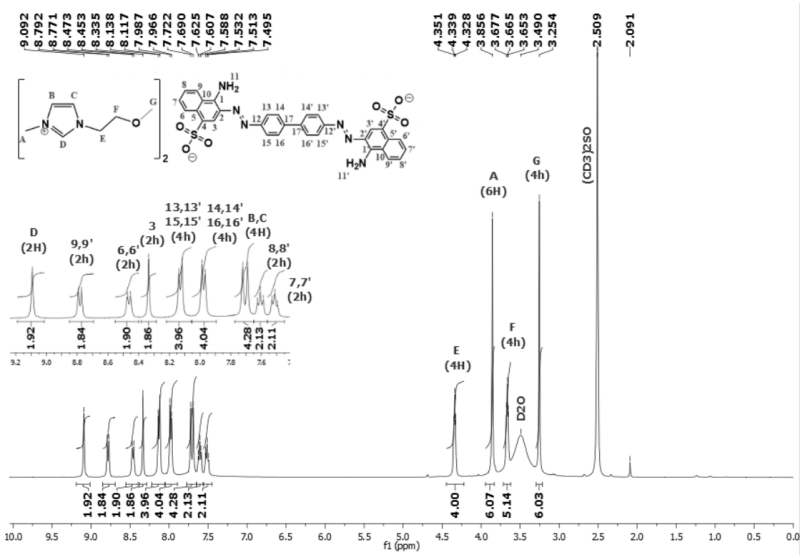

Figure SI 109 | ^{1}H-NMR spectra of $[C_2MIM]_2[CR]$ in $(CD3)_2SO$.

ITQB NOVA, Avenida da República, 2780-157 Oeiras, Portugal | Tel +351 214 469 100 | itqb.unl.pt